THE STRUCTURE, DYNAMICS AND FUNCTION OF NEURAL MICRO-CIRCUITS FOR PERCEPTION AND BEHAVIOR

EDITED BY: Yoshiyuki Kubota, Allan T. Gulledge and M. Victoria Puig

PUBLISHED IN: Frontiers in Neural Circuits

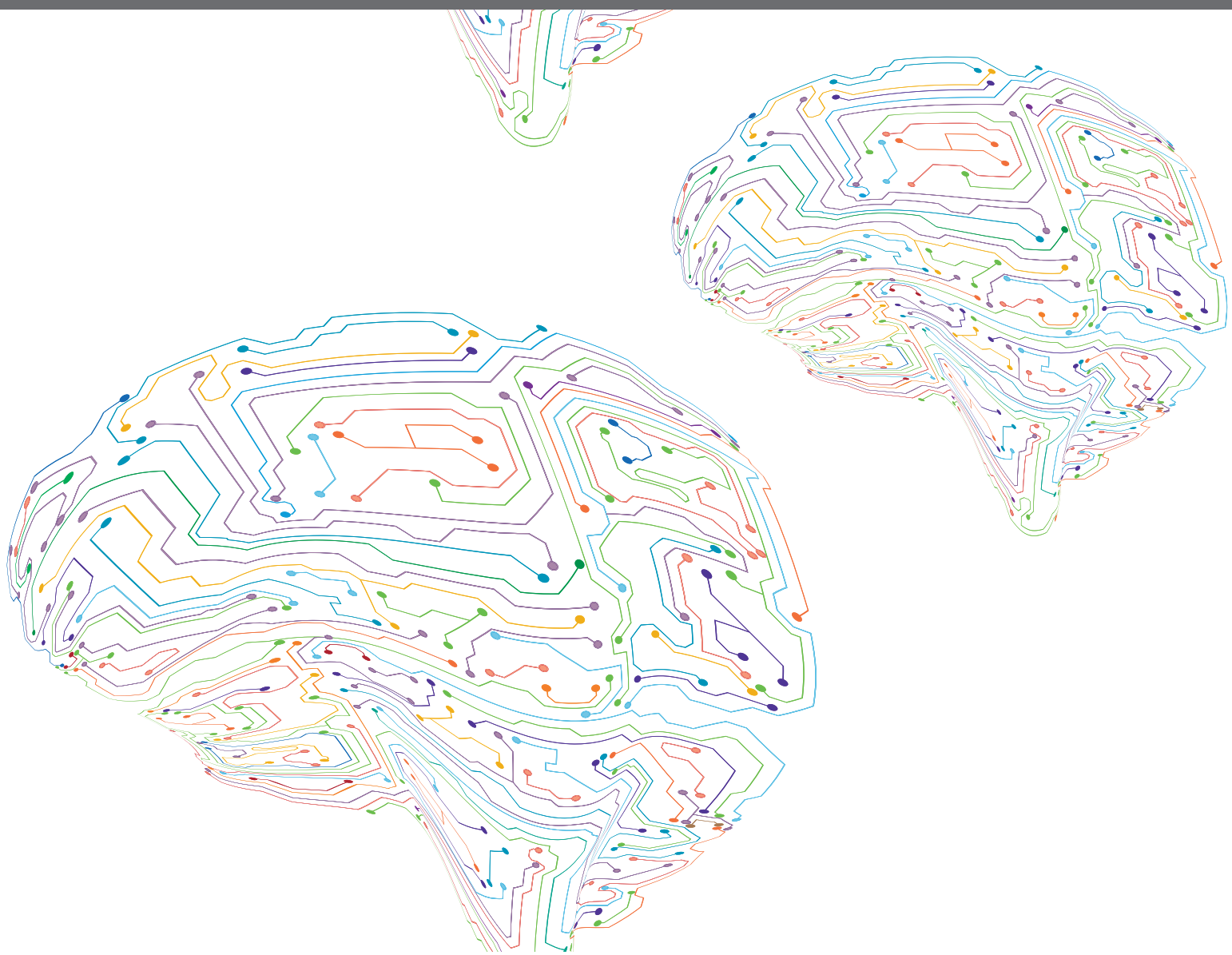

frontiers Research Topics

ISSN 1664-8714
ISBN 978-2-83250-152-8
DOI 10.3389/978-2-83250-152-8

About Frontiers

Frontiers is more than just an open-access publisher of scholarly articles: it is a pioneering approach to the world of academia, radically improving the way scholarly research is managed. The grand vision of Frontiers is a world where all people have an equal opportunity to seek, share and generate knowledge. Frontiers provides immediate and permanent online open access to all its publications, but this alone is not enough to realize our grand goals.

Frontiers Journal Series

The Frontiers Journal Series is a multi-tier and interdisciplinary set of open-access, online journals, promising a paradigm shift from the current review, selection and dissemination processes in academic publishing. All Frontiers journals are driven by researchers for researchers; therefore, they constitute a service to the scholarly community. At the same time, the Frontiers Journal Series operates on a revolutionary invention, the tiered publishing system, initially addressing specific communities of scholars, and gradually climbing up to broader public understanding, thus serving the interests of the lay society, too.

Dedication to Quality

Each Frontiers article is a landmark of the highest quality, thanks to genuinely collaborative interactions between authors and review editors, who include some of the world's best academicians. Research must be certified by peers before entering a stream of knowledge that may eventually reach the public - and shape society; therefore, Frontiers only applies the most rigorous and unbiased reviews.
Frontiers revolutionizes research publishing by freely delivering the most outstanding research, evaluated with no bias from both the academic and social point of view. By applying the most advanced information technologies, Frontiers is catapulting scholarly publishing into a new generation.

What are Frontiers Research Topics?

Frontiers Research Topics are very popular trademarks of the Frontiers Journals Series: they are collections of at least ten articles, all centered on a particular subject. With their unique mix of varied contributions from Original Research to Review Articles, Frontiers Research Topics unify the most influential researchers, the latest key findings and historical advances in a hot research area! Find out more on how to host your own Frontiers Research Topic or contribute to one as an author by contacting the Frontiers Editorial Office: frontiersin.org/about/contact

THE STRUCTURE, DYNAMICS AND FUNCTION OF NEURAL MICRO-CIRCUITS FOR PERCEPTION AND BEHAVIOR

Topic Editors:
Yoshiyuki Kubota, National Institute for Physiological Sciences (NIPS), Japan
Allan T. Gulledge, Dartmouth College, United States
M. Victoria Puig, Catalan Institute of Nanoscience and Nanotechnology (CIN2), Spain

Citation: Kubota, Y., Gulledge, A. T., Puig, M. V., eds. (2022). The Structure, Dynamics and Function of Neural Micro-Circuits for Perception and Behavior. Lausanne: Frontiers Media SA. doi: 10.3389/978-2-83250-152-8

Table of Contents

frontiers in Neural Circuits

ORIGINAL RESEARCH
published: 30 October 2020
doi: 10.3389/fncir.2020.553208

A Layer 3→5 Circuit in Auditory Cortex That Contributes to Pre-pulse Inhibition of the Acoustic Startle Response

*Aldis P. Weible, Iryna Yavorska, Donna Kayal, Ulysses Duckler and Michael Wehr**

Department of Psychology, Institute of Neuroscience, University of Oregon, Eugene, OR, United States

While connectivity within sensory cortical circuits has been studied extensively, how these connections contribute to perception and behavior is not well understood. Here we tested the role of a circuit between layers 3 and 5 of auditory cortex in sound detection. We measured sound detection using a common variant of pre-pulse inhibition of the acoustic startle response, in which a silent gap in background noise acts as a cue that attenuates startle. We used the Nr5a-Cre driver line, which we found drove expression in the auditory cortex restricted predominantly to layer 3. Photoactivation of these cells evoked short-latency, highly reliable spiking in downstream layer 5 neurons, and attenuated startle responses similarly to gaps in noise. Photosuppression of these cells did not affect behavioral gap detection. Our data provide the first demonstration that direct activation of auditory cortical neurons is sufficient to attenuate the acoustic startle response, similar to the detection of a sound.

Keywords: auditory cortex, startle response modulation, canonical microcircuit, gap detection, layer 3

OPEN ACCESS

Edited by:
Allan T. Gulledge, Dartmouth College, United States

Reviewed by:
Daniel Llano, University of Illinois at Urbana-Champaign, United States
Torfi Sigurdsson, Goethe University Frankfurt, Germany

***Correspondence:**
Michael Wehr
wehr@uoregon.edu

Received: *17 April 2020*
Accepted: *28 September 2020*
Published: *30 October 2020*

Citation:
Weible AP, Yavorska I, Kayal D, Duckler U and Wehr M (2020) A Layer 3→5 Circuit in Auditory Cortex That Contributes to Pre-pulse Inhibition of the Acoustic Startle Response. Front. Neural Circuits. 14:553208. doi: 10.3389/fncir.2020.553208

INTRODUCTION

How cortical circuits contribute to sensory perception and behavioral output remains a fundamental question in systems neuroscience. Building on more than a century of research into cortical physiology and connectivity (Grünbaum and Sherrington, 1902; Campbell, 1905; Ramon y Cajal, 1911), recent advances in the ability to manipulate and record from identified cell types have provided new insights into the computations performed by cortical circuits (for review, see Adesnik and Naka, 2018). Here, we focus on gap detection, a common variant of pre-pulse inhibition of the acoustic startle response, in which a silent gap inserted into continuous background noise acts as a cue that attenuates the startle reflex. Auditory cortex plays a critical role in reflex modification for gaps <32–64 ms in duration (Ison et al., 1991; Kelly et al., 1996; Bowen et al., 2003; Threlkeld et al., 2008; Masini et al., 2012; Weible et al., 2014b, 2020). Thus auditory cortical circuits contribute to the normal operation of this sensorimotor behavior. How sensory information flows through cortical circuits to mediate this behavior remains unknown.

A good starting point for understanding the flow of information through the cortex is the canonical cortical microcircuit, first proposed for the visual system (Gilbert and Wiesel, 1983; Douglas and Martin, 1991). In this model, sensory information from the thalamus first enters the cortex in layer 4, then ascends to superficial layers 2/3, then descends to deep layers 5/6, from where it either exits the cortex or closes the loop *via* an L6→L4 projection. One approach to understanding how information is transformed in the cortex is to measure neuronal responses at each stage of this circuit and test how manipulations at one stage impact responses at the next.

Since the original conception of the canonical cortical microcircuit, however, the picture has grown more complicated. For example, thalamocortical inputs are known to terminate throughout layers 1–6 (Harris and Shepherd, 2015). Numerous pathways that interconnect layers and sublayers have also been identified (Douglas and Martin, 2004; for review, see Adesnik and Naka, 2018). Furthermore, neighboring neurons within a given layer, even when focusing specifically on excitatory neurons and ignoring the broad diversity of interneurons, can exhibit different morphology, physiology, and connectivity patterns, and thus appear to be functionally distinct. These factors indicate that the components of cortical circuits are not individual layers, but rather classes of cells, which are typically intermingled with other cell classes within and among layers (Harris and Shepherd, 2015; Williamson and Polley, 2019). This suggests that recording from and manipulating specific cell classes, such as genetically identified cell types, maybe a useful strategy for understanding how cortical circuitry contributes to sensorimotor computation.

Here we tested the role of a genetically-identified class of cells in the mouse auditory cortex in brief gap detection. We used the Nr5a-Cre driver line (Harris et al., 2014, 2019; Tomorsky et al., 2017), which has not previously been characterized in the auditory cortex. Nr5a expression was restricted almost exclusively to layer 3. Photoactivation of these cells drove robust spiking in layer 5 cells, and also produced a behavioral inhibition of the startle response that was indistinguishable from that evoked by acoustic gaps in noise. A subset of layer 5 cells are known to send a major corticofugal projection to the inferior colliculus (IC), which is a critical component of the pre-pulse inhibition pathway (Li et al., 1998). This suggests a scenario in which Nr5a+ cells in layer 3 contribute to behavioral inhibition of the startle response by acting through layer 5 cortico-collicular cells in an L3→L5→IC circuit.

MATERIALS AND METHODS

Mice

All procedures were performed in strict accordance with the National Institutes of Health guidelines, as approved by the University of Oregon Animal Care and Use Committee. We used +/+ offspring of crosses between hemizygous Tg(Nr5a1-Cre)2Lowl ("Nr5a"; 006364; The Jackson Laboratory, Bar Harbor, ME, USA) and homozygous CAG-ChR2-eYFP ("ChR2"; 012569, Ai32, The Jackson Laboratory, Bar Harbor, ME, USA), CAG-Arch-eGFP ("Arch"; 012735, Ai35D, The Jackson Laboratory, Bar Harbor, ME, USA), or Rosa-CAG-LSL-tdTomato-WPRE ("tdTomato"; Ai14, 007914, The Jackson Laboratory, Bar Harbor, ME, USA) lines. In these offspring, Cre-dependent ChR2 (behavior: $n = 6$ mice; physiology: $n = 3$), Arch (behavior: $n = 9$; physiology: $n = 6$), or tdTomato ($n = 5$) was expressed in Nr5a-positive (Nr5a+) pyramidal neurons. The mice are on a C57BL/6J background. For behavioral and electrophysiological experiments, we used Nr5a-negative (Nr5a−) littermates as controls (behavior: $n = 9$; physiology: $n = 5$).

Anatomy

We crossed Nr5a-Cre mice with Cre-dependent tdTomato mice. We collected 50 μm coronal sections spanning auditory cortex from 5 Nr5a-tdTomato mice (8–12 weeks of age) and took photomicrographs of alternating sections on a Zeiss microscope using Zen software (Carl Zeiss Microscopy GmbH 2011). Seven of these sections were matched to the closest representative atlas section (**Figure 1A**; Paxinos and Franklin, 2004). We selected a rectangular region oriented perpendicular to the cortical surface, with a height extending from the pia to the external capsule, and a width 1/8th of this height, through the middle of primary auditory cortex (A1). To establish laminar boundaries as shown in **Figure 1B**, we subdivided this rectangular region as described by Anderson et al. (2009): layers 1, 2, 3, and 4 each represent 12.5% of the cortical thickness, and layers 5 and 6 each represent another 25%. We further subdivided each layer into two equal sublayers, to obtain finer-grained measures of penetrance with depth (**Figure 1C**). A sample count of cells was taken from the rectangular region. Counts of tdTomato-labeled cells were taken from 7 coronal sections, at 100 μm spacing. Cells were counted manually by two scorers and averaged. For three of the mice, we then performed *in situ* hybridization on the sections to label putative pyramidal neurons positive for Ca+/calmodulin protein kinase II (CaMKII). We used a digoxygenin (DIG)-labeled riboprobe (1:500), visualized by Anti Fluor-POD (1:1,000; Invitrogen, Cat. A21253) and Fluorescein (1:50; PerkinElmer, Cat. NEL741), as described previously (Weible et al., 2014a). We were not able to test for co-localization of tdTomato and CaMKII at cellular resolution, because *in situ* hybridization processing quenched the fluorescent tdTomato signal and also slightly distorted the tissue, which prevented precise spatial registration of before-and-after images. We therefore quantified CaMKII-labeled cells across lamina, using the same rectangular regions, to measure the penetrance of Nr5a+ cells proportional to the broader population of excitatory cells.

Fiber Implantation

We administered atropine (0.03 mg/kg) pre-surgically to reduce respiratory irregularities. Mice were anesthetized with isoflurane (1.25–2.0%). One craniotomy was drilled in each hemisphere dorsal to auditory cortex (AP: −2.9 mm, ML: 4.4 mm, relative to Bregma) for the placement of 200 μm-diameter optic fibers (on the pial surface). We used cyanoacrylate and dental cement to secure the fibers to the skull. We administered ketoprofen (4.0 mg/kg) postoperatively. Mice were housed individually following the surgery and were given 7 days to recover.

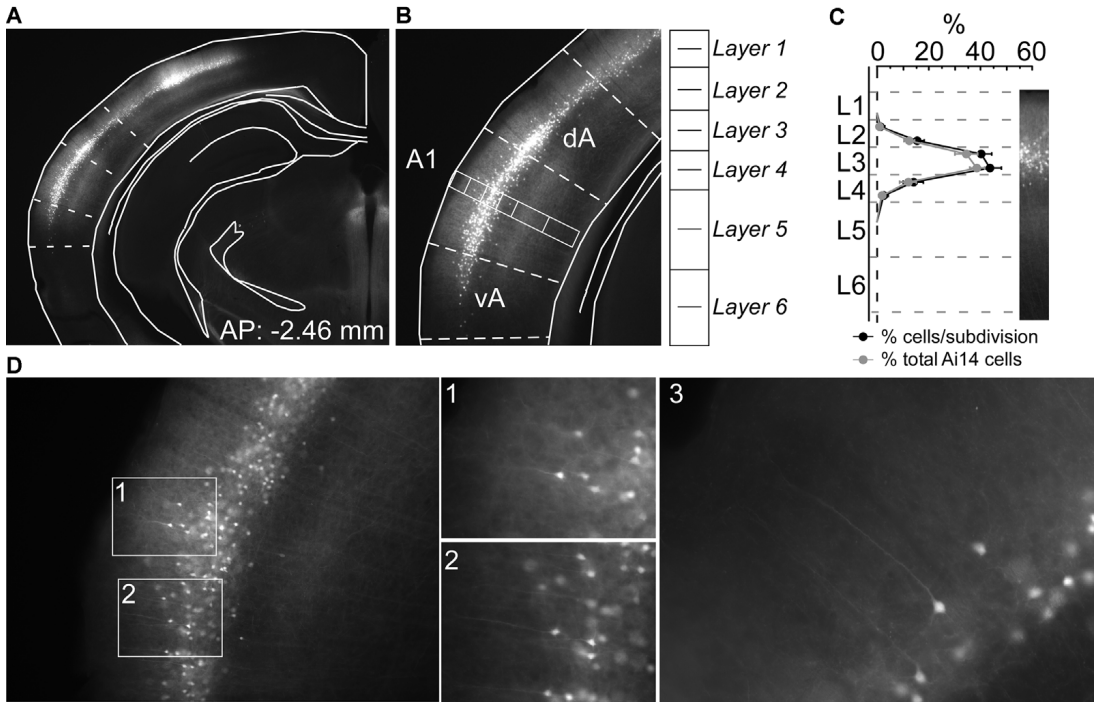

FIGURE 1 | Nr5a-positive (Nr5a+) labeling is restricted primarily to layer 3. **(A)** tdTomato-labeled Nr5a+ cells in auditory cortex. We determined boundaries for the primary auditory cortex (A1) by aligning photomicrographs to atlas sections (Paxinos and Franklin, 2004). **(B)** We counted cells in a rectangular region spanning the depth of the cortex in the middle of A1. **(C)** We counted tdTomato-labeled Nr5a+ cells and CaMKII+ cells labeled by *in situ* hybridization from the rectangular sample regions. Penetrance (shown in black) is the proportion of tdTomato-labeled cells relative to CaMKII+ cells within each sublayer. The distribution of tdTomato-labeled cells across layers (shown in gray) is the percent of tdTomato-labeled cells in each sublayer relative to the total number of tdTomato-labeled cells, and sums to 100%. We did not quantify co-localization due to the quenching of the tdTomato signal and distortion of the tissue following *in situ* hybridization. Values are mean ± SEM. **(D)** Higher magnification views of labeled cells. Panels 1 and 2 are views of the insets in panel **(D)**. Panels 1–3 reveal pyramidal-shaped soma and apical dendrites extending toward layer 1. AP, anterior-posterior coordinate relative to Bregma; dA and vA, dorsal and ventral auditory cortex, respectively.

Behavioral Data Acquisition and Stimulus Delivery

All behavioral data were collected in a sound-attenuating chamber. Sounds were delivered from a free-field speaker directly facing the animal. The speaker was calibrated to within ±1 dB using a Brüel and Kjær 4939 microphone positioned where the ear would be but without the animal present. Mice were loosely restrained in a plastic tube (35 mm inner diameter, 1.5 mm wall thickness) affixed to a flat base. The tube was perforated (∼3 mm diameter holes) to allow effective transmission of sound, with no more than 5 dB attenuation. The head was loosely clamped in position. An open slot along the top enabled access to the implanted fibers. Startle responses were measured with a piezo transducer positioned beneath the tube.

We inserted silent gaps into continuous 80 dB background white noise and measured how these gaps attenuated startle responses elicited by a 100 dB, 25 ms white noise burst. Gaps were 1, 2, 4, 8, 16, and 32 ms in duration, and there was a 50 ms interval between the end of the gap and the start of the startle stimulus. We also presented startle stimuli in isolation, without a gap ("gap-free" trials) to provide a baseline startle response. Each combination of gap duration and laser condition (see below) was presented 20 times per session, randomly interleaved and separated by a random inter-trial interval of 15 ± 5 s.

We separately examined how photostimulation and photosuppression of Nr5a+ cells affected behavior. For photostimulation, we used mice expressing Channelrhodopsin-2 (Nr5a-ChR2) and 445 nm wavelength laser diodes set to an output power of 50, 100, 200, or 300 mW/mm^2. For photosuppression, we used mice expressing Archaerhodopsin (Nr5a-Arch) and 520 nm wavelength laser diodes with an output power of 300 mW/mm^2. We chose these intensities based on the previous characterization of their spatial spread in the auditory cortex (Weible et al., 2014a,b). Laser-on trials were randomly interleaved with laser-off trials. For Nr5a-Arch mice, we delivered a 50 ms light pulse, starting 50 ms before the onset of the startle stimulus (see inset to **Figure 4A**). For Nr5a-ChR2 mice, we delivered a 25 ms pulse starting 50 ms before the startle on gap-free trials only (see inset to **Figure 3A**). To visually mask light delivery, we used strobe lights equipped with blue or green filters that pulsed continuously for the duration of the session. We confirmed the presence or absence of transgene expression (based on eGFP or eYFP fluorescence) and fiber placement in auditory cortex histologically after the experiment.

Behavioral Analysis

We quantified startle amplitudes by calculating the area of the rectified startle signal within a 100 ms window following onset of the startle stimulus, and taking the median across trials. Only sessions with significant gap detection for at least one gap duration (laser-off) were included for analysis. We tested whether gap detection was significant by comparing startle amplitudes associated with each gap duration to startle amplitudes on gap-free trials (paired t-test, $p < 0.05$). Because data for some gap durations were not normally distributed, group analyses were performed using non-parametric tests. For analysis of Nr5a-Arch data, laser-on and laser-off data within each session were normalized to that session's median laser-off response. Comparisons between laser-on and laser-off conditions were performed with the Kruskal–Wallis test. For analysis of Nr5a-ChR2 data, we used the Wilcoxon signed-rank test to compare raw (non-normalized) laser-on and laser-off gap-free startles (because normalization of the data to the laser-off gap-free startles would artificially decrease variance). Data were collected from the same mouse for no more than four sessions, to minimize the likelihood of introducing experience-related shifts in startle behavior at brief gap durations (Swetter et al., 2010; Weible et al., 2014b).

Electrophysiology

Mice were anesthetized with isoflurane (1.25–2.0%). A head post was secured to the skull and a mark was made on the skull over auditory cortex for a future craniotomy (AP: −2.9 mm, ML: 4.4 mm, relative to Bregma). Mice were housed individually following the surgery and were allowed at least 5 days of post-operative recovery. On the day of recording, mice were anesthetized with isoflurane (1.25–2.0%), the head was clamped with the head post, and a small craniotomy was made over auditory cortex (1 × 1 mm). Craniotomies were covered with a thin layer of agar and mice were allowed to recover for at least 1 h before recording.

All electrophysiological recordings were performed while the animal was awake and head-fixed on a styrofoam ball inside a double-walled acoustic isolation booth. Neurons in auditory cortex were recorded with a 32-channel silicon probe (25 μm spacing between sites, 750 μm shank, Neuronexus A1 × 32-Poly2–5mm-50s-177), Intan RHD2000 board, and Open Ephys software (Siegle et al., 2017). The silicon probe was positioned with a micromanipulator (MP-285, Sutter) orthogonal to the cortical surface such that the electrode sites spanned cortical layers. Spiking and local field potential signals were filtered online (600–6,000 and 0.1–400 Hz, respectively). Single neurons were identified offline using MClust spike sorting software (Redish, 2008) as described previously (Weible et al., 2020). To measure the depth of recorded cells, we used current-source density analysis of the local field potential evoked by 25 ms white noise bursts. We identified the robust sink with the shortest latency in upper L4 and assigned it a depth of 400 μm (Intskirveli and Metherate, 2012). We assigned the depths of individual neurons relative to this, based on the channel exhibiting the maximum waveform amplitude for each neuron. We assigned laminar boundaries using the same percentages as described above (see "Anatomy" section), applied to a total cortical thickness of 1,045 μm (Intskirveli and Metherate, 2012). This allowed us to relate recording depth to our histological analysis and laminar boundaries.

Neural data were collected during the presentation of gap-in-noise stimuli (Nr5a-Arch and Nr5a-ChR2), as well as light-pulse train stimuli for photo-identification of Nr5a+ neurons (Nr5a-ChR2 only). Laser intensities were 200 mW/mm^2 for Nr5a-ChR2 recordings and 300 mW/mm^2 for Nr5a-Arch recordings. The presentations of gaps-in-noise stimuli differed from the behavioral protocol in two respects. First, no startle stimuli were presented. Second, a shorter inter-trial interval was used (1 s vs. the 15 ± 5 s used during behavioral experiments). Recording sessions included 20 presentations each of gaps 1, 2, 4, 8, 16, and 32 ms in duration, as well as 20 gap-free trials. Gap Termination Responses (GTRs) were defined as a significant increase (paired t-test) in spiking activity during the 50 ms post-gap interval (i.e., following the resumption of noise) for at least two consecutive gap durations. Paired t-tests were also used to identify the within-cell effects of the laser. Between-group comparisons of spiking data were performed using non-parametric tests because some of the comparisons involved non-normally distributed data (Lilliefors), and because statistical power was comparable even when the underlying assumptions for the corresponding parametric analysis were met (Kitchen, 2009). GTRs were normalized using z-values (calculated relative to either the gap-free baseline interval or the laser-off trials of the same gap duration). We used the Kruskal–Wallis test (non-parametric alternative to the one-way ANOVA) to assess group differences across gap durations. We used the Wilcoxon rank-sum test (non-parametric alternative to the unpaired t-test) for laminar comparisons. We report effect sizes as eta-squared (η^2; Lenhard and Lenhard, 2016). η^2 varies between 0 and 1 and corresponds to the proportion of variance in the dependent variable explained by the independent variable. η^2 values of 0.01–0.06 are generally considered to be small effects, η^2 of 0.06–0.14 moderate effects, and $\eta^2 > 0.14$ large effects.

We classified neurons with significant GTRs as all-pass, band-pass, short-pass, or long-pass based on their duration tuning curves (Casseday et al., 1994; Fuzessery and Hall, 1999). All-pass neurons responded above 50% of the peak firing rate across all gap durations. Band-pass neurons exhibited ≤50% of peak firing rate at durations both shorter and longer than the preferred duration. Short-pass neurons preferred brief durations and exhibited a decrease to ≤50% of the peak firing rate at longer durations. Long-pass neurons typically preferred longer durations and did not fire ≤50% of the peak firing rate at longer durations.

We used light-pulse trains to identify putative Nr5a+ neurons (Lima et al., 2009). Blue light pulses (445 nm, 5 ms duration, 200 mW/mm^2) were delivered at a frequency of 10 Hz for 1 s. Twenty repetitions of this train were presented. To distinguish directly light-activated cells from downstream, indirectly-activated cells, we quantified light-evoked responses using three measures: response significance, peak response latency, and response reliability. We measured response significance as the p-value of a paired t-test comparing spiking activity in a

25 ms window following the onset of each light pulse to an equivalent laser-off baseline window. We measured response latency as the time-to-peak of the gaussian-smoothed (5 ms S.D.) trial-averaged firing rate following the onset of each light pulse. We measured response reliability as the proportion of trials on which light evoked 1 or more spikes in a 50 ms window following the onset of each light pulse. We could not identify any trends from the first to the last (tenth) pulse in the train that distinguished between putative directly-activated or indirectly-activated cells, so we averaged these measures across all pulses in the train. We also computed the Stimulus-Associated spike Latency Test (SALT) statistic (Kvitsiani et al., 2013), which was developed to detect light-evoked responses. We defined "putative directly-activated cells" as those that met one of two sets of criteria: (1) significance <0.0001, peak latency <20 ms, and reliability >0.5; or (2) significance <0.0001 and peak latency <15 ms. However, we note that putative directly-activated cells almost certainly included indirectly-activated cells in layer 5, as described below.

RESULTS

The detection of brief gaps in noise requires auditory cortex and specifically relies on spiking evoked by the end of the gap (termed the gap termination response, or GTR; Ison et al., 1991; Kelly et al., 1996; Bowen et al., 2003; Threlkeld et al., 2008; Weible et al., 2014b, 2020). The circuit mechanisms by which this activity contributes to gap detection remain unknown. Here we tested the role of a genetically-identified class of layer 3 pyramidal cells in this behavior. First, we characterized the expression pattern in the primary auditory cortex (A1). We then examined whether and how photoactivating (Nr5a-ChR2) and photosuppressing (Nr5a-Arch) these cells influenced startle responses and gap detection.

Nr5a+ Cells Are Found in Layer 3

We first quantified the laminar expression pattern and penetrance in A1 for the Nr5a-Cre line. We counted tdTomato-labeled cells across layers in Nr5a-tdTomato mice (**Figures 1A,B**, n= 5 mice), and then counted CaMKII-positive (excitatory) cells in the same sections labeled by *in situ* hybridization (ISH). We did not measure whether individual cells showed co-localization of tdTomato and CaMKII (due to tissue processing effects; see "Materials and Methods" section), and therefore quantified penetrance as the percentage of tdTomato-labeled cells relative to the total number of excitatory neurons in each layer. The expression of the Nr5a-Cre line in A1 has not previously been described in detail. In primary visual cortex (V1), expression is restricted to layer 4 (Harris et al., 2014; Tomorsky et al., 2017). We found instead that expression in A1 was more superficial, with tdTomato labeled cell bodies limited predominantly to layer 3 (**Figure 1C**). Penetrance in layer 3 reached 42%. Immediately adjacent to layer 3, 15% of cells in sub-layer 2b and 17% of cells in sub-layer 4a expressed tdTomato (**Figure 1C**). Labeled cells were pyramidal-shaped with apical dendrites projecting toward the pial surface (see examples in **Figure 1D**), and with axonal projections descending to deep layers of cortex (**Figures 1A,B,D**). We only saw cells with pyramidal morphology, although we did not examine all labeled cells so we cannot rule out the existence of non-pyramidal Nr5a+ cells. No labeled neurons were observed in layers 1, 5, or 6.

Layer 3 Nr5a+ Cells Strongly Drive Layer 5 Cells

What influence do these layer 3 Nr5a+ cells have on other cells in the cortical microcircuit during sensorimotor integration? To test this, we recorded from neurons across layers of auditory cortex with a linear silicon probe in Nr5a-ChR2 mice. To accurately measure the depth of recorded neurons, we used current-source density analysis to identify the sound-evoked robust short-latency sink in L4 (Intskirveli and Metherate, 2012). We recorded from a total of 192 cells (three mice, 14 penetrations), of which we could unambiguously assign precise laminar depth to 156 cells. Light evoked significant spiking responses in 48 of these cells, which were distributed throughout layers 2–6. The majority of these cells were activated with relatively long latency and low reliability, suggesting that they are likely to be indirectly-activated cells, postsynaptic to directly-activated cells expressing ChR2. Because Nr5a+ cells have a pyramidal morphology (**Figure 1D**), they are almost certainly excitatory and would be expected to broadly drive downstream neurons in the cortical circuit. In an attempt to distinguish between directly- and indirectly-activated neurons, we adapted a set of criteria based on the latency and reliability of light-evoked spiking responses (Lima et al., 2009). With these criteria, we identified 27 putative directly-activated cells from 3 Nr5a-ChR2 mice, of which we could unambiguously assign depths to 23 cells (**Figure 2A**; putative directly-activated cells: 27/192, or 14.1% of all cells recorded; 23/156, or 14.7% of cells with verifiable depths). These putative directly-activated cells were distributed across layers 2–5 (blue and black dots in **Figure 2A**) and formed two distinct spatial clusters: a superficial cluster (nine cells ranging in depth from 150 μm to 425 μm; 29% of cells in this depth range, blue dots in **Figure 2A**) and a deep cluster (14 cells ranging in depth from 525–825 μm; 13% of cells in this depth range, black dots in **Figure 2A**). The superficial cluster corresponded to the band of tdTomato-labeled cells centered in layer 3 (**Figure 2B**). Both the superficial and deep clusters corresponded to two robust light-evoked current-source density sinks in layers 3 and 5 (**Figure 2C**). However, the median latency to peak response of the deep cluster was significantly delayed relative to the superficial cluster (**Figures 2D,E**; latency difference was 3.5 ms, $p = 0.04$, $\eta^2 = 0.18$, rank-sum test). Despite this delay at the group level, when cells were segregated by the depth we could not identify a set of spike latency or reliability criteria with which we could differentiate light-evoked responses from cells in the superficial and deep clusters. We also computed the SALT statistic, a latency-based test for detecting light-evoked responses (Kvitsiani et al., 2013). SALT values were significantly higher for putative directly-activated cells than for non-responsive cells (rank-sum $p = 10^{-5}$), but cells in the superficial and deep clusters were not different from each other.

The proportion of superficial directly-activated cells mirrored the penetrance that we observed in Nr5a-tdTomato mice. Within layer 3, 33% of cells (5 of 15) were directly activated,

compared with 42% that were labeled by tdTomato. Spanning layers 2b-4a, 23% of cells (7 of 31) were directly activated, compared with 29% labeled by tdTomato. Taken together, the correspondence with tdTomato-labeled cells in the superficial layers, the complete absence of tdTomato cells in the deeper layers, and the delayed response timing with depth provide strong evidence that the putative directly-activated cells in the superficial cluster (150–425 μm) were indeed directly-activated Nr5a-ChR2-expressing cells, whereas those in the deep cluster (525–825 μm) were downstream, indirectly-activated cells in layer 5. The short latency and high reliability of the light-evoked responses in these layer 5 cells suggest that they were driven by an exceptionally powerful monosynaptic projection from layer 3 Nr5a+ cells. This is consistent with the position of layer 5 immediately downstream of layer 3 in the canonical cortical circuit (Gilbert and Wiesel, 1983; Douglas and Martin, 1991, 2004). The fact that these two groups of cells were not separable based on the timing or reliability of light-evoked spikes (and could only be segregated by depth) provides an important and cautionary note about the limitations of these measures for accurately classifying optogenetically-tagged cells. For example, a recording technique with less spatial accuracy (such as chronically-implanted tetrodes) could potentially yield false-positive classification, at least with populations of strongly-connected excitatory neurons like those described here.

Nr5a+ Cells Show Typical Responses to Gap Stimuli

Putative Nr5a+ cells and neighboring Nr5a- cells recorded in layers 2b-4a responded similarly to brief gaps in noise. The proportion of Nr5a+ cells exhibiting GTRs did not differ from neighboring cells (6/9 Nr5a+ cells vs. 15/39 Nr5a− cells; $\chi^2 = 2.36$, $p = 0.12$). Tuning properties of the observed GTRs also did not differ between Nr5a+ and neighboring Nr5a− cells. The proportion of band-pass and long-pass tuned responses was comparable between groups (Nr5a+: band-pass $n = 2$, long-pass $n = 4$; Nr5a−: band-pass $n = 3$, long-pass $n = 12$; $\chi^2 = 0.42$, $p = 0.51$; for examples, see **Figure 2G**), as was the median preferred gap duration (Nr5a+: 32 ms; Nr5a−: 20 ms; $p = 0.13$ rank-sum). No all-pass or short-pass responses were observed in either group.

Nr5a+ Cells Drive Behavioral Startle Attenuation

Next, we asked whether the stimulation of these Nr5a+ cells would directly impact behavior. For this, we turned to a well-established sensorimotor paradigm: attenuation of the acoustic startle response. Auditory cortex makes a critical contribution to this behavior. A brief gap in continuous background noise attenuates the startle reflex, and the GTRs of auditory cortical neurons are required for this to occur (Weible et al., 2014b, 2020). The amount of attenuation increases with gap duration. We found that optogenetic stimulation of Nr5a+ cells preceding the startle pulse on gap-free trials strongly attenuated the startle reflex (**Figure 3A**, filled blue box; laser intensity: 200 mW/mm^2). This attenuation was comparable to that seen following the longest gap duration presented

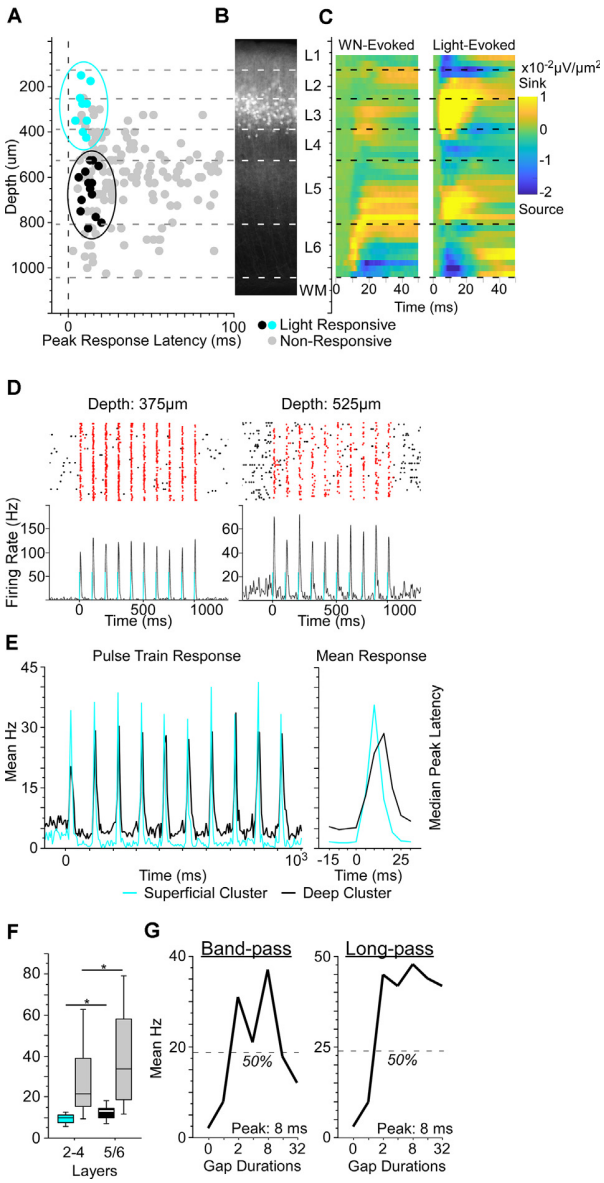

FIGURE 2 | Optogenetically-identified Nr5a+ neurons in layer 3 respond to brief gaps in noise. **(A)** We established depths for 156 cells from three Nr5a-ChR2 mice. Of these, 23 were putative directly-activated cells (blue and black dots). For response criteria, see "Materials and Methods: Electrophysiology" section. Gray dots show the other 133 "non-responsive" cells; light intensity: 200 mW/mm^2. When plotting depth by peak response latency, these 23 cells fell into one of two clusters, a superficial cluster (blue dots in the blue oval) with a median depth of 275 μm and a deep cluster (black dots in the black oval) with a median depth of 638 μm. **(B)** Cells in the superficial cluster matched the locations of tdTomato labeled cells from the Nr5a-Ai14 cross. **(C)** Left: white-noise-evoked current source density profile used for depth calibration. Right: both superficial and deep clusters corresponded to light-evoked current source density sinks (yellow hot-spots). Both panels are averages of 11 penetrations. **(D)** Two examples of neuronal responses to laser pulse-trains. Blue bars indicate light pulses (5 ms duration, 10 Hz). Spikes within 50 ms of light onset are shown in red. **(E)** The population-averaged responses from superficial and deep cluster cells were similar in shape but shifted in time, as illustrated pulse-by-pulse across

(*Continued*)

FIGURE 2 | Continued
the train (left) and in the mean pulse response (right). Color code as in panel **(A)**. **(F)** The median peak latency of cells in the superficial cluster preceded those of deeper responses by 3.5 ms. Non-responsive cells (gray bars) also showed a shift to longer median peak latency with depth ($p = 0.03$, $\eta^2 = 0.03$). Boxes show median and interquartile range (IQR), whiskers show 10th and 90th percentiles. **(G)** Two examples of gap duration tuning curves from Nr5a+ cells (left, a band-pass tuned cell; right, a long-pass tuned cell). Nr5a+ cells were responsive to brief gaps and exhibited tuning similar to that of the broader population at the same depth. *$p < 0.05$.

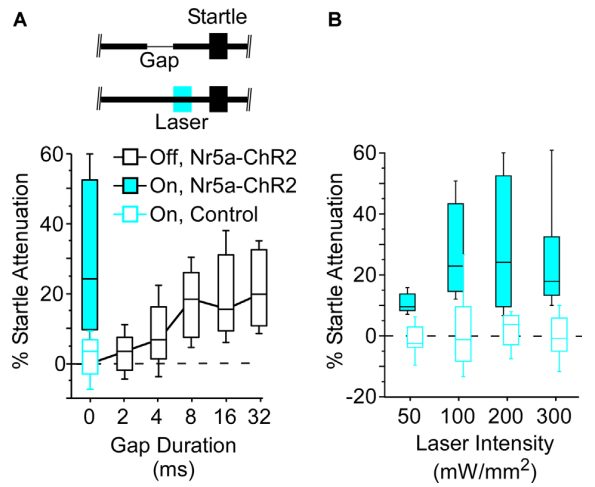

FIGURE 3 | Optogenetic stimulation of Nr5a+ cells robustly attenuates the startle reflex. **(A)** Open black-box plot shows gap detection; longer gaps evoke progressively stronger startle attenuation. Boxes show median and IQR, whiskers show 10th and 90th percentiles. A 25 ms pulse of 445 nm blue light (200 mW/mm^2), presented 50 ms before a 100 dB startle stimulus embedded in 80 dB continuous white noise without a gap, robustly attenuated evoked startle responses in Nr5a-ChR2 mice (filled blue box). No effect of light was seen with Nr5a- controls (open blue box). Inset depicts the laser pulse, background noise without a gap, and the startle stimulus. **(B)** Activation of Nr5a+ cells attenuated the startle response across a range of laser intensities (Wilcoxon signed-rank; 50 mW/mm^2: $p = 0.005$; 100 mW/mm^2: $p = 0.003$; 200 mW/mm^2: $p = 0.003$; 300 mW/mm^2: $p = 0.008$).

(32 ms). Illumination had no effect in control mice that did not express ChR2 (**Figure 3A**, open blue box), ruling out artifactual attenuation due to visual or intracranial detection of the light pulses. Thus, stimulation of the Nr5a+ cells alone was sufficient to attenuate the startle reflex.

Startle attenuation was significant across a range of laser intensities (**Figure 3B**; range: 50–300 mW/mm^2). Because a subset of layer 5 cells project corticofugally to the inferior colliculus (IC), a brain region known to be critically involved in startle attenuation, we speculate that activation of Nr5a+ neurons in layer 3, which in turn activates layer 5 cells (**Figure 2**), could act *via* an L3→L5→IC pathway.

Suppression of Nr5a+ Cells Does Not Affect Gap Detection

Because Nr5a+ cells appeared to be sufficient for attenuating the startle response, we next asked whether optogenetic suppression of these cells could interfere with the normal startle attenuation evoked by gaps in background noise. We used Nr5a-Arch mice that expressed Archaerhodopsin in Nr5a+ cells and found that optogenetic suppression had no discernable impact on behavior (**Figure 4A**). Illumination in control mice also did not affect behavior (data not shown).

To test whether illumination caused optogenetic suppression of spiking in Nr5a+ cells, we recorded from neurons in all layers of auditory cortex with a linear silicon probe in Nr5a-Arch mice. We verified transgene expression by fluorescence in all mice histologically after the recordings. We recorded the activity of 350 neurons from six Nr5a-Arch mice and 340 neurons from four Nr5a- control mice while presenting gap-in-noise stimuli. Of these, we established reliable depths for 271 and 291 cells based on current-source density analysis, respectively (**Figures 4B,C**). Across all layers, illumination did not produce a significant change in activity in cells from Nr5a-Arch mice relative to controls, although there was a trend toward reduced activity ($p = 0.08$, $\eta^2 = 0.005$, rank-sum). The same analysis performed layer-by-layer revealed a significant decrease in activity (z-scores) with illumination in cells from Nr5a-Arch mice in layer 3 relative to controls (**Figure 4D**; $p = 0.0004$, $\eta^2 = 0.22$, rank-sum). This decrease in layer 3 activity was only significant for non-GTR cells, though a trend was also observed for GTR cells ($p = 0.002$, $\eta^2 = 0.2$ and $p = 0.053$, respectively, rank-sum). We conclude that although Arch was indeed expressed in Nr5a+ cells and could modestly suppress their spiking activity, this optogenetic suppression was not robust enough to test whether gap responses in these neurons are necessary for startle attenuation.

DISCUSSION

Here, we identified a potent L3→L5 component of the canonical microcircuit in auditory cortex that contributes to behavioral startle attenuation. We found that Nr5a+ cells were pyramidal neurons located predominantly in layer 3 of auditory cortex, which showed gap responses similar in all major respects to those of other cortical neurons. Photoactivation of these layer 3 cells evoked short-latency and highly reliable spiking in layer 5 neurons, and robustly attenuated startle responses even at the lowest laser intensity tested. This behavioral inhibition of the startle response was indistinguishable from that evoked by acoustic gaps in noise. It therefore seems likely that some or all of these synaptically-driven layer 5 cells project corticofugally to inferior colliculus, which is a critical component of the pre-pulse inhibition pathway. These results are thus consistent with a scenario in which Nr5a+ cells in layer 3 contribute to behavioral inhibition of the startle response by acting through layer 5 cortico-collicular cells in an L3→L5→IC circuit.

Interestingly, Nr5a expression in mouse visual cortex is predominantly found in layer 4 (Bolser, 2004; Harris et al., 2014; Oh et al., 2014; Tomorsky et al., 2017), in contrast to our findings that these cells are primarily found in layer 3 of auditory cortex. The pial branching patterns of apical dendrites, axonal projections to deep layers, and strong synaptic activation

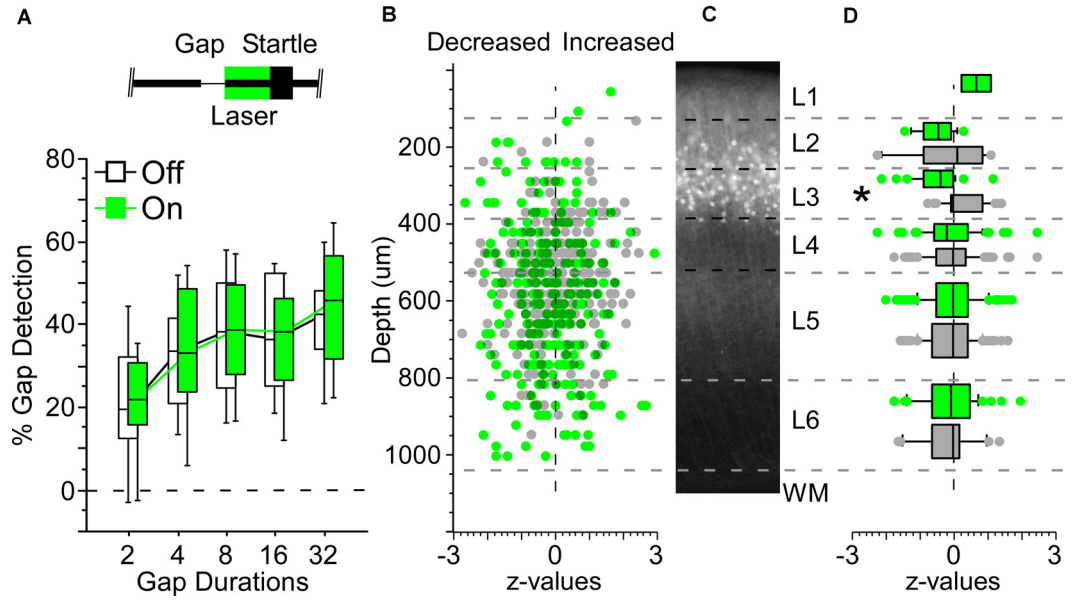

FIGURE 4 | Illumination in the Nr5a-Arch line produced only weak suppression of spiking activity. **(A)** Box plots show gap detection, measured as percent startle attenuation; longer gaps evoked progressively stronger startle attenuation. Boxes show median and IQR, whiskers show 10th and 90th percentiles. A 50 ms pulse of 520 nm green light during the post-gap interval did not alter startle responses in Nr5a-Arch mice (green boxes; light intensity: 300 mW/mm^2). Black boxes show gap detection on interleaved laser-off trials in the same mice. Inset depicts the laser pulse, background noise with a gap, and the startle stimulus. **(B)** Effect of illumination on each cell. Values are *z*-scores of firing rates averaged across all gap durations (laser-on relative to laser-off). Positive *z*-values indicate increased firing during illumination, negative *z*-values indicate suppression during illumination. Green dots are 267 cells from six Nr5a-Arch mice, gray dots are 287 cells from 4 Nr5a-control mice. **(C)** Expression pattern of tdTomato labeled cells from the Nr5a-Ai14 mouse for comparison. **(D)** Illumination significantly suppressed activity in Nr5a-Arch layer 3 neurons compared with those from controls. Same data as **(B)**, binned by layer. *$p < 0.05$.

of layer 5 neurons provide anatomical and physiological evidence consistent with the identification of Nr5a+ cells as layer 3 pyramidal neurons. Although layer 4 neurons in mouse sensory cortex do project to layer 5, the axonal projection from layer 2/3 to layer 5 is potent and densely branched, and is a prominent and consistent feature of cortical circuits across areas and species (Thomson and Bannister, 2003; Douglas and Martin, 2004; Harris and Shepherd, 2015). Indeed, the strongest projection from layer 3 is to layer 5, and this projection is a hallmark of the canonical microcircuit (Harris and Shepherd, 2015). We independently confirmed the location of these neurons in layer 3 of auditory cortex using anatomical (tdTomato expression) and physiological (ChR2-tagging and current-source density) characterization. We used anatomical laminar boundaries established in CBA mice (Anderson et al., 2009), which could in principle differ from those in our C57BL/6J mice, but agreed with our physiological characterization. We conclude that the laminar expression pattern of Nr5a differs between mouse auditory and visual cortex, with layer 3 expression in auditory cortex and layer 4 expression in visual cortex. The expression patterns of other laminar markers such as cytochrome oxidase and acetylcholinesterase also differ between mouse auditory and visual cortex (Anderson et al., 2009), as does the distribution of thalamocortical input (Linden and Schreiner, 2003). Why the Nr5a gene (a transcription factor in nuclear receptor subfamily five group A) shows different laminar expression patterns across cortical areas is unknown.

The canonical cortical microcircuit was first described in the visual system, in which its feedforward LGN→L4→L2/3 pathway has a natural interpretation in terms of the hierarchical representation of visual features, from circularly-symmetric to simple-cell to complex-cell receptive fields (Gilbert and Wiesel, 1983; Douglas and Martin, 1991). An alternative account views the canonical microcircuit in terms of predictive coding (Bastos et al., 2012; Adesnik and Naka, 2018; Keller and Mrsic-Flogel, 2018). In this view, ascending information (L4→L2/3) encodes prediction error, and prediction error neurons in layer 2/3 in turn provide feedforward connections that update internal representation neurons in layer 5. Central to the idea of predictive coding is the role of internal representation neurons, such as those in layer 5, which send a suppressive descending projection that cancels the activity of prediction error neurons at lower levels, presumably by engaging local inhibitory circuits. This cancellation corresponds to the "explaining away" of successfully predicted information. Pre-pulse inhibition of the startle response has a natural interpretation in this framework. A gap in continuous background noise, randomly timed so as to be unpredictable, generates a prediction error that is manifested as gap-evoked spiking in layer 2/3 neurons. This prediction error updates the internal representation in layer 5 neurons *via* the potent L3→L5 pathway that we have identified here. In turn, the corticofugal projection from layer 5 to the inferior and superior colliculus is relayed through the pedunculopontine tegmental

nucleus, which produces long-lasting inhibition of premotor neurons in the caudal pontine reticular nucleus that mediates the startle response (Fendt et al., 2001). This long-lasting inhibition can be thought of as the cancellation of activity corresponding to a predicted event. In this framework, direct activation of layer 3 neurons with ChR2 generates a prediction error that drives the representation of an anticipated event in layer 5 neurons, canceling the corresponding startle response.

In contrast, a more conventional view of the functional significance of pre-pulse inhibition is that it serves to protect stimulus recognition (Graham, 1979; Fendt et al., 2001). The duration of pre-pulse inhibition (∼150 ms) corresponds to a period of pre-attentive processing during which an unanticipated stimulus is recognized. A startle response during this period would evoke widespread behavioral and neural effects, which could interfere with stimulus recognition; pre-pulse inhibition might thus serve to protect sensory processing. This reflects a trade-off between the importance of recognizing an unexpected stimulus, and the importance of a startle response (such as a jump or an eyeblink) to avoid potential impact. Approaches that enable direct manipulation of the L3→L5 pathway, such as that described here or by others (Pluta et al., 2019), will help test the validity of these competing views.

Here we provide the first demonstration that direct activation of auditory cortical neurons is sufficient to attenuate the acoustic startle response. It remains unclear how an animal perceives the activation of layer 3 neurons (which in turn activates layer 5 and other downstream neurons). Because the ability of a pre-pulse stimulus (whether acoustic, tactile, or visual) to inhibit the startle response is closely tied to the extent to which the pre-pulse is consciously perceived (Fendt et al., 2001), pre-pulse inhibition has often been interpreted as an index of perception. For example, electrical stimulation of the cochlear nucleus can elicit pre-pulse inhibition, which led Zhang and Zhang (2010) to argue that electrical stimulation of the cochlear nucleus induces hearing. However, electrical stimulation of superior colliculus or the pedunculopontine tegmental nucleus can also elicit pre-pulse inhibition, and it seems less clear that stimulation of those multimodal structures would produce an acoustic percept. Nevertheless, animals can be trained to report electrical or optogenetic stimulation of remarkably small populations of neurons in the sensory cortex (Houweling and Brecht, 2008; Huber et al., 2008), and intracortical electrical stimulation of the auditory cortex in humans can evoke the auditory perception of sounds (Penfield and Perot, 1963; Fenoy et al., 2006). It, therefore, seems conceivable that optogenetic activation of layer 3 Nr5a+ neurons in the auditory cortex could evoke a phantom acoustic percept.

DATA AVAILABILITY STATEMENT

The raw data supporting the conclusions of this article will be made available by the authors, without undue reservation.

ETHICS STATEMENT

The animal study was reviewed and approved by University of Oregon Institutional Animal Care and Use Committee.

AUTHOR CONTRIBUTIONS

AW, IY, DK, and UD performed research. AW and MW designed research, analyzed data, and wrote the article. All authors contributed to the article and approved the submitted version.

FUNDING

This work was supported by the National Institutes of Health National Institute on Deafness and Other Communication Disorders Grant R01 DC-015828.

REFERENCES

Adesnik, H., and Naka, A. (2018). Cracking the function of layers in the sensory cortex. *Neuron* 100, 1028–1043. doi: 10.1016/j.neuron.2018.10.032

Anderson, L. A., Christianson, G. B., and Linden, J. F. (2009). Mouse auditory cortex differs from visual and somatosensory cortices in the laminar distribution of cytochrome oxidase and acetylcholinesterase. *Brain Res.* 1252, 130–142. doi: 10.1016/j.brainres.2008.11.037

Bastos, A. M., Martin Usrey, W., Adams, R. A., Mangun, G. R., Fries, P., and Friston, K. J. (2012). Canonical microcircuits for predictive coding. *Neuron* 76, 695–711. doi: 10.1016/j.neuron.2012.10.038

Bolser, D. (2004). Allen brain atlas. *Dict. Bioinform. Comput. Biol.* doi: 10.1002/9780471650126.dob080510.1002/9780471650126.dob0805

Bowen, G. P., Lin, D., Taylor, M. K., and Ison, J. R. (2003). Auditory cortex lesions in the rat impair both temporal acuity and noise increment thresholds, revealing a common neural substrate. *Cereb. Cortex* 13, 815–822. doi: 10.1093/cercor/13.8.815

Campbell, A. (1905). *Histological Studies on the Localization of Cerebral Function*. Cambridge, UK: Cambridge University Press.

Casseday, J. H., Ehrlich, D., and Covey, E. (1994). Neural tuning for sound duration: role of inhibitory mechanisms in the inferior colliculus. *Science* 264, 847–850. doi: 10.1126/science.8171341

Douglas, R. J., and Martin, K. A. (1991). A functional microcircuit for cat visual cortex. *J. Physiol.* 440, 735–769. doi: 10.1113/jphysiol.1991.sp018733

Douglas, R. J., and Martin, K. A. C. (2004). Neuronal circuits of the neocortex. *Annu. Rev. Neurosci.* 27, 419–451. doi: 10.1146/annurev.neuro.27.070203.144152

Fendt, M., Li, L., and Yeomans, J. S. (2001). Brain stem circuits mediating prepulse inhibition of the startle reflex. *Psychopharmacology* 156, 216–224. doi: 10.1007/s002130100794

Fenoy, A. J., Severson, M. A., Volkov, I. O., Brugge, J. F., and Howard, M. A. III. (2006). Hearing suppression induced by electrical stimulation of human auditory cortex. *Brain Res.* 1118, 75–83. doi: 10.1016/j.brainres.2006.08.013

Fuzessery, Z. M., and Hall, J. C. (1999). Sound duration selectivity in the pallid bat inferior colliculus. *Hear. Res.* 137, 137–154. doi: 10.1016/s0378-5955(99)00133-1

Gilbert, C. D., and Wiesel, T. N. (1983). Functional organization of the visual cortex. *Prog. Brain Res.* 58, 209–218. doi: 10.1016/S0079-6123(08)60022-9

Graham, K. F. (1979). "Distinguishing among orienting, defense, and startle reflexes," in *The Orienting Reflex in Humans* eds H. D. Kimmel, E. H. van Olst, and J. F. Orlebeke. (New York, NY: Erlbaum). Available online at: https://ci.nii.ac.jp/naid/10019297625/. Accessed May 6, 2019.

Grünbaum, A. S. F., and Sherrington, C. S. (1902). Observations on the physiology of the cerebral cortex of some of the higher apes (Preliminary communication.). *Proc. R. Soc. Lond.* 69, 451–458. doi: 10.1098/rspl.1901.0100

Harris, J. A., Hirokawa, K. E., Sorensen, S. A., Gu, H., Mills, M., Ng, L. L., et al. (2014). Anatomical characterization of Cre driver mice for neural circuit mapping and manipulation. *Front. Neural Circuits* 8:76. doi: 10.3389/fncir.2014.00076

Harris, J. A., Mihalas, S., Hirokawa, K. E., Whitesell, J. D., Choi, H., Bernard, A., et al. (2019). Hierarchical organization of cortical and thalamic connectivity. *Nature* 575, 195–202. doi: 10.1038/s41586-019-1716-z

Harris, K. D., and Shepherd, G. M. G. (2015). The neocortical circuit: themes and variations. *Nat. Neurosci.* 18, 170–181. doi: 10.1038/nn.3917

Houweling, A. R., and Brecht, M. (2008). Behavioural report of single neuron stimulation in somatosensory cortex. *Nature* 451, 65–68. doi: 10.1038/nature06447

Huber, D., Petreanu, L., Ghitani, N., Ranade, S., Hromádka, T., Mainen, Z., et al. (2008). Sparse optical microstimulation in barrel cortex drives learned behaviour in freely moving mice. *Nature* 451, 61–64. doi: 10.1038/nature06445

Intskirveli, I., and Metherate, R. (2012). Nicotinic neuromodulation in auditory cortex requires MAPK activation in thalamocortical and intracortical circuits. *J. Neurophysiol.* 107, 2782–2793. doi: 10.1152/jn.01129.2011

Ison, J. R., O'Connor, K., Bowen, G. P., and Bocirnea, A. (1991). Temporal resolution of gaps in noise by the rat is lost with functional decortication. *Behav. Neurosci.* 105, 33–40. doi: 10.1037/0735-7044.105.1.33

Keller, G. B., and Mrsic-Flogel, T. D. (2018). Predictive processing: a canonical cortical computation. *Neuron* 100, 424–435. doi: 10.1016/j.neuron.2018.10.003

Kelly, J. B., Rooney, B. J., and Phillips, D. P. (1996). Effects of bilateral auditory cortical lesions on gap-detection thresholds in the ferret *(Mustela putorius)*. *Behav. Neurosci.* 110, 542–550. doi: 10.1037/0735-7044.110.3.542

Kitchen, C. M. R. (2009). Nonparametric vs. parametric tests of location in biomedical research. *Am. J. Ophthalmol.* 147, 571–572. doi: 10.1016/j.ajo.2008.06.031

Kvitsiani, D., Ranade, S., Hangya, B., Taniguchi, H., Huang, J. Z., and Kepecs, S. (2013). Distinct behavioural and network correlates of two interneuron types in prefrontal cortex. *Nature* 498, 363–366. doi: 10.1038/nature12176

Lenhard, W., and Lenhard, A. (2016). Calculation of effect sizes. *Psychometrica* doi: 10.13140/RG.2.2.17823.92329

Li, L., Korngut, L. M., Frost, B. J., and Beninger, R. J. (1998). Prepulse inhibition following lesions of the inferior colliculus: prepulse intensity functions. *Physiol. Behav.* 65, 133–139. doi: 10.1016/s0031-9384(98)00143-7

Lima, S. Q., Hromádka, T., Znamenskiy, P., and Zador, A. M. (2009). PINP: a new method of tagging neuronal populations for identification during *in vivo* electrophysiological recording. *PLoS One* 4:e6099. doi: 10.1371/journal.pone.0006099

Linden, J. F., and Schreiner, C. E. (2003). Columnar transformations in auditory cortex? A comparison to visual and somatosensory cortices. *Cereb. Cortex* 13, 83–89. doi: 10.1093/cercor/13.1.83

Masini, C. V., Babb, J. A., Nyhuis, T. J., Day, H. E. W., and Campeau, S. (2012). Auditory cortex lesions do not disrupt habituation of HPA axis responses to repeated noise stress. *Brain Res.* 1443, 18–26. doi: 10.1016/j.brainres.2012.01.002

Oh, S. W., Harris, J. A., Ng, L., Winslow, B., Cain, N., Mihalas, S., et al. (2014). A mesoscale connectome of the mouse brain. *Nature* 508, 207–214. doi: 10.1038/nature13186

Paxinos, G., and Franklin, K. B. J. (2004). *The Mouse Brain in Stereotaxic Coordinates.* San Diego, CA: Gulf Professional Publishing.

Penfield, W., and Perot, P. (1963). The brain's record of auditory and visual experience. *Brain* 86, 595–696. doi: 10.1093/brain/86.4.595

Pluta, S. R., Telian, G. I., Naka, A., and Adesnik, H. (2019). Superficial layers suppress the deep layers to fine-tune cortical coding. *J. Neurosci.* 39, 2052–2064. doi: 10.1523/JNEUROSCI.1459-18.2018

Ramon y Cajal, S. (1911). *Histologie du Systeme Nerveux de l'Homme et des Vertebres*. Vol. 2. Paris: Maloine.

Redish, D. A. (2008). *MClust Spike Sorting Toolbox*. Available online at: http://redishlab.neuroscience.umn.edu/MClust/MClust.html.

Siegle, J. H., López, A. C., Patel, Y. A., Abramov, K., Ohayon, S., and Voigts, J. (2017). Open Ephys: an open-source, plugin-based platform for multichannel electrophysiology. *J. Neural Eng.* 14:045003. doi: 10.1088/1741-2552/aa5eea

Swetter, B. J., Fitch, R. H., and Markus, E. J. (2010). Age-related decline in auditory plasticity: experience dependent changes in gap detection as measured by prepulse inhibition in young and aged rats. *Behav. Neurosci.* 124, 370–380. doi: 10.1037/a0019519

Thomson, A. M., and Bannister, A. P. (2003). Interlaminar connections in the neocortex. *Cereb. Cortex* 13, 5–14. doi: 10.1093/cercor/13.1.5

Threlkeld, S. W., Penley, S. C., Rosen, G. D., and Fitch, R. H. (2008). Detection of silent gaps in white noise following cortical deactivation in rats. *Neuroreport* 19, 893–898. doi: 10.1097/WNR.0b013e3283013d7e

Tomorsky, J., DeBlander, L., Kentros, C. G., Doe, C. Q., and Niell, C. M. (2017). TU-tagging: a method for identifying layer-enriched neuronal genes in developing mouse visual cortex. *eNeuro* 4:ENEURO.0181-17.2017. doi: 10.1523/ENEURO.0181-17.2017

Weible, A. P., Liu, C., Niell, C. M., and Wehr, M. (2014a). Auditory cortex is required for fear potentiation of gap detection. *J. Neurosci.* 34, 15437–15445. doi: 10.1523/JNEUROSCI.3408-14.2014

Weible, A. P., Moore, A. K., Liu, C., DeBlander, L., Wu, H., Kentros, C., et al. (2014b). Perceptual gap detection is mediated by gap termination responses in auditory cortex. *Curr. Biol.* 24, 1447–1455. doi: 10.1016/j.cub.2014.05.031

Weible, A. P., Yavorska, I., and Wehr, M. (2020). A cortico-collicular amplification mechanism for gap detection. *Cereb. Cortex* 30, 3590–3607. doi: 10.1093/cercor/bhz328

Williamson, R. S., and Polley, D. B. (2019). Parallel pathways for sound processing and functional connectivity among layer 5 and 6 auditory corticofugal neurons. *eLife* 8:e42974. doi: 10.7554/eLife.42974

Zhang, J., and Zhang, X. (2010). Electrical stimulation of the dorsal cochlear nucleus induces hearing in rats. *Brain Res.* 1311, 37–50. doi: 10.1016/j.brainres.2009.11.032

Conflict of Interest: The authors declare that the research was conducted in the absence of any commercial or financial relationships that could be construed as a potential conflict of interest.

frontiers in Neural Circuits

ORIGINAL RESEARCH
published: 26 November 2020
doi: 10.3389/fncir.2020.581435

Learning-Dependent Dendritic Spine Plasticity Is Reduced in the Aged Mouse Cortex

Lianyan Huang[1,2], Hang Zhou[3], Kai Chen[3], Xiao Chen[2] and Guang Yang[1,3]**

[1]Department of Anesthesiology, New York University School of Medicine, New York, NY, United States, [2]Guangdong Provincial Key Laboratory of Brain Function and Disease, Zhongshan School of Medicine, Sun Yat-Sen University, Guangzhou, China, [3]Department of Anesthesiology, Columbia University Medical Center, New York, NY, United States

Aging is accompanied by a progressive decrease in learning and memory function. Synaptic loss, one of the hallmarks of normal aging, likely plays an important role in age-related cognitive decline. But little is known about the impact of advanced age on synaptic plasticity and neuronal function *in vivo*. In this study, we examined the structural dynamics of postsynaptic dendritic spines as well as calcium activity of layer 5 pyramidal neurons in the cerebral cortex of young and old mice. Using transcranial two-photon microscopy, we found that in both sensory and motor cortices, the elimination rates of dendritic spines were comparable between young (3–5 months) and mature adults (8–10 months), but seemed higher in old mice (>20 months), contributing to a reduction of total spine number in the old brain. During the process of motor learning, old mice compared to young mice had fewer new spines formed in the primary motor cortex. Motor training-evoked somatic calcium activity in layer 5 pyramidal neurons of the motor cortex was also lower in old than young mice, which was associated with the decline of motor learning ability during aging. Together, these results demonstrate the effects of aging on learning-dependent synapse remodeling and neuronal activity in the living cortex and suggest that synaptic deficits may contribute to age-related learning impairment.

Keywords: aging, dendritic spine, synaptic plasticity, learning, two-photon imaging, cortex

OPEN ACCESS

Edited by:
Yoshiyuki Kubota, National Institute for Physiological Sciences (NIPS), Japan

Reviewed by:
Jun Noguchi, National Center of Neurology and Psychiatry, Japan
Simon Chen, University of Ottawa, Canada

****Correspondence:***
Guang Yang
gy2268@cumc.columbia.edu
Lianyan Huang
huangly55@mail.sysu.edu.cn

Received: *08 July 2020*
Accepted: *05 November 2020*
Published: *26 November 2020*

Citation:
Huang L, Zhou H, Chen K, Chen X and Yang G (2020) Learning-Dependent Dendritic Spine Plasticity Is Reduced in the Aged Mouse Cortex. Front. Neural Circuits 14:581435. doi: 10.3389/fncir.2020.581435

INTRODUCTION

The normal aging process is accompanied by a progressive decrease in cognitive and learning ability (Hedden and Gabrieli, 2004; Brayne, 2007; Deary et al., 2009). Neuropsychological tests have revealed that people older than 60 years of age often show impairments in certain types of memory, especially recall of recent events (Shimamura, 1994; Zelinski and Burnight, 1997). Elder people also experience increased difficulties in a variety of mental tasks (Rhodes, 2004). Aging-related cognitive decline leads to decreased quality of life and lowered ability to function. As the average lifespan is increasing worldwide, it becomes increasingly important to understand the neural mechanisms of age-related cognitive impairment.

Despite many efforts, the cellular basis of age-related cognitive decline remains unclear. It was once believed that a generalized neuronal loss in the cerebral cortex and deterioration of dendritic branching occurs during normal aging and contributes to cognitive impairment

(Brody, 1955; Coleman and Flood, 1987). Yet stereological studies have documented minimal aging-related neuronal loss in the cortex and hippocampus (West et al., 1994; Morrison and Hof, 1997). It is now generally accepted that age-related cognitive decline is accompanied by minimum loss of neurons and subtle changes of neuronal arborization (Buell and Coleman, 1981; Flood et al., 1987; Flood, 1993; Morrison and Hof, 2002). On the other hand, changes in synapse number and plasticity have been reported in the brains of aging people and experimental animals (Terry and Katzman, 2001; Hof and Morrison, 2004; Burke and Barnes, 2006; Dickstein et al., 2007). Because neuronal circuit function is highly dependent on synaptic connectivity, age-related synapse loss and dysfunction likely contribute to the impairment in cognitive and learning capacities in the aged brain.

Dendritic spines are small protrusions extending from the shafts of dendrites, which represent postsynaptic sites of most excitatory synapses in the mammalian brain (Bhatt et al., 2009). During aging, an approximate 20–40% loss of dendritic spines has been demonstrated in the cortex and hippocampus of human and experimental animals (Mervis, 1978; Jacobs et al., 1997; Hedden and Gabrieli, 2004; Dumitriu et al., 2010). Consistent with the loss of dendritic spines, electrophysiological studies have shown that the field excitatory postsynaptic potential is reduced in aged rats (Barnes, 1979; Barnes and McNaughton, 1980; Luebke et al., 2004). Recent *in vivo* imaging studies reported that aging alters the dynamics of dendritic spines in the cortex of old mice (Mostany et al., 2013; Davidson et al., 2020). But how aging affects dendritic spine plasticity associated with learning remains unknown.

Previous studies have shown that novel sensory and learning experiences lead to rapid dendritic spine formation and elimination in functionally relevant cortical regions (Hofer et al., 2009; Xu et al., 2009; Yang et al., 2009; Kim and Nabekura, 2011; Lai et al., 2012; Hayashi-Takagi et al., 2015), raising the possibility that age-related decline in cognitive and memory function might attribute to the impairment in learning-dependent dendritic spine plasticity. To test this hypothesis, we examined the dynamics of dendritic spines in the mouse cortex *in vivo*. Our results showed that old mice (>20 months) had higher rates of spine elimination compared to young (3–5 months) and mature adults (8–10 months). During the process of motor learning, training-induced spine formation and somatic calcium activity were significantly lower in the motor cortex of old mice than young adults. These findings suggest that the ability of neurons to maintain and regenerate synapses declines during aging, which may contribute to learning and memory impairment.

MATERIALS AND METHODS

Experimental Animals

Thy1-YFP-H mice (Stock No.: 003782) were purchased from the Jackson Laboratory and used for dendritic spine imaging experiments. *Thy1*-GCaMP6slow mice (Founder line 1) were used for Ca^{2+} imaging experiments (Cichon et al., 2020). Mice were group-housed in animal facilities at New York University Medical Center and Columbia University Medical Center. All animal procedures were carried out following protocols approved by Institutional Animal Care and Use Committees (IACUC) at New York University and Columbia University as consistent with National Institutes of Health (NIH) Guidelines for the Care and Use of Laboratory Animals.

In vivo Imaging of Dendritic Spines and Data Analysis

The surgical procedure for transcranial two-photon imaging has been described previously (Yang et al., 2010). While the animal was under deep anesthesia induced by 100 mg/kg ketamine and 15 mg/kg xylazine, the skull surface was exposed with a midline scalp incision. A small skull region (∼0.2 mm in diameter) located over the primary somatosensory cortex or the primary motor cortex was identified based on stereotaxic coordinates. A custom-made, stainless steel plate was glued to the skull with a central opening over the identified brain region. To create a cranial window for imaging, the skull surface was immersed in artificial cerebrospinal fluid (ACSF), and a high-speed drill and a microsurgical blade were used to reduce the thickness of the skull to approximately 20 μm under a dissection microscope. After the skull thinning, the animal was placed under an Olympus two-photon microscope with the laser tuned to the optimal excitation wavelength for YFP (920 nm). Low laser power (20–30 mW at the sample) was used during imaging to minimize phototoxicity. Stacks of image planes within a depth of 100 μm from the pial surface was collected with a 60× water-immersion objective (1.1 N.A.) at a digital zoom of 1.0–3.0. The step size was 2 μm for the initial low magnification image (1.0× zoom) for relocation at later time points and 0.75 μm for all the other experiments (3.0× zoom). After imaging, the steel plate was gently detached from the skull, and the scalp was sutured with 6–0 silk. The animals were returned to their home cages until the next view.

Data analysis was performed with NIH ImageJ software as described previously (Huang et al., 2016). The same dendritic segments were identified from three-dimensional image stacks taken at both time points. The number and location of dendritic protrusions were identified in each view. Filopodia were identified as long, thin structures without enlarged heads, and the rest of the protrusions were classified as spines. Spines were considered the same between two views based on their spatial relationship to adjacent landmarks. Spines in the second view were considered different if they were more than 0.7 μm away from their expected positions based on the first view. The formation or elimination rates of spines were measured as the number of spines formed or eliminated divided by the number of spines existing in the first view.

Rotarod Training

An EZRod system with a test chamber (44.5 × 14 × 51 cm dimensions, Accuscan Instruments, Columbus, OH, USA) was used in this study. Animals were placed on the motorized rod (30 mm in diameter) in the chamber. The rotation speed gradually increased from 0 to 60 rpm for 3 min. The time latency and rotation speed were recorded when the animal was unable to keep up with the increasing speed and fell. Rotarod

training was performed in one 30-min session (20 trials) per day. The performance was measured as the average speed animals achieved during the training session.

Treadmill Training

A treadmill task was introduced to provide mild motor training, as well as to perform *in vivo* Ca^{2+} imaging and motor training at the same time. A custom-built treadmill (46 × 15 × 10 cm dimensions) was used to allow head-fixed mice to move their limbs freely on a moving belt. Following the onset of a training trial, the belt speed was gradually increased from 0 to 4 cm/s within ∼3 s and maintained at 4 cm/s through the rest of the trial. Mice walked on the moving belt and adjusted their gait patterns progressively. To obtain footprints, mouse paws were coated with ink and a sheet of white construction paper was placed on top of the belt during treadmill training. Gait analysis was performed manually offline. The animal's gait pattern was classified as drag, wobble, sweep, and steady run as previously described (Cichon and Gan, 2015). Treadmill performance was presented as the percentage of time spent in a steady run, averaged over five trials.

Immunohistochemistry

Mice were deeply anesthetized and perfused with a phosphate-buffered solution (PBS) and 4% paraformaldehyde (PFA). The brain was removed and post-fixed in 4% PFA for 3 days and rinsed three times with PBS. Following gradient dehydration in 10%, 20%, and 30% sucrose solution at 4°C, the brain (from AP −0.4 to −1.2 mm) was sectioned with a Leica vibratome (VT 1000 S) at 50 μm thickness. Sections were post-fixed in 4% PFA for 1 h and washed three times with PBS. Sections were permeabilized and blocked at room temperature in 0.2% Triton X-100 and 5% goat or donkey serum in PBS for 1.5 h and then incubated overnight at 4°C with primary antibodies: rabbit anti-Iba1 (Wako, 019-19741, 1:2,000); mouse anti-GFAP (Sigma–Aldrich, AMAB91033, 1:1,000); rabbit anti-GFP (Abcam, ab6556, 1:1,500) and chicken anti-MAP2 (Abcam, ab5392). The sections were then washed three times with PBS and incubated for 2 h at room temperature with secondary antibodies: goat anti-rabbit Alexa Fluor 488 (1:500), donkey anti-rabbit Alexa Fluor 555 (1:500), donkey anti-mouse Alexa Fluor 488 (1:500), and goat anti-chicken Alexa Fluor 647 (1:500). The sections were washed as before and then mounted in a mounting medium containing DAPI (VectorLabs, H-2000) for confocal imaging.

Confocal Imaging and Quantification

Confocal images were taken with a 20× objective at 1,024 × 1,024 pixels (0.62249 μm/pixel) using a Nikon Ti laser scanning confocal system. The fluorophores of DAPI, Alexa Fluor 488, and Alexa Fluor 647 were excited by 405, 488, and 640 nm laser, respectively. A *z*-stack of images was obtained at 2 μm step size and projected at a maximal intensity to generate the final three-channel images, which were then analyzed in ImageJ. For *Thy1*-GCaMP6s Line 1 mice, the mean fluorescent intensity of individual Alexa Fluor 488-positive cells ($F_{\text{Anti-GFP}}$) in layer 5 (L5) of the cortex was normalized by that of Alexa Fluor 647 ($F_{\text{Anti-MAP2}}$), where the expression level of neuronal skeleton marker MAP2 was used as an internal reference to correct the potential variations introduced by experimental procedures. The ratio ($F_{\text{Anti-GFP}}/F_{\text{Anti-MAP2}}$) was used to represent the expression level of GCaMP6s in individual neurons. The ratio ($F_{\text{Anti-GFP}}/F_{\text{Anti-MAP2}}$) in individual MAP2-positive cells in wild type (WT) mice was quantified as a negative control.

In vivo Ca^{2+} Imaging

In vivo Ca^{2+} imaging was performed in *Thy1*-GCaMP6s mice under awake states. The surgical procedure for preparing mice for awake imaging has been described previously (Yang et al., 2013). In brief, a head holder composed of two metal bars was attached to the animal's skull to reduce motion artifact during imaging. Following surgical anesthesia and a midline scalp incision, the region of the skull located over the primary motor cortex was identified and marked with ink. The head holder was attached to the skull surface first with cyanoacrylate-based glue (Loctite 495) and then with dental acrylic cement, leaving the marked skull region in between the two metal bars. After the cement was completely dry, a craniotomy was made over the motor cortex and covered with a glass coverslip custom to the size (1.0–1.5 mm diameter) of the bone removed. The coverslip was glued to the skull to stabilize the exposed brain. Before imaging, mice were given 1 day to recover from the surgical anesthesia and habituated several times (10 min each time) to minimize the potential stress of head restraining and imaging.

In vivo Ca^{2+} imaging was performed using an Olympus two-photon system equipped with a Ti:sapphire laser (Mai Tai DeepSee; Spectra-Physics) tuned to 920 nm. To examine the somatic activity of L5 pyramidal neurons, Ca^{2+} images were collected at the depth of 500–600 μm below the pial surface, at a frame size of 256 × 256 pixels and a rate of 2 Hz, using a 25× objective immersed in ACSF. Image acquisition was performed using Olympus FV1000 software and analyzed *post hoc* using NIH ImageJ software. Ca^{2+} analysis was performed as previously described (Zhao et al., 2018). $\Delta F/F_0$ was calculated as $(F - F_0)/F_0$, where F_0 is the baseline fluorescence averaged over a 2-s period corresponding to the lowest recording signal over the resting period (i.e., treadmill off). The average integrated Ca^{2+} activity was the average of $\Delta F/F_0$ over 2.5 min recording.

Statistics

Prism software (GraphPad 7.0) was used to conduct statistical analysis. Data were presented as mean ± SEM. For spine imaging and calcium imaging data, tests for differences between populations were performed using two-tailed Mann–Whitney's test. For behavioral data, tests for differences between groups were performed using the two-tailed Student's *t*-test. Immunostaining data were compared using Kolmogorov–Smirnov tests. Significant levels were set at $P \leq 0.05$.

RESULTS

More Spines Are Eliminated in the Sensory Cortex of Old Mice

To examine age-related changes in dendritic spine plasticity, we first compared spine turnover rates in the cortex of young

adult (3–5 months of age), mature adult (8–10 months of age), and old mice (>20 months of age). Apical dendrites of L5 pyramidal neurons in the sensory cortex of *Thy1*-YFP-H transgenic mice were repeatedly imaged using transcranial two-photon microscopy (**Figure 1A**). Consistent with previous studies (Grutzendler et al., 2002; Yang et al., 2009), we found a small and equivalent degree of dendritic spine formation and elimination over 2 days in young, mature, and old brains (**Figures 1A,B**). In young adult mice, 2.7 ± 0.3% dendritic spines were formed and 2.9 ± 0.6% were eliminated over 2 days (658 spines, n = 4 mice). Similar turnover rates were found in mature adult mice over 2 days (formation: 2.9 ± 0.3%; elimination: 2.2 ± 0.6%; 569 spines, n = 4 mice). In old mice, the rates of spine formation (3.9 ± 0.5%) and elimination (4.11 ± 0.4%) increased slightly (515 spines, n = 4 mice), although not significantly different compared to young and mature adult mice.

To determine long-term changes of dendritic spines, we repeatedly imaged dendritic segments in the sensory cortex over a 2-week interval (**Figure 1C**). We found that 4.6 ± 0.2% of dendritic spines were formed and 5.1 ± 0.2% were eliminated over 2 weeks in young adult mice (639 spines, n = 4 mice). In mature adults, spine formation and elimination over 2 weeks were 4.7 ± 0.4% and 5.9 ± 0.3%, respectively, compared to those in young adults (**Figure 1C**). Notably, in old mice, the percentage of spines eliminated (7.4 ± 0.3%) over 2 weeks was significantly higher than those in young and mature adults. Moreover, the percentage of spines eliminated over 2 weeks was slightly, but not significantly, higher than the percentage of spines formed (7.4 ± 0.3% vs. 5.9 ± 0.4%, P = 0.0571) in old mice, leading to a trend of spine loss in the sensory cortex. Consistently, dendritic spine density in layer 1 of the sensory cortex was significantly lower in old mice as compared with young adult mice (**Figure 1D**). Together, these results indicate a net loss of dendritic spines in the old sensory cortex due to a higher number of spines being eliminated than formed.

In a separate experiment, we stained microglia and astrocytes in the cortex of old mice after the thinning-skull surgery. Consistent with the previous report that the properly performed thinning-skull surgery does not cause glial activation (Xu et al., 2007), we did not observe noticeable changes in microglial morphology and density in the old cortex within 2 days after the surgery (**Figure 2**). Moreover, the expression levels of glial fibrillary acidic protein (GFAP) in the cortical areas under the cranial window was comparable to those in the contralateral hemisphere, indicating no activation of astrocytes (**Figure 2**). These results suggest that the increased turnover of spine dynamics in the old cortex is unlikely due to the surgery-induced glial activation.

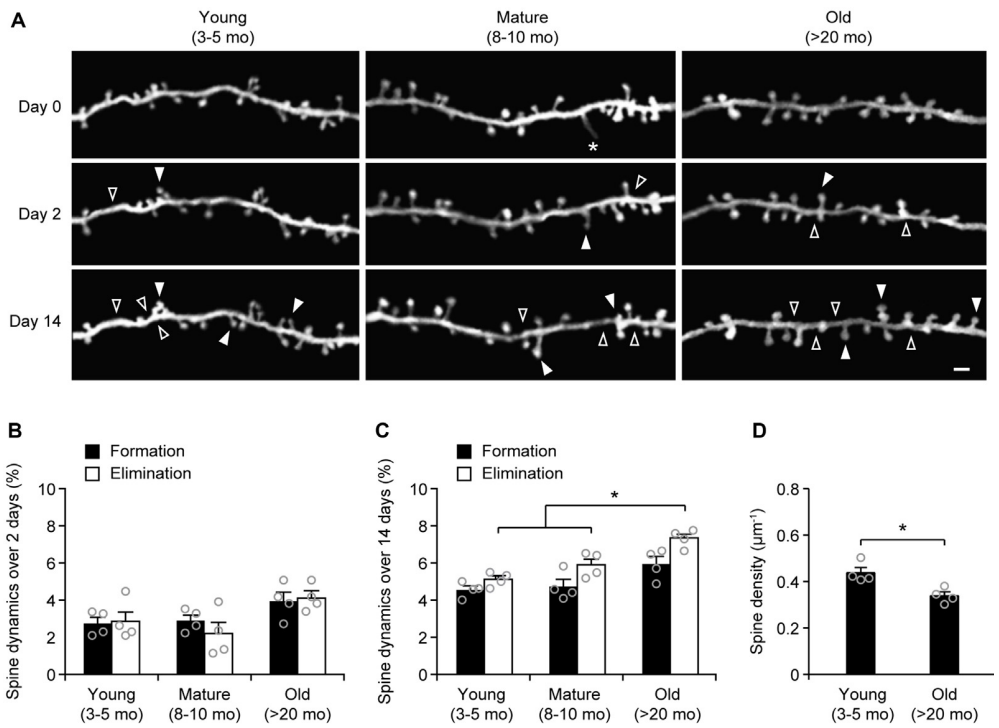

FIGURE 1 | Aging increases dendritic spine elimination in the sensory cortex. **(A)** *In vivo* time-lapse imaging of the same dendritic segments over 2 and 14 days in the sensory cortex of young and old mice. Filled and empty arrowheads indicate dendritic spines that were formed and eliminated relative to the first view, respectively. Asterisks indicate filopodia. Scale bar, 2 μm. **(B)** Percentages of dendritic spines that were formed and eliminated over 2 days. **(C)** Percentages of dendritic spines that were formed and eliminated over 14 days. **(D)** The density of dendritic spines on the apical tuft dendrites of L5 pyramidal neurons in young adult and old mice. Throughout, individual circles represent data from a single mouse. Summary data are presented as mean ± SEM. *P < 0.05 by two-tailed Mann–Whitney test.

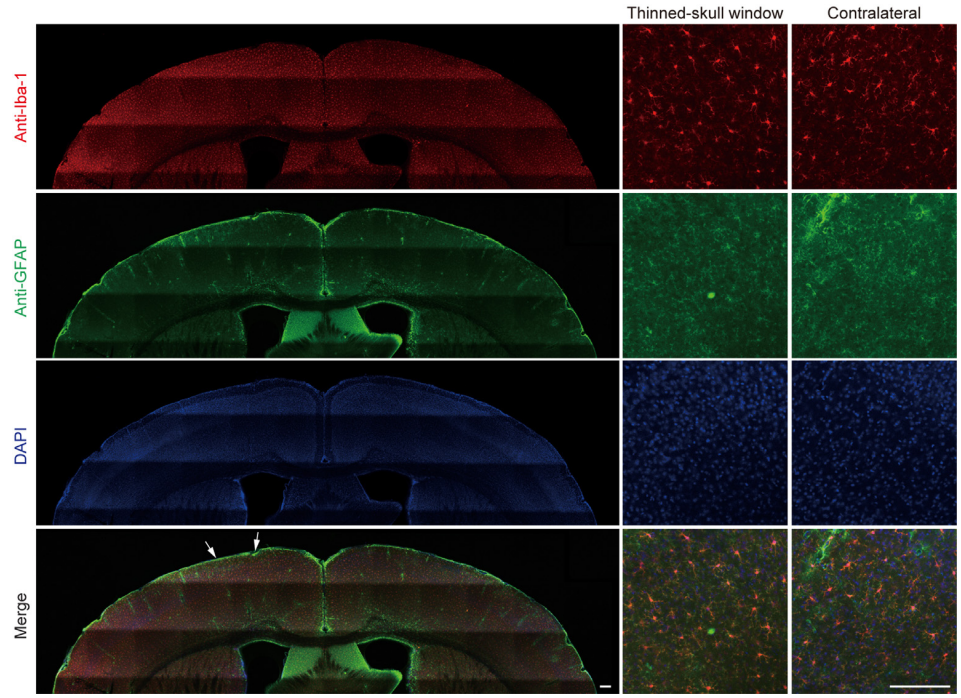

FIGURE 2 | No obvious glial activation is observed under the thinned-skull window. Two days after thinning-skull surgery in 20-month-old mice, iba1-stained microglia appeared normal both on the contralateral control side and under the thinned-skull window. Little GFAP expression was found under the thinned-skull window (between arrows) or on the contralateral control side. Scale bar, 200 μm.

More Spines Are Eliminated in the Motor Cortex of Old Mice

Next, we measured the rates of spine turnover in the primary motor cortex during aging. Previous studies have shown that the rates of spine turnover are comparable across different cortical regions in adult mice (Zuo et al., 2005). Consistent with those studies, we found that 3.1 ± 0.2% and 3.1 ± 0.4% of dendritic spines were formed and eliminated, respectively, over 2 days in the motor cortex of young adult mice (539 spines, $n = 4$ mice; **Figures 3A–C**), comparable to those in the sensory cortex at the same age (**Figure 1B**). There were no differences in the rates of spine formation in the motor cortex between young adults and old mice (3.1 ± 0.2% vs. 3.3 ± 0.3%, $P = 0.9714$). In the motor cortex of old mice, the rate of spine elimination increased slightly as compared to that in young adults (5.2 ± 0.2% vs. 3.1 ± 0.4%, $P = 0.0286$) and was significantly higher than the rate of spine formation in the same mice ($P = 0.0286$; **Figures 3A–C**). In line with the trend of more spines being eliminated than formed in the old motor cortex, dendritic spine density in layer 1 of the motor cortex was significantly lower in old mice as compared with young adult mice (**Figure 3D**). These results indicate that during aging, a loss of dendritic spines also occurs in the motor cortex.

Motor Learning-Induced Spine Formation Is Reduced in Old Mice

Experience-dependent remodeling of synaptic connections is essential for learning and memory. Previous studies have shown that motor skill learning promotes the rapid formation of new spines in the motor cortex and the extent of spine remodeling strongly correlates with behavioral improvement after learning (Yang et al., 2009; Liston et al., 2013). To examine the effects of aging on motor learning-dependent spine plasticity, we trained young adult and old mice on the rotarod task for 2 days. Dendritic spines in the primary motor cortex were imaged before and after rotarod training to determine learning-induced spine formation and elimination (**Figure 3**). Consistent with previous findings (Yang et al., 2009, 2014), we found that in 4-month-old adult mice, rotarod training over 2 days significantly increased the formation of new spines in the motor cortex (7.1 ± 0.2% vs. 3.1 ± 0.2%; 605 spines, 4 mice; $P = 0.0286$; **Figures 3A,B**). By contrast, motor training had little effect on spine formation in old mice (4.0 ± 0.4% vs. 3.3 ± 0.3%; $P = 0.0857$). The degree of learning-induced spine formation was significantly lower in old mice as compared to that in young adults ($P = 0.0286$), indicating that learning-induced spine formation is compromised during aging. Moreover, we found that motor training for 2 days had no significant effect on dendritic spine elimination in young adult mice (3.5 ± 0.2% vs. 3.1 ± 0.4%; $P = 0.6286$) but lowered the elevated spine elimination in old mice (3.5 ± 0.6% vs. 5.2 ± 0.2%; $P = 0.0286$; **Figures 3A,C**), suggesting a beneficial effect of motor training in preventing age-related synapse loss.

Consistent with the reduction of new spine formation after learning, we found that old mice compared to young adults showed less performance improvement after training in the rotarod task (**Figure 3E**). Notably, we observed a strong

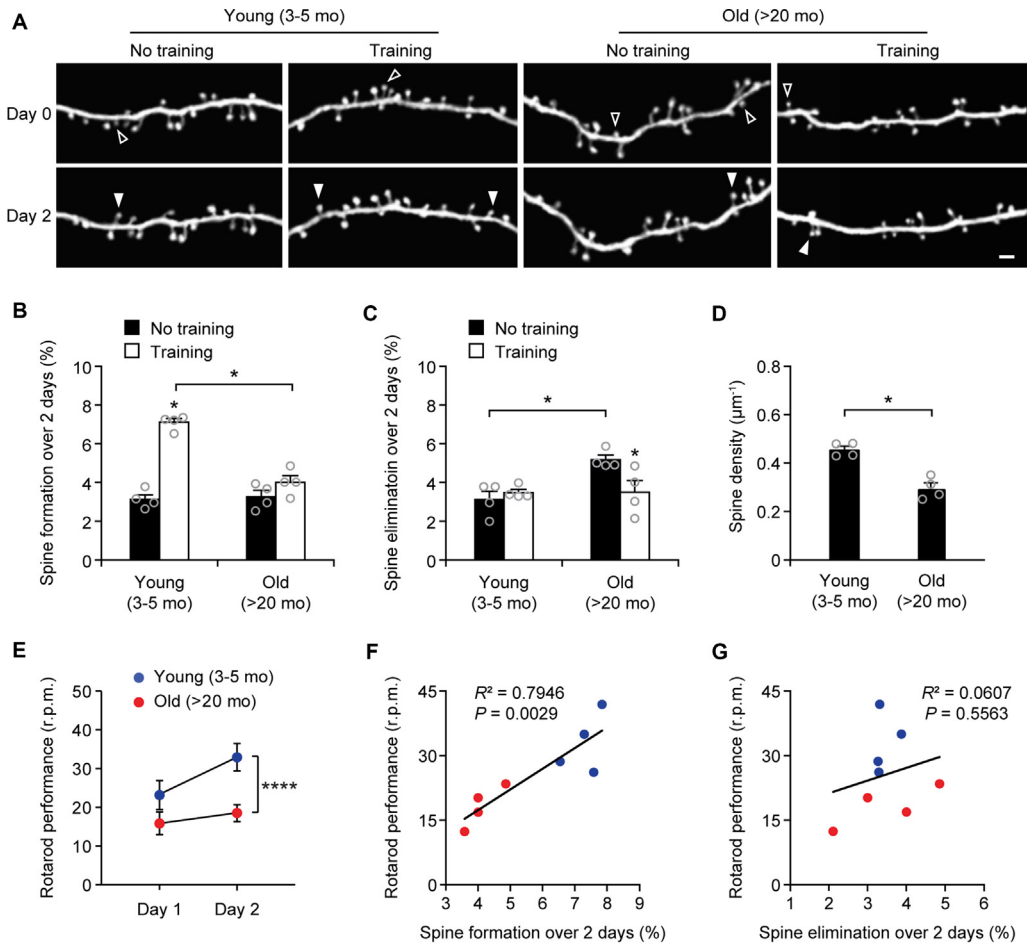

FIGURE 3 | Aging decreases learning-induced spine formation in the motor cortex. **(A)** *In vivo* time-lapse imaging of the same dendritic segments over 2 days in the primary motor cortex of young and old mice, with or without motor training. Empty and filled arrowheads indicate individual spines that were eliminated or newly formed, respectively. Scale bar, 2 μm. **(B)** Percentages of dendritic spines formed over 2 days in young and old mice. **(C)** Percentages of dendritic spines eliminated over 2 days in young and old mice. **(D)** The density of dendritic spines on the apical tuft dendrites of L5 pyramidal neurons in young adult and old mice. **(E)** Rotarod performance in young and old mice (n = 8 mice per group). After 2-day training, old mice showed less performance improvement than young mice (Day 1: t = 2.065; P = 0.0580; Day 2: t = 6.230; P < 0.0001). **(F,G)** Following 2-day training, animals' performance on the rotarod strongly correlated with the number of new spines formed but not with the number of spines eliminated (Pearson correlation). Throughout, individual circles represent data from a single mouse. Summary data are presented as mean ± SEM. *P < 0.05, ****P < 0.0001 by two-tailed Mann–Whitney test in panels **(B–D)** and two-tailed Student's t-test in panel **(E)**.

correlation between the percentages of new spines formed over 2-day training and the animals' performance on the rotarod on day 2 (Pearson correlation: R^2 = 0.7946, P = 0.0029; **Figure 3F**). There was no significant correlation between the rates of spine elimination over 2 days and the animals' rotarod performance on day 2 (Pearson correlation: R^2 = 0.0607, P = 0.5563; **Figure 3G**).

Motor Training-Evoked Neuronal Activity Is Lower in the Cortex of Old Mice

Because the neuronal activity is critical for regulating dendritic spine plasticity, we next examined the impact of aging on the activity of cortical neurons during behavior. In this experiment, head-restrained mice were trained on the treadmill task on the stage of a two-photon microscope (**Figure 4**). With the belt moving at a walking speed, the treadmill task is mild in intensity and requires little physical strength to achieve. Consistent with previous studies (Huang et al., 2016), naive mice displayed large percentages of untrained gait feature, such as drag, wobble, sweep, when they first walked on the treadmill, whereas the proportion of trained feature (i.e., steady run) increased after training (**Figure 4A**). Five hours after initial 1-h training, both young and adult mice showed substantial increases in the steady run in their gait patterns (post-training vs. pre-training: young, P < 0.0001; mature, P = 0.009, paired t-test), whereas old mice showed less improvement in treadmill performance (**Figure 4B**).

Using *in vivo* two-photon imaging, we recorded the Ca^{2+} activity of L5 pyramidal neurons in the primary motor cortex using transgenic mice (*Thy1*-GCaMP6s line 1) expressing the genetically encoded Ca^{2+} indicator GCaMP6s in L5 pyramidal neurons of the cortex (**Figure 4C**). We found that under the quiet resting state (i.e., treadmill off), the average integrated Ca^{2+} activity ($\Delta F/F_0$) of L5 somas was significantly lower in old

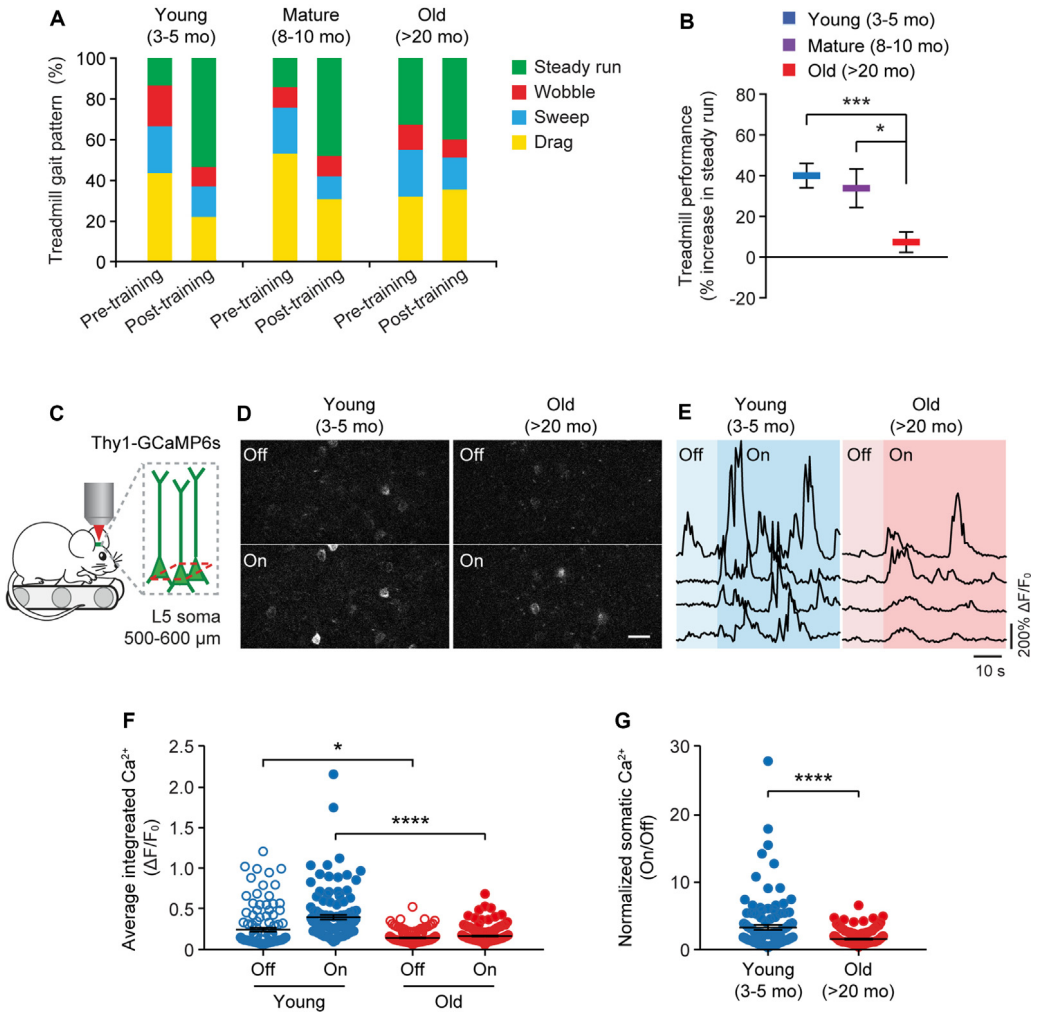

FIGURE 4 | Aging decreases neuronal calcium activity in the motor cortex during resting and movement states. **(A)** Analysis of the animals' gait patterns when walking on a treadmill. Old mice displayed higher proportions of drag, wobble, and sweep but less steady run after 1-h training. **(B)** Treadmill performance in young adults, mature adults, and old mice. Treadmill performance is expressed as a percent increase in the fraction of time spent in a steady run between post-training and pre-training (n = 10, 8, 13 mice per group). **(C)** Schematic showing two-photon Ca^{2+} imaging in the primary motor cortex of head-restrained mice walking on a treadmill. **(D)** Representative images of L5 somas expressing GCaMP6s when the treadmill is off and on. Scale bar, 20 μm. **(E)** Calcium fluorescence traces of representative pyramidal somas in young adult and old mice. **(F)** The average integrated activity of somatic calcium transients while the treadmill is off and on (Young: n = 116 cells from 6 mice; Old: n = 187 cells from 9 mice). **(G)** Normalized somatic calcium activity in young adult and old mice during treadmill training. Individual circles represent data from a single cell. Summary data are presented as mean ± SEM. $^*P < 0.05$, $^{***}P < 0.001$, $^{****}P < 0.0001$ by two-tailed Student's t-test in panel **(B)** and two-tailed Mann–Whitney tests in panels **(F,G)**.

mice compared to young adults (0.13 ± 0.01 vs. 0.24 ± 0.02; P = 0.0485; **Figures 4D–F**). When mice were trained on the treadmill (i.e., treadmill on), there was a marked increase in somatic Ca^{2+} levels relative to resting states in young adult mice (0.39 ± 0.03 vs. 0.24 ± 0.02; $P < 0.0001$; **Figures 4D–G**). Compared to young adults, both the absolute (0.15 ± 0.01 vs. 0.39 ± 0.03; $P < 0.0001$) and normalized (on/off: 1.41 ± 0.07 vs. 3.15 ± 0.36; $P < 0.0001$) levels of somatic Ca^{2+} during treadmill training were substantially lower in old mice (**Figures 4F,G**).

To rule out the possibility that the reduction of $\Delta F/F_0$ in old mice might be due to extensive changes of cytoplasmic GCaMP6s concentration, we performed immunostaining to characterize the protein levels of GCaMP6s in individual cells. As shown in **Figure 5A**, at both 4 and 23 months of age, GCaMP6s was primarily expressed in L5 of the motor cortex in *Thy1*-GCaMP6s line 1 mice. We found that the expression pattern of GCaMP6s was largely similar between young adults and old mice (**Figures 5A–C**). The average level of GCaMP6s per cell in old mice was about 1.1-folds of that in young adults (**Figures 5A–C**). Thus, the cellular concentration of GCaMP6s changed little between young adult and old mice, allowing for an appropriate comparison of $\Delta F/F_0$ between them. Together, these results show that aging decreases pyramidal neuronal activity in the motor cortex under both resting and movement states.

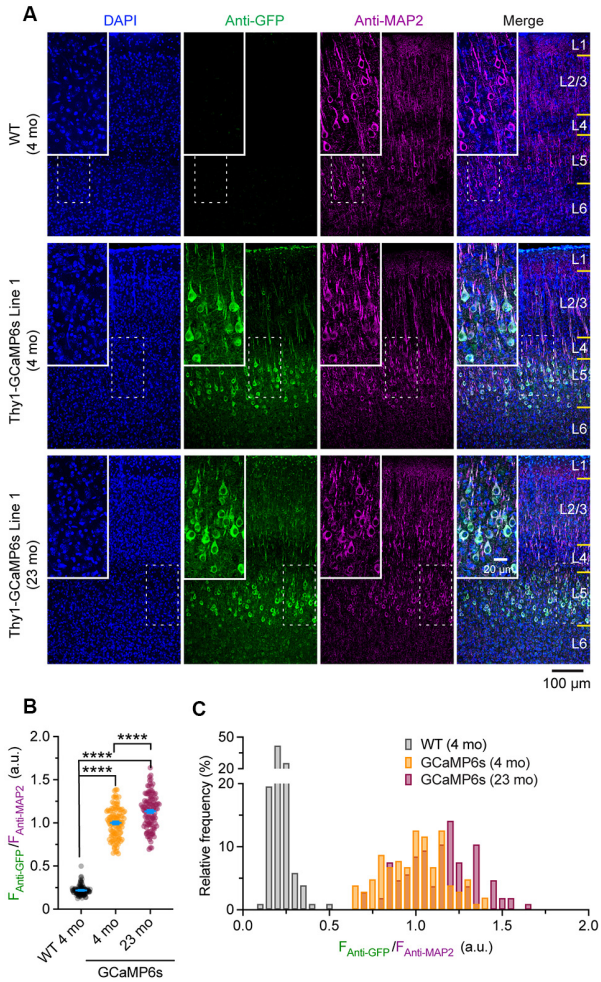

FIGURE 5 | Characterization of GCaMP6 expression in young adult and old mice. **(A)** Representative coronal sections of the mouse cortex stained for GFP and MAP2 in 4-month-old wild type (WT), 4- and 23-month-old transgenic *Thy1*-GCaMP6s line 1 mice. **(B)** Expression levels of GCaMP6s ($F_{Anti\text{-}GFP}/F_{Anti\text{-}MAP2}$) in individual L5 pyramidal neurons. **(C)** Distribution of GCaMP6s levels in individual neurons. Summary data are presented as mean ± SEM. ****$P < 0.0001$ by Kolmogorov–Smirnov tests.

DISCUSSION

Aging decreases synapse number and function in the brain and drives a progressive decline in cognition, yet the link between synaptic alterations and learning impairment during normal aging remains unclear. Using the *in vivo* imaging approach, we examined dendritic spine formation and elimination in response to motor skill learning in young adult and old mice. We found that spine elimination was higher in old than young adult mice under basal conditions, while motor learning-induced spine formation was reduced in old mice. Additionally, we found that motor training-evoked neuronal activity in the motor cortex was markedly decreased in old mice. These findings reveal age-related alterations in synaptic plasticity and neuronal activity in the mouse cortex *in vivo*.

With the high-resolution two-photon imaging technique and the behavioral learning assays, we sought to answer several long-standing questions regarding the effects of aging on synaptic plasticity in the mammalian brain. Specifically, how does aging affect the degree of synapse formation and elimination in the living cerebral cortex? Does advanced age compromise synaptic remodeling associated with learning and memory formation? To address these questions, we first compared the dynamics of dendritic spines between young adults (3–5 months), mature adults (8–10 months), and old mice (>20 months) in the basal state (i.e., no training). We found that in the sensory cortex, the elimination rate of existing spines is comparable between young and mature adults, but significantly higher in old mice. Aging has no significant effect on the rate of spine formation under basal conditions. A similar finding was also observed in the motor cortex. These findings support the notion that synapse loss is a prominent feature of the aged brain and suggest that the disruption of the synaptic connectivity established early in life may contribute to the decline of cognitive function during aging. It is worth noting that the results of the present study seem to contradict a recent report of elevated dendritic spine density and dynamics in the primary motor cortex of aged mice (Davidson et al., 2020). Such discrepancy can be attributed to different transgenic mouse lines (*Thy1*-YFP-H vs. *Thy1*-GFP line M) and types of observation windows (thinned skull vs. open skull) used for spine imaging, as well as different data analysis methods (manual vs. automated). Indeed, previous studies have linked different observation windows to different turnover rates of dendritic spines (Xu et al., 2007).

It is well established that sensory and behavioral experiences have a profound impact on synaptic connections in cortical circuits (Wiesel, 1982; Knott et al., 2002; Xu et al., 2009; Lai et al., 2012; Yang et al., 2014; Ma et al., 2016). We have previously shown that rotarod skill learning induces the rapid formation of new spines over days as well as the elimination of existing spines over a longer period (Yang et al., 2009). Importantly, the extent of spine remodeling correlates with behavioral improvement after learning, underscoring a critical role of structural synaptic plasticity in learning and memory formation. In this study, we examined dendritic spine formation and elimination in response to motor skill learning in the motor cortex of young adult and old mice. We found that in young adults, motor-learning induced a ∼5% increase in new spine formation. By contrast, old mice did not show an obvious increase in spine formation over the 2 days of motor training. This decrease of learning-induced new spine formation correlated with the compromised motor learning abilities in old mice. These results suggest that the reduction of learning-dependent synaptic plasticity may play a role in age-related cognitive decline in old mice, although the weakening of other organs, such as muscle and sensory organs, cannot be excluded.

Another interesting finding from the current study is that motor training improves the stability of existing spines in the old motor cortex, supporting the beneficial effects of exercise on brain function. It is well acknowledged that exercise counteracts cognitive decline in aging and neurodegenerative diseases (Ahlskog et al., 2011). Exercise has been shown to enhance

learning and hippocampal neurogenesis in aged mice (van Praag et al., 2005). At the level of synapses, exercise attenuates age-related changes in neuromuscular synapses (Valdez et al., 2010; Nishimune et al., 2012) and hippocampal synapses (Siette et al., 2013) in rodents. In conformity with these studies, our results provide evidence that motor training may help maintain synaptic connectivity in the old brain.

By performing Ca^{2+} imaging in the motor cortex of mice performing a treadmill task, we found that motor training-evoked neuronal activity is markedly lower in old mice relative to young adults. Together with the finding of decreased dendritic spine formation after motor training, these results suggest that cortical circuits in the old brain may be less responsive to modulation by learning experiences, and the plastic reserve of the brain declines during aging. Many age-related molecular changes in the brain and blood may contribute to the reduction of neuronal activity and synaptic plasticity in the cortex. Previous studies have shown that the amounts of synaptic proteins such as synaptophysin (Smith et al., 2000) and NMDA receptor subunits (GluN1, GluN2B; Magnusson et al., 2002) are decreased during aging. Moreover, age-related decline in protein expression of GluN1 and GluN2B subunits in both the frontal cortex and hippocampus correlates with impaired memory function in old rodents (Magnusson et al., 2007; Zhao et al., 2009). Additionally, emerging studies suggest that young blood contains specific factors that mediate age-associated changes in brain function (Katsimpardi et al., 2014; Middeldorp et al., 2016). A recent study reported that systemic factors enriched in young serum, such as thrombospondin-4 and SPARCL1, can act directly on neurons to promote synapse formation and NMDA receptor recruitment in cultured cells (Gan and Südhof, 2019). It would be interesting to examine whether the administration of these systemic factors into the old brain could improve synaptic plasticity and function *in vivo*.

It is important to point out that all the imaging experiments in this study were performed using fluorescence-expressing transgenic animals (*Thy1*-YFP-H and *Thy1*-GCaMP6s). Although we expect that these experiments will provide important information on age-related alterations of dendritic spine plasticity and neuronal function, some of the results could be confounded by the long-term expression of fluorescent protein in neurons. Future studies using other labeling methods, such as virus-mediated fluorescence expression, may help address these concerns.

In summary, we found that in the cortex of old mice, more dendritic spines were eliminated under basal conditions and fewer new spines were generated after learning. These findings reveal the effects of aging on the formation and maintenance of synaptic connections and provide the missing links between synaptic alterations and learning impairment during normal aging.

DATA AVAILABILITY STATEMENT

The original contributions presented in the study are included in the article, further inquiries can be directed to the corresponding author/s.

ETHICS STATEMENT

The animal study was reviewed and approved by Institutional Animal Care and Use Committees (IACUC) at New York University Medical Center and Columbia University Medical Center.

AUTHOR CONTRIBUTIONS

LH and GY designed research studies and wrote the manuscript. LH, HZ, KC, and GY conducted experiments. LH, HZ, KC, XC, and GY analyzed data. All authors contributed to data interpretation. All authors contributed to the article and approved the submitted version.

FUNDING

This work was partly supported by the American Federation for Aging Research (GY), Columbia University Medical Center Target of Opportunity Award (GY), National Natural Science Foundation of China (81871048 and 81741063 to LH), Guangdong Natural Science Foundation (2016A030313531 and 2018B030311034 to LH), and Guangdong Provincial Key R&D Programs (Key Technologies for Treatment of Brain Disorders 2018B030332001 to LH).

ACKNOWLEDGMENTS

We thank all the members of the Yang laboratory for comments on the manuscript.

REFERENCES

Ahlskog, J. E., Geda, Y. E., Graff-Radford, N. R., and Petersen, R. C. (2011). Physical exercise as a preventive or disease-modifying treatment of dementia and brain aging. *Mayo Clin. Proc.* 86, 876–884. doi: 10.4065/mcp.2011.0252

Barnes, C. A. (1979). Memory deficits associated with senescence: a neurophysiological and behavioral study in the rat. *J. Comp. Physiol. Psychol.* 93, 74–104. doi: 10.1037/h0077579

Barnes, C. A., and McNaughton, B. L. (1980). Physiological compensation for loss of afferent synapses in rat hippocampal granule cells during senescence. *J. Physiol.* 309, 473–485. doi: 10.1113/jphysiol.1980.sp013521

Bhatt, D. H., Zhang, S., and Gan, W. B. (2009). Dendritic spine dynamics. *Annu. Rev. Physiol.* 71, 261–282. doi: 10.1146/annurev.physiol.010908.163140

Brayne, C. (2007). The elephant in the room—healthy brains in later life, epidemiology and public health. *Nat. Rev. Neurosci.* 8, 233–239. doi: 10.1038/nrn2091

Brody, H. (1955). Organization of the cerebral cortex. III. A study of aging in the human cerebral cortex. *J. Comp. Neurol.* 102, 511–516. doi: 10.1002/cne.901020206

Buell, S. J., and Coleman, P. D. (1981). Quantitative evidence for selective dendritic growth in normal human aging but not in senile dementia. *Brain Res.* 214, 23–41. doi: 10.1016/0006-8993(81)90436-4

Burke, S. N., and Barnes, C. A. (2006). Neural plasticity in the ageing brain. *Nat. Rev. Neurosci.* 7, 30–40. doi: 10.1038/nrn1809

Cichon, J., and Gan, W. B. (2015). Branch-specific dendritic Ca^{2+} spikes cause persistent synaptic plasticity. *Nature* 520, 180–185. doi: 10.1038/nature14251

Cichon, J., Magrane, J., Shtridler, E., Chen, C., Sun, L., Yang, G., et al. (2020). Imaging neuronal activity in the central and peripheral nervous systems using new Thy1.2-GCaMP6 transgenic mouse lines. *J. Neurosci. Methods* 334:108535. doi: 10.1016/j.jneumeth.2019.108535

Coleman, P. D., and Flood, D. G. (1987). Neuron numbers and dendritic extent in normal aging and Alzheimer's disease. *Neurobiol. Aging* 8, 521–545. doi: 10.1016/0197-4580(87)90127-8

Davidson, A. M., Mejia-Gomez, H., Jacobowitz, M., and Mostany, R. (2020). Dendritic spine density and dynamics of layer 5 pyramidal neurons of the primary motor cortex are elevated with aging. *Cereb. Cortex* 30, 767–777. doi: 10.1093/cercor/bhz124

Deary, I. J., Corley, J., Gow, A. J., Harris, S. E., Houlihan, L. M., Marioni, R. E., et al. (2009). Age-associated cognitive decline. *Br. Med. Bull.* 92, 135–152. doi: 10.1093/bmb/ldp033

Dickstein, D. L., Kabaso, D., Rocher, A. B., Luebke, J. I., Wearne, S. L., and Hof, P. R. (2007). Changes in the structural complexity of the aged brain. *Aging Cell* 6, 275–284. doi: 10.1111/j.1474-9726.2007.00289.x

Dumitriu, D., Hao, J., Hara, Y., Kaufmann, J., Janssen, W. G., Lou, W., et al. (2010). Selective changes in thin spine density and morphology in monkey prefrontal cortex correlate with aging-related cognitive impairment. *J. Neurosci.* 30, 7507–7515. doi: 10.1523/JNEUROSCI.6410-09.2010

Flood, D. G. (1993). Critical issues in the analysis of dendritic extent in aging humans, primates and rodents. *Neurobiol. Aging* 14, 649–654. doi: 10.1016/0197-4580(93)90058-j

Flood, D. G., Buell, S. J., Horwitz, G. J., and Coleman, P. D. (1987). Dendritic extent in human dentate gyrus granule cells in normal aging and senile dementia. *Brain Res.* 402, 205–216. doi: 10.1016/0006-8993(87)90027-8

Gan, K. J., and Südhof, T. C. (2019). Specific factors in blood from young but not old mice directly promote synapse formation and NMDA-receptor recruitment. *Proc. Natl. Acad. Sci. U S A* 116, 12524–12533. doi: 10.1073/pnas.1902672116

Grutzendler, J., Kasthuri, N., and Gan, W. B. (2002). Long-term dendritic spine stability in the adult cortex. *Nature* 420, 812–816. doi: 10.1038/nature01276

Hayashi-Takagi, A., Yagishita, S., Nakamura, M., Shirai, F., Wu, Y. I., Loshbaugh, A. L., et al. (2015). Labelling and optical erasure of synaptic memory traces in the motor cortex. *Nature* 525, 333–338. doi: 10.1038/nature15257

Hedden, T., and Gabrieli, J. D. (2004). Insights into the ageing mind: a view from cognitive neuroscience. *Nat. Rev. Neurosci.* 5, 87–96. doi: 10.1038/nrn1323

Hof, P. R., and Morrison, J. H. (2004). The aging brain: morphomolecular senescence of cortical circuits. *Trends Neurosci.* 27, 607–613. doi: 10.1016/j.tins.2004.07.013

Hofer, S. B., Mrsic-Flogel, T. D., Bonhoeffer, T., and Hubener, M. (2009). Experience leaves a lasting structural trace in cortical circuits. *Nature* 457, 313–317. doi: 10.1038/nature07487

Huang, L., Cichon, J., Ninan, I., and Yang, G. (2016). Post-anesthesia AMPA receptor potentiation prevents anesthesia-induced learning and synaptic deficits. *Sci. Transl. Med.* 8:344ra385.doi: 10.1126/scitranslmed.aaf7151

Jacobs, B., Driscoll, L., and Schall, M. (1997). Life-span dendritic and spine changes in areas 10 and 18 of human cortex: a quantitative Golgi study. *J. Comp. Neurol.* 386, 661–680.

Katsimpardi, L., Litterman, N. K., Schein, P. A., Miller, C. M., Loffredo, F. S., Wojtkiewicz, G. R., et al. (2014). Vascular and neurogenic rejuvenation of the aging mouse brain by young systemic factors. *Science* 344, 630–634. doi: 10.1126/science.1251141

Kim, S. K., and Nabekura, J. (2011). Rapid synaptic remodeling in the adult somatosensory cortex following peripheral nerve injury and its association with neuropathic pain. *J. Neurosci.* 31, 5477–5482. doi: 10.1523/JNEUROSCI.0328-11.2011

Knott, G. W., Quairiaux, C., Genoud, C., and Welker, E. (2002). Formation of dendritic spines with GABAergic synapses induced by whisker stimulation in adult mice. *Neuron* 34, 265–273. doi: 10.1016/s0896-6273(02)00663-3

Lai, C. S., Franke, T. F., and Gan, W.-B. (2012). Opposite effects of fear conditioning and extinction on dendritic spine remodelling. *Nature* 483, 87–91. doi: 10.1038/nature10792

Liston, C., Cichon, J. M., Jeanneteau, F., Jia, Z., Chao, M. V., and Gan, W. B. (2013). Circadian glucocorticoid oscillations promote learning-dependent synapse formation and maintenance. *Nat. Neurosci.* 16, 698–705. doi: 10.1038/nn.3387

Luebke, J. I., Chang, Y. M., Moore, T. L., and Rosene, D. L. (2004). Normal aging results in decreased synaptic excitation and increased synaptic inhibition of layer 2/3 pyramidal cells in the monkey prefrontal cortex. *Neuroscience* 125, 277–288. doi: 10.1016/j.neuroscience.2004.01.035

Ma, L., Qiao, Q., Tsai, J. W., Yang, G., Li, W., and Gan, W. B. (2016). Experience-dependent plasticity of dendritic spines of layer 2/3 pyramidal neurons in the mouse cortex. *Dev. Neurobiol.* 76, 277–286. doi: 10.1002/dneu.22313

Magnusson, K. R., Nelson, S. E., and Young, A. B. (2002). Age-related changes in the protein expression of subunits of the NMDA receptor. *Mol. Brain Res.* 99, 40–45. doi: 10.1016/s0169-328x(01)00344-8

Magnusson, K. R., Scruggs, B., Zhao, X., and Hammersmark, R. (2007). Age-related declines in a two-day reference memory task are associated with changes in NMDA receptor subunits in mice. *BMC Neurosci.* 8:43. doi: 10.1186/1471-2202-8-43

Mervis, R. (1978). Structural alterations in neurons of aged canine neocortex: a Golgi study. *Exp. Neurol.* 62, 417–432. doi: 10.1016/0014-4886(78)90065-1

Middeldorp, J., Lehallier, B., Villeda, S. A., Miedema, S. S., Evans, E., Czirr, E., et al. (2016). Preclinical assessment of young blood plasma for Alzheimer disease. *JAMA Neurol.* 73, 1325–1333. doi: 10.1001/jamaneurol.2016.3185

Morrison, J. H., and Hof, P. R. (1997). Life and death of neurons in the aging brain. *Science* 278, 412–419. doi: 10.1126/science.278.5337.412

Morrison, J. H., and Hof, P. R. (2002). Selective vulnerability of corticocortical and hippocampal circuits in aging and Alzheimer's disease. *Prog. Brain Res.* 136, 467–486. doi: 10.1016/s0079-6123(02)36039-4

Mostany, R., Anstey, J. E., Crump, K. L., Maco, B., Knott, G., and Portera-Cailliau, C. (2013). Altered synaptic dynamics during normal brain aging. *J. Neurosci.* 33, 4094–4104. doi: 10.1523/JNEUROSCI.4825-12.2013

Nishimune, H., Numata, T., Chen, J., Aoki, Y., Wang, Y., Starr, M. P., et al. (2012). Active zone protein Bassoon co-localizes with presynaptic calcium channel, modifies channel function, and recovers from aging related loss by exercise. *PLoS One* 7:e38029. doi: 10.1371/journal.pone.0038029

Rhodes, M. G. (2004). Age-related differences in performance on the Wisconsin card sorting test: a meta-analytic review. *Psychol. Aging* 19, 482–494. doi: 10.1037/0882-7974.19.3.482

Shimamura, A. P. (1994). Neuropsychological perspectives on memory and cognitive decline in normal human aging. *Semin. Neurosci.* 6, 387–394. doi: 10.1006/smns.1994.1050

Siette, J., Westbrook, R. F., Cotman, C., Sidhu, K., Zhu, W., Sachdev, P., et al. (2013). Age-specific effects of voluntary exercise on memory and the older brain. *Biol. Psychiatry* 73, 435–442. doi: 10.1016/j.biopsych.2012.05.034

Smith, T. D., Adams, M. M., Gallagher, M., Morrison, J. H., and Rapp, P. R. (2000). Circuit-specific alterations in hippocampal synaptophysin immunoreactivity predict spatial learning impairment in aged rats. *J. Neurosci.* 20, 6587–6593. doi: 10.1523/JNEUROSCI.20-17-06587.2000

Terry, R. D., and Katzman, R. (2001). Life span and synapses: will there be a primary senile dementia? *Neurobiol. Aging* 22, 347–348; discussion 353–344. doi: 10.1016/s0197-4580(00)00250-5

Valdez, G., Tapia, J. C., Kang, H., Clemenson, G. D. Jr., Gage, F. H., Lichtman, J. W., et al. (2010). Attenuation of age-related changes in mouse neuromuscular synapses by caloric restriction and exercise. *Proc. Natl. Acad. Sci. U S A* 107, 14863–14868. doi: 10.1073/pnas.1002220107

van Praag, H., Shubert, T., Zhao, C., and Gage, F. H. (2005). Exercise enhances learning and hippocampal neurogenesis in aged mice. *J. Neurosci.* 25, 8680–8685. doi: 10.1523/JNEUROSCI.1731-05.2005

West, M. J., Coleman, P. D., Flood, D. G., and Troncoso, J. C. (1994). Differences in the pattern of hippocampal neuronal loss in normal ageing and Alzheimer's disease. *Lancet* 344, 769–772. doi: 10.1016/s0140-6736(94)92338-8

Wiesel, T. N. (1982). Postnatal development of the visual cortex and the influence of environment. *Nature* 299, 583–591. doi: 10.1038/299583a0

Xu, H.-T., Pan, F., Yang, G., and Gan, W.-B. (2007). Choice of cranial window type for *in vivo* imaging affects dendritic spine turnover in the cortex. *Nat. Neurosci.* 10, 549–551. doi: 10.1038/nn1883

Xu, T., Yu, X., Perlik, A. J., Tobin, W. F., Zweig, J. A., Tennant, K., et al. (2009). Rapid formation and selective stabilization of synapses for enduring motor memories. *Nature* 462, 915–919. doi: 10.1038/nature08389

Yang, G., Lai, C. S., Cichon, J., Ma, L., Li, W., and Gan, W. B. (2014). Sleep promotes branch-specific formation of dendritic spines after learning. *Science* 344, 1173–1178. doi: 10.1126/science.1249098

Yang, G., Pan, F., Chang, P. C., Gooden, F., and Gan, W. B. (2013). Transcranial two-photon imaging of synaptic structures in the cortex of awake head-restrained mice. *Methods Mol. Biol.* 1010, 35–43. doi: 10.1007/978-1-62703-411-1_3

Yang, G., Pan, F., and Gan, W. B. (2009). Stably maintained dendritic spines are associated with lifelong memories. *Nature* 462, 920–924. doi: 10.1038/nature08577

Yang, G., Pan, F., Parkhurst, C. N., Grutzendler, J., and Gan, W. B. (2010). Thinned-skull cranial window technique for long-term imaging of the cortex in live mice. *Nat. Protoc.* 5, 201–208. doi: 10.1038/nprot.2009.222

Zelinski, E. M., and Burnight, K. P. (1997). Sixteen-year longitudinal and time lag changes in memory and cognition in older adults. *Psychol. Aging* 12, 503–513. doi: 10.1037/0882-7974.12.3.503

Zhao, X., Rosenke, R., Kronemann, D., Brim, B., Das, S. R., Dunah, A. W., et al. (2009). The effects of aging on *N*-methyl-D-aspartate receptor subunits in the synaptic membrane and relationships to long-term spatial memory. *Neuroscience* 162, 933–945. doi: 10.1016/j.neuroscience.2009.05.018

Zhao, R., Zhou, H., Huang, L., Xie, Z., Wang, J., Gan, W. B., et al. (2018). Neuropathic pain causes pyramidal neuronal hyperactivity in the anterior cingulate cortex. *Front. Cell. Neurosci.* 12:107. doi: 10.3389/fncel.2018.00107

Zuo, Y., Lin, A., Chang, P., and Gan, W. B. (2005). Development of long-term dendritic spine stability in diverse regions of cerebral cortex. *Neuron* 46, 181–189. doi: 10.1016/j.neuron.2005.04.001

Conflict of Interest: The authors declare that the research was conducted in the absence of any commercial or financial relationships that could be construed as a potential conflict of interest.

frontiers in Neural Circuits

ORIGINAL RESEARCH
published: 14 April 2021
doi: 10.3389/fncir.2021.643230

Whole-Brain Mapping the Direct Inputs of Dorsal and Ventral CA1 Projection Neurons

Sijue Tao[1,2], Yihang Wang[2], Jundan Peng[2], Yang Zhao[2], Xiaobin He[2,3], Xuefeng Yu[5], Qing Liu[2,3,4,6], Sen Jin[5]* and Fuqiang Xu[1,2,3,4,6,7]**

[1] Wuhan National Laboratory for Optoelectronics, Huazhong University of Science and Technology, Wuhan, China, [2] State Key Laboratory of Magnetic Resonance and Atomic and Molecular Physics, Key Laboratory of Magnetic Resonance in Biological Systems, Wuhan Center for Magnetic Resonance, Wuhan Institute of Physics and Mathematics, Innovation Academy for Precision Measurement Science and Technology, Chinese Academy of Sciences, Wuhan, China, [3] University of Chinese Academy of Sciences, Beijing, China, [4] Shenzhen Key Lab of Neuropsychiatric Modulation, Guangdong Provincial Key Laboratory of Brain Connectome and Behavior, CAS Key Laboratory of Brain Connectome and Manipulation, The Brain Cognition and Brain Disease Institute (BCBDI), Shenzhen Institute of Advanced Technology, Chinese Academy of Sciences, Shenzhen, China, [5] Materials and Interfaces Center, Shenzhen Institute of Advanced Technology, Chinese Academy of Sciences, Shenzhen, China, [6] Shenzhen-Hong Kong Institute of Brain Science-Shenzhen Fundamental Research Institutions, Shenzhen, China, [7] Center for Excellence in Brain Science and Intelligence Technology, Chinese Academy of Sciences, Shanghai, China

The CA1, an important subregion of the hippocampus, is anatomically and functionally heterogeneous in the dorsal and ventral hippocampus. Here, to dissect the distinctions between the dorsal (dCA1) and ventral CA1 (vCA1) in anatomical connections, we systematically analyzed the direct inputs to dCA1 and vCA1 projection neurons (PNs) with the rabies virus-mediated retrograde trans-monosynaptic tracing system in Thy1-Cre mice. Our mapping results revealed that the input proportions and distributions of dCA1 and vCA1 PNs varied significantly. Inside the hippocampal region, dCA1 and vCA1 PNs shared the same upstream brain regions, but with distinctive distribution patterns along the rostrocaudal axis. The intrahippocampal inputs to the dCA1 and vCA1 exhibited opposite trends, decreasing and increasing gradually along the dorsoventral axis, respectively. For extrahippocampal inputs, dCA1 and vCA1 shared some monosynaptic projections from certain regions such as pallidum, striatum, hypothalamus, and thalamus. However, vCA1, not dCA1, received innervations from the subregions of olfactory areas and amygdala nuclei. Characterization of the direct input networks of dCA1 and vCA1 PNs may provide a structural basis to understand the differential functions of dCA1 and vCA1.

Keywords: dorsal CA1, ventral CA1, projection neurons, direct inputs, rabies virus tracing

OPEN ACCESS

Edited by:
Yoshiyuki Kubota, National Institute for Physiological Sciences (NIPS), Japan

Reviewed by:
Kelly Dougherty, Rhodes College, United States
Takuya Sasaki, The University of Tokyo, Japan

***Correspondence:**
Qing Liu
liuqing@wipm.ac.cn
Sen Jin
sen.jin@siat.ac.cn
Fuqiang Xu
fuqiang.xu@wipm.ac.cn

Received: *17 December 2020*
Accepted: *01 March 2021*
Published: *14 April 2021*

Citation:
Tao S, Wang Y, Peng J, Zhao Y, He X, Yu X, Liu Q, Jin S and Xu F (2021) Whole-Brain Mapping the Direct Inputs of Dorsal and Ventral CA1 Projection Neurons. Front. Neural Circuits 15:643230. doi: 10.3389/fncir.2021.643230

INTRODUCTION

Since the dorsal and ventral hippocampi are proposed to participate in different functions (Amaral and Witter, 1989; Moser et al., 1995), evidence on the anatomical and functional segregations along the dorsoventral axis (also referred to as the longitudinal or septotemporal axis) has been cumulated (Dong et al., 2009; Fanselow and Dong, 2010; Bannerman et al., 2014; Strange et al., 2014). Generally, the dorsal hippocampus encodes spatial and cognitive information (Moser et al., 1995; Rogers and Kesner, 2006; Taube, 2007; Kim et al., 2018), while the ventral hippocampus processes emotion-related information (Kjelstrup et al., 2002; Maren and Holt, 2004; Ruediger et al., 2012; Chawla et al., 2018; McDonald et al., 2018). Structurally, spatial and non-spatial afferents to the hippocampus are relatively segregated along the dorsoventral axis (Andersen et al., 2006; Leonardo et al., 2006; Hunsaker et al., 2008; Dong et al., 2009; Fanselow and Dong, 2010; Strange et al., 2014). Differences in hippocampal connectivity along the dorsoventral axis may explain functional diversifications of the hippocampus.

As a pivotal subregion of hippocampus, the CA1 is important for the integration of different streams of information and participation in many hippocampus-related behaviors such as memory, cognition, and emotion (Lisman and Otmakhova, 2001; Cenquizca and Swanson, 2007; Igarashi et al., 2014; Kaifosh and Losonczy, 2016). Previous studies using classical tracers have provided much information about the classic extrinsic and intrinsic hippocampal circuitry of CA1. For example, CA3 projects to CA1 *via* their ipsilateral Schaffer collaterals and contralateral commissural fibers (Nakashiba et al., 2008), the entorhinal cortex (ENT) provides inputs through the temporo-ammonic pathway (Witter et al., 2000; van Strien et al., 2009), and the medial septum and diagonal band (MS-DB) areas correlate with CA1 as well (Mamad et al., 2015; Muller and Remy, 2018). Additionally, some studies have demonstrated functional and anatomical segregations between dorsal and ventral CA1 regions (referred to as dCA1 and vCA1). Literature has shown that dCA1 processes information involved in spatial location and memory (Hunsaker et al., 2008; Fanselow and Dong, 2010), while the vCA1 modulates mood-related behavior like stress and anxiety (Jacobson and Sapolsky, 1991; Parfitt et al., 2017; Jimenez et al., 2018; Padilla-Coreano et al., 2019). Distinctive heterogeneities between dCA1 and vCA1 were also found in dendritic morphology, synaptic physiology, intrinsic excitability, and gene expressions (Leonardo et al., 2006; Dougherty et al., 2012, 2013; Malik et al., 2016; Malik and Johnston, 2017; Evans and Dougherty, 2018; Dougherty, 2020).

However, traditional tracers are unable to exclusively map the cell-type specific monosynaptic input networks. There is also a relative paucity of systematic analysis and comparison of differences in the presynaptic circuit of dCA1 and vCA1 quantitatively. This paper focuses on systematic quantification and detailed analysis of the direct inputs of projection neurons (PNs) in dCA1 and vCA1. By employing the genetically modified rabies virus (RV) tracing system and Thy1-Cre transgenic mice, we represented the complex and varied circuity of CA1 along the hippocampal dorsoventral axis. Our whole-brain mapping revealed that inputs to the dCA1 and vCA1 PNs were different along the rostrocaudal axis (RC axis): vCA1 PNs directly integrated information from both intrinsic and extrinsic hippocampal subregions, while the dCA1 PNs preferentially received information from intrinsic hippocampal subregions.

RESULTS

Overview of the Whole-Brain Inputs to Dorsal and Ventral CA1 Projection Neurons

We applied the RV-based monosynaptic tracing system to Thy1-Cre mice ($N = 4$ in each tracing group) in which the hippocampal PNs expressed Cre recombinase (**Figure 1A**) to identify the monosynaptic inputs of PNs in dCA1 and vCA1. For both tracing groups, the starter cells were restricted to the injected dCA1 and vCA1 areas and distributed across the RC range of the injected site with peak around the targeted coordinates (**Figures 1D,G**). We counted the number of the starter cells (coexpressing GFP and DsRed) and RV-labeled input neurons (only expressing DsRed) within each brain region or subregion (**Figures 1C,F**).

For quantitative analysis, we counted 21,526–24,727 input neurons in each brain of the dCA1 tracing group and 37,971–58,357 input neurons in each brain of the vCA1 tracing group (**Figures 1E,H**; see **Supplementary Table 1** for specific data values). Then, we calculated the mean convergence index (defined as the number of whole-brain presynaptic DsRed+ cells divided by the number of starter cells) of both tracing groups. The mean convergence index of the dCA1 tracing group was 30.54 ± 1.60 (mean ± SEM) and that of the vCA1 tracing group was 28.40 ± 1.15. Since there was no significant difference in convergence index ($P = 0.317$) between the two experiment groups, the differences in the monosynaptic afferents represent the differences in the connection strength between the CA1 PNs and their upstream neurons.

Quantitative analysis of the whole-brain connections to the dCA1 and vCA1 PNs revealed that they both received extensive inputs from the brain regions along the RC axis (**Figure 2A**). To compare the input distribution patterns in each brain region of the two groups, the number of the input neurons within each brain region from bilateral hemispheres was normalized relative to the total number of input neurons in the whole brain. Our results showed that most of the inputs to the dCA1 PNs were observed within the HIP (79.19 ± 2.12%), followed by isocortex (10.23 ± 2.53%), and thalamus (TH) (6.10 ± 2.33%). The other regions, such as pallium (PAL) (3.42 ± 0.34%), striatum (STR) (0.28 ± 0.08%), and hypothalamus (HY) (0.40 ± 0.08%) were sparsely labeled (**Figures 2A,B**). Meanwhile, our results revealed that most of the input neurons to vCA1 PNs were also from the HIP (61.09 ± 1.70%), along with minor contributions of widely distributed inputs from TH (7.98 ± 1.28%), isocortex (0.26 ± 0.14%), PAL (6.25 ± 0.22%), STR (1.24 ± 0.09%), and HY (1.39 ± 0.19%). However, the olfactory area (OLF) (12.01 ± 1.41%) and amygdala nuclei of cortical subplate

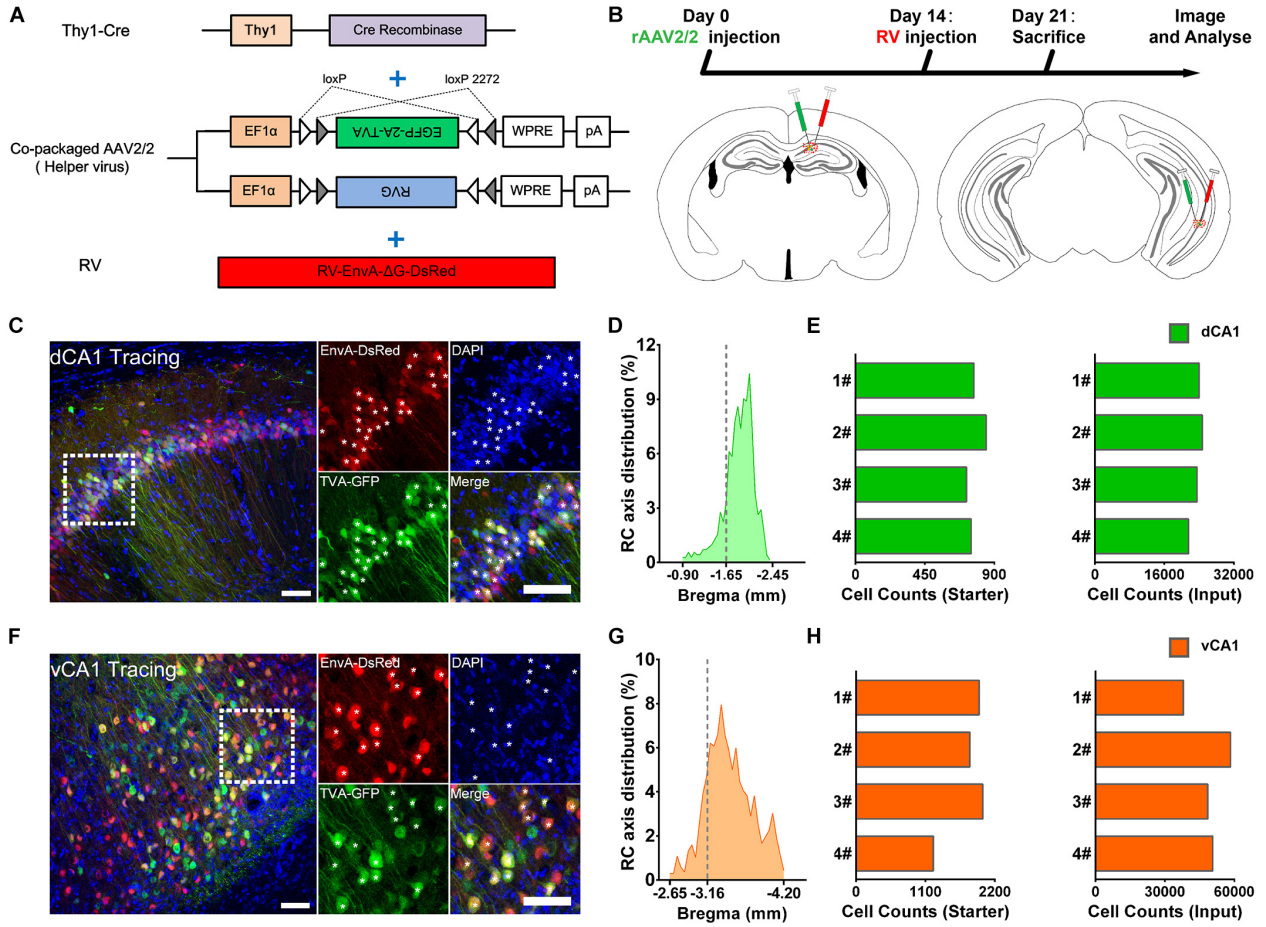

FIGURE 1 | Experimental procedures for the cell-type-specific retrograde monosynaptic tracing of dorsal CA1 or ventral CA1 PNs. **(A)** Thy1-Cre transgenic mice treated with co-packaged recombinant adeno-associated virus (AAV) strains and rabies virus (RV). **(B)** Experimental design showing timeline and injection site for dCA1 and vCA1 tracing group. **(C,F)** Representative images of coronal brain sections containing the injection sites and the magnifications of the starter cells (**C**, the dorsal CA1 tracing group; **(E)**, the ventral CA1 tracing group). The starter cells coexpressing GFP and DsRed are indicated by white asterisks. Scale bar: 50 μm. **(D,G)** Distribution patterns of the starter cells in the injected CA1 regions as detected along the RC axis. **(E,H)** Numbers of the starter cells and numbers of input neurons in whole brain in each mouse of dCA1 and vCA1 tracing groups (quantified with all slices; *N* = 4).

(CTXsp) (7.51 ± 0.53%) both projected to the vCA1 but not dCA1 PNs (**Figures 2A,B**).

Both Dorsal and Ventral CA1 Projection Neurons Receive Extensive Intrahippocampal Inputs

We found it was very hard to separate ipsilateral CA1-to-CA1 and ipsilateral SUB-to-CA1 inputs near the injection site. Therefore, we analyzed the intrahippocampal inputs in the contralateral CA1, bilateral CA2, bilateral CA3, and bilateral ENT in this paper. Our results showed that the HIP projects to both dCA1 and vCA1 PNs (**Figures 2B**, **3**, **4**), dominantly from the ipsilateral intrahippocampus in both tracing groups (**Figures 5D,E** and **Supplementary Table 2**). The quantitative comparison showed that the bilateral intrahippocampal monosynaptic inputs to dCA1 PNs were stronger than those to vCA1 PNs (dCA1: 24.15 ± 1.19; vCA1: 17.24 ± 0.83, $P < 0.01$) (**Figure 2C**). Meanwhile, we found that the intrahippocampal inputs to dCA1 and vCA1 PNs shared quite different distribution patterns along both transverse and rostrocaudal axes (**Figures 3**, **4**).

CA3 projects densely to the CA1 region *via* the Schaffer Collateral pathway and contralateral commissural pathway (Andersen et al., 2006; Schultz and Engelhardt, 2014). According to our calculations, CA3 inputs were made up of 84.29 ± 1.52% and 75.50 ± 2.56% of the total HIP inputs to the dCA1 and vCA1 PNs, respectively, as the largest input contribution to both tracing groups. Between the two groups, we found that the connection strength of CA3-dCA1 PNs and CA3-vCA1 PNs differed quantitatively (dCA1: 20.40 ± 1.29 versus vCA1: 13.03 ± 0.78, $P < 0.01$) (**Figure 5A**). The input strength differences of CA3 to dCA1 and vCA1 were bilateral and significant in contralateral (dCA1: ipsi-CSI = 11.36 ± 0.77, vCA1: ipsi-CSI = 9.11 ± 0.49, $P < 0.05$; dCA1: contra-CSI = 9.04 ± 0.64; vCA1: contra-CSI = 3.91 ± 0.30, $P < 0.01$) (**Figures 5B,C**). Along the radial axis, the CA3 input neurons of both tracing

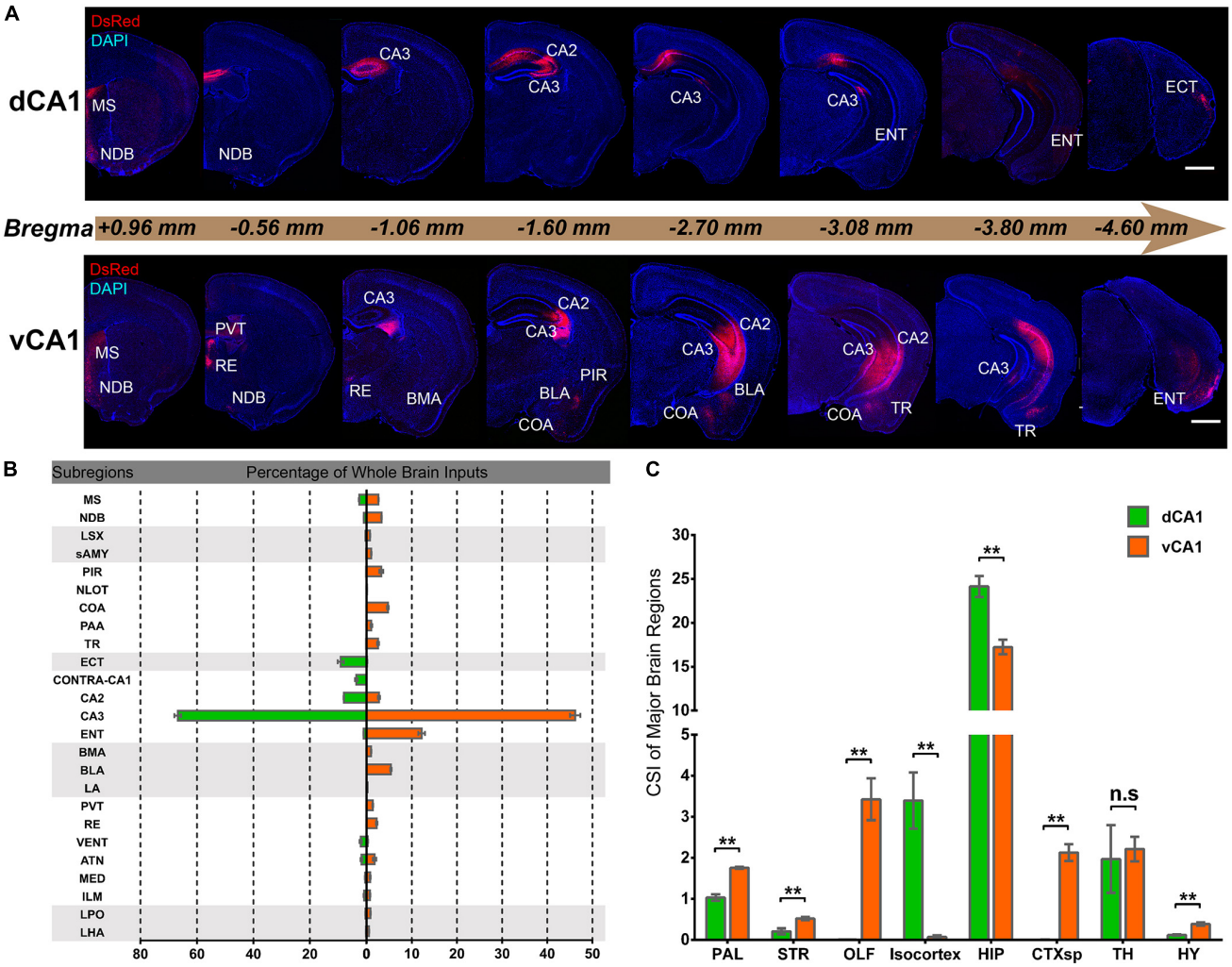

FIGURE 2 | Distribution patterns of whole-brain inputs to dorsal or ventral CA1 PNs. **(A)** Representative coronal sections showing labeling of monosynaptic inputs to the dorsal or ventral CA1 PNs along the RC axis. Scale bar: 1 mm. **(B)** The proportion of input neurons within subregions of the whole brain in two tracing groups, quantified with all slices (left, dCA1 tracing group; right, vCA1 tracing group). **(C)** The CSI of eight major input brain regions, quantified with all slices. n.s., no significant difference; $^{**}P < 0.01$.

groups were mostly located in both the sublayer and deep layer of the stratum pyramidale (SP) (**Figures 3A,B**). However, both the dorsoventral and transverse distributions of the CA3 input cells were quite different between the two groups. The bilateral CA3 input neurons of the dCA1 group mostly resided in the rostral part (**Figures 3**, **4**). The bilateral CA3 input neurons of the vCA1 group disseminated in both rostral and caudal parts but were largely located in the caudal part (**Figures 3C**, **4C**). For the dCA1 group, the input neurons in the rostral part of bilateral CA3 were distributed in both distal and proximal regions (**Figures 3A**, **4A**), and the input neurons in the caudal part of CA3 were only found in the proximal region bilaterally (**Figures 3B**, **4B**). For the vCA1 group, input neurons in the rostral part of CA3 were mostly situated in the distal region bilaterally (**Figures 3A**, **4A**), and the input neurons in the caudal part of CA3 were located in the middle region bilaterally (**Figures 3B**, **4B**).

We have found some DsRed+ neurons in contralateral CA1 of the dCA1 but not the vCA1 tracing group (**Figure 4**). Our analysis demonstrated that contralateral CA1 made almost no interhemispheric/contralateral connections to vCA1 PNs (only two cells were found in mouse 1 in contralateral CA1 of the vCA1 tracing group, data not shown) (**Figures 4A,B**). Some labeled input neurons were discovered in the contralateral CA1 for dCA1 PNs (dCA1: 1.05 ± 0.22) (**Figures 4**, **5C**). Furthermore, we analyzed the cell body distribution details of input neurons in contra-CA1 of the dCA1 tracing group. Here, the PNs received integrated contralateral inputs from the distal region in rostral CA1 (**Figure 4A**), with very few projections from the caudal CA1 (**Figure 4B**).

The entorhinal area (ENT) is regarded as the core of the parahippocampal region, since it has extensive reciprocal connections with the hippocampal region. In our data, ENT

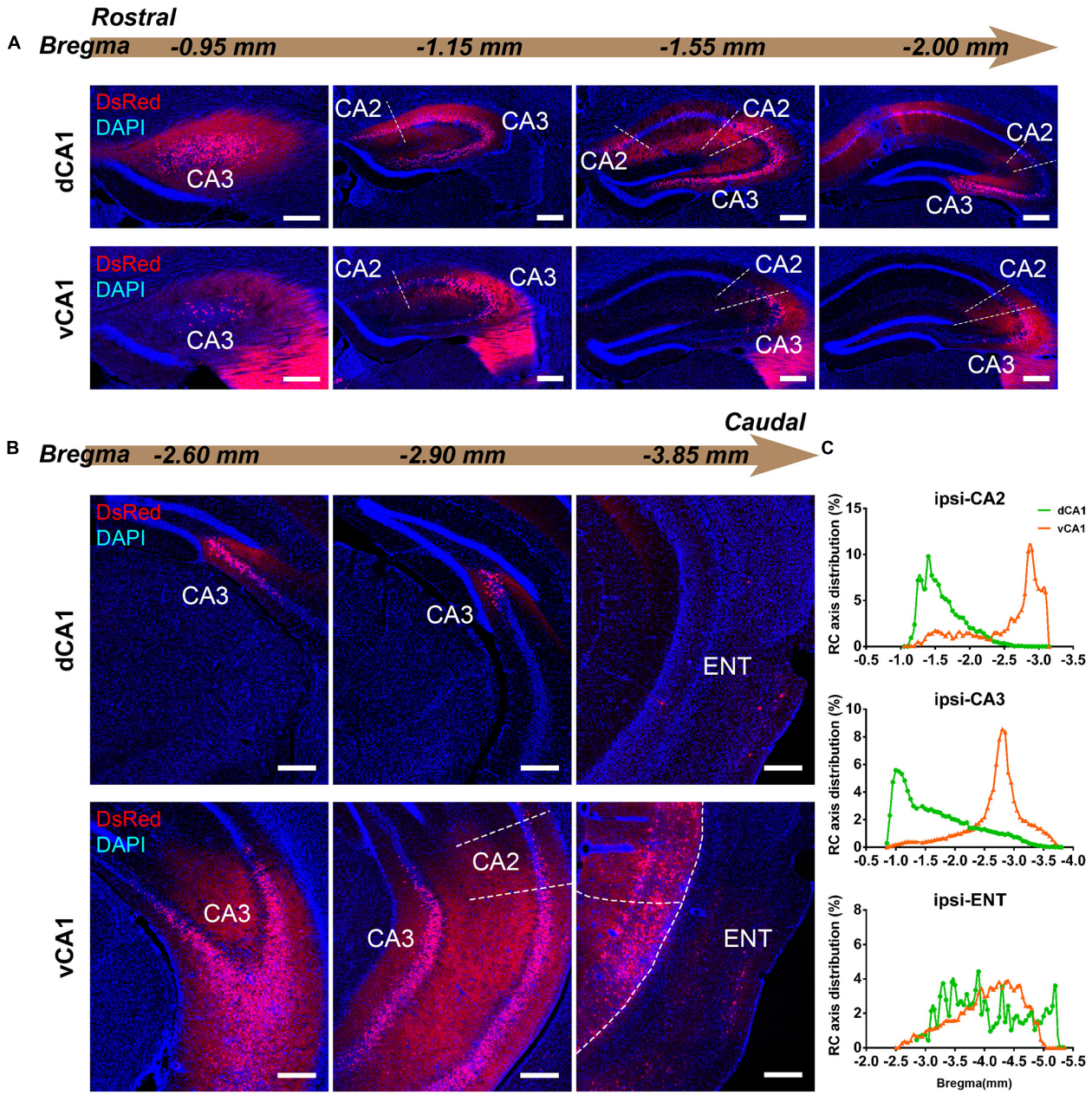

FIGURE 3 | Inputs to CA1 PNs from ipsilateral HIP subregions. **(A,B)** Representative images showing distributions of the input neurons located in ipsilateral HIP. Scale bar: 250 μm. **(C)** Distribution patterns of the input neurons along the RC axis in different subregions of the ipsilateral HIP. In the ipsilateral HIP, the input neurons were found located in CA2, CA3, and ENT in both tracing groups.

was an essential input source of whole brain to the vCA1 but not dCA1 PNs (dCA1: 0.95 ± 0.19%; vCA1: 12.19 ± 1.46%). Analysis revealed that vCA1 PNs received more inputs from ENT than dCA1 (dCA1: 0.29 ± 0.06 versus vCA1: 3.4 ± 0.47, $P < 0.01$) (**Figure 5A**). Meanwhile, in the dCA1 group, the PNs only integrated inputs from ipsilateral ENT (**Figure 3B**). In the vCA1 group, the PNs integrated inputs from bilateral ENT (**Figures 3B**, **4B**). Of these, the lateral ENT (ENTl) projections are stronger than the medial ENT (ENTm) in both groups (**Figure 5F**). In the case of ENTl projections, a significant difference was found between the two groups, with stronger connections in the ENTl-vCA1 projection than in the ENTl-dCA1 (dCA1: 0.28 ± 0.06 versus vCA1: 2.55 ± 0.33, $P < 0.01$) (**Figure 5F**). No ENTm projections were found in the dCA1 tracing group (**Figure 5F**). Furthermore, the distribution patterns of ENT input neurons were different along the RC axis. In the dCA1 tracing group, the labeled neurons were distributed evenly along the RC axis in ipsilateral

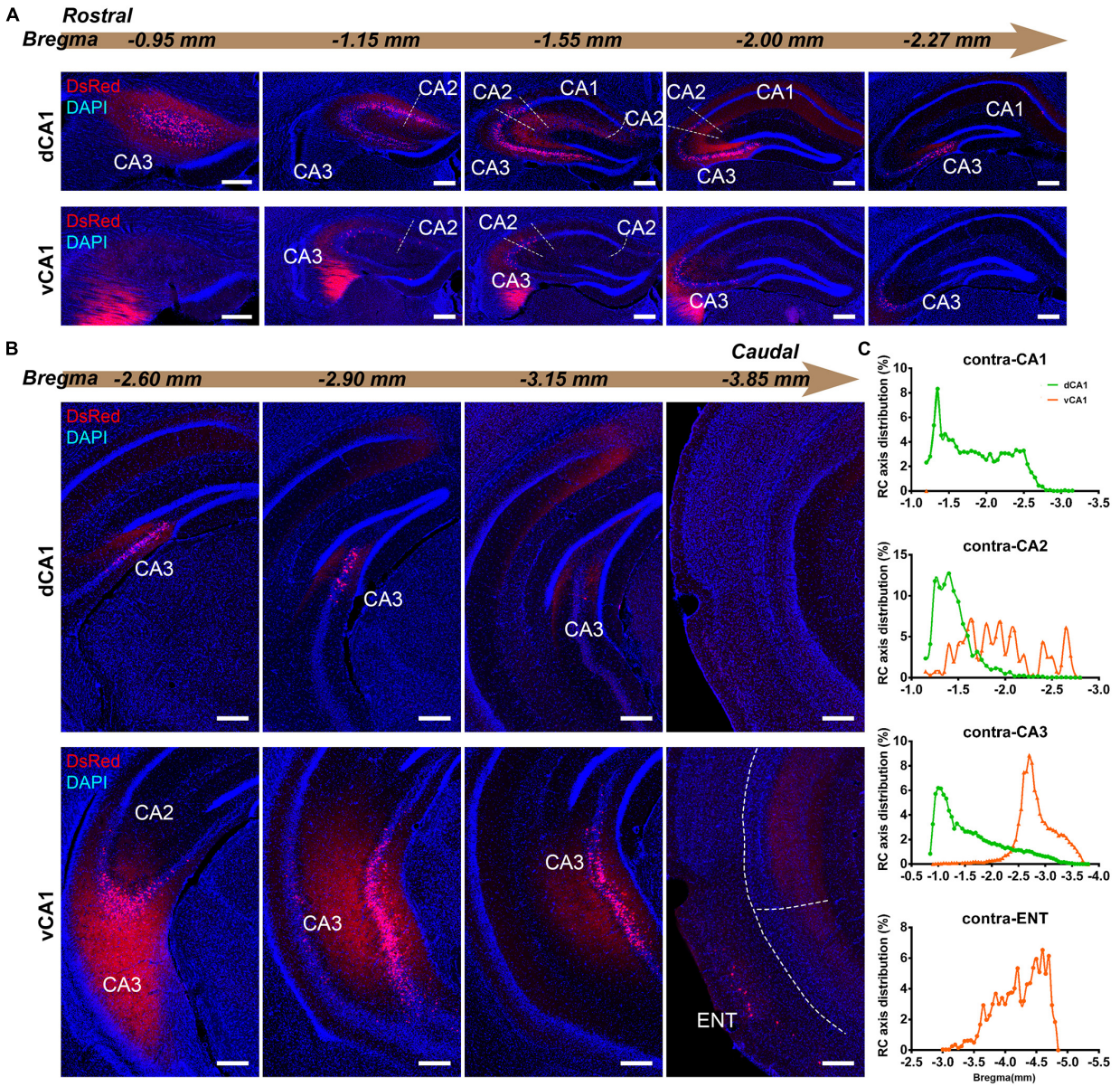

FIGURE 4 | Inputs to CA1 PNs from contralateral HIP subregions. **(A,B)** Representative images showing distributions of the input neurons located in contralateral HIP. Scale bar: 250 μm. **(C)** Distribution patterns of the input neurons along the RC axis in different subregions of the contralateral HIP. In the contralateral HIP, the input neurons were found located in the CA1, CA2, and CA3 for the dorsal CA1 tracing group and in the CA1, CA2, CA3, and ENT for the ventral CA1 tracing group.

ENT (**Figure 3C**). In the vCA1 tracing group, the number of input neurons increased along the RC axis in bilateral ENT (**Figures 3C**, **4C**).

Earlier researches reported that the projections from the CA2 to CA1 spread along the dorsoventral axis of the hippocampus (Ropireddy et al., 2012; Kohara et al., 2014; Dudek et al., 2016). In our results, robust labeling signals were observed in CA2 in both tracing groups. The analysis showed that dCA1 appears to receive stronger CA2 inputs relative to vCA1 bilaterally, with CSIs being 2.41 ± 0.08 and 0.76 ± 0.12, respectively ($P < 0.01$) (**Figure 5A**). The input CSIs of ipsilateral CA2 to dCA1 and vCA1 PNs were 1.68 ± 0.08 and 0.73 ± 0.11 ($P < 0.01$) and the input CSIs of contralateral CA2 to dCA1 and vCA1 PNs were 0.73 ± 0.04 and 0.02 ± 0.01 ($P < 0.01$) (**Figures 5B,C**). Essentially, all of the labeled CA2 cells were located in the SP (**Figures 3**, **4**). In both groups, the labeled neurons in CA2 were mostly found in the ipsilateral part (**Figures 5D,E**). For the dCA1 tracing group, the input cells in CA2 were mostly located in the rostral hippocampus (**Figures 3A,C**, **4A,C**). For the vCA1 tracing group, the input cells in CA2 were mostly located in the caudal hippocampus (**Figures 3B,C**, **4B,C**).

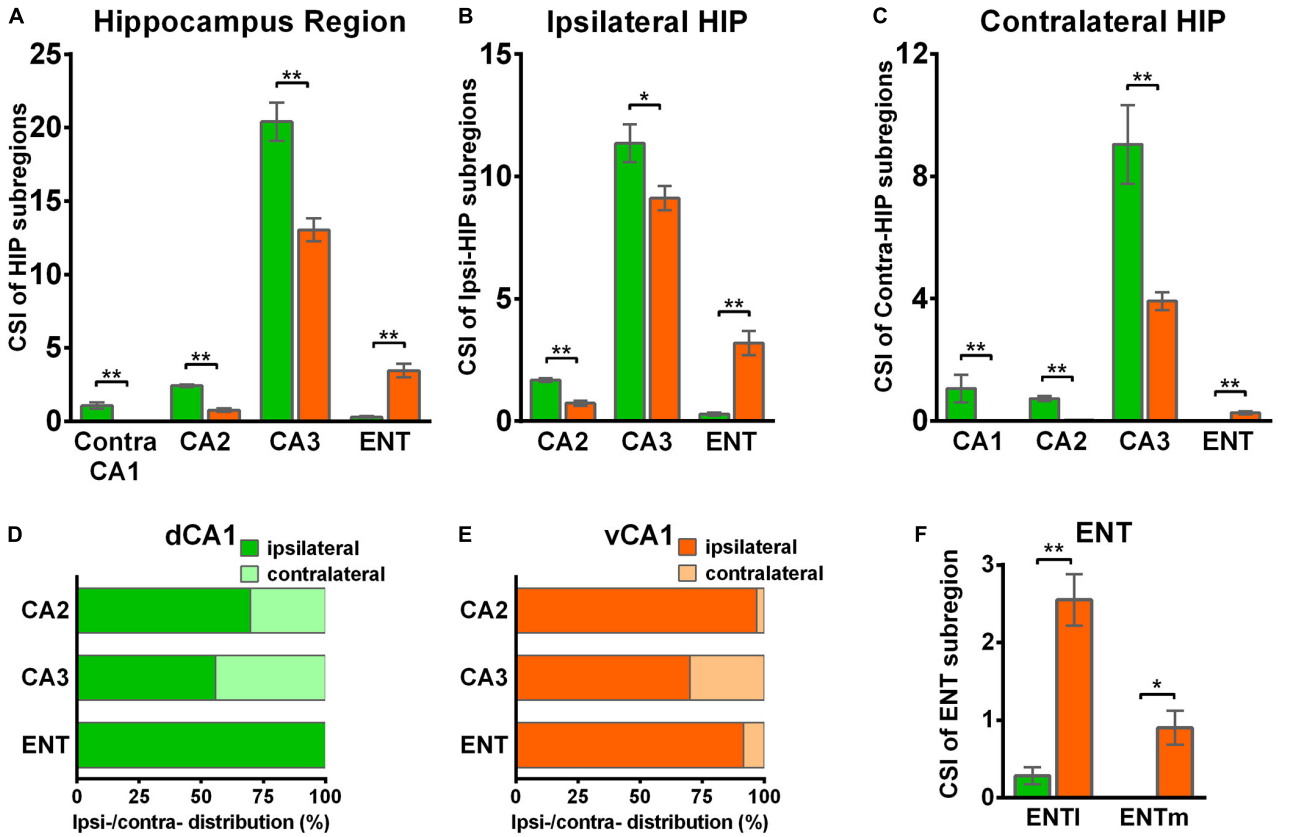

FIGURE 5 | Distribution patterns of HIP inputs between the two CA1 tracing groups. **(A)** CSI of the bilateral inputs in the different HIP subregions between two CA1 tracing groups. **(B)** CSI of the inputs in the ipsilateral HIP subregions between two CA1 tracing groups. **(C)** CSI of the inputs in the contralateral HIP subregions between two CA1 tracing groups. **(D)** Distributions of ipsilateral and contralateral input neurons within five subregions of HIP. **(E)** Distributions of ipsilateral and contralateral input neurons within five subregions of HIP. **(F)** CSI of the inputs in bilateral ENT subregions. n.s., no significant difference; $^{*}P < 0.05$; $^{**}P < 0.01$.

Both Dorsal and Ventral CA1 Projection Neurons Receive Pallidum and Cortical Inputs

In both the dCA1 and vCA1 tracing groups, the input neurons were found distributed widely in the medial septal complex subregion of PAL (**Figure 6A**). The inputs from the medial septal complex to the hippocampus play important roles in hippocampal spatial representation and cognition (Mamad et al., 2015; Jiang et al., 2018; Muller and Remy, 2018). As shown in **Figure 6B**, the inputs from MS to dCA1 and vCA1 PNs were similar (dCA1: 0.76 ± 0.06 versus vCA1: 0.74 ± 0.02, $P = 0.748$), while NDB contributed more direct afferents to vCA1 than dCA1 with CSIs of 0.93 ± 0.03 and 0.27 ± 0.03 ($P < 0.01$), respectively (**Figure 6B**). The input neurons in the MS/NDB region shared similar distribution patterns along the RC axis and the dorsal-ventral line between the two groups (**Figures 6C,E**). In both groups, the input neurons in MS/NDB were mostly located in the ipsilateral hemisphere (**Figure 6D**).

Our results showed that the notable input region in isocortex was the ipsilateral ectorhinal area (ECT) (**Figure 7A**), demonstrating that CA1 is the direct target of the posterior cortex. The connection strength between ECT and dCA1 was much stronger than that of vCA1, with CSIs of 2.70 ± 0.55 versus 0.04 ± 0.02 ($P < 0.01$) (**Figure 7B**). The density of labeled neurons in ECT increased along the RC axis in the dCA1 group (**Figure 7C**). As the ECT was rarely labeled in the vCA1 group (**Figure 7B**), the RC axis distribution was not shown. Furthermore, dCA1 received bilateral ECT inputs, while all the inputs to vCA1 were limited in ipsilateral ECT.

Both Dorsal and Ventral CA1 Projection Neurons Receive Inputs From the Striatum, the Hypothalamus, and the Thalamus

Our data revealed that a few subregions in STR, HY, and TH yielded weak projections to both dCA1 and vCA1 PNs with CSI < 1.00. The LSX, subregion of STR, provided projections to both dCA1 and vCA1 PNs. In our data, LSX generated more inputs to vCA1 than dCA1 PNs (dCA1: 0.08 ± 0.03 versus vCA1: 0.21 ± 0.01, $P < 0.05$) (**Figures 7D,E**). The labeled neurons in LSX shared quite different distribution patterns along the medial-lateral line. In the dCA1 group, the percentage of input neurons has a peak in the midline, while the input neurons spread evenly in vCA1 group along the medial-lateral line. In

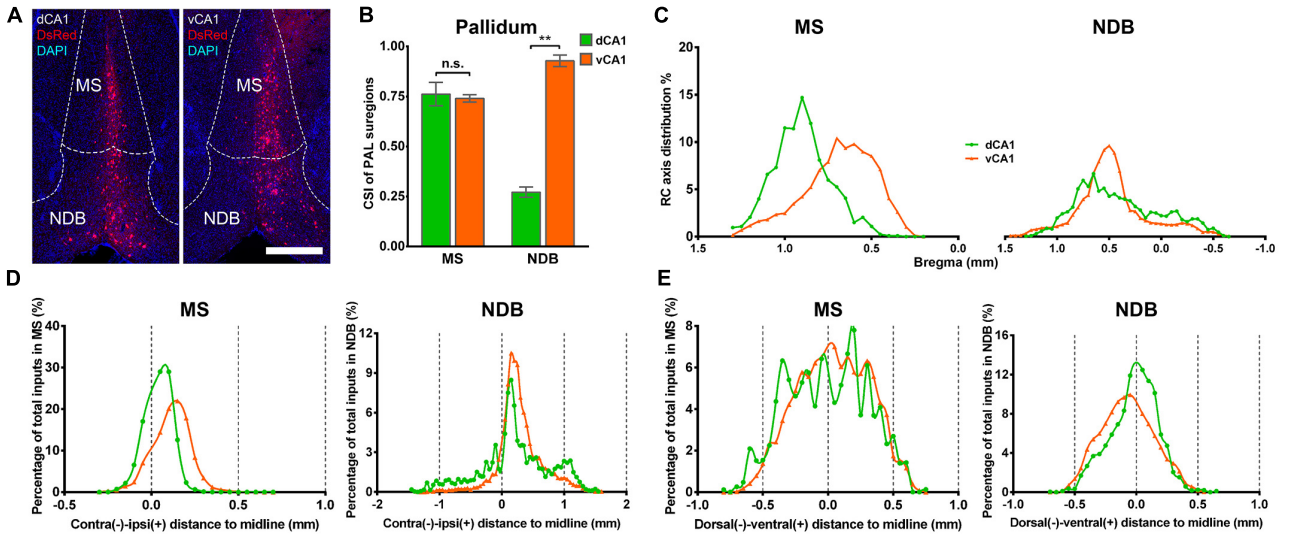

FIGURE 6 | Distribution patterns of bilateral inputs in PAL subregions between the two CA1 tracing groups. **(A)** Representative images showing MS and NDB inputs to the dorsal or ventral CA1 PNs. Scale bar: 500 μm. **(B)** CSI of the inputs in bilateral PAL subregions. **(C)** Distribution patterns of the input neurons along the RC axis in the bilateral MS or NDB. **(D)** The contralateral-ipsilateral distribution patterns of monosynaptic inputs in MS or NDB of two tracing groups. **(E)** The dorsal-ventral distribution patterns of monosynaptic inputs in MS or NDB of two tracing groups. n.s., no significant difference; $^{**}P < 0.01$.

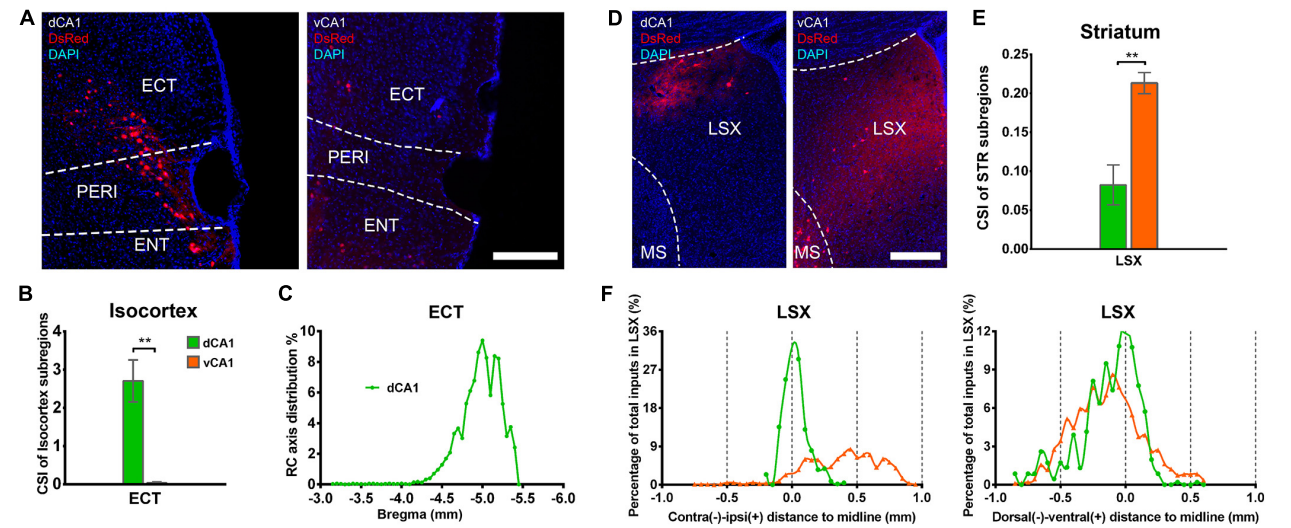

FIGURE 7 | Distribution patterns of bilateral isocortex and STR inputs between the two CA1 tracing groups. **(A)** Representative images showing labeling of monosynaptic inputs to the dorsal or ventral CA1 PNs in ipsilateral ECT. Scale bar: 250 μm. **(B)** CSI of the bilateral inputs in ECT. **(C)** Distribution patterns of the bilateral input neurons to dorsal CA1 PNs along the RC axis in ECT. **(D)** Representative images showing LSX inputs to the dorsal or ventral CA1 PNs. Scale bar, 250 μm. **(E)** CSI of the inputs in bilateral STR subregions-LSX. **(F)** The contralateral-ipsilateral and dorsal-ventral distribution patterns of monosynaptic inputs in LSX of two tracing groups. $^{**}P < 0.01$.

addition, we found that the labeled neurons in LSX shared similar distribution patterns along the dorsal-ventral line for both the two groups (**Figure 7F**).

The connection strength of HY-dCA1 and HY-vCA1 differed significantly (dCA1: 0.12 ± 0.02 versus vCA1: 0.38 ± 0.04, $P < 0.01$) (**Figure 2C**). The discrete subregions, including LHA and LPO, projected significantly more to vCA1 than dCA1 PNs (LHA: dCA1: 0.02 ± 0.01 versus vCA1: 0.15 ± 0.02, $P < 0.01$; LPO: dCA1: 0.09 ± 0.01 versus vCA1: 0.24 ± 0.03, $P < 0.01$) but both weakly (**Figures 8A,B**).

A few thalamus subregions projected sparsely to both dCA1 and vCA1 PNs. Their inputs to dCA1 and vCA1 PNs were not significantly different, for ILM (CSI: 0.25 ± 0.15 versus 0.20 ± 0.05), ATN (CSI: 0.53 ± 0.22 versus 0.48 ± 0.19), MED (CSI: 0.12 ± 0.05 versus 0.21 ± 0.07), and VENT (CSI: 0.63 ± 0.26 versus 0.07 ± 0.04) (**Figures 8A,C**). However, two thalamus

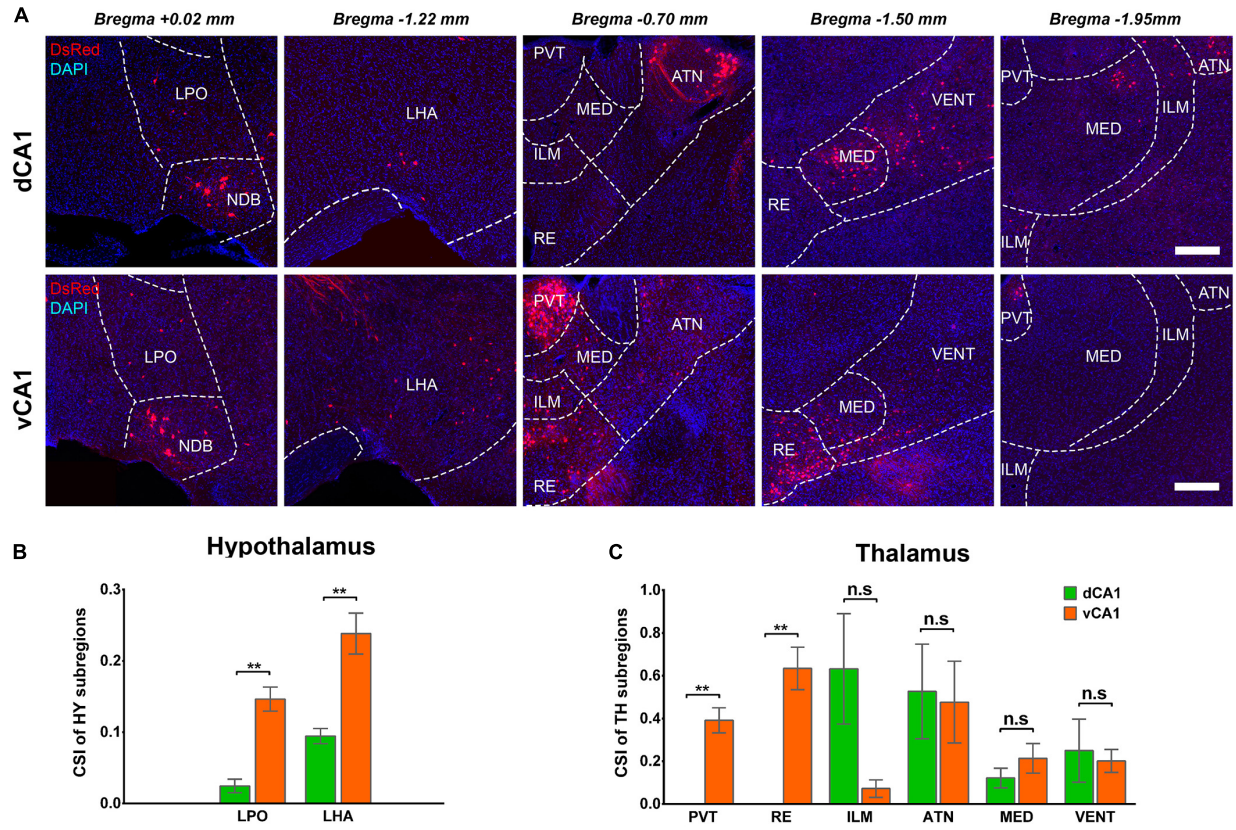

FIGURE 8 | Distribution patterns of HY and TH inputs between the two CA1 tracing groups. **(A)** Representative images showing inputs from the selected subregions of HY and TH to the dCA1 or vCA1 PNs. Scale bar: 250 μm. **(B)** CSI of the inputs in HY subregions. **(C)** CSI of the inputs in TH subregions. n.s., no significant difference; $^{**}P < 0.01$.

subregions, the midline nucleus reuniens (RE, CSI = 0.63 ± 0.10) and, to a lesser degree, the paraventricular nucleus of the thalamus (PVT, CSI = 0.39 ± 0.06) directly projected to vCA1, not dCA1 PNs (**Figures 8A,C**). Previous research found that by injecting traditional retrograde tracers in CA1, the RE form a predominant contact on both dCA1 and vCA1 (Hoover and Vertes, 2012). Our results demonstrated that vCA1 PNs received significant inputs from the RE (CSI = 0.63 ± 0.10). However, in the dCA1 group, no cells in RE were labeled in DsRed (**Figures 8A,C**).

Ventral but Not Dorsal CA1 Projection Neurons Receive Inputs From Amygdala Nuclei and Olfactory Areas

The amygdala nuclei only projected ipsilaterally to vCA1 PNs, with the basolateral nuclei of the amygdala (BLA) contributing the highest proportions of amygdala inputs [70.63 ± 3.03%, $F(2,9) = 285.143$, $P < 0.01$], followed by striatum-like amygdala groups (sAMY), basomedial amygdala nucleus (BMA), and the lateral amygdala nucleus (LA) with the percentage of 13.56 ± 2.23, 12.92 ± 1.84, and 2.89 ± 0.70%, respectively (**Figures 9A,B**). The RC axis distributions of the input neurons were inconsistent between the subregions of amygdala nuclei in CTXsp (**Figure 9C**). Within BLA, the afferent neurons were largely located in the posterior part (BLAp) with 78.23 ± 2.52% [$F(2,9) = 1{,}339.696$, $P < 0.01$], with fewer in the anterior (BLAa) and ventral BLA (BLAv) (12.85 ± 2.14, 8.92 ± 1.62%) (**Figure 9D**). The results indicated that BLAp may play a more important role in BLA-vCA1 circuit-related behavior.

Ventral CA1 PNs received significant monosynaptic inputs from OLFs, including the nucleus of the lateral olfactory tract (NLOT, 0.68 ± 0.39%), piriform area (PIR, 26.05 ± 4.24%), cortical amygdalar area (COA, 40.90 ± 5.60%), postpiriform transition area (TR, 21.35 ± 3.1%), and the piriform-amygdalar area (PAA, 8.07 ± 2.08%) [$F(4,15) = 19.568$, $P < 0.01$]. Among them, the COA, PIR, and TR were the fundamental input sources and contributed about 90% of total olfactory inputs, while NLOT and PAA were sparsely labeled (**Figures 9E,F**). Our results indicated that vCA1 PNs may be modulated by olfactory information.

DISCUSSION

In this study, our findings highlighted the heterogeneity in monosynaptic inputs of CA1 PNs across the longitudinal axis of the hippocampus. Our results corroborated with some

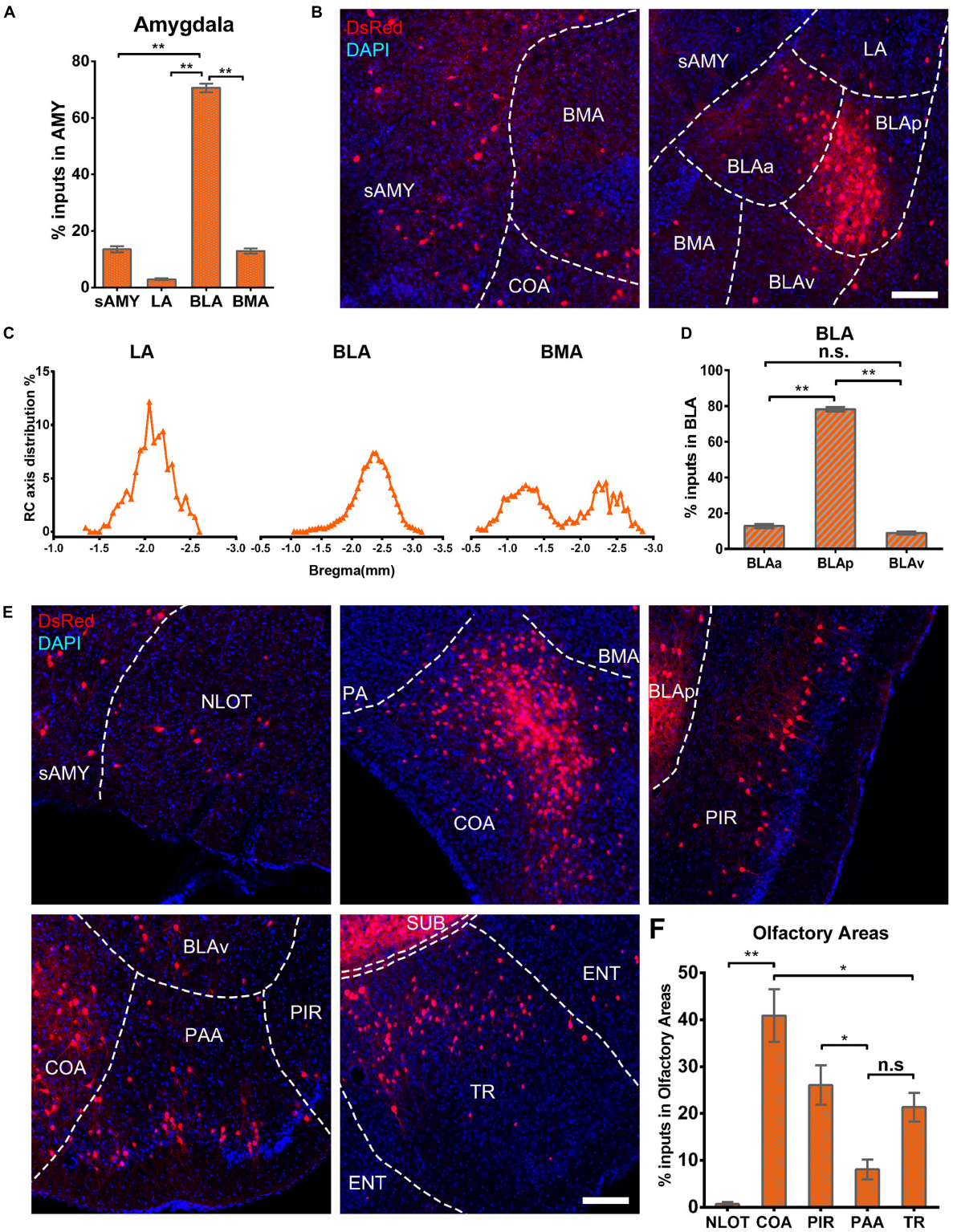

FIGURE 9 | Amygdala nuclei and OLF inputs to ventral CA1. **(A)** Distribution of the input neurons within the subregions of amygdala nuclei. **(B)** Representative images showing inputs from the subregions of amygdala nuclei to the projection cells of ventral CA1. Scale bar: 250 μm. **(C)** Distribution patterns of the input neurons along the RC axis in LA, BMA, and BLA. **(D)** Distribution of the input neurons within the subregions of BLA. The BLA was mainly divided into the BLAa, BLAp, and BLAv. **(E)** Representative images showing presynaptic neurons in the subregions of OLF to the projection cells of ventral CA1. Scale bar: 250 μm. **(F)** Distribution of the input neurons within subregions of the OLF. n.s., no significant difference; $^{*}P < 0.05$; $^{**}P < 0.01$.

previous tracing studies using traditional tracers, but in a cell-type-specific manner. As there are relatively few papers with quantitative analysis, we described proportions and distributions of whole-brain inputs to the dCA1 and vCA1 PNs and quantitatively compared the relative contributions of ipsilateral and contralateral projections from the whole brain. In this study, we provided a systematic and quantitative description of whole-brain direct inputs of CA1 PNs in separate dorsal and ventral parts, with statistical evaluation.

Our results showed that the dCA1 and vCA1 PNs shared some upstream brain regions/subregions but displayed distinctive input organizations of their own. The key findings of this study are that we confirmed that the intrahippocampal circuitries provide the majority of the direct afferents to PNs in both dCA1 and vCA1 (**Figures 2B,C**), and quantitative analysis revealed that PNs in the dCA1 received much stronger intrahippocampal monosynaptic inputs. Specifically, PNs in the dCA1 receive higher input from CA2 and CA3, while PNs in the vCA1 receive higher input from CA3 and ENT (**Figure 5A**). Regarding the extrahippocampal circuitry, we found some minor inputs to CA1, which was previously underexplored, such as ECT to dCA1. We also determined some inputs which only projected to vCA1 but not dCA1 PNs, such as RE, PVT, OLF, and amygdala nuclei.

TABLE 1 | Abbreviations.

Abbreviation	Definition
PAL	**Pallidum**
MS	Medial septal nucleus
NDB	Diagonal band nucleus
STR	**Striatum**
LSX	Lateral septal complex
sAMY	Striatum-like amygdalar nucleus
OLF	**Olfactory areas**
PIR	Piriform area
NLOT	Nucleus of the lateral olfactory tract
COA	Cortical amygdalar area
PAA	Piriform-amygdalar area
TR	Postpiriform transition area
Isocortex	
ECT	Ectorhinal area
HIP	**Hippocampal region**
CA1	Field CA1
CA2	Field CA2
CA3	Field CA3
ENT	Entorhinal area
ENTl	Entorhinal area lateral part
ENTm	Entorhinal area medial part
CTXsp	**Cortical subplate**
BMA	Basomedial amygdalar nucleus
BLA	Basolateral amygdalar nucleus
BLAa	Basolateral amygdalar nucleus anterior part
BLAp	Basolateral amygdalar nucleus posterior part
BLAv	Basolateral amygdalar nucleus ventral part
LA	Lateral amygdalar nucleus
TH	**Thalamus**
PVT	Paraventricular nucleus of the thalamus
RE	Nucleus of reuniens
VENT	Ventral group of the dorsal thalamus
ATN	Anterior group of the dorsal thalamus
MED	Medial group of the dorsal thalamus
ILM	Intralaminar nuclei of the dorsal thalamus
HY	**Hypothalamus**
LPO	Lateral preoptic area
LHA	Lateral hypothalamic area

The bold terms and normal terms in Table 1 stand for brain regions and subregions, respectively.

Monosynaptic Intrahippocampal Input Patterns to Different Subarea of CA1 Projection Neurons

Our results showed that most direct intrahippocampal connections of CA1 PNs were organized as a topographic gradient across the rostrocaudal hippocampus (**Figures 3**, **4**). The input neurons of dCA1 PNs in bilateral CA2, CA3, and contralateral CA1 exhibited a decreasing gradient along the RC axis, while that of vCA1 PNs in ipsilateral CA2 and bilateral CA3 and ENT presented the increasing gradient.

Previous studies demonstrated that memory encoding and rapid generalization are dependent on the symmetrical interhemispheric dCA1 circuit (Zhou et al., 2017). Our results showed that the interhemispheric CA1 connection only occurred in dCA1 not vCA1 PNs.

Previous studies using classical tracing methods have established that CA2 forms functional synaptic connections with CA1 cells with a vast caudal spread along the longitudinal axis of the rat hippocampus (Tamamaki et al., 1988; Shinohara et al., 2012; Kohara et al., 2014; Dudek et al., 2016). However, the degree to which this longitudinal spread differs for dCA1 and vCA1 PNs is unclear. Our results showed that the connection strength of CA2 to dCA1 PNs was significantly stronger than CA2 to vCA1 PNs bilaterally. Different innervation strengths may suggest differential information processing efficiency in the dendrites of the dCA1 and vCA1 PNs.

Our evaluation revealed distribution details about the CA3–CA1 circuitry. The CA3–CA1 connectivity was organized as a topographic gradient. The input neurons in CA3 of dCA1 PNs exhibited a decreasing gradient bilaterally along the dorsoventral axis, while that of vCA1 PNs presented the increasing gradient on both hemispheres. Meanwhile, our findings demonstrated that the dCA1 PNs received much stronger overall CA3 inputs than vCA1 PNs. It could be speculated that the CA3-associated Schaffer collateral and contralateral commissural inputs have much stronger influence on the neural activity of dCA1 than vCA1 PNs.

Previous studies had confirmed that ENT directly projects to the hippocampus (Amaral and Witter, 1989; Witter et al., 2000; van Strien et al., 2009; Kitamura et al., 2015; Li et al., 2017; Chenani et al., 2019). Complementing this work, our results illustrated that ENT domains projected bilaterally to vCA1, but only ipsilaterally to dCA1 PNs. Our findings of the differences between ENT-dCA1 and ENT-vCA1 connectivity may help

elucidate the different mechanisms underlying ENT-CA1 circuit-related behavior.

Monosynaptic Extrahippocampal Inputs to Different Subarea of CA1 Projection Neurons

Previous researches have confirmed that CA1 is highly connected with brain regions beside HIP. We found some more extrahippocampal brain regions made monosynaptic projections to dCA1 or vCA1 PNs with differential distributions and connection strengths.

Previous studies employing traditional tracers have found some weak projections from vCA1 to ECT, but no feedback projection was mentioned. With the high-efficiency RV monosynaptic tracing system, we were able to notice that both dCA1 and vCA1 PNs received weak direct inputs from ECT. However, the ECT provided stronger connectivity to dCA1 than vCA1 PNs. Considering that ECT is an important isocortex subregion involved in sensory signals processing (Wang et al., 2012; Nishio et al., 2018), our results may provide new conjecture about how dCA1 PNs directly participate in information processing and memory formation in the cortex.

We also found that some brain regions only project to vCA1 PNs. For example, amygdala nuclei, RE, and PVT only provided direct input to vCA1 PNs. The amygdala nuclei are functionally associated with mental disorders including multiple anxiety disorders, addiction, and autism (Janak and Tye, 2015). Traditional tracing techniques have discovered that the BLA innervate CA1, along with limited inputs from other subregions of the amygdala nuclei (Yang et al., 2016; McDonald and Mott, 2017). Our results contributed more details about the projection preferences of different subregions in amygdala nuclei to vCA1 PNs. These results may provide more explanations as to how vCA1 PNs participate in amygdala-related functions.

Nucleus reuniens has been proven to modulate hippocampus-related navigation (Ito et al., 2018) and aversive memory consolidation (Troyner et al., 2018). Meanwhile, as a prominent component of the hypothalamo-pituitary-adrenal (HPA) axis, PVT has been reported to associate with stress-related anxiety and responsiveness (Wigger et al., 2004; Bergstrom, 2016; van Bodegom et al., 2017; Careaga et al., 2019). In previous studies with electrophysiological methods, the RE and PVT of the hypothalamus are reciprocally connected with both dCA1 and vCA1 (Zhang and Hernandez, 2013; Dolleman-van der Weel et al., 2017; Eichenbaum, 2017). Our data showed that only vCA1 PNs received direct inputs with RE and PVT. It may indicate that RE and PVT control dCA1 activity mostly through interneurons but not PNs.

Moreover, the previous CA1 lesion experiment confirmed that the vCA1, but not dCA1, is involved in sensory (odor) discrimination events (Roullet et al., 2005; Hunsaker et al., 2008; Kesner et al., 2010). Our tracing results may help to demonstrate that the anatomical evidence of subregions in OLFs made direct projections to vCA1 PNs in different connection strengths.

Technical Considerations

Due to technical limitations, this study still has a few inadequacies that need to be improved. In order to get accurate results, we only target most dorsal or ventral areas which are not enough for whole dCA1 and vCA1 analysis. In recent studies of CA1 subdivisions, some single-cell RNA approaches such as multiplexed seqFISH mapping have suggested that the gene expression of CA1 cell types showed a gradual transition along the dorsoventral axis rather than having discrete boundaries between subregions (Malik et al., 2016; Shah et al., 2017; Soltesz and Losonczy, 2018; Cembrowski and Spruston, 2019). Therefore, without gene expression-specific classification of the dCA1 or vCA1 PNs, we can only analyze neuronal connectivity patterns of CA1 along the dorsoventral axis on the rather large scale of dorsal and ventral areas. In the experiments, we assumed that projection cells in the dorsal or ventral position shared the same input regions. In order to distinguish the different inputs of newly defined subpopulations of projection cells, additional criteria such as gene markers and comprehensive transcriptomes are needed for systematic examination and validation in subtype-specific connectivity of CA1 projection cells. Further studies using various mouse strains and new elaborate tracing systems are required to address the connectome of fine subdivisions in CA1.

CONCLUSION

In summary, we mapped the input networks in the whole brain for PNs of two different subregions of CA1 by using a co-packaged rAAV helper virus and a modified RV tracing system, which allows us to target a limited subregion of CA1 with relatively high transfection efficiency. Our retrograde tracing experiments have determined statistically significant differences between whole-brain inputs of dCA1 and vCA1 PNs. Overall, our data showed that the dCA1 and vCA1 PNs shared similar monosynaptic upstream regions, but the comparative input strengths of the afferent connectivity may be related to distinct non-uniform information processing circuits. Our findings provide a necessary anatomical basis that may help elucidate the roles of dCA1 and vCA1 PNs in various behaviors, including the processing of parallel information.

MATERIALS AND METHODS

Animals

All surgery and experimental procedures were performed in accordance with the guidelines of the Animal Experimentation Ethics Committee of Huazhong University of Science and Technology, and the Animal Care and Use Committees at the Wuhan Innovation Academy for Precision Measurement Science and Technology Chinese Academy of Sciences. Thy1-Cre mice (Jackson Laboratory stocknumber: 006143, a kind gift from Prof. Shumin Duan's Lab of Zhejiang University) were mated with C57BL/6J mice which were purchased from Hunan SJA Laboratory Animal Company. All mice used in the experiments

were young adult (8–12 weeks of age) male mice with weight of 20–25 g. C57BL/6 were used as control. Mice were group-housed in a quiet room with a 12/12-h light/dark cycle, and a thermostatically controlled environment with the temperature of 22–25°C. Food and water were provided *ad libitum*.

Virus Preparation

We applied the RV-based monosynaptic tracing system and Thy1-Cre mice to identify the monosynaptic inputs of PNs in dCA1 and vCA1. All viruses used in this study were produced by our lab or provided by BrainVTA Science and Technology Company (Wuhan, China).

The retrograde trans-monosynaptic system consisted of the genetically modified EnvA-pseudotyped RV (RV-EnvA-ΔG-DsRed, 2.0×10^8 infectious particles per ml) and the Cre-dependent co-packaged rAAV helper virus (AAV2/2, 5.27×10^{12} genomic copies per ml). Production of rAAVs and genetically modified RV were prepared as previously described (Sun et al., 2020). The co-packaged helper rAAV particles (AAV2/2) were constructed by cotransfection of two packaging plasmids AAV-EF1α-DIO-EGFP-TVA (GT) and AAV-EF1α-DIO-RVG into HEK293T cells at a ratio of 1:2. The RV, whose glycoprotein (RVG) gene was substituted to DsRed gene, was pseudotyped with an avian virus envelope protein (EnvA) (**Figure 1A**). The Cre-dependent rAAV helper virus encodes the GFP for the visualization of targeted neurons, TVA receptors for strict infection of RV, and the RVG protein for the transsynapptic spread of the modified RV as previously reported (Zhang et al., 2017). All viruses used in this study were stored at −80°C until use.

Surgery Procedure

For trans-synaptic retrograde tracing, mice were anesthetized with sodium pentobarbital (80 mg/kg, i.p.) and fixed on stereotaxic apparatus (Item: 68030, RWD, Shenzhen, China). All viruses were injected with a pulled glass micropipette at a rate of 10 nl/min. The glass microelectrode remained for additional 10 min before withdrawal from the brain. The surface of mouse brain was embedded with lincomycin lidocaine gel before suturing. Mice were placed on electric heating blankets until entire recovery. After recovery, the mice were rehoused carefully, until being given additional injections or killed. The coordinates for the injection based on the Allen Mouse Brain Atlas were as follows: dCA1 (AP: −1.65 mm; ML: −1.20 mm; DV: −1.52 mm); vCA1 (AP: −3.10 mm; ML: −3.06 mm; DV: −4.00 mm). Sixty nanoliters of co-packaged rAAV helper (serotype = 2/2) was stereotactically injected into the dCA1 or vCA1, respectively (dCA1, $n = 4$; vCA1, $n = 4$).

Two weeks after rAAV helper virus injection into dCA1 or vCA1 of Thy1-Cre mice, we injected 120 nl of RV (RV-EnvA-ΔG-DsRed) in the same location. RV selectively infected TVA-expressing cells, which should be restricted to PNs in CA1 (**Figure 1C**). RV trans-synaptically spread to direct presynaptic cells after being complemented with RVG protein provided by rAAV. Mice were killed 7 days after RV injection for further analysis (**Figure 1B**).

We performed the same procedure in C57BL/6J mice as the control experiment to test the leakage of the tracing system. We found that a few RV-labeled DsRed-positive neurons were only detected at the injection site (**Supplementary Figure 1**). These results showed that our tracing system worked well with very little local leakage.

Perfusion and Slicing

One week after RV injection, mice were transcardially perfused with 0.01 M PBS followed by 4% paraformaldehyde (PFA) in 0.01 M PBS. Brain tissue was carefully collected, postfixed overnight at 4°C, dehydrated in 30% sucrose in PBS for 48–72 h, and 50-μm frozen sections were performed across the whole brain with the freezing microtome (CryoStar NX50 cryostat, Thermo Fisher Scientific, San Jose, CA, United States). All continuous brain slices were collected one by one in a strict sequence in a 24-well plate with antifreeze liquid (50% = PBS, 20% = glycerine, and 30% = ethylene glycol) for further staining and imaging.

Imaging

All brain slices were imaged with the virtual microscopy slide scanning system (VS120, Olympus, Japan) or confocal laser scanning system (SP8, Leica, Germany) for further analysis.

Cell Counting and Data Analysis

To map the whole-brain monosynaptic distribution of the RV-labeled presynaptic neurons of CA1 PNs, we imaged serial coronal sections and analyzed them. For cell counting, we manually examined each brain slice to pinpoint the locations of the postsynaptic starter cells (coexpressing GFP and DsRed) (**Figure 1C**) and the labeled presynaptic neurons (expressing DsRed only). We marked each neuron according to their locations in anatomical brain region or subregion for specific region quantification according to the ARA2011 (**Figure 2A**). The numbers of all the marked cells were then counted and analyzed as reported (Do et al., 2016); meanwhile, their location details were classified and registered in the reference atlas. For quality control, we double checked the cell numbers in some subregions using the cell-counter plugin in ImageJ.

The Allen Mouse Brain Atlas (ARA2011) was used as the criterion to perform quantitative analysis of every brain section across different brain samples. In this study, the divisions of major brain regions and discrete subregions were mainly defined according to the Allen Brain Atlas 2011 (**Figures 2B,C**). Specifically, the whole brain was divided into eight major brain regions, comprising the PAL, STR, OLF, isocortex, HIP, CTXsp, TH, and HY. Each major brain region was further subdivided into several discrete brain subregions for better analysis of transverse or dorsoventral distribution. All related subregions and their abbreviations are listed in **Table 1**.

Then, the total number of the input neurons within the whole-brain or a certain brain region was quantified by adding up the numbers of the DsRed+ neurons within all involved brain areas. For precise quantitative evaluation of the whole-brain monosynaptic input distribution patterns in each tracing group, the number of the input neurons within a certain

brain region/subregion/lamina was evaluated relative to the total number of the defined input neurons in the whole brain/a certain major brain region/subregion, and the proportions of whole-brain inputs/certain brain region inputs/a certain brain subregion were quantified and analyzed individually. The quantitative comparison of the distribution patterns of the input neurons between the two tracing groups was performed as the input connection strength index (CSI, defined as the ratio of the number of rabies-labeled presynaptic neurons versus the number of starter neurons).

For statistical comparisons, two-tailed unpaired Student's *t*-tests were performed between two tracing groups. For statistical comparisons across more than two data, one-way ANOVA tests followed by Bonferroni tests were used for determining statistical differences using SPSS (version 22.0), with the significance set at $^{*}P < 0.05$, $^{**}P < 0.01$. All data values were presented as mean ± SEM.

DATA AVAILABILITY STATEMENT

The original contributions presented in the study are included in the article/**Supplementary Material**, further inquiries can be directed to the corresponding author/s.

ETHICS STATEMENT

The animal study was reviewed and approved by the Animal Care and Use Committees at the Wuhan Innovation Academy for Precision Measurement Science and Technology Chinese Academy of Sciences.

AUTHOR CONTRIBUTIONS

ST, SJ, and FX designed the experiments. ST, SJ, YW, JP, and YZ performed the experiments. ST and SJ collected the data. ST analyzed the data and generated the figures. XH helped the virus preparation. ST and FX contributed to manuscript writing. XY, SJ, QL, and FX contributed to manuscript modification. All authors contributed to the article and approved the submitted version.

FUNDING

This work was supported in part by the Funding Program for the Key-Area Research and Development Program of Guangdong Province (2018B030331001), the Strategic Priority Research Program of the Chinese Academy of Sciences (XDB32030200), the National Natural Science Foundation of China (31830035), and the Chinese Postdoctoral Science Foundation (2020M682964).

ACKNOWLEDGMENTS

We would like to express our gratitude to Shumin Duan of Zhejiang University for providing the breeding pair of Thy1-Cre mice. We thank Lingling Xu from Wuhan Institute of Physics and Mathematics for guiding imaging and Yanqiu Li from Wuhan Institute of Physics and Mathematics for genotyping the transgenic mice. We also thank Min Xu and Lizhao Wang from the Institute of Neuroscience Chinese Academy of Sciences and Siyu Zhang of Shanghai Jiao Tong University for their kind help on data analysis.

SUPPLEMENTARY MATERIAL

The Supplementary Material for this article can be found online at: https://www.frontiersin.org/articles/10.3389/fncir.2021.643230/full#supplementary-material

REFERENCES

Amaral, D. G., and Witter, M. P. (1989). The three-dimensional organization of the hippocampal formation: a review of anatomical data. *Neuroscience* 31, 571–591. doi: 10.1016/0306-4522(89)90424-7

Andersen, P., Morris, R., Amaral, D., Bliss, T., and O'Keefe, J. (2006). *The Hippocampus Book*. Oxford: Oxford University Press.

Bannerman, D. M., Sprengel, R., Sanderson, D. J., McHugh, S. B., Rawlins, J. N., Monyer, H., et al. (2014). Hippocampal synaptic plasticity, spatial memory and anxiety. *Nat. Rev. Neurosci.* 15, 181–192. doi: 10.1038/nrn3677

Bergstrom, H. C. (2016). The neurocircuitry of remote cued fear memory. *Neurosci. Biobehav. Rev.* 71, 409–417. doi: 10.1016/j.neubiorev.2016.09.028

Careaga, M. B. L., Girardi, C. E. N., and Suchecki, D. (2019). Variability in response to severe stress: highly reactive rats exhibit changes in fear and anxiety-like behavior related to distinct neuronal co-activation patterns. *Behav. Brain Res.* 373:112078. doi: 10.1016/j.bbr.2019.112078

Cembrowski, M. S., and Spruston, N. (2019). Heterogeneity within classical cell types is the rule: lessons from hippocampal pyramidal neurons. *Nat. Rev. Neurosci.* 20, 193–204. doi: 10.1038/s41583-019-0125-5

Cenquizca, L. A., and Swanson, L. W. (2007). Spatial organization of direct hippocampal field CA1 axonal projections to the rest of the cerebral cortex. *Brain Res. Rev.* 56, 1–26. doi: 10.1016/j.brainresrev.2007.05.002

Chawla, M. K., Sutherland, V. L., Olson, K., McNaughton, B. L., and Barnes, C. A. (2018). Behavior-driven arc expression is reduced in all ventral hippocampal subfields compared to CA1, CA3, and dentate gyrus in rat dorsal hippocampus. *Hippocampus* 28, 178–185. doi: 10.1002/hipo.22820

Chenani, A., Sabariego, M., Schlesiger, M. I., Leutgeb, J. K., Leutgeb, S., and Leibold, C. (2019). Hippocampal CA1 replay becomes less prominent but more rigid without inputs from medial entorhinal cortex. *Nat. Commun.* 10:1341. doi: 10.1038/s41467-019-09280-0

Do, J. P., Xu, M., Lee, S. H., Chang, W. C., Zhang, S. Y., Chung, S., et al. (2016). Cell type-specific long-range connections of basal forebrain circuit. *eLife* 5:e13214. doi: 10.7554/eLife.13214

Dolleman-van der Weel, M. J., Lopes da Silva, F. H., and Witter, M. P. (2017). Interaction of nucleus reuniens and entorhinal cortex projections in hippocampal field CA1 of the rat. *Brain Struct. Funct.* 222, 2421–2438. doi: 10.1007/s00429-016-1350-6

Dong, H. W., Swanson, L. W., Chen, L., Fanselow, M. S., and Toga, A. W. (2009). Genomic-anatomic evidence for distinct functional domains in hippocampal field CA1. *Proc. Natl. Acad. Sci. U.S.A.* 106, 11794–11799. doi: 10.1073/pnas.0812608106

Dougherty, K. A. (2020). Differential developmental refinement of the intrinsic electrophysiological properties of CA1 pyramidal neurons from the rat dorsal and ventral hippocampus. *Hippocampus* 30, 233–249. doi: 10.1002/hipo.23152

Dougherty, K. A., Islam, T., and Johnston, D. (2012). Intrinsic excitability of CA1 pyramidal neurones from the rat dorsal and ventral hippocampus. *J. Physiol* 590, 5707–5722. doi: 10.1113/jphysiol.2012.242693

Dougherty, K. A., Nicholson, D. A., Diaz, L., Buss, E. W., Neuman, K. M., Chetkovich, D. M., et al. (2013). Differential expression of HCN subunits alters voltage-dependent gating of h-channels in CA1 pyramidal neurons from dorsal and ventral hippocampus. *J. Neurophysiol.* 109, 1940–1953. doi: 10.1152/jn.00010.2013

Dudek, S. M., Alexander, G. M., and Farris, S. (2016). Rediscovering area CA2: unique properties and functions. *Nat. Rev. Neurosci.* 17, 89–102. doi: 10.1038/nrn.2015.22

Eichenbaum, H. (2017). Prefrontal-hippocampal interactions in episodic memory. *Nat. Rev. Neurosci.* 18, 547–558. doi: 10.1038/nrn.2017.74

Evans, M. C., and Dougherty, K. A. (2018). Carbamazepine-induced suppression of repetitive firing in CA1 pyramidal neurons is greater in the dorsal hippocampus than the ventral hippocampus. *Epilepsy Res.* 145, 63–72. doi: 10.1016/j.eplepsyres.2018.05.014

Fanselow, M. S., and Dong, H. W. (2010). Are the dorsal and ventral hippocampus functionally distinct structures? *Neuron* 65, 7–19. doi: 10.1016/j.neuron.2009.11.031

Hoover, W. B., and Vertes, R. P. (2012). Collateral projections from nucleus reuniens of thalamus to hippocampus and medial prefrontal cortex in the rat: a single and double retrograde fluorescent labeling study. *Brain Struct. Funct.* 217, 191–209. doi: 10.1007/s00429-011-0345-6

Hunsaker, M. R., Fieldsted, P. M., Rosenberg, J. S., and Kesner, R. P. (2008). Dissociating the roles of dorsal and ventral CA1 for the temporal processing of spatial locations, visual objects, and odors. *Behav. Neurosci.* 122, 643–650. doi: 10.1037/0735-7044.122.3.643

Igarashi, K. M., Ito, H. T., Moser, E. I., and Moser, M. B. (2014). Functional diversity along the transverse axis of hippocampal area CA1. *FEBS Lett.* 588, 2470–2476. doi: 10.1016/j.febslet.2014.06.004

Ito, H. T., Moser, E. I., and Moser, M. B. (2018). Supramammillary nucleus modulates spike-time coordination in the prefrontal-thalamo-hippocampal circuit during navigation. *Neuron* 99, 576–587.e5. doi: 10.1016/j.neuron.2018.07.021

Jacobson, L., and Sapolsky, R. (1991). The role of the hippocampus in feedback regulation of the hypothalamic-pituitary-adrenocortical axis. *Endocr. Rev.* 12, 118–134. doi: 10.1210/edrv-12-2-118

Janak, P. H., and Tye, K. M. (2015). From circuits to behaviour in the amygdala. *Nature* 517, 284–292. doi: 10.1038/nature14188

Jiang, Y. Y., Shao, S., Zhang, Y., Zheng, J., Chen, X., Cui, S., et al. (2018). Neural pathways in medial septal cholinergic modulation of chronic pain: distinct contribution of the anterior cingulate cortex and ventral hippocampus. *Pain* 159, 1550–1561. doi: 10.1097/j.pain.0000000000001240

Jimenez, J. C., Su, K., Goldberg, A. R., Luna, V. M., Biane, J. S., Ordek, G., et al. (2018). Anxiety cells in a hippocampal-hypothalamic circuit. *Neuron* 97, 670–683.e6. doi: 10.1016/j.neuron.2018.01.016

Kaifosh, P., and Losonczy, A. (2016). Mnemonic functions for nonlinear dendritic integration in hippocampal pyramidal circuits. *Neuron* 90, 622–634. doi: 10.1016/j.neuron.2016.03.019

Kesner, R. P., Hunsaker, M. R., and Ziegler, W. (2010). The role of the dorsal CA1 and ventral CA1 in memory for the temporal order of a sequence of odors. *Neurobiol. Learn. Mem.* 93, 111–116. doi: 10.1016/j.nlm.2009.08.010

Kim, J., Castro, L., Wasserman, E. A., and Freeman, J. H. (2018). Dorsal hippocampus is necessary for visual categorization in rats. *Hippocampus* 28, 392–405. doi: 10.1002/hipo.22839

Kitamura, T., Macdonald, C. J., and Tonegawa, S. (2015). Entorhinal-hippocampal neuronal circuits bridge temporally discontiguous events. *Learn. Mem.* 22, 438–443. doi: 10.1101/lm.038687.115

Kjelstrup, K. G., Tuvnes, F. A., Steffenach, H. A., Murison, R., Moser, E. I., and Moser, M. B. (2002). Reduced fear expression after lesions of the ventral hippocampus. *Proc. Natl. Acad. Sci. U.S.A.* 99, 10825–10830. doi: 10.1073/pnas.152112399

Kohara, K., Pignatelli, M., Rivest, A. J., Jung, H. Y., Kitamura, T., Suh, J., et al. (2014). Cell type-specific genetic and optogenetic tools reveal hippocampal CA2 circuits. *Nat. Neurosci.* 17, 269–279. doi: 10.1038/nn.3614

Leonardo, E. D., Richardson-Jones, J. W., Sibille, E., Kottman, A., and Hen, R. (2006). Molecular heterogeneity along the dorsal-ventral axis of the murine hippocampal CA1 field: a microarray analysis of gene expression. *Neuroscience* 137, 177–186. doi: 10.1016/j.neuroscience.2005.08.082

Li, Y. D., Xu, J. M., Liu, Y. F., Zhu, J., Liu, N., Zeng, W. B., et al. (2017). A distinct entorhinal cortex to hippocampal CA1 direct circuit for olfactory associative learning. *Nat. Neurosci.* 20, 559–570. doi: 10.1038/nn.4517

Lisman, J. E., and Otmakhova, N. A. (2001). Storage, recall, and novelty detection of sequences by the hippocampus: elaborating on the SOCRATIC model to account for normal and aberrant effects of dopamine. *Hippocampus* 11, 551–568. doi: 10.1002/hipo.1071

Malik, R., Dougherty, K. A., Parikh, K., Byrne, C., and Johnston, D. (2016). Mapping the electrophysiological and morphological properties of CA1 pyramidal neurons along the longitudinal hippocampal axis. *Hippocampus* 26, 341–361. doi: 10.1002/hipo.22526

Malik, R., and Johnston, D. (2017). Dendritic GIRK channels gate the integration window, plateau potentials, and induction of synaptic plasticity in dorsal but not ventral CA1 neurons. *J. Neurosci.* 37, 3940–3955. doi: 10.1523/JNEUROSCI.2784-16.2017

Mamad, O., McNamara, H. M., Reilly, R. B., and Tsanov, M. (2015). Medial septum regulates the hippocampal spatial representation. *Front. Behav. Neurosci.* 9:166. doi: 10.3389/fnbeh.2015.00166

Maren, S., and Holt, W. G. (2004). Hippocampus and Pavlovian fear conditioning in rats: muscimol infusions into the ventral, but not dorsal, hippocampus impair the acquisition of conditional freezing to an auditory conditional stimulus. *Behav. Neurosci.* 118, 97–110. doi: 10.1037/0735-7044.118.1.97

McDonald, A. J., and Mott, D. D. (2017). Functional neuroanatomy of amygdalohippocampal interconnections and their role in learning and memory. *J. Neurosci. Res.* 95, 797–820. doi: 10.1002/jnr.23709

McDonald, R. J., Balog, R. J., Lee, J. Q., Stuart, E. E., Carrels, B. B., and Hong, N. S. (2018). Rats with ventral hippocampal damage are impaired at various forms of learning including conditioned inhibition, spatial navigation, and discriminative fear conditioning to similar contexts. *Behav. Brain Res.* 351, 138–151. doi: 10.1016/j.bbr.2018.06.003

Moser, M. B., Moser, E. I., Forrest, E., Andersen, P., and Morris, R. G. (1995). Spatial learning with a minislab in the dorsal hippocampus. *Proc. Natl. Acad. Sci. U.S.A.* 92, 9697–9701. doi: 10.1073/pnas.92.21.9697

Muller, C., and Remy, S. (2018). Septo-hippocampal interaction. *Cell Tissue Res.* 373, 565–575. doi: 10.1007/s00441-017-2745-2

Nakashiba, T., Young, J. Z., McHugh, T. J., Buhl, D. L., and Tonegawa, S. (2008). Transgenic inhibition of synaptic transmission reveals role of CA3 output in hippocampal learning. *Science* 319, 1260–1264. doi: 10.1126/science.1151120

Nishio, N., Tsukano, H., Hishida, R., Abe, M., Nakai, J., Kawamura, M., et al. (2018). Higher visual responses in the temporal cortex of mice. *Sci. Rep.* 8:11136. doi: 10.1038/s41598-018-29530-3

Padilla-Coreano, N., Canetta, S., Mikofsky, R. M., Alway, E., Passecker, J., Myroshnychenko, M. V., et al. (2019). Hippocampal-prefrontal theta transmission regulates avoidance behavior. *Neuron* 104, 601–610.e4. doi: 10.1016/j.neuron.2019.08.006

Parfitt, G. M., Nguyen, R., Bang, J. Y., Aqrabawi, A. J., Tran, M. M., Seo, D. K., et al. (2017). Bidirectional control of anxiety-related behaviors in mice: role of inputs arising from the ventral hippocampus to the lateral septum and medial prefrontal cortex. *Neuropsychopharmacology* 42, 1715–1728. doi: 10.1038/npp.2017.56

Rogers, J. L., and Kesner, R. P. (2006). Lesions of the dorsal hippocampus or parietal cortex differentially affect spatial information processing. *Behav. Neurosci.* 120, 852–860. doi: 10.1037/0735-7044.120.4.852

Ropireddy, D., Bachus, S. E., and Ascoli, G. A. (2012). Non-homogeneous stereological properties of the rat hippocampus from high-resolution 3D serial reconstruction of thin histological sections. *Neuroscience* 205, 91–111. doi: 10.1016/j.neuroscience.2011.12.055

Roullet, F., Datiche, F., Lienard, F., and Cattarelli, M. (2005). Learning-stage dependent Fos expression in the rat brain during acquisition of an olfactory discrimination task. *Behav. Brain Res.* 157, 127–137. doi: 10.1016/j.bbr.2004.06.017

Ruediger, S., Spirig, D., Donato, F., and Caroni, P. (2012). Goal-oriented searching mediated by ventral hippocampus early in trial-and-error learning. *Nat. Neurosci.* 15, 1563–1571. doi: 10.1038/nn.3224

Schultz, C., and Engelhardt, M. (2014). Anatomy of the hippocampal formation. *Front. Neurol. Neurosci.* 34:925. doi: 10.1159/000360925

Shah, S., Lubeck, E., Zhou, W., and Cai, L. (2017). seqFISH accurately detects transcripts in single cells and reveals robust spatial organization in the hippocampus. *Neuron* 94, 752–758.e1. doi: 10.1016/j.neuron.2017.05.008

Shinohara, Y., Hosoya, A., Yahagi, K., Ferecsko, A. S., Yaguchi, K., Sik, A., et al. (2012). Hippocampal CA3 and CA2 have distinct bilateral innervation patterns to CA1 in rodents. *Eur. J. Neurosci.* 35, 702–710. doi: 10.1111/j.1460-9568.2012.07993.x

Soltesz, I., and Losonczy, A. (2018). CA1 pyramidal cell diversity enabling parallel information processing in the hippocampus. *Nat. Neurosci.* 21, 484–493. doi: 10.1038/s41593-018-0118-0

Strange, B. A., Witter, M. P., Lein, E. S., and Moser, E. I. (2014). Functional organization of the hippocampal longitudinal axis. *Nat. Rev. Neurosci.* 15, 655–669. doi: 10.1038/nrn3785

Sun, P., Jin, S., Tao, S., Wang, J., Li, A., Li, N., et al. (2020). Highly efficient and super-bright neurocircuit tracing using vector mixing-based virus cocktail. *bioRxiv [Preprint]* doi: 10.1101/705772

Tamamaki, N., Abe, K., and Nojyo, Y. (1988). Three-dimensional analysis of the whole axonal arbors originating from single CA2 pyramidal neurons in the rat hippocampus with the aid of a computer graphic technique. *Brain Res.* 452, 255–272. doi: 10.1016/0006-8993(88)90030-3

Taube, J. S. (2007). The head direction signal: origins and sensory-motor integration. *Annu. Rev. Neurosci.* 30, 181–207. doi: 10.1146/annurev.neuro.29.051605.112854

Troyner, F., Bicca, M. A., and Bertoglio, L. J. (2018). Nucleus reuniens of the thalamus controls fear memory intensity, specificity and long-term maintenance during consolidation. *Hippocampus* 28, 602–616. doi: 10.1002/hipo.22964

van Bodegom, M., Homberg, J. R., and Henckens, M. (2017). Modulation of the hypothalamic-pituitary-adrenal axis by early life stress exposure. *Front. Cell Neurosci.* 11:87. doi: 10.3389/fncel.2017.00087

van Strien, N. M., Cappaert, N. L., and Witter, M. P. (2009). The anatomy of memory: an interactive overview of the parahippocampal-hippocampal network. *Nat. Rev. Neurosci.* 10, 272–282. doi: 10.1038/nrn2614

Wang, Q., Sporns, O., and Burkhalter, A. (2012). Network analysis of corticocortical connections reveals ventral and dorsal processing streams in mouse visual cortex. *J. Neurosci.* 32, 4386–4399. doi: 10.1523/JNEUROSCI.6063-11.2012

Wigger, A., Sanchez, M. M., Mathys, K. C., Ebner, K., Frank, E., Liu, D., et al. (2004). Alterations in central neuropeptide expression, release, and receptor binding in rats bred for high anxiety: critical role of vasopressin. *Neuropsychopharmacology* 29, 1–14. doi: 10.1038/sj.npp.1300290

Witter, M. P., Wouterlood, F. G., Naber, P. A., and Van Haeften, T. (2000). Anatomical organization of the parahippocampal-hippocampal network. *Ann. N. Y. Acad. Sci.* 911, 1–24. doi: 10.1111/j.1749-6632.2000.tb06716.x

Yang, Y., Wang, Z. H., Jin, S., Gao, D., Liu, N., Chen, S. P., et al. (2016). Opposite monosynaptic scaling of BLP-vCA1 inputs governs hopefulness- and helplessness-modulated spatial learning and memory. *Nat. Commun.* 7:11935. doi: 10.1038/ncomms11935

Zhang, L., and Hernandez, V. S. (2013). Synaptic innervation to rat hippocampus by vasopressin-immuno-positive fibres from the hypothalamic supraoptic and paraventricular nuclei. *Neuroscience* 228, 139–162. doi: 10.1016/j.neuroscience.2012.10.010

Zhang, Z. J., Zhang, H. R., Wen, P. J., Zhu, X. T., Wang, L., Liu, Q., et al. (2017). Whole-brain mapping of the inputs and outputs of the medial part of the olfactory tubercle. *Front. Neural Circ.* 11:52. doi: 10.3389/fncir.2017.00052

Zhou, H., Xiong, G. J., Jing, L., Song, N. N., Pu, D. L., Tang, X., et al. (2017). The interhemispheric CA1 circuit governs rapid generalisation but not fear memory. *Nat. Commun.* 8:2190. doi: 10.1038/s41467-017-02315-4

Conflict of Interest: The authors declare that the research was conducted in the absence of any commercial or financial relationships that could be construed as a potential conflict of interest.

frontiers in Neural Circuits

ORIGINAL RESEARCH
published: 28 June 2021
doi: 10.3389/fncir.2021.676891

An Autism-Associated Neuroligin-3 Mutation Affects Developmental Synapse Elimination in the Cerebellum

*Esther Suk King Lai[1], Hisako Nakayama[2], Taisuke Miyazaki[3,4], Takanobu Nakazawa[5], Katsuhiko Tabuchi[6], Kouichi Hashimoto[7], Masahiko Watanabe[3] and Masanobu Kano[1,8]**

[1] Department of Neurophysiology, Graduate School of Medicine, The University of Tokyo, Tokyo, Japan, [2] Department of Physiology, Division of Neurophysiology, School of Medicine, Tokyo Women's Medical University, Tokyo, Japan, [3] Department of Anatomy, Hokkaido University Graduate School of Medicine, Sapporo, Japan, [4] Department of Functioning and Disability, Faculty of Health Sciences, Hokkaido University, Sapporo, Japan, [5] Department of Bioscience, Tokyo University of Agriculture, Tokyo, Japan, [6] Department of Molecular and Cellular Physiology, Shinshu University School of Medicine, Matsumoto, Japan, [7] Department of Neurophysiology, Graduate School of Biomedical and Health Sciences, Hiroshima University, Hiroshima, Japan, [8] International Research Center for Neurointelligence (IRCN), The University of Tokyo Institutes for Advanced Study, The University of Tokyo, Tokyo, Japan

OPEN ACCESS

Edited by:
Yoshiyuki Kubota, National Institute for Physiological Sciences (NIPS), Japan

Reviewed by:
Tetsuya Takano, Keio University, Japan
Aleksandra Badura, Erasmus Medical Center, Netherlands

***Correspondence:**
Masanobu Kano
mkano-tky@m.u-tokyo.ac.jp

Received: *06 March 2021*
Accepted: *31 May 2021*
Published: *28 June 2021*

Citation:
Lai ESK, Nakayama H, Miyazaki T, Nakazawa T, Tabuchi K, Hashimoto K, Watanabe M and Kano M (2021) An Autism-Associated Neuroligin-3 Mutation Affects Developmental Synapse Elimination in the Cerebellum. Front. Neural Circuits 15:676891. doi: 10.3389/fncir.2021.676891

Neuroligin is a postsynaptic cell-adhesion molecule that is involved in synapse formation and maturation by interacting with presynaptic neurexin. Mutations in neuroligin genes, including the arginine to cystein substitution at the 451st amino acid residue (R451C) of neuroligin-3 (NLGN3), have been identified in patients with autism spectrum disorder (ASD). Functional magnetic resonance imaging and examination of post-mortem brain in ASD patients implicate alteration of cerebellar morphology and Purkinje cell (PC) loss. In the present study, we examined possible association between the R451C mutation in NLGN3 and synaptic development and function in the mouse cerebellum. In NLGN3-R451C mutant mice, the expression of NLGN3 protein in the cerebellum was reduced to about 10% of the level of wild-type mice. Elimination of redundant climbing fiber (CF) to PC synapses was impaired from postnatal day 10–15 (P10–15) in NLGN3-R451C mutant mice, but majority of PCs became mono-innervated as in wild-type mice after P16. In NLGN3-R451C mutant mice, selective strengthening of a single CF relative to the other CFs in each PC was impaired from P16, which persisted into juvenile stage. Furthermore, the inhibition to excitation (I/E) balance of synaptic inputs to PCs was elevated, and calcium transients in the soma induced by strong and weak CF inputs were reduced in NLGN3-R451C mutant mice. These results suggest that a single point mutation in NLGN3 significantly influences the synapse development and refinement in cerebellar circuitry, which might be related to the pathogenesis of ASD.

Keywords: synapse elimination, neuroligin-3 mutation, autism, developing cerebellum, climbing fibers, Purkinje cell, mouse

INTRODUCTION

Establishment of proper neural circuits relies on dynamic processes of synapse formation and elimination/pruning. Supernumerary synapses are formed transiently around birth, yielding excessive excitatory synaptic connections. Subsequently during postnatal development, some synapses are strengthened, whereas others are weakened and eventually eliminated in a neural activity-dependent manner (Purves and Lichtman, 1980; Lichtman and Colman, 2000; Hua and Smith, 2004; Kano and Hashimoto, 2009). Accumulating evidence strongly suggests that abnormality in developmental synapse elimination underlies the pathophysiology of neurodevelopmental and psychiatric disorders including autism spectrum disorder (ASD) (Zoghbi, 2003; Penzes et al., 2011). ASD is a category of pervasive developmental disorder characterized by impaired social interaction or communication, and stereotyped or repetitive behaviors (Geschwind and Levitt, 2007; Fombonne, 2009). ASD is highly hereditary, numerous ASD-associated genes have been identified, and a number of ASD mouse models have been reported (Abrahams and Geschwind, 2008; Bourgeron et al., 2009; Tsai et al., 2012a). Majority of ASD-associated genes are thought to encode synaptic proteins such as synaptic cell adhesion molecules, neuroligin and neurexin families (Südhof, 2008; Singh and Eroglu, 2013; Maćkowiak et al., 2014; Stewart, 2015) and a scaffold protein in the postsynaptic density, SHANK/ProSAP (Berkel et al., 2010; Arons et al., 2012; Guilmatre et al., 2014).

Previous studies show that some autism-related genes are involved in synapse elimination/pruning. For instance, myocyte enhancer factor 2 (MEF2) and Fragile X mental retardation 1 (Fmr1) induce excitatory synapse elimination in mouse hippocampal neurons. Deletion of these genes resulted in excessive dendritic spine formation (Pfeiffer et al., 2010; Tsai et al., 2012a). Moreover, mutations in genes that act to inhibit mammalian target of rapamycin (mTOR) kinase, including Tsc1/Tsc2, NF1, and Pten are reported to increase the dendritic spine density with reduced spine pruning in layer V pyramidal neurons of the temporal lobe of postmortem ASD patients and in cortical projection neurons of Tsc2-deficient mice (Tang et al., 2014). However, it remains unclear how impairment of synapse elimination/pruning contributes to the pathophysiology of ASD.

Neuroligins are postsynaptic cell-adhesion molecules that are comprised of four isoforms and are involved in synapse formation and maintenance by interacting with presynaptic neurexin. While neuroligin-1 (NLGN1), neuroligin-2 (NLGN2), and neuroligin-4 (NLGN4) are specifically expressed in excitatory, inhibitory and glycinergic synapses, respectively; neuroligin-3 (NLGN3) is present at both excitatory and inhibitory synapses (Chih et al., 2005; Varoqueaux et al., 2006; Craig and Kang, 2007; Bolliger et al., 2008). Single gene mutation in the arginine to cysteine substitution at the 451st amino acid (R451C) of NLGN3 has been identified in several ASD patients (Jamain et al., 2003; Yan et al., 2005). The R451C point mutation in mice shows a deviation of the balance between excitatory and inhibitory synaptic inputs from that of wild-type mice in the hippocampus and somatosensory cortex (Tabuchi et al., 2007; Etherton et al., 2011). However, it is unclear whether the R451C point mutation of NLGN3 affects synapse elimination/pruning in the developing brain.

The cerebellum has been suggested to be associated with the pathophysiology of ASD by studies on human patients and various animal models. Live imaging studies in ASD patients showed cerebellar abnormalities including hypoplasia of the vermis, gray and white matter abnormalities and cerebellar undergrowth, which are present in early life and persist into adulthood (Courchesne et al., 1988; Becker et al., 2001; Palmen and van Engeland, 2004; DiCicco-Bloom et al., 2006; Webb et al., 2009; Aldinger et al., 2013; Sundberg and Sahin, 2015). Postmortem studies in ASD patients showed loss of Purkinje cells (PCs), excessive number of Bergmann glia, or activation of microglia and production of cytokine in the cerebellar white matter (Bailey et al., 1998; Kern, 2003; Bauman and Kemper, 2005; Vargas et al., 2005; Sundberg and Sahin, 2015). Moreover, studies on ASD-related animal models revealed reduced number of PCs, dysfunction of PCs and deficits in cerebellum-dependent associative learning (Shahbazian et al., 2001; Tsai et al., 2012b; Reith et al., 2013; Kloth et al., 2015; Peter et al., 2016; Hoxha et al., 2017; Xiao et al., 2020; Yamashiro et al., 2020). These studies raise a further question whether and how altered development of synaptic wiring in the cerebellum is related to ASD.

To address these issues, we examined whether climbing fiber (CF) to PC synapse elimination in the developing cerebellum, a representative model of developmental synapse elimination, is affected in mice with R451C point mutation of NLGN3 (NLGN3-R451C mutant mice) (Tabuchi et al., 2007). In the neonatal mouse cerebellum, each PC receives excitatory synaptic inputs on the soma from multiple (more than five) CFs that originate from neurons in the inferior olive of the medulla. The strengths of multiple CF synaptic inputs are similar around birth, but inputs from a single CF selectively become stronger relative to those from the other CFs in each PC during the first postnatal week. Then, only the strongest CF extends its synaptic territory along the growing PC dendrite. In parallel, synapses from weaker CFs are eliminated from the soma, and most PCs become innervated by single strong CFs on their proximal dendrites by the end of the third postnatal week (Watanabe and Kano, 2011; Hashimoto and Kano, 2013; Kano et al., 2018; Kano and Watanabe, 2019). We found a marked reduction of NLGN3 protein expression in the cerebellum and enhanced synaptic inhibition of PCs leading to an elevation of the inhibition to excitation balance of synaptic inputs to PCs in NLGN3-R451C mutant mice. CF to PC synapse elimination was impaired transiently from postnatal day 10–15 (P10–P15), but CF innervation pattern became normal after P16. Furthermore, selective strengthening of a single CF relative to the other weaker CFs in each PC was impaired from P16 to juvenile stage because the weaker CFs remained abnormally strong. We assume that these changes during CF to PC synapse development leave persistent effects on the operation of cerebellar neural circuits, which might contribute to the ASD-like behavioral abnormalities in NLGN3-R451C mutant mice.

MATERIALS AND METHODS

Animals

All experiments were performed in accordance with the guidelines for the care and use of laboratory animals of the University of Tokyo and the Japan Neuroscience Society. NLGN3-R451C mutant mice were generated on the 129/SvJ background and have been backcrossed to the C57BL/6 strain for more than 10 generations (Tabuchi et al., 2007). Litters of mice were kept in a room at 22°C with 12 h dark-light cycles and were weaned at P21. Weaned pups were housed in the same-sex group of 4–6. Standard rodent pellets and water were provided *ad libitum*. In total, 77 male wild-type and 74 male homozygote NLGN3-R451C mice were used in the present study. All experiments in the present study were performed under the conditions in which the experimenters were blind to the mouse genotypes.

Electrophysiology and Ca^{2+} Imaging

Mice were deeply anesthetized with CO_2 and killed by decapitation. The brain was quickly removed and placed in the chilled (0–4°C) artificial cerebrospinal fluid (ACSF) containing (in mM) 125 NaCl, 2.5 KCl, 2 $CaCl_2$, 1 $MgSO_4$, 1.25 NaH_2PO_4, 26 $NaHCO_3$, and 20 glucose, bubbled with 95% O_2 and 5% CO_2 (pH 7.4). Parasagittal cerebellar slices (250 μm thick) were prepared from the cerebellar vermis of mice aged P4–P35 using a vibratome slicer (VT-1200S, Leica, Germany). Whole-cell recordings were made from visually identified somata of PCs at 32°C as described previously (Hashimoto et al., 2009b) using an upright microscope (BX50WI, Olympus, Japan). We used three intracellular solutions with the following compositions (in mM): (1) 60 CsCl, 10 D-gluconate, 20 TEA-Cl, 20 BAPTA, 4 $MgCl_2$, 4 ATP, 0.4 GTP, and 30 HEPES (pH 7.3, adjusted with CsOH) for recording excitatory postsynaptic currents (EPSCs), (2) 124 CsCl, 10 HEPES, 10 BAPTA, 1 $CaCl_2$, 4.6 $MgCl_2$, 4 ATP, 0.4 GTP (pH 7.3, adjusted with CsOH) for recording inhibitory postsynaptic currents (IPSCs), and (3) 135 K-gluconate, 10 Na-gluconate, 5 KCl, 0.5 EGTA, 10 HEPES, 4 Mg-ATP, 0.4 Na_3-GTP (pH 7.3, adjusted with NaOH), and 0.1 Oregon Green 488 BAPTA1 for recording CF-induced complex spikes and resultant calcium transients. Picrotoxin (100 μM) was added to block GABA receptor-mediated inhibitory currents for recording EPSCs, and NBQX (10 μM) and D-AP5 (50 μM) were included to block AMPA receptor-mediated and NMDA receptor-mediated excitatory synaptic currents, respectively, for recording IPSCs. To stimulate CFs in the granular layer underneath the recorded PCs, electrical pulses (duration of 0.1 ms, amplitude of 0–100 V) were applied at 0.2 Hz through a glass pipette filled with the normal ACSF (Hashimoto and Kano, 2003; Hashimoto et al., 2009b). CF-mediated EPSCs (CF-EPSCs) were recorded at a holding potential of −10 mV to avoid inadvertent generation of voltage-dependent regenerative responses (Hashimoto and Kano, 2003; Hashimoto et al., 2009b). The number of CFs innervating the recorded PC was estimated according to the number of discrete CF-EPSC steps as previously described (Hashimoto and Kano, 2003; Hashimoto et al., 2009b). To search all CFs innervating the recorded PC, we moved the stimulation pipette systematically around the PC soma and increased the stimulus intensity gradually at each stimulation site (Nakayama et al., 2012; Kawata et al., 2014). To measure the inhibitory/excitatory (I/E) ratio, PFs were stimulated in the molecular layer at the position where a maximum response was elicited with the stimulus current of 5 μA. D-AP5 was present throughout the experiment to block NMDA receptors. AMPA receptor-mediated currents evoked by PF-stimulation were first recorded at a holding potential of −60 mV, the reversal potential for GABA receptor-mediated current under our experimental conditions. PCs were subsequently depolarized to −20 mV, NBQX was applied to block AMPARs, and $GABA_A$ receptor-mediated synaptic currents were recorded. The I/E ratio was calculated by dividing the peak $GABA_A$ receptor-mediated current by the peak AMPA receptor-mediated current.

For Ca^{2+}-imaging, Oregon Green 488 BAPTA-1 (0.1 mM; Molecular Probes) was included in the internal solution and applied to the recorded PC by diffusion for at least 20 min. Fluorescence images were acquired by using a high-speed confocal laser scanning microscope (CSU22, Yokogawa, Japan) before and after the application of a 1 s depolarization pulse from −70 to 0 mV to the recorded PCs, as described previously (Tanimura et al., 2009). At each time point, the Ca^{2+}-dependent fluorescence signals from selected regions of interest (ROIs) in the soma and dendrite were corrected by subtracting the background fluorescence signal from a ROI outside the recorded PC. The Ca^{2+}-dependent fluorescence signal was expressed as an increase in fluorescence divided by the pre-stimulus fluorescence values (ΔF/F0) using the Image J software (http://rsbweb.nih.gov/ij/). The changes in fluorescence signals induced by CF inputs in PC somatic or dendritic regions were recorded (Nakayama et al., 2012).

Quantification of Disparity in Multiple CF-EPSCs

To quantify the disparity in multiple CF-EPSCs of a given PC, we calculated disparity ratio, a parameter which reflects the average of the inverse proportion of the strongest CF-EPSC amplitude to each of the other weaker CF-EPSCs (Hashimoto and Kano, 2003). For calculating the disparity ratio, the amplitude of individual CF-EPSCs in a given multiply innervated PC were measured and they were numbered in the order of their amplitudes (A_1, A_2,…, A_N, $N \geqq 2$, A_N represents the largest CF-EPSC). The disparity ratio was obtained from the following formula.

$$\text{Disparity ratio} = (A_1/A_N + A_2/A_N + \ldots\ldots + A_{N-1}/A_N)/(N-1)$$

Western Blot Analysis

Proteins from the cerebella of 2-month-old NLGN3-R451C mutant mice and wild-type mice were extracted and homogenized in RIPA buffer (125 mM Tris-HCl, ph 6.8; 10% Mercaptoethanol, 0.004% Bromophenol Blue, 10% Sucrose, and 4% SDS) with a pestle and mortar. Protein concentrations were determined using the Bradford assay (Bio-Rad Laboratories). Equal amounts of proteins were loaded to the 10% polyacrylamide gel and run at 196 V

and 40 mA for 90 min. The blot was performed at 25 V and 100 mA for 2 h. The primary antibodies were applied overnight at 4°C and HRP-conjugated secondary antibodies were incubated for 1 h at room temperature. The development was performed with Western Lightning Plus ECL (PerkinElmer) and ImageQuant LAS 4000 (GE Healthcare) was used to visualize the bands.

Immunohistochemistry

All primary antibodies were purchased from Nittobo Medical Co., Ltd. (Tokyo, Japan). Under deep pentobarbital anesthesia (100 μg/g of body weight, i.p.), wild-type and NLGN3-R451C mutant mice with 30–35 days of age were fixed with ice-cold 4% paraformaldehyde in 0.1 M sodium phosphate buffer (pH 7.4) and processed for preparation of parasagittal cerebellar sections (50 μm thickness). Free-floating sections were incubated overnight with affinity-purified primary antibodies against the following molecules (host species, final concentration, RRID): NLGN3 (rabbit, 1μg/ml, AB_2571813), anti-calbindin (goat, 1μg/ml, AB_2571569), VGluT2 (rabbit, 1 μg/ml, AB_2619683), parvalbumin (guinea pig, 1 μg/ml, AB_2571615), and vesicular inhibitory amino acid transporter (VIAAT) (rabbit, 0.5 μg/ml, AB_2571622). Sections were incubated subsequently with a mixture of species-specific secondary antibodies labeled with Alexa 488 (1:200, Invitrogen, Carlsbad, CA), Cy3, and Cy5 (1:200, Jackson ImmunoResearch, West Grove, PA) for 2 h. Slices were then washed and mounted on glass slides with Vectashield mounting media (Vector Laboratories). Images were taken with confocal laser-scanning microscope (LSM510, Zeiss). Quantitative analyses of the number of PCs, the length of primary PC dendrite and the number of molecular layer interneurons (**Figures 5O–Q**) were performed on lobule 3, 4/5, and 6 of the cerebellar slices by using MetaMorph software (Molecular Devices, Sunnyvale, CA).

Anterograde Tracer Labeling

Three wild-type and three NLGN3-R451C mutant mice were used for the following analyses. Under anesthesia by inhalation of 3.5% isoflurane, a glass pipette filled with 2–3 μl of 10% solution of dextran Alexa Fluor-594 (DA-594, Invitrogen) in PBS was inserted stereotaxically into the inferior olive by the dorsal approach, as described previously (Miyazaki and Watanabe, 2011). The tracer was injected by air pressure (Pneumatic Picopump; World Precision Instruments). After 4 days of the tracer injection, mice were deeply anesthetized with sodium pentobarbital (100 μg/g of body weight, i.p.) and fixed by transcardial perfusion at P14 or P28. To visualize tracer-labeled CFs, all CF terminals, and PC somata and dendrites, microslicer sections of the cerebellum from DA-594-injected mice were incubated overnight with a mixture of primary antibodies against calbindin (a marker for PC; rabbit serum, 1:10,000 dilution; AB_2571568) and VGluT2 (a marker for CF terminals; goat, 1 μg/ml, AB_2571620), followed by 2 h incubation with a mixture of species-specific secondary antibodies as described above. Images of the triple labeling were taken with a confocal laser-scanning microscope (FV1000, Olympus, Tokyo, Japan).

Post-embedding Immunogold Electronmicroscopy

For postembedding immunogold, three NLGN3-R451C mutant and three wild-type mice with 30–35 days of age were used. Cerebellar sections (250 μm in thickness) were embedded in Lowicryl HM20 (Lowi) medium and polymerized with ultraviolet. The ultrathin sections processed with an ultramicrotome (ULTRACUT UCT, Lecia) were incubated overnight with rabbit anti-NLGN3 antibody (5 μg/ml) and then with 10-nm colloidal gold-conjugated anti-rabbit IgG (1:100; British Bio Cell International). Subsequently, the sections were incubated overnight with guinea pig anti-VGluT1 (10 μg/ml), anti-VGluT2 (10 μg/ml), and anti-VIAAT (10 μg/ml) antibodies and then with 15-nm colloidal gold-conjugated anti-guinea pig IgG (1:100; British Bio Cell International). Electron micrographs were taken with an JEM1400 electron microscope (JEOL, Tokyo, Japan). For the quantitative analysis of synaptic localization of immune-gold particles (**Figure 4G**), we used MetaMorph software (Molecular Devices, Sunnyvale, CA).

Statistics

Data are presented as mean ± SD unless indicated otherwise. Unpaired two-tailed Student's *t*-test, Mann-Whitney U-test or the Kolmogorov-Smirnov test was used for comparison of two independent samples. Two-way ANOVA and the non-parametric Kruskal-Wallis H test were used for multiple comparisons. Statistical analysis was conducted with GraphPad Prism 8 software (GraphPad Software, La Jolla, CA, USA) and IBM SPSS statistics (IBM SPSS Inc., Chicago, IL, USA). $p < 0.05$ was considered as statistically significant.

RESULTS

Selective Strengthening of Single CF Inputs Relative to Others Is Compromised in NLGN3-R451C Mutant Mice

To determine CF innervation patterns of PCs in juvenile wild-type and mutant mice, we performed whole-cell recordings from PCs in cerebellar slices from mice aged P21–P35. In 80% (68/85) of PCs in wild-type mice and 79% (60/76) in NLGN3-R451C mutant mice, single large CF-EPSCs were induced in an all-or-none fashion as the stimulus intensity was gradually increased (**Figure 1A**). There was no significant difference in the frequency distribution of PCs in terms of the number of CF-EPSC steps between wild-type and NLGN3-R451C mutant mice (**Figure 1B**). This result suggests that CF elimination is completed normally in PCs of juvenile NLGN3-R451C mutant mice.

We then examined whether the selective strengthening of a single CF among multiple CFs in each PC was affected in NLGN3-R451C mutant mice. We calculated the disparity ratio for each multiply innervated PC (see section Materials and Methods), which reflects the average of the inverse proportion of the strongest CF-EPSC amplitude to each of the other weaker CF-EPSCs (Hashimoto and Kano, 2003). We found that the disparity ratio was significantly larger in juvenile NLGN3-R451C mutant mice than in wild-type mice (**Figure 1C**), suggesting that

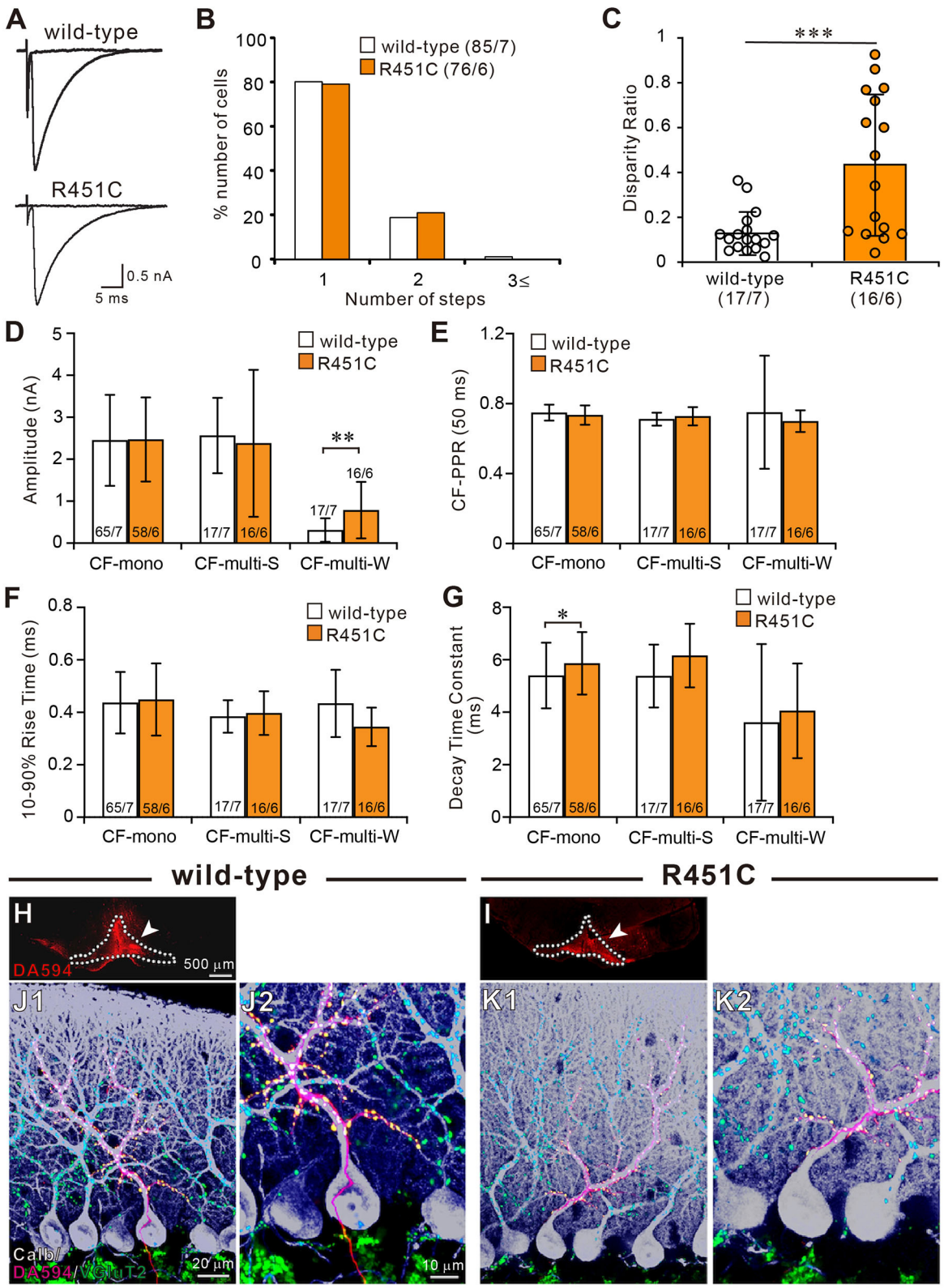

FIGURE 1 | The NLGN3-R451C mutation impairs functional differentiation of multiple CF inputs during synapse elimination. **(A)** Specimen traces of CF-EPSC recorded from Purkinje cell soma in wild-type and NLGN3-R451C mutant (R451C) mice at P21–P35 at a holding potential (Vh) of −10 mV in the presence of 100 µM picrotoxin. Scale bars, 5 ms and 0.5 nA. **(B)** Frequency distribution of the number of CF-EPSC steps in each PCs for wild-type (open columns) and NLGN3-R451C

(Continued)

FIGURE 1 | mutant (orange columns) mice at P21–P35. $p = 0.9$ by Mann-Whitney U test. Numbers of PCs/mice are shown in parentheses. **(C)** Summary plots of disparity ratio in wild-type (open circles and open column) and NLGN3-R451C mutant (orange circles and orange column) mice during P21–P35. ***$p < 0.001$ by Mann-Whitney U test. Numbers of PCs/mice are shown in parentheses below the graph. Data are expressed as mean ± SD. **(D–G)** Summary bar graphs for the amplitude **(D)**, paired-pulse ratio **(E)**, 10–90% rise time **(F)**, and decay time constant **(G)** of EPSCs elicited by stimulating CF-mono, CF-multi-S, and CF-multi-W in wild-type (open column) and NLGN3-R451C mutant (orange column) mice. Data were obtained from P21–P35 mice and are expressed as mean ± SD. **$p = 0.0061$ in **(D)** and *$p = 0.033$ in **(G)** by Mann-Whitney U test. Numbers of PCs/mice are shown inside or above the bar. **(H,I)** Fluorescent images of the anterograde tracer (red, DA-594) showing its injection sites (arrows) in the inferior olive (dotted lines) of wild-type **(H)** and NLGN3-R451C mutant **(I)** mice. **(J,K)** Triple immunostaining for calbindin (white), anterogradely labeled CFs (red, DA-594), and VGluT2 (green) in wild-type **(J1,J2)** and NLGN3-R451C mutant **(K1,K2)** mice at P28. **(J2,K2)** are the magnified views of **(J1,K1)**, respectively. Scale bars represent 500 μm for **(D,E)**, 20 μm for **(J1,K1)**, and 10 μm for **(J2,K2)**. Three mice at P28 of each genotype were used for **(H–K)**.

selective strengthening of a single CF in each PC is severely impaired in NLGN3-R451C mutant mice. Since each PC is either mono innervated by a single strong CF (CF-mono) or multiply innervated by a strong CF (CF-multi-S) and a few weaker CFs (CF-multi-W), we compared the amplitude of EPSCs for these three categories of CFs (**Figure 1D**). Whereas the amplitudes of EPSCs for CF-mono and for CF-multi-S were similar between the two genotypes, those for CF-multi-W were significantly larger in NLGN3-R451C mutant mice than in wild-type mice (**Figure 1D**), which appeared to be the basis for the elevated disparity ratio in NLGN3-R451C mutant mice. In contrast, basic electrophysiological properties of EPSCs for the three categories of CFs were similar between the two genotypes (**Figures 1E–G**) except that the decay time constant for CF-mono was longer in NLGN3-R451C mutant mice (**Figure 1G**).

Next, we examined the innervation pattern of CFs morphologically by labeling a subset of CFs with an anterograde tracer, DA-594, injected into the inferior olive (**Figures 1H,I**). Combining with immunofluorescence for a PC marker, calbindin and a global CF terminal marker, VGluT2, we found that DA-594-labeled CFs precisely followed the PC's proximal dendrites and climbed up to the four-fifths of the molecular layer in both wild-type and NLGN3-R451C mutant mice (**Figures 1J,K**). VGluT2 signals were only found on proximal dendrites but not in the somatic regions of PCs, which indicates essentially all the VGluT2 signals overlapped with DA-594 signals. This result demonstrates that most of the wild-type and NLGN3-R451C mutant PCs are innervated by single CFs on their proximal dendrites. There was no appreciable difference between the two genotypes.

CF Synapse Elimination Is Delayed From P10 to P15 in NLGN3-R451C Mutant Mice

Although majority of PCs in juvenile NLGN3-R451C mutant mice were innervated by single CFs, functional differentiation of multiple CFs during postnatal development appeared to be affected. We therefore investigated whether CF innervation patterns during the first three postnatal weeks are altered in NLGN3-R451C mutant mice. From P5 to P9, majority of PCs were multiply innervated by CFs in both wild-type and NLGN3-R451C mutant mice. Although the number of CFs innervating individual PCs decreased from P5–P6 to P7–P9, no significant differences were found between the genotypes (**Figures 2A,B**). In contrast, a significantly higher number of CFs innervated individual PCs in NLGN3-R451C mutant mice than in wild-type mice from P10 to P12 (**Figure 2C**) and from P13 to P15 (**Figure 2D**). Then, the CF innervation pattern in NLGN3-R451C mutant mice became identical to that of wild-type from P16 to P20 (**Figure 2E**), which persisted into juvenile stage (**Figure 1**). We also calculated the disparity ratio at each of the five developmental stages (**Figure 2F**) and found that the disparity ratio in NLGN3-R451C mutant mice became larger than that in wild-type mice after P16. To check whether there is any structural change transiently in the developing cerebellum, we examined the innervation pattern of CFs morphologically at P14 by labeling a subset of CFs with DA-594 (**Supplementary Figure 1**). We found no perceptive difference between the genotypes in the morphology of PC dendrites and CF innervation pattern. These results indicate that regression of multiple CF innervation initially occurs normally until P9, is impaired transiently from P10 to P15, and then is resumed to yield normal pattern of CF innervation after P16. In contrast, impairment in the strengthening of a single CF relative to the other weaker CFs in each PC became obvious at around P16 and persisted thereafter.

Reduced NLGN3 Expression but Normal Gross Anatomy and Cellular Morphology in the Cerebellum of NLGN3-R451C Mutant Mice

In a previous work on the NLGN3-R451C mutation, Etherton and coworkers (Etherton et al., 2011) showed that NLGN3 controls excitatory and inhibitory synaptic transmission in circuit-dependent and brain region-specific manners. For instance, mutant mice displayed an increase in synaptic inhibition in the somatosensory cortex while an increase in AMPA receptor-mediated excitatory synaptic transmission and NMDA receptor containing GluN2B subunits in the hippocampus. Given NLGN3 is localized to both glutamatergic and GABAergic synapses, organizes the scaffolding protein recruitment and maintains the synapse stability, we explored a possibility that the NLGN3-R451C mutation delays the CF to PC synapse elimination process by changing the expression level of synaptic molecules. We first analyzed the expression of synaptic proteins in the cerebellum. Consistent with the previous studies on other brain regions, we found that the NLGN3-R451C substitution caused a nearly 90% reduction of NLGN3 total protein (**Figure 3A**). However, we did not observe any significant changes in the expression of other NLGN isoforms (NLGN1 and NLGN2), PSD-95 (a marker of

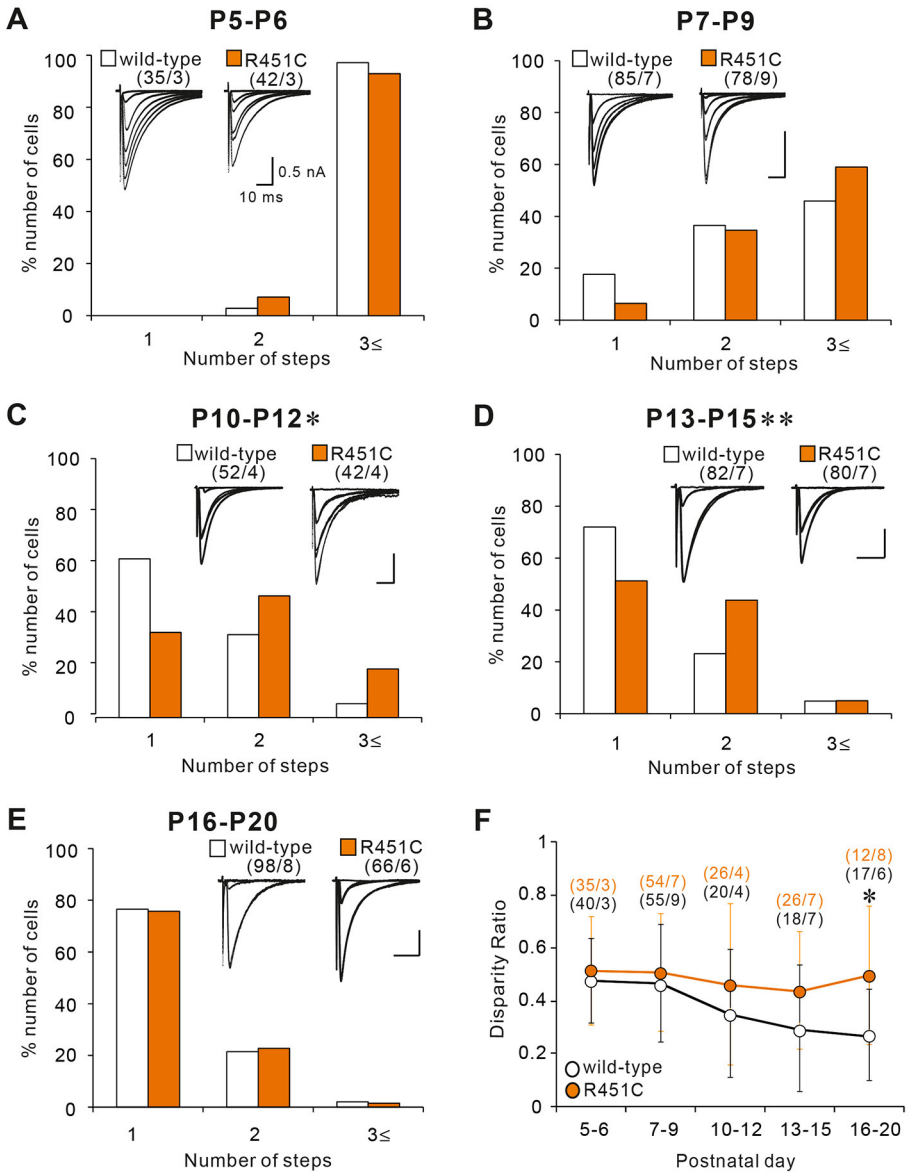

FIGURE 2 | The NLGN3-R451C mutation impairs CF synapse elimination during postnatal development. **(A–E)** Specimen records of CF-EPSCs (inserts, five to eight traces were superimposed at each threshold intensity; Vh = −10 mV) and frequency distribution histogram for the number of discrete CF-EPSCs for wild-type (open columns) and NLGN3-R451C mutant mice (orange columns) at indicated ages. There is no significant difference in the frequency distribution in **(A,B,E)** between wild-type and NLGN3-R451C mutant mice [**(A)**, $p = 0.143$, **(B)**, $p = 0.063$, and **(E)**, $p = 0.6$ by Mann-Whitney U test]. In contrast, frequency distributions for **(C,D)** are significantly different between wild-type and NLGN3-R451C mutant mice (**C**, $^{*}p = 0.024$ and **D**, $^{**}p < 0.001$ by Mann-Whitney U test). Scale bars, 10 ms and 0.5 nA. Numbers of PCs/mice are shown in parentheses. **(F)** Summary plots of disparity ratio in wild-type (open circles) and NLGN3-R451C mutant (orange circles) mice at indicated ages. There is a significant difference between wild-type and NLGN3-R451C mutant mice aged P16–P20 (P5–P6, $p = 0.961$; P7–P9, $p = 0.877$; P10–P12, $p = 0.409$; P13–P15, $p = 0.173$; P16–P20; $^{*}p = 0.039$ by Two-way ANOVA with Tukey's *post-hoc* test). Numbers of PCs/mice are shown in parentheses. Data are expressed as mean ± SD.

excitatory synapses), Gephyrin (a marker of inhibitory synapses) and $GABA_AR\alpha1$ ($GABA_A$ receptor subunit α1) (**Figure 3A**). To further characterize possible effects of the R451C mutation, we checked the cellular expression of NLGN3 within the cerebellum. Immunohistochemical study using an NLGN3-specific antibody showed that NLGN3 was strongly localized in the molecular layer, granular layer and PC layer in wild-type mice (**Figures 3B,C**), which is similar to a previous study (Baudouin et al., 2012). However, in NLGN3-R451C mutant mice, NLGN3 expression was decreased in both the molecular and the granular layers (**Figures 3D,E**). Post-embedding immunogold electron microscopy showed that the density of metal particles for NLGN3 at the postsynaptic membrane was not different between wild-type and NLGN3-R451C mutant mice for parallel fiber (PF) to PC synapses (**Figures 4A,D,G**) and for CF to PC synapses (**Figures 4B,E,G**). In contrast, the postsynaptic

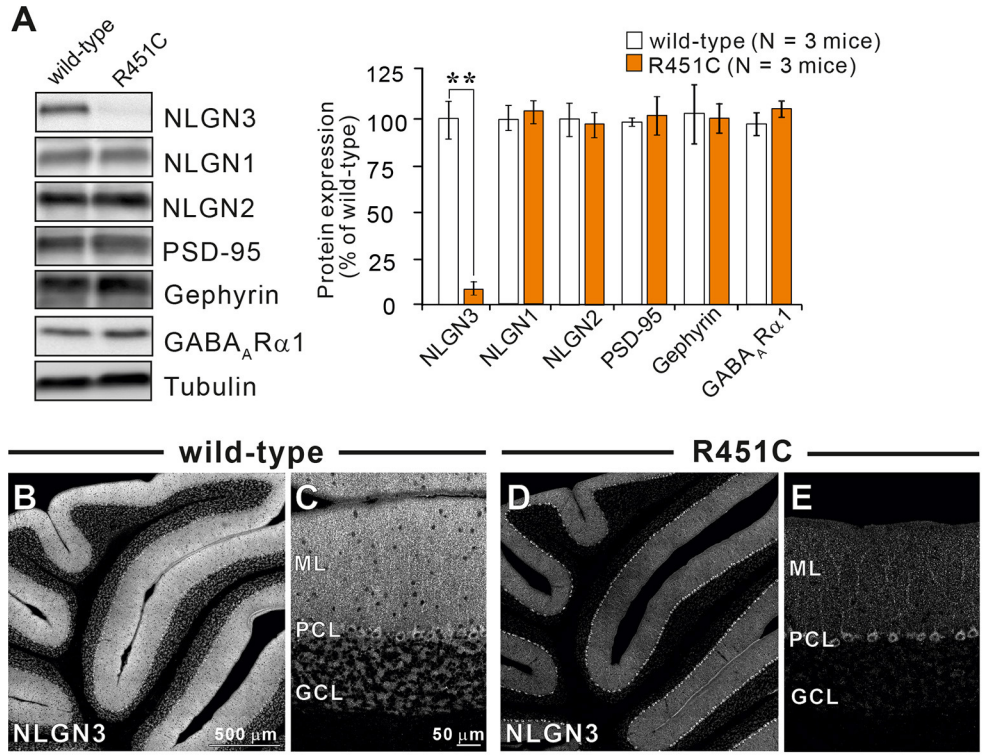

FIGURE 3 | The NLGN3-R451C mutation greatly reduces the expression of NLGN3 but not other synaptic proteins in the cerebellum. **(A)** Representative immunoblots (left panel) and summary bar graphs (right panel) showing the expression levels of several synaptic proteins in cerebellar homogenates from 2-month-old wild-type (open columns) and age-matched NLGN3-R451C mutant mice (orange columns) ($N = 3$ mice/group). Representative synaptic proteins (NLGN1, neuroligin-1; NLGN2, neuroligin-2; NLGN3, neuroligin-3; PSD-95, Gephyrin, $GABA_A$ receptor subunit α1) were analyzed by quantitative immunoblotting. Data are expressed as mean ± SD. $^{**}p < 0.001$ by Student's *t*-test. **(B–E)** Immunohistochemistry for NLGN3 in the cerebellum with a low magnification **(B,D)** and with a high magnification **(C,E)** in 2-month-old wild-type **(B,C)** and age-matched NLGN3-R451C mutant **(D,E)** mice. ML, molecular layer; PCL, Purkinje cell layer; GCL, granule cell layer. In wild-type mice, NLGN3 signal is intense in ML and GL, whereas that in NLGN3-R451C mutant mice is decreased. Scales bars represent 500 μm for **(B,D)**, and 50 μm for **(C,E)**.

NLGN3 density was significantly lower in NLGN3-R451C mutant than in wild-type mice at inhibitory interneuron (InT) to PC synapses (**Figures 4C,F,G**). We also checked global histo- and cytoarchitecture of the cerebellum. No apparent difference between genotypes were observed in the size and lobular organization of the cerebellum (**Figures 5A–D**), the cellular arrangement and dendritic arborization of PCs (**Figures 5E1,F1**), the distribution and density of CF terminals (**Figures 5E2,F2**), PF terminals (**Figures 5G,I**), inhibitory terminals (**Figures 5H,J**), and cell bodies of molecular layer interneurons (**Figures 5K,M**), and the palisade-like arrangement of Bergmann glia's fibers (**Figures 5L,N**). No difference was found in the number of PCs (**Figure 5O**), the length of primary PC dendrite (**Figure 5P**) or the number of molecular layer interneurons (MLIs) (**Figure 5Q**).

Elevated Inhibition to Excitation Balance in PCs of NLGN3-R451C Mutant Mice

How does the NLGN3-R451C mutation delays CF synapse elimination and compromises the strengthening of a single CF relative to the other weaker CFs? Because post-embedding immunogold electron microscopy showed a significant reduction of NLGN3 expression at inhibitory synapses of PC, we hypothesized that alteration in inhibitory synaptic strength to PCs may have caused the changes in CF to PC synapse development in NLGN-R451C mutant mice. We first examined miniature inhibitory postsynaptic currents (mIPSCs) from PCs of mice aged P22 to P35 and found that the amplitude but not the frequency was increased by ∼50% in NLGN3-R451C mutant mice when compared to wild-type mice (**Figure 6A**). We then examined mIPSCs during postnatal development of CF to PC synapses. We found that the amplitude of mIPSCs was consistently larger in NLGN3-R451C mutant mice than in wild-type mice during P7–P9, P10–P12, P13–P15, and P16–P20 (**Figure 6B**). Our previous study shows that inhibitory synaptic inputs to PCs from around P10 to P12 are important for CF synapse elimination (Nakayama et al., 2012). We therefore scrutinized mIPSCs at this developmental stage and found that the amplitude of mIPSCs larger than 100 pA, which presumably arose from basket cells, and that smaller than 100 pA, which presumably represent inhibitory inputs from stellate cells, were both increased in NLGN3-R451C mutant mice compared to wild-type mice (**Figures 6E–G**).

In contrast to mIPSC, no significant differences were found in either the amplitude or the frequency of miniature excitatory

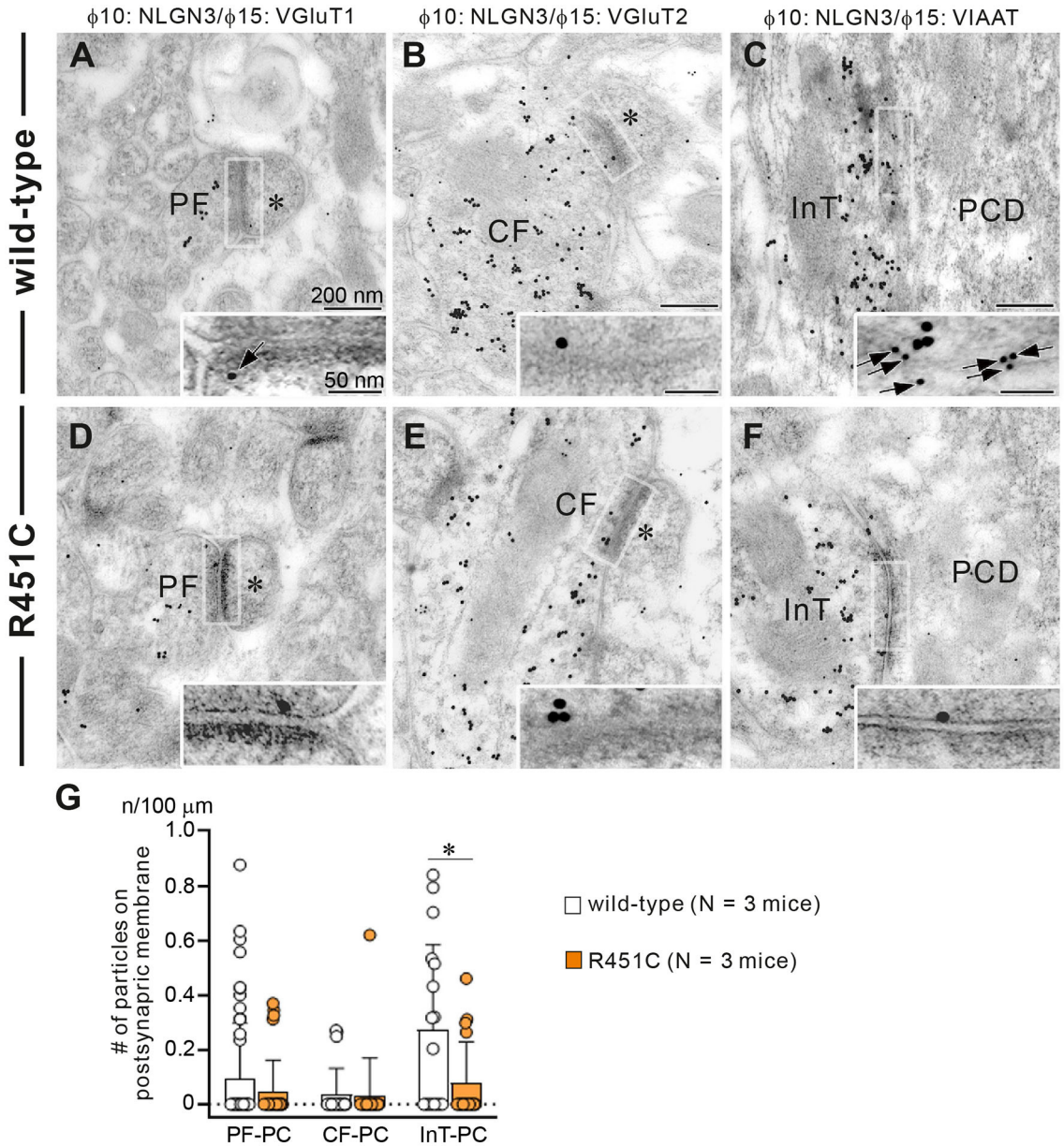

FIGURE 4 | Reduced NLGN3 expression at inhibitory interneurons to PC synapses in NLGN3-R451C mutant mice. **(A–F)** Post-embedding immunogold electron microscopy for NLGN3 in wild-type **(A–C)** and NLGN3-R451C mutant **(D–F)** mice. **(A,D)** Indicate PC spines (asterisks) contacting to PF presynaptic terminals labeled for VGluT1. **(B,E)** Indicate PC spines (asterisks) contacting to CF presynaptic terminals labeled for VGluT2. **(C,F)** Indicate PC dendrites (PCD) contacting to presynaptic terminals of inhibitory interneurons (InT). Scale bars, 200 nm and 50 nm for inset. **(G)** Summary bar graphs showing the average number of NLGN3 immunogold particles (n) per 100 μm of the postsynaptic membrane of PF-PC, CF-PC, and InT-PC synapses in wild-type (open circles and columns, $N = 3$ mice aged 30–35 days) and NLGN3-R451C mutant (orange circles and columns, $N = 3$ mice aged 30–35 days) mice. Data are expressed as mean ± SD. $p = 0.33$ for PF-PC, $p = 0.61$ for CF-PC and $^*p = 0.035$ for InT-PC synapses by Mann-Whitney U test.

postsynaptic currents (mEPSCs) between wild-type and NLGN3-R451C mutant mice aged P22–P35 (**Figure 6C**). Furthermore, the amplitude of mEPSCs was similar between genotypes throughout postnatal development (**Figure 6D**). We further examined EPSCs evoked by PF stimulation (PF-EPSCs) and found that the input-output relation and the response to paired stimulation (paired-pulse ratio) for PF-EPSCs were not altered in NLGN3-R451C mutant mice (**Supplementary Figures 2A,B**). Moreover, the paired-pulse ratio for CF-EPSCs was also not altered in NLGN3-R451C mutant mice (**Supplementary Figures 2C,D**).

Many previous studies indicate that the deviation of balance between inhibition and excitation in individual neurons underlies the pathophysiology of ASD (Tabuchi et al., 2007;

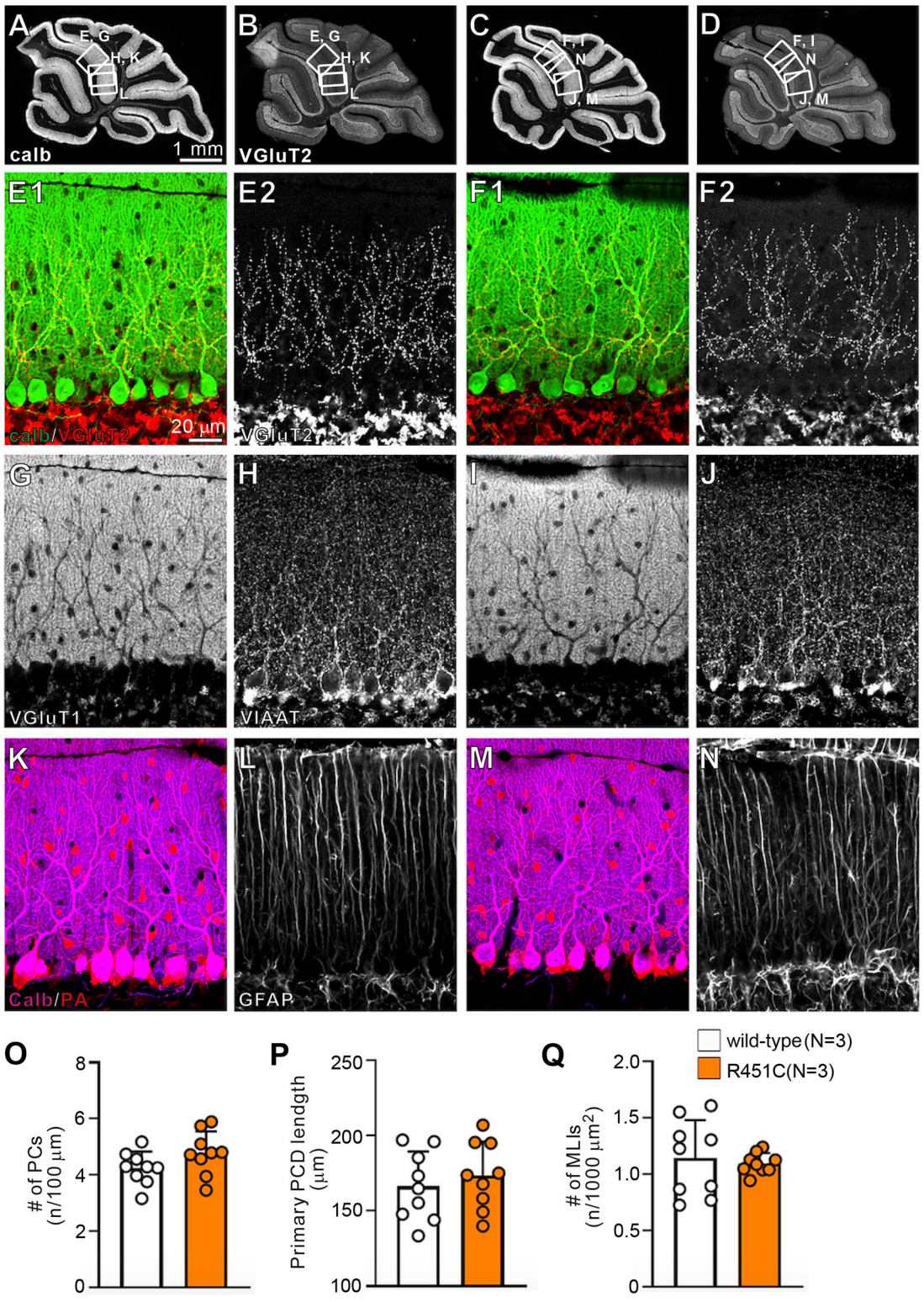

FIGURE 5 | Gross anatomy of the cerebellum, morphology of major cell types, and density of major excitatory and inhibitory synapses appear normal in NLGN3-R451C mutant mice. **(A–D)** Immunofluorescence for the PC marker calbindin **(A,C)** and for the CF terminal marker VGluT2 **(B,D)** of the cerebellum of wild-type **(A,B)** and NLGN3-R451C mutant **(C,D)** mice. The boxed regions in **(A,B)** and those in **(C,D)** indicate the portions of the cerebellum from which the images

(Continued)

FIGURE 5 | in **(E,G,H,K,L)** and those in **(F,I,J,M,N)** were obtained, respectively. Scale bar, 1 mm. **(E–N)** Immunofluorescence for calbindin (green, **E1,F1**) and VGluT2 [red for **(E1,F1)**, white for **(E2,F2)**], for the PF marker VGluT1 **(G,I)**, for the inhibitory synaptic terminal marker vesicular inhibitory amino acid transporter (VIAAT) **(H,J)**, for a marker of PC and inhibitory interneurons, parvalbumin (PA) **(K,M)**, and for the astrocyte marker glial fibrillary acidic protein (GFAP) **(L,N)** in wild-type **(A,E,G,H,K,L)** and NLGN3-R451C mutant **(F,I,J,M,N)** mice. Scale bar, 20 μm. **(O–Q)** Histograms for wild-type (open circles and columns, $N = 3$ mice aged 30–35 days) and NLGN3-R451C mutant mice (orange circles and columns, $N = 3$ mice aged 30–35 days) showing the number of PCs (n) per 100 μm of Purkinje cell layer **(O)**, the length of primary PC dendrite **(P)** and the number of MLIs (n) per 1000 μm^2 **(Q)**. Data were obtained from the straight portions of lobule 3, 4/5, and 6, and are expressed as mean ± SD. $p = 0.11$ for **(O)**, $p = 0.55$ for **(P)** and $p = 0.80$ for **(Q)** by Mann-Whitney *U* test.

Chao et al., 2010; Delorme et al., 2013). We therefore directly estimated the ratio of inhibition to excitation in individual PCs in response to stimulation in the molecular layer (**Figures 6H–K**). We first recorded PF-EPSCs that are mediated by AMPA receptors at a holding potential of −60 mV, which is equivalent to the Cl^- equilibrium potential, in the presence of the NMDA receptor antagonist D-AP5. Then we added NBQX to completely block AMPA receptor-mediated PF-EPSCs and recorded $GABA_A$ receptor-mediated IPSCs at a holding potential of −20 mV, which were abolished by addition of PTX (**Figures 6H,I**). We then calculated the ratio of the amplitude of PF-EPSC to that of IPSC (I/E ratio) in each PC and found that the I/E ratio was markedly increased in NLGN3-R451C mutant mice (**Figures 6J,K**). Taken together, these results indicate that inhibitory synaptic inputs to PCs are enhanced but the overall strength of excitatory synaptic inputs to PCs are not altered, leading to elevated I/E balance in NLGN3-R451C mutant mice when compared to wild-type mice.

Decreased CF-Induced Ca^{2+} Transients in the PC Soma in NLGN3-R451C Mutant Mice

We have reported previously that diminished GABAergic transmission from putative basket cell to PC resulted in larger Ca^{2+} transients elicited by the weaker CFs in multiply innervated PCs from P10 to P13 (Nakayama et al., 2012). Because the R451C substitution of NLGN3 increases the amplitude of mIPSCs in PCs, CF-induced Ca^{2+} transients may be affected. To test this possibility, we recorded postsynaptic membrane potentials and Ca^{2+} transients from multiply innervated PCs from P10 to P13 during stimulation of CF-multi-S or CF-multi-W under current-clamp mode in the normal external solution. Stimulation of CF-multi-S induced characteristic complex spikes accompanied by clear Ca^{2+} transients in proximal dendrites and somata in both wild-type and NLGN3-R451C mutant mice (**Figures 7A,B**). We quantified the magnitude of CF-induced Ca^{2+} transients by measuring the integral of Ca^{2+} signals (for 1.5 s from the onset). We found that the Ca^{2+} transients in the soma were significantly smaller but those in dendrites were similar in NLGN3-R451C mutant mice compared to wild-type mice (**Figure 7C**). Stimulation of CF-multi-W induced smaller EPSPs with a few action potentials and much smaller Ca^{2+} transients when compared to those induced by stimulating CF-multi-S (**Figures 7D,E**). Notably, dendritic Ca^{2+} transients were very small and sometimes undetectable, which is consistent with the fact that CF-multi-W does not undergo dendritic translocation but stays around the PC soma (Hashimoto and Kano, 2003; Hashimoto et al., 2009a). Nevertheless, dendritic Ca^{2+} transients were similar between the two genotypes. In contrast, somatic Ca^{2+} transients induced by CF-multi-W were significantly smaller in NLGN3-R451C mutant mice than in wild-type mice (**Figure 7F**). These results indicate that increased inhibition to PCs results in reduced somatic Ca^{2+} transients elicited by CF-multi-S and CF-multi-W in PCs of NLGN3-R451C mutant mice presumably because of weaker activation of P/Q-type voltage-dependent calcium channels (P/Q-VDCCs) and resultant reduction of Ca^{2+} influx into the PC soma.

DISCUSSION

Several previous studies suggest that abnormal synaptic pruning/elimination in the developing brain underlies the pathophysiology of ASD (Weiler and Greenough, 1999; Bourgeron, 2009; Tsai et al., 2012a). For instance, in Fragile X syndrome patients and Fmr1 knockout mice, the number of dendritic spines in mature cortical neurons was increased because of the deficit in MEF2-dependent synapse elimination (Irwin et al., 2001, 2002; Pfeiffer et al., 2010). In Tsc2 mutant mice, the density of dendritic spines in cortical neurons was elevated because of over-activation of mTOR signaling, leading to the reduction of autophagy for spine pruning (Bourgeron, 2009; Tang et al., 2014). However, it is not clear whether and how ASD-associated genes are involved in synapse pruning/elimination in the developing cerebellum. In the present study, we show that an autism-associated genetic mutation of NLGN3 affects developmental synaptic refinement in the mouse cerebellum. In NLGN3-R451C mutant mice, CF to PC synapse elimination was delayed transiently from P10 to P15. Although CF innervation pattern became normal in juvenile mice, the weaker CF synaptic inputs were abnormally strong in NLGN3-R451C mutant PCs, which became evident from P16 and persisted into juvenile stage. These results indicate that abnormalities during postnatal development may perturb proper formation of cerebellar neural circuits and may cause lifelong effects on animal's behavior. However, it should be noted that NLGN3-R451C mutation is present not only in PCs but also in all the cell types that express NLG3 in the mutant mice. It is therefore possible that the abnormality of CF to PC synapse development in the mutant mice may result from, or at least may be influenced by, NLGN3-R451C mutation in cells other than PCs such as neurons in the inferior olive. It would be interesting in future to examine whether a PC-specific introduction of NLGN3-R451C mutation in mice causes abnormalities seen in global NLGN3-R451C mutant mice.

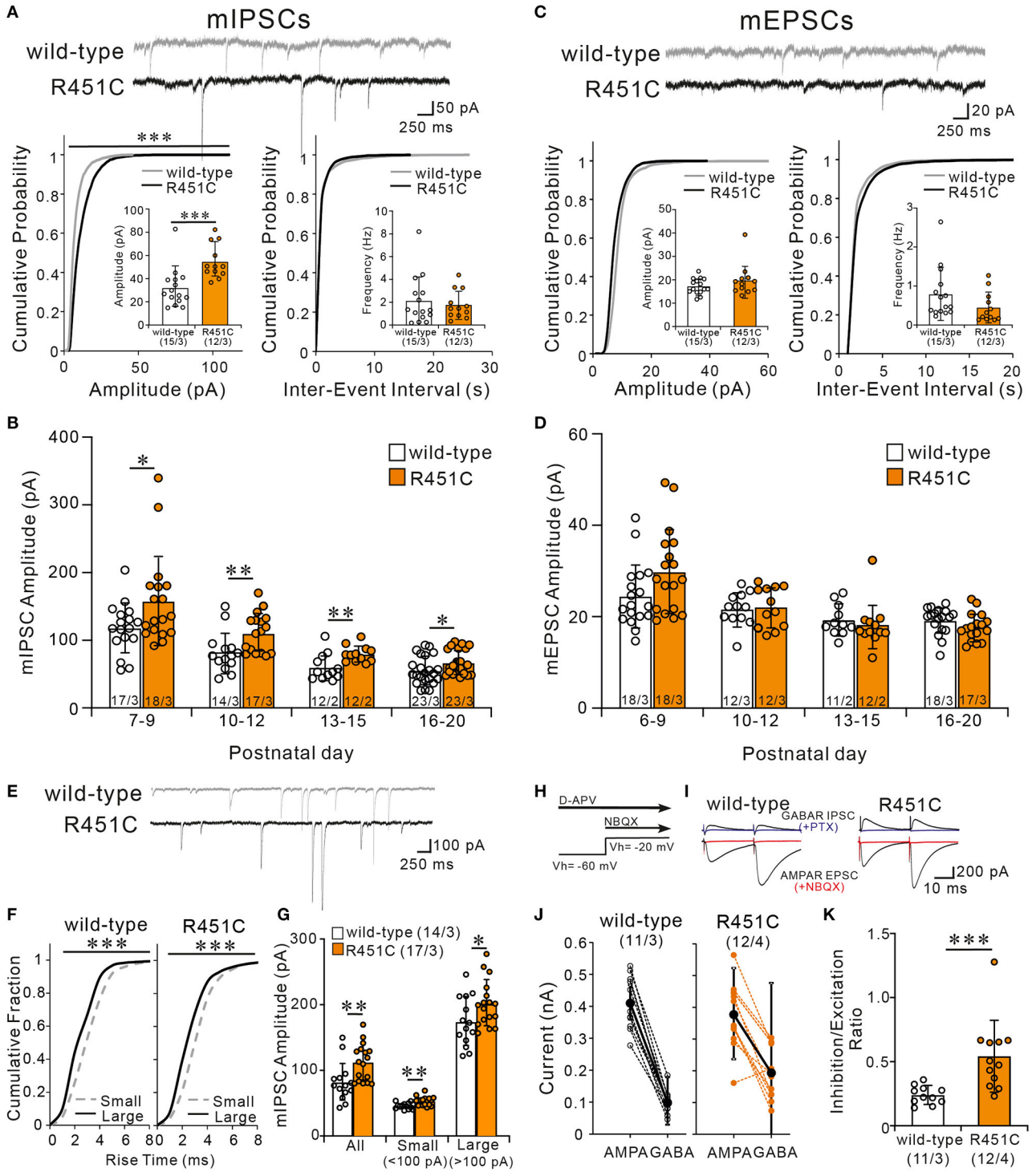

FIGURE 6 | The NLGN3-R451C mutation causes the enhancement of inhibitory synaptic transmission and the elevation of inhibition/excitation ratio of synaptic inputs to PCs. **(A)** Representative traces of mIPSC recorded from PCs of wild-type (upper trace) and NLGN3-R451C mutant (lower trace) mice (top) at Vh of −70 mV in the presence of 1 μM tetrodotoxin, 10 μM NBQX, and 5 μM R-CPP ($N = 3$/group). Scale bars, 250 ms and 50 pA. Cumulative distribution plots and summary bar graphs for the mIPSC amplitude (lower left; inset shows the average mIPSC amplitude) and for the inter-event interval (lower right; inset shows the average mIPSC frequency) in PCs of wild-type and NLGN3-R451C mutant mice aged P21–P35. For the mIPSC amplitude, $^{***}p < 0.0001$ by Kolmogorov-Smirnov test in the cumulative distribution plot and $^{***}p = 0.0002$ by Mann-Whitney U test in the bar graph. For the inter-event interval, $p = 0.99$ by Kolmogorov-Smirnov test in the cumulative distribution plot and $p = 0.9$ by Mann-Whitney U test in the bar graph. **(B)** Summary graph for the mIPSC amplitude of wild-type (open columns) and NLGN3-R451C mutant (orange columns) mice at indicated ages. Note that the mean amplitudes of mIPSCs in NLGN3-R451C mutant mice are significantly larger than those of

(Continued)

FIGURE 6 | wild-type mice during postnatal development (P7–P9, $^{*}p = 0.029$; P10–P12, $^{**}p = 0.0053$; P13–P15, $^{**}p = 0.0083$; P16–P20, $^{*}p = 0.024$ by Mann-Whitney U test). **(C)** Representative traces of mEPSC recorded from PCs of wild-type (upper trace) and NLGN3-R451C mutant (lower trace) mice (top) at Vh of −70 mV in the presence of 1 μM tetrodotoxin and 100 μM PTX ($N = 3$/group). Scale bars, 250 ms and 20 pA. Cumulative distribution plots for the mEPSC amplitude (lower left; inset shows the average mEPSC amplitude) and for the inter-event interval (lower right; inset shows the average mEPSC frequency) in PCs of wild-type and NLGN3-R451C mutant mice aged P21–P35. For the mEPSC amplitude, $p = 0.17$ by Kolmogorov-Smirnov test in the cumulative distribution plot and $p = 0.40$ by Mann-Whitney U test in the bar graph. For the inter-event interval, $p = 0.84$ by Kolmogorov-Smirnov test in the cumulative distribution plot and $p = 0.59$ by Mann-Whitney U test in the bar graph. **(D)** Summary graph for the mEPSC amplitude of wild-type (open columns) and NLGN3-R451C mutant (orange columns) mice at indicated ages (P6–P9, $p = 0.074$; P10–P12, $p = 0.76$; P13–P15, $p = 0.350$; P16–P20, $p = 0.10$ by Mann-Whitney U test). **(E)** Representative traces of mIPSC recorded from PCs of wild-type (upper) and NLGN3-R451C mutant (lower) mice at P10 in the presence of 1 μM tetrodotoxin, 10 μM NBQX, and 5 μM R-CPP. Vh = −70 mV. Scale bars, 250 ms and 100 pA. **(F)** Cumulative fractions of the rise time of small (<100 pA) (gray dotted line) and large (>100 pA) (black line) mIPSCs in wild-type (left) and NLGN3-R451C mutant (right) mice from P10 to P12. $^{***}p < 0.0001$ by Kolmogorov-Smirnov test for both genotypes. **(G)** Summary bar graphs for the mIPSC amplitude for all, small and large events in wild-type (open columns) and NLGN3-R451C mutant (orange columns) mice from P10 to P12. $^{**}p = 0.0053$ (All); $^{**}p = 0.0014$ (Small); $^{*}p = 0.0484$ (Large) by Mann-Whitney U test. **(H)** Experimental protocol used to measure the inhibition/excitation ratio. **(I)** Representative traces of evoked AMPAR- and $GABA_A$R-mediated synaptic currents in wild-type (left) and NLGN3-R451C mutant (right) mice. Scale bars, 10 ms and 200 pA. **(J)** Amplitudes of AMPAR- (left) and $GABA_A$R- (right) mediated synaptic currents from wild-type (black) and NLGN3-R451C mutant (orange) mice. **(K)** Average inhibition/excitation ratio from wild-type (open column) and NLGN3-R451C mutant (orange column) mice aged P19–P25. $^{***}p = 0.0004$ by Mann-Whitney U test. Data are expressed as mean ± SD. Total number of cells recorded/total number of mice used is indicated within or beneath individual columns.

We found that the R451C substitution of NLGN3 caused a marked reduction of NLGN3 expression within the cerebellum to about 10% of the level of wild-type mice, and that significant reduction was found at inhibitory interneuron to PC synapses. During the postnatal development in NLGN3-R451C mutant mice, inhibitory neurotransmission onto PCs was enhanced without a noticeable effect on excitatory transmission. We found that both large and small mIPSCs recorded from NLGN3-R451C mutant PCs, which presumably arise from basket cells and stellate cells, respectively, were increased and the I/E ratio was elevated significantly. We therefore assume that NLGN3 in the cerebellar circuitry is mainly responsible for the regulation of inhibitory interneuron to PC synaptic transmission, although NLGN3 is widely localized at glutamatergic and GABAergic synapses.

How does a reduction of NLGN3 expression leads to an enhancement of inhibitory synaptic transmission in PCs? Tabuchi et al. (2007) reported increased inhibitory but normal excitatory synaptic transmission in the somatosensory cortex of NLGN3-R451C mutant mice (Tabuchi et al., 2007). They found increased levels of an inhibitory presynaptic protein, VIAAT, and an inhibitory postsynaptic protein, gephyrin, increased density of VIAAT puncta, but normal number of inhibitory synapses. The frequency of mIPSC was elevated, the response to applied GABA was increased, but the amplitude of mIPSC and short-term plasticity were normal. These changes in inhibitory synapses are not consistent with those found in cerebellar PCs of NLGN3-R451C mutant mice. We found an increase in the amplitude but no change in the frequency of mIPSCs and apparently normal intensity of VIAAT immunostaining in the cerebellum of NLGN3-R451C mutant mice. These results suggest that NLGN3-R451C mutation alters inhibitory synaptic function in cell type- and brain region-specific manners, while the outcome of increased inhibitory synaptic transmission and elevated I/E balance are the same. Moreover, Foldy et al. (2013) reported an increase in inhibitory synaptic transmission from cholecystokinin (CCK) basket cells to pyramidal cells in the hippocampus of NLGN3 R451C mutant, which resulted from the absence of endocannabinoid-mediated tonic inhibition (Foldy et al., 2013). It remains to be investigated in future studies how NLGN3-R451C mutation in PCs enhances inhibitory synaptic transmission and whether endocannabinoid-mediated tonic inhibition is absent in PCs of NLGN3-R451C mutant mice.

As the involvement of inhibitory transmission in autism-related synapse pruning was unclear in the previous studies, the cerebellum of NLGN3-R451C mutant mice provides a good model to examine whether and how inhibitory transmission contributes to developmental synapse elimination in ASD. The enhanced inhibition of PCs is considered to be a cause of transient impairment of CF synapse elimination from P10 to P15. On the other hand, our previous study on $GAD67^{+/GFP}$ mice showed that reduced GABAergic inhibition to PCs from P10 impairs CF synapse elimination (Nakayama et al., 2012). It is currently unknown why enhancement and reduction of PC inhibition resulted in apparently similar phenotypes. It is possible that proper balance of excitation and inhibition is crucial for proper CF synapse elimination and deviation of the I/E balance from the normal range may lead to its impairment (see below).

Another key finding in the present study is that the synaptic strength of weaker CFs of multiply innervated juvenile PCs was stronger in NLGN3-R451C mutant mice than in wild-type mice, albeit normal CF innervation of PCs in juvenile mice. In neonatal mice, PCs were innervated by multiple CFs with similar synaptic strengths. From P3 to P7, a single CF is selectively strengthened among the multiple CFs in each PC (functional differentiation) (Hashimoto and Kano, 2005; Hashimoto et al., 2009a; Watanabe and Kano, 2011). Then, only the strengthened CF ("winner" CF) extends its innervation along growing dendrites in each PC (CF translocation) from P9 (Hashimoto and Kano, 2005; Hashimoto et al., 2009a; Watanabe and Kano, 2011). In parallel, the other weaker CFs ("loser" CFs) remaining on the soma are eliminated from P7 to P11 (early phase of CF innervation, which is independent of PF to PC synapse formation) and from P12 to P17 (late phase of CF innervation, which requires normal PF to PC synapse formation) (Hashimoto and Kano, 2005; Hashimoto et al., 2009a; Watanabe and Kano, 2011). Our previous study on PC-selective P/Q-type VDCC knockout mice demonstrated that preferential strengthening of a single CF input from multiple CFs in each PC is severely impaired from P5 to P8. During this

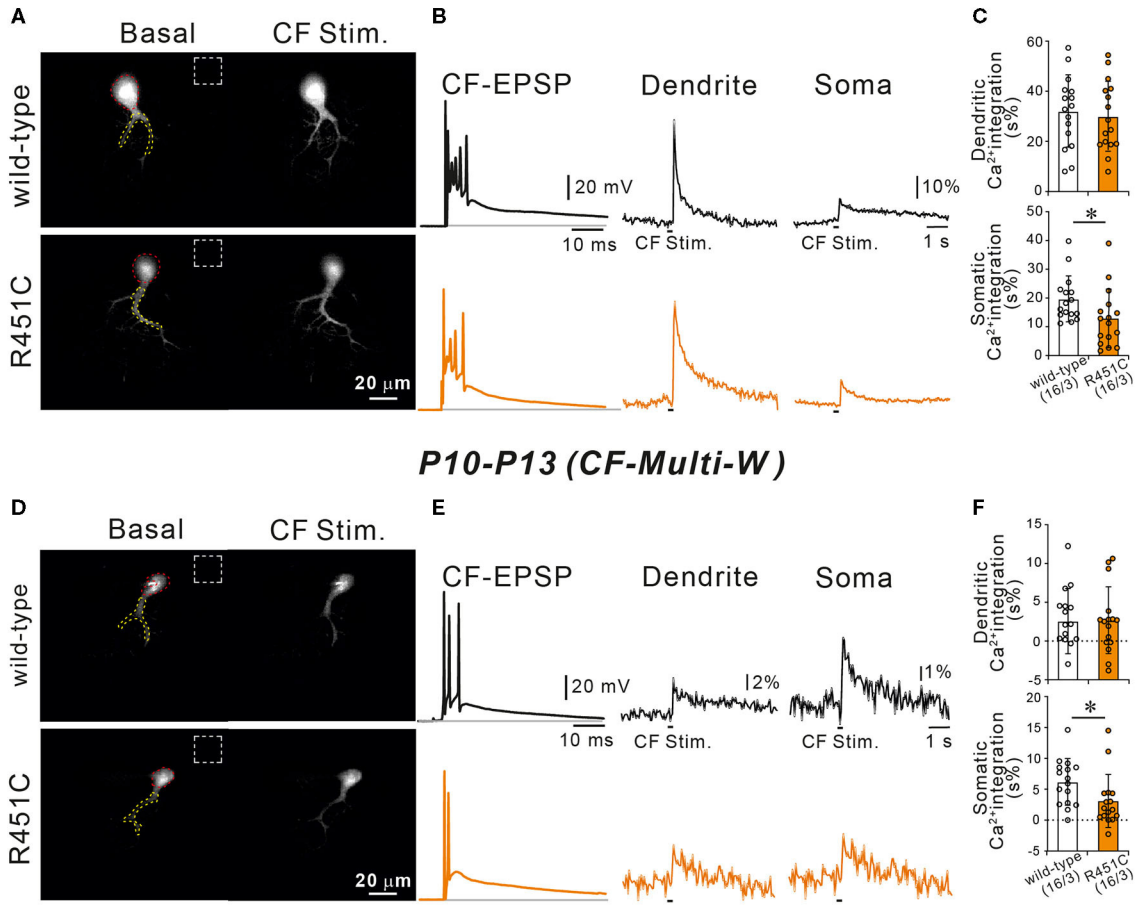

FIGURE 7 | Ca^{2+} transients induced by strong and weak CF inputs are smaller in NLGN3-R451C mutant mice than in wild-type mice. **(A)** Representative images of a wild-type (upper left) and a NLGN3-R451C mutant (lower left) PC. Areas demarcated by red and yellow dotted lines represent ROIs for somatic and dendritic Ca^{2+} transients, respectively. Dashed rectangles represent the ROIs where the background fluorescence signals were measured. Scale bar, 20 μm. **(B)** Representative traces of CF-induced EPSP (right) and those of Ca^{2+} transients recorded in the dendrite (middle) and the soma (right) of multiply-innervated PCs in response to stimulation of the strongest CF in wild-type (black) and NLGN3-R451C mutant (orange) mice. Scale bars, 20 mV and 10 ms for CF-EPSC, 10% and 1 s for Ca^{2+} transients. **(C)** Average magnitudes of Ca^{2+} transients from the soma and the dendrite by stimulating the strongest CF in wild-type (open columns) and NLGN3-R451C mutant (orange columns) mice. $p = 0.77$ (Dendrite) and $^*p = 0.026$ (Soma) by Mann-Whitney U test. **(D)** Representative images of a wild-type (upper left) and a NLGN3-R451C mutant (lower left) PC shown similarly to **(A)**. Scale bar, 20 μm. **(E,F)** Representative traces **(E)** and average magnitudes of Ca^{2+} transients **(F)** shown similarly to **(A,B)**, respectively, but for responses to stimulation of a weak CF of a multiply innervated PC. Scale bars, 20 mV and 10 ms for CF-EPSC, 2% or 1% and 1 s for Ca^{2+} transients. $p = 0.86$ (Dendrite) and $^*p = 0.015$ (Soma) by Mann-Whitney U test. Data for **(A–F)** were obtained from P10 to P13 mice. Data in **(C,F)** are expressed as mean ± SD. Numbers of PCs/mice are shown in parentheses.

developmental period, Ca^{2+} transients induced by spontaneous CF inputs were smaller in PCs of knockout mice (Hashimoto et al., 2011). These results indicate that Ca^{2+} transients in PCs by activation of P/Q-type VDCC are crucial for selective strengthening of a single winner CF and suppressing the other loser CFs in each PC.

We hypothesize that activation of the strong CF may produce "punishment signals" that depress the other weaker CF inputs without affecting the strong CF itself. The hypothetical "punishment signals" are assumed to require large Ca^{2+} transients for their production and can depress only weak CF inputs that generate small Ca^{2+}-transients. We also hypothesize the presence of "survival signals" that are produced by Ca^{2+} transients in PCs and are necessary for the maintenance of CF inputs. In NLGN3-R451C mutant mice, activation of the strong CF induced smaller Ca^{2+} transients in the soma than in wild-type mice, which may have not produced sufficient "punishment signals." Therefore, the weaker CFs may have not been eliminated and CF synapse elimination was transiently impaired from P10 to P15 in NLGN3-R451C mutant mice. However, subsets of the weaker CFs in NLGN3-R451C mutant mice may have not been able to produce sufficient "survival signals" and therefore they were eventually eliminated. Thus, the weaker CF inputs of NLGN3-R451C mutant mice that survived into juvenile stage

may be stronger than those of wild-type mice presumably because of the reduced production of the hypothetical punishment signals from the strongest CF inputs. It is demonstrated that semaphorin 3A (Uesaka et al., 2014), progranulin (Uesaka et al., 2018), and Bai3 (Kakegawa et al., 2015; Sigoillot et al., 2015) in PCs function as "maintenance factors" for CFs, but it is not known whether these molecules require Ca^{2+} transients in PCs for their action. It is also reported that Arc/Arg3.1 (Mikuni et al., 2013), semaphorin 7A (Uesaka et al., 2014), and BDNF (Choo et al., 2017) in PCs function as "punishment signals" for weak CFs. While Arc/Arg3.1 is activated by Ca^{2+} elevation in PCs through P/Q-VDCC (Mikuni et al., 2013), semaphorin 7A and BDNF function at the downstream of metabotropic glutamate receptor 1 but not P/Q-VDCC (Uesaka et al., 2014; Choo et al., 2017). It remains to be investigated whether and how these reported molecules are involved or yet unidentified molecules play roles in shaping CF to PC synaptic wiring during postnatal development.

Many studies indicate that defects in neural circuits including the cerebellum are critical for ASD (O'Halloran et al., 2012; Piochon et al., 2014; Wang et al., 2014; Kloth et al., 2015; Stoodley et al., 2017; Kelley et al., 2020). The cerebellum has connections not only with motor areas of the cerebral cortex but also with the association cortices responsible for higher brain functions (Schmahmann, 2019). Live imaging and postmortem studies in ASD patients showed abnormalities in the cerebellum (Palmen et al., 2004; Wegiel et al., 2010; Becker and Stoodley, 2013) and damage to the cerebellum in neonates is a high risk of ASD (Limperopoulos et al., 2014; Wang et al., 2014). In mouse models of ASD, the cerebellum is reported to be responsible for ASD-like behaviors. For example, PC-specific knockout of an ASD-associated gene, Tsc, is shown to exhibit behavioral abnormalities relevant to ASD including impaired sociality and enhanced repetitive behavior (Tsai et al., 2012b). The results of the present study suggest that the second postnatal week of CF to PC synapse elimination may be critical for shaping neural circuits involving the cerebellum and the cerebrum, and impairment of this process may contribute to ASD-like behavioral abnormalities in NLGN3 R451C mutant mice (Tabuchi et al., 2007). Moreover, NLGN3-R451C mutant mice have been reported to display a significantly increased performance in the accelerating rotarod test because of their elevated trait of repetitive behavior, which is thought to result from impaired neural circuit function in the striatum (Rothwell et al., 2014).

DATA AVAILABILITY STATEMENT

The raw data supporting the conclusions of this article will be made available by the authors.

ETHICS STATEMENT

The animal study was reviewed and approved by the experimental animal ethics committees of the University of Tokyo.

AUTHOR CONTRIBUTIONS

EL and MK designed the project and wrote the manuscript. EL, HN, TM, and TN conducted experiments. EL, TM, and TN analyzed the data. KT provided the NLGN3-R451C mutant mice. All authors contributed to the article and approved the submitted version.

FUNDING

This work was partly supported by Grants-in-Aid for Scientific Research (18H04012 to MK) from the Japan Society for the Promotion of Science (JSPS) and by Grants-in-Aid for Transformative Research Areas (A) (20H05915 to MK) from the Ministry of Education, Culture, Sports, Science and Technology (MEXT) of Japan.

ACKNOWLEDGMENTS

We thank N. Uesaka, S. Kawata, T.-H. Kao, and M. J. Choo for helpful advice and discussion, and K. Matsuyama and M. Sekiguchi for technical assistance.

SUPPLEMENTARY MATERIAL

The Supplementary Material for this article can be found online at: https://www.frontiersin.org/articles/10.3389/fncir.2021.676891/full#supplementary-material

REFERENCES

Abrahams, B. S., and Geschwind, D. H. (2008). Advances in autism genetics: on the threshold of a new neurobiology. *Nat. Rev. Genet.* 9, 341–355. doi: 10.1038/nrg2346

Aldinger, K. A., Kogan, J., Kimonis, V., Fernandez, B., Horn, D., Klopocki, E., et al. (2013). Cerebellar and posterior fossa malformations in patients with autism-associated chromosome 22q13 terminal deletion. *Am. J. Med. Genet. A* 161A, 131–136. doi: 10.1002/ajmg.a.35700

Arons, M. H., Thynne, C. J., Grabrucker, A. M., Li, D., Schoen, M., Cheyne, J. E., et al. (2012). Autism-associated mutations in ProSAP2/Shank3 impair synaptic transmission and neurexin-neuroligin-mediated transsynaptic signaling. *J. Neurosci.* 32, 14966–14978. doi: 10.1523/JNEUROSCI.2215-12.2012

Bailey, A., Luthert, P., Dean, A., Harding, B., Janota, I., Montgomery, M., et al. (1998). A clinicopathological study of autism. *Brain* 121(Pt 5), 889–905. doi: 10.1093/brain/121.5.889

Baudouin, S. J., Gaudias, J., Gerharz, S., Hatstatt, L., Zhou, K., Punnakkal, P., et al. (2012). Shared synaptic pathophysiology in syndromic and nonsyndromic rodent models of autism. *Science* 338, 128–132. doi: 10.1126/science.1224159

Bauman, M. L., and Kemper, T. L. (2005). Neuroanatomic observations of the brain in autism: a review and future directions. *Int. J. Dev. Neurosci.* 23, 183–187. doi: 10.1016/j.ijdevneu.2004.09.006

Becker, E. B., and Stoodley, C. J. (2013). Autism spectrum disorder and the cerebellum. *Int. Rev. Neurobiol.* 113, 1–34. doi: 10.1016/B978-0-12-418700-9.00001-0

Becker, R., Stiemer, B., Neumann, L., and Entezami, M. (2001). Mild ventriculomegaly, mild cerebellar hypoplasia, and dysplastic choroid plexus as

early prenatal signs of CHARGE association. *Fetal Diagn. Ther.* 16, 280–283. doi: 10.1159/000053928

Berkel, S., Marshall, C. R., Weiss, B., Howe, J., Roeth, R., Moog, U., et al. (2010). Mutations in the SHANK2 synaptic scaffolding gene in autism spectrum disorder and mental retardation. *Nat. Genet.* 42, 489–491. doi: 10.1038/ng.589

Bolliger, M. F., Pei, J., Maxeiner, S., Boucard, A. A., Grishin, N. V., and Südhof, T. C. (2008). Unusually rapid evolution of Neuroligin-4 in mice. *Proc. Natl. Acad. Sci. U.S.A.* 105, 6421–6426. doi: 10.1073/pnas.0801383105

Bourgeron, T. (2009). A synaptic trek to autism. *Curr. Opin. Neurobiol.* 19, 231–234. doi: 10.1016/j.conb.2009.06.003

Bourgeron, T., Leboyer, M., and Delorme, R. (2009). [Autism: more evidence of a genetic cause]. *Bull. Acad. Natl. Med.* 193, 299–304. discussion 304–295. doi: 10.1016/S0001-4079(19)32583-X

Chao, H. T., Chen, H., Samaco, R. C., Xue, M., Chahrour, M., Yoo, J., et al. (2010). Dysfunction in GABA signalling mediates autism-like stereotypies and Rett syndrome phenotypes. *Nature* 468, 263–269. doi: 10.1038/nature09582

Chih, B., Engelman, H., and Scheiffele, P. (2005). Control of excitatory and inhibitory synapse formation by neuroligins. *Science* 307, 1324–1328. doi: 10.1126/science.1107470

Choo, M., Miyazaki, T., Yamazaki, M., Kawamura, M., Nakazawa, T., Zhang, J., et al. (2017). Retrograde BDNF to TrkB signaling promotes synapse elimination in the developing cerebellum. *Nat. Commun.* 8:195. doi: 10.1038/s41467-017-00260-w

Courchesne, E., Yeung-Courchesne, R., Press, G. A., Hesselink, J. R., and Jernigan, T. L. (1988). Hypoplasia of cerebellar vermal lobules VI and VII in autism. *N. Engl. J. Med.* 318, 1349–1354. doi: 10.1056/NEJM198805263182102

Craig, A. M., and Kang, Y. (2007). Neurexin-neuroligin signaling in synapse development. *Curr. Opin. Neurobiol.* 17, 43–52. doi: 10.1016/j.conb.2007.01.011

Delorme, R., Ey, E., Toro, R., Leboyer, M., Gillberg, C., and Bourgeron, T. (2013). Progress toward treatments for synaptic defects in autism. *Nat. Med.* 19, 685–694. doi: 10.1038/nm.3193

DiCicco-Bloom, E., Lord, C., Zwaigenbaum, L., Courchesne, E., Dager, S. R., Schmitz, C., et al. (2006). The developmental neurobiology of autism spectrum disorder. *J. Neurosci.* 26, 6897–6906. doi: 10.1523/JNEUROSCI.1712-06.2006

Etherton, M., Földy, C., Sharma, M., Tabuchi, K., Liu, X., Shamloo, M., et al. (2011). Autism-linked neuroligin-3 R451C mutation differentially alters hippocampal and cortical synaptic function. *Proc. Natl. Acad. Sci. U.S.A.* 108, 13764–13769. doi: 10.1073/pnas.1111093108

Foldy, C., Malenka, R. C., and Sudhof, T. C. (2013). Autism-associated neuroligin-3 mutations commonly disrupt tonic endocannabinoid signaling. *Neuron* 78, 498–509. doi: 10.1016/j.neuron.2013.02.036

Fombonne, E. (2009). Epidemiology of pervasive developmental disorders. *Pediatr. Res.* 65, 591–598. doi: 10.1203/PDR.0b013e31819e7203

Geschwind, D. H., and Levitt, P. (2007). Autism spectrum disorders: developmental disconnection syndromes. *Curr. Opin. Neurobiol.* 17, 103–111. doi: 10.1016/j.conb.2007.01.009

Guilmatre, A., Huguet, G., Delorme, R., and Bourgeron, T. (2014). The emerging role of SHANK genes in neuropsychiatric disorders. *Dev. Neurobiol.* 74, 113–122. doi: 10.1002/dneu.22128

Hashimoto, K., Ichikawa, R., Kitamura, K., Watanabe, M., and Kano, M. (2009a). Translocation of a "winner" climbing fiber to the Purkinje cell dendrite and subsequent elimination of "losers" from the soma in developing cerebellum. *Neuron* 63, 106–118. doi: 10.1016/j.neuron.2009.06.008

Hashimoto, K., and Kano, M. (2003). Functional differentiation of multiple climbing fiber inputs during synapse elimination in the developing cerebellum. *Neuron* 38, 785–796. doi: 10.1016/S0896-6273(03)00298-8

Hashimoto, K., and Kano, M. (2005). Postnatal development and synapse elimination of climbing fiber to Purkinje cell projection in the cerebellum. *Neurosci. Res.* 53, 221–228. doi: 10.1016/j.neures.2005.07.007

Hashimoto, K., and Kano, M. (2013). Synapse elimination in the developing cerebellum. *Cell. Mol. Life Sci.* 70, 4667–4680. doi: 10.1007/s00018-013-1405-2

Hashimoto, K., Tsujita, M., Miyazaki, T., Kitamura, K., Yamazaki, M., Shin, H. S., et al. (2011). Postsynaptic P/Q-type Ca2+ channel in Purkinje cell mediates synaptic competition and elimination in developing cerebellum. *Proc. Natl. Acad. Sci. U.S.A.* 108, 9987–9992. doi: 10.1073/pnas.1101488108

Hashimoto, K., Yoshida, T., Sakimura, K., Mishina, M., Watanabe, M., and Kano, M. (2009b). Influence of parallel fiber-Purkinje cell synapse formation on postnatal development of climbing fiber-Purkinje cell synapses in the cerebellum. *Neuroscience* 162, 601–611. doi: 10.1016/j.neuroscience.2008.12.037

Hoxha, E., Lippiello, P., Scelfo, B., Tempia, F., Ghirardi, M., and Miniaci, M. C. (2017). Maturation, refinement, and serotonergic modulation of cerebellar cortical circuits in normal development and in murine models of autism. *Neural Plast.* 2017:6595740. doi: 10.1155/2017/6595740

Hua, J. Y., and Smith, S. J. (2004). Neural activity and the dynamics of central nervous system development. *Nat. Neurosci.* 7, 327–332. doi: 10.1038/nn1218

Irwin, S. A., Idupulapati, M., Gilbert, M. E., Harris, J. B., Chakravarti, A. B., Rogers, E. J., et al. (2002). Dendritic spine and dendritic field characteristics of layer V pyramidal neurons in the visual cortex of fragile-X knockout mice. *Am. J. Med. Genet.* 111, 140–146. doi: 10.1002/ajmg.10500

Irwin, S. A., Patel, B., Idupulapati, M., Harris, J. B., Crisostomo, R. A., Larsen, B. P., et al. (2001). Abnormal dendritic spine characteristics in the temporal and visual cortices of patients with fragile-X syndrome: a quantitative examination. *Am. J. Med. Genet.* 98, 161–167. doi: 10.1002/1096-8628(20010115)98:2<161::aid-ajmg1025>3.0.co;2-b

Jamain, S., Quach, H., Betancur, C., Råstam, M., Colineaux, C., Gillberg, I. C., et al. (2003). Mutations of the X-linked genes encoding neuroligins NLGN3 and NLGN4 are associated with autism. *Nat. Genet.* 34, 27–29. doi: 10.1038/ng1136

Kakegawa, W., Mitakidis, N., Miura, E., Abe, M., Matsuda, K., Takeo, Y. H., et al. (2015). Anterograde C1ql1 signaling is required in order to determine and maintain a single-winner climbing fiber in the mouse cerebellum. *Neuron* 85, 316–329. doi: 10.1016/j.neuron.2014.12.020

Kano, M., and Hashimoto, K. (2009). Synapse elimination in the central nervous system. *Curr. Opin. Neurobiol.* 19, 154–161. doi: 10.1016/j.conb.2009.05.002

Kano, M., and Watanabe, T. (2019). Developmental synapse remodeling in the cerebellum and visual thalamus. *F1000Res*. 8:F1000 Faculty Rev-1191. doi: 10.12688/f1000research.18903.1

Kano, M., Watanabe, T., Uesaka, N., and Watanabe, M. (2018). Multiple phases of climbing fiber synapse elimination in the developing cerebellum. *Cerebellum* 17, 722–734. doi: 10.1007/s12311-018-0964-z

Kawata, S., Miyazaki, T., Yamazaki, M., Mikuni, T., Yamasaki, M., Hashimoto, K., et al. (2014). Global scaling down of excitatory postsynaptic responses in cerebellar Purkinje cells impairs developmental synapse elimination. *Cell Rep.* 8, 1119–1129. doi: 10.1016/j.celrep.2014.07.014

Kelley, L. T., Coderre-Ball, A. M., Dalgarno, N., McKeown, S., and Egan, R. (2020). Continuing professional development for primary care providers in palliative and end-of-life care: a systematic review. *J. Palliat. Med.* 23, 1104–1124. doi: 10.1089/jpm.2020.0060

Kern, J. K. (2003). Purkinje cell vulnerability and autism: a possible etiological connection. *Brain Dev.* 25, 377–382. doi: 10.1016/S0387-7604(03)00056-1

Kloth, A. D., Badura, A., Li, A., Cherskov, A., Connolly, S. G., Giovannucci, A., et al. (2015). Cerebellar associative sensory learning defects in five mouse autism models. *Elife* 4:e06085. doi: 10.7554/eLife.06085.017

Lichtman, J. W., and Colman, H. (2000). Synapse elimination and indelible memory. *Neuron* 25, 269–278. doi: 10.1016/S0896-6273(00)80893-4

Limperopoulos, C., Chilingaryan, G., Sullivan, N., Guizard, N., Robertson, R. L., and du Plessis, A. J. (2014). Injury to the premature cerebellum: outcome is related to remote cortical development. *Cereb. Cortex* 24, 728–736. doi: 10.1093/cercor/bhs354

Maćkowiak, M., Mordalska, P., and Wedzony, K. (2014). Neuroligins, synapse balance, and neuropsychiatric disorders. *Pharmacol. Rep.* 66, 830–835. doi: 10.1016/j.pharep.2014.04.011

Mikuni, T., Uesaka, N., Okuno, H., Hirai, H., Deisseroth, K., Bito, H., et al. (2013). Arc/Arg3.1 is a postsynaptic mediator of activity-dependent synapse elimination in the developing cerebellum. *Neuron* 78, 1024–1035. doi: 10.1016/j.neuron.2013.04.036

Miyazaki, T., and Watanabe, M. (2011). Development of an anatomical technique for visualizing the mode of climbing fiber innervation in Purkinje cells and its application to mutant mice lacking GluRδ2 and Ca(v)2.1. *Anat. Sci. Int.* 86, 10–18. doi: 10.1007/s12565-010-0095-1

Nakayama, H., Miyazaki, T., Kitamura, K., Hashimoto, K., Yanagawa, Y., Obata, K., et al. (2012). GABAergic inhibition regulates developmental synapse elimination in the cerebellum. *Neuron* 74, 384–396. doi: 10.1016/j.neuron.2012.02.032

O'Halloran, C. J., Kinsella, G. J., and Storey, E. (2012). The cerebellum and neuropsychological functioning: a critical review. *J. Clin. Exp. Neuropsychol.* 34, 35–56. doi: 10.1080/13803395.2011.614599

Palmen, S. J., and van Engeland, H. (2004). Review on structural neuroimaging findings in autism. *J. Neural Transm. (Vienna)* 111, 903–929. doi: 10.1007/s00702-003-0068-9

Palmen, S. J., van Engeland, H., Hof, P. R., and Schmitz, C. (2004). Neuropathological findings in autism. *Brain* 127(Pt 12), 2572–2583. doi: 10.1093/brain/awh287

Penzes, P., Cahill, M. E., Jones, K. A., VanLeeuwen, J. E., and Woolfrey, K. M. (2011). Dendritic spine pathology in neuropsychiatric disorders. *Nat. Neurosci.* 14, 285–293. doi: 10.1038/nn.2741

Peter, S., Ten Brinke, M. M., Stedehouder, J., Reinelt, C. M., Wu, B., Zhou, H., et al. (2016). Dysfunctional cerebellar Purkinje cells contribute to autism-like behaviour in Shank2-deficient mice. *Nat. Commun.* 7:12627. doi: 10.1038/ncomms12627

Pfeiffer, B. E., Zang, T., Wilkerson, J. R., Taniguchi, M., Maksimova, M. A., Smith, L. N., et al. (2010). Fragile X mental retardation protein is required for synapse elimination by the activity-dependent transcription factor MEF2. *Neuron* 66, 191–197. doi: 10.1016/j.neuron.2010.03.017

Piochon, C., Kloth, A. D., Grasselli, G., Titley, H. K., Nakayama, H., Hashimoto, K., et al. (2014). Cerebellar plasticity and motor learning deficits in a copy-number variation mouse model of autism. *Nat. Commun.* 5:5586. doi: 10.1038/ncomms6586

Purves, D., and Lichtman, J. W. (1980). Elimination of synapses in the developing nervous system. *Science* 210, 153–157. doi: 10.1126/science.7414326

Reith, R. M., McKenna, J., Wu, H., Hashmi, S. S., Cho, S. H., Dash, P. K., et al. (2013). Loss of Tsc2 in Purkinje cells is associated with autistic-like behavior in a mouse model of tuberous sclerosis complex. *Neurobiol. Dis.* 51, 93–103. doi: 10.1016/j.nbd.2012.10.014

Rothwell, P. E., Fuccillo, M. V., Maxeiner, S., Hayton, S. J., Gokce, O., Lim, B. K., et al. (2014). Autism-associated neuroligin-3 mutations commonly impair striatal circuits to boost repetitive behaviors. *Cell* 158, 198–212. doi: 10.1016/j.cell.2014.04.045

Schmahmann, J. D. (2019). The cerebellum and cognition. *Neurosci. Lett.* 688, 62–75. doi: 10.1016/j.neulet.2018.07.005

Shahbazian, M. D., Orr, H. T., and Zoghbi, H. Y. (2001). Reduction of Purkinje cell pathology in SCA1 transgenic mice by p53 deletion. *Neurobiol. Dis.* 8, 974–981. doi: 10.1006/nbdi.2001.0444

Sigoillot, S. M., Iyer, K., Binda, F., Gonzalez-Calvo, I., Talleur, M., Vodjdani, G., et al. (2015). The secreted protein C1QL1 and its receptor BAI3 control the synaptic connectivity of excitatory inputs converging on cerebellar purkinje cells. *Cell Rep.* 10, 820–832. doi: 10.1016/j.celrep.2015.01.034

Singh, S. K., and Eroglu, C. (2013). Neuroligins provide molecular links between syndromic and nonsyndromic autism. *Sci. Signal* 6:re4. doi: 10.1126/scisignal.2004102

Stewart, L. T. (2015). Cell adhesion proteins and the pathogenesis of autism spectrum disorders. *J. Neurophysiol.* 113, 1283–1286. doi: 10.1152/jn.00780.2013

Stoodley, C. J., D'Mello, A. M., Ellegood, J., Jakkamsetti, V., Liu, P., Nebel, M. B., et al. (2017). Altered cerebellar connectivity in autism and cerebellar-mediated rescue of autism-related behaviors in mice. *Nat. Neurosci.* 20, 1744–1751. doi: 10.1038/s41593-017-0004-1

Südhof, T. C. (2008). Neuroligins and neurexins link synaptic function to cognitive disease. *Nature* 455, 903–911. doi: 10.1038/nature07456

Sundberg, M., and Sahin, M. (2015). Cerebellar development and autism spectrum disorder in tuberous sclerosis complex. *J. Child Neurol.* 30, 1954–1962. doi: 10.1177/0883073815600870

Tabuchi, K., Blundell, J., Etherton, M. R., Hammer, R. E., Liu, X., Powell, C. M., et al. (2007). A neuroligin-3 mutation implicated in autism increases inhibitory synaptic transmission in mice. *Science* 318, 71–76. doi: 10.1126/science.1146221

Tang, G., Gudsnuk, K., Kuo, S. H., Cotrina, M. L., Rosoklija, G., Sosunov, A., et al. (2014). Loss of mTOR-dependent macroautophagy causes autistic-like synaptic pruning deficits. *Neuron* 83, 1131–1143. doi: 10.1016/j.neuron.2014.07.040

Tanimura, A., Kawata, S., Hashimoto, K., and Kano, M. (2009). Not glutamate but endocannabinoids mediate retrograde suppression of cerebellar parallel fiber to Purkinje cell synaptic transmission in young adult rodents. *Neuropharmacology* 57, 157–163. doi: 10.1016/j.neuropharm.2009.04.015

Tsai, N. P., Wilkerson, J. R., Guo, W., Maksimova, M. A., DeMartino, G. N., Cowan, C. W., et al. (2012a). Multiple autism-linked genes mediate synapse elimination via proteasomal degradation of a synaptic scaffold PSD-95. *Cell* 151, 1581–1594. doi: 10.1016/j.cell.2012.11.040

Tsai, P. T., Hull, C., Chu, Y., Greene-Colozzi, E., Sadowski, A. R., Leech, J. M., et al. (2012b). Autistic-like behaviour and cerebellar dysfunction in Purkinje cell Tsc1 mutant mice. *Nature* 488, 647–651. doi: 10.1038/nature11310

Uesaka, N., Abe, M., Konno, K., Yamazaki, M., Sakoori, K., Watanabe, T., et al. (2018). Retrograde signaling from progranulin to sort1 counteracts synapse elimination in the developing cerebellum. *Neuron* 97, 796 e795–805 e795. doi: 10.1016/j.neuron.2018.01.018

Uesaka, N., Uchigashima, M., Mikuni, T., Nakazawa, T., Nakao, H., Hirai, H., et al. (2014). Retrograde semaphorin signaling regulates synapse elimination in the developing mouse brain. *Science* 344, 1020–1023. doi: 10.1126/science.1252514

Vargas, D. L., Nascimbene, C., Krishnan, C., Zimmerman, A. W., and Pardo, C. A. (2005). Neuroglial activation and neuroinflammation in the brain of patients with autism. *Ann. Neurol.* 57, 67–81. doi: 10.1002/ana.20315

Varoqueaux, F., Aramuni, G., Rawson, R. L., Mohrmann, R., Missler, M., Gottmann, K., et al. (2006). Neuroligins determine synapse maturation and function. *Neuron* 51, 741–754. doi: 10.1016/j.neuron.2006.09.003

Wang, S. S., Kloth, A. D., and Badura, A. (2014). The cerebellum, sensitive periods, and autism. *Neuron* 83, 518–532. doi: 10.1016/j.neuron.2014.07.016

Watanabe, M., and Kano, M. (2011). Climbing fiber synapse elimination in cerebellar Purkinje cells. *Eur. J. Neurosci.* 34, 1697–1710. doi: 10.1111/j.1460-9568.2011.07894.x

Webb, S. J., Sparks, B. F., Friedman, S. D., Shaw, D. W., Giedd, J., Dawson, G., et al. (2009). Cerebellar vermal volumes and behavioral correlates in children with autism spectrum disorder. *Psychiatry Res.* 172, 61–67. doi: 10.1016/j.pscychresns.2008.06.001

Wegiel, J., Kuchna, I., Nowicki, K., Imaki, H., Marchi, E., Ma, S. Y., et al. (2010). The neuropathology of autism: defects of neurogenesis and neuronal migration, and dysplastic changes. *Acta Neuropathol.* 119, 755–770. doi: 10.1007/s00401-010-0655-4

Weiler, I. J., and Greenough, W. T. (1999). Synaptic synthesis of the Fragile X protein: possible involvement in synapse maturation and elimination. *Am. J. Med. Genet.* 83, 248–252.

Xiao, R., Zhong, H., Li, X., Ma, Y., Zhang, R., Wang, L., et al. (2020). Abnormal cerebellar development is involved in dystonia-like behaviors and motor dysfunction of autistic BTBR mice. *Front. Cell Dev. Biol.* 8:231. doi: 10.3389/fcell.2020.00231

Yamashiro, K., Hori, K., Lai, E. S. K., Aoki, R., Shimaoka, K., Arimura, N., et al. (2020). AUTS2 governs cerebellar development, purkinje cell maturation, motor function and social communication. *iScience* 23:101820. doi: 10.1016/j.isci.2020.101820

Yan, J., Oliveira, G., Coutinho, A., Yang, C., Feng, J., Katz, C., et al. (2005). Analysis of the neuroligin 3 and 4 genes in autism and other neuropsychiatric patients. *Mol. Psychiatry* 10, 329–332. doi: 10.1038/sj.mp.4001629

Zoghbi, H. Y. (2003). Postnatal neurodevelopmental disorders: meeting at the synapse? *Science* 302, 826–830. doi: 10.1126/science.1089071

Conflict of Interest: The authors declare that the research was conducted in the absence of any commercial or financial relationships that could be construed as a potential conflict of interest.

frontiers in Neural Circuits

REVIEW
published: 12 July 2021
doi: 10.3389/fncir.2021.716408

Prefrontal GABAergic Interneurons Gate Long-Range Afferents to Regulate Prefrontal Cortex-Associated Complex Behaviors

*Sha-Sha Yang[1,2], Nancy R. Mack[1], Yousheng Shu[2] and Wen-Jun Gao[1]**

[1] Department of Neurobiology and Anatomy, College of Medicine, Drexel University, Philadelphia, PA, United States,
[2] Institute for Translational Brain Research, Fudan University, Shanghai, China

Prefrontal cortical GABAergic interneurons (INs) and their innervations are essential for the execution of complex behaviors such as working memory, social behavior, and fear expression. These behavior regulations are highly dependent on primary long-range afferents originating from the subcortical structures such as mediodorsal thalamus (MD), ventral hippocampus (vHPC), and basolateral amygdala (BLA). In turn, the regulatory effects of these inputs are mediated by activation of parvalbumin-expressing (PV) and/or somatostatin expressing (SST) INs within the prefrontal cortex (PFC). Here we review how each of these long-range afferents from the MD, vHPC, or BLA recruits a subset of the prefrontal interneuron population to exert precise control of specific PFC-dependent behaviors. Specifically, we first summarize the anatomical connections of different long-range inputs formed on prefrontal GABAergic INs, focusing on PV versus SST cells. Next, we elaborate on the role of prefrontal PV- and SST- INs in regulating MD afferents-mediated cognitive behaviors. We also examine how prefrontal PV- and SST- INs gate vHPC afferents in spatial working memory and fear expression. Finally, we discuss the possibility that prefrontal PV-INs mediate fear conditioning, predominantly driven by the BLA-mPFC pathway. This review will provide a broad view of how multiple long-range inputs converge on prefrontal interneurons to regulate complex behaviors and novel future directions to understand how PFC controls different behaviors.

Keywords: prefrontal cortex, interneurons, mediodorsal thalamus, ventral hippocampus, basolateral amygdala, complex behavior

OPEN ACCESS

Edited by:
Allan T. Gulledge, Dartmouth College, United States

Reviewed by:
Kuei Y. Tseng, University of Illinois at Chicago, United States
Alexei Morozov, Virginia Tech, United States

***Correspondence:**
Wen-Jun Gao
wg38@drexel.edu

Received: *28 May 2021*
Accepted: *14 June 2021*
Published: *12 July 2021*

Citation:
Yang S-S, Mack NR, Shu Y and Gao W-J (2021) Prefrontal GABAergic Interneurons Gate Long-Range Afferents to Regulate Prefrontal Cortex-Associated Complex Behaviors. Front. Neural Circuits 15:716408. doi: 10.3389/fncir.2021.716408

Abbreviations: ACC, anterior cingulate cortex; BLA, basolateral amygdala; DNMST, delayed non-match to sample T-maze task; DREADDs, designer receptors exclusively activated by designer drugs; EPSCs, excitatory postsynaptic currents; FFI, feedforward inhibition; GABA, gamma-aminobutyric acid; IL, infralimbic; INs, interneurons; L1, layer 1; MD, mediodorsal thalamus; mPFC, medial prefrontal cortex; PL, prelimbic; PTSD, post-traumatic stress disorder; PV, parvalbumin; SAD, social anxiety disorder; SST, somatostatin; SZ, schizophrenia.

HIGHLIGHTS

- PV-INs recruitment by MD inputs is crucial for working memory and social preference.
- SST-INs facilitate the coherence between vHPC-PFC during a working memory task.
- The vHPC inputs target on PV-INs in IL to inhibit CS-induced fear renewal.
- BLA innervates both PV- and SST- INs, but its function remains to be determined.

INTRODUCTION

The prefrontal cortex (PFC) is well known for its top-down control of multiple distinct complex behaviors, including cognitive, emotional, and social behaviors, by selectively processing different input information (Carmichael and Price, 1996; Amodio and Frith, 2006; Hoover and Vertes, 2007; Yizhar and Levy, 2021). Multiple excitatory glutamatergic pathways are involved in controlling these complex behaviors with the PFC as an executive center. Canonically, the mediodorsal thalamus (MD)-PFC pathway is widely believed to be involved in controlling high-order cognitive performance, such as working memory, goal-directed behavior, and decision making (Mitchell and Chakraborty, 2013; Ferguson and Gao, 2015; Parnaudeau et al., 2018; Wolff and Vann, 2019). Whereas afferents originating from the ventral hippocampus (vHPC) are responsible for spatial working memory or navigation related tasks (Gordon, 2011; Neill et al., 2013). On the other hand, inputs from the basolateral amygdala (BLA) are thought to participate in expressing negative emotional behaviors such as fear, anxiety, and aggression (Nelson and Trainor, 2007; Arruda-Carvalho and Clem, 2015; Likhtik and Paz, 2015). However, the functions of these neural circuits are often not singular and complicated by overlapping roles in regulating specific behavioral components. This increases the complexity of categorizing the function of each particular pathway formed with the PFC.

As a convergent target of multiple long-range inputs, the medial PFC (mPFC) is required to precisely filter essential information from the numerous signals it receives from cortical and subcortical brain regions. Local GABAergic interneurons (INs) are critical for gating incoming long-range inputs. In the neocortex, interneurons comprise more than 20 molecularly-, morphologically- or physiologically-defined subpopulations, raising a major challenge in characterizing their regulatory function in controlling specific behaviors (Rudy et al., 2011; He et al., 2016; Paul et al., 2017). Among the cortical interneuron subpopulations, parvalbumin-expressing (PV-) and somatostatin-expressing (SST-) INs are the two most abundant subtypes. By taking advantage of newly developed transgenic mouse lines, researchers have comprehensively studied the distinct physiological properties of these two types of interneurons within the mPFC in recent years. Extensive research unveiled the unique abilities of PV- and SST- INs in gating inputs and controlling nearby pyramidal neurons (Cardin, 2018). PV-INs exert robust control over the information integration by targeting cell bodies and proximal dendrites of pyramidal neurons. In contrast, SST-INs enhance excitatory inputs' selectivity by forming inhibitory synapses on distal dendritic branches of pyramidal neurons (Markram et al., 2004). Excitatory synaptic transmission onto PV- and SST- INs also exhibits differences in short-term plasticity (Gibson et al., 1999; Hofer et al., 2011). Briefly, the excitatory transmission is depressed on PV-INs but facilitated on SST-INs (Xiang et al., 2002; Ma et al., 2012). Therefore, different levels of the stimulation are required to activate PV- and SST- INs. A single burst of high-frequency stimulation is sufficient to excite PV-INs, resulting in brief but precise inhibition on targeted cell; whereas repeated stimulation is required to activate SST- INs, producing long-lasting and temporally delayed inhibition. Therefore, long-range inputs from a single brain region could play distinct and diverse roles in different complex behaviors by recruiting a separate subpopulation of INs. Indeed, due to their different excitabilities, PV- and SST- INs display distinct activity patterns in spatial working memory tasks (Kim et al., 2016). It is well established that all regions mentioned above, including MD, vHPC, and BLA, send projections to the PFC INs to form feedforward inhibition (Delevich et al., 2015; McGarry and Carter, 2016; Abbas et al., 2018). Here we review how each of those long-range afferents recruits particular INs to exert precise control of the mPFC local circuits involved in specific behaviors. We will dissect the anatomical connection of the MD, vHPC, and BLA with PV- or SST-INs in the PFC, demonstrate the roles of PV- and SST- INs in regulating these long-range inputs, and in mediating complex behaviors such as working memory, social interaction, and fear expression. Here, we focus on PV- and SST-INs as these two subpopulations are the largest expressed INs in the neocortex. The physiological and functional connection of long-range inputs to other types of interneurons, such as the vasoactive intestinal polypeptide expressing interneuron subtype, remains sparse and requires more studies to be characterized.

ANATOMICAL AND PHYSIOLOGICAL CONNECTIONS THE LONG-RANGE AFFERENTS FORMED WITH PREFRONTAL INs

Similar to other cortices, the mPFC also consists of laminar structures. Long-range inputs typically show laminar preference in the mPFC, with a higher proportion of them accumulating in layer I/II/III while layer V and VI mainly serve as output originators. Local interneurons also receive long-range inputs, which form the primary driving force of feedforward inhibition to the local circuits. Given the challenge in elucidating the multiple complex behaviors related to two different INs and three afferents, especially the technologies used in studying the enormous complexity of the relevant prefrontal cortical microcircuit, here we will focus on rodent studies. For the purpose of this review, we define the rodent mPFC as comprised of the anterior cingulate, prelimbic, and infralimbic cortex.

MD-mPFC

As corresponding thalamic and cortical partners, the MD and mPFC are reciprocally connected with one another (Heidbreder and Groenewegen, 2003; Mitchell and Chakraborty, 2013; Collins et al., 2018). Similar to the connection between sensory thalamic nuclei and their cortical partners, MD inputs can not only drive feedforward excitation but also inhibition on principal pyramidal neurons by activating PV-INs in the mPFC (**Figure 1A**). The activation of PV-INs by MD afferents is critical for maintaining the excitation/inhibition (E/I) balance in local prefrontal circuits (Anastasiades et al., 2018; Ferguson and Gao, 2018a). Using a retrograde tracing method and *ex vivo* electrophysiological recording, Delevich et al. (2015) found that the lateral and central part of the MD sends projections to layer 1 (L1), L3, and L5 of the dorsal anterior cingulate cortex (ACC), a subregion of the mPFC. These inputs directly target PV-INs to form a feedforward inhibitory circuit in the mPFC (Delevich et al., 2015), in support of a morphological study (Rotaru et al., 2005). Optical activation of MD afferents induces both monosynaptic excitatory and disynaptic inhibitory current in pyramidal neurons (Delevich et al., 2015). The monosynaptic excitatory postsynaptic currents (EPSCs) are detected on L3 PV-INs which are responsible for the disynaptic inhibitory current in pyramidal neurons. Interestingly, although both PV- and SST- INs fire action potential in response to activation of MD afferents in the mPFC, the latency of SST-INs is significantly longer than that of PV-INs. This finding suggested that SST-IN spiking might be driven mainly by local ploy-synaptic inputs rather than direct MD innervation (Delevich et al., 2015). However, a retrograde tracing study revealed that MD afferents form direct contact with SST-INs in the mPFC, although the literature has long been biased to PV-INs (Ährlund-Richter et al., 2019). The functional connection between MD afferents and prefrontal SST-INs needs further characterization in future studies.

vHPC-mPFC

Although often overlooked in the literature, vHPC afferents form excitatory synapses not only on pyramidal neurons but also INs to promote feedforward inhibition (**Figure 1B**) (Thierry et al., 2000; Gabbott et al., 2002; Dégenètais et al., 2003; Dembrow et al., 2015; Liu and Carter, 2018; Marek et al., 2018). These inputs synapse on both PV- and SST- INs in the mPFC, and stimulation of vHPC inputs successfully induces EPSCs on both excitatory and inhibitory cells (Abbas et al., 2018; Phillips et al., 2019). In the mPFC, corticocortical projecting neurons in L5 preferentially receive inputs from the vHPC (Liu and Carter, 2018). Therefore, this subset of pyramidal neurons could be the primary regulatory target of the vHPC-driving feedforward inhibition in the mPFC. This assumption, however, remains to be tested. Further, optically activating vHPC inputs in the PFC triggers both AMPA and NMDA receptor-mediated EPSCs in fast-spiking PV-INs (Bogart and O'Donnell, 2018). Particularly, NMDARs in PV-INs play a critical role in forming functional connections between vHPC and mPFC during adolescent development (Alvarez et al., 2020).

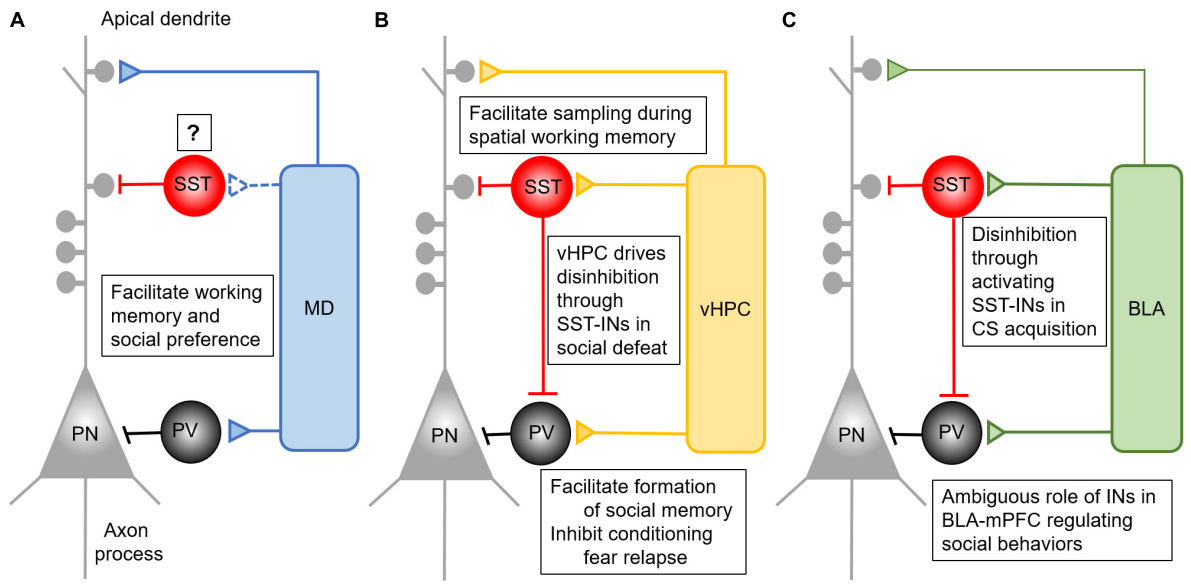

FIGURE 1 | Anatomical and functional connectivity between mPFC and its major long-range inputs. **(A)** MD afferents form feedforward inhibition in the mPFC by driving the activity of PV- INs. This feedforward inhibition is critical for the performance of mPFC dependent working memory and social interaction, but its connection and role via SST-INs remains to be determined. **(B)** The vHPC afferents form feedforward inhibition in the mPFC by driving the activity of both PV- and SST- INs. Activation of prefrontal SST-INs by vHPC inputs facilitates spatial working memory performance. The inhibition of conditioning fear relapse is mediated by vHPC activating PV- INs, while vHPC activates SST-INs to inhibit PV-INs in the mPFC. This results in disinhibition of mPFC for the performance of social fear during the social defeat. **(C)** The BLA afferents form feedforward inhibition in the mPFC by driving the activity of both PV- and SST- INs. Presentation of CS in fear conditioning can activate SST-INs, which inhibit the PV-INs to form disinhibition in the mPFC. This process facilitates the acquisition of CS. Despite the importance of the BLA-mPFC pathway in regulating social behaviors, there is no concrete evidence elaborating the detailed function of PV- and SST-IN in it.

However, despite the well-founded anatomical connection of vHPC afferents to SST-INs (Sun et al., 2019), similar studies at the receptor level have not been done to characterize the synaptic properties in SST-INs in the mPFC. Activation of vHPC afferents will likely induce distinct responses in prefrontal SST-INs compared with PV-INs due to their different physiological properties and connectivity (Rudy et al., 2011; He et al., 2016; Paul et al., 2017), but this intriguing assumption remains to be determined.

BLA-mPFC

The mPFC is a major top-down control center for the BLA in regulating the extinction of learned fear and other types of emotional behavior (Sotres-Bayon and Quirk, 2010). Anatomically, the mPFC and BLA are reciprocally connected (Gabbott et al., 2005; Hoover and Vertes, 2007). Although the BLA sends glutamatergic afferents to the mPFC, they preferentially target GABAergic INs to drive feedforward inhibition (**Figure 1C**) (Gabbott et al., 2005, 2006; Floresco and Tse, 2007; Dilgen et al., 2013; Klavir et al., 2017). Specifically, activating BLA inhibits most pyramidal neurons in the mPFC by activating PV-INs (Floresco and Tse, 2007; Dilgen et al., 2013), indicating a powerful inhibitory control of the prefrontal network activity by the BLA. McGarry and Carter (2016) reported that BLA inputs synapsed on cortico-amygdalar excitatory neurons but formed stronger connections with nearby PV- and SST- INs. Furthermore, these amygdalar-mPFC connections in PV-INs are more robust than those in SST-INs (McGarry and Carter, 2016). Interestingly, the presynaptic release of glutamate from BLA axon terminals is depressed on PV-INs but facilitated on SST-INs, enabling faster recruitment of PV-INs by BLA afferents (McGarry and Carter, 2016). Remarkably, both PV- and SST-INs fire action potential earlier than pyramidal neurons in the mPFC, suggesting that BLA inputs recruit INs faster to primarily trigger feedforward inhibition once activated (McGarry and Carter, 2016).

DISTINCT ROLES OF THREE LONG-RANGE AFFERENTS IN THE MPFC IN REGULATING COMPLEX BEHAVIOR

Working Memory

In rodents, working memory is a representation of an object, stimulus, or spatial location that is used to guide behaviors (Dudchenko, 2004). The working memory deficit is a primary cognitive symptom of schizophrenia (SZ) (Saykin et al., 1991, 1994; Park and Holzman, 1993) and other psychiatric disorders (Landrø et al., 2001; Martinussen et al., 2005; Arts et al., 2008; Lai et al., 2017). The dysfunction of mPFC, especially impaired GABAergic transmission, is believed to underlie the working memory deficits seen in SZ. Evidence from postmortem studies in SZ patients identified that both PV- and SST- INs displayed morphological (reduced immunopositivity), physiological (hypo-excitability), and molecular (reduced mRNA expression) dysfunction in the mPFC (Hartman et al., 2003; Hashimoto, 2008; Fung et al., 2010, 2014). It appears that SST- and PV- INs participate in different phases of working memory. Unlike PV-INs, which exhibit consistently increased activity during the delay period, SST-INs show more complex firing patterns with a strong target preference (Pinto and Dan, 2015). Direct inhibition of SST-INs, but not PV-INs, during the sample phase of the delayed non-match to sample T-maze task (DNMST) impaired performance (Abbas et al., 2018). Unlike the work done in 8-shape maze (Kim et al., 2016), inhibition of PV-INs in DNMST does not affect working memory performance (Abbas et al., 2018), which contradicts the canonical theory that prefrontal PV-INs play a more critical role in working memory. The discrepancy of functions between SST- and PV-INs during working memory are likely derived from different and specific upstream inputs. In this section, we depict how these long-range inputs regulate working memory through prefrontal INs.

PV-INs Regulate MD-PFC-Dependent Cognitive Function

The MD-mPFC pathway is widely involved in controlling high-order cognitive performance, such as working memory, goal-directed behavior, and decision making (Ferguson and Gao, 2015; Parnaudeau et al., 2018). Reduced functional connectivity between MD and mPFC is a central pathological mechanism underlying cognitive deficits in many neuropsychiatric disorders, including SZ (Block et al., 2006). A previous study discovered that the MD-mFPC pathway is critical for cognitive functional performance, decreasing MD activity impaired not only the flexibility in reversal learning, but also the ability to make correct choices in the DNMST (Parnaudeau et al., 2013). This study provides a piece of direct evidence for the role of MD-mPFC pathway in cognitive function. Recently, we reported that inhibiting MD activity by Designer Receptors Exclusively Activated by Designer Drugs (DREADDs, hM4Di) impaired the performance of the T-maze working memory task, which requires the information to be retained during varied delay periods (5, 15, or 60s) (Ferguson and Gao, 2018a). Activating PV- INs by a novel excitatory DREADDs via a parvalbumin promoter (PV-hM3Dq) successfully restored the working memory function impaired in long- (60 s) but not short- (5 and 15 s) delay trials. Presumably, activating PV-INs rescues working memory by correcting the disrupted E/I balance caused by compromised excitatory MD inputs to the mPFC (Ferguson and Gao, 2018a). Prefrontal pyramidal neuron activity features sequential firing during the delay period of working memory tasks (Bolkan et al., 2017; Schmitt et al., 2017). These pyramidal neurons' sequential activity probably depends on both MD afferents and PV-INs driving feedforward inhibition. Although both PV- and SST-INs display high firing rates during the delay period of the working memory task (Kim et al., 2016), no study has been done to explore whether the activity of SST-INs in the mPFC is driven by MD inputs while performing the task. Interestingly, disrupting SST-INs activity could affect mouse working memory performance in relatively short-delay trials (10 s) (Kim et al., 2016). Collectively, this evidence suggests that SST-INs may mediate short delay working memory, but the role of MD inputs remains to be determined.

SST-INs Facilitate vHPC-mPFC Synchrony and Prefrontal Spatial Coding

Besides the MD-mPFC pathway, synchronization between mPFC and vHPC is also important for the performance of working memory. The communication between vHPC and mPFC through synchronized oscillations critically regulates spatial working memory (Gordon, 2011), whereas functional dissociation between these two brain regions is an important feature of SZ etiology (Ford et al., 2002; Meyer-Lindenberg et al., 2005; Esmaeili and Grace, 2013; Alvarez et al., 2020). Spellman et al. (2015) demonstrated that optically inhibiting the vHPC projection to the PFC impaired spatial working memory performance in mice. Interestingly, the power of both theta and gamma-band oscillations are increased in both mPFC and HPC in spatial working memory tasks (Jones and Wilson, 2005; Sigurdsson et al., 2010; Neill et al., 2013; Hallock et al., 2016; Lagler et al., 2016). INs are crucial for oscillation synchrony between these two long-range connected regions. Indeed, Abbas et al. (2018) found that inhibiting SST-INs during the sample phase, when the cue was presented to animals, impaired spatial working memory performance. More interestingly, the phase-locking between mPFC single-unit activity and theta oscillation in the vHPC is decreased when SST-INs were inhibited during the sample phase. It is thus possible that GABAergic INs facilitate the synchronously enhanced theta and gamma-band oscillations between mPFC and vHPC during spatial working memory. By doing this, SST-INs would be expected to encode information during the sample phase through facilitating the communication between vHPC and mPFC, which is critically important for the subsequent delay period neural activity. Inhibition of SST-INs activity during the sample phase leads to disinhibition of pyramidal neurons, which could continuously fire action potentials in the subsequent delay phase of the spatial working memory task. Altogether, there is strong evidence supporting the conclusion that SST-INs gate the vHPC inputs to the mPFC to encode spatial information in the spatial working memory task (Abbas et al., 2018). In contrast, inhibiting PV-INs at any phases did not affect phase-locking activity to the vHPC theta nor working memory accuracy (Abbas et al., 2018). One possible explanation is that the vHPC activation of PV-INs mediated feedforward inhibition in mPFC is involved in other complex behaviors, such as social memory (Phillips et al., 2019; Sun et al., 2020), as described below, rather than spatial working memory.

Amygdala Inputs Drive Feedforward Inhibition in the mPFC

Basolateral amygdala is a universally acknowledged regulatory center of emotional behaviors rather than participating in cognitive functions. Few studies have explored the role this pathway plays in high-order cognitive functions such as decision-making and goal-directed behaviors (Bechara et al., 1999; Ghods-Sharifi et al., 2009). Previous studies also indicated that the BLA interacts with the mPFC in regulating glucocorticoid effects on working memory impairment (Roozendaal et al., 2004) and memory consolidation (Roozendaal et al., 2009). BLA mainly impacts cognition through its tight control of impulsive behaviors (Yin et al., 2019), whereas the subthalamic nucleus-projection-defined prefrontal pyramidal neurons suppress impulsive behavior (Li et al., 2020). However, whether and how these two brain regions coordinate to influence high-order cognitive functions like working memory and spatial memory and the potential roles prefrontal INs may play are still open questions.

Social Cognition

The mPFC exerts robust control on cognition not only in working memory, but also in social interaction. Social interaction is a complex behavior that requires the coordination of social learning, social memory, and cognitive skills (Bachevalier and Mishkin, 1986; Courchesne et al., 2004; Yizhar et al., 2011; Brumback et al., 2018). Major psychiatric disorders, including depression, autism, SZ, and social anxiety disorder (SAD), all share impaired sociability as a distinctive feature, bringing hefty economic and affection burden on patients and their families (American psychiatric association, 2013). Social behavior performance is influenced by many social skill domains, including social memory, social recognition, and affective discrimination. The mPFC is a key node of the social neuronal network – the social brain (Bicks et al., 2015; Lieberman et al., 2019). Particularly, GABAergic deficits appear to be a convergent point for understanding the neural mechanism of social dysfunction in neuropsychiatric disorders. Imbalanced E/I ratio has been seen in multiple ASD animal models (Rubenstein and Merzenich, 2003; Chao et al., 2010; Han et al., 2012; Gogolla et al., 2014; Karayannis et al., 2014; Vogt et al., 2015; Inan et al., 2016; Antoine et al., 2019). Both PV- and SST- INs contribute to the progress of these psychiatric disorders. For example, knockdown of either PV or SST in the mPFC impaires social interaction performance by dramatically decreasing the interaction time (Perez et al., 2019). Notwithstanding, these two types of medial ganglionic eminence-derived interneurons distinctly control different components of social behaviors. Early life stress, a common risk factor for numerous psychiatric disorders such as SZ, anxiety, and autism, causes social deficits in a sex-specific manner, with a significant loss of PV-INs in the mPFC in juvenile female but not male mice (Holland et al., 2014). Juvenile social isolation preferentially diminishes the activity of PV-INs in the mPFC during social approach in adulthood (Bicks et al., 2020), indicating that early life disturbance triggers social deficits are dominantly mediated by prefrontal PV-INs. In contrast, the function of SST-INs social behaviors differs based on the identify of the social conspecifics. Oxytocin receptor-positive SST-INs, a subset of SST-INs in the mPFC, specifically regulate sexual social behaviors, and inhibiting this group of INs in female mice reduces their interaction with male mice (Nakajima et al., 2014). However, disinhibition of prefrontal SST-INs through inhibition of vasoactive intestinal peptide INs, which are derived from caudal ganglionic eminence, decreases social preference (Koukouli et al., 2017). *In mice,* knockout of *Pten*, a high-risk autism gene, preferentially reduces the intensity of SST-INs, increasing PV/SST ratio, although not specifically in the mPFC (Vogt et al., 2015). Therefore, both PV- and SST- INs in the mPFC play important, complex roles in regulating social

cognition and this section will reveal how MD, vHPC, and BLA afferents uniquely and differentially regulate this function.

MD-mPFC Pathway Appears to Be Important for Social Preference and Dominance but Not Social Memory and Social Fear

Reduced functional connectivity between MD and mPFC is found to be a major pathological mechanism underlying cognitive dysfunctions, including social deficits (Block et al., 2006; Foss-Feig et al., 2017). It has been found that both mPFC and MD are activated when rats are performing social interaction behaviors (Jodo et al., 2010). As the mPFC and MD are reciprocally connected, concurrent activation of these two brain regions may occur during a social interaction task. Studies in our lab reported that inhibiting MD led to a reduction in social preference in rats (Ferguson and Gao, 2018a,b). In the three-chamber sociability test, rats subjected to MD inhibition via inhibitory DREADDs spend less time in the social chamber containing a novel rat compared to the control group. This behavioral deficit is successfully rescued by elevating PV-INs activity through a PV-promoter-driven excitatory DREADD (Ferguson and Gao, 2018a). This evidence demonstrates that PV-INs play a critical role in mediating the effects of the MD-mPFC pathway in social behaviors. Therefore, the MD-mPFC pathway is involved in regulating not only working memory via PV-INs, but also social interaction. However, it is not clear whether MD-mPFC pathway effects on SST-INs are also important for social interaction. Although prefrontal SST-INs play a powerful control of social fear (Xu et al., 2019), it is unclear whether activating mPFC SST-INs would similarly rescue the MD inhibition-induced social interaction deficit.

vHPC-mPFC Connections Regulate Social Memory via PV-INs

As one of the key brain regions for memory consolidation and social memory, the vHPC is essential for the recall of social memory during social interaction. Studies in both humans (Tavares et al., 2015) and rodents (Hitti and Siegelbaum, 2014; Okuyama et al., 2016; Meira et al., 2018) found that vHPC activity is highly involved in social skills requiring social memory. The vHPC appears to be an essential brain region in keeping the memory of familiar conspecifics through a close connection with multiple upstream inputs and downstream target brain regions (Okuyama et al., 2016). For example, the vHPC receives direct inputs from the dCA2 to maintain social memory (Hitti and Siegelbaum, 2014; Meira et al., 2018). The outputs originated from vHPC innervate nucleus accumbens shell to regulate social discrimination (Okuyama et al., 2016). The mPFC is another downstream target recruited by the vHPC to regulate social memory. Due to the abundant projections the vHPC sends to the mPFC, the social-related memory might be retrieved by vHPC-mPFC to help guide social interaction. The mPFC-projecting vHPC neurons are selectively activated when encounter to a live mouse rather than a toy mouse. By combining retrograde tracer with c-fos immunostaining, a study has found that the c-fos expression is significantly higher in mPFC-projecting vHPC neurons in the social interaction trained group comparing with the control group (Phillips et al., 2019). Chronically enhancing the mPFC-projecting neurons in the vHPC significantly impaires social memory retrieval, suggesting a negative correlation between social memory and the vHPC-mPFC pathway activity. Prefrontal neurons are very diverse in responding to social exploration. There are both ON and OFF ensembles tuned to social performance, which requires selectively activation and inhibition of the local circuit that is controlled by inhibitory neurons, although their specific role in social cognition remain unexplored (Liang et al., 2018). Imbalanced E/I ratio has appeared to be a keynote in understanding the pathological mechanism of social deficits underlying multiple psychiatric disorders (van Heukelum et al., 2019). Disrupting the E/I balance in the mPFC mimics autism social deficits featured with severe social defeats (Yizhar et al., 2011) and social cognition in SZ (Bicks et al., 2015). Long-range vHPC afferents to the mPFC innervate both major types of INs (Sun et al., 2019). However, PV-INs appear to be a more important regulator of functional vHPC-mPFC connection in social performance (Alvarez et al., 2020; Sun et al., 2020). Both PV-IN deficiency and impaired social behaviors were seen in SZ model, in which vHPC-mPFC show impaired functional connectivity (Mukherjee et al., 2019). Selective activation of pyramidal neurons disrupted social preference whereas activation of PV-INs via optogenetic method in the mPFC rescues social preference deficit (Yizhar et al., 2011). Phillips et al. (2019) have identified that mPFC projecting vHPC neurons not only innervate pyramidal neurons but also PV- and SST-INs in the mPFC. These exciting results intrigue the hypothesis that increasing activity of mPFC projecting neurons in the vHPC may disrupt the social memory retrieval through enhancing the feedforward inhibition. Still, the detailed function a specific IN subpopulation plays in gating vHPC inputs in social memory requires further studies in the future.

BLA-mPFC Pathway Plays an Important Role in Social Cognition but the Involvement of GABAergic INs in the mPFC Remains to Be Determined

The implication of amygdala in social memory is supported by evidence collected from both primate (Kling and Cornell, 1971; Kling and Steklis, 1976; Machado et al., 2008) and rodent studies (Bunnell et al., 1970; Jonason and Enloe, 1971; Sanders and Shekhar, 1995). Beside to MD and vHPC, the participation of mPFC in social interaction behaviors also subjects to the modulation of the excitatory input from BLA (Felix-Ortiz et al., 2016) although its role in social cognition remains untested. BLA inputs to the mPFC function as a suppressor of social exploration (Felix-Ortiz et al., 2016). Stimulation of BLA induces disynaptic response in prefrontal neurons with shorter latency of the inhibitory current (Dilgen et al., 2013). Therefore, the decrease of social interaction following activation of BLA axon terminals in the mPFC might result from elevated inhibition driven by the BLA. Both SST- and PV- INs mediate the BLA-driven feedforward inhibition. Due to distinct biophysical properties of excitatory synapses on these two types of INs, BLA synaptic transmission is facilitated in SST-INs but depressed in PV-INs. These could further create two temporal windows for BLA-mediated inhibition in the mPFC (McGarry and Carter,

2016). Therefore, these two parallel inhibitory pathways might contribute to different influences on social behaviors but further study in the context of social memory is warranted.

Fear Conditioning Expression and Extinction

Fear is an unpleasant emotion when the subject is aware of the presence of danger, and functions to keep animals alert to avoid harm. However, fear can be maladaptive when normal stimuli are detected as dangerous. The mPFC serves as a top-down regulating center of emotional behaviors, including conditioned fear expression. In the past few decades, plenty of research was devoted to better understand the role of mPFC in the process of conditioned fear acquisition, expression, and extinction, as recently reviewed (Giustino and Maren, 2015; Gourley and Taylor, 2016). Temporal inhibition or permanent lesion of the mPFC significantly reduces the freezing behaviors in the fear-conditioned group in rats (Frysztak and Neafsey, 1991, 1994; Resstel et al., 2006). In contrast, elevating the neural activity of mPFC enhances fear expression and memory formation following the conditioning stimulus (CS) (Shibano et al., 2020). Etkin et al. (2011) elaborate on the recruitment of ACC and mPFC, two subdivisions of the PFC in emotion regulation and found that the activation of mPFC was seen in the fear expression, retention, and extinction, suggesting that mPFC conveys both safety and danger information. More specifically, as reviewed by Giustino and Maren (2015), the prelimbic (PL) and infralimbic (IL) subdivisions of the rodent mPFC respectively regulate the expression and suppression of fear in rodents. Under certain conditions, the PL and IL act in concert, exhibiting similar patterns of neural activity in response to aversive conditioned stimuli and during the expression or inhibition of conditioned fear; albeit these mPFC subdivisions may code opposing behavioral outcomes, with PL biased toward fear expression and IL toward suppression (Giustino and Maren, 2015). The question raised by this intriguing hypothesis is whether and how this opposing action is achieved.

Recently, the functional importance of mPFC GABAergic INs in regulating conditioned fear expression has been evidenced. Calcium activity of prefrontal SST-INs in mice is increased during and after the conditioning, suggesting that the activity of SST-INs in the mPFC may underlie the fear acquisition and memory consolidation (Cummings and Clem, 2020). Furthermore, photoactivation of SST-INs increases freezing behaviors during memory retrieval. Conditioning pair electrical shock with neutral stimulus enhances the inhibition from SST-INs to PV-INs, resulting in the disinhibition of PNs in the mPFC (Cummings and Clem, 2020; Flores-Barrera et al., 2020). MK-801 (an NMDAR antagonist) treatment primarily diminishes the GABAergic transmission and increases excitation and inhibition ratio (Flores-Barrera et al., 2020). However, the dysfunction of inhibitory transmission does not disrupt the acquisition of fear conditioning (Flores-Barrera et al., 2020). Instead, it enhances fear memory retrieval and impairs extinction. Direct infusion of GABAa receptor agonist generates an opposite effect on freezing response (Flores-Barrera et al., 2020). These findings depict a local disinhibition circuit onto excitatory pyramidal neurons through SST-mediated dendritic inhibition and PV-mediated perisomatic inhibition, respectively. In the following sections, we will review and summarize how primary long-range afferents regulate this disinhibition circuit in the mPFC in fear conditioning.

MD-mPFC Pathway for Both Fear Expression and Extinction

Both MD and mPFC are main structures in controlling fear expression and extinction (Oyoshi et al., 1996; Herry and Garcia, 2002; Li et al., 2004; Padilla-Coreano et al., 2012). In the establishment of conditioned fear, MD serves as a relay to transfer information from the superior colliculus to both the mPFC and amygdala. Tonic but not burst activity of MD is required for the fear extinction induced by alternative bilateral visual stimulation, a task known to promote fear extinction by increasing visual attention (Baek et al., 2019). Enhancing burst firing by knocking out phospholipase C-beta4 abolishes the effect of alternating bilateral stimulation-induced attenuation on fear relapse (Baek et al., 2019). In contrast, the activity of BLA neurons is inhibited by the alternating bilateral stimulation. MD drives feedforward inhibition in the BLA to support long-lasting fear attenuation (Baek et al., 2019). Surprisingly, the role of MD-mediated regulation of GABAergic INs in the mPFC and other fear-associated brain regions has yet to be examined for fear expression and extinction behavior. It has been shown that activating MD afferents in the BLA induces monosynaptic EPSC and disynaptic IPSC (McGarry and Carter, 2017), but the specific IN subtypes in the BLA gating MD inputs, and more relevant to the MD-mPFC inputs, during a different fear conditioning phase, remains to be explored.

vHPC-mPFC in Social Fear

Social fear is one type of maladaptive fear shown in SAD. Patients usually experience intense social anxiety, which severely affects their daily life. In rodents, social fear can be induced by a social defeat paradigm through the resident-intruder test, followed by social interaction test to measure the fear memory (Qi et al., 2018). Both mPFC and vHPC are involved in the regulation of social behavior. However, controversy about this pathway's complex function in the expression of social fear has remained due to several reasons. First, the vHPC inputs innervate both excitatory and inhibitory neurons in the mPFC. This broadens the range of diversity of the role the vHPC-mPFC pathway plays in controlling social fear. Second, the reported activity of the mPFC in social fear expression is controversial. For example, after social defeat, the expression of early response genes suggests that the suppression of mPFC activity can last for 7 days from the initial social fear induction (Qi et al., 2018), emphasizing the inhibition of mPFC is essential for fear memory maintenance. However, *in vivo* recording of prefrontal neuron activity discovers an increase of firing rate of pyramidal neurons in the PL region of mPFC during social fear expression (Abe et al., 2019; Xu et al., 2019). Interestingly, activating SST-INs, which are known to inhibit PV-INs, facilitates the expression of social fear. SST-INs in the mPFC participate in conditioned social

fear behavior by disinhibiting excitatory networks via suppressing PV-INs activity (Xu et al., 2019). Indeed, SST-INs have been reported to gate the vHPC input in the mPFC. PFC projecting vHPC neurons show higher activity during a social encounter (Phillips et al., 2019). Therefore, during the resident-intruder test, the vHPC activity may drive SST-INs to disinhibit the prefrontal network activity via PV-INs. However, during social encounters following the social fear conditioning, the BLA may inhibit both vHPC and mPFC to allow stress expression and enhance social fear memory (Qi et al., 2018). Further experiments are needed to explore the specific roles of prefrontal INs in regulating vHPC-mPFC pathway-dependent social interaction.

vHPC-mPFC Connection Drives Fear Extinction via PV-INs

Preventing the renewal of fear following extinction could be a novel and effective clinical intervention procedure for treating maladaptive learned fear responses. The expression of a conditioned stimulus (CS)-evoked fear during the extinction is a context-dependent fear renewal, which involves re-expression of fear when encountering the CS outside the extinction context. Previous studies reported that context-independent expression of extinct fear could be induced by inactivating the vHPC (Corcoran and Maren, 2001; Hobin et al., 2006; Zelikowsky et al., 2013), suggesting that vHPC might be a fear suppressor. A study conducted by Marek et al. (2018) supports this notion. The researchers find that pharmacologically activating the vHPC input to the mPFC results in a decrease of freezing behavior in the extinction context (Marek et al., 2018). More importantly, they discover that the vHPC controls fear relapse through feedforward inhibition of amygdala-projecting prefrontal pyramidal neurons (Marek et al., 2018). The IL region of the mPFC is critical for fear relapse. Activating IL axon terminals in the amygdala inhibits the re-expression of fear when encountering the CS. Interestingly, a subsequent *ex vivo* study discovers that vHPC projections primarily target inhibitory neurons in L2/3 of the IL. Moreover, these INs mainly comprise PV- rather than SST-INs, as inhibiting SST- INs in the IL does not affect vHPC evoked feedforward inhibition on IL pyramidal neurons (Marek et al., 2018). Together, although both SST- and PV- INs in the IL receive vHPC inputs, PV-INs are more important than SST- INs in regulating the vHPC-mPFC pathway in fear relapse.

BLA-mPFC in Fear Acquisition, Expression, Extinction

Although BLA is the hub for emotional learning, the mPFC serves as a suppressor to control maladaptive fear learning (Likhtik and Paz, 2015). The communication between the amygdala and the mPFC is critical for expressing learned fear (Likhtik et al., 2013; Likhtik and Paz, 2015). The synaptic transmission from BLA to mPFC can be blocked by selectively stimulating the BLA inputs at high frequency, and blocking the BLA-mPFC pathway activity attenuated the conditioning-stimulus evoked increase of firing in mPFC (Klavir et al., 2017). This effect suggests that BLA projection transmits learned CS-US associations to the mPFC (Garcia et al., 1999; Sotres-Bayon et al., 2012; Senn et al., 2014). The function of prefrontal INs in regulating the amygdala-mPFC pathway in this behavioral performance remains to be fully characterized. Given the diversity of IN subpopulations in the mPFC, each phase of the fear conditioning process might be differentially regulated by GABAergic INs in a cell-type-specific manner. Indeed, a recent study reported that the presentation of CS inhibited PV-INs to disinhibit pyramidal neurons in the mPFC to drive fear expression (Courtin et al., 2013). Theta oscillation, which is coupled with the presentation of CS (Likhtik et al., 2014), is enhanced by the inhibition of PV-INs (Courtin et al., 2013). The inhibition of PV-INs may originate from the activation of SST-INs, which inhibit both excitatory and inhibitory neurons in the mPFC. Indeed, CS paired with footshock enhances not only the activity of SST-INs but also the inhibition of PV-INs in the PL (Cummings and Clem, 2020). Interestingly, the synaptic transmission BLA formed on both SST-INs and pyramidal neurons are enhanced, while the connection between BLA inputs to PV-INs is weakened. This finding fills the blank of how BLA inputs regulate the fear conditioning association through mPFC inhibitory circuits mediated by both SST- and PV-INs.

How are vHPC and amygdala inputs integrated into the PL and IL subregions in the mPFC to influence fear expression and extinction? The existing evidence shows that in responding to the presence of conditioned cues, BLA inputs primarily activate projecting pyramidal neurons in the PL to drive fear expression (Sotres-Bayon et al., 2012) (**Figure 2A**). The mechanism for this effect may be explained by the fact that after learning a CS-US pairing, BLA afferent activity favors the recruitment of SST-INs over PV-INs, resulting in the disinhibition of pyramidal neurons and the promotion of fear expression (Cummings and Clem, 2020). At the same time, vHPC afferents drive feedforward inhibition by recruiting PV-INs to prevent the activation of projecting neurons from the fear response. Therefore, vHPC inputs are believed to gate the BLA inputs via prelimbic PV-INs (Sotres-Bayon et al., 2012). In contrast, the extinction of fear is predominantly regulated by vHPC-driving feedforward inhibition onto the amygdala projecting neurons in the IL (Sotres-Bayon et al., 2012; Marek et al., 2018). Activation of vHPC increases the activity of PV-INs in the IL to suppress the prefrontal-amygdala projecting neurons (**Figure 2B**). These studies suggests that multiple long-range afferents may cooperate to regulate distinct complex behavior by activating specific cell types in a region-specific manner.

However, it is important to note that when it comes to fear conditioning, different modes of fear acquisition recruit different components of mPFC microcircuitry. Evidence shows that levels of freezing response are sensitive to the expression of PV in the mPFC (Caballero et al., 2020) or local disruption of vHIP and BLA inputs (Miguelez Fernández et al., 2021). For example, the amygdalar inputs in the mPFC are regulated by the vHPC inputs-driving feedforward inhibition (Caballero et al., 2014). The recruitment of vHPC and amygdalar inputs in fear expression and/or extinction is also regulated by PV-IN activity magnitude (Caballero et al., 2020). Specifically, although vHPC recruitment of PV interneurons can suppress fear expression in contextual fear conditioning, reducing PV

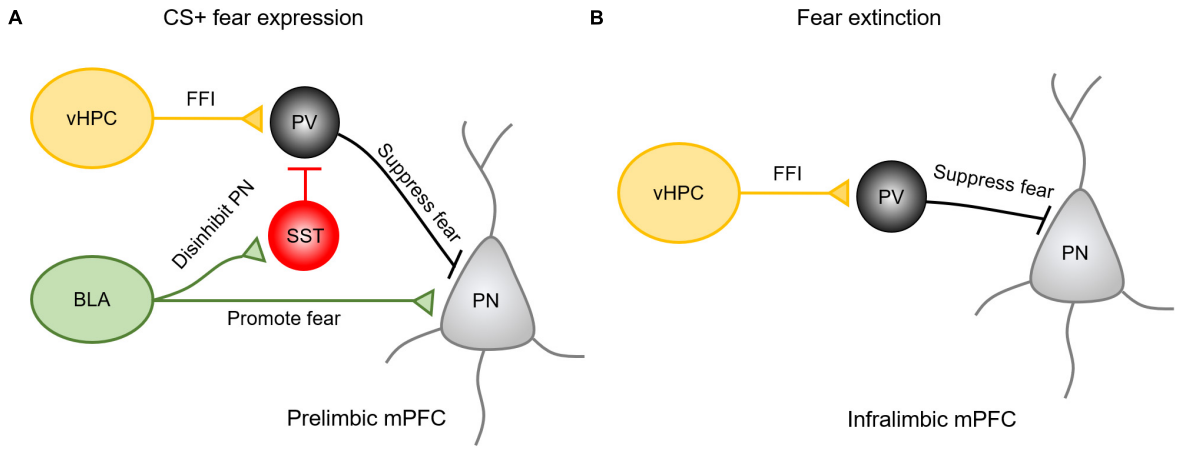

FIGURE 2 | The vHPC and amygdala inputs in the mPFC exhibit regional specificity and differential mechanisms in regulating fear expression and extinction. **(A)** Upon presenting conditioned cues, BLA inputs could activate projecting pyramidal neurons in the PL to drive fear expression or activate SST-INs to disinhibit pyramidal neurons in promoting the fear expression. Meanwhile, vHPC inputs drive feedforward inhibition (FFI) by recruiting PV-INs to prevent these projecting neurons from the fear response. **(B)** During extinction, vHPC inputs drive feedforward inhibition onto the amygdala projecting neurons in the IL to suppress the relapse of fear.

expression by 25% in the mPFC through shRNA knockdown in adolescence has no effect on the expression of conditioned fear when using a trace-fear conditioning paradigm (Caballero et al., 2020). Prefrontal infusion of a7nAChR antagonist methyllycaconitine also differentially modulates the gain of vHPC and amygdalar inputs and fear responses in an age-dependent manner (Miguelez Fernández et al., 2021).

CONCLUSION AND FUTURE DIRECTIONS

In this review, as summarized in **Figure 1**, we dissect the anatomical connection the MD, vHPC, and BLA formed with PV- or SST- INs in the PFC. All three brain regions form feedforward inhibition in the mPFC by targeting certain IN subpopulations. The MD mainly innervates PV-INs. Activation of the MD-PFC feedforward inhibitory circuit is critical for working memory performance and social preference. However, although SST-INs in the mPFC participate in the encoding of working memory, social interaction, and fear expression, what roles they play in the mPFC in gating MD inputs in these complex behaviors remains ambiguous. It is still unclear whether MD inputs form functional synaptic connections with SST-INs in the mPFC.

In contrast, it has been shown that the vHPC sends projection onto both PV- and SST- INs in the mPFC. These two subpopulations of INs separately regulate vHPC-mPFC control of distinct complex behaviors. SST-INs facilitate the coherence between prefrontal single-unit activity with vHPC theta oscillation during the sample phase of the spatial working memory task. Afferents from the vHPC target PV-INs in the IL to inhibit CS-induced fear renewal, and these connections also appear to be important for social cognition. When it comes to social fear expression, vHPC regulation of SST-INs may play a more important role.

The BLA-mPFC pathway plays an essential role in social cognition and fear acquisition, expression and extinction, but the specific mechanisms remain unclear. Although BLA inputs innervate both PV- and SST- INs to drive feedforward inhibition to the local prefrontal circuit, the unique functions of these feedforward inhibition driven by the BLA-mPFC pathway is largely understudied. The BLA inputs in the mPFC mainly serve as a suppressor of social exploration, which may require the feedforward inhibition driven by BLA inputs. In the expression of conditioned fear, synaptic transmission the BLA formed onto SST-INs is enhanced, which could inhibit PV-INs and disinhibit pyramidal neurons in the mPFC.

Dissecting the function of these long-range inputs that drive feedforward inhibition in a cell-type-specific manner is valuable for understanding the mechanisms underlying multiple behavioral impairments associated with neuropsychiatric diseases and potential novel therapeutic targets for better control over pathological development. However, outstanding questions are raised to be addressed in future studies.

- Although functional overlaps exist among different PFC-associated pathways, each IN subtype may be preferentially coupled with specific components of complex behaviors when engaged by distinct afferents. However, cell type-specific regulation of PFC-associated behaviors is overly understudied. For example, the function of BLA-prefrontal GABAergic pathways in cognitive behaviors other than emotional control is barely explored.
- One of the prominent shared features of PFC-associated psychiatric disorders is the developmental onset of pathology. However, the time course of each type of psychiatric disorder, such as SZ and ASD, are not identical. The onset of SZ could vary between 12 and 14 years old and encounter the first peak from 15 to 30 years old, which is adolescence and young adult age (Häfner, 2019).

In contrast, ASD could be presented in the first 18 months of life (Zwaigenbaum et al., 2021), which may be phase-locked with the developmental trajectories of specific interneuron populations. For example, disturbance of interneuron development during adolescence may have a stronger effect on the onset of SZ. Furthermore, embryonic and early life development, including the processes of proliferation and migration, may underlie the pathology of ASD. Therefore, characterizing the developing features of each subtype of INs, and the long-range pathway they dominantly regulate is essential for a better understanding of the pathological process.

- GABAergic INs, even within the same subtype, are highly heterogeneous based on physiological and biological features. PV-INs can be divided into two subtypes according to their morphology-basket cells and chandelier cells. SST-INs also consist of few subtypes which possess distinct physiological properties - Martinotti cells, and non-Martinotti cells. The functional differences among these small subgroups are not well studied yet. For example, in the phenomenon of cell loss seen in ASD, the population of basket cells remain relatively stable, while chandelier cells subject to a persistent decrease of intensity (Ariza et al., 2018). It thus increases the difficulty to fully understand the properties of each long-range pathway connected with the mPFC and their functions in driving complex behaviors. Bottom-Up research combining *in vivo* active cell labeling markers with molecular and electrophysiological techniques may be helpful to address this question.
- Finally, the mechanisms underlying different long-range afferents' abilities to activate distinct IN subpopulations for distinct behaviors remain unknown. For example, vHPC innervates SST- and PV- INs, but vHPC control of PV-INs is important for fear renewal or social interaction. In contrast, vHPC control of SST-INs is vital for spatial memory. Understanding how a particular input is able to engage distinct subpopulations of INs to regulate different behaviors is a great unknown question for future study.

AUTHOR CONTRIBUTIONS

S-SY, NM, YS, and W-JG wrote and edited the manuscript. All authors contributed to the article and approved the submitted version.

FUNDING

This study was supported by NIH R21MH110678 and the NIH R01MH085666 to W-JG.

REFERENCES

Abbas, A. I., Sundiang, M. J. M., Henoch, B., Morton, M. P., Bolkan, S. S., Park, A. J., et al. (2018). Somatostatin Interneurons Facilitate Hippocampal-Prefrontal Synchrony and Prefrontal Spatial Encoding. *Neuron* 100, 926.e–939.e.

Abe, R., Okada, S., Nakayama, R., Ikegaya, Y., and Sasaki, T. (2019). Social defeat stress causes selective attenuation of neuronal activity in the ventromedial prefrontal cortex. *Sci. Rep.* 9:9447.

Ährlund-Richter, S., Xuan, Y., van Lunteren, J. A., Kim, H., Ortiz, C., Pollak Dorocic, I., et al. (2019). A whole-brain atlas of monosynaptic input targeting four different cell types in the medial prefrontal cortex of the mouse. *Nat. Neurosci.* 22, 657–668. doi: 10.1038/s41593-019-0354-y

Alvarez, R. J., Pafundo, D. E., Zold, C. L., and Belforte, J. E. (2020). Interneuron NMDA Receptor Ablation Induces Hippocampus-Prefrontal Cortex Functional Hypoconnectivity after Adolescence in a Mouse Model of Schizophrenia. *J. Neurosci.* 40:3304. doi: 10.1523/jneurosci.1897-19.2020

Amodio, D. M., and Frith, C. D. (2006). Meeting of minds: the medial frontal cortex and social cognition. *Nat. Rev. Neurosci.* 7, 268–277. doi: 10.1038/nrn1884

Anastasiades, P. G., Marlin, J. J., and Carter, A. G. (2018). Cell-Type Specificity of Callosally Evoked Excitation and Feedforward Inhibition in the Prefrontal Cortex. *Cell Rep.* 22, 679–692. doi: 10.1016/j.celrep.2017.12.073

Antoine, M. W., Langberg, T., Schnepel, P., and Feldman, D. E. (2019). Increased Excitation-Inhibition Ratio Stabilizes Synapse and Circuit Excitability in Four Autism Mouse Models. *Neuron* 101, 648.e–661.e.

Ariza, J., Rogers, H., Hashemi, E., Noctor, S. C., and Martinez-Cerdeno, V. (2018). The Number of Chandelier and Basket Cells Are Differentially Decreased in Prefrontal Cortex in Autism. *Cereb. Cortex* 28, 411–420. doi: 10.1093/cercor/bhw349

Arruda-Carvalho, M., and Clem, R. L. (2015). Prefrontal-amygdala fear networks come into focus. *Front. Syst. Neurosci.* 2015:9. doi: 10.3389/fnsys.2015.00145

Arts, B., Jabben, N., Krabbendam, L., and van Os, J. (2008). Meta-analyses of cognitive functioning in euthymic bipolar patients and their first-degree relatives. *Psychol. Med.* 38, 771–785. doi: 10.1017/s0033291707001675

Bachevalier, J., and Mishkin, M. (1986). Visual recognition impairment follows ventromedial but not dorsolateral prefrontal lesions in monkeys. *Behav. Brain Res.* 20, 249–261. doi: 10.1016/0166-4328(86)90225-1

Baek, J., Lee, S., Cho, T., Kim, S.-W., Kim, M., Yoon, Y., et al. (2019). Neural circuits underlying a psychotherapeutic regimen for fear disorders. *Nature* 566, 339–343. doi: 10.1038/s41586-019-0931-y

Bechara, A., Damasio, H., Damasio, A. R., and Lee, G. P. (1999). Different Contributions of the Human Amygdala and Ventromedial Prefrontal Cortex to Decision-Making. *J. Neurosci.* 19, 5473–5481. doi: 10.1523/jneurosci.19-13-05473.1999

Bicks, L. K., Koike, H., Akbarian, S., and Morishita, H. (2015). Prefrontal Cortex and Social Cognition in Mouse and Man. *Front. Psychol.* 6:1805. doi: 10.3389/fpsyg.2015.01805

Bicks, L. K., Yamamuro, K., Flanigan, M. E., Kim, J. M., Kato, D., Lucas, E. K., et al. (2020). Prefrontal parvalbumin interneurons require juvenile social experience to establish adult social behavior. *Nat. Commun.* 11:1003.

Block, A. E., Dhanji, H., Thompson-Tardif, S. F., and Floresco, S. B. (2006). Thalamic–Prefrontal Cortical–Ventral Striatal Circuitry Mediates Dissociable Components of Strategy Set Shifting. *Cereb. Cortex* 17, 1625–1636. doi: 10.1093/cercor/bhl073

Bogart, L. J., and O'Donnell, P. (2018). Multiple long-range inputs evoke NMDA currents in prefrontal cortex fast-spiking interneurons. *Neuropsychopharmacology* 2018:3543590.

Bolkan, S. S., Stujenske, J. M., Parnaudeau, S., Spellman, T. J., Rauffenbart, C., Abbas, A. I., et al. (2017). Thalamic projections sustain prefrontal activity during working memory maintenance. *Nat. Neurosci.* 20:987. doi: 10.1038/nn.4568

Brumback, A. C., Ellwood, I. T., Kjaerby, C., Iafrati, J., Robinson, S., Lee, A. T., et al. (2018). Identifying specific prefrontal neurons that contribute to autism-associated abnormalities in physiology and social behavior. *Mole. Psychiatr.* 23, 2078–2089. doi: 10.1038/mp.2017.213

Bunnell, B. N., Sodetz, F. J. Jr., and Shalloway, D. I. (1970). Amygdaloid lesions and social behavior in the golden hamster. *Physiol. Behav.* 5, 153–161. doi: 10.1016/0031-9384(70)90059-4

Caballero, A., Flores-Barrera, E., Thomases, D. R., and Tseng, K. Y. (2020). Downregulation of parvalbumin expression in the prefrontal cortex during adolescence causes enduring prefrontal disinhibition in adulthood. *Neuropsychopharmacology* 45, 1527–1535. doi: 10.1038/s41386-020-0709-9

Caballero, A., Thomases, D. R., Flores-Barrera, E., Cass, D. K., and Tseng, K. Y. (2014). Emergence of GABAergic-dependent regulation of input-specific plasticity in the adult rat prefrontal cortex during adolescence. *Psychopharmacology* 231, 1789–1796. doi: 10.1007/s00213-013-3216-4

Cardin, J. A. (2018). Inhibitory Interneurons Regulate Temporal Precision and Correlations in Cortical Circuits. *Trends Neurosci.* 41, 689–700. doi: 10.1016/j.tins.2018.07.015

Carmichael, S. T., and Price, J. L. (1996). Connectional networks within the orbital and medial prefrontal cortex of macaque monkeys. *J. Comparat. Neurol.* 371, 179–207. doi: 10.1002/(sici)1096-9861(19960722)371:2<179::aid-cne1>3.0.co;2-#

Chao, H. T., Chen, H., Samaco, R. C., Xue, M., Chahrour, M., Yoo, J., et al. (2010). Dysfunction in GABA signalling mediates autism-like stereotypies and Rett syndrome phenotypes. *Nature* 468, 263–269. doi: 10.1038/nature09582

Collins, D. P., Anastasiades, P. G., Marlin, J. J., and Carter, A. G. (2018). Reciprocal circuits linking the prefrontal cortex with dorsal and ventral thalamic nuclei. *Neuron* 98, 366.e–379.e.

Corcoran, K. A., and Maren, S. (2001). Hippocampal Inactivation Disrupts Contextual Retrieval of Fear Memory after Extinction. *J. Neurosci.* 21, 1720–1726. doi: 10.1523/jneurosci.21-05-01720.2001

Courchesne, E., Sedaghat, F., Haist, F., and Pierce, K. (2004). The brain response to personally familiar faces in autism: findings of fusiform activity and beyond. *Brain* 127, 2703–2716. doi: 10.1093/brain/awh289

Courtin, J., Chaudun, F., Rozeske, R. R., Karalis, N., Gonzalez-Campo, C., Wurtz, H., et al. (2013). Prefrontal parvalbumin interneurons shape neuronal activity to drive fear expression. *Nature* 505:92. doi: 10.1038/nature12755

Cummings, K. A., and Clem, R. L. (2020). Prefrontal somatostatin interneurons encode fear memory. *Nat. Neurosci.* 23, 61–74. doi: 10.1038/s41593-019-0552-7

Dégenètais, E., Thierry, A.-M., Glowinski, J., and Gioanni, Y. (2003). Synaptic Influence of Hippocampus on Pyramidal Cells of the Rat Prefrontal Cortex: An In Vivo Intracellular Recording Study. *Cereb. Cortex* 13, 782–792. doi: 10.1093/cercor/13.7.782

Delevich, K., Tucciarone, J., Huang, Z. J., and Li, B. (2015). The mediodorsal thalamus drives feedforward inhibition in the anterior cingulate cortex via parvalbumin interneurons. *J. Neurosci.* 35, 5743–5753. doi: 10.1523/jneurosci.4565-14.2015

Dembrow, N. C., Zemelman, B. V., and Johnston, D. (2015). Temporal dynamics of L5 dendrites in medial prefrontal cortex regulate integration versus coincidence detection of afferent inputs. *J. Neurosci.* 35, 4501–4514. doi: 10.1523/jneurosci.4673-14.2015

Dilgen, J., Tejeda, H. A., and O'Donnell, P. (2013). Amygdala inputs drive feedforward inhibition in the medial prefrontal cortex. *J. Neurophys.* 110, 221–229. doi: 10.1152/jn.00531.2012

Dudchenko, P. A. (2004). An overview of the tasks used to test working memory in rodents. *Neurosci. Biobehav. Rev.* 28, 699–709. doi: 10.1016/j.neubiorev.2004.09.002

Esmaeili, B., and Grace, A. A. (2013). Afferent drive of medial prefrontal cortex by hippocampus and amygdala is altered in MAM-treated rats: evidence for interneuron dysfunction. *Neuropsychopharmacology* 38, 1871–1880. doi: 10.1038/npp.2013.64

Etkin, A., Egner, T., and Kalisch, R. (2011). Emotional processing in anterior cingulate and medial prefrontal cortex. *Trends Cogn. Sci.* 15, 85–93. doi: 10.1016/j.tics.2010.11.004

Felix-Ortiz, A. C., Burgos-Robles, A., Bhagat, N. D., Leppla, C. A., and Tye, K. M. (2016). Bidirectional modulation of anxiety-related and social behaviors by amygdala projections to the medial prefrontal cortex. *Neuroscience* 321, 197–209. doi: 10.1016/j.neuroscience.2015.07.041

Ferguson, B. R., and Gao, W. J. (2015). Development of thalamocortical connections between the mediodorsal thalamus and the prefrontal cortex and its implication in cognition. *Front. Hum. Neurosci.* 8:1027. doi: 10.3389/fnhum.2014.01027

Ferguson, B. R., and Gao, W-J. (2018a). Thalamic Control of Cognition and Social Behavior Via Regulation of Gamma-Aminobutyric Acidergic Signaling and Excitation/Inhibition Balance in the Medial Prefrontal Cortex. *Biol. Psychiatr.* 83, 657–669. doi: 10.1016/j.biopsych.2017.11.033

Ferguson, B. R., and Gao, W. J. (2018b). PV Interneurons: Critical Regulators of E/I Balance for Prefrontal Cortex-Dependent Behavior and Psychiatric Disorders. *Front. Neural. Circuit.* 12:37. doi: 10.3389/fncir.2018.00037

Flores-Barrera, E., Thomases, D. R., and Tseng, K. Y. (2020). MK-801 Exposure during Adolescence Elicits Enduring Disruption of Prefrontal E-I Balance and Its Control of Fear Extinction Behavior. *J. Neurosci.* 40, 4881–4887. doi: 10.1523/jneurosci.0581-20.2020

Floresco, S. B., and Tse, M. T. (2007). Dopaminergic Regulation of Inhibitory and Excitatory Transmission in the Basolateral Amygdala–Prefrontal Cortical Pathway. *J. Neurosci.* 27, 2045–2057. doi: 10.1523/jneurosci.5474-06.2007

Ford, J. M., Mathalon, D. H., Whitfield, S., Faustman, W. O., and Roth, W. T. (2002). Reduced communication between frontal and temporal lobes during talking in schizophrenia. *Biol. Psychiatr.* 51, 485–492. doi: 10.1016/s0006-3223(01)01335-x

Foss-Feig, J. H., Adkinson, B. D., Ji, J. L., Yang, G., Srihari, V. H., McPartland, J. C., et al. (2017). Searching for Cross-Diagnostic Convergence: Neural Mechanisms Governing Excitation and Inhibition Balance in Schizophrenia and Autism Spectrum Disorders. *Biol. Psychiatr.* 81, 848–861. doi: 10.1016/j.biopsych.2017.03.005

Frysztak, R. J., and Neafsey, E. J. (1991). The Effect of Medial Frontal Cortex Lesions on Respiration, "Freezing," and Ultrasonic Vocalizations during Conditioned Emotional Responses in Rats. *Cereb. Cortex* 1, 418–425. doi: 10.1093/cercor/1.5.418

Frysztak, R. J., and Neafsey, E. J. (1994). The effect of medial frontal cortex lesions on cardiovascular conditioned emotional responses in the rat. *Brain Res.* 643, 181–193. doi: 10.1016/0006-8993(94)90024-8

Fung, S. J., Fillman, S. G., Webster, M. J., and Shannon Weickert, C. (2014). Schizophrenia and bipolar disorder show both common and distinct changes in cortical interneuron markers. *Schizophr. Res.* 155, 26–30. doi: 10.1016/j.schres.2014.02.021

Fung, S. J., Webster, M. J., Sivagnanasundaram, S., Duncan, C., Elashoff, M., and Weickert, C. S. (2010). Expression of interneuron markers in the dorsolateral prefrontal cortex of the developing human and in schizophrenia. *Am. J. Psychiatr.* 167, 1479–1488. doi: 10.1176/appi.ajp.2010.09060784

Gabbott, P., Headlam, A., and Busby, S. (2002). Morphological evidence that CA1 hippocampal afferents monosynaptically innervate PV-containing neurons and NADPH-diaphorase reactive cells in the medial prefrontal cortex (Areas 25/32) of the rat. *Brain Res.* 946, 314–322. doi: 10.1016/s0006-8993(02)02487-3

Gabbott, P. L. A., Warner, T. A., and Busby, S. J. (2006). Amygdala input monosynaptically innervates parvalbumin immunoreactive local circuit neurons in rat medial prefrontal cortex. *Neuroscience* 139, 1039–1048. doi: 10.1016/j.neuroscience.2006.01.026

Gabbott, P. L. A., Warner, T. A., Jays, P. R. L., Salway, P., and Busby, S. J. (2005). Prefrontal cortex in the rat: Projections to subcortical autonomic, motor, and limbic centers. *J. Comparat. Neurol.* 492, 145–177. doi: 10.1002/cne.20738

Garcia, R., Vouimba, R.-M., Baudry, M., and Thompson, R. F. (1999). The amygdala modulates prefrontal cortex activity relative to conditioned fear. *Nature* 402, 294–296. doi: 10.1038/46286

Ghods-Sharifi, S., St Onge, J. R., and Floresco, S. B. (2009). Fundamental contribution by the basolateral amygdala to different forms of decision making. *J. Neurosci.* 29, 5251–5259. doi: 10.1523/jneurosci.0315-09.2009

Gibson, J. R., Beierlein, M., and Connors, B. W. (1999). Two networks of electrically coupled inhibitory neurons in neocortex. *Nature* 402:75. doi: 10.1038/47035

Giustino, T. F., and Maren, S. (2015). The Role of the Medial Prefrontal Cortex in the Conditioning and Extinction of Fear. *Front. Behav. Neurosci.* 9:298. doi: 10.3389/fnbeh.2015.00298

Gogolla, N., Takesian, A. E., Feng, G., Fagiolini, M., and Hensch, T. K. (2014). Sensory integration in mouse insular cortex reflects GABA circuit maturation. *Neuron* 83, 894–905. doi: 10.1016/j.neuron.2014.06.033

Gordon, J. A. (2011). Oscillations and hippocampal–prefrontal synchrony. *Curr. Opin. Neurobiol.* 21, 486–491. doi: 10.1016/j.conb.2011.02.012

Gourley, S. L., and Taylor, J. R. (2016). Going and stopping: Dichotomies in behavioral control by the prefrontal cortex. *Nat. Neurosci.* 19, 656–664. doi: 10.1038/nn.4275

Häfner, H. (2019). From Onset and Prodromal Stage to a Life-Long Course of Schizophrenia and Its Symptom Dimensions: How Sex, Age, and Other Risk Factors Influence Incidence and Course of Illness. *Psychiatr. J.* 2019:980 4836.

Hallock, H. L., Wang, A., and Griffin, A. L. (2016). Ventral Midline Thalamus Is Critical for Hippocampal–Prefrontal Synchrony and Spatial Working Memory. *J. Neurosci.* 36, 8372–8389. doi: 10.1523/jneurosci.0991-16.2016

Han, S., Tai, C., Westenbroek, R. E., Yu, F. H., Cheah, C. S., Potter, G. B., et al. (2012). Autistic-like behaviour in Scn1a+/- mice and rescue by enhanced GABA-mediated neurotransmission. *Nature* 489, 385–390. doi: 10.1038/nature11356

Hartman, M., Steketee, M. C., Silva, S., Lanning, K., and McCann, H. (2003). Working memory and schizophrenia: evidence for slowed encoding. *Schizophr. Res.* 59, 99–113. doi: 10.1016/s0920-9964(01)00366-8

Hashimoto, K. (2008). Microglial activation in schizophrenia and minocycline treatment. *Prog. Neuro-Psychopharm. Biol. Psychiatr.* 32, 1758–1759. doi: 10.1016/j.pnpbp.2008.06.012

He, M., Tucciarone, J., Lee, S., Nigro Maximiliano, J., Kim, Y., Levine Jesse, M., et al. (2016). Strategies and Tools for Combinatorial Targeting of GABAergic Neurons in Mouse Cerebral Cortex. *Neuron* 92:555. doi: 10.1016/j.neuron.2016.10.009

Heidbreder, C. A., and Groenewegen, H. J. (2003). The medial prefrontal cortex in the rat: evidence for a dorso-ventral distinction based upon functional and anatomical characteristics. *Neurosci. Biobehav. Rev.* 27, 555–579. doi: 10.1016/j.neubiorev.2003.09.003

Herry, C., and Garcia, R. (2002). Prefrontal cortex long-term potentiation, but not long-term depression, is associated with the maintenance of extinction of learned fear in mice. *J. Neurosci.* 22, 577–583. doi: 10.1523/jneurosci.22-02-00577.2002

Hitti, F. L., and Siegelbaum, S. A. (2014). The hippocampal CA2 region is essential for social memory. *Nature* 508, 88–92. doi: 10.1038/nature13028

Hobin, J. A., Ji, J., and Maren, S. (2006). Ventral hippocampal muscimol disrupts context-specific fear memory retrieval after extinction in rats. *Hippocampus* 16, 174–182. doi: 10.1002/hipo.20144

Hofer, S. B., Ko, H., Pichler, B., Vogelstein, J., Ros, H., Zeng, H., et al. (2011). Differential connectivity and response dynamics of excitatory and inhibitory neurons in visual cortex. *Nat. Neurosci.* 14:1045. doi: 10.1038/nn.2876

Holland, F. H., Ganguly, P., Potter, D. N., Chartoff, E. H., and Brenhouse, H. C. (2014). Early life stress disrupts social behavior and prefrontal cortex parvalbumin interneurons at an earlier time-point in females than in males. *Neurosci. Lett.* 566, 131–136. doi: 10.1016/j.neulet.2014.02.023

Hoover, W. B., and Vertes, R. P. (2007). Anatomical analysis of afferent projections to the medial prefrontal cortex in the rat. *Brain Struct. Funct.* 212, 149–179. doi: 10.1007/s00429-007-0150-4

Inan, M., Zhao, M., Manuszak, M., Karakaya, C., Rajadhyaksha, A. M., Pickel, V. M., et al. (2016). Energy deficit in parvalbumin neurons leads to circuit dysfunction, impaired sensory gating and social disability. *Neurobiol. Dis.* 93, 35–46. doi: 10.1016/j.nbd.2016.04.004

Jodo, E., Katayama, T., Okamoto, M., Suzuki, Y., Hoshino, K., and Kayama, Y. (2010). Differences in responsiveness of mediodorsal thalamic and medial prefrontal cortical neurons to social interaction and systemically administered phencyclidine in rats. *Neuroscience* 170, 1153–1164. doi: 10.1016/j.neuroscience.2010.08.017

Jonason, K. R., and Enloe, L. J. (1971). Alterations in social behavior following septal and amygdaloid lesions in the rat. *J. Compar. Physiol. Psychol.* 75, 286–301. doi: 10.1037/h0030808

Jones, M. W., and Wilson, M. A. (2005). Theta Rhythms Coordinate Hippocampal–Prefrontal Interactions in a Spatial Memory Task. *PLoS Biology* 3:e402. doi: 10.1371/journal.pbio.0030402

Karayannis, T., Au, E., Patel, J. C., Kruglikov, I., Markx, S., Delorme, R., et al. (2014). Cntnap4 differentially contributes to GABAergic and dopaminergic synaptic transmission. *Nature* 511, 236–240. doi: 10.1038/nature13248

Kim, D., Jeong, H., Lee, J., Ghim, J.-W., Her, E. S., Lee, S.-H., et al. (2016). Distinct Roles of Parvalbumin- and Somatostatin-Expressing Interneurons in Working Memory. *Neuron* 92, 902–915. doi: 10.1016/j.neuron.2016.09.023

Klavir, O., Prigge, M., Sarel, A., Paz, R., and Yizhar, O. (2017). Manipulating fear associations via optogenetic modulation of amygdala inputs to prefrontal cortex. *Nat. Neurosci.* 20, 836–844. doi: 10.1038/nn.4523

Kling, A., and Cornell, R. (1971). Amygdalectomy and social behavior in the caged stump-tailed macaque (Macaca speciosa). *Intern. J. Primatol.* 14, 190–208. doi: 10.1159/000155350

Kling, A., and Steklis, H. D. (1976). A neural substrate for affiliative behavior in nonhuman primates. *Brain Behav. Evol.* 13, 216–238. doi: 10.1159/000123811

Koukouli, F., Rooy, M., Tziotis, D., Sailor, K. A., O'Neill, H. C., Levenga, J., et al. (2017). Nicotine reverses hypofrontality in animal models of addiction and schizophrenia. *Nat. Med.* 23, 347–354. doi: 10.1038/nm.4274

Lagler, M., Ozdemir, A. T., Lagoun, S., Malagon-Vina, H., Borhegyi, Z., Hauer, R., et al. (2016). Divisions of identified parvalbumin-expressing basket cells during working memory-guided decision making. *Neuron* 91, 1390–1401. doi: 10.1016/j.neuron.2016.08.010

Lai, C. L. E., Lau, Z., Lui, S. S. Y., Lok, E., Tam, V., Chan, Q., et al. (2017). Meta-analysis of neuropsychological measures of executive functioning in children and adolescents with high-functioning autism spectrum disorder. *Off. J. Intern. Soc. Autism Res.* 10, 911–939. doi: 10.1002/aur.1723

Landrø, N. I., Stiles, T. C., and Sletvold, H. (2001). Neuropsychological function in nonpsychotic unipolar major depression. *Neuropsychiatr. Neuropsychol. Behav. Neurol.* 14, 233–240.

Li, B., Nguyen, T. P., Ma, C., and Dan, Y. (2020). Inhibition of impulsive action by projection-defined prefrontal pyramidal neurons. *Proc. Natl. Acad. Sci.* 117, 17278–17287. doi: 10.1073/pnas.2000523117

Li, X. B., Inoue, T., Nakagawa, S., and Koyama, T. (2004). Effect of mediodorsal thalamic nucleus lesion on contextual fear conditioning in rats. *Brain Res.* 1008, 261–272. doi: 10.1016/j.brainres.2004.02.038

Liang, B., Zhang, L., Barbera, G., Fang, W., Zhang, J., Chen, X., et al. (2018). Distinct and Dynamic ON and OFF Neural Ensembles in the Prefrontal Cortex Code Social Exploration. *Neuron* 100, 700.e–714.e.

Lieberman, M. D., Straccia, M. A., Meyer, M. L., Du, M., and Tan, K. M. (2019). Social, self, (situational), and affective processes in medial prefrontal cortex (MPFC): Causal, multivariate, and reverse inference evidence. *Neurosci. Biobehav. Rev.* 99, 311–328. doi: 10.1016/j.neubiorev.2018.12.021

Likhtik, E., and Paz, R. (2015). Amygdala–prefrontal interactions in (mal)adaptive learning. *Trends Neurosci.* 38, 158–166. doi: 10.1016/j.tins.2014.12.007

Likhtik, E., Stujenske, J. M., Topiwala, M., Harris, A. Z., and Gordon, J. A. (2013). Prefrontal entrainment of amygdala activity signals safety in learned fear and innate anxiety. *Nat. Neurosci.* 17:106. doi: 10.1038/nn.3582

Likhtik, E., Stujenske, J. M., Topiwala, M. A., Harris, A. Z., and Gordon, J. A. (2014). Prefrontal entrainment of amygdala activity signals safety in learned fear and innate anxiety. *Nat. Neurosci.* 17, 106–113.

Liu, X., and Carter, A. G. (2018). Ventral Hippocampal Inputs Preferentially Drive Corticocortical Neurons in the Infralimbic Prefrontal Cortex. *J. Neurosci.* 38, 7351–7363. doi: 10.1523/jneurosci.0378-18.2018

Ma, Y., Hu, H., and Agmon, A. (2012). Short-Term Plasticity of Unitary Inhibitory-to-Inhibitory Synapses Depends on the Presynaptic Interneuron Subtype. *J. Neurosci.* 32, 983–988. doi: 10.1523/jneurosci.5007-11.2012

Machado, C. J., Emery, N. J., Capitanio, J. P., Mason, W. A., Mendoza, S. P., and Amaral, D. G. (2008). Bilateral neurotoxic amygdala lesions in rhesus monkeys (*Macaca mulatta*): consistent pattern of behavior across different social contexts. *Behav. Neurosci.* 122, 251–266. doi: 10.1037/0735-7044.122.2.251

Marek, R., Jin, J., Goode, T. D., Giustino, T. F., Wang, Q., Acca, G. M., et al. (2018). Hippocampus-driven feed-forward inhibition of the prefrontal cortex mediates relapse of extinguished fear. *Nat. Neurosci.* 21, 384–392. doi: 10.1038/s41593-018-0073-9

Markram, H., Toledo-Rodriguez, M., Wang, Y., Gupta, A., Silberberg, G., and Wu, C. (2004). Interneurons of the neocortical inhibitory system. *Nat. Rev. Neurosci.* 5:793. doi: 10.1038/nrn1519

Martinussen, R., Hayden, J., Hogg-Johnson, S., and Tannock, R. (2005). A Meta-Analysis of Working Memory Impairments in Children With Attention-Deficit/Hyperactivity Disorder. *J. Am. Acad. Child Adolescent Psychiatr.* 44, 377–384.

McGarry, L. M., and Carter, A. G. (2016). Inhibitory Gating of Basolateral Amygdala Inputs to the Prefrontal Cortex. *J. Neurosci.* 36, 9391–9406. doi: 10.1523/jneurosci.0874-16.2016

McGarry, L. M., and Carter, A. G. (2017). Prefrontal Cortex Drives Distinct Projection Neurons in the Basolateral Amygdala. *Cell Rep.* 21, 1426–1433. doi: 10.1016/j.celrep.2017.10.046

Meira, T., Leroy, F., Buss, E. W., Oliva, A., Park, J., and Siegelbaum, S. A. (2018). A hippocampal circuit linking dorsal CA2 to ventral CA1 critical for social memory dynamics. *Nat. Commun.* 9:4163.

Meyer-Lindenberg, A. S., Olsen, R. K., Kohn, P. D., Brown, T., Egan, M. F., Weinberger, D. R., et al. (2005). Regionally specific disturbance of dorsolateral prefrontal-hippocampal functional connectivity in schizophrenia. *Arch. Gen. Psychiatr.* 62, 379–386. doi: 10.1001/archpsyc.62.4.379

Miguelez Fernández, A. M. M., Molla, H. M., Thomases, D. R., and Tseng, K. Y. (2021). Prefrontal α7nAChR Signaling Differentially Modulates Afferent Drive and Trace Fear Conditioning Behavior in Adolescent and Adult Rats. *J. Neurosci.* 41, 1908–1916. doi: 10.1523/jneurosci.1941-20.2020

Mitchell, A. S., and Chakraborty, S. (2013). What does the mediodorsal thalamus do? *Front. Neurosci.* 7:37. doi: 10.3389/fnsys.2013.00037

Mukherjee, A., Carvalho, F., Eliez, S., and Caroni, P. (2019). Long-Lasting Rescue of Network and Cognitive Dysfunction in a Genetic Schizophrenia Model. *Cell* 178, 1387.e–1402.e.

Nakajima, M., Görlich, A., and Heintz, N. (2014). Oxytocin Modulates Female Sociosexual Behavior through a Specific Class of Prefrontal Cortical Interneurons. *Cell* 159, 295–305. doi: 10.1016/j.cell.2014.09.020

Neill, P.-K., Gordon, J. A., and Sigurdsson, T. (2013). Theta Oscillations in the Medial Prefrontal Cortex Are Modulated by Spatial Working Memory and Synchronize with the Hippocampus through Its Ventral Subregion. *J. Neurosci.* 33:14211. doi: 10.1523/jneurosci.2378-13.2013

Nelson, R. J., and Trainor, B. C. (2007). Neural mechanisms of aggression. *Nat. Rev. Neurosci.* 8:536.

Okuyama, T., Kitamura, T., Roy, D. S., Itohara, S., and Tonegawa, S. (2016). Ventral CA1 neurons store social memory. *Science* 353, 1536–1541. doi: 10.1126/science.aaf7003

Oyoshi, T., Nishijo, H., Asakura, T., Takamura, Y., and Ono, T. (1996). Emotional and behavioral correlates of mediodorsal thalamic neurons during associative learning in rats. *J. Neurosci.* 16, 5812–5829. doi: 10.1523/jneurosci.16-18-05812.1996

Padilla-Coreano, N., Do-Monte, F. H., and Quirk, G. J. (2012). A time-dependent role of midline thalamic nuclei in the retrieval of fear memory. *Neuropharmacology* 62, 457–463. doi: 10.1016/j.neuropharm.2011.08.037

Park, S., and Holzman, P. S. (1993). Association of working memory deficit and eye tracking dysfunction in schizophrenia. *Schizophr. Res.* 11, 55–61. doi: 10.1016/0920-9964(93)90038-k

Parnaudeau, S., Bolkan, S. S., and Kellendonk, C. (2018). The mediodorsal thalamus: an essential partner of the prefrontal cortex for cognition. *Biol. Psychiatr.* 83, 648–656. doi: 10.1016/j.biopsych.2017.11.008

Parnaudeau, S., O'Neill, P. K., Bolkan, S. S., Ward, R. D., Abbas, A. I., Roth, B. L., et al. (2013). Inhibition of mediodorsal thalamus disrupts thalamofrontal connectivity and cognition. *Neuron* 77, 1151–1162. doi: 10.1016/j.neuron.2013.01.038

Paul, A., Crow, M., Raudales, R., He, M., Gillis, J., and Huang, Z. J. (2017). Transcriptional architecture of synaptic communication delineates GABAergic neuron identity. *Cell* 171, 522.e–539.e.

Perez, S. M., Boley, A., and Lodge, D. J. (2019). Region specific knockdown of Parvalbumin or Somatostatin produces neuronal and behavioral deficits consistent with those observed in schizophrenia. *Translat. Psychiatr.* 9, 264–264.

Phillips, M. L., Robinson, H. A., and Pozzo-Miller, L. (2019). Ventral hippocampal projections to the medial prefrontal cortex regulate social memory. *eLife* 8:e44182.

Pinto, L., and Dan, Y. (2015). Cell-Type-Specific Activity in Prefrontal Cortex during Goal-Directed Behavior. *Neuron* 87, 437–450. doi: 10.1016/j.neuron.2015.06.021

Qi, C.-C., Wang, Q.-J., Ma X-z, Chen, H.-C., Gao, L.-P., Yin, J., et al. (2018). Interaction of basolateral amygdala, ventral hippocampus and medial prefrontal cortex regulates the consolidation and extinction of social fear. *Behav. Brain Funct.* 14:7.

Resstel, L. B. M., Joca, S. R. L., Guimarães, F. G., and Corrêa, F. M. A. (2006). Involvement of medial prefrontal cortex neurons in behavioral and cardiovascular responses to contextual fear conditioning. *Neuroscience* 143, 377–385. doi: 10.1016/j.neuroscience.2006.08.002

Roozendaal, B., McEwen, B. S., and Chattarji, S. (2009). Stress, memory and the amygdala. *Nat. Rev. Neurosci.* 10, 423–433. doi: 10.1038/nrn2651

Roozendaal, B., de Quervain, D. J. F., Schelling, G., and McGaugh, J. L. (2004). A systemically administered β-adrenoceptor antagonist blocks corticosterone-induced impairment of contextual memory retrieval in rats. *Neurobiol. Learn. Memory* 81, 150–154. doi: 10.1016/j.nlm.2003.10.001

Rotaru, D. C., Barrionuevo, G., and Sesack, S. R. (2005). Mediodorsal thalamic afferents to layer III of the rat prefrontal cortex: Synaptic relationships to subclasses of interneurons. *J. Comp. Neurol.* 490, 220–238. doi: 10.1002/cne.20661

Rubenstein, J. L. R., and Merzenich, M. M. (2003). Model of autism: increased ratio of excitation/inhibition in key neural systems. *Genes Brain Behav.* 2, 255–267. doi: 10.1034/j.1601-183x.2003.00037.x

Rudy, B., Fishell, G., Lee, S., and Hjerling-Leffler, J. (2011). Three groups of interneurons account for nearly 100% of neocortical GABAergic neurons. *Dev. Neurobiol.* 71, 45–61. doi: 10.1002/dneu.20853

Sanders, S. K., and Shekhar, A. (1995). Regulation of anxiety by GABAA receptors in the rat amygdala. *Pharm. Biochem. Behav.* 52, 701–706. doi: 10.1016/0091-3057(95)00153-n

Saykin, A. J., Shtasel, D. L., Gur, R. E., Kester, D. B., Mozley, L. H., Stafiniak, P., et al. (1994). Neuropsychological deficits in neuroleptic naive patients with first-episode schizophrenia. *Arch. Gen. Psychiatr.* 51, 124–131. doi: 10.1001/archpsyc.1994.03950020048005

Saykin, A. J., Gur, R. C., Gur, R. E., Mozley, P. D., Mozley, L. H., Resnick, S. M., et al. (1991). Neuropsychological function in schizophrenia. Selective impairment in memory and learning. *Arch. Gen. Psychiatr.* 48, 618–624. doi: 10.1001/archpsyc.1991.01810310036007

Schmitt, L. I., Wimmer, R. D., Nakajima, M., Happ, M., Mofakham, S., and Halassa, M. M. (2017). Thalamic amplification of cortical connectivity sustains attentional control. *Nature* 545:219. doi: 10.1038/nature22073

Senn, V., Wolff, S. B., Herry, C., Grenier, F., Ehrlich, I., Gründemann, J., et al. (2014). Long-range connectivity defines behavioral specificity of amygdala neurons. *Neuron* 81, 428–437. doi: 10.1016/j.neuron.2013.11.006

Shibano, N., Yamazaki, M., Arima, T., Abe, K., Kuroda, M., Kobayashi, Y., et al. (2020). Excitation of prefrontal cortical neurons during conditioning enhances fear memory formation. *Sci. Rep.* 10:8613.

Sigurdsson, T., Stark, K. L., Karayiorgou, M., Gogos, J. A., and Gordon, J. A. (2010). Impaired hippocampal–prefrontal synchrony in a genetic mouse model of schizophrenia. *Nature* 464:763. doi: 10.1038/nature08855

Sotres-Bayon, F., and Quirk, G. J. (2010). Prefrontal control of fear: more than just extinction. *Curr. Opin. Neurobiol.* 20, 231–235. doi: 10.1016/j.conb.2010.02.005

Sotres-Bayon, F., Sierra-Mercado, D., Pardilla-Delgado, E., and Quirk, G. J. (2012). Gating of fear in prelimbic cortex by hippocampal and amygdala inputs. *Neuron* 76, 804–812. doi: 10.1016/j.neuron.2012.09.028

Spellman, T., Rigotti, M., Ahmari, S. E., Fusi, S., Gogos, J. A., and Gordon, J. A. (2015). Hippocampal–prefrontal input supports spatial encoding in working memory. *Nature* 522:309. doi: 10.1038/nature14445

Sun, Q., Li, X., Li, A., Zhang, J., Ding, Z., Gong, H., et al. (2020). Ventral Hippocampal-Prefrontal Interaction Affects Social Behavior via Parvalbumin Positive Neurons in the Medial Prefrontal Cortex. *iScience* 2020:23.

Sun, Q., Li, X., Ren, M., Zhao, M., Zhong, Q., Ren, Y., et al. (2019). A whole-brain map of long-range inputs to GABAergic interneurons in the mouse medial prefrontal cortex. *Nat. Neurosci.* 22, 1357–1370. doi: 10.1038/s41593-019-0429-9

Tavares, R. M., Mendelsohn, A., Grossman, Y., Williams, C. H., Shapiro, M., Trope, Y., et al. (2015). A Map for Social Navigation in the Human Brain. *Neuron* 87, 231–243. doi: 10.1016/j.neuron.2015.06.011

Thierry, A. M., Gioanni, Y., Degenetais, E., and Glowinski, J. (2000). Hippocampo-prefrontal cortex pathway: anatomical and electrophysiological characteristics. *Hippocampus* 10, 411–419. doi: 10.1002/1098-1063(2000)10:4<411::aid-hipo7>3.0.co;2-a

van Heukelum, S., Mogavero, F., van de Wal, M. A. E., Geers, F. E., França, A. S. C., Buitelaar, J. K., et al. (2019). Gradient of Parvalbumin- and Somatostatin-Expressing Interneurons Across Cingulate Cortex Is Differentially Linked to Aggression and Sociability in BALB/cJ Mice. *Front. Psychiatr.* 10, 809–809. doi: 10.3389/fpsyt.2019.00809

Vogt, D., Cho, K. K. A., Lee, A. T., Sohal, V. S., and Rubenstein, J. L. R. (2015). The Parvalbumin/Somatostatin Ratio Is Increased in Pten Mutant Mice and by Human PTEN ASD Alleles. *Cell Rep.* 11, 944–956. doi: 10.1016/j.celrep.2015.04.019

Wolff, M., and Vann, S. D. (2019). The cognitive thalamus as a gateway to mental representations. *J. Neurosci.* 39, 3–14. doi: 10.1523/jneurosci.0479-18.2018

Xiang, Z., Huguenard, J. R., and Prince, D. A. (2002). Synaptic Inhibition of Pyramidal Cells Evoked by Different Interneuronal Subtypes in Layer V of Rat Visual Cortex. *J. Neurophysiol.* 88, 740–750. doi: 10.1152/jn.2002.88.2.740

Xu, H., Liu, L., Tian, Y., Wang, J., Li, J., Zheng, J., et al. (2019). A Disinhibitory Microcircuit Mediates Conditioned Social Fear in the Prefrontal Cortex. *Neuron* 102, 662–683.

Yin, F., Guo, H., Cui, J., Shi, Y., Su, R., Xie, Q., et al. (2019). The basolateral amygdala regulation of complex cognitive behaviours in the five-choice serial reaction time task. *Psychopharmacol.* 236, 3135–3146. doi: 10.1007/s00213-019-05260-w

Yizhar, O., and Levy, D. R. (2021). The social dilemma: prefrontal control of mammalian sociability. *Curr. Opin. Neurobiol.* 68, 67–75. doi: 10.1016/j.conb.2021.01.007

Yizhar, O., Fenno, L. E., Prigge, M., Schneider, F., Davidson, T. J., O'Shea, D. J., et al. (2011). Neocortical excitation/inhibition balance in information processing and social dysfunction. *Nature* 477:171. doi: 10.1038/nature10360

Zelikowsky, M., Bissiere, S., Hast, T. A., Bennett, R. Z., Abdipranoto, A., Vissel, B., et al. (2013). Prefrontal microcircuit underlies contextual learning after hippocampal loss. *Proc. Natl. Acad. Sci.* 110, 9938–9943. doi: 10.1073/pnas.1301691110

Zwaigenbaum, L., Brian, J., Smith, I. M., Sacrey, L.-A. R., Franchini, M., Bryson, S. E., et al. (2021). Symptom trajectories in the first 18 months and autism risk in a prospective high-risk cohort. *J. Child Psychol. Psychiatr.* 2021:13417.

Conflict of Interest: The authors declare that the research was conducted in the absence of any commercial or financial relationships that could be construed as a potential conflict of interest.

frontiers in Neural Circuits

ORIGINAL RESEARCH
published: 23 July 2021
doi: 10.3389/fncir.2021.714780

Corticofugal VIP Gabaergic Projection Neurons in the Mouse Auditory and Motor Cortex

*Alice Bertero, Charles Garcia and Alfonso junior Apicella**

Department of Biology, Neurosciences Institute, University of Texas at San Antonio, San Antonio, TX, United States

Anatomical and physiological studies have described the cortex as a six-layer structure that receives, elaborates, and sends out information exclusively as excitatory output to cortical and subcortical regions. This concept has increasingly been challenged by several anatomical and functional studies that showed that direct inhibitory cortical outputs are also a common feature of the sensory and motor cortices. Similar to their excitatory counterparts, subsets of Somatostatin- and Parvalbumin-expressing neurons have been shown to innervate distal targets like the sensory and motor striatum and the contralateral cortex. However, no evidence of long-range VIP-expressing neurons, the third major class of GABAergic cortical inhibitory neurons, has been shown in such cortical regions. Here, using anatomical anterograde and retrograde viral tracing, we tested the hypothesis that VIP-expressing neurons of the mouse auditory and motor cortices can also send long-range projections to cortical and subcortical areas. We were able to demonstrate, for the first time, that VIP-expressing neurons of the auditory cortex can reach not only the contralateral auditory cortex and the ipsilateral striatum and amygdala, as shown for Somatostatin- and Parvalbumin-expressing long-range neurons, but also the medial geniculate body and both superior and inferior colliculus. We also demonstrate that VIP-expressing neurons of the motor cortex send long-range GABAergic projections to the dorsal striatum and contralateral cortex. Because of its presence in two such disparate cortical areas, this would suggest that the long-range VIP projection is likely a general feature of the cortex's network.

Keywords: long-range, GABAergic, VIP, Som, Parv, auditory cortex, motor cortex

Edited by:
M. Victoria Puig, Hospital del Mar Medical Research Institute (IMIM), Spain

Reviewed by:
Kathleen S. Rockland, Boston University, United States
Jeffrey Garrett Mellott, Northeast Ohio Medical University, United States

***Correspondence:**
Alfonso junior Apicella
alfonso.apicella@utsa.edu

Received: *25 May 2021*
Accepted: *05 July 2021*
Published: *23 July 2021*

Citation:
Bertero A, Garcia C and Apicella Aj (2021) Corticofugal VIP GABAergic Projection Neurons in the Mouse Auditory and Motor Cortex. Front. Neural Circuits 15:714780. doi: 10.3389/fncir.2021.714780

INTRODUCTION

The auditory cortex is a six-layer structure characterized by different cell types. In a very simplistic way, these neurons, according to the neurotransmitter they release, can be divide into two main groups: glutamatergic/excitatory pyramidal neurons (about 70–80%) and GABAergic/inhibitory neurons (about 20–30%). Moreover, this neuronal subdivision of the cortex leads to the

Abbreviations: AC, auditory cortex; ACA, anterior cingulate cortex; ACB, nucleus accumbens; CA1, Cornu Ammonis of the hippocampus subfield 1; CA3, Cornu Ammonis of the hippocampus subfield 3; cc, corpus callosum; CP, caudoputamen; DG, dentate gyrus; ENT, enthorinal cortex; HPF, hippocampal formation; HY, hypothalamus; IC, inferior colliculus; ICe, inferior colliculus, external; LA, lateral amygdala; LGN, lateral geniculate nucleus; LS, lateral septal nucleus; MB, midbrain; MC, motor cortex; MGB, medial geniculate body; MS, medial septal nucleus; NB, nucleus of the brachium of the inferior colliculus; PAG, periacqueductal grey; PG, pontine gray; PIR, piriform cortex; RSP, retrosplenial cortex; SC, superior colliculus; SN, substantia nigra; SS, somatosensory cortex; STR, striatum; TeA, temporal association cortex; TH, thalamus; VIS, visual cortex; VTA, ventrotegmental area.

overall principle of cortical organization that excitation is both local and long-range, while inhibition is described as being exclusively local (for review, see Isaacson and Scanziani, 2011). However, the existence of long-range GABAergic neurons in rats, cats, and monkeys has been reported anatomically since the 80s (Seress and Ribak, 1983; Ribak et al., 1986; Toth and Freund, 1992; McDonald and Burkhalter, 1993; Toth et al., 1993; Tomioka et al., 2005, 2015; Higo et al., 2007, 2009; Tomioka and Rockland, 2007; Caputi et al., 2013). Only recent investigation has been engaged to understand how different subtypes of long-range GABAergic projections play distinct roles in cortical processing according to their differences in anatomical, electrophysiological, molecular content, and synaptic connectivity patterns (Melzer et al., 2012, 2017; Lee et al., 2014; Rock and Apicella, 2015; Rock et al., 2016, 2018; Zurita et al., 2018a; Bertero et al., 2019, 2020). Our lab showed that both Parvalbumin- and Somatostatin-expressing neurons in the sensory and motor cortices provide direct inhibitory projection to multiple cortical and subcortical areas (Rock et al., 2016, 2018; Zurita et al., 2018a; Bertero et al., 2019, 2020). However, no long-range GABAergic VIP-expressing neurons from these cortical regions have been shown yet. We addressed this fundamental question using anterograde and retrograde anatomical methods. Using these techniques, we demonstrate, for the first time, the existence of VIP-expressing GABAergic neurons in the auditory and motor cortices with cortico-cortical and cortico-subcortical long-range GABAergic projections.

MATERIALS AND METHODS

Animals

All animal procedures were approved by the Institutional Animal Care and Use. Procedures followed animal welfare guidelines set by the National Institutes of Health. Mice were housed in a vivarium maintaining a 12 h light/dark schedule and given ad libitum access to mouse chow and water. Male and female homozygous VIP-Cre mice were used in this study and were injected at postnatal day 35: B6J.Cg-Viptm1(cre)Zjh/AreckJ (the Jackson Laboratory, stock number 031628). Auditory Cortex injections (anterograde): $N = 5$ mice from 3 litters; Motor cortex injections (anterograde): $N = 3$ mice from 2 litters; Auditory Cortex injections (retrograde): $N = 3$ mice from 2 litters.

Stereotaxic Injections

As described in our previous studies mice were initially anesthetized with isoflurane (3%; 1 L/min O_2 flow) and head-fixed on a stereotaxic frame (Model 1900; Kopf Instruments) using non-rupture ear bars. Anesthesia was maintained at 1–1.5% isoflurane for the duration of the surgery. A warming pad was used to maintain body temperature during the procedure. Standard aseptic technique was followed for all surgical procedures. Injections were performed using a pressure injector (Nanoject II; Drummond Scientific) mounted on the stereotaxic frame. Injections were delivered through a borosilicate glass injection pipette (Wiretrol II; Drummond Scientific) with a taper length of ∼30 mm and a tip diameter of ∼50 μm. The pipette remained in place for 5 min before starting injecting at 1 nl/s rate, 15 s waiting period after each nl, and was left in place for 5 min after the injection to avoid viral backflow along the injection tract. Both male and female mice, P35–40 at the time of the injection, were utilized in these experiments. Viral preparation used in this study: AAV1-Syn-Flex-ChrimsonR-tdTomato (AAV-flex-ChRimson-tdTomato, titer 4.1×10^{12} GC/ml (UNC Gene Therapy Center Vector Core); AAV1-CAG-Flex-EGFP-WPRE, titer 3.1×10^{13} VG/ml (AAV1-flex-GFP, Addgene viral prep #51502-AAV1). Coordinates for injections for the right auditory cortex: 2.6 mm posterior and 4.5 mm lateral from Bregma, 0.9 mm below the brain's surface. Coordinates for injections for right motor cortex: 1 mm posterior and 1.7 mm lateral from Bregma, 0.9 mm below the brain's surface.

Immunohistochemistry

Four to Five weeks after injection, mice were anesthetized with isoflurane and decapitated. Coronal slices (200 or 300 μm thick) were sectioned on a vibratome (VT1200S; Leica) in a chilled cutting solution containing the following (in mM): 100 choline chloride, 25 $NaHCO_3$, 25 D-glucose, 11.6 sodium ascorbate, 7 $MgSO_4$, 3.1 sodium pyruvate, 2.5 KCl, 1.25 NaH_2 PO_4, 0.5 $CaCl_2$. Slices were then imaged acutely on an Olympus Macroscope with an appropriate RFP filter at a 1.6×, 5×, or 6.4× magnification lens. Slices were then postfixed for 3 h at room temperature in PBS buffered 1% PFA solution with gentle shaking. For retrograde experiments, 2 weeks after injection, mice were transcardially perfused with 4% PFA in Phosphate Buffered Saline (PBS), the brain was extracted and postfixed overnight in 4% PFA solution and sliced with a vibratome at 100 μm thick coronal slices.

Immunohistochemical procedures were performed on free-floating sections using rabbit anti-RFP (for tdTomato, 1:500, Abcam, cat #ab62341) or Chicken-anti-GFP (1:1,000; Abcam, ab13970) primary antibody, followed by Alexa Fluor 594 goat anti-rabbit IgG (1:500, Life Technologies) or AlexaFluor 488 goat anti-chicken IgG (1:500; Life Technologies) secondary antibody. Briefly, slices were washed 3–6 times in PBS 0.3% Triton X-100, and then incubated 1 h at room temperature with blocking solution (PBS with 0.3% Triton X-100 and 5% Goat serum), and overnight at 4°C with primary antibody solution with gentle shaking. After 16–24 h, slices were thoroughly washed with PBS containing 0.3% Triton X-100 at least three times for at least 10 min each wash, and then incubated 2 h at room temperature with secondary antibody solution (blocking solution with the appropriate combination of secondary antibodies). Before mounting, the slices were washed again at least three times with PBS containing 0.3% Triton X-100 for at least 10 min each wash and then mounted in Fluoromount-G (Southern Biotech). Confocal images were taken with a Zeiss LSM-710 microscope at 10×, 20×, 40× magnifications with an appropriate filter set for AlexaFluor-488/594.

Image adjustment was performed with ImageJ (National Institutes of Health) or Adobe Photoshop for brightness/contrast

corrections and pseudo coloring. Atlas reference tables were modified from the Allen Brain Atlas.

Quantification of laminar distribution of GFP-expressing VIP neurons was performed in the injection site of VIP-Cre mice injected with AAV-flex-GFP in the right auditory cortex and used for retro experiments. 100 μm thick slices ($n = 12$ slices from two mice, one litter) were acquired at 4× magnification, and a normalized 50 μm spaced grid was superimposed to cover the whole cortical thickness from Pia (0 μm) to white matter (1 mm). GFP-expressing cells were counted using the Cell Counter plugin of ImageJ.

Slice Preparation and Recording

Mice were anesthetized with isoflurane and decapitated. Coronal slices (300 μm) containing the injection site were sectioned on a vibratome (VT1200S; Leica) in a chilled cutting solution containing the following (in mM): 100 choline chloride, 25 $NaHCO_3$, 25 D-glucose, 11.6 sodium ascorbate, 7 $MgSO_4$, 3.1 sodium pyruvate, 2.5 KCl, 1.25 NaH_2PO_4, 0.5 $CaCl_2$. These slices were incubated in oxygenated artificial cerebrospinal fluid (ACSF) in a submerged chamber at 35–37°C for 30 min and then room temperature (21–25°C) until recordings were performed. ACSF contained the following (in mM): 126 NaCl, 26 $NaHCO_3$, 10 D-glucose, 2.5 KCl, 2 $CaCl_2$, 1.25 NaH_2PO_4, 1 $MgCl_2$; osmolarity was ∼290 Osm/L. Cell-attached and whole-cell recordings were performed in 31–33°C ACSF. Thin-walled borosilicate glass pipettes (Warner Instruments) were pulled on a vertical pipette puller (PC-10; Narishige) and typically were in the range of 3–5 MΩ resistance when filled with a potassium-based intracellular solution containing the following (in mM): 120 potassium gluconate, 20 KCl, 10 HEPES, 10 phosphocreatine, 4 ATP, 0.3 GTP, 0.2 EGTA, and 0.3–0.5% biocytin). Signals were sampled at 10 kHz and filtered at 4 kHz. Hardware control and data acquisition were performed by Ephus[1] (Suter et al., 2010). ChRimson positive VIP neurons in the injection site were patched and photostimulated in cell-attach: recordings were coupled with photostimulation with 615 nm wavelength red LED (CoolLED pE excitation system) and 60× water-immersion objective at 0.2 and 0.4 mW/mm2 LED power. During whole-cell recordings, neurons were filled with an internal solution containing 0.3–0.5% biocytin. Filled neurons were held for at least 20 min, and then the slices were fixed in a formalin solution (neutral buffered, 10% solution; Sigma-Aldrich) for 1–5 days at 4°C. The slices were washed in PBS (six times, 10 min per wash) and placed in a 4% streptavidin-AlexaFluor-488 conjugated (Life Technologies) solution, incubated at 4°C overnight, washed in PBS (six times, 10 min per wash), and mounted with Fluoromount-G (SouthernBiotech) on a glass microscope slide. Confocal images were taken with a Zeiss LSM-710 microscope at 40× magnifications. Image adjustment was performed in ImageJ (National Institutes of Health) for brightness/contrast corrections and pseudocoloring. Neurons were morphologically reconstructed in three dimensions using the Simple Neuritre Tracer plugin on ImageJ software (Schindelin et al., 2012).

[1]www.ephus.org

RESULTS

First, we injected a cre-dependent AAV virus expressing a cytoplasmic reporter (AAV-flex-GFP) in the right auditory cortex of VIP-Cre mice (**Figures 1A,B**) and determined the laminar distribution of GFP positive neurons. This allowed us to clearly identify GFP+/VIP-Cre soma in the auditory cortex (**Figures 1B,C**) and their characteristic distributions among cortical layers, with a peak in layer 1 and 2/3 (**Figure 1D**), as already described in genetically labeled VIP neurons (Mesik et al., 2015; Pronneke et al., 2015). Interestingly, since our lab and others (Rothermel et al., 2013; Rock et al., 2016, 2018; Zurita et al., 2018a; Bertero et al., 2019, 2020) have described that AAV1-Flex viral vectors exhibited both anterograde and retrograde transfection capabilities, we checked the contralateral auditory cortex and found GFP-labeled neurons (**Figure 1E**). The retrograde labeled neuron's bipolar morphology and aspiny dendritic arborization are compatible with VIP-expressing neurons (**Figures 1F,G**). This experiment supports the hypothesis that not only Parv- and Som-expressing neurons (Rock et al., 2016, 2018; Zurita et al., 2018a; Bertero et al., 2019, 2020), but also VIP-expressing neurons send long-range projections from the auditory cortex.

To better investigate this hypothesis, at the whole-brain scale, we used an anterograde viral tracing approach injecting the right auditory cortex of VIP-Cre driver mice with a Cre-dependent AAV-flex-ChRimson-tdTomato (**Figure 2A**). This method allowed us to visualize VIP-expressing neurons in the right auditory cortex (**Figures 2B–D**) and their axonal projection far from the injection site (i.e., long-range). Although AAV1 viruses can display both anterograde and retrograde expression in our experience, this viral preparation exhibits only anterograde features. We also checked every animal injected, and we found no labeled neuron outside the injection site with no evidence of Chrimson-tdTomato deposit or spillover in the hippocampus and/or other subcortical structures (**Figure 2C**). We also confirmed that tdTomato positive neurons in the injection site (**Figure 2D**) were expressing ChRimson, patching them while flashing red LED light on the slices to elicit action potentials (**Figure 2E**). The dendritic arborization of six patched and biocytin-filled neurons was also reconstructed and showed various characteristic somatodendritic features of VIP-like including four bipolar, one modified bipolar (i.e., tripolar), and one multipolar morphology, as previously described (Mesik et al., 2015; Pronneke et al., 2015; **Figure 2F**).

We then systematically imaged every slice, from the most posterior to the most anterior, that displayed VIP-tdTomato axons in $n = 5$ mice from three litters. In midbrain structures, known to be innervated by corticofugal excitatory axons from the auditory cortex (Zurita et al., 2018b), we could observe labeling in the ipsilateral inferior colliculus (**Figures 3A–C**), superior colliculus (**Figures 4A–C**), and in the inferior colliculus (**Figure 4D**) with thick beaded tdTomato+ axons. Moreover, we found a dense arborization of tdTomato+ axons in the temporal association cortex's upper layer (TeA, **Figure 4E**). Moving forward on the anteroposterior axis, high magnification images close to the injection site (**Figures 5A,B**)

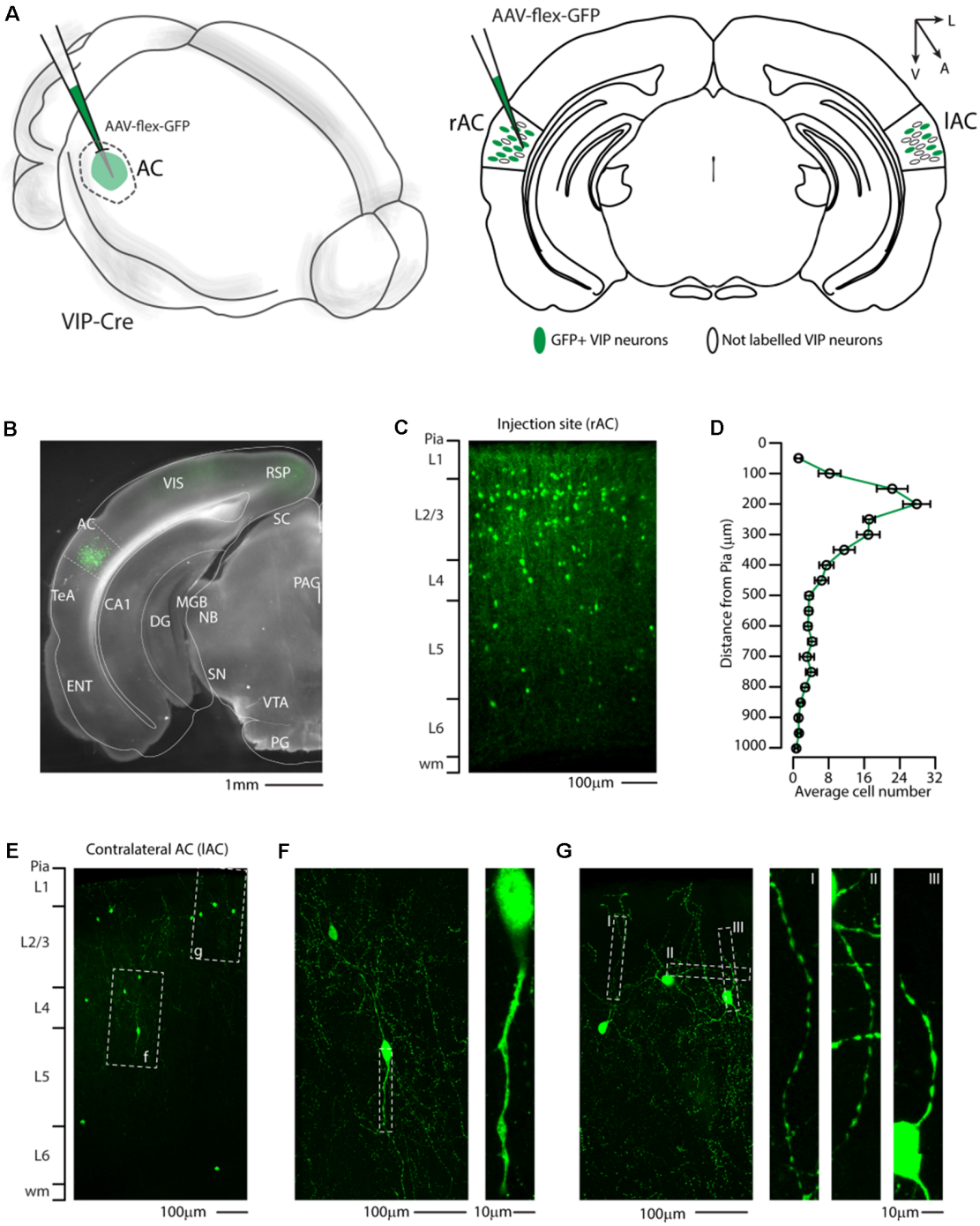

FIGURE 1 | Distribution of VIP-expressing neurons in the auditory cortex. **(A)** Schematic representation of right auditory cortex viral injection of AAV-flex-GFP. VIP-expressing neurons in both the injected (right AC, rAC) and contralateral (left, lAC) auditory cortex express GFP in a Cre-dependent manner. **(B)** Representative coronal section of an acute slice of the injection site (200 µm thick), with bright field (gray) and GFP expressing neurons (green). The Allen brain atlas coronal table superimposed for reference indicates the correct targeting of the auditory cortex. Scale bar: 1 mm. **(C)** High magnification confocal image of the injection site showing GFP expressing neurons in the right auditory cortex. Scale bars: 100 µm. **(D)** Laminar distribution of VIP neurons in the auditory cortex, quantified every 50 µm from Pia (0) to white matter (1 mm). Data are expressed ad mean ± s.e.m. **(E)** Representative high magnification confocal image of the contralateral Auditory cortex showing retrograde labeled GFP expressing neurons. Scale bars: 100 µm. **(F,G)** Details of dashed square (f and g) of **(E)**, with corresponding high magnification of the dendritic arborization of GFP+ VIP-expressing neurons showing their characteristic thin and aspiny morphology. Scale bars: 100 µm and 10 µm. RSP, retrosplenial cortex; VIS, visual cortex; TeA, temporal association cortex; AC, auditory cortex; ENT, enthorinal cortex; CA1, Cornu Ammonis of the hippocampus subfield 1; DG, dentate gyrus; SC, superior colliculus; MGB, medial geniculate body; NB, nucleus of the brachium of the inferior colliculus; PAG, periacqueductal gray; SN, substantia nigra; VTA, ventrotegmental area; PG, pontine gray.

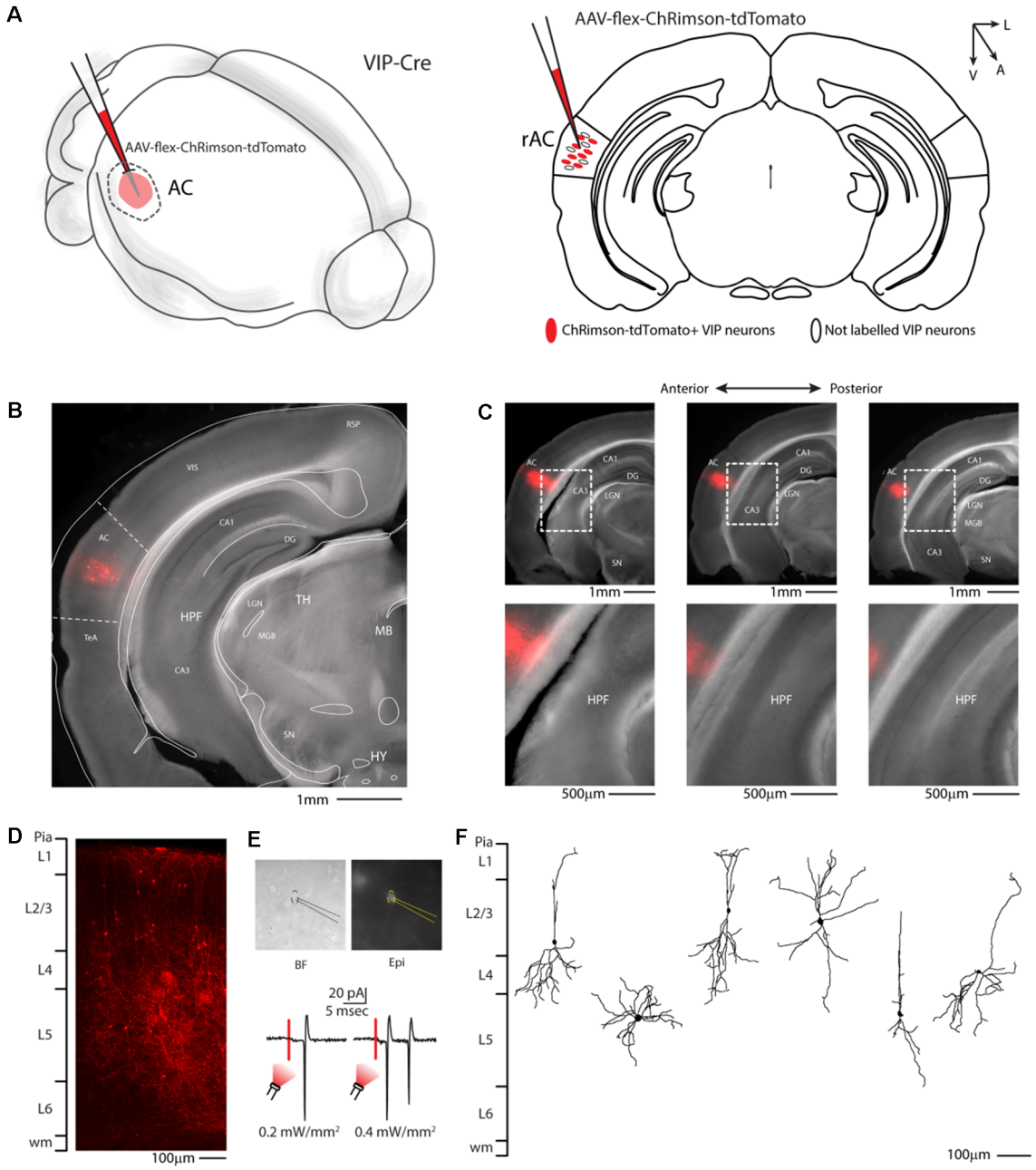

FIGURE 2 | Auditory cortex injection of AAV-flex-ChRimson-tdTomato. **(A)** Schematic representation of right auditory cortex viral injection. **(B)** Representative coronal section of an acute slice of the injection site (200 µm thick), with bright field (gray) and tdTomato expressing neurons (red). The Allen brain atlas coronal table superimposed for reference indicates the correct targeting of the Auditory cortex. Scale bar: 1 mm. **(C)** Top panel: antero-posterior and dorsal ventral spread of ChRimson-tdTomato injection in AC. Scale Bars: 1 mm. Bottom panel: high magnification image of the injection site showing no evidence of ChRimson-tdTomato deposit or spillover in the hippocampus and/or other subcortical structures. Scale Bars: 500 µm. **(D)** High magnification confocal image of the injection site showing tdTomato expressing neurons. Scale bar: 100 µm. **(E)** Top panel: bright field and epifluorescence image of tdTomato expressing VIP neuron used in whole-cell patch clamp recordings. Bottom panel: example of responses recorded from a VIP neuron using red LED at two different powers. **(F)** Reconstruction of the dendritic arborization of biocytin-filled tdTomato expressing VIP neurons. Scale bar: 100 µm. RSP, retrosplenial cortex; VIS, visual cortex; TeA, temporal association cortex; AC, auditory cortex; HPF, hippocampal formation; CA1, Cornu Ammonis of the hippocampus subfield 1; CA3, Cornu Ammonis of the hippocampus subfield 3; DG, dentate gyrus; TH, thalamus; MGB, medial geniculate body; LGN, lateral geniculate nucleus; MB, midbrain; SN, substantia nigra; HY, hypothalamus.

showed axonal arborization infiltrating the white matter, an indication of potential corticofugal projections. Previous studies from our lab have reported long-range cortico-cortical Parvalbumin-expressing neurons in the auditory cortex that provide local inhibition onto nearby pyramidal neurons and receive thalamocortical input. When looking at the contralateral

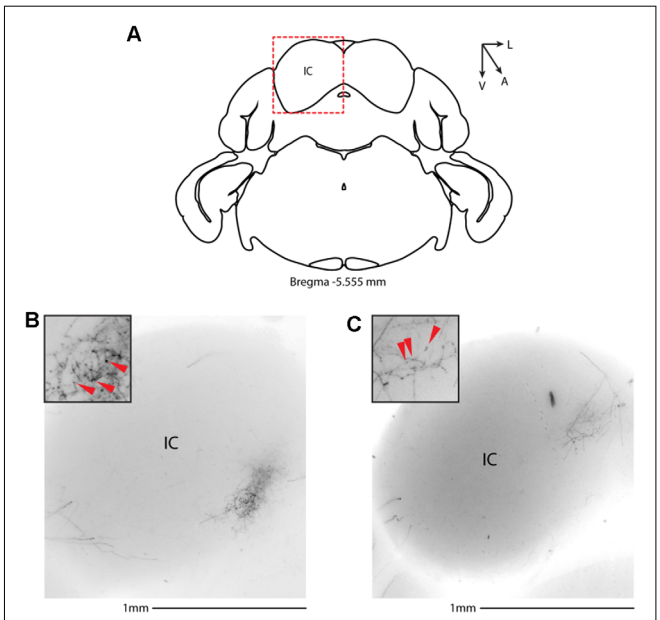

FIGURE 3 | Subcortical target of long-range VIP-expressing neurons: midbrain. **(A)** Allen Brain reference coronal section at −5.555 mm from Bregma. Red dashed squares indicate the region imaged in the panels below. **(B,C)** Two examples of the inferior colliculus, from two animals. Scale bars: 1 mm. Insets indicate axonal branches and the red arrowheads boutons. Inset size 190 μm. IC, inferior colliculus.

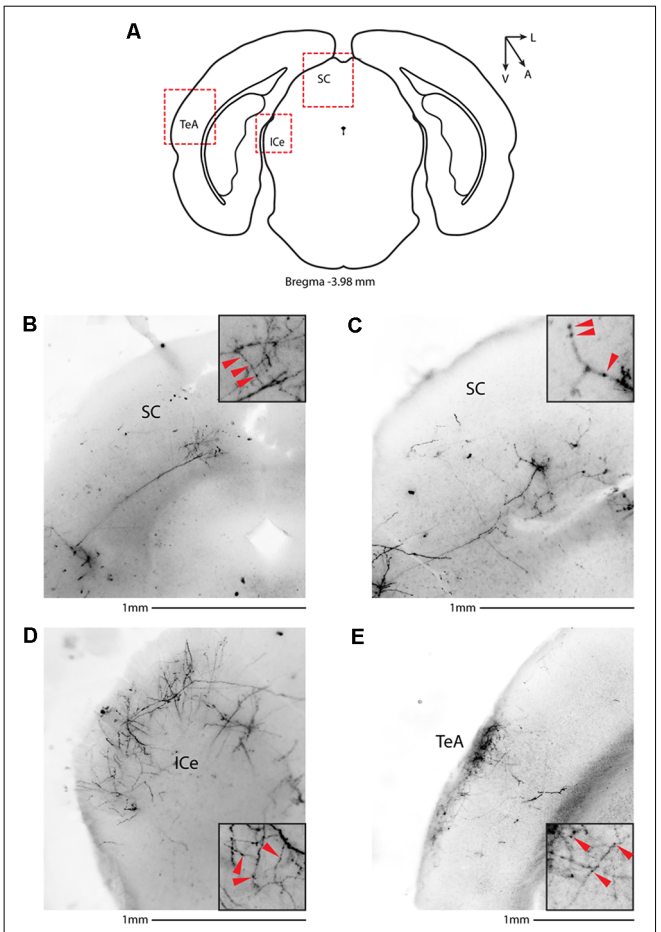

FIGURE 4 | Subcortical target of long-range VIP-expressing neurons: midbrain. **(A)** Allen Brain reference coronal section at −3.98 mm from Bregma. Red dashed squares indicate the regions imaged in the panels below. **(B,C)** Two examples of the superior colliculus, from two animals. **(D)** Representative image of the external cortex of inferior colliculus. **(E)** Representative image of the temporal association cortex. Scale bars: 1 mm. Insets indicate axonal branches and the red arrowheads boutons. Inset size 190 μm. SC, superior colliculus; ICe, inferior colliculus, external; TeA, temporal association cortex.

auditory cortex, we observed a dense tdTomato+ axonal arborization spanning all layers, with a higher concentration in the upper ones (**Figures 5C–E**), also demonstrating that the VIP-expressing neurons establish cortico-cortical connections. In thalamic areas, we found axons in the medial geniculate body (MGB), the primary auditory thalamus (**Figure 6**), while in more anterior slices, we found axons in the corpus callosum (**Figures 7A,B**), and a dense arborization in the striatum and lateral amygdala, spanning at least 600 μm anterior to posterior and almost 1 mm medial to lateral, with a higher concentration of terminal field axons (thin and twisted) in the ventral part of the striatum and thick straight axons of passage in the upper striae (**Figures 7C–E**).

Since our lab and others have already demonstrated that the motor cortex sends long-range Parvalbumin- and Somatostatin-expressing axons to the dorsal striatum (Rock et al., 2016; Melzer et al., 2017), a cortical area involved not only in sensory processing but also in planned and motivated behavior, we asked whether long-range VIP neurons are specific for the auditory cortex or are a common feature of the corticofugal circuit organization. We injected the right motor cortex of VIP-Cre mice with AAV-flex-ChRimson-tdTomato (**Figures 8A,B**), and we looked for long-range projections. We also checked every animal injected, and we found no labeled neuron outside the injection site with no evidence of Chrimson-tdTomato deposit or spillover in the striatum (**Figures 8C,D**). Not only we could find axons in the white matter underneath the injection site (**Figures 8E,F**), and in the striatum, with thick axons of passages in the upper striae (**Figure 8G**) and twisted mesh of axonal arborization in the ventral and lateral striatum (**Figures 8G,H**), but also in the contralateral motor cortex (**Figure 8F**), suggesting that the three major classes of GABAergic neurons are organized in long-range projection to reach the major cortical and subcortical target of the area of interest.

DISCUSSION

In this study, we test the hypothesis that a class of GABAergic neurons, VIP-expressing neurons, establish a long-range GABAergic inhibitory projection in the mouse neocortex. Our results support this hypothesis and additionally conclude that the auditory and motor cortices send long-range GABAergic projections to their corresponding cortex and subcortical structures, such as the dorsal striatum, *via* long-range VIP-expressing neurons (**Figure 9**). Because of its presence in two such disparate cortical areas, this would suggest that the

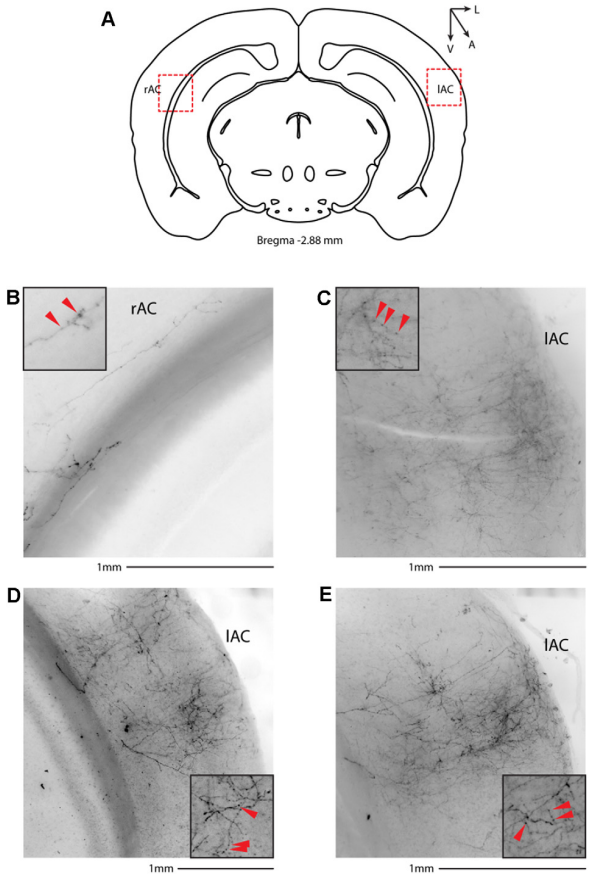

FIGURE 5 | Cortical target of long-range VIP-expressing neurons: auditory cortex. **(A)** Allen Brain reference coronal section at −2.88 mm from Bregma. Red dashed squares indicate the regions imaged in the panels below. **(B)** Representative image of white matter infiltrating axons in correspondence to the injection site. **(C–E)** Three examples of contralateral auditory cortex from two animals. Scale bars: 1 mm. Insets indicate axonal branches and the red arrowheads boutons. Inset size 190 μm. lAC, left auditory cortex; rAC, right auditory cortex.

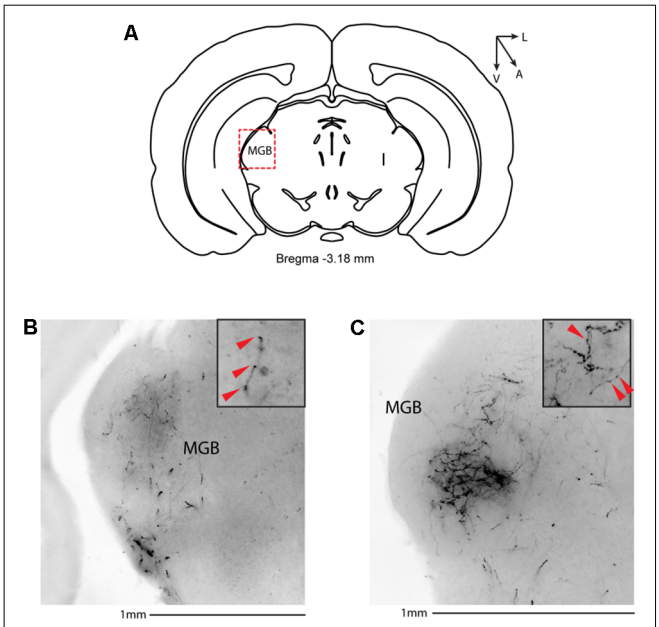

FIGURE 6 | Subcortical target of long-range VIP-expressing neurons: thalamus. **(A)** Allen Brain reference coronal section at −3.18 mm from Bregma. The Red dashed square indicates the region imaged in the panels below. **(B,C)** Two examples of the medial geniculate body from two different animals. Scale bar: 1 mm. Insets indicate axonal branches and the red arrowheads boutons. Inset size 190 μm. MGB, medial geniculate body.

long-range VIP projection is likely a general feature of the cortex's network.

A central question of modern neuroscience is determining the whole connectome of the mammalian brain (Abbott et al., 2020) and how many different cell types contribute to signal processing within specific neuronal networks to control behavior. The interaction between two forces, excitation (pyramidal neurons) and inhibition (GABAergic neurons), orchestrate the flow of information within cortical networks. GABAergic neurons are the primary source of inhibition in the adult brain, and they represent a minority of all cortical neurons (10–15% in rodents; Meyer et al., 2011) but are composed of a highly heterogeneous cell population (for review, Ascoli et al., 2008; Xu et al., 2010; Rudy et al., 2011). All our previous knowledge about the cortical cell types has led to a general principle of the organization of the cortical circuit, in which pyramidal neurons are both local and long-range while the GABAergic neurons are only local. However, recent studies from our lab and others (Lee et al., 2014; Rock and Apicella, 2015; Basu et al., 2016; Rock et al., 2016, 2018; Melzer et al., 2017; Zurita et al., 2018a; Bertero et al., 2019, 2020) are demonstrating that long-range GABAergic projections originate from Parvalbumin- and Somatostatin-expressing neurons may be more prevalent than previously assumed.

The present study's main finding is that the VIP-expressing neuronal population projects through the corpus callosum to connect the two hemispheres of AC and MC, and also reaches subcortical structures such as the dorsal striatum. In addition, our results indicate that the auditory cortex long-range GABAergic VIP-expressing neurons also project to the medial geniculate body, amygdala, temporal association cortex, and superior and inferior colliculus.

Even though we were able to identify long-range VIP-expressing neurons in this study, our approach is limited by caveats (limited injection volume and variability in transfection, which leads to incomplete coverage of the cortical area analyzed) that can preclude us from performing experiments aimed to determine the absolute number and ratio of long-range vs. short–range VIP-expressing neurons. Our findings, together with previous studies, in which long-range GABAergic projections were found to connect different brain areas in different species both ipsi- and contralaterally (Buhl and Singer, 1989; McDonald and Burkhalter, 1993; Tomioka et al., 2005, 2015; Apergis-Schoute et al., 2007; Higo et al., 2007; Tomioka and Rockland, 2007; Tamamaki and Tomioka, 2010; Rock et al., 2016, 2018; Zurita et al., 2018a; Bertero et al., 2019, 2020) lead to a new concept in which not only glutamatergic

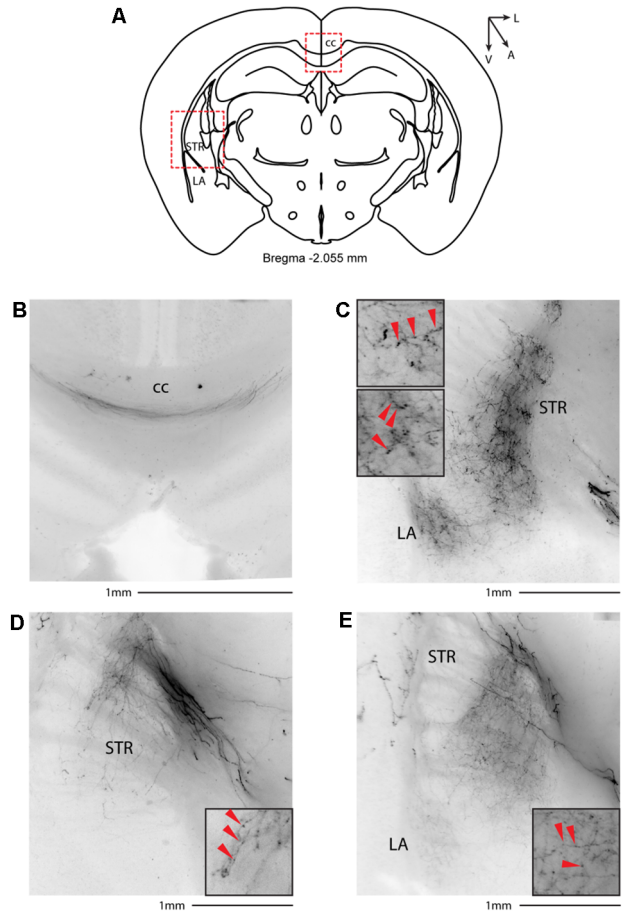

FIGURE 7 | Subcortical target of long-range VIP-expressing neurons: striatum. **(A)** Allen Brain reference coronal section at −2.055 mm from Bregma. Red dashed squares indicate the regions imaged in the panels below. **(B)** Thick axons of passage in the corpus callosum. **(C–E)** Three representative images of VIP axons in the striatum and lateral amygdala from two animals. Scale bars: 1 mm. Insets indicate axonal branches and the red arrowheads boutons. Inset size 190 μm. cc, corpus callosum; STR, striatum; LA, lateral amygdala.

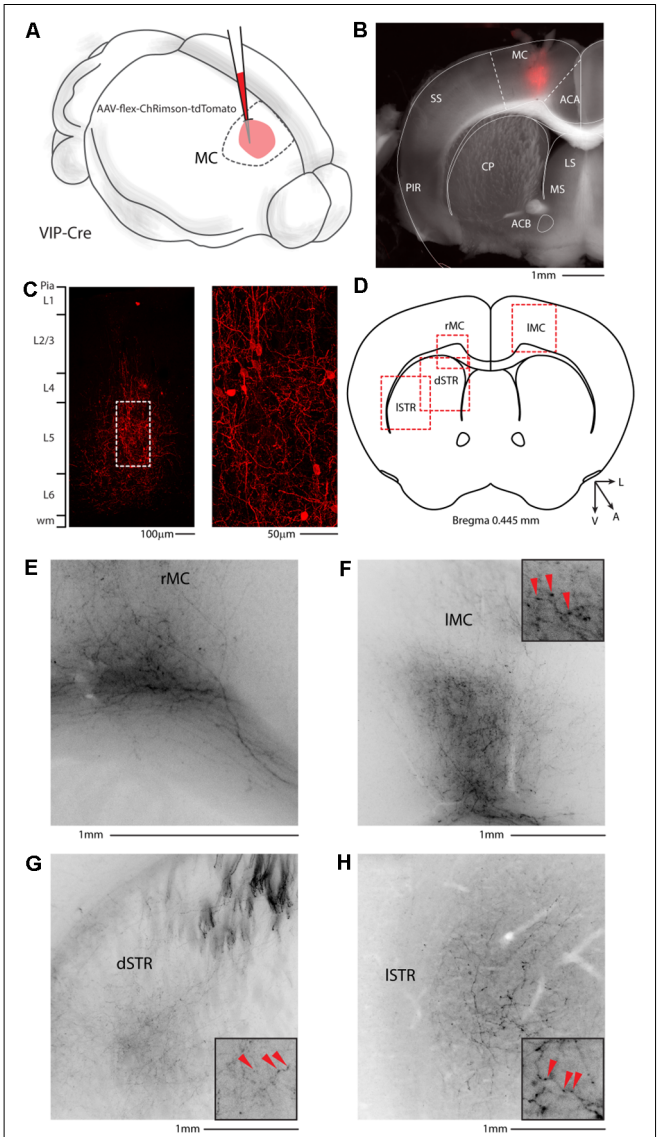

FIGURE 8 | Motor cortex injection of AAV-flex-ChRimson-tdTomato. **(A)** Schematic representation of right motor cortex viral injection. **(B)** Representative coronal section of an acute slice of the injection site (200 μm thick), with bright field (gray) and tdTomato expressing neurons (red). The Allen brain atlas coronal table superimposed for reference indicates the correct targeting of the motor cortex. Scale bar: 1 mm. The image of the injection site showing no evidence of ChRimson-tdTomato deposit or spillover in the striatum and/or other subcortical structures. **(C)** High magnification confocal image of the injection site showing tdTomato expressing neurons. Right panel: high magnification of dashed square in the left panel. Scale bars: 100 and 50 μm. **(D)** Allen Brain reference coronal section at +0.445 mm from Bregma. Red dashed squares indicate the regions imaged in the panels below. **(E)** Representative image of the contralateral motor cortex. **(F)** Representative image of white matter infiltrating axons in correspondence to the injection site. **(G)** Representative image of dorsal motor striatum with thick axons of passage in the upper striae and terminal field axonal arborization in the striatal parenchyma. **(H)** Representative image of lateral motor striatum VIP axons. Scale bars: 1 mm. Insets indicate axonal branches and the red arrowheads boutons. Inset size 190 μm. ACA, anterior cingulate cortex; MC, motor cortex; SS, somatosensory cortex; PIR, piriform cortex; STR, striatum; CP, caudoputamen; ACB, nucleus accumbens; LS, lateral septal nucleus; MS, medial septal nucleus; dSTR, dorsal striatum; lSTR, lateral striatum.

but also long-range GABAergic cortical neurons are carrying information to far stations (for review, see Isaacson and Scanziani, 2011; Caputi et al., 2013; Melzer and Monyer, 2020). Future experiments will provide insight into the complexity of the long-range VIP GABAergic projections' anatomical, electrophysiological, and molecular composition.

VIP neurons: A Disinhibitory Circuits Motif Involved in Synaptic Integration and Plasticity?

In a recent work, Lee et al. (2013) studied a long-range excitatory projection from the motor cortex to the whisker somatosensory cortex. By photo-activating channelrhodopsin-expressing axons originated in the motor cortex and targeting the somatosensory cortex, they found that VIP-expressing neurons received the strongest excitation, compared to Parvalbumin- and Somatostatin-expressing neurons, leading to action potentials

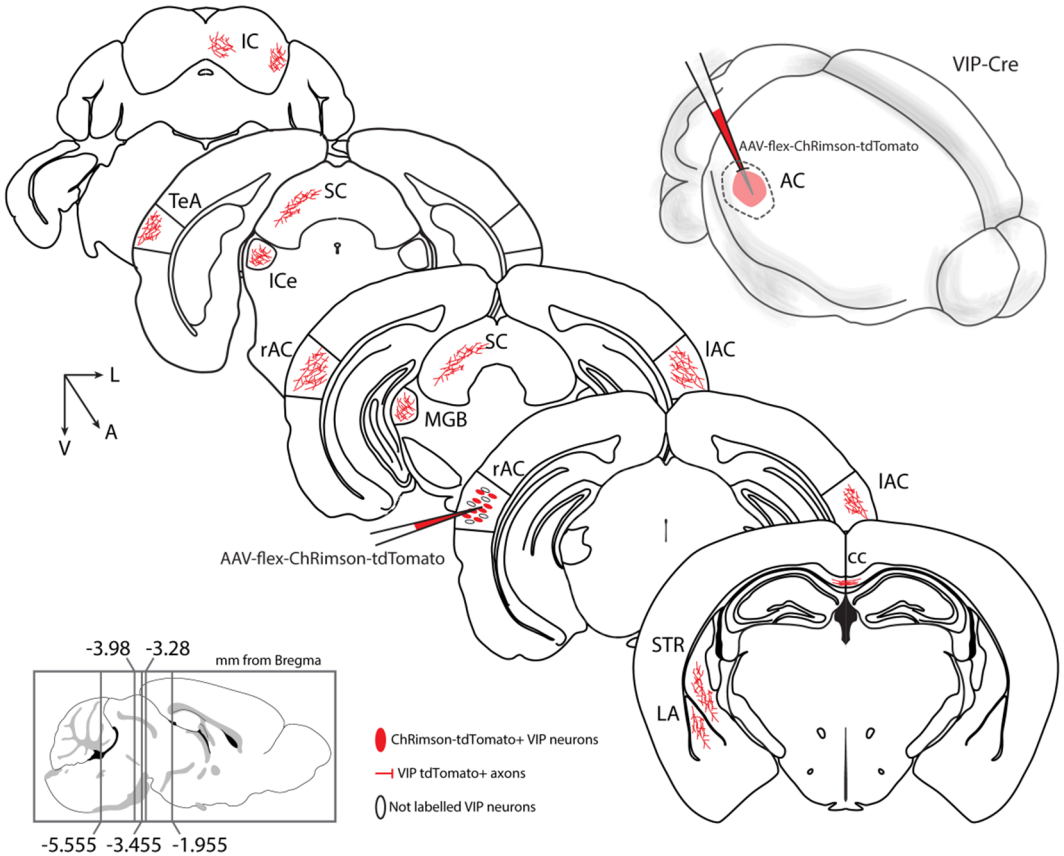

FIGURE 9 | Summary diagram: long-range VIP-expressing neuron projections. Top right: schematic representation of auditory cortex injection with AAV-flex-ChRimson-tdTomato. VIP long-range axons were found in several areas: AC, auditory cortex, right, and left; cc, corpus callosum; ipsilateral ICe, inferior colliculus, external; ipsilateral IC, inferior colliculus; ipsilateral LA, lateral amygdala; ipsilateral MGB, medial geniculate body, ipsilateral SC, superior colliculus; ipsilateral STR, striatum; ipsilateral TeA, temporal association cortex.

only in the VIP-neurons. One of the questions that now needs an answer is if the long-range GABAergic neurons can be recruited by activating long-range associated projection neurons.

Previous work (Dalezios et al., 2002; Pfeffer et al., 2013) has shown that VIP-expressing neurons preferentially inhibit Somatostatin-expressing inhibitory neurons. In line with these findings, recently, Keller et al. (2020) showed that VIP-expressing neurons preferentially inhibit Somatostatin-expressing neurons in the visual cortex, which leads to relief of excitatory neurons from suppression that contributes to contextual modulation in the primary visual cortex. The finding from is similar to what previously Lee et al. (2013) and Pi et al. (2013) observed in the somatosensory and auditory cortex, respectively. Although beyond the target of the present study, it is intriguing to speculate that long-range VIP-expressing neurons could play a role in interhemispheric communication through strong inhibition of Somatostatin-expressing neurons in the contralateral cortex, leading to relief of pyramidal neurons from suppression and eventually entrain the two cortical areas in specific brain oscillations.

In addition, Pi et al. (2013) measured neurons' activity in the auditory cortex while the mice performed an auditory discrimination behavioral task. In this task, the mice were trained to discriminate two different tones, in which one tone was associated with a water reward and the other with a punishment (Pi et al., 2013). Remarkably, VIP-expressing neurons were strongly activated by reward and punishment signals. However, the strong recruitment of the VIP-expressing neurons did not correlate with an increased spiking of other nearby neurons, as can be expected by the identified canonical cortical disinhibitory circuit motif (for review, see Pfeffer, 2014). One other important aspect of this disinhibitory circuit is that the VIP-expressing neurons, by strongly inhibiting the Somatostatin-expressing neurons, which in turn preferentially inhibit the pyramidal neurons' distal dendrites (Somogyi et al., 1998), can open a window to increase synaptic integration or plasticity along the distal dendrites of the pyramidal neurons. Are the long-range cortical VIP-expressing neurons part of a long-range disinhibitory circuit leading to integration and plasticity across cortical and subcortical areas? Future experiments will need to address these open questions on the role of the long-range VIP-expressing neurons that can dynamically affect the cortico-cortical processing. On the other hand, it is also intriguing to speculate about the role of long-range VIP-expressing

neurons in cortico-subcortical processing: are they establishing a disinhibitory local circuit in their subcortical target, mirroring their main organization in the cortex? For example, in the MGB, only a negligible fraction of the neuronal population express GABA (Lu et al., 2009; Jager et al., 2021) and inhibition has been described to come mainly from the thalamic reticular complex and the inferior colliculus (Rouiller et al., 1985; Winer et al., 1996): would this novel long-range VIP neuron population target the few local GABA-ergic neurons or perform direct inhibition of excitatory neurons in the MGB? A direct source of inhibition from high order auditory stations like the auditory cortex would add a further level of complexity in the modulation of auditory thalamus activity and plasticity not only during perception but also associative learning. Moreover, we showed long range VIP-expressing neurons reaching both the external cortex of the inferior colliculus and the multisensory deeper layers of the superior colliculus, two interconnected midbrain regions involved in orienting behavior (Masullo et al., 2019), suggesting a role for inhibitory long-range VIP-expressing neurons of the auditory cortex in movement selection.

Recent studies from Bigelow et al. (2019), and Yavorska and Wehr (2021) measured movement, and VIP-expressing neurons activation can differentially modulate auditory processing in the mouse auditory cortex. Nevertheless, it is not presently understood whether these differential changes in firing rate, resulting from movement and due to the activation of long-range-GABAergic VIP-expressing neurons, produce corresponding changes in information transfer to the targeted areas. Future studies will provide anatomical, electrophysiological, and molecular features of the long-range VIP-expressing neurons aimed to understand their circuit organization involved in reward-learning and action-selection behavior driven by auditory and motor stimuli.

DATA AVAILABILITY STATEMENT

The raw data supporting the conclusions of this article will be made available by the authors, without undue reservation.

ETHICS STATEMENT

The animal study was reviewed and approved by IACUC.

AUTHOR CONTRIBUTIONS

AjA designed research, performed experiments, analyzed data, and wrote the article. AB performed experiments, analyzed data, and wrote the article. CG performed experiments. All authors contributed to the article and approved the submitted version.

FUNDING

AjA was supported by two NIH grants: GM122645 and MH123260.

REFERENCES

Abbott, L. F., Bock, D. D., Callaway, E. M., Denk, W., Dulac, C., Fairhall, A. L., et al. (2020). The Mind of a Mouse. *Cell* 182, 1372–1376. doi: 10.1016/j.cell.2020.08.010

Apergis-Schoute, J., Pinto, A., and Pare, D. (2007). Muscarinic control of long-range gabaergic inhibition within the rhinal cortices. *J. Neurosci.* 27, 4061–4071. doi: 10.1523/JNEUROSCI.0068-07.2007

Ascoli, G. A., Alonso-Nanclares, L., Anderson, S. A., Barrionuevo, G., Benavides-Piccione, R., Burkhalter, A., et al. (2008). Petilla terminology: nomenclature of features of GABAergic interneurons of the cerebral cortex. *Nat. Rev. Neurosci.* 9, 557–568. doi: 10.1038/nrn2402

Basu, J., Zaremba, J. D., Cheung, S. K., Hitti, F. L., Zemelman, B. V., Losonczy, A., et al. (2016). Gating of hippocampal activity, plasticity and memory by entorhinal cortex long-range inhibition. *Science* 351:aaa5694. doi: 10.1126/science.aaa5694

Bertero, A., Feyen, P. L. C., Zurita, H., and Apicella, A. J. (2019). A non-canonical cortico-amygdala inhibitory loop. *J. Neurosci.* 39, 8424–8438. doi: 10.1523/JNEUROSCI.1515-19.2019

Bertero, A., Zurita, H., Normandin, M., and Apicella, A. J. (2020). Auditory long-range parvalbumin cortico-striatal neurons. *Front. Neural Circuits* 14:45.doi: 10.3389/fncir.2020.00045

Bigelow, J., Morrill, R. J., Dekloe, J., and Hasenstaub, A. R. (2019). Movement and VIP interneuron activation differentially modulate encoding in mouse auditory cortex. *eNeuro*6: ENEURO.0164-19.2019. doi: 10.1523/ENEURO.0164-19.2019

Buhl, E. H., and Singer, W. (1989). The callosal projection in cat visual cortex as revealed by a combination of retrograde tracing and intracellular injection. *Exp. Brain Res.* 75, 470–476. doi: 10.1007/BF00249898

Caputi, A., Melzer, S., Michael, M., and Monyer, H. (2013). The long and short of GABAergic neurons. *Curr. Opin. Neurobiol.* 23, 179–186. doi: 10.1016/j.conb.2013.01.021

Dalezios, Y., Lujan, R., Shigemoto, R., Somogyi, P., and Roberts, J. D. (2002). Enrichment of mGluR7a in the presynaptic active zones of GABAergic and non-GABAergic terminals on interneurons in the rat somatosensory cortex. *Cereb. Cortex.* 12, 961–974. doi: 10.1093/cercor/12.9.961

Higo, S., Akashi, K., Sakimura, K., and Tamamaki, N. (2009). Subtypes of GABAergic neurons project axons in the neocortex. *Front. Neuroanat.* 3:25. doi: 10.3389/neuro.05.025.2009

Higo, S., Udaka, N., and Tamamaki, N. (2007). Long-range GABAergic projection neurons in the cat neocortex. *J. Comp. Neurol.* 503, 421–431. doi: 10.1002/cne.21395

Isaacson, J. S., and Scanziani, M. (2011). How inhibition shapes cortical activity. *Neuron* 72, 231–243. doi: 10.1016/j.neuron.2011.09.027

Jager, P., Moore, G., Calpin, P., Durmishi, X., Salgarella, I., Menage, L., et al. (2021). Dual midbrain and forebrain origins of thalamic inhibitory interneurons. *eLife* 10:e59272. doi: 10.7554/eLife.59272

Keller, A. J., Dipoppa, M., Roth, M. M., Caudill, M. S., Ingrosso, A., Miller, K. D., et al. (2020). A disinhibitory circuit for contextual modulation in primary visual cortex. *Neuron.* 108, 1181.e8–1193.e8. doi: 10.1016/j.neuron.2020.11.013

Lee, S., Kruglikov, I., Huang, Z. J., Fishell, G., and Rudy, B. (2013). A disinhibitory circuit mediates motor integration in the somatosensory cortex. *Nat. Neurosci.* 16, 1662–1670. doi: 10.1038/nn.3544

Lee, A. T., Vogt, D., Rubenstein, J. L., and Sohal, V. S. (2014). A class of GABAergic neurons in the prefrontal cortex sends long-range projections to the nucleus accumbens and elicits acute avoidance behavior. *J. Neurosci.* 34, 11519–11525. doi: 10.1523/JNEUROSCI.1157-14.2014

Lu, E., Llano, D. A., and Sherman, S. M. (2009). Different distributions of calbindin and calretinin immunostaining across the medial and dorsal divisions of the mouse medial geniculate body. *Hear. Res.* 257, 16–23. doi: 10.1016/j.heares.2009.07.009

Masullo, L., Mariotti, L., Alexandre, N., Freire-Pritchett, P., Boulanger, J., and Tripodi, M. (2019). Genetically defined functional modules for spatial orienting

in the mouse superior colliculus. *Curr. Biol.* 29, 2892.e8–2904.e8. doi: 10.1016/j.cub.2019.07.083

McDonald, C. T., and Burkhalter, A. (1993). Organization of long-range inhibitory connections with rat visual cortex. *J. Neurosci.* 13, 768–781. doi: 10.1523/JNEUROSCI.13-02-00768.1993

Melzer, S., Gil, M., Koser, D. E., Michael, M., Huang, K. W., and Monyer, H. (2017). Distinct corticostriatal GABAergic neurons modulate striatal output neurons and motor activity. *Cell Rep.* 19, 1045–1055. doi: 10.1016/j.celrep.2017.04.024

Melzer, S., Michael, M., Caputi, A., Eliava, M., Fuchs, E. C., Whittington, M. A., et al. (2012). Long-range-projecting GABAergic neurons modulate inhibition in hippocampus and entorhinal cortex. *Science* 335, 1506–1510. doi: 10.1126/science.1217139

Melzer, S., and Monyer, H. (2020). Diversity and function of corticopetal and corticofugal GABAergic projection neurons. *Nat. Rev. Neurosci.* 21, 499–515. doi: 10.1038/s41583-020-0344-9

Mesik, L., Ma, W. P., Li, L. Y., Ibrahim, L. A., Huang, Z. J., Zhang, L. I., et al. (2015). Functional response properties of VIP-expressing inhibitory neurons in mouse visual and auditory cortex. *Front. Neural Circuits* 9:22. doi: 10.3389/fncir.2015.00022

Meyer, H. S., Schwarz, D., Wimmer, V. C., Schmitt, A. C., Kerr, J. N., Sakmann, B., et al. (2011). Inhibitory interneurons in a cortical column form hot zones of inhibition in layers 2 and 5A. *Proc. Natl. Acad. Sci. U S A* 108, 16807–16812. doi: 10.1073/pnas.1113648108

Pfeffer, C. K. (2014). Inhibitory neurons: vip cells hit the brake on inhibition. *Curr. Biol.* 24, R18–R20. doi: 10.1016/j.cub.2013.11.001

Pfeffer, C. K., Xue, M., He, M., Huang, Z. J., and Scanziani, M. (2013). Inhibition of inhibition in visual cortex: the logic of connections between molecularly distinct interneurons. *Nat. Neurosci.* 16, 1068–1076. doi: 10.1038/nn.3446

Pi, H. J., Hangya, B., Kvitsiani, D., Sanders, J. I., Huang, Z. J., and Kepecs, A. (2013). Cortical interneurons that specialize in disinhibitory control. *Nature* 503, 521–524. doi: 10.1038/nature12676

Pronneke, A., Scheuer, B., Wagener, R. J., Mock, M., Witte, M., and Staiger, J. F. (2015). Characterizing VIP neurons in the barrel cortex of vipcre/tdtomato mice reveals layer-specific differences. *Cereb. Cortex* 25, 4854–4868. doi: 10.1093/cercor/bhv202

Ribak, C. E., Seress, L., Peterson, G. M., Seroogy, K. B., Fallon, J. H., and Schmued, L. C. (1986). A GABAergic inhibitory component within the hippocampal commissural pathway. *J. Neurosci.* 6, 3492–3498. doi: 10.1523/JNEUROSCI.06-12-03492.1986

Rock, C., and Apicella, A. J. (2015). Callosal projections drive neuronal-specific responses in the mouse auditory cortex. *J. Neurosci.* 35, 6703–6713. doi: 10.1523/JNEUROSCI.5049-14.2015

Rock, C., Zurita, H., Lebby, S., Wilson, C. J., and Apicella, A. J. (2018). Cortical circuits of callosal gabaergic neurons. *Cereb. Cortex* 28,1154–1167. doi: 10.1093/cercor/bhx025

Rock, C., Zurita, H., Wilson, C., and Apicella, A. J. (2016). An inhibitory corticostriatal pathway. *eLife* 5:e15890. doi: 10.7554/eLife.15890

Rothermel, M., Brunert, D., Zabawa, C., Diaz-Quesada, M., and Wachowiak, M. (2013). Transgene expression in target-defined neuron populations mediated by retrograde infection with adeno-associated viral vectors. *J. Neurosci.* 33, 15195–15206. doi: 10.1523/JNEUROSCI.1618-13.2013

Rouiller, E. M., Colomb, E., Capt, M., and Ribaupierre, F. D. (1985). Projections of the reticular complex of the thalamus onto physiologically characterized regions of the medial geniculate body. *Neurosci. Lett.* 53, 227–232. doi: 10.1016/0304-3940(85)90190-9

Rudy, B., Fishell, G., Lee, S., and Hjerling-Leffler, J. (2011). Three groups of interneurons account for nearly 100% of neocortical GABAergic neurons. *Dev. Neurobiol.* 71, 45–61. doi: 10.1002/dneu.20853

Schindelin, J., Arganda-Carreras, I., Frise, E., Kaynig, V., Longair, M., Pietzsch, T., et al. (2012). Fiji: an open-source platform for biological-image analysis. *Nat. Methods.* 9, 676–682. doi: 10.1038/nmeth.2019

Seress, L., and Ribak, C. E. (1983). GABAergic cells in the dentate gyrus appear to be local circuit and projection neurons. *Exp. Brain Res.* 50, 173–182. doi: 10.1007/BF00239181

Somogyi, P., Tamás, G., Lujan, R., and Buhl, E. H. (1998). Salient features of synaptic organisation in the cerebral cortex. *Brain Res. Brain Res. Rev.* 26, 113–135. doi: 10.1016/s0165-0173(97)00061-1

Suter, B. A., O'Connor, T., Iyer, V., Petreanu, L. T., Hooks, B. M., Kiritani, T., et al. (2010). Ephus: multipurpose data acquisition software for neuroscience experiments. *Front. Neural Circuits* 4:100. doi: 10.3389/fncir.2010.00100

Tamamaki, N., and Tomioka, R. (2010). Long-range GABAergic connections distributed throughout the neocortex and their possible function. *Front. Neurosci.* 4:202. doi: 10.3389/fnins.2010.00202

Tomioka, R., Okamoto, K., Furuta, T., Fujiyama, F., Iwasato, T., Yanagawa, Y., et al. (2005). Demonstration of long-range GABAergic connections distributed throughout the mouse neocortex. *Eur. J. Neurosci.* 21, 1587–1600. doi: 10.1111/j.1460-9568.2005.03989.x

Tomioka, R., and Rockland, K. S. (2007). Long-distance corticocortical GABAergic neurons in the adult monkey white and gray matter. *J. Comp. Neurol.* 505, 526–538. doi: 10.1002/cne.21504

Tomioka, R., Sakimura, K., and Yanagawa, Y. (2015). Corticofugal GABAergic projection neurons in the mouse frontal cortex. *Front. Neuroanat.* 9:133.doi: 10.3389/fnana.2015.00133

Toth, K., Borhegyi, Z., and Freund, T. F. (1993). Postsynaptic targets of GABAergic hippocampal neurons in the medial septum-diagonal band of broca complex. *J. Neurosci.* 13, 3712–3724. doi: 10.1523/JNEUROSCI.13-09-03712.1993

Toth, K., and Freund, T. F. (1992). Calbindin D28k-containing nonpyramidal cells in the rat hippocampus: their immunoreactivity for GABA and projection to the medial septum. *Neurosci.* 49, 793–805. doi: 10.1016/0306-4522(92)90357-8

Yavorska, I., and Wehr, M. (2021). Effects of locomotion in auditory cortex are not mediated by the VIP network. *Front. Neural. Circuits* 15:618881. doi: 10.3389/fncir.2021.618881

Winer, J. A., Saint Marie, R. L., Larue, D. T., and Oliver, D. L. (1996). GABAergic feedforward projections from the inferior colliculus to the medial geniculate body. *Proc. Natl. Acad. Sci. U S A* 93, 8005–8010. doi: 10.1073/pnas.93.15.8005

Xu, X., Roby, K. D., and Callaway, E. M. (2010). Immunochemical characterization of inhibitory mouse cortical neurons: three chemically distinct classes of inhibitory cells. *J. Comp. Neurol.* 518, 389–404. doi: 10.1002/cne.22229

Zurita, H., Feyen, P. L. C., and Apicella, A. J. (2018a). Layer 5 callosal parvalbumin-expressing neurons: a distinct functional group of gabaergic neurons. *Front. Cell Neurosci.* 12:53. doi: 10.3389/fncel.2018.00053

Zurita, H., Rock, C., Perkins, J., and Apicella, A. J. (2018b). A layer-specific corticofugal input to the mouse superior colliculus. *Cereb. Cortex* 28, 2817–2833. doi: 10.1093/cercor/bhx161

Conflict of Interest: The authors declare that the research was conducted in the absence of any commercial or financial relationships that could be construed as a potential conflict of interest.

Publisher's Note: All claims expressed in this article are solely those of the authors and do not necessarily represent those of their affiliated organizations, or those of the publisher, the editors and the reviewers. Any product that may be evaluated in this article, or claim that may be made by its manufacturer, is not guaranteed or endorsed by the publisher.

frontiers in Neural Circuits

REVIEW
published: 24 September 2021
doi: 10.3389/fncir.2021.728832

Mechanisms Underlying Target Selectivity for Cell Types and Subcellular Domains in Developing Neocortical Circuits

Alan Y. Gutman-Wei[1] and Solange P. Brown[1,2]**

[1] Solomon H. Snyder Department of Neuroscience, Johns Hopkins University School of Medicine, Baltimore, MD, United States, [2] Kavli Neuroscience Discovery Institute, Johns Hopkins University School of Medicine, Baltimore, MD, United States

The cerebral cortex contains numerous neuronal cell types, distinguished by their molecular identity as well as their electrophysiological and morphological properties. Cortical function is reliant on stereotyped patterns of synaptic connectivity and synaptic function among these neuron types, but how these patterns are established during development remains poorly understood. Selective targeting not only of different cell types but also of distinct postsynaptic neuronal domains occurs in many brain circuits and is directed by multiple mechanisms. These mechanisms include the regulation of axonal and dendritic guidance and fine-scale morphogenesis of pre- and postsynaptic processes, lineage relationships, activity dependent mechanisms and intercellular molecular determinants such as transmembrane and secreted molecules, many of which have also been implicated in neurodevelopmental disorders. However, many studies of synaptic targeting have focused on circuits in which neuronal processes target different lamina, such that cell-type-biased connectivity may be confounded with mechanisms of laminar specificity. In the cerebral cortex, each cortical layer contains cell bodies and processes from intermingled neuronal cell types, an arrangement that presents a challenge for the development of target-selective synapse formation. Here, we address progress and future directions in the study of cell-type-biased synaptic targeting in the cerebral cortex. We highlight challenges to identifying developmental mechanisms generating stereotyped patterns of intracortical connectivity, recent developments in uncovering the determinants of synaptic target selection during cortical synapse formation, and current gaps in the understanding of cortical synapse specificity.

Keywords: neocortex, pyramidal cell, inhibitory interneuron, synapse formation, development, cell-type specificity, targeting

OPEN ACCESS

Edited by:
Yoshiyuki Kubota, National Institute for Physiological Sciences (NIPS), Japan

Reviewed by:
Dirk Feldmeyer, Julich-Forschungszentrum, Helmholtz-Verband Deutscher Forschungszentren (HZ), Germany
Naofumi Uesaka, The University of Tokyo, Japan

****Correspondence:***
Alan Y. Gutman-Wei
awei9@jhmi.edu
Solange P. Brown
spbrown@jhmi.edu

Received: *22 June 2021*
Accepted: *25 August 2021*
Published: *24 September 2021*

Citation:
Gutman-Wei AY and Brown SP (2021) Mechanisms Underlying Target Selectivity for Cell Types and Subcellular Domains in Developing Neocortical Circuits. Front. Neural Circuits 15:728832. doi: 10.3389/fncir.2021.728832

CELL-TYPE-BIASED CONNECTIVITY IN THE NEOCORTEX

The mammalian neocortex is an extensively interconnected network of neurons underlying a broad repertoire of behaviors including perception, decision-making, and voluntary action. Approximately 80–90% of cortical neurons are excitatory while the remaining are inhibitory, and both excitatory and inhibitory neurons are further subdivided into different cell types based on their molecular, morphological and functional characteristics (Kawaguchi and Kubota, 1997;

Markram et al., 2004, 2015; Lefort et al., 2009; Meyer et al., 2011; DeFelipe et al., 2013; Greig et al., 2013; Lodato and Arlotta, 2015; Kubota et al., 2016; Tremblay et al., 2016; Baker et al., 2018; Lim et al., 2018a; Tasic et al., 2018; Huang and Paul, 2019; Fishell and Kepecs, 2020; Gouwens et al., 2020; Yuste et al., 2020; Anastasiades and Carter, 2021). The neocortex is traditionally divided into six layers, and each cortical layer is composed of different sets of these neuronal cell types (Callaway, 1998; Thomson and Lamy, 2007; Feldmeyer, 2012; Harris and Mrsic-Flogel, 2013; Harris and Shepherd, 2015; Anastasiades and Carter, 2021; Staiger and Petersen, 2021), most of which also send dendrites and intracortical axons outside their home layer. The function of the mature neocortex relies on stereotyped patterns of intracortical connections among these neuronal cell types both within and across layers as well as predictable properties of their synaptic connections (Thomson and Lamy, 2007; Feldmeyer, 2012; Harris and Shepherd, 2015; Kubota et al., 2016; Tremblay et al., 2016; Adesnik and Naka, 2018; Anastasiades and Carter, 2021; Staiger and Petersen, 2021). Although much progress has been made in identifying mechanisms regulating cell-type-specific synapse formation in other brain areas and model organisms (Kolodkin and Tessier-Lavigne, 2011; Rawson et al., 2017; Favuzzi and Rico, 2018; Apostolo and De Wit, 2019; Kast and Levitt, 2019; Agi et al., 2020; Honig and Shapiro, 2020; Sanes and Zipursky, 2020), how the synaptic organization of intracortical connections arises during development to generate the circuits of the mature mammalian neocortex is only beginning to be understood.

During development, the intracortical axons and dendrites of cortical cell types reach their appropriate laminar destinations (Larsen and Callaway, 2006; Fame et al., 2011; Gibson and Ma, 2011; Kalil and Dent, 2014; Hand et al., 2015; Dorskind and Kolodkin, 2021), and there encounter multiple classes of synaptic targets. They must then select the correct cell types and postsynaptic domains within those cell types with which to form synaptic connections (Thomson and Lamy, 2007; Brown and Hestrin, 2009a; Krook-Magnuson et al., 2012; Harris and Shepherd, 2015; Kubota et al., 2016; Tremblay et al., 2016; Chevée and Brown, 2018; Kast and Levitt, 2019; Anastasiades and Carter, 2021). The appropriate synaptic machinery must also be recruited to the pre- and postsynaptic membranes to establish synaptic properties specific to each connection type (Larsen and Sjöström, 2015; Nusser, 2018; Südhof, 2018; Sanes and Zipursky, 2020). Here, we highlight some of the long-standing barriers to understanding these developmental processes in the neocortex, some mechanisms that have been recently implicated in the development of cell-type-biased intracortical connectivity, and remaining challenges to understanding the cell-type-dependent development of intracortical circuits.

PETERS' RULE: AXODENDRITIC OVERLAP CONSTRAINS THE DEVELOPMENT OF INTRACORTICAL CIRCUITS

A conceptual barrier to identifying mechanisms that contribute to the development of cell-type dependent synaptic organization in intracortical circuits has been the debate over whether the organization of cortical circuits is fully explained by the dendritic and axonal morphologies of different cell types, or whether additional mechanisms contribute to cell-type-biased connectivity. One hypothesis is that the synaptic connectivity between two cortical cell types reflects their average axodendritic overlap and thus depends only on the densities of the axonal processes of the presynaptic cell types and the dendritic processes of the postsynaptic cell types in the target region (**Figure 1A**). This concept, known as Peters' rule, was first posited when describing the connectivity between thalamocortical axons and the postsynaptic elements in layer 4 (L4) of the visual cortex (Peters and Feldman, 1976), and has been extensively applied to studies of cortical connectivity (Braitenberg and Schüz, 1998; Stepanyants and Chklovskii, 2005; Rees et al., 2017). Although Peters' rule has been extended to different spatial scales (Rees et al., 2017), Peters originally proposed that the synaptic connectivity between cell types reflects the average spatial overlap between the presynaptic axon of one cell type and the different postsynaptic targets in a volume of cortex. If Peters' rule explains the connectivity patterns of the neocortex, mechanisms governing the development of each cell type's characteristic axonal and dendritic morphologies, including their vertical and horizontal distribution and their density, would establish the predictable patterns of intracortical synaptic connectivity among cortical cell types by regulating the average axodendritic overlap for different cell-type combinations (Hill et al., 2012; Ramaswamy et al., 2012; Reimann et al., 2017). Additional developmental mechanisms for establishing biases in synaptic connections would not be required. Since synapse formation requires apposition between a presynaptic neuron's axon and a postsynaptic neuron's dendrite, by necessity, the synaptic connectivity among different neuron types is constrained by the morphological patterning of their axons and dendrites. However, studies comparing the rate of synaptic connectivity among different cortical cell types with their axodendritic overlap suggest that additional mechanisms must contribute to establishing intracortical circuits.

BEYOND PETERS' RULE: THE CHALLENGE OF IDENTIFYING ADDITIONAL CELL-TYPE-DEPENDENT DEVELOPMENTAL MECHANISMS

Directly testing whether Peters' rule fully explains stereotyped patterns of intracortical connectivity is technically challenging for several reasons. First, one must know the identity of the cell types in the cortex to compare the synaptic connectivity and morphological relationships for different combinations of cell types. However, despite much progress, a full catalog of the cell types in the neocortex remains out of reach. Indeed, what constitutes a cell type is still debated (Zeng and Sanes, 2017), and increasingly sophisticated methods for determining cell types in the cortex have revealed more and more complexity

(Zeisel et al., 2015; Tasic et al., 2016, 2018; Paul et al., 2017; Huang and Paul, 2019; Loo et al., 2019; Gouwens et al., 2020; Kim et al., 2020; Scala et al., 2020; Yao et al., 2020; Yuste et al., 2020). For example, parvalbumin-positive (PV) interneurons, one of the three major classes of cortical inhibitory neurons, have long been further subdivided into two morphological subclasses, basket cells and Chandelier cells (Kawaguchi and Kubota, 1997; Tremblay et al., 2016). However, prior studies using morphological, electrophysiological and molecular criteria as well as recent studies using single cell transcriptomics combined with other characteristics such as cellular morphology have identified multiple types of PV interneurons even within a single cortical layer (DeFelipe et al., 1989; Gupta et al., 2000; Wang et al., 2002; Blatow et al., 2003; Kumar and Ohana, 2008; Tan et al., 2008; Buchanan et al., 2012; Bortone et al., 2014; Jiang et al., 2015; Koelbl et al., 2015; Tasic et al., 2016, 2018; Frandolig et al., 2019; Gouwens et al., 2020; Scala et al., 2020; Yao et al., 2020). These differences have functional consequences. For example, the synapses of deep layer pyramidal neurons onto two types of PV interneurons, one with locally ramifying axons and one that sends axons toward more superficial layers, differ in whether or not they contain presynaptic NMDA receptors (Buchanan et al., 2012). To fully evaluate any selectivity in synaptic connectivity, these different cell types must be taken into account.

In addition to an evolving classification of cortical cell types, methods for comparing the patterns of functional synaptic connectivity with those predicted by neuronal morphology remain low-throughput and technically challenging. Three-dimensional volume electron microscopy reveals the physical connectivity among cells within volumes of cortex, but identifying different cell types within these blocks based on criteria such as long-range axonal targets or transcriptomic classes remains challenging, and the functional properties of the synapses cannot be fully ascertained (Briggman and Bock, 2012; Helmstaedter, 2013; Kubota et al., 2018). Performing paired whole-cell recordings of unitary synaptic connections followed by cell filling and morphological reconstruction is also laborious (Miles and Poncer, 1996; Thomson and Lamy, 2007; Qi et al., 2020). Importantly, these technical limitations have also hindered the ability to test for effects of perturbations of processes hypothesized to underlie the development of intracortical synaptic connections. Despite these obstacles, exceptions to Peters' rule have been identified, implying the existence of additional mechanisms that contribute to specifying intracortical circuits during development.

INTRACORTICAL CIRCUITS, SYNAPTIC TARGETING AND SYNAPTIC SPECIALIZATION

As experimentally measured synaptic connectivity and anatomically predicted connectivity patterns among different cortical cell types have been directly compared, more and more exceptions to connectivity rates based solely on average axodendritic overlap have been observed (Dantzker and Callaway, 2000; Shepherd et al., 2005; Brown and Hestrin, 2009b; Petreanu et al., 2009; Little and Carter, 2012; Kasthuri et al., 2015; Lee et al., 2016; Schmidt et al., 2017; Motta et al., 2019; Karimi et al., 2020). For example, layer 5 corticocortical neurons (L5 CCNs) synapse onto neighboring L5 corticotectal neurons (L5 CTectNs) at a higher rate than predicted from their axodendritic overlap (Brown and Hestrin, 2009b). This general preference for intratelencephalic pyramidal neurons (L5 IT neurons), of which L5 CCNs are a subtype, to synapse onto L5 pyramidal tract neurons (L5 PT neurons), of which L5 CTectNs are a subtype, but not the reverse, has been found across cortical areas (Morishima and Kawaguchi, 2006; Brown and Hestrin, 2009b; Kiritani et al., 2012; Harris and Shepherd, 2015). Similarly, a reconstruction of mouse visual cortex using electron microscopy showed that neurons with similar orientation tuning were preferentially connected even though the axons and dendrites of neurons of all orientation selectivities were intermingled (Lee et al., 2016). Although it remains possible that additional structural constraints contribute to predictable patterns of intracortical connectivity, such as the packing density of neuronal processes of different cortical cell types in sublamina within the cortex (Udvary et al., 2021), these results suggest that mechanisms beyond axodendritic overlap must contribute to preferential synapse formation among some cell types in the cortex.

Synaptic biases for particular neuronal domains have also been shown to be inconsistent with mechanisms for establishing synaptic connections based solely on average axodendritic overlap (Petreanu et al., 2009; Little and Carter, 2012; Reimann et al., 2015; Motta et al., 2019; Schneider-Mizell et al., 2020). For example, different classes of cortical inhibitory neurons target distinct regions of the dendritic and axonal arbors of pyramidal neurons (Jiang et al., 2013; Kubota et al., 2016; Paul et al., 2017), a feature that plays an important role in determining how these inputs are integrated by pyramidal neurons. Chandelier cells (ChCs) form specialized synaptic connections onto the axon initial segments (AISs) of pyramidal neurons (Somogyi, 1977; Fairen and Valverde, 1980; Somogyi et al., 1982; Gallo et al., 2020), in contrast to PV basket cells that preferentially target pyramidal cell somas and proximal dendritic shafts, and somatostatin-expressing (SST) Martinotti cells that synapse onto distal apical dendrites (Kubota, 2014; Kubota et al., 2016; Tremblay et al., 2016; Fishell and Kepecs, 2020). The subcellular preference of neither ChCs (Schneider-Mizell et al., 2020) nor SST Martinotti cells (Reimann et al., 2015) is fully predicted by axodendritic overlap. The developmental targeting of subcellular domains is likely not limited to inhibitory neuron types. For example, the distribution of excitatory and inhibitory synapses around the initial bifurcation of the apical dendritic tuft differs across different classes of pyramidal neurons (Karimi et al., 2020). Similarly, a recent ultrastructural reconstruction of layer 4 (L4) in mouse somatosensory cortex showed that a fraction of both excitatory and inhibitory axons preferentially innervated specific subcellular domains, inconsistent with a purely geometric mechanism (Motta et al., 2019).

Finally, the properties of synaptic connections formed during development can depend on the identity of the pre- or postsynaptic cell type. For example, single pyramidal neurons form both depressing synapses onto PV basket cells and facilitating synapses onto SST Martinotti cells (Reyes et al., 1998; Koester and Johnston, 2005). Similarly, the synapses of deep layer pyramidal neurons onto other pyramidal neurons, SST Martinotti cells and translaminar PV neurons contain presynaptic NMDA receptors while those onto PV basket cells do not (Buchanan et al., 2012). These studies indicate that synaptic machinery must be selectively recruited to particular synapse types to determine connection-type-biased synaptic properties (Nusser, 2018; Südhof, 2018; Sanes and Zipursky, 2020). Together, these results suggest that, although Peters' rule sets a minimum necessary constraint on synapse formation, additional mechanisms contribute to the predictable synaptic target choices and the development of synaptic properties formed by some cortical cell types during development.

CELL-TYPE-SPECIFIC NEURITE MORPHOLOGIES CONSTRAIN POSSIBLE SYNAPTIC PARTNERS

The development of the distinctive intracortical axonal and dendritic morphologies of different cortical cell types, as well as their cell number and position within the cortex, set baseline constraints on the synaptic connectivity between cell types (**Figure 1A**; Hill et al., 2012; Reimann et al., 2017;

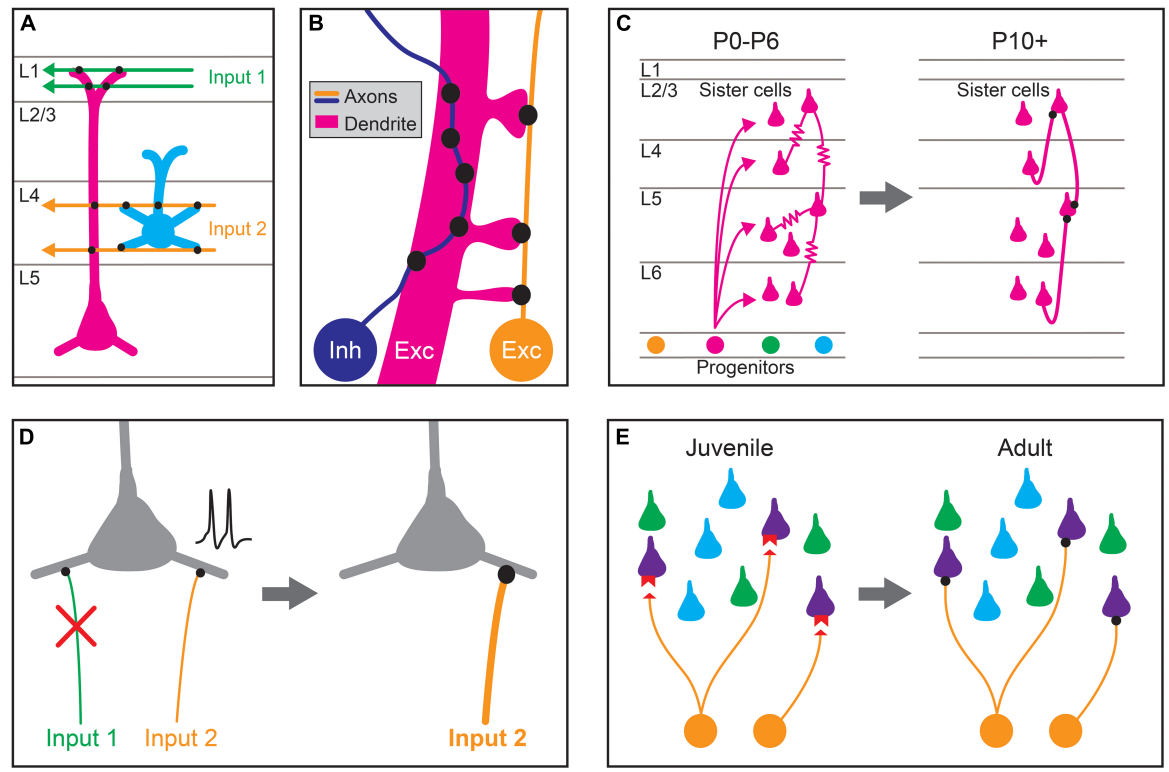

FIGURE 1 | Proposed mechanisms for establishing stereotyped patterns of synaptic connectivity in the neocortex. **(A)** Predictable patterns of synaptic connectivity may be defined by anatomical relationships between presynaptic axons and postsynaptic dendrites. For example, the axodendritic overlap between Input 1 (green) and the two pyramidal cell types (magenta, blue) precludes synapse formation with the blue cell type. The axodendritic overlap of Input 2 (orange) and the two pyramidal cell types predicts a higher probability of connection with the blue type than the magenta type. **(B)** Fine-scale neurite geometry such as axon tortuosity and dendritic spine outgrowth may contribute to synaptic partner selection. Growth patterns of axons and dendrites at small scales alter the amount of apposed membrane between cells, and thus the number of potential synaptic sites. Inhibitory interneuron axons (Inh, blue) in the cortex are highly tortuous, which can increase potential sites of contact with the dendrites of preferred synaptic partners, allowing the formation of more synapses between them. The axons of excitatory pyramidal neurons (Exc, orange) are more linear but directed dendritic spine growth in postsynaptic neurons (Exc, magenta) could also allow for the preferential formation of synaptic sites. **(C)** Lineage relationships affect synaptic connectivity. Clonally related pyramidal cells (sister cells) arising from the same neural progenitor lineage are preferentially interconnected by gap junctions (⊸⊷⊸) during the first postnatal week (postnatal day 0–6; P0–P6). These gap junctions disappear during the second postnatal week (~P10+), and chemical synapses are preferentially formed between clonally related pyramidal cells. **(D)** Activity-dependent plasticity may guide cell-type biased synaptic targeting. Different axonal inputs to a cortical cell type may have distinct neural activity patterns, and synapses between specific cell-type combinations may be selectively strengthened (orange input) or weakened (green input) through activity-dependent mechanisms, leading to preferential connectivity between cortical cell types. **(E)** Specific expression of recognition molecules may mediate cell-type or domain-specific synaptic targeting and synapse-type-specific functional properties. During development, preferred synaptic partner cell types may express cognate receptors and ligands (red) on the pre- (orange) and postsynaptic processes (purple). These molecular signals guide growth and synaptogenesis, leading to cell-type-biased connectivity and function in adulthood.

Udvary et al., 2021). Mechanisms establishing the characteristic intracortical axonal guidance and branching of different cell types remain incompletely understood but likely include extrinsic molecular cues such as semaphorin, Wnt, netrin, and ephrin family members, interactions with radial glia, selective stabilization of axon collaterals and the cellular migration patterns of inhibitory neurons (Fame et al., 2011; Leyva-Diaz and Lopez-Bendito, 2013; Hand et al., 2015; Dorskind and Kolodkin, 2021). For example, both SST Martinotti cells and translaminar PV interneurons migrate through the marginal zone before arriving into position in the cortex, and preventing this migration impairs the growth of their axonal arbors into the appropriate target layers (Lim et al., 2018b). The size and shape of the dendritic arbors of different classes of cortical neurons are also regulated by multiple mechanisms including extrinsic secreted cues that orient the apical dendrites of pyramidal neurons toward the pial surface (Polleux et al., 2000) as well as intrinsic expression of transcription factors that regulate dendritic arbor complexity and lamination (Chen et al., 2005; Tran et al., 2009; Cubelos et al., 2010, 2015; Lefebvre et al., 2015; Fazel Darbandi et al., 2018). Because the mechanisms regulating axonal and dendritic morphogenesis, together with neuronal positioning and cell number, limit the possible connectivity between cortical cell types during development, they may lead to some predictable patterns of connectivity.

Directed axon growth at finer spatial scales during development (**Figure 1B**), guided by short-range secreted or contact based cues, may increase the amount of membrane surface apposed to preferred postsynaptic targets, and thus the number of potential synapse sites. The local axonal structure of cortical inhibitory neurons is highly correlated with the dendritic structure of their synaptic target cells, and their axons exhibit high tortuosity (Stepanyants et al., 2004; Portera-Cailliau et al., 2005). This tortuosity suggests that short-range interactions affecting axon outgrowth may generate inhibitory synapse selectivity through increasing membrane contact with target cell types or specific postsynaptic domains, but this hypothesis has not been directly tested. Axon tortuosity may also affect the angular alignment between axons and different dendritic segments, which has been shown to influence the number of synapses formed between axons and target dendrites in the spinal cord (Balaskas et al., 2019). In contrast, the axons of pyramidal neurons are less tortuous and exhibit little spatial correlation with connected neurons (Stepanyants et al., 2004; Kalisman et al., 2005).

The fine-scale structure of dendritic branches and spines may also influence synaptic connectivity with preferred partners (**Figure 1B**). Not only do the dendritic arbors of cortical pyramidal neurons exceed the theoretical density required for sampling all potential synaptic partners in their dendritic field, they are also studded with dendritic spines that further increase the number of potential sites for synapse formation (Stepanyants et al., 2008; Wen et al., 2009; Bird et al., 2021). Yet pyramids form synapses with only a small subset of available synaptic partners (Song et al., 2005; Stepanyants and Chklovskii, 2005; Kasthuri et al., 2015). Types of nominally aspiny inhibitory interneurons also exhibit spines, albeit at very low densities (Kawaguchi et al., 2006). Spine density and distribution, which varies across cell types and cellular domains, is controlled by a large number of cell-intrinsic and extrinsic factors, including competition between different spine types (Koleske, 2013; Bian et al., 2015; Moyer and Zuo, 2018; Henderson et al., 2019). Directed growth and stabilization of dendritic filopodia has been proposed as a potential strategy for increasing the probability of connection between preferred synaptic partners in the cortex, although direct evidence for such mechanisms has not yet been reported (Dailey and Smith, 1996; Ziv and Smith, 1996; Jontes and Smith, 2000; Bonhoeffer and Yuste, 2002; Konur and Yuste, 2004; Stepanyants et al., 2004; Yuste, 2011).

NEURONAL LINEAGE INFLUENCES SYNAPSE FORMATION OF CLONALLY RELATED NEURONS

Developmental mechanisms contributing to the pattern of intracortical circuits also reflect the lineage relationships of neurons (**Figure 1C**). Clonally related excitatory neurons are more likely to be synaptically connected than expected based on their cell types (Yu et al., 2009, 2012; Cadwell et al., 2020), first through the preferential formation of gap junctions among clonally related neurons followed by a transition to chemical synapses (Yu et al., 2009, 2012). Rather than exhibiting increased connectivity within a cell type or cortical layer, these interconnected, clonally related excitatory neurons span multiple cell types and show increased interlaminar connectivity (Cadwell et al., 2020). Formation of these synaptically connected clusters requires normal processes of radial migration and is disrupted by the depletion of DNA-methyltransferase 3 or clustered protocadherins (Tarusawa et al., 2016). Interestingly, clonally related excitatory neurons have similar selectivity for visual stimuli (Li et al., 2012; Ohtsuki et al., 2012). Clonally related inhibitory neurons also preferentially form electrical synapses during development, but do not go on to form preferential chemical synapses (Zhang et al., 2017). Instead, these electrically coupled, clonally related inhibitory neurons tend to target the same set of excitatory neurons (Zhang et al., 2017), but how these synaptic relationships are established is not yet known.

ACTIVITY-DEPENDENT MECHANISMS SCULPT CELL-TYPE-BIASED CONNECTIVITY

Both spontaneous and evoked neuronal activity play central roles in the development of the neocortex, affecting the number of cells, their position, their intracortical axonal and dendritic morphology and their synaptic connectivity (Katz and Shatz, 1996; Kirischuk et al., 2017; Lim et al., 2018a; Simi and Studer, 2018; Bragg-Gonzalo et al., 2021; Hanganu-Opatz et al., 2021). Activity-dependent strengthening or elimination of specific types of intracortical connections may work in concert with cell-type-specific molecular mechanisms to establish stereotyped patterns of connectivity in cortical circuits (**Figure 1D**). For

example, the preferential connectivity between neurons with similar receptive field properties or activity state suggests that cell-type-biased connectivity is influenced by neuronal activity patterns (Yassin et al., 2010; Ko et al., 2011, 2014; Cossell et al., 2015; Lee et al., 2016). Similarly, while the initial subcellular domain-specific targeting of AISs by ChCs is regulated through molecular mechanisms (Favuzzi et al., 2019; Tai et al., 2019), subsequent changes in neuronal activity modify the location of the AIS and the density of ChC synapses onto AISs (Grubb and Burrone, 2010; Wefelmeyer et al., 2015; Pan-Vazquez et al., 2020). Nonetheless, some stereotyped targeting is maintained despite abnormal cortical activity patterns. For example, the preferential innervation of different subcellular domains by inhibitory neuron subclasses is preserved in organotypic slices (Di Cristo et al., 2004), even though neuronal activity patterns are drastically altered in culture. Although activity-dependent mechanisms likely shape cell-type and domain selectivity of intracortical synaptic connections, the molecular cascades evoked by neuronal activity to affect these processes are still not clear.

MOLECULAR MECHANISMS FOR BIASING CELL-TYPE AND DOMAIN-SELECTIVE TARGETING IN THE NEOCORTEX DURING DEVELOPMENT

In addition to processes regulating axodendritic overlap and directed neurite outgrowth, neural activity, and cell lineage relationships, molecular recognition mechanisms contribute to the stereotyped patterns of connectivity among cortical cell types (**Figure 1E**). Molecular pathways for establishing cell-type and domain-selective neuronal connections have been well characterized in other model systems and brain areas, including the retina, olfactory bulb, cerebellum, and spinal cord (Sanes and Yamagata, 2009; Shen and Scheiffele, 2010; De Wit and Ghosh, 2016; Rawson et al., 2017; Apostolo and De Wit, 2019; Honig and Shapiro, 2020; Sanes and Zipursky, 2020). Most of these molecules belong to a few families of cell-surface and secreted proteins capable of trans-cellular interactions (Apostolo and De Wit, 2019; Sanes and Zipursky, 2020). The identification of cell-type-biased connectivity in the neocortex suggests that similar mechanisms contribute to cortical development, and recent studies have identified molecular recognition processes that play a role in neocortical synaptic targeting. In the following sections, we first focus on the contributions of molecular mechanisms to domain-specific and cell-type specific synapse formation of inhibitory synapses, including examples where such mechanisms are hypothesized but not yet known (see the sections "Chandelier Cells and Synaptic Targeting at the Axon Initial Segment," "Somatostatin and Parvalbumin-Expressing Interneurons and Subcellular Targeting," "Cell-Type-Biased Connections From Inhibitory Interneurons to Pyramidal Neurons," and "Cell-Type-Specific Inhibitory Networks"). In the subsequent sections (see the sections "Mechanisms Shaping the Synaptic Connectivity of Pyramidal Neurons," "Mechanisms for Targeting Excitatory Input to Subcellular Domains of Pyramidal Neurons," and "Cell-Type-Biased Connections From Pyramidal Neuron to Inhibitory Neuron Types"), we describe molecular mechanisms involved in the cell-type and domain-selective targeting of excitatory synapses. Finally, in Section "The Development of Synapse-Type-Specific Functional Properties," we describe molecular mechanisms implicated in establishing synapse-type-specific functional properties.

Chandelier Cells and Synaptic Targeting at the Axon Initial Segment

A notable example of subcellular domain targeting by a cortical inhibitory neuron is the ChC, an inhibitory interneuron type that preferentially synapses on the AISs of pyramidal neurons while avoiding somatic and dendritic domains (Somogyi, 1977; Fairen and Valverde, 1980; Somogyi et al., 1982; Gallo et al., 2020). This level of specificity requires additional mechanisms beyond axodendritic overlap (Schneider-Mizell et al., 2020). The preference of ChCs for AISs appears before their specialized axonal cartridges are formed (Gour et al., 2021). Although immature ChCs initially generate some axonal varicosities not associated with AISs, these are subsequently pruned during postnatal development so that by postnatal day 28 (P28) in the mouse, the cells exhibit adult selectivity with the majority of their synapses formed onto AISs (Steinecke et al., 2017; Gour et al., 2021).

Recent work has uncovered a number of molecular pathways that underlie ChC synaptic targeting (**Figure 2**; Contreras et al., 2019; Gallo et al., 2020). One recent study compared results from

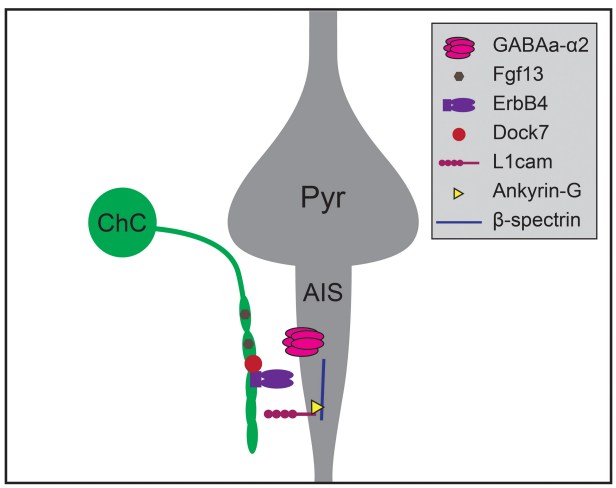

FIGURE 2 | Molecular mechanisms regulating chandelier cell (ChC) targeting of the axon initial segment of pyramidal neurons. Chandelier cells form synapses preferentially on the axon initial segment (AIS) of pyramidal neurons (Pyr), generating specialized axonal structures called cartridges (green). Chandelier cell-AIS targeting requires the expression of Fgf13 and ErbB4 in chandelier cells, and the expression of L1cam and α2 subunit-containing $GABA_A$ receptors in the AIS. ErbB4 is further regulated by the expression of intracellular Dock7 in chandelier cells, while L1cam interacts with Ankyrin-G and β-spectrin within the AIS to mediate axo-axonic synaptogenesis.

cell-type-specific RNA sequencing of three classes of developing interneurons – ChC, PV, and SST interneurons – and identified Fgf13, a fibroblast growth factor family member, as required for ChCs to correctly target AISs (Favuzzi et al., 2019). Another recent study found that the interaction of L1cam, a member of the immunoglobulin cell adhesion molecule superfamily, with ankyrin-G at the AIS, is also required to target ChC synapses to AISs (Tai et al., 2019). This mechanism is similar to the process for GABAergic innervation of Purkinje cell AISs directed by the L1cam family member, neurofascin (Ango et al., 2004; Kriebel et al., 2011). Expression of ErbB4, a receptor tyrosine kinase, in ChCs also promotes the formation of axoaxonic synapses, likely through the ErbB4 receptor Neuregulin 1 which is expressed in pyramidal neurons (Fazzari et al., 2010; Del Pino et al., 2013, but see Neddens et al., 2011). ErbB4 is further regulated by the protein Dock7, a member of the DOCK180 family of atypical Rac or Cdc42 GTPase guanine nucleotide exchange factors. Dock7 is required to activate ErbB4 autophosphorylation and promote ChC synaptogenesis (Tai et al., 2014), and may also interact with the α2 subunit of the $GABA_A$ receptor which is itself required for synaptogenesis at AISs in the hippocampus (Hines et al., 2018; Yang et al., 2019). Notably, perturbations of most of these mechanisms do not result in complete absence of ChC-AIS targeting, suggesting that multiple molecular mechanisms act together to mediate synaptic specificity.

Somatostatin and Parvalbumin-Expressing Interneurons and Subcellular Targeting

Another example of target selectivity of inhibitory synapses in the neocortex is the biased innervation of different dendritic regions of pyramidal neurons by PV and SST interneurons (**Figure 3**). Cortical pyramidal neurons are distinguished by their apical dendrite ending in an apical tuft near the pial surface and a domain of basal dendrites surrounding the cell soma. These dendritic domains differ in their integration properties and influence on pyramidal neuron computations (Spruston, 2008; Stuart and Spruston, 2015). SST Martinotti cells and PV interneurons exhibit different preferences for these two dendritic regions: SST Martinotti cells synapse onto the distal apical dendrites of pyramidal neurons while PV interneurons preferentially synapse onto the perisomatic region (Kubota, 2014; Kubota et al., 2016; Tremblay et al., 2016). Comparisons of the transcriptional profiles of developing ChCs, SST and PV interneurons not only identified a role for Fgf13 in directing ChC synapses to the AIS, but also identified molecules contributing to SST and PV targeting of dendritic domains (Favuzzi et al., 2019). Cbln4, a member of the C1q family, is necessary for specifying distal dendrite targeting of SST Martinotti cells and Lgi2, a leucine-rich glioma inactivated family member, for perisomatic targeting of PV basket cells (**Figure 3**). Furthermore, Cbln4 is sufficient to direct non-SST interneurons to form synapses onto distal dendrites, while not affecting normal targeting of somatic and proximal regions. However, these molecular mechanisms work in concert with additional developmental mechanisms to generate the synaptic patterns seen in the mature cortex: while

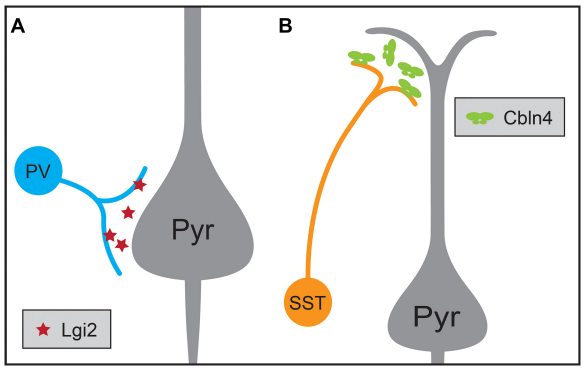

FIGURE 3 | Molecular mechanisms regulating the synaptic targeting of two inhibitory interneuron types to the perisomatic and distal dendritic regions of pyramidal neurons (Pyr), respectively. **(A)** Parvalbumin-positive (PV) interneurons preferentially form synapses onto the perisomatic region of pyramidal neurons, a process that requires the expression of the secreted protein Lgi2 in PV neurons. **(B)** Somatostatin-positive (SST) interneurons preferentially form synapses on the distal dendrites of pyramidal neurons, a process that requires the expression of secreted Cbln4 in SST neurons.

the synapses of SST interneurons are biased for apical dendrites at the earliest time points tested, those of soma-targeting basket cells also rely on pruning of inappropriate synapses during development (Gour et al., 2021). Similarly, the development of basket cell synapses from cholecystokinin-expressing (CCK) basket cells but not PV interneurons onto pyramidal neurons is regulated by dystroglycan (Fruh et al., 2016; Contreras et al., 2019). These experiments show that interneuron targeting of subcellular domains during development relies on distinct cell-type-specific mechanisms.

Cell-Type-Biased Connections From Inhibitory Interneurons to Pyramidal Neurons

Cortical inhibitory interneuron types not only exhibit specificity for a particular cellular region when forming synaptic connections during development but also exhibit cell-type-biased synaptic targeting. As cell types among cortical pyramidal neurons have become better defined, instances of striking specificity in inhibitory targeting of pyramidal neuron subtypes have been identified (Krook-Magnuson et al., 2012; Anastasiades and Carter, 2021). For example, although some studies showed that innervation of pyramidal neurons by PV basket cells and SST Martinotti cells is consistent with Peters' Rule (Fino and Yuste, 2011; Packer and Yuste, 2011), PV neurons in the mouse medial prefrontal cortex (mPFC) have a higher connection probability with L5 PT cells than IT pyramids (Lee et al., 2014; Anastasiades et al., 2018). Recent work has shown that transsynaptic signaling through chemokine C-X-C motif proteins may play a role in this targeting. In L5 pyramidal neurons, the ligand Cxcl12 is secreted from PT pyramids and helps direct PV neuron axon terminals, which express its receptors Cxcr4 and Cxcr7, to synapse onto perisomatic regions of PT neurons (**Figure 4**; Wu et al., 2017). Conditional knockout of *Cxcl12* in a subset of

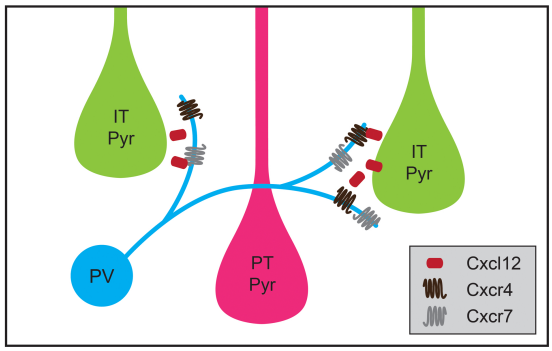

FIGURE 4 | Chemokine signaling regulates cell-type-specific parvalbumin-positive (PV) interneuron targeting in medial prefrontal cortex (mPFC). PV interneurons in mPFC preferentially innervate intratelencephalic pyramidal (IT Pyr) neurons over neighboring pyramidal tract (PT Pyr) neurons. This process is mediated by the selective expression of the secreted protein Cxcl12 at higher levels in IT pyramidal neurons compared to PT pyramidal neurons. Cxcl12 likely acts through its receptors Cxcr4 and Cxcr7, which are expressed in PV interneurons.

L5 pyramidal neurons using the Rbp4-Cre mouse line resulted in a ∼30% decrease in perisomatic inhibitory synapses on L5 pyramidal neurons in mPFC and decreased inhibitory input onto L5 PT but not IT pyramids (Wu et al., 2017). Additional examples of inhibitory neuron types biasing their synaptic output to particular classes of pyramidal neurons have been identified, but the developmental mechanisms establishing these patterns are not yet understood. For example, in layer 2 (L2) of the medial entorhinal cortex, CCK basket cells preferentially innervate one subtype of pyramidal neuron that projects to contralateral entorhinal cortex while avoiding a pyramidal cell subtype that projects to the ipsilateral dentate gyrus (Varga et al., 2010). Similarly, a study using electron microscopy showed that inhibitory axons targeted L1 apical tufts from superficial or deep layer neurons, but not both (Karimi et al., 2020).

Chandelier cells also exhibit cell-type-biased synaptic targeting in addition to selective targeting of AISs. ChCs form axoaxonic synapses onto pyramidal neurons and other ChCs but not onto other interneuron types (Somogyi, 1977; Jiang et al., 2015; Shapson-Coe et al., 2021). Furthermore, ChCs do not synapse onto all the neurons within range of their axonal arbor, and pyramidal cell types receive different numbers of ChC synapses (Somogyi, 1979; Fairen and Valverde, 1980; De Carlos et al., 1985; DeFelipe et al., 1985; Farinas and DeFelipe, 1991; Wang and Sun, 2012; Inan et al., 2013; Lu et al., 2017; Schneider-Mizell et al., 2020). For example, in cat visual cortex, ChCs form more synaptic inputs onto corticocortical neurons whereas corticothalamic neurons receive relatively fewer ChC synapses (Farinas and DeFelipe, 1991). Furthermore, a recent electrophysiological study of connectivity between ChCs and identified pyramidal cell types in prelimbic cortex of mice indicated that L2 ChCs preferentially synapsed onto pyramidal neurons projecting to the basolateral amygdala as compared to those projecting to the contralateral cortex (Lu et al., 2017). Whether differential laminar positioning of pyramidal neurons (Lu et al., 2017; Schneider-Mizell et al., 2020) combined with the distinct morphologies of different types of ChCs (Wang et al., 2019) explains cell-type-specific biases in connectivity must be assessed in concert with testing for molecular mechanisms that may contribute to the formation of these additional levels of selectivity. Nonetheless, these examples suggest that currently unidentified developmental mechanisms sculpt the intracortical connections from inhibitory neurons onto different excitatory cell types.

Cell-Type-Specific Inhibitory Networks

In addition to forming synapses onto specific neuronal domains and types of cortical excitatory neurons, inhibitory interneurons form cell-type-specific inhibitory networks within the neocortex (Hestrin and Galarreta, 2005; Tremblay et al., 2016; Fishell and Kepecs, 2020; Anastasiades and Carter, 2021). Although the molecular mechanisms underlying the development of these stereotyped patterns of connectivity remain unclear, the increasing availability of genetic tools for identifying and manipulating interneuron subtypes make them potentially tractable systems for investigating molecular recognition mechanisms in neocortical development. For example, PV, SST, and layer 1 (L1) neurogliaform neuron types are each strongly interconnected via electrical synapses (Galarreta and Hestrin, 1999; Gibson et al., 1999; Beierlein et al., 2000; Amitai et al., 2002; Simon et al., 2005). PV interneurons are also interconnected through GABAergic synapses, while rarely innervating other inhibitory neuron subtypes (Galarreta and Hestrin, 1999; Gibson et al., 1999; Pfeffer et al., 2013; Jiang et al., 2015). Studies of inhibitory neuron types have also identified cell-type-biased patterns of connectivity between different inhibitory subtypes (Hestrin and Galarreta, 2005; Tremblay et al., 2016; Fishell and Kepecs, 2020). For example, SST cells are thought to avoid forming chemical synapses onto other SST interneurons while forming GABAergic synapses onto PV interneurons (Gibson et al., 1999; Pfeffer et al., 2013; Xu et al., 2013 but see Jiang et al., 2015), and vasoactive intestinal polypeptide-expressing (VIP) interneurons synapse onto SST Martinotti cells and PV neurons but not onto more numerous neighboring pyramidal neurons (Lee et al., 2013; Pfeffer et al., 2013; Pi et al., 2013). Many additional examples of preferences in synaptic connectivity among inhibitory neuron types indicate that such biases are common in neocortical circuits (Chittajallu et al., 2013; Jiang et al., 2013; Lee et al., 2013, 2015; Pfeffer et al., 2013; Pi et al., 2013; Xu et al., 2013; Kubota et al., 2016; Feldmeyer et al., 2018). As inhibitory neuron types represent only 10–20% of the neurons in the neocortex, these networks represent remarkable stereotyped biases in synaptic targeting. In contrast to interneuron targeting of excitatory cells, molecular mechanisms contributing to the cell-type-specific patterns of electrical and chemical synapses among inhibitory cell types are still unclear.

Mechanisms Shaping the Synaptic Connectivity of Pyramidal Neurons

The diversity of excitatory cell types in L5 has served as a model for understanding synapse specificity among cortical excitatory

neurons. L5 contains two main classes of pyramidal neurons: PT neurons, which project to subcortical brain regions including the spinal cord, brainstem and thalamus, and IT neurons, which confine their axons within the telencephalon, and each may be further subdivided into subtypes (Harris and Shepherd, 2015; Yuste et al., 2020; Anastasiades and Carter, 2021). Studies of mouse sensory cortex showed that the probability of synaptic connectivity reflects the pre- and postsynaptic identity of L5 pyramids and not solely their axodendritic overlap (Brown and Hestrin, 2009b). For example, CCNs, an IT cell class, form more frequent synaptic connections onto CTectNs, a PT cell class, as compared to neighboring CCNs than predicted by their axodendritic overlap (Brown and Hestrin, 2009b). A similar dependence of synaptic connectivity and functional properties on cell type was identified for L5 pyramidal cell types in other cortical areas including motor and frontal cortex (Morishima and Kawaguchi, 2006; Anderson et al., 2010; Morishima et al., 2011; Kiritani et al., 2012). The intracortical connections of L5 neurons thus provide an example of cell-type-biased synaptic targeting among cortical excitatory neurons.

Recent work has uncovered potential mechanisms for the development of L5 pyramidal neuron connectivity. The formation of the layer 2/3 (2/3) pyramidal projection onto L5 pyramids requires expression of Sonic Hedgehog (*Shh*) by L5 PT neurons and of its receptor, Brother of CDO (*BoC*), in L2/3 axons (**Figure 5**; Harwell et al., 2012). Perturbing expression of either the receptor or ligand results in decreased L2/3-to-L5 connectivity without affecting connectivity within L2/3 (Harwell et al., 2012). However, whether Shh-Boc signaling alone is sufficient to specify this targeting remains unknown. Furthermore, whether this signaling pathway affects differential innervation of L5 cell types by L2/3 pyramids is also not clear (Otsuka and Kawaguchi, 2008, 2011; Anderson et al., 2010; Collins et al., 2018). Shh may instead establish laminar identity, as suggested by recent work implicating Shh in establishing L5 astrocytic identity (Xie et al., 2020). Competitive signaling between dendritic spines and potential presynaptic partner axons may also play a role in determining cell-type-biased connectivity between L5 pyramidal neurons. Henderson et al. (2019) showed that levels of ephrin B3, a ligand for the Eph family of receptor tyrosine kinases, in postsynaptic spines determine synaptogenesis rates via competitive signaling through EphB2 receptors. Ephrin B3 is significantly enriched in Ctip2+ L5 PT neurons as compared to neighboring Satb2+ L5 IT neurons, providing a potential basis for cell-type-specific synaptic targeting between these cell types (**Figure 5**; Henderson et al., 2019). New tools, including better genetic access to different L5 cell types, will be required to fully elucidate these mechanisms, including disambiguating layer- and cell-type targeting mechanisms and determining whether competitive expression of signaling molecules in spines underlie such targeting.

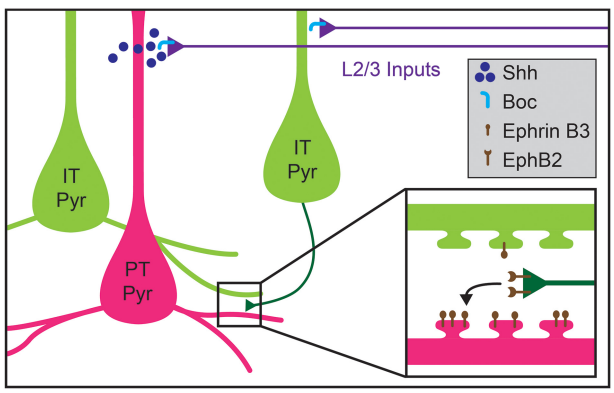

FIGURE 5 | Molecular mechanisms regulating cell-type-specific excitatory connections in cortical layer 5 (L5). Inputs to L5 from layer 2/3 (L2/3) callosal projection neurons are guided by the expression of Shh in pyramidal tract (PT Pyr) neurons (magenta), which signals through its receptor Boc expressed on L2/3 axons (blue). Within L5, intralaminar synapses formed by intratelencephalic pyramidal (IT Pyr) neurons (green) preferentially innervate PT pyramidal neurons over other pyramidal IT neurons. PT pyramidal neurons express higher levels of ephrin B3, which competitively signals through its receptor EphB2 to mediate biased synaptogenesis (inset). This competitive ephrin signaling may underlie the targeting preferences of IT pyramidal neurons.

Mechanisms for Targeting Excitatory Input to Subcellular Domains of Pyramidal Neurons

Just as inhibitory neuron subtypes prefer specific subcellular domains of pyramidal neurons, some excitatory inputs are also biased to particular postsynaptic regions. For example, channelrhodopsin-assisted circuit mapping showed that different local and long-range excitatory inputs to L2/3 and L5 pyramidal neurons formed synapses on different regions of their dendritic arbors at relative strengths inconsistent with average axodendritic overlap (Petreanu et al., 2009; Little and Carter, 2012). Similarly, thalamocortical input and the input from different subtypes of L4 excitatory neurons are biased toward different regions of the dendritic arbors of L6 pyramidal neurons (Da Costa and Martin, 2009; Qi and Feldmeyer, 2016). Because the apical dendrites of pyramidal neurons traverse multiple cortical layers, it is possible that developmental mechanisms underlying laminar targeting in the neocortex also contribute to excitatory targeting of subcellular domains, but how these interact with domain-specific mechanisms remains to be tested.

Insights into how these circuits develop in the neocortex may come from developmental processes identified in hippocampal circuits. The hippocampus is a highly laminated structure, with the cell bodies of hippocampal pyramidal neurons contained primarily within a single layer, and their dendrites oriented perpendicularly to layer borders such that each lamina contains dendritic processes of a similar distance from the soma. Excitatory inputs from the entorhinal cortex and from other hippocampal regions segregate into these different laminae, targeting specific dendritic regions of pyramidal neurons (**Figure 6A**). After being initially directed to the appropriate laminae and regions by interaction with pioneer neurons, guidance molecules, and the expression of topographic partner-matching cues (Skutella and Nitsch, 2001; Förster et al., 2006; Berns et al., 2018), these long-range axons are then directed

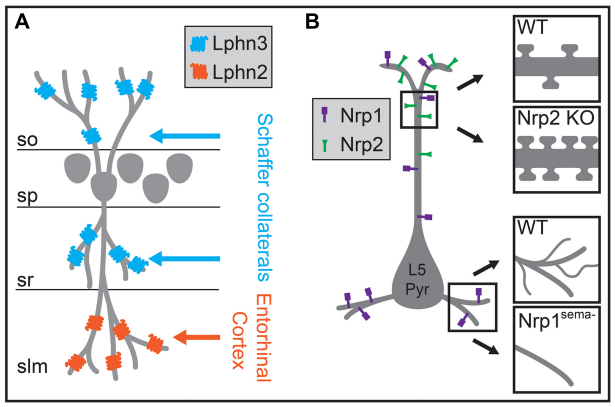

FIGURE 6 | Molecular mechanisms regulating the biased formation of excitatory inputs onto different regions of the postsynaptic dendrite. **(A)** In hippocampal CA1, excitatory Schaffer collateral inputs innervate pyramidal neuron dendrites within the *stratum oriens* (*so*) and the *stratum radiatum* (*sr*), whereas excitatory inputs from the entorhinal cortex form synapses onto distal dendritic regions in the *stratum lacunosum moleculare* (*slm*). In CA1 pyramidal neurons, Lphn3 is localized to *so* and *sr* and is required for Schaffer collateral input targeting to these layers, while Lphn2 is localized to *slm* and is required for targeting of entorhinal cortex inputs to dendrites in *slm*. **(B)** In layer 5 pyramidal (L5 Pyr) neurons in the neocortex, different semaphorin signaling pathways regulate morphology and spine density in distinct dendritic regions. The distribution of the Sema3F receptor Nrp2 is biased to apical dendritic regions, and a null mutation in Nrp2 results in increased spine density on the apical dendrite (upper insets). The Sema3A receptor Nrp1 is localized across the entire dendritic arbor, and a genetic mutation rendering Nrp1 unable to bind Sema3A results in reduced branching complexity of basal dendrites (lower insets). *sp*, stratum pyramidale.

to the appropriate subcellular domain through domain-specific molecular interactions. Axons originating from each input selectively express binding partners that interact with a diverse complement of transmembrane proteins that are selectively distributed along pyramidal neuron dendrites. For example, in CA1, two closely related G-protein coupled receptors (GPCRs) differentially regulate synapse formation across hippocampal pyramidal neuron dendrites. Lphn2 is enriched in *stratum lacunosum moleculare* and required for the targeting of entorhinal cortex inputs to distal dendrites, while Lphn3 is enriched in both CA1 *stratum radiatum* and *stratum oriens* and is required for the targeting of those layers by Schaffer collateral axons from CA3 and commissural fibers from the contralateral hippocampus (**Figure 6A**; Anderson et al., 2017; Sando et al., 2019). Subsequent structural studies have shown that this mechanism relies on heterotrimeric transsynaptic binding complexes, and that synapse formation relies on GPCR intracellular signaling (Del Toro et al., 2020; Li et al., 2020b; Sando and Südhof, 2021). These results agree in general with other studies of the hippocampus highlighting the roles of selectively distributed transmembrane molecules in generating laminar or subcellular-domain-specific synaptic targeting. In CA3, interactions between members of the Plexin A family of receptors and the transmembrane semaphorin, Sema6a, restrict mossy fiber axons to the proximal region of pyramidal neuron dendrites (Suto et al., 2007). Similarly, differentially distributed leucine-rich repeat family proteins in CA1 pyramidal neuron dendrites play a role in subcellular targeting by CA3 inputs and play domain-specific roles in controlling synaptic properties (Nishimura-Akiyoshi et al., 2007; DeNardo et al., 2012; Schroeder et al., 2018).

Although the laminar organization of the hippocampus is more precise than in neocortex, the differential distribution of postsynaptic molecules along the dendritic arbors of pyramidal neurons combined with specific expression of binding partners on subsets of presynaptic axons may also play a role in establishing intracortical circuits. Molecular mechanisms that control domain-specific excitatory synaptic density have been discovered in the neocortex (Tran et al., 2009; Cubelos et al., 2015). In L5 pyramidal neurons, expression of the Sema3F receptor Nrp2 is localized to apical dendrites, while the closely related Sema3A receptor Nrp1 is distributed across the dendritic arbor (**Figure 6B**). Nrp2 controls the density and abundance of spines on apical dendrites, while Nrp1 plays a role in basal dendritic arborization in these neurons (**Figure 6B**; Gu et al., 2003; Tran et al., 2009). Whether these proteins affect input-type synaptic targeting onto different dendritic regions of L5 pyramidal neurons is still uncertain, but these or related molecular pathways may play a role in excitatory synaptic targeting in the neocortex.

Cell-Type-Biased Connections From Pyramidal Neuron to Inhibitory Neuron Types

Excitatory cortical pyramidal neurons also selectively target different subtypes of local inhibitory neurons, although molecular recognition processes underlying the development of these circuits are still poorly understood. One study found that L5 IT pyramids that project to contralateral striatum synapsed more frequently onto one particular subtype of low threshold spiking (LTS) interneurons while L5 PT neurons projecting to the pons synapse with similar frequency on all types of L5 LTS interneurons (Morishima et al., 2017). Layer 6 corticothalamic neurons (L6 CThNs) also exhibit biased synaptic targeting of interneurons. L6 CThNs appear to form infrequent or weak synapses onto SST interneurons as well as neighboring excitatory neurons in L6, but target rarer PV interneurons in L6 and L4 via intracortical axon collaterals (Beierlein and Connors, 2002; West et al., 2006; Bortone et al., 2014; Kim et al., 2014; Crandall et al., 2017; Frandolig et al., 2019). The developmental mechanisms that underlie the biases of L5 and L6 pyramids for specific interneuron subtypes remain unclear.

The Development of Synapse-Type-Specific Functional Properties

Not only do cell types within the cortex form stereotyped patterns of connectivity, but synapses between different cell types can also acquire distinct signaling characteristics. For example, individual L2/3 pyramidal neurons form depressing synapses onto PV interneurons while forming facilitating synapses onto SST interneurons (**Figure 7**; Reyes et al., 1998;

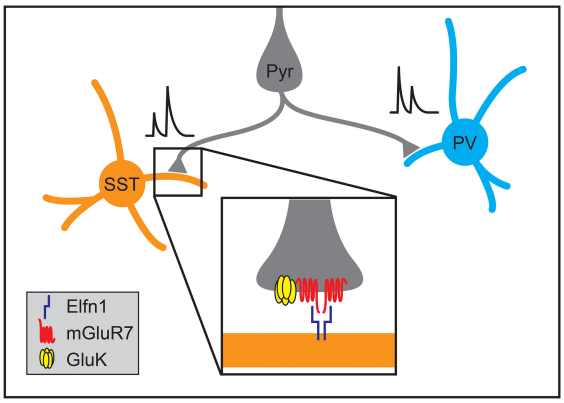

FIGURE 7 | Molecular mechanisms regulating the formation of synapse-type-specific functional properties. The short-term plasticity of pyramidal neuron synapses onto somatostatin-positive (SST) and parvalbumin-positive (PV) interneurons depends on the identity of the postsynaptic cell type. Single pyramidal neurons form facilitating synapses onto SST interneurons while forming depressing synapses onto PV interneurons. The development of facilitation of excitatory synapses onto SST neurons in the hippocampus and neocortex relies on postsynaptic expression of Elfn1 (inset), which then signals through presynaptic metabotropic glutamate receptors (mGluR7). At some synapse types, activation of mGluR7 also interacts with kainate receptors (GluK2) that further enhance synaptic facilitation.

Koester and Johnston, 2005). The smaller presynaptic calcium transients and facilitating postsynaptic potentials of the synapses onto SST cells suggest lower release probabilities at Pyr➔SST synapses relative to Pyr➔PV connections (Reyes et al., 1998; Koester and Johnston, 2005; Glasgow et al., 2019). Elfn1 has recently been found to regulate the development of synapse-type-specific facilitation in the neocortex and hippocampus, where pyramidal neurons similarly form depressing synapses onto PV neurons and facilitating synapses on SST neurons. In hippocampal CA1, SST neurons in the *stratum oriens* express the transmembrane protein Elfn1, which is localized to excitatory postsynaptic structures and is required to form facilitating synapses (Sylwestrak and Ghosh, 2012). As in CA1, Elfn1 knockout results in the loss of synaptic facilitation at neocortical excitatory synapses on L2/3 and L5 SST neurons (Stachniak et al., 2019) as well as a decrease in facilitation at excitatory connections onto multipolar vasoactive intestinal polypeptide-expressing (VIP) interneurons but not bipolar VIP interneurons (Stachniak et al., 2021). Overexpression of Elfn1 in hippocampal PV neurons is also sufficient to generate facilitating excitatory synapses where depressing synapses would normally occur (Sylwestrak and Ghosh, 2012) as is overexpression in bipolar VIP interneurons (Stachniak et al., 2021).

The mechanisms by which Elfn1 regulates synaptic transmission are being elucidated. Elfn1, localized postsynaptically, binds in *trans* to the metabotropic glutamate receptor, mGluR7, which is localized to presynaptic terminals of Elfn1-positive synapses in both the hippocampus and neocortex (**Figure 7**; Tomioka et al., 2014; Dunn et al., 2018; Stachniak et al., 2019, 2021). Elfn1 recruits mGluR7 and other group III mGluRs, and can allosterically activate them, modulating their downstream signaling (Dunn et al., 2019). These mechanisms alone or in combination with presynaptic GluK2-containing kainate receptors increase facilitation at different types of synapses in the neocortex and hippocampus (**Figure 7**; Sylwestrak and Ghosh, 2012; Tomioka et al., 2014; Stachniak et al., 2019, 2021). In VIP interneurons, the transcription factor Prox1 has been implicated in regulating Elfn1 expression (Stachniak et al., 2021).

Many additional examples of synapse-type-specific properties exist in the cortex. Facilitation distinguishes other subsets of cortical synapses, including, for example, thalamocortical (TC) synapses onto SST neurons which facilitate versus TC synapses on PV neurons which depress (Beierlein et al., 2003; Tan et al., 2008). Some pyramidal cell types also form facilitating synapses onto other excitatory cells (Ferster and Lindström, 1985; Stratford et al., 1996; Beierlein and Connors, 2002; Wang et al., 2006; West et al., 2006; Frandolig et al., 2019). The complement of receptors also varies in a synapse-type specific manner. For example, in L5 pyramidal neurons of visual cortex, presynaptic NMDA receptors are specifically localized to synapses made on SST neurons and locally projecting PV neurons, but not on translaminar PV neurons (Buchanan et al., 2012). Similarly, excitatory synapses onto the dendritic shafts and dendritic spines of PV interneurons differ in their enrichment for NMDA receptors (Sancho and Bloodgood, 2018). How these synapse-type-specific properties are established remains unknown.

CONCLUSION

Recent studies have begun to reveal developmental mechanisms for biasing the connectivity of cortical cell types and have implicated specific molecules in these processes. However, many challenges to fully understanding these mechanisms remain.

First, a catalog of cell types making up the cortex has not yet been fully established, although an increasingly large repertoire of cortical cell types has been defined using combinations of transcriptional, morphological and electrophysiological data (Zeisel et al., 2015; Tasic et al., 2016, 2018; Paul et al., 2017; Huang and Paul, 2019; Loo et al., 2019; Gouwens et al., 2020; Kim et al., 2020; Scala et al., 2020; Yao et al., 2020; Yuste et al., 2020). Relatedly, although some progress has been made in identifying approaches for directing gene expression in these different cortical cell types, genetic access for many of these is still lacking, preventing manipulation of these cell types during development. Genetic access allows tests of the sufficiency of a developmental mechanism for establishing synaptic connections by, for example, assessing synapse formation with ectopic expression of one or a small number of genes within a pathway, a strong indication that the identified molecules direct synaptic targeting itself.

Second, methods for determining cell-type-biased synaptic connectivity and function remain laborious; thus, not only do the synaptic relationships of cortical cell types remain to be fully elucidated, but it remains difficult to assess how these synaptic relationships change across development or following specific experimental perturbations. Although a recent study successfully

used electron microscopy at multiple developmental timepoints to assess the development of intracortical target specificity of different types of inhibitory interneurons (Gour et al., 2021), such studies remain technically difficult.

Third, multiple mechanisms likely work in concert to establish the specificity of intracortical connectivity as is illustrated by ChC targeting of AISs (**Figure 2**; Gallo et al., 2020), further complicating experimental approaches. Perturbing any single molecule may generate only a subtle phenotype, making it even more difficult to assess any effects.

Fourth, the protein families implicated in synaptic targeting in the neocortex are multifunctional and often affect other aspects of cortical development (De Wit and Ghosh, 2016; Sanes and Zipursky, 2020). Synaptic targeting mechanisms may only function properly in the context of an appropriate temporal sequence of developmental events, requiring tools for temporally specific manipulation such as inducible recombinase systems.

Fifth, most of the work on mechanisms of intracortical synaptic targeting has focused on cell-intrinsic signaling pathways or transcellular interactions between neurons. The roles of additional cortical cell types, like microglia, astrocytes and oligodendrocyte precursor cells, in establishing cell-type-biased connections in the cortex remain underexplored. Glial cells may mediate specific synapse growth or elimination (Schafer and Stevens, 2015; Bosworth and Allen, 2017; Stogsdill and Eroglu, 2017; Buchanan et al., 2021). Furthermore, just as radial glia guide axon growth directions in the cortex, glial cells may act directly to guide cortical synaptic partners to each other, as has been observed for cerebellar Bergmann glia (Ango et al., 2008). More work is required to understand the role glial cells play in cortical synaptic target specificity.

Despite these difficulties, methods such as projection-specific barcoding and profiling of growth cones are being developed that enable unbiased and high-throughput analyses of candidate molecular mechanisms for cortical synaptic targeting (Biesemann et al., 2014; Poulopoulos et al., 2019; Apostolo et al., 2020; Sun et al., 2021). Furthermore, proximity-based labeling methods such as APEX and BioID can be used to specifically tag proteins in the synapses of cell populations of interest, allowing for cell-type and domain-specific profiling of candidate molecules (Loh et al., 2016; Spence et al., 2019; Li et al., 2020a). These new molecular methods provide a toolbox that is particularly useful in the cortex, where the visualization and purification of synapses is difficult amid intermingled cell classes.

Understanding how the intracortical patterns of connectivity are established during development not only has implications for normal cortical development, but also for disease processes. Alterations to the molecular mechanisms of cell-type-biased and synapse-type-specific development may underlie aspects of neurodevelopmental disorders like autism and schizophrenia, as shown by the associations between mutations in *Elfn1* and ASDs, epilepsy, and ADHD (Matsunaga and Aruga, 2021). Similarly, mutations in genes involved in synaptic targeting by ChCs onto the AISs of pyramidal neurons including *L1CAM*, *ERBB4*, and *FGF13* have been implicated in epilepsy, schizophrenia or intellectual disability (Contreras et al., 2019; Gallo et al., 2020). As more mechanisms for specific synaptic targeting are uncovered, it is likely that other links to neurodevelopmental disorders will emerge given the importance of patterned synaptic connectivity to the function of the healthy neocortex (Chen et al., 2014; Nelson and Valakh, 2015).

AUTHOR CONTRIBUTIONS

Both authors conceptualized and wrote this review together. Both authors contributed to the article and approved the submitted version.

FUNDING

SB was supported by the National Institutes of Health (R01 NS085121 and RF1 MH121539), the National Science Foundation (NSF 1656592), and a Klingenstein-Simons Fellowship in the Neurosciences. AG-W was supported by the National Science Foundation Graduate Research Fellowship Program.

ACKNOWLEDGMENTS

The authors thank Seong Yeol An, Kenji Johnson, Su-Jeong Kim, and Alina Spiegel for comments on the manuscript.

REFERENCES

Adesnik, H., and Naka, A. (2018). Cracking the function of layers in the sensory cortex. *Neuron* 100, 1028–1043. doi: 10.1016/j.neuron.2018.10.032

Agi, E., Kulkarni, A., and Hiesinger, P. R. (2020). Neuronal strategies for meeting the right partner during brain wiring. *Curr. Opin. Neurobiol.* 63, 1–8. doi: 10.1016/j.conb.2020.01.002

Amitai, Y., Gibson, J. R., Beierlein, M., Patrick, S. L., Ho, A. M., Connors, B. W., et al. (2002). The spatial dimensions of electrically coupled networks of interneurons in the neocortex. *J. Neurosci.* 22, 4142–4152. doi: 10.1523/JNEUROSCI.22-10-04142.2002

Anastasiades, P. G., and Carter, A. G. (2021). Circuit organization of the rodent medial prefrontal cortex. *Trends Neurosci.* 44, 550–563. doi: 10.1016/j.tins.2021.03.006

Anastasiades, P. G., Marlin, J. J., and Carter, A. G. (2018). Cell-type specificity of callosally evoked excitation and feedforward inhibition in the prefrontal cortex. *Cell Rep.* 22, 679–692. doi: 10.1016/j.celrep.2017.12.073

Anderson, C. T., Sheets, P. L., Kiritani, T., and Shepherd, G. M. (2010). Sublayer-specific microcircuits of corticospinal and corticostriatal neurons in motor cortex. *Nat. Neurosci.* 13, 739–744. doi: 10.1038/nn.2538

Anderson, G. R., Maxeiner, S., Sando, R., Tsetsenis, T., Malenka, R. C., and Südhof, T. C. (2017). Postsynaptic adhesion GPCR latrophilin-2 mediates target recognition in entorhinal-hippocampal synapse assembly. *J. Cell Biol.* 216, 3831–3846. doi: 10.1083/jcb.201703042

Ango, F., Di Cristo, G., Higashiyama, H., Bennett, V., Wu, P., and Huang, Z. J. (2004). Ankyrin-based subcellular gradient of neurofascin, an immunoglobulin family protein, directs GABAergic innervation at purkinje axon initial segment. *Cell* 119, 257–272. doi: 10.1016/j.cell.2004.10.004

Ango, F., Wu, C., Van Der Want, J. J., Wu, P., Schachner, M., and Huang, Z. J. (2008). Bergmann glia and the recognition molecule CHL1 organize GABAergic axons and direct innervation of Purkinje cell dendrites. *PLoS Biol.* 6:e103. doi: 10.1371/journal.pbio.0060103

Apostolo, N., and De Wit, J. (2019). Compartmentalized distributions of neuronal and glial cell-surface proteins pattern the synaptic network. *Curr. Opin. Neurobiol.* 57, 126–133. doi: 10.1016/j.conb.2019.01.025

Apostolo, N., Smukowski, S. N., Vanderlinden, J., Condomitti, G., Rybakin, V., Ten Bos, J., et al. (2020). Synapse type-specific proteomic dissection identifies IgSF8 as a hippocampal CA3 microcircuit organizer. *Nat. Commun.* 11:5171. doi: 10.1038/s41467-020-18956-x

Baker, A., Kalmbach, B., Morishima, M., Kim, J., Juavinett, A., Li, N., et al. (2018). Specialized subpopulations of deep-layer pyramidal neurons in the neocortex: bridging cellular properties to functional consequences. *J. Neurosci.* 38, 5441–5455. doi: 10.1523/JNEUROSCI.0150-18.2018

Balaskas, N., Abbott, L. F., Jessell, T. M., and Ng, D. (2019). Positional strategies for connection specificity and synaptic organization in spinal sensory-motor circuits. *Neuron* 102, 1143–1156.e4. doi: 10.1016/j.neuron.2019.04.008

Beierlein, M., and Connors, B. W. (2002). Short-term dynamics of thalamocortical and intracortical synapses onto layer 6 neurons in neocortex. *J. Neurophysiol.* 88, 1924–1932. doi: 10.1152/jn.2002.88.4.1924

Beierlein, M., Gibson, J. R., and Connors, B. W. (2000). A network of electrically coupled interneurons drives synchronized inhibition in neocortex. *Nat. Neurosci.* 3, 904–910. doi: 10.1038/78809

Beierlein, M., Gibson, J. R., and Connors, B. W. (2003). Two dynamically distinct inhibitory networks in layer 4 of the neocortex. *J. Neurophysiol.* 90, 2987–3000. doi: 10.1152/jn.00283.2003

Berns, D. S., DeNardo, L. A., Pederick, D. T., and Luo, L. (2018). Teneurin-3 controls topographic circuit assembly in the hippocampus. *Nature* 554, 328–333. doi: 10.1038/nature25463

Bian, W. J., Miao, W. Y., He, S. J., Qiu, Z., and Yu, X. (2015). Coordinated spine pruning and maturation mediated by inter-spine competition for cadherin/catenin complexes. *Cell* 162, 808–822. doi: 10.1016/j.cell.2015.07.018

Biesemann, C., Gronborg, M., Luquet, E., Wichert, S. P., Bernard, V., Bungers, S. R., et al. (2014). Proteomic screening of glutamatergic mouse brain synaptosomes isolated by fluorescence activated sorting. *EMBO J.* 33, 157–170. doi: 10.1002/embj.201386120

Bird, A. D., Deters, L. H., and Cuntz, H. (2021). Excess neuronal branching allows for local innervation of specific dendritic compartments in mature cortex. *Cereb. Cortex* 31, 1008–1031. doi: 10.1093/cercor/bhaa271

Blatow, M., Rozov, A., Katona, I., Hormuzdi, S. G., Meyer, A. H., Whittington, M. A., et al. (2003). A novel network of multipolar bursting interneurons generates theta frequency oscillations in neocortex. *Neuron* 38, 805–817. doi: 10.1016/S0896-6273(03)00300-3

Bonhoeffer, T., and Yuste, R. (2002). Spine motility: phenomenology, mechanisms, and function. *Neuron* 35, 1019–1027. doi: 10.1016/s0896-6273(02)00906-6

Bortone, D. S., Olsen, S. R., and Scanziani, M. (2014). Translaminar inhibitory cells recruited by layer 6 corticothalamic neurons suppress visual cortex. *Neuron* 82, 474–485. doi: 10.1016/j.neuron.2014.02.021

Bosworth, A. P., and Allen, N. J. (2017). The diverse actions of astrocytes during synaptic development. *Curr. Opin. Neurobiol.* 47, 38–43. doi: 10.1016/j.conb.2017.08.017

Bragg-Gonzalo, L., De León Reyes, N. S., and Nieto, M. (2021). Genetic and activity dependent-mechanisms wiring the cortex: two sides of the same coin. *Semin. Cell Dev. Biol.* doi: 10.1016/j.semcdb.2021.05.011

Braitenberg, V., and Schüz, A. (1998). *Cortex: Statistics and Geometry of Neuronal Connectivity*. Berlin: Springer-Verlag.

Briggman, K. L., and Bock, D. D. (2012). Volume electron microscopy for neuronal circuit reconstruction. *Curr. Opin. Neurobiol.* 22, 154–161. doi: 10.1016/j.conb.2011.10.022

Brown, S. P., and Hestrin, S. (2009a). Cell-type identity: a key to unlocking the function of neocortical circuits. *Curr. Opin. Neurobiol.* 19, 415–421. doi: 10.1016/j.conb.2009.07.011

Brown, S. P., and Hestrin, S. (2009b). Intracortical circuits of pyramidal neurons reflect their long-range axonal targets. *Nature* 457, 1133–1136. doi: 10.1038/nature07658

Buchanan, J., Elabbady, L., Collman, F., Jorstad, N. L., Bakken, T. E., Ott, C., et al. (2021). Oligodendrocyte precursor cells prune axons in the mouse neocortex. *bioRxiv* doi: 10.1101/2021.05.29.446047 [Preprint].

Buchanan, K. A., Blackman, A. V., Moreau, A. W., Elgar, D., Costa, R. P., Lalanne, T., et al. (2012). Target-specific expression of presynaptic NMDA receptors in neocortical microcircuits. *Neuron* 75, 451–466. doi: 10.1016/j.neuron.2012.06.017

Cadwell, C. R., Scala, F., Fahey, P. G., Kobak, D., Mulherkar, S., Sinz, F. H., et al. (2020). Cell type composition and circuit organization of clonally related excitatory neurons in the juvenile mouse neocortex. *eLife* 9:e52951. doi: 10.7554/eLife.52951

Callaway, E. M. (1998). Local circuits in primary visual cortex of the macaque monkey. *Annu. Rev. Neurosci.* 21, 47–74. doi: 10.1146/annurev.neuro.21.1.47

Chen, E. S., Gigek, C. O., Rosenfeld, J. A., Diallo, A. B., Maussion, G., Chen, G. G., et al. (2014). Molecular convergence of neurodevelopmental disorders. *Am. J. Hum. Genet.* 95, 490–508. doi: 10.1016/j.ajhg.2014.09.013

Chen, J. G., Rasin, M. R., Kwan, K. Y., and Sestan, N. (2005). Zfp312 is required for subcortical axonal projections and dendritic morphology of deep-layer pyramidal neurons of the cerebral cortex. *Proc. Natl. Acad. Sci. U. S. A.* 102, 17792–17797. doi: 10.1073/pnas.0509032102

Chevée, M., and Brown, S. P. (2018). The development of local circuits in the neocortex: recent lessons from the mouse visual cortex. *Curr. Opin. Neurobiol.* 53, 103–109. doi: 10.1016/j.conb.2018.06.009

Chittajallu, R., Pelkey, K. A., and Mcbain, C. J. (2013). Neurogliaform cells dynamically regulate somatosensory integration via synapse-specific modulation. *Nat. Neurosci.* 16, 13–15. doi: 10.1038/nn.3284

Collins, D. P., Anastasiades, P. G., Marlin, J. J., and Carter, A. G. (2018). Reciprocal circuits linking the prefrontal cortex with dorsal and ventral thalamic nuclei. *Neuron* 98, 366–379.e4. doi: 10.1016/j.neuron.2018.03.024

Contreras, A., Hines, D. J., and Hines, R. M. (2019). Molecular specialization of GABAergic synapses on the soma and axon in cortical and hippocampal circuit function and dysfunction. *Front. Mol. Neurosci.* 12:154. doi: 10.3389/fnmol.2019.00154

Cossell, L., Iacaruso, M. F., Muir, D. R., Houlton, R., Sader, E. N., Ko, H., et al. (2015). Functional organization of excitatory synaptic strength in primary visual cortex. *Nature* 518, 399–403. doi: 10.1038/nature14182

Crandall, S. R., Patrick, S. L., Cruikshank, S. J., and Connors, B. W. (2017). Infrabarrels are layer 6 circuit modules in the barrel cortex that link long-range inputs and outputs. *Cell Rep.* 21, 3065–3078. doi: 10.1016/j.celrep.2017.11.049

Cubelos, B., Briz, C. G., Esteban-Ortega, G. M., and Nieto, M. (2015). Cux1 and Cux2 selectively target basal and apical dendritic compartments of layer II-III cortical neurons. *Dev. Neurobiol.* 75, 163–172. doi: 10.1002/dneu.22215

Cubelos, B., Sebastian-Serrano, A., Beccari, L., Calcagnotto, M. E., Cisneros, E., Kim, S., et al. (2010). Cux1 and Cux2 regulate dendritic branching, spine morphology, and synapses of the upper layer neurons of the cortex. *Neuron* 66, 523–535. doi: 10.1016/j.neuron.2010.04.038

Da Costa, N. M., and Martin, K. A. (2009). Selective targeting of the dendrites of corticothalamic cells by thalamic afferents in area 17 of the cat. *J. Neurosci.* 29, 13919–13928. doi: 10.1523/JNEUROSCI.2785-09.2009

Dailey, M. E., and Smith, S. J. (1996). The dynamics of dendritic structure in developing hippocampal slices. *J. Neurosci.* 16, 2983–2994. doi: 10.1523/JNEUROSCI.16-09-02983.1996

Dantzker, J. L., and Callaway, E. M. (2000). Laminar sources of synaptic input to cortical inhibitory interneurons and pyramidal neurons. *Nat. Neurosci.* 3, 701–707. doi: 10.1038/76656

De Carlos, J. A., Lopez-Mascaraque, L., and Valverde, F. (1985). Development, morphology and topography of chandelier cells in the auditory cortex of the cat. *Brain Res.* 354, 293–300. doi: 10.1016/0165-3806(85)90182-8

De Wit, J., and Ghosh, A. (2016). Specification of synaptic connectivity by cell surface interactions. *Nat. Rev. Neurosci.* 17, 22–35. doi: 10.1038/nrn.2015.3

DeFelipe, J., Hendry, S. H., and Jones, E. G. (1989). Visualization of chandelier cell axons by parvalbumin immunoreactivity in monkey cerebral cortex. *Proc. Natl. Acad. Sci. U. S. A.* 86, 2093–2097. doi: 10.1073/pnas.86.6.2093

DeFelipe, J., Hendry, S. H., Jones, E. G., and Schmechel, D. (1985). Variability in the terminations of GABAergic chandelier cell axons on initial segments of pyramidal cell axons in the monkey sensory-motor cortex. *J. Comp. Neurol.* 231, 364–384. doi: 10.1002/cne.902310307

DeFelipe, J., Lopez-Cruz, P. L., Benavides-Piccione, R., Bielza, C., Larranaga, P., Anderson, S., et al. (2013). New insights into the classification and nomenclature of cortical GABAergic interneurons. *Nat. Rev. Neurosci.* 14, 202–216. doi: 10.1038/nrn3444

Del Pino, I., Garcia-Frigola, C., Dehorter, N., Brotons-Mas, J. R., Alvarez-Salvado, E., Martinez De Lagran, M., et al. (2013). Erbb4 deletion from fast-spiking interneurons causes schizophrenia-like phenotypes. *Neuron* 79, 1152–1168. doi: 10.1016/j.neuron.2013.07.010

Del Toro, D., Carrasquero-Ordaz, M. A., Chu, A., Ruff, T., Shahin, M., Jackson, V. A., et al. (2020). Structural basis of teneurin-latrophilin interaction in repulsive guidance of migrating neurons. *Cell* 180, 323–339.e19. doi: 10.1016/j.cell.2019.12.014

DeNardo, L. A., De Wit, J., Otto-Hitt, S., and Ghosh, A. (2012). NGL-2 regulates input-specific synapse development in CA1 pyramidal neurons. *Neuron* 76, 762–775. doi: 10.1016/j.neuron.2012.10.013

Di Cristo, G., Wu, C., Chattopadhyaya, B., Ango, F., Knott, G., Welker, E., et al. (2004). Subcellular domain-restricted GABAergic innervation in primary visual cortex in the absence of sensory and thalamic inputs. *Nat. Neurosci.* 7, 1184–1186. doi: 10.1038/nn1334

Dorskind, J. M., and Kolodkin, A. L. (2021). Revisiting and refining roles of neural guidance cues in circuit assembly. *Curr. Opin. Neurobiol.* 66, 10–21. doi: 10.1016/j.conb.2020.07.005

Dunn, H. A., Orlandi, C., and Martemyanov, K. A. (2019). Beyond the ligand: extracellular and transcellular G protein-coupled receptor complexes in physiology and pharmacology. *Pharmacol. Rev.* 71, 503–519. doi: 10.1124/pr.119.018044

Dunn, H. A., Patil, D. N., Cao, Y., Orlandi, C., and Martemyanov, K. A. (2018). Synaptic adhesion protein ELFN1 is a selective allosteric modulator of group III metabotropic glutamate receptors in trans. *Proc. Natl. Acad. Sci. U. S. A.* 115, 5022–5027. doi: 10.1073/pnas.1722498115

Fairen, A., and Valverde, F. (1980). A specialized type of neuron in the visual cortex of cat: a Golgi and electron microscope study of chandelier cells. *J. Comp. Neurol.* 194, 761–779. doi: 10.1002/cne.901940405

Fame, R. M., Macdonald, J. L., and Macklis, J. D. (2011). Development, specification, and diversity of callosal projection neurons. *Trends Neurosci.* 34, 41–50. doi: 10.1016/j.tins.2010.10.002

Farinas, I., and DeFelipe, J. (1991). Patterns of synaptic input on corticocortical and corticothalamic cells in the cat visual cortex. II. The axon initial segment. *J. Comp. Neurol.* 304, 70–77. doi: 10.1002/cne.903040106

Favuzzi, E., Deogracias, R., Marques-Smith, A., Maeso, P., Jezequel, J., Exposito-Alonso, D., et al. (2019). Distinct molecular programs regulate synapse specificity in cortical inhibitory circuits. *Science* 363, 413–417. doi: 10.1126/science.aau8977

Favuzzi, E., and Rico, B. (2018). Molecular diversity underlying cortical excitatory and inhibitory synapse development. *Curr. Opin. Neurobiol.* 53, 8–15. doi: 10.1016/j.conb.2018.03.011

Fazel Darbandi, S., Robinson Schwartz, S. E., Qi, Q., Catta-Preta, R., Pai, E. L., Mandell, J. D., et al. (2018). Neonatal Tbr1 dosage controls Cortical layer 6 connectivity. *Neuron* 100, 831–845.e7. doi: 10.1016/j.neuron.2018.09.027

Fazzari, P., Paternain, A. V., Valiente, M., Pla, R., Lujan, R., Lloyd, K., et al. (2010). Control of cortical GABA circuitry development by Nrg1 and ErbB4 signalling. *Nature* 464, 1376–1380. doi: 10.1038/nature08928

Feldmeyer, D. (2012). Excitatory neuronal connectivity in the barrel cortex. *Front. Neuroanat.* 6:24. doi: 10.3389/fnana.2012.00024

Feldmeyer, D., Qi, G., Emmenegger, V., and Staiger, J. F. (2018). Inhibitory interneurons and their circuit motifs in the many layers of the barrel cortex. *Neuroscience* 368, 132–151. doi: 10.1016/j.neuroscience.2017.05.027

Ferster, D., and Lindström, S. (1985). Augmenting responses evoked in area 17 of the cat by intracortical axon collaterals of cortico-geniculate cells. *J. Physiol.* 367, 217–232.

Fino, E., and Yuste, R. (2011). Dense inhibitory connectivity in neocortex. *Neuron* 69, 1188–1203. doi: 10.1016/j.neuron.2011.02.025

Fishell, G., and Kepecs, A. (2020). Interneuron types as attractors and controllers. *Annu. Rev. Neurosci.* 43, 1–30. doi: 10.1146/annurev-neuro-070918-050421

Förster, E., Zhao, S., and Frotscher, M. (2006). Laminating the hippocampus. *Nat. Rev. Neurosci.* 7, 259–267. doi: 10.1038/nrn1882

Frandolig, J. E., Matney, C. J., Lee, K., Kim, J., Chevée, M., Kim, S. J., et al. (2019). The synaptic organization of layer 6 circuits reveals inhibition as a major output of a neocortical sublamina. *Cell Rep.* 28, 3131–3143.e5. doi: 10.1016/j.celrep.2019.08.048

Fruh, S., Romanos, J., Panzanelli, P., Burgisser, D., Tyagarajan, S. K., Campbell, K. P., et al. (2016). Neuronal dystroglycan is necessary for formation and maintenance of functional CCK-positive basket cell terminals on pyramidal cells. *J. Neurosci.* 36, 10296–10313. doi: 10.1523/JNEUROSCI.1823-16.2016

Galarreta, M., and Hestrin, S. (1999). A network of fast-spiking cells in the neocortex connected by electrical synapses. *Nature* 402, 72–75. doi: 10.1038/47029

Gallo, N. B., Paul, A., and Van Aelst, L. (2020). Shedding light on Chandelier cell development, connectivity, and contribution to neural disorders. *Trends Neurosci.* 43, 565–580. doi: 10.1016/j.tins.2020.05.003

Gibson, D. A., and Ma, L. (2011). Developmental regulation of axon branching in the vertebrate nervous system. *Development* 138, 183–195. doi: 10.1242/dev.046441

Gibson, J. R., Beierlein, M., and Connors, B. W. (1999). Two networks of electrically coupled inhibitory neurons in neocortex. *Nature* 402, 75–79. doi: 10.1038/47035

Glasgow, S. D., Mcphedrain, R., Madranges, J. F., Kennedy, T. E., and Ruthazer, E. S. (2019). Approaches and limitations in the investigation of synaptic transmission and plasticity. *Front. Synaptic Neurosci.* 11:20. doi: 10.3389/fnsyn.2019.00020

Gour, A., Boergens, K. M., Heike, N., Hua, Y., Laserstein, P., Song, K., et al. (2021). Postnatal connectomic development of inhibition in mouse barrel cortex. *Science* 371:eabb4534. doi: 10.1126/science.abb4534

Gouwens, N. W., Sorensen, S. A., Baftizadeh, F., Budzillo, A., Lee, B. R., Jarsky, T., et al. (2020). Integrated morphoelectric and transcriptomic classification of cortical GABAergic cells. *Cell* 183, 935–953.e19. doi: 10.1016/j.cell.2020.09.057

Greig, L. C., Woodworth, M. B., Galazo, M. J., Padmanabhan, H., and Macklis, J. D. (2013). Molecular logic of neocortical projection neuron specification, development and diversity. *Nat. Rev. Neurosci.* 14, 755–769. doi: 10.1038/nrn3586

Grubb, M. S., and Burrone, J. (2010). Activity-dependent relocation of the axon initial segment fine-tunes neuronal excitability. *Nature* 465, 1070–1074. doi: 10.1038/nature09160

Gu, C., Rodriguez, E. R., Reimert, D. V., Shu, T., Fritzsch, B., Richards, L. J., et al. (2003). Neuropilin-1 conveys semaphorin and VEGF signaling during neural and cardiovascular development. *Dev. Cell* 5, 45–57. doi: 10.1016/s1534-5807(03)00169-2

Gupta, A., Wang, Y., and Markram, H. (2000). Organizing principles for a diversity of GABAergic interneurons and synapses in the neocortex. *Science* 287, 273–278. doi: 10.1126/science.287.5451.273

Hand, R. A., Khalid, S., Tam, E., and Kolodkin, A. L. (2015). Axon dynamics during neocortical laminar innervation. *Cell Rep.* 12, 172–182. doi: 10.1016/j.celrep.2015.06.026

Hanganu-Opatz, I. L., Butt, S. J. B., Hippenmeyer, S., De Marco Garcia, N. V., Cardin, J. A., Voytek, B., et al. (2021). The logic of developing neocortical circuits in health and disease. *J. Neurosci.* 41, 813–822. doi: 10.1523/JNEUROSCI.1655-20.2020

Harris, K. D., and Mrsic-Flogel, T. D. (2013). Cortical connectivity and sensory coding. *Nature* 503, 51–58. doi: 10.1038/nature12654

Harris, K. D., and Shepherd, G. M. (2015). The neocortical circuit: themes and variations. *Nat. Neurosci.* 18, 170–181. doi: 10.1038/nn.3917

Harwell, C. C., Parker, P. R., Gee, S. M., Okada, A., Mcconnell, S. K., Kreitzer, A. C., et al. (2012). Sonic hedgehog expression in corticofugal projection neurons directs cortical microcircuit formation. *Neuron* 73, 1116–1126. doi: 10.1016/j.neuron.2012.02.009

Helmstaedter, M. (2013). Cellular-resolution connectomics: challenges of dense neural circuit reconstruction. *Nat. Methods* 10, 501–507. doi: 10.1038/nmeth.2476

Henderson, N. T., Le Marchand, S. J., Hruska, M., Hippenmeyer, S., Luo, L., and Dalva, M. B. (2019). Ephrin-B3 controls excitatory synapse density through cell-cell competition for EphBs. *eLife* 8:e41563. doi: 10.7554/eLife.41563

Hestrin, S., and Galarreta, M. (2005). Electrical synapses define networks of neocortical GABAergic neurons. *Trends Neurosci.* 28, 304–309. doi: 10.1016/j.tins.2005.04.001

Hill, S. L., Wang, Y., Riachi, I., Schurmann, F., and Markram, H. (2012). Statistical connectivity provides a sufficient foundation for specific functional connectivity in neocortical neural microcircuits. *Proc. Natl. Acad. Sci. U. S. A.* 109, E2885–E2894. doi: 10.1073/pnas.1202128109

Hines, R. M., Maric, H. M., Hines, D. J., Modgil, A., Panzanelli, P., Nakamura, Y., et al. (2018). Developmental seizures and mortality result from reducing GABAA receptor alpha2-subunit interaction with collybistin. *Nat. Commun.* 9:3130. doi: 10.1038/s41467-018-05481-1

Honig, B., and Shapiro, L. (2020). Adhesion protein structure, molecular affinities, and principles of cell-cell recognition. *Cell* 181, 520–535. doi: 10.1016/j.cell.2020.04.010

Huang, Z. J., and Paul, A. (2019). The diversity of GABAergic neurons and neural communication elements. *Nat. Rev. Neurosci.* 20, 563–572. doi: 10.1038/s41583-019-0195-4

Inan, M., Blazquez-Llorca, L., Merchan-Perez, A., Anderson, S. A., DeFelipe, J., and Yuste, R. (2013). Dense and overlapping innervation of pyramidal neurons by chandelier cells. *J. Neurosci.* 33, 1907–1914. doi: 10.1523/JNEUROSCI.4049-12.2013

Jiang, X., Shen, S., Cadwell, C. R., Berens, P., Sinz, F., Ecker, A. S., et al. (2015). Principles of connectivity among morphologically defined cell types in adult neocortex. *Science* 350:aac9462. doi: 10.1126/science.aac9462

Jiang, X., Wang, G., Lee, A. J., Stornetta, R. L., and Zhu, J. J. (2013). The organization of two new cortical interneuronal circuits. *Nat. Neurosci.* 16, 210–218. doi: 10.1038/nn.3305

Jontes, J. D., and Smith, S. J. (2000). Filopodia, spines, and the generation of synaptic diversity. *Neuron* 27, 11–14. doi: 10.1016/s0896-6273(00)00003-9

Kalil, K., and Dent, E. W. (2014). Branch management: mechanisms of axon branching in the developing vertebrate CNS. *Nat. Rev. Neurosci.* 15, 7–18. doi: 10.1038/nrn3650

Kalisman, N., Silberberg, G., and Markram, H. (2005). The neocortical microcircuit as a tabula rasa. *Proc. Natl. Acad. Sci. U. S. A.* 102, 880–885. doi: 10.1073/pnas.0407088102

Karimi, A., Odenthal, J., Drawitsch, F., Boergens, K. M., and Helmstaedter, M. (2020). Cell-type specific innervation of cortical pyramidal cells at their apical dendrites. *eLife* 9:e46876. doi: 10.7554/eLife.46876

Kast, R. J., and Levitt, P. (2019). Precision in the development of neocortical architecture: from progenitors to cortical networks. *Prog. Neurobiol.* 175, 77–95. doi: 10.1016/j.pneurobio.2019.01.003

Kasthuri, N., Hayworth, K. J., Berger, D. R., Schalek, R. L., Conchello, J. A., Knowles-Barley, S., et al. (2015). Saturated reconstruction of a volume of neocortex. *Cell* 162, 648–661. doi: 10.1016/j.cell.2015.06.054

Katz, L. C., and Shatz, C. J. (1996). Synaptic activity and the construction of cortical circuits. *Science* 274, 1133–1138. doi: 10.1126/science.274.5290.1133

Kawaguchi, Y., Karube, F., and Kubota, Y. (2006). Dendritic branch typing and spine expression patterns in cortical nonpyramidal cells. *Cereb. Cortex* 16, 696–711. doi: 10.1093/cercor/bhj015

Kawaguchi, Y., and Kubota, Y. (1997). GABAergic cell subtypes and their synaptic connections in rat frontal cortex. *Cereb. Cortex* 7, 476–486. doi: 10.1093/cercor/7.6.476

Kim, E. J., Zhang, Z., Huang, L., Ito-Cole, T., Jacobs, M. W., Juavinett, A. L., et al. (2020). Extraction of distinct neuronal cell types from within a genetically continuous population. *Neuron* 107, 274–282.e6. doi: 10.1016/j.neuron.2020.04.018

Kim, J., Matney, C. J., Blankenship, A., Hestrin, S., and Brown, S. P. (2014). Layer 6 corticothalamic neurons activate a cortical output layer, layer 5a. *J. Neurosci.* 34, 9656–9664. doi: 10.1523/JNEUROSCI.1325-14.2014

Kirischuk, S., Sinning, A., Blanquie, O., Yang, J. W., Luhmann, H. J., and Kilb, W. (2017). Modulation of neocortical development by early neuronal activity: physiology and pathophysiology. *Front. Cell Neurosci.* 11:379. doi: 10.3389/fncel.2017.00379

Kiritani, T., Wickersham, I. R., Seung, H. S., and Shepherd, G. M. (2012). Hierarchical connectivity and connection-specific dynamics in the corticospinal-corticostriatal microcircuit in mouse motor cortex. *J. Neurosci.* 32, 4992–5001. doi: 10.1523/JNEUROSCI.4759-11.2012

Ko, H., Hofer, S. B., Pichler, B., Buchanan, K. A., Sjöström, P. J., and Mrsic-Flogel, T. D. (2011). Functional specificity of local synaptic connections in neocortical networks. *Nature* 473, 87–91. doi: 10.1038/nature09880

Ko, H., Mrsic-Flogel, T. D., and Hofer, S. B. (2014). Emergence of feature-specific connectivity in cortical microcircuits in the absence of visual experience. *J. Neurosci.* 34, 9812–9816. doi: 10.1523/JNEUROSCI.0875-14.2014

Koelbl, C., Helmstaedter, M., Lubke, J., and Feldmeyer, D. (2015). A barrel-related interneuron in layer 4 of rat somatosensory cortex with a high intrabarrel connectivity. *Cereb. Cortex* 25, 713–725. doi: 10.1093/cercor/bht263

Koester, H. J., and Johnston, D. (2005). Target cell-dependent normalization of transmitter release at neocortical synapses. *Science* 308, 863–866. doi: 10.1126/science.1100815

Koleske, A. J. (2013). Molecular mechanisms of dendrite stability. *Nat. Rev. Neurosci.* 14, 536–550. doi: 10.1038/nrn3486

Kolodkin, A. L., and Tessier-Lavigne, M. (2011). Mechanisms and molecules of neuronal wiring: a primer. *Cold Spring Harb. Perspect. Biol.* 3:a001727 doi: 10.1101/cshperspect.a001727

Konur, S., and Yuste, R. (2004). Imaging the motility of dendritic protrusions and axon terminals: roles in axon sampling and synaptic competition. *Mol. Cell. Neurosci.* 27, 427–440. doi: 10.1016/j.mcn.2004.07.005

Kriebel, M., Metzger, J., Trinks, S., Chugh, D., Harvey, R. J., Harvey, K., et al. (2011). The cell adhesion molecule neurofascin stabilizes axo-axonic GABAergic terminals at the axon initial segment. *J. Biol. Chem.* 286, 24385–24393. doi: 10.1074/jbc.M110.212191

Krook-Magnuson, E., Varga, C., Lee, S. H., and Soltesz, I. (2012). New dimensions of interneuronal specialization unmasked by principal cell heterogeneity. *Trends Neurosci.* 35, 175–184. doi: 10.1016/j.tins.2011.10.005

Kubota, Y. (2014). Untangling GABAergic wiring in the cortical microcircuit. *Curr. Opin. Neurobiol.* 26, 7–14. doi: 10.1016/j.conb.2013.10.003

Kubota, Y., Karube, F., Nomura, M., and Kawaguchi, Y. (2016). The diversity of cortical inhibitory synapses. *Front. Neural. Circuits* 10:27. doi: 10.3389/fncir.2016.00027

Kubota, Y., Sohn, J., and Kawaguchi, Y. (2018). Large volume electron microscopy and neural microcircuit analysis. *Front. Neural. Circuits* 12:98. doi: 10.3389/fncir.2018.00098

Kumar, P., and Ohana, O. (2008). Inter- and intralaminar subcircuits of excitatory and inhibitory neurons in layer 6a of the rat barrel cortex. *J. Neurophysiol.* 100, 1909–1922. doi: 10.1152/jn.90684.2008

Larsen, D. D., and Callaway, E. M. (2006). Development of layer-specific axonal arborizations in mouse primary somatosensory cortex. *J. Comp. Neurol.* 494, 398–414. doi: 10.1002/cne.20754

Larsen, R. S., and Sjöström, P. J. (2015). Synapse-type-specific plasticity in local circuits. *Curr. Opin. Neurobiol.* 35, 127–135. doi: 10.1016/j.conb.2015.08.001

Lee, A. J., Wang, G., Jiang, X., Johnson, S. M., Hoang, E. T., Lante, F., et al. (2015). Canonical organization of layer 1 neuron-led cortical inhibitory and disinhibitory interneuronal circuits. *Cereb. Cortex* 25, 2114–2126. doi: 10.1093/cercor/bhu020

Lee, A. T., Gee, S. M., Vogt, D., Patel, T., Rubenstein, J. L., and Sohal, V. S. (2014). Pyramidal neurons in prefrontal cortex receive subtype-specific forms of excitation and inhibition. *Neuron* 81, 61–68. doi: 10.1016/j.neuron.2013.10.031

Lee, S., Kruglikov, I., Huang, Z. J., Fishell, G., and Rudy, B. (2013). A disinhibitory circuit mediates motor integration in the somatosensory cortex. *Nat. Neurosci.* 16, 1662–1670. doi: 10.1038/nn.3544

Lee, W. C., Bonin, V., Reed, M., Graham, B. J., Hood, G., Glattfelder, K., et al. (2016). Anatomy and function of an excitatory network in the visual cortex. *Nature* 532, 370–374. doi: 10.1038/nature17192

Lefebvre, J. L., Sanes, J. R., and Kay, J. N. (2015). Development of dendritic form and function. *Annu. Rev. Cell Dev. Biol.* 31, 741–777. doi: 10.1146/annurev-cellbio-100913-013020

Lefort, S., Tomm, C., Floyd Sarria, J. C., and Petersen, C. C. (2009). The excitatory neuronal network of the C2 barrel column in mouse primary somatosensory cortex. *Neuron* 61, 301–316. doi: 10.1016/j.neuron.2008.12.020

Leyva-Diaz, E., and Lopez-Bendito, G. (2013). In and out from the cortex: development of major forebrain connections. *Neuroscience* 254, 26–44. doi: 10.1016/j.neuroscience.2013.08.070

Li, J., Han, S., Li, H., Udeshi, N. D., Svinkina, T., Mani, D. R., et al. (2020a). Cell-surface proteomic profiling in the fly brain uncovers wiring regulators. *Cell* 180, 373–386.e15. doi: 10.1016/j.cell.2019.12.029

Li, J., Xie, Y., Cornelius, S., Jiang, X., Sando, R., Kordon, S. P., et al. (2020b). Alternative splicing controls teneurin-latrophilin interaction and synapse specificity by a shape-shifting mechanism. *Nat. Commun.* 11:2140. doi: 10.1038/s41467-020-16029-7

Li, Y., Lu, H., Cheng, P. L., Ge, S., Xu, H., Shi, S. H., et al. (2012). Clonally related visual cortical neurons show similar stimulus feature selectivity. *Nature* 486, 118–121. doi: 10.1038/nature11110

Lim, L., Mi, D., Llorca, A., and Marin, O. (2018a). Development and functional diversification of cortical interneurons. *Neuron* 100, 294–313. doi: 10.1016/j.neuron.2018.10.009

Lim, L., Pakan, J. M. P., Selten, M. M., Marques-Smith, A., Llorca, A., Bae, S. E., et al. (2018b). Optimization of interneuron function by direct coupling of cell migration and axonal targeting. *Nat. Neurosci.* 21, 920–931. doi: 10.1038/s41593-018-0162-9

Little, J. P., and Carter, A. G. (2012). Subcellular synaptic connectivity of layer 2 pyramidal neurons in the medial prefrontal cortex. *J. Neurosci.* 32, 12808–12819. doi: 10.1523/JNEUROSCI.1616-12.2012

Lodato, S., and Arlotta, P. (2015). Generating neuronal diversity in the mammalian cerebral cortex. *Annu. Rev. Cell Dev. Biol.* 31, 699–720. doi: 10.1146/annurev-cellbio-100814-125353

Loh, K. H., Stawski, P. S., Draycott, A. S., Udeshi, N. D., Lehrman, E. K., Wilton, D. K., et al. (2016). Proteomic analysis of unbounded cellular compartments: synaptic clefts. *Cell* 166, 1295–1307.e21. doi: 10.1016/j.cell.2016.07.041

Loo, L., Simon, J. M., Xing, L., Mccoy, E. S., Niehaus, J. K., Guo, J., et al. (2019). Single-cell transcriptomic analysis of mouse neocortical development. *Nat. Commun.* 10:134. doi: 10.1038/s41467-018-08079-9

Lu, J., Tucciarone, J., Padilla-Coreano, N., He, M., Gordon, J. A., and Huang, Z. J. (2017). Selective inhibitory control of pyramidal neuron ensembles and cortical subnetworks by chandelier cells. *Nat. Neurosci.* 20, 1377–1383. doi: 10.1038/nn.4624

Markram, H., Muller, E., Ramaswamy, S., Reimann, M. W., Abdellah, M., Sanchez, C. A., et al. (2015). Reconstruction and simulation of neocortical microcircuitry. *Cell* 163, 456–492. doi: 10.1016/j.cell.2015.09.029

Markram, H., Toledo-Rodriguez, M., Wang, Y., Gupta, A., Silberberg, G., and Wu, C. (2004). Interneurons of the neocortical inhibitory system. *Nat. Rev. Neurosci.* 5, 793–807. doi: 10.1038/nrn1519

Matsunaga, H., and Aruga, J. (2021). Trans-synaptic regulation of metabotropic glutamate receptors by Elfn proteins in health and disease. *Front. Neural. Circuits* 15:634875. doi: 10.3389/fncir.2021.634875

Meyer, H. S., Schwarz, D., Wimmer, V. C., Schmitt, A. C., Kerr, J. N., Sakmann, B., et al. (2011). Inhibitory interneurons in a cortical column form hot zones of inhibition in layers 2 and 5A. *Proc. Natl. Acad. Sci. U. S. A.* 108, 16807–16812. doi: 10.1073/pnas.1113648108

Miles, R., and Poncer, J. C. (1996). Paired recordings from neurones. *Curr. Opin. Neurobiol.* 6, 387–394. doi: 10.1016/s0959-4388(96)80124-3

Morishima, M., and Kawaguchi, Y. (2006). Recurrent connection patterns of corticostriatal pyramidal cells in frontal cortex. *J. Neurosci.* 26, 4394–4405. doi: 10.1523/JNEUROSCI.0252-06.2006

Morishima, M., Kobayashi, K., Kato, S., and Kawaguchi, Y. (2017). Segregated excitatory-inhibitory recurrent subnetworks in Layer 5 of the rat frontal cortex. *Cereb. Cortex* 27, 5846–5857. doi: 10.1093/cercor/bhx276

Morishima, M., Morita, K., Kubota, Y., and Kawaguchi, Y. (2011). Highly differentiated projection-specific cortical subnetworks. *J. Neurosci.* 31, 10380–10391. doi: 10.1523/JNEUROSCI.0772-11.2011

Motta, A., Berning, M., Boergens, K. M., Staffler, B., Beining, M., Loomba, S., et al. (2019). Dense connectomic reconstruction in layer 4 of the somatosensory cortex. *Science* 366:eaay3134. doi: 10.1126/science.aay3134

Moyer, C. E., and Zuo, Y. (2018). Cortical dendritic spine development and plasticity: insights from in vivo imaging. *Curr. Opin. Neurobiol.* 53, 76–82. doi: 10.1016/j.conb.2018.06.002

Neddens, J., Fish, K. N., Tricoire, L., Vullhorst, D., Shamir, A., Chung, W., et al. (2011). Conserved interneuron-specific ErbB4 expression in frontal cortex of rodents, monkeys, and humans: implications for schizophrenia. *Biol. Psychiatry* 70, 636–645. doi: 10.1016/j.biopsych.2011.04.016

Nelson, S. B., and Valakh, V. (2015). Excitatory/inhibitory balance and circuit homeostasis in autism spectrum disorders. *Neuron* 87, 684–698. doi: 10.1016/j.neuron.2015.07.033

Nishimura-Akiyoshi, S., Niimi, K., Nakashiba, T., and Itohara, S. (2007). Axonal netrin-Gs transneuronally determine lamina-specific subdendritic segments. *Proc. Natl. Acad. Sci. U. S. A.* 104, 14801–14806. doi: 10.1073/pnas.0706919104

Nusser, Z. (2018). Creating diverse synapses from the same molecules. *Curr. Opin. Neurobiol.* 51, 8–15. doi: 10.1016/j.conb.2018.01.001

Ohtsuki, G., Nishiyama, M., Yoshida, T., Murakami, T., Histed, M., Lois, C., et al. (2012). Similarity of visual selectivity among clonally related neurons in visual cortex. *Neuron* 75, 65–72. doi: 10.1016/j.neuron.2012.05.023

Otsuka, T., and Kawaguchi, Y. (2008). Firing-pattern-dependent specificity of cortical excitatory feed-forward subnetworks. *J. Neurosci.* 28, 11186–11195. doi: 10.1523/JNEUROSCI.1921-08.2008

Otsuka, T., and Kawaguchi, Y. (2011). Cell diversity and connection specificity between callosal projection neurons in the frontal cortex. *J. Neurosci.* 31, 3862–3870. doi: 10.1523/JNEUROSCI.5795-10.2011

Packer, A. M., and Yuste, R. (2011). Dense, unspecific connectivity of neocortical parvalbumin-positive interneurons: a canonical microcircuit for inhibition? *J. Neurosci.* 31, 13260–13271. doi: 10.1523/JNEUROSCI.3131-11.2011

Pan-Vazquez, A., Wefelmeyer, W., Gonzalez Sabater, V., Neves, G., and Burrone, J. (2020). Activity-dependent plasticity of axo-axonic synapses at the axon initial segment. *Neuron* 106, 265–276.e6. doi: 10.1016/j.neuron.2020.01.037

Paul, A., Crow, M., Raudales, R., He, M., Gillis, J., and Huang, Z. J. (2017). Transcriptional architecture of synaptic communication delineates GABAergic neuron identity. *Cell* 171, 522–539.e20. doi: 10.1016/j.cell.2017.08.032

Peters, A., and Feldman, M. L. (1976). The projection of the lateral geniculate nucleus to area 17 of the rat cerebral cortex. I. General description. *J. Neurocytol.* 5, 63–84. doi: 10.1007/BF01176183

Petreanu, L., Mao, T., Sternson, S. M., and Svoboda, K. (2009). The subcellular organization of neocortical excitatory connections. *Nature* 457, 1142–1145. doi: 10.1038/nature07709

Pfeffer, C. K., Xue, M., He, M., Huang, Z. J., and Scanziani, M. (2013). Inhibition of inhibition in visual cortex: the logic of connections between molecularly distinct interneurons. *Nat. Neurosci.* 16, 1068–1076. doi: 10.1038/nn.3446

Pi, H. J., Hangya, B., Kvitsiani, D., Sanders, J. I., Huang, Z. J., and Kepecs, A. (2013). Cortical interneurons that specialize in disinhibitory control. *Nature* 503, 521–524. doi: 10.1038/nature12676

Polleux, F., Morrow, T., and Ghosh, A. (2000). Semaphorin 3A is a chemoattractant for cortical apical dendrites. *Nature* 404, 567–573. doi: 10.1038/35007001

Portera-Cailliau, C., Weimer, R. M., De Paola, V., Caroni, P., and Svoboda, K. (2005). Diverse modes of axon elaboration in the developing neocortex. *PLoS Biol.* 3:e272. doi: 10.1371/journal.pbio.0030272

Poulopoulos, A., Murphy, A. J., Ozkan, A., Davis, P., Hatch, J., Kirchner, R., et al. (2019). Subcellular transcriptomes and proteomes of developing axon projections in the cerebral cortex. *Nature* 565, 356–360. doi: 10.1038/s41586-018-0847-y

Qi, G., and Feldmeyer, D. (2016). Dendritic target region-specific formation of synapses between excitatory layer 4 neurons and layer 6 pyramidal cells. *Cereb. Cortex* 26, 1569–1579. doi: 10.1093/cercor/bhu334

Qi, G., Yang, D., Ding, C., and Feldmeyer, D. (2020). Unveiling the synaptic function and structure using paired recordings from synaptically coupled neurons. *Front. Synaptic Neurosci.* 12:5. doi: 10.3389/fnsyn.2020.00005

Ramaswamy, S., Hill, S. L., King, J. G., Schurmann, F., Wang, Y., and Markram, H. (2012). Intrinsic morphological diversity of thick-tufted layer 5 pyramidal neurons ensures robust and invariant properties of in silico synaptic connections. *J. Physiol.* 590, 737–752. doi: 10.1113/jphysiol.2011.219576

Rawson, R. L., Martin, E. A., and Williams, M. E. (2017). Mechanisms of input and output synaptic specificity: finding partners, building synapses, and fine-tuning communication. *Curr. Opin. Neurobiol.* 45, 39–44. doi: 10.1016/j.conb.2017.03.006

Rees, C. L., Moradi, K., and Ascoli, G. A. (2017). Weighing the evidence in Peters' rule: does neuronal morphology predict connectivity? *Trends Neurosci.* 40, 63–71. doi: 10.1016/j.tins.2016.11.007

Reimann, M. W., Horlemann, A. L., Ramaswamy, S., Muller, E. B., and Markram, H. (2017). Morphological diversity strongly constrains synaptic connectivity and plasticity. *Cereb. Cortex* 27, 4570–4585. doi: 10.1093/cercor/bhx150

Reimann, M. W., King, J. G., Muller, E. B., Ramaswamy, S., and Markram, H. (2015). An algorithm to predict the connectome of neural microcircuits. *Front. Comput. Neurosci.* 9:120. doi: 10.3389/fncom.2015.00120

Reyes, A., Lujan, R., Rozov, A., Burnashev, N., Somogyi, P., and Sakmann, B. (1998). Target-cell-specific facilitation and depression in neocortical circuits. *Nat. Neurosci.* 1, 279–285. doi: 10.1038/1092

Sancho, L., and Bloodgood, B. L. (2018). Functional distinctions between spine and dendritic synapses made onto parvalbumin-positive interneurons in mouse cortex. *Cell Rep.* 24, 2075–2087. doi: 10.1016/j.celrep.2018.07.070

Sando, R., Jiang, X., and Südhof, T. C. (2019). Latrophilin GPCRs direct synapse specificity by coincident binding of FLRTs and teneurins. *Science* 363:eaav7969. doi: 10.1126/science.aav7969

Sando, R., and Südhof, T. C. (2021). Latrophilin GPCR signaling mediates synapse formation. *eLife* 10:e65717. doi: 10.7554/eLife.65717

Sanes, J. R., and Yamagata, M. (2009). Many paths to synaptic specificity. *Annu. Rev. Cell Dev. Biol.* 25, 161–195. doi: 10.1146/annurev.cellbio.24.110707.175402

Sanes, J. R., and Zipursky, S. L. (2020). Synaptic specificity, recognition molecules, and assembly of neural circuits. *Cell* 181, 536–556. doi: 10.1016/j.cell.2020.04.008

Scala, F., Kobak, D., Bernabucci, M., Bernaerts, Y., Cadwell, C. R., Castro, J. R., et al. (2020). Phenotypic variation of transcriptomic cell types in mouse motor cortex. *Nature* doi: 10.1038/s41586-020-2907-3 [Epub ahead of print].

Schafer, D. P., and Stevens, B. (2015). Microglia function in central nervous system development and plasticity. *Cold Spring Harb. Perspect. Biol.* 7:a020545. doi: 10.1101/cshperspect.a020545

Schmidt, H., Gour, A., Straehle, J., Boergens, K. M., Brecht, M., and Helmstaedter, M. (2017). Axonal synapse sorting in medial entorhinal cortex. *Nature* 549, 469–475. doi: 10.1038/nature24005

Schneider-Mizell, C. M., Bodor, A. L., Collman, F., Brittain, D., Bleckert, A. A., Dorkenwald, S., et al. (2020). Chandelier cell anatomy and function reveal a variably distributed but common signal. *bioRxiv* doi: 10.1101/2020.03.31.018952 [Preprint].

Schroeder, A., Vanderlinden, J., Vints, K., Ribeiro, L. F., Vennekens, K. M., Gounko, N. V., et al. (2018). A modular organization of LRR protein-mediated synaptic adhesion defines synapse identity. *Neuron* 99, 329–344.e7. doi: 10.1016/j.neuron.2018.06.026

Shapson-Coe, A., Januszewski, M., Berger, D. R., Pope, A., Wu, Y. E., Blakely, T., et al. (2021). A connectomic study of a petascale fragment of human cerebral cortex. *bioRxiv* [Preprint].

Shen, K., and Scheiffele, P. (2010). Genetics and cell biology of building specific synaptic connectivity. *Annu. Rev. Neurosci.* 33, 473–507. doi: 10.1146/annurev.neuro.051508.135302

Shepherd, G. M., Stepanyants, A., Bureau, I., Chklovskii, D., and Svoboda, K. (2005). Geometric and functional organization of cortical circuits. *Nat. Neurosci.* 8, 782–790. doi: 10.1038/nn1447

Simi, A., and Studer, M. (2018). Developmental genetic programs and activity-dependent mechanisms instruct neocortical area mapping. *Curr. Opin. Neurobiol.* 53, 96–102. doi: 10.1016/j.conb.2018.06.007

Simon, A., Olah, S., Molnar, G., Szabadics, J., and Tamas, G. (2005). Gap-junctional coupling between neurogliaform cells and various interneuron types in the neocortex. *J. Neurosci.* 25, 6278–6285. doi: 10.1523/JNEUROSCI.1431-05.2005

Skutella, T., and Nitsch, R. (2001). New molecules for hippocampal development. *Trends Neurosci.* 24, 107–113. doi: 10.1016/s0166-2236(00)01717-3

Somogyi, P. (1977). A specific 'axo-axonal' interneuron in the visual cortex of the rat. *Brain Res.* 136, 345–350. doi: 10.1016/0006-8993(77)90808-3

Somogyi, P. (1979). An interneurone making synapses specifically on the axon initial segment of pyramidal cells in the cerebral cortex of the cat [proceedings]. *J. Physiol.* 296, 18–19.

Somogyi, P., Freund, T. F., and Cowey, A. (1982). The axo-axonic interneuron in the cerebral cortex of the rat, cat and monkey. *Neuroscience* 7, 2577–2607. doi: 10.1016/0306-4522(82)90086-0

Song, S., S̈jöström, P. J., Reigl, M., Nelson, S., and Chklovskii, D. B. (2005). Highly nonrandom features of synaptic connectivity in local cortical circuits. *PLoS Biol.* 3:e68. doi: 10.1371/journal.pbio.0030068

Spence, E. F., Dube, S., Uezu, A., Locke, M., Soderblom, E. J., and Soderling, S. H. (2019). In vivo proximity proteomics of nascent synapses reveals a novel regulator of cytoskeleton-mediated synaptic maturation. *Nat. Commun.* 10:386. doi: 10.1038/s41467-019-08288-w

Spruston, N. (2008). Pyramidal neurons: dendritic structure and synaptic integration. *Nat. Rev. Neurosci.* 9, 206–221. doi: 10.1038/nrn2286

Stachniak, T. J., Kastli, R., Hanley, O., Argunsah, A. O., Van Der Valk, E. G. T., Kanatouris, G., et al. (2021). Post-mitotic Prox1 expression controls the final specification of cortical VIP interneuron subtypes. *J. Neurosci.* doi: 10.1523/JNEUROSCI.1021-21.2021 [Epub ahead of print].

Stachniak, T. J., Sylwestrak, E. L., Scheiffele, P., Hall, B. J., and Ghosh, A. (2019). Elfn1-induced constitutive activation of mGluR7 determines frequency-dependent recruitment of somatostatin interneurons. *J. Neurosci.* 39, 4461–4474. doi: 10.1523/JNEUROSCI.2276-18.2019

Staiger, J. F., and Petersen, C. C. H. (2021). Neuronal circuits in barrel cortex for whisker sensory perception. *Physiol. Rev.* 101, 353–415. doi: 10.1152/physrev.00019.2019

Steinecke, A., Hozhabri, E., Tapanes, S., Ishino, Y., Zeng, H., Kamasawa, N., et al. (2017). Neocortical chandelier cells developmentally shape axonal arbors through reorganization but establish subcellular synapse specificity without refinement. *eNeuro* 4:ENEURO.0057-17.2017. doi: 10.1523/ENEURO.0057-17.2017

Stepanyants, A., and Chklovskii, D. B. (2005). Neurogeometry and potential synaptic connectivity. *Trends Neurosci.* 28, 387–394. doi: 10.1016/j.tins.2005.05.006

Stepanyants, A., Hirsch, J. A., Martinez, L. M., Kisvarday, Z. F., Ferecsko, A. S., and Chklovskii, D. B. (2008). Local potential connectivity in cat primary visual cortex. *Cereb. Cortex* 18, 13–28. doi: 10.1093/cercor/bhm027

Stepanyants, A., Tamas, G., and Chklovskii, D. B. (2004). Class-specific features of neuronal wiring. *Neuron* 43, 251–259. doi: 10.1016/j.neuron.2004.06.013

Stogsdill, J. A., and Eroglu, C. (2017). The interplay between neurons and glia in synapse development and plasticity. *Curr. Opin. Neurobiol.* 42, 1–8. doi: 10.1016/j.conb.2016.09.016

Stratford, K. J., Tarczy-Hornoch, K., Martin, K. A., Bannister, N. J., and Jack, J. J. (1996). Excitatory synaptic inputs to spiny stellate cells in cat visual cortex. *Nature* 382, 258–261. doi: 10.1038/382258a0

Stuart, G. J., and Spruston, N. (2015). Dendritic integration: 60 years of progress. *Nat. Neurosci.* 18, 1713–1721. doi: 10.1038/nn.4157

Südhof, T. C. (2018). Towards an understanding of synapse formation. *Neuron* 100, 276–293. doi: 10.1016/j.neuron.2018.09.040

Sun, Y. C., Chen, X., Fischer, S., Lu, S., Zhan, H., Gillis, J., et al. (2021). Integrating barcoded neuroanatomy with spatial transcriptional profiling enables identification of gene correlates of projections. *Nat. Neurosci.* 24, 873–885. doi: 10.1038/s41593-021-00842-4

Suto, F., Tsuboi, M., Kamiya, H., Mizuno, H., Kiyama, Y., Komai, S., et al. (2007). Interactions between plexin-A2, plexin-A4, and semaphorin 6A control lamina-restricted projection of hippocampal mossy fibers. *Neuron* 53, 535–547. doi: 10.1016/j.neuron.2007.01.028

Sylwestrak, E. L., and Ghosh, A. (2012). Elfn1 regulates target-specific release probability at CA1-interneuron synapses. *Science* 338, 536–540. doi: 10.1126/science.1222482

Tai, Y., Gallo, N. B., Wang, M., Yu, J. R., and Van Aelst, L. (2019). Axo-axonic innervation of neocortical pyramidal neurons by GABAergic Chandelier cells requires AnkyrinG-associated L1CAM. *Neuron* 102, 358–372.e9. doi: 10.1016/j.neuron.2019.02.009

Tai, Y., Janas, J. A., Wang, C. L., and Van Aelst, L. (2014). Regulation of chandelier cell cartridge and bouton development via DOCK7-mediated ErbB4 activation. *Cell Rep.* 6, 254–263. doi: 10.1016/j.celrep.2013.12.034

Tan, Z., Hu, H., Huang, Z. J., and Agmon, A. (2008). Robust but delayed thalamocortical activation of dendritic-targeting inhibitory interneurons. *Proc. Natl. Acad. Sci. U. S. A.* 105, 2187–2192. doi: 10.1073/pnas.0710628105

Tarusawa, E., Sanbo, M., Okayama, A., Miyashita, T., Kitsukawa, T., Hirayama, T., et al. (2016). Establishment of high reciprocal connectivity between clonal cortical neurons is regulated by the Dnmt3b DNA methyltransferase and clustered protocadherins. *BMC Biol.* 14:103. doi: 10.1186/s12915-016-0326-6

Tasic, B., Menon, V., Nguyen, T. N., Kim, T. K., Jarsky, T., Yao, Z., et al. (2016). Adult mouse cortical cell taxonomy revealed by single cell transcriptomics. *Nat. Neurosci.* 19, 335–346. doi: 10.1038/nn.4216

Tasic, B., Yao, Z., Graybuck, L. T., Smith, K. A., Nguyen, T. N., Bertagnolli, D., et al. (2018). Shared and distinct transcriptomic cell types across neocortical areas. *Nature* 563, 72–78. doi: 10.1038/s41586-018-0654-5

Thomson, A. M., and Lamy, C. (2007). Functional maps of neocortical local circuitry. *Front. Neurosci.* 1:19–42. doi: 10.3389/neuro.01.1.1.002.2007

Tomioka, N. H., Yasuda, H., Miyamoto, H., Hatayama, M., Morimura, N., Matsumoto, Y., et al. (2014). Elfn1 recruits presynaptic mGluR7 in trans and its loss results in seizures. *Nat. Commun.* 5:4501. doi: 10.1038/ncomms5501

Tran, T. S., Rubio, M. E., Clem, R. L., Johnson, D., Case, L., Tessier-Lavigne, M., et al. (2009). Secreted semaphorins control spine distribution and morphogenesis in the postnatal CNS. *Nature* 462, 1065–1069. doi: 10.1038/nature08628

Tremblay, R., Lee, S., and Rudy, B. (2016). GABAergic interneurons in the neocortex: from cellular properties to circuits. *Neuron* 91, 260–292. doi: 10.1016/j.neuron.2016.06.033

Udvary, D., Harth, P., Macke, J. H., Hege, H.-C., De Kock, C. P., Sakmann, B., et al. (2021). The impact of neuronal structure on cortical network architecture. *bioRxiv* doi: 10.1101/2020.11.13.381087 [Preprint].

Varga, C., Lee, S. Y., and Soltesz, I. (2010). Target-selective GABAergic control of entorhinal cortex output. *Nat. Neurosci.* 13, 822–824. doi: 10.1038/nn.2570

Wang, X., and Sun, Q. Q. (2012). Characterization of axo-axonic synapses in the piriform cortex of Mus musculus. *J. Comp. Neurol.* 520, 832–847. doi: 10.1002/cne.22792

Wang, X., Tucciarone, J., Jiang, S., Yin, F., Wang, B. S., Wang, D., et al. (2019). Genetic single neuron anatomy reveals fine granularity of cortical axo-axonic cells. *Cell Rep.* 26, 3145–3159.e5. doi: 10.1016/j.celrep.2019.02.040

Wang, Y., Gupta, A., Toledo-Rodriguez, M., Wu, C. Z., and Markram, H. (2002). Anatomical, physiological, molecular and circuit properties of nest basket cells in the developing somatosensory cortex. *Cereb. Cortex* 12, 395–410. doi: 10.1093/cercor/12.4.395

Wang, Y., Markram, H., Goodman, P. H., Berger, T. K., Ma, J., and Goldman-Rakic, P. S. (2006). Heterogeneity in the pyramidal network of the medial prefrontal cortex. *Nat. Neurosci.* 9, 534–542. doi: 10.1038/nn1670

Wefelmeyer, W., Cattaert, D., and Burrone, J. (2015). Activity-dependent mismatch between axo-axonic synapses and the axon initial segment controls neuronal output. *Proc. Natl. Acad. Sci. U. S. A.* 112, 9757–9762. doi: 10.1073/pnas.1502902112

Wen, Q., Stepanyants, A., Elston, G. N., Grosberg, A. Y., and Chklovskii, D. B. (2009). Maximization of the connectivity repertoire as a statistical principle governing the shapes of dendritic arbors. *Proc. Natl. Acad. Sci. U. S. A.* 106, 12536–12541. doi: 10.1073/pnas.0901530106

West, D. C., Mercer, A., Kirchhecker, S., Morris, O. T., and Thomson, A. M. (2006). Layer 6 cortico-thalamic pyramidal cells preferentially innervate interneurons and generate facilitating EPSPs. *Cereb. Cortex* 16, 200–211. doi: 10.1093/cercor/bhi098

Wu, P. R., Cho, K. K. A., Vogt, D., Sohal, V. S., and Rubenstein, J. L. R. (2017). The cytokine CXCL12 promotes basket interneuron inhibitory synapses in the medial prefrontal cortex. *Cereb. Cortex* 27, 4303–4313. doi: 10.1093/cercor/bhw230

Xie, Y., Hkuan, A. T., Wang, W., Herbert, Z. T., Mosto, O., Olukoya, O., et al. (2020). Astrocyte-neuron crosstalk through Hedgehog signaling mediates cortical circuit assembly. *bioRxiv* [Preprint].

Xu, H., Jeong, H. Y., Tremblay, R., and Rudy, B. (2013). Neocortical somatostatin-expressing GABAergic interneurons disinhibit the thalamorecipient layer 4. *Neuron* 77, 155–167. doi: 10.1016/j.neuron.2012.11.004

Yang, J. M., Shen, C. J., Chen, X. J., Kong, Y., Liu, Y. S., Li, X. W., et al. (2019). *erbb4* deficits in Chandelier cells of the medial prefrontal cortex confer cognitive dysfunctions: implications for schizophrenia. *Cereb. Cortex* 29, 4334–4346. doi: 10.1093/cercor/bhy316

Yao, Z., Liu, H., Xie, F., Fischer, S., Booeshaghi, A. S., Adkins, R. S., et al. (2020). An integrated transcriptomic and epigenomic atlas of mouse primary motor cortex cell types. *bioRxiv* doi: 10.1101/2020.02.29.970558 [Preprint].

Yassin, L., Benedetti, B. L., Jouhanneau, J. S., Wen, J. A., Poulet, J. F., and Barth, A. L. (2010). An embedded subnetwork of highly active neurons in the neocortex. *Neuron* 68, 1043–1050. doi: 10.1016/j.neuron.2010.11.029

Yu, Y. C., Bultje, R. S., Wang, X., and Shi, S. H. (2009). Specific synapses develop preferentially among sister excitatory neurons in the neocortex. *Nature* 458, 501–504. doi: 10.1038/nature07722

Yu, Y. C., He, S., Chen, S., Fu, Y., Brown, K. N., Yao, X. H., et al. (2012). Preferential electrical coupling regulates neocortical lineage-dependent microcircuit assembly. *Nature* 486, 113–117. doi: 10.1038/nature10958

Yuste, R. (2011). Dendritic spines and distributed circuits. *Neuron* 71, 772–781. doi: 10.1016/j.neuron.2011.07.024

Yuste, R., Hawrylycz, M., Aalling, N., Aguilar-Valles, A., Arendt, D., Armananzas, R., et al. (2020). A community-based transcriptomics classification and nomenclature of neocortical cell types. *Nat. Neurosci.* 23, 1456–1468. doi: 10.1038/s41593-020-0685-8

Zeisel, A., Munoz-Manchado, A. B., Codeluppi, S., Lonnerberg, P., La Manno, G., Jureus, A., et al. (2015). Brain structure. Cell types in the mouse cortex and hippocampus revealed by single-cell RNA-seq. *Science* 347, 1138–1142. doi: 10.1126/science.aaa1934

Zeng, H., and Sanes, J. R. (2017). Neuronal cell-type classification: challenges, opportunities and the path forward. *Nat. Rev. Neurosci.* 18, 530–546. doi: 10.1038/nrn.2017.85

Zhang, X. J., Li, Z., Han, Z., Sultan, K. T., Huang, K., and Shi, S. H. (2017). Precise inhibitory microcircuit assembly of developmentally related neocortical interneurons in clusters. *Nat. Commun.* 8:16091. doi: 10.1038/ncomms16091

Ziv, N. E., and Smith, S. J. (1996). Evidence for a role of dendritic filopodia in synaptogenesis and spine formation. *Neuron* 17, 91–102. doi: 10.1016/s0896-6273(00)80283-4

Conflict of Interest: The authors declare that the research was conducted in the absence of any commercial or financial relationships that could be construed as a potential conflict of interest.

Publisher's Note: All claims expressed in this article are solely those of the authors and do not necessarily represent those of their affiliated organizations, or those of the publisher, the editors and the reviewers. Any product that may be evaluated in this article, or claim that may be made by its manufacturer, is not guaranteed or endorsed by the publisher.

frontiers in Neural Circuits

ORIGINAL RESEARCH
published: 24 September 2021
doi: 10.3389/fncir.2021.718270

The Role of Hub Neurons in Modulating Cortical Dynamics

Eyal Gal[1,2†], Oren Amsalem[2*†], Alon Schindel[2], Michael London[1,2], Felix Schürmann[3], Henry Markram[3] and Idan Segev[1,2*]*

[1] The Edmond & Lily Safra Center for Brain Sciences, The Hebrew University of Jerusalem, Jerusalem, Israel, [2] Department of Neurobiology, The Hebrew University of Jerusalem, Jerusalem, Israel, [3] Blue Brain Project, École Polytechnique Fédérale de Lausanne (EPFL), Campus Biotech, Geneva, Switzerland

Many neurodegenerative diseases are associated with the death of specific neuron types in particular brain regions. What makes the death of specific neuron types particularly harmful for the integrity and dynamics of the respective network is not well understood. To start addressing this question we used the most up-to-date biologically realistic dense neocortical microcircuit (NMC) of the rodent, which has reconstructed a volume of 0.3 mm^3 and containing 31,000 neurons, ∼37 million synapses, and 55 morphological cell types arranged in six cortical layers. Using modern network science tools, we identified hub neurons in the NMC, that are connected synaptically to a large number of their neighbors and systematically examined the impact of abolishing these cells. In general, the structural integrity of the network is robust to cells' attack; yet, attacking hub neurons strongly impacted the small-world topology of the network, whereas similar attacks on random neurons have a negligible effect. Such hub-specific attacks are also impactful on the network dynamics, both when the network is at its spontaneous synchronous state and when it was presented with synchronized thalamo-cortical visual-like input. We found that attacking layer 5 hub neurons is most harmful to the structural and functional integrity of the NMC. The significance of our results for understanding the role of specific neuron types and cortical layers for disease manifestation is discussed.

Keywords: network science, cortical microcircuitry, network synchronicity, scale free network, hub neurons, small world topology, cell ablation strategy

OPEN ACCESS

Edited by:
Yoshiyuki Kubota, National Institute for Physiological Sciences (NIPS), Japan

Reviewed by:
Yasuhiro Tsubo, Ritsumeikan University, Japan
Diana Martinez, Cooper Medical School of Rowan University, United States

***Correspondence:**
Eyal Gal
eyal.gal@mail.huji.ac.il
Oren Amsalem
oren.amsalem1@mail.huji.ac.il
Idan Segev
idan@lobster.ls.huji.ac.il

† These authors have contributed equally to this work and share first authorship

Received: *31 May 2021*
Accepted: *24 August 2021*
Published: *24 September 2021*

Citation:
Gal E, Amsalem O, Schindel A, London M, Schürmann F, Markram H and Segev I (2021) The Role of Hub Neurons in Modulating Cortical Dynamics. Front. Neural Circuits 15:718270. doi: 10.3389/fncir.2021.718270

INTRODUCTION

Research at the macro- and peso-scale brain anatomy has demonstrated a clear connection between structure and function. Indeed, the global network structure of the brain was shown to be altered in diseases such as schizophrenia (Rubinov and Bullmore, 2013), bipolar disorder (Syan et al., 2018) and others (Stam, 2014). Yet, pathology takes place at the micro-scale, at the cellular and synaptic level architecture of neuronal microcircuits. How the connectomics at this level shape the dynamics and functionality of biological circuits is indeed a key question in neuroscience (Abbott et al., 2020; Amsalem et al., 2020; Turner et al., 2020). Of particular interest is the impact of structural disruption of the connectome, whether due to natural aging or due to disease. These two types of disruption are rather different. Whereas a non-selective general reduction in the number of cells was found in the aging brain, recent studies showed selective cell vulnerability associated with certain pathologies. For example, a significant decrease in the number of specific cell types in

cortical areas were found in Alzheimer's disease (Stranahan and Mattson, 2010; Fu et al., 2018; Murray et al., 2018), multiple sclerosis (Schirmer et al., 2019) and Parkinson's disease (Hammond et al., 2007).

Experimental investigation of the role of specific cell populations in the neocortex has advanced significantly in recent years. Optogenetic methods (Deisseroth, 2015) together with genetic dissection of specific neurons (Luo et al., 2018) enables precise recording and manipulation (silencing and activating) of specific neuronal populations. Manipulating the neural activity of specific cell types during *in vivo* experiments is presently used to affect animal behavior (Guo et al., 2015; Carrillo-Reid et al., 2019; Robinson et al., 2020), but the effects of such cell-type-specific manipulations on circuit dynamics are rarely characterized at the network scale (Cardin et al., 2009; Pouille et al., 2009; Adesnik and Scanziani, 2010; Xue et al., 2014; Bitzenhofer et al., 2017). Consequently, we currently lack understanding of the role of particular cell populations, e.g., in the case of specific diseases, in shaping neural network dynamics and eventually network functionality.

To address this gap, we hereby utilized network theoretical approaches to explore the correlates between microcircuitry structure and function, as theoretical approaches provided new insights into the relationship between structure and function of neural networks (Newman, 2003; Avena-Koenigsberger et al., 2017; Nolte et al., 2020). Toward this end we simulated the most up-to-date, biologically realistic, dense digital reconstruction of a neocortical microcircuit, NMC (Markram et al., 2015). This 0.3 mm^3 cortical circuit contains some 31,000 neurons, ∼37 million excitatory and inhibitory synapses, and 55 morphological cell types (m-types). This model circuit enables an unprecedented opportunity to directly investigate the impact of network structure on system dynamics by introducing cell-specific and layer-specific attack/damage while measuring the collective neural activity under different physiological conditions.

This cortical microcircuit displays structured architecture with multiple emerging network features at multiple levels, from the local single-cell level, through clusters and motifs of two and three neurons, to the global network-wide architectures (Gal et al., 2017). In particular, at the single-cell level, the circuit contained highly connected neurons ("hub neurons") that either received or made significantly more connections than average. Moreover, these hub neurons belong to a surprisingly small number of cell-type subclasses and are densely interconnected among themselves forming a cell-type-specific core of hubs ("rich club"). Among all 55 m-types that constitute the mouse somatosensory cortex, the hubs belonged mainly to pyramidal cells from the deeper layers 4–6. Hub neurons with a high number of outgoing connections ("out hubs") tend to arise from the intermediate layers (4–5), and those with a high number of incoming connections ("in hubs") were positioned more deeply (in layers 5–6). Surprisingly, the existence of such cell-type-specific wiring specificities was found to be essentially unavoidable, emerging mostly from the asymmetrical structure of individual cortical neurons (Gal et al., 2019). However, determining the functional role of such ubiquitous wiring specificities in shaping the cortical circuit dynamics remains elusive (Setareh et al., 2017; Luccioli et al., 2018). Indeed, the question emerges: is the death ("attack") of these hub cells, or of specific cell types, in realistic cortical microcircuits more harmful to the network dynamics as compared to that of other cell types?

Using network science tools, we first analyzed how the circuit structural connectivity was impacted after removing these cells. At the global level, the structural connectivity demonstrated small-world topology with an average synaptic distance of 2.5 synapses separating any two neurons. In the present study, we measured the increase in the average synaptic distance (mean shortest path in a network; see section "Materials and Methods") before and after hub attacks; this measure is related to the efficiency of information flow across the network (Watts and Strogatz, 1998). Another respective measure of the network topology is the clustering coefficient, which measures by the tendency of nodes to cluster together (see section "Materials and Methods"). When a network simultaneously displays a short-averaged path length and a high clustering level it is termed as a "small-world network" (Watts and Strogatz, 1998). Reduction in the "small-worldness" of the networks might imply a reduction in efficiency of information exchange and capacity for associative memory (Bullmore and Sporns, 2009).

We next used several measures to evaluate network dynamics such as mean firing rate, coefficient of variation (CV), SPIKE-synchronization (Kreuz et al., 2015), etc. Each measure provides us with different aspects of the circuit activity and, hence, helps us understand how targeted attacks on hub neurons are more disruptive to the network functionality than attacking the same number of neurons randomly. Combining these results with structural network measures following cells' attack sheds new light on the robustness of the NMC to a variety of attacks and, at the same time, on the functional sensitivity of the network to some of these attacks. These findings provided important insights into the impact of the death of specific cell types (e.g., due to certain diseases) on the dynamics and functionality of local cortical microcircuits.

RESULTS

Hub Neuron Attacks Impact the NMC Small-World Topology

To explore the structural and functional impact of attacking highly-connected hub neurons we started by ranking all neurons according to their total degree (total number of pre- and post-synaptic cells connected to a given neuron). We then removed (attacked) different quantities of these neurons, starting from the highest degree hub cells to the lowest degree.

To quantify the structural effect, we first measured the overall connectedness of the network, as captured by the size of the network's largest connected component (giant component size; see section "Materials and Methods"). We highlight two extreme outcomes on network architecture following hubs attack (**Figure 1A**). On one extreme, the removal of hub neurons may completely break the network into multiple smaller unconnected components (**Figure 1A** top; "breakable"). On the other extreme, the removal of hub neurons will not break

the network and the remaining neurons will remain in one connected giant component (**Figure 1A** bottom; "unbreakable"). A finer structural feature utilized here, which relates to the efficiency of network communication and computation, is the small-world topology of the network. This measure relies on two opposing requirements: a short path length between any pair of nodes/neurons (**Figure 1B**, right; see section "Materials and Methods") and clustered interconnectivity, *c*, within groups of nodes (**Figure 1B**, left; see section "Materials and Methods"). Thus, the "small-worldness" of a neural network reflects the degree in which it balances the needs for global integration and local segregation of neural information (Sporns, 2013a).

We found that the giant component of the NMC is not broken by hub-attack as its size only negligibly decreased when a large number of hub neurons are attacked (**Figure 1C**, black line; see section "Materials and Methods"), showing that the global integrity of the circuit is robust to such attacks. Moreover, the effect was similar to respective random cell attacks (**Figure 1C**, orange line) in which a similar number of cells were selected randomly (see section "Materials and Methods"). This implies that the NMC circuit is of the unbreakable type. In contrast, the small-world topology of the circuit is more sensitive to attacks on hub neurons. For example, attacking 5,000 hub neurons increased the path length from 2.48 to 2.69 (8% increase, **Figure 1D**) while reducing *c* from 0.029 to 0.025 (12% reduction, **Figure 1E**). To test whether this disrupted small-world topology is expected by chance and resulting merely due to the number of eliminated nodes, we performed control random attacks with matching number of nodes (**Figures 1C–E**). We found that the disruption of both path-length and clustering due to hub attacks were significantly stronger than that expected from the random attacks ($p < 0.001$ for both, two-tailed Wilcoxon rank sum test; $n_1 = 10$, $n_2 = 100$; see section "Materials and Methods"). Additionally, the observed disruptions were found significant ($P < 0.001$, two-tailed Wilcoxon rank sum test; $n_1 = 10$, $n_2 = 100$; see section "Materials and Methods") compared to that of randomly attacked networks with similar numbers of eliminated edges (**Supplementary Figure 1**).

Hub Neurons Are Key for Network Synchrony

The structural analysis has uncovered the disruptive effect of hub attacks on the small-world properties of the neocortical microcircuit. However, the functional implications of such structural changes are not trivial. To elucidate the functional impact of hub neurons on network dynamics, we simulated NMC networks following different cells' attacks and examined various functional features of network activity.

It has been shown (Markram et al., 2015) that at an extracellular calcium concentration of 1.4 mM the NMC network generates spontaneously synchronous bursts at ∼1 Hz (**Figure 2A** and see section "Materials and Methods"). At this synchronous state, the cells' mean firing rate is 3.7 Hz, their CV is 2.16 and SPIKE-synchronization measure is 0.25 (see section "Materials and Methods"). We simulated the circuit after removing 2,977 hub neurons (**Figure 2B**) or 2,977 random neurons (**Figure 2D**). Removal of hub neurons markedly reduced the number of bursts in the network (**Figure 2B**), whereas the bursting properties of the network were unaltered for the respective random attack (**Figure 2D**). Increasing further the number of attacked hub neurons to 7,993 completely abolished the bursting activity of the network, shifting it to the asynchronous state (**Figure 2C**) whereas it did not change the burstiness in the case of random cells removal (**Figure 2E**). **Figure 2F** summarizes the change in burst number due to different strengths of attacks. In addition to the reduction in burst activity due to removal of hub cells from the circuit, the coefficient of variation (std divided by mean ISI), CV, firing rate and spike-synchronization all showed a stronger reduction compared to removal of random neurons (**Figures 2G–I**).

Because hub neurons are mostly excitatory (Gal et al., 2017), hub attacks primarily remove excitatory neurons from the network. Indeed, in all analyzed hub attacks, ranging up to 15,000 neurons, the percentage of excitatory neurons in the attacked neurons was above 97%, but when attacking random nodes, we converge to the full circuit distribution of E/I neurons (85% excitatory). To address this discrepancy, we performed random attacks that matched both the number and the E/I identity of nodes (**Supplementary Figure 2** and see section "Materials and Methods"). Indeed, this attack was more disruptive than the completely random attacks, but still less than the hub attacks. We also show that the number of edges attacked is not the main factor for this effect (**Supplementary Figure 2**). This analysis demonstrates that, in the synchronous state, the impact of a neuron on the generations of collective synchrony in the NMC is more affected by their embedding in the network ("hubiness") rather than by their physiological effect (the network E/I distribution).

Finally, we repeated the above analysis also for the asynchronous state, which is induced by setting the calcium concentration in the NMC simulations to 1.25 mM (Markram et al., 2015). At this state, the difference between attacking hubs versus random neurons is still significant, but not prominent as in the asynchronous case (**Supplementary Figure 3**; see section "Materials and Methods"). Indeed, the asynchronous state is, in general, more robust to cell-attacks.

Functional Implication of Layer-Specific Hub Attacks

We showed that hub neurons are more effective in driving network synchrony. These hubs potentially belong to multiple cell-types at the different layers. To further detail the impact layer-specific hubs, we measured the connectivity among excitatory and inhibitory cells within and between layers (**Figure 3A**). To compactly examine the connectivity among all 55 cell types in the NMC, we employed a force-directed graph drawing algorithm, whose 55 nodes depict the cell types whereas edge strengths correspond to the pairwise connection probability. In this presentation, tightly connected nodes will tend to appear closer. Inspecting the original network, the existence of large cell-type groups and clusters can be seen within each layer (**Figure 3B** large nodes). After attacking 15,000 hub neurons, several changes

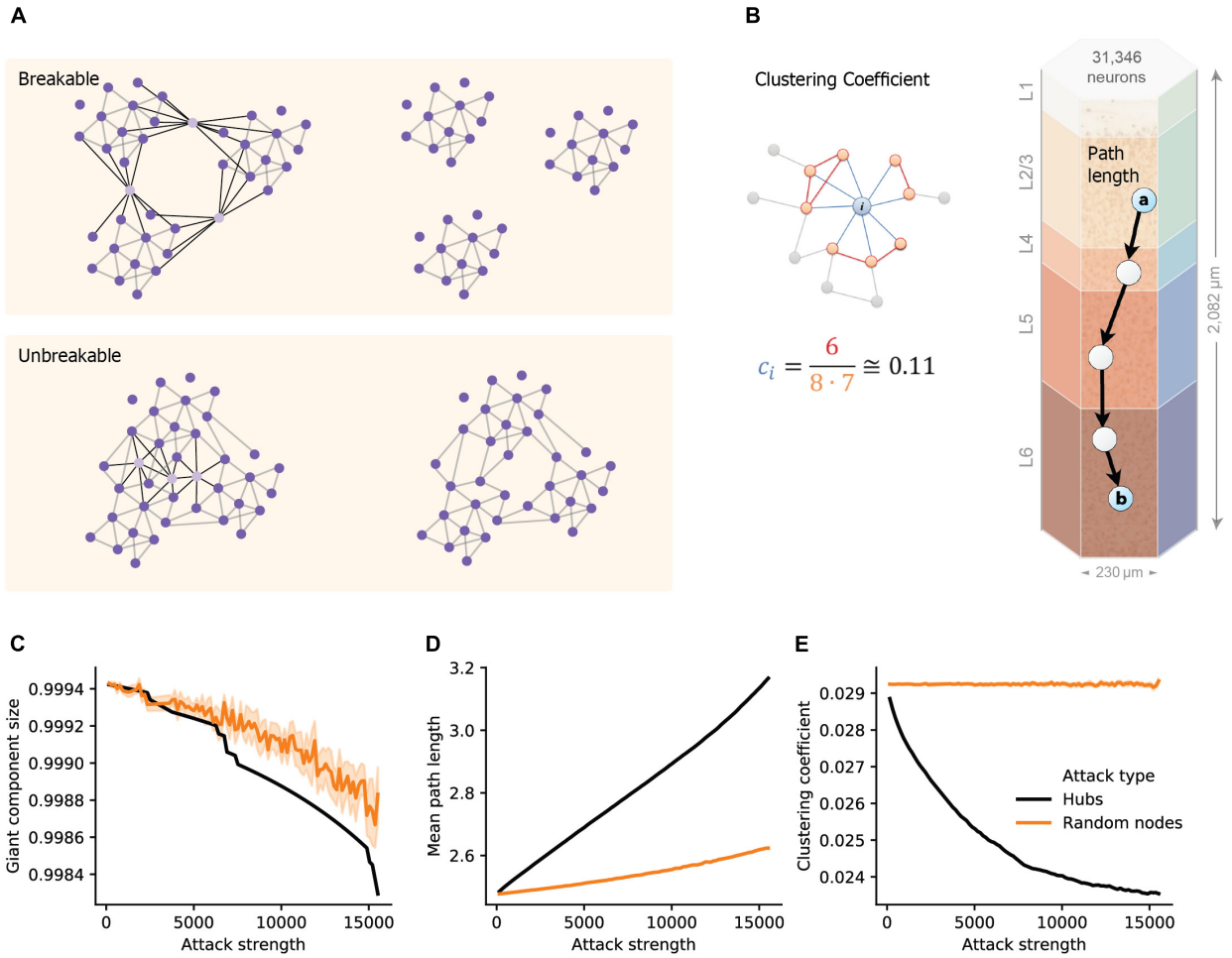

FIGURE 1 | Structural disruption of cortical microcircuits following attacks on hub neurons. **(A)** Schematic illustration of two network architectures having different sensitivity to a similar targeted hubs attack. (Top) The case of breakable network whereby an attack on 3 hub neurons disintegrates the network into 3 separate sub-networks. (Bottom) The case of an unbreakable network which, after an attack on 3 hub neurons, remains fully connected. **(B)** Schematic illustration of the two features used to define small-world networks. (Right) The shortest path length connecting two nodes (cells "a" and "b", overplayed on the modeled neocortical microcircuit). (Left) The local clustering coefficient of a node *i*, c_i, which is the density of connections among the neighbors of this node. In the example shown, node *i*, has 8 neighbors; among them only 6 connections out of all 8·(8–1) = 56 possible connections (c_i = 6/56 ≅ 0.11). **(C)** The size of the giant component in the NMC as a function of the number of hubs attacked (Attack strength), black line, compared to the corresponding random attacks (orange line), demonstrating that the NMC network is "unbreakable." **(D)** Mean path-length and **(E)** mean clustering coefficient following hub attacks (black) versus random attack (orange). These two features are particularly sensitive to hub attack. Light orange depicts 95% confidence interval in all figures.

were prominent (**Figure 3C**). The network layout had spread more widely, indicating that the strength of the connections between cell types is reduced. Additionally, the large nodes of L5 almost disappeared, hinting to their possible impact on disruption of network functionality (see below).

To test the importance of the different layers for network activity we performed layer-specific hub attacks by simulating the circuit while removing hub neurons in specific layers. We found that, in general, attacking L5 hub neurons is the most disruptive attack as it caused the largest change in all the functional measures used (**Figures 3D,F,G**, but see the impact of L4 in **Figure 3E**). When revisiting the high-level circuit connectivity (**Figure 3A**) one observes that L5 excitatory cells are the most interconnected population in the circuit per cell (the overall percentage of incoming and outgoing connections); this is probably the reason for the high functional influence of L5 attack. L6 attacks also resulted in a large change of the functional measurements except for the number of bursts; similarly, L6 excitatory cells are also relatively highly interconnected (**Figure 3A**). We also note that when attacking L2/3 there is a slight increase in the network firing rate, this might be due to the relatively large part of inhibitory neurons in this layer.

We summarize this section by noting that attacking hub neurons is most disruptive to network dynamics when hub neurons are attacked at all layers (**Figures 3D–G**, dashed black line). Layer 5 is the most-sensitive layer to such an attack. As neurons in different cortical layers belong to different genetic

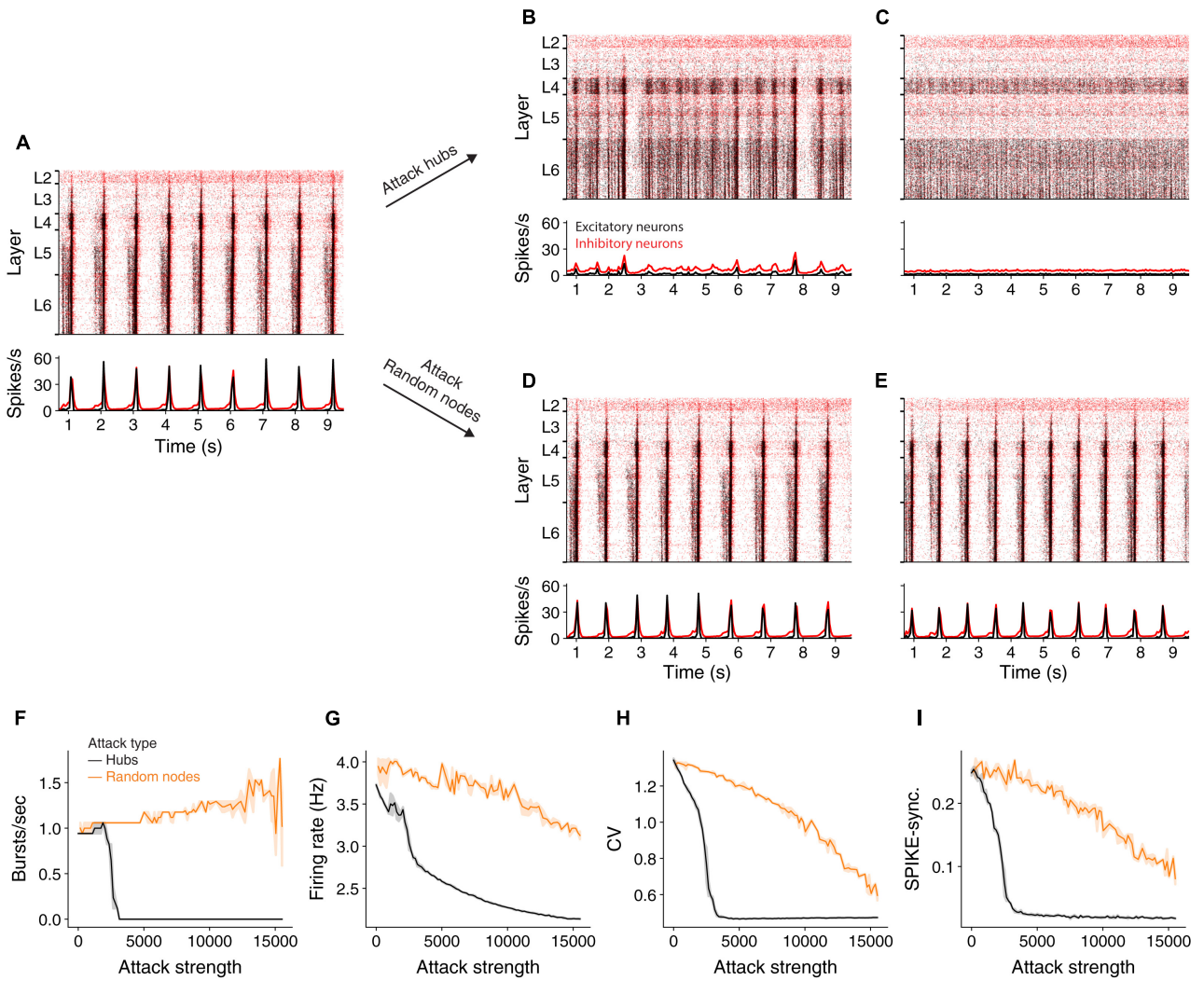

FIGURE 2 | Effect of hub attacks on the dynamics of the NMC network in the synchronous regime. **(A)** Raster plot (top) and time histogram (bottom) of the NMC spiking activity during spontaneous bursting state (see section "Materials and Methods"). In this state, all cortical layers tend to burst synchronously at about 1 Hz, with lower layers starting to fire earlier. **(B,C)** Same as **(A)** after attacking 2,977 and 7,993 hub neurons, respectively. **(D,E)** As in **(B,C)** but for respective random attacks. **(F,G)** Impact of hubs attack (black) versus random attack (orange) on network activity as a function of attack strength. **(F)** Impact on the number of bursts/sec. **(G)** Impact on average firing rate. **(H)** The impact on the coefficient of variation. **(I)** On global SPIKE synchronization measure. For all measures, hub attack is significantly more impactful (light orange depicts 95% confidence interval).

types (Gouwens et al., 2019; Yuste et al., 2020), this result shows that, although the same number of neurons might be degraded due to different pathologies that target specific genetic cell types (e.g., L5 thick-tufted pyramidal cells), they will have a very different impact on the overall dynamics of the cortical network and, thus, on the manifestation of specific diseases.

Functional Implication of Hub Cells on Thalamic Input Processing

The above sections have demonstrated that hub attacks are significantly more effective in disrupting circuit-wide synchronization in the spontaneous synchronized case. In this section, we set to test whether this observation is general enough, and also valid for the case where the synchronized activity is generated by realistic sensory input. Toward this end we innervated the NMC circuit by 574 thalamic fibers (the thalamo-cortical, TC, input). These TC axons project mostly to neurons in lower layers 3 and 5 (**Figure 4A**), where some neurons might receive up to 750 thalamic synapses. Each reconstructed axon is making synapses on dendrites that are adjacent to its path (**Figure 4B**; see section "Materials and Methods"), functionally impacting a vertically confined space (Amsalem et al., 2020).

For these simulations we set the calcium concentration value to 1.25 mM; this results in the network being in a spontaneous asynchronous state (as in **Supplementary Figure 3A**; see

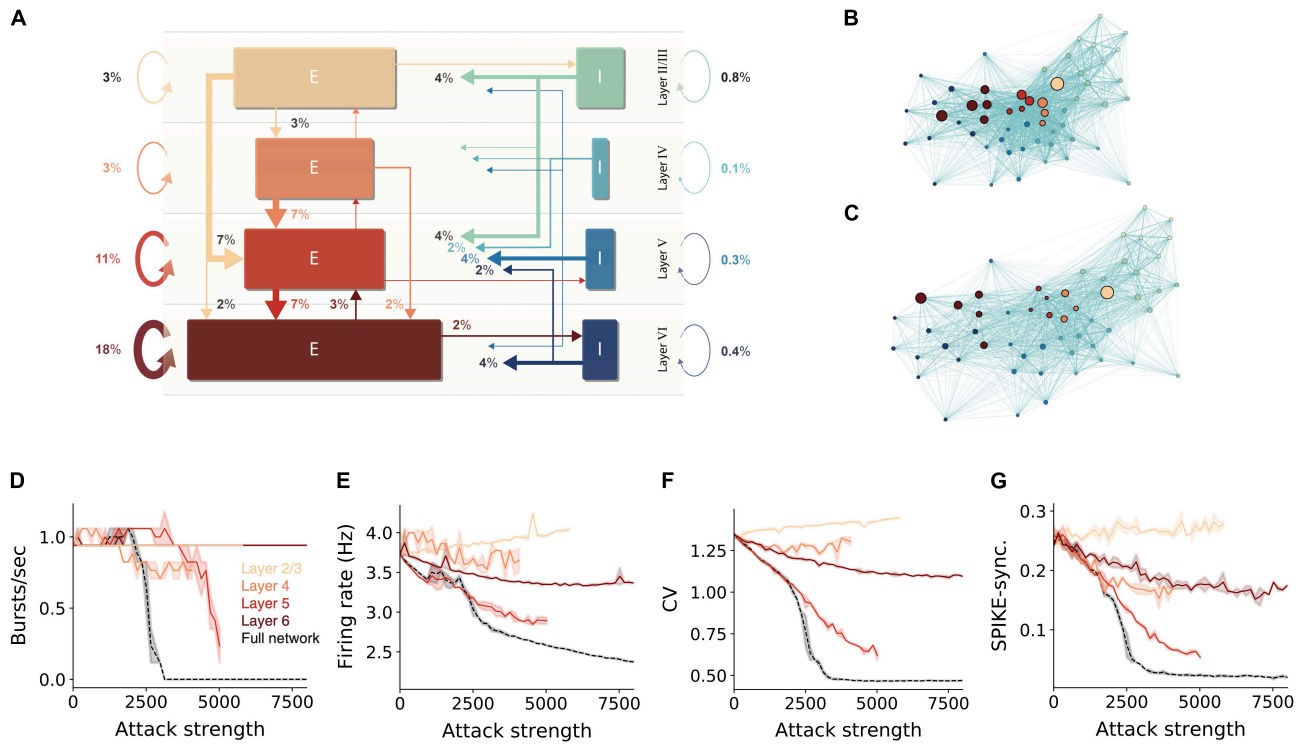

FIGURE 3 | Sensitivity of network dynamic to hub attack is mostly attributed to attacks on L5 PCs. **(A)** Percentages of synapses for excitatory (brown-red arrows) and inhibitory (blue-green arrows) connections in the NMC microcircuit (layer 1 omitted). Arrow width and corresponding numbers indicate the percentage of total synapses formed by this pathway (omitted for pathways with <1% of synapses). The total percentage of plotted synapses is 98%; the remaining 2% originate in layer 1. Rectangle sizes are proportional to the sizes of the corresponding number of excitatory or inhibitory populations. **(B)** The connectivity among layers and cell-types is visualized using the force-directed graph algorithm (see section "Materials and Methods"). The network is composed of 55 morphological cell-types (circular nodes, colors match to that in **A**); edges strength corresponds to pairwise connection probabilities. Strongly connected cell-types are displayed closer in space. **(C)** Same as **(B)**, but for the network following an attack on 15,000 hub neurons. Note the disappearance of the large nodes in Layer 5. **(D–G)** Different quantification of network activity for layer-specific hub attack, global hub attack and random nodes attack. **(D)** Number of bursts/sec, **(E)** average network firing rate, **(F)** coefficient of variation, **(G)** global SPIKE synchronization measure (see section "Materials and Methods"). Note that attack of L5 pyramidal cells is the most disruptive layer attack.

also **Figure 15** and **Supplementary Figure 12** in Markram et al., 2015). We then simulated a grating drifting at 1 Hz by generating the firing rate of the thalamic axons from an inhomogeneous Poisson process with a time-varying rate that followed a sinusoidal function (**Figure 4C**; see section "Materials and Methods"). The circuit responded by following the oscillatory input firing with highly time-locked synchronized bursts of spikes at 1 Hz (**Figure 4D**). We repeated the simulation following the attack on 2,500 random neurons (**Figure 4E**) or 2,500 hub neurons (**Figure 4F**). In the random attack the circuit continued to follow the oscillatory input and the response remained synchronized to the input. However, following attack on hub neurons, the circuit response was much less synchronized.

We next quantified the circuit activity using SPIKE-synchronization time profile in response to the thalamic input for different cases (**Figure 4G**). The blue line in this figure shows the spike-synchronization measure of the TC axons whereas the gray line depicts the spike-synchronization of the cortical neurons. We found that the circuit strongly sharpens the synchronicity of the thalamic input (**Figure 4G**, compare gray to blue line), and that attacking random nodes (in this case 2,500) only slightly reduced this sharpening (orange line). In contrast, attacking (2,500) hub neurons reduced the synchronization in response to the TC input dramatically (**Figure 4G**, black line); this case is even less synchronized than the thalamic input itself (**Figure 4G**, compare black line to blue line). We further conducted a complete set of simulations while attacking random or hubs neurons, and quantified different functional features (**Figures 4H–K**). Hub attacks were much more destructive compared to the random attacks and caused a larger change of all measures. Interestingly removing hub neurons reduced the SPIKE-synchronization profile to a value which is lower than that of the input, showing the strong dependence of the circuit ability to follow and sharpen synchronized input on hub neurons. These results highlight the importance of hub neurons in processing sensory input, clearly demonstrating that the integrity of the cortical hub neurons is critical for the fast and reliable response of the cortical circuit to sensory information.

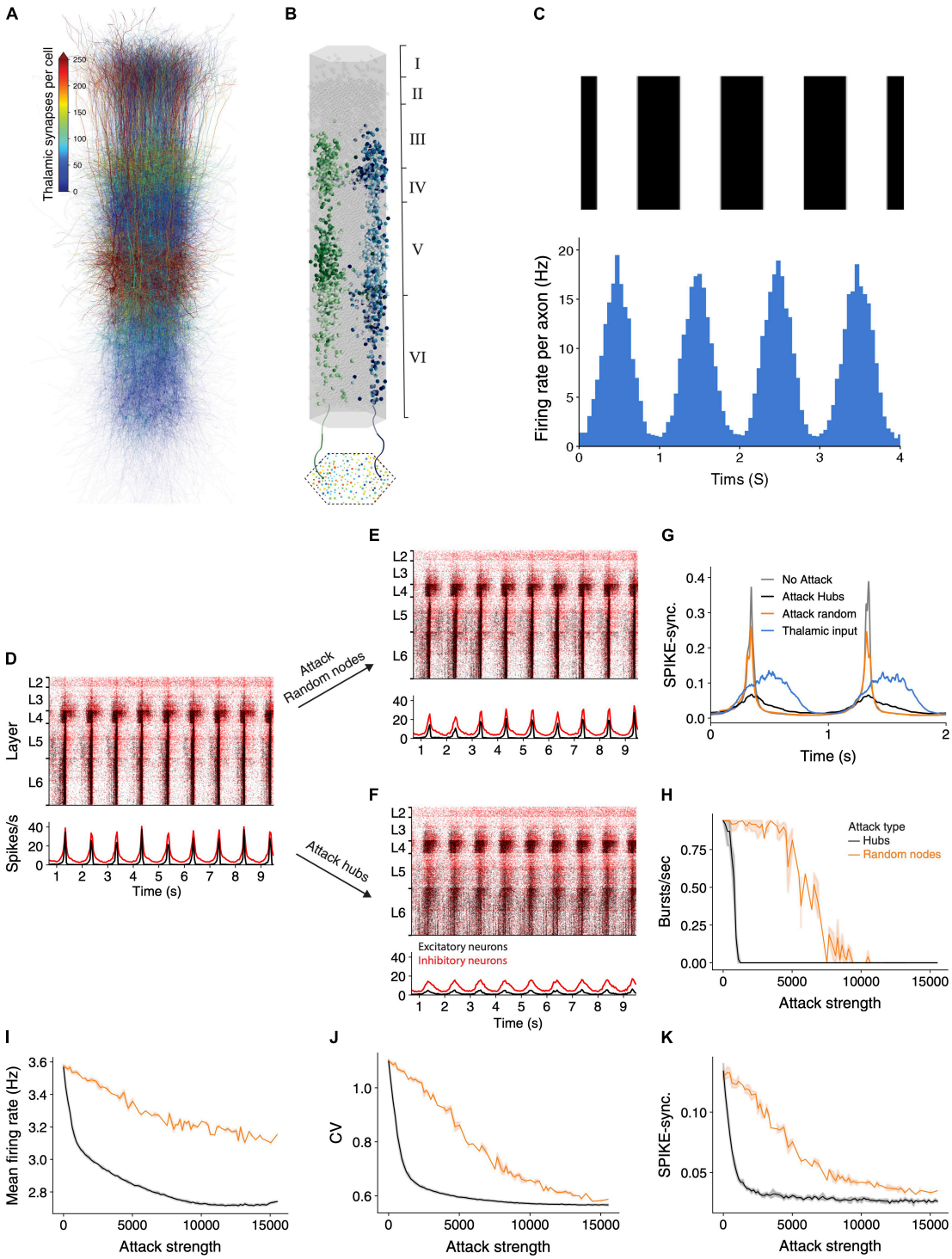

FIGURE 4 | Network synchrony due to thalamic input is disrupted following attack on hub neurons. **(A)** Schematic illustration of the NMC circuit, each neuron is color-coded by the number of thalamic synapses it receives. **(B)** The spatial distribution of the thalamic input is illustrated by showing the cortical postsynaptic neurons receiving inputs from two exemplar TC axons (green and blue axons and respective colored cortical neurons). **(C)** Mean thalamic activity **(bottom)** simulating their response moving bars at 1 Hz (**top**, see section "Materials and Methods"). Bin size = 45 ms. **(D)** Raster plots of the circuit responding to the thalamic input. This circuit fires asynchronously at its spontaneous state ($[Ca^{2+}]_0$ = 1.25 mM; see **Supplementary Figure 3A** and section "Materials and Methods"). Red, inhibitory neurons; black, excitatory neurons. **(E,F)** The response of the circuit to the thalamic input after attack of 2,500 random nodes **(E)** and 2,500 hub neurons **(F)**. **(G)** Circuit's SPIKE-synchronization profile (Kreuz et al., 2015) in response to thalamic input is sharpened in the intact and randomly-attacked networks as compared to that of the TC input itself (blue line) and it decreased dramatically after hub attacks (black line), even below that of the TC input. **(H–K)** Different quantifications of network activity under thalamic input for hub and random attacks (as in **Figures 2F,G**).

DISCUSSION

We introduced in this work a network-based approach to investigate the relation between a cortical circuit structure to its function by removing cells according to different criteria in a highly detailed simulation. Additionally, we proposed a network-based approach for identifying potentially interesting neurons. Our analysis shows that the importance of a neuron in maintaining synchronous activity is more affected by their embedding in the network (e.g., the neurons' in/out degree, its "hubness") rather than strictly by their physiology.

To examine the importance of different cells and layers, we simulated the network activity after removing hub cells globally or from specific layers and compared the results to control models where random cells were removed. We discovered that hub neuron attacks have the largest change of structural network measures, leading to loss of the small-world properties of the simulated NMC (**Figures 1C–E**). Accordingly, attacks on this population resulted in the largest decrease in the network synchrony, firing rate and number of bursts (**Figure 2**). The attack changed the network response from spontaneously synchronous to asynchronous, resulting in no bursts and reduced CV, as noted by another recent research (Nolte et al., 2019).

Among attacks targeting specific layers, mimicking a more biologically plausible scenario, we found that attacking L5 hub neurons resulted in the largest effect on all functional measures (**Figures 3D–G**) and therefore is the most distributive attack. We believe that this phenomenon is rooted in the high interconnectivity of L5 excitatory neurons (**Figure 3A**). Interestingly the specific genetic profile of L5 excitatory neurons is widely used to optogenetically target and record from this subset of neurons (de Vries et al., 2020), and open the possibility of examining our predictions by specifically silencing this subpopulation while recording from the neocortex.

Hub neurons play an important role not only in maintaining spontaneous network oscillatory activity but also in the processing of sensory input from other brain areas. When thalamic (sensory) drifting sinusoidal input impinged on our modeled cortical circuit, the circuit not only followed the thalamic synchrony, but resulted in activity that was more synchronized. We then found that attacking hub cells caused a significant reduction of the synchrony of the cortical column with respect to the oscillation of the TC input (**Figures 4G–K**), eventually resulting in activity that is less synchronized than the input. Nevertheless, random attacks seem to have a minor effect on thalamic input processing by the network, demonstrating yet again the robustness of the cortical microcircuit to random cell death. These results highlight the functional role of hub neurons in fast processing of sensory information in the cortical microcircuit.

In a previous study we have demonstrated that both in-hubs and out-hubs neurons belong to a small subset of cortical neuron types (Gal et al., 2017; **Figures 3A,B**). It was recently shown that, although any disease-associated genes are expressed in multiple cell types, the pathologic variants affect primarily specific cell types (Guan et al., 2021), and see also related recent work of disease map and specific cell type in the retina by Siegert et al. (2012). Therefore, it is highly likely that dysfunction of specific genes might abolish specific hub cells. We further emphasize that hub neurons (both in-hubs and out-hubs) require more metabolic energy as they receive/form a larger number of synapses and this might entail earlier death (e.g., in neurodegenerative diseases) compared to non-hub neurons (see e.g., Pathak et al., 2013).

Our findings can also be seen as a demonstration of how network science theory is implemented in realistic networks. As the modeled cortical microcircuit was shown to display small-world topology with a high clustering coefficient and short mean path, we now can systematically characterize how the targeting of fundamental components of the network, the hubs, indeed leads to loss of this topology in the neural microcircuit, and results in major functional disruptions. Robustness of complex networks to random attacks and vulnerability to removal of highly connected nodes was previously shown theoretically (Watts and Strogatz, 1998; Boccaletti et al., 2006). Here, we provided concrete evidence that hubs fulfill their theoretical key role in affecting the dynamics of the network, in a highly detailed biological model circuit. The loss of small-world topology among brain regions was shown to be related to neurodegenerative diseases using fMRI data (Sporns, 2013b). Our theoretical experiments suggest that a decrease in network clustering and an increase in the mean short path length can cause functional failures also at the microscale level of resolution.

To conclude, while neurons are usually characterized according to genetic markers, morphology and physiology (Berg et al., 2020; Yuste et al., 2020), we showed how a specific structural measure such as the number of synapses that defines hub cells, has a direct effect on the network functionality. As hub cells are specific subtypes of neurons, it is possible to use *in vivo* cell-specific knockout experiments to explore the behavioral implications of the neural network functional disruption suggested in our work.

MATERIALS AND METHODS

NMC Connectedness Measures

The general connectedness of the NMC was characterized by identifying connected components of the network. A strongly connected component is a group of nodes in which any node is reachable from any other node through a directed path (a series of nodes and directed edges). Intuitively, a strongly connected component reflects a group of recurrently interlinked neurons that could give rise to an anatomical module with functional specialization.

Small-World Properties

The first property of the small-world analysis is based on the length of the shortest path l_{ij} between pairs of nodes in the network. A path length between two nodes in the network is expressed as the number of connections along that path. To generalize this property for the entire network, the characteristic path length (l) of a network was used, which is the mean shortest

path length averaged over all pairs of neurons.

$$l = \frac{1}{n(n-1)} \sum_{i,j:i \neq j} l_{ij}$$

Clearly, this measure is well-defined in connected networks where any node is reachable from any other node. The NMC network initially contained a single giant component of 31,329 ± 5 neurons that were mutually reachable (99.95% ± 0.01% of all neurons; see above).

The second property of the small-world analysis is captured by the tendency of nodes to cluster together. The local clustering of individual nodes measures the level at which the neighbors of a node are interconnected among themselves. Let the binary (unweighted) adjacency matrix of a directed network be denoted by A; then the local clustering coefficient c_i of a node i is defined as,

$$c_i = \frac{\left(A + A^T\right)^3_{ii}}{2\left(d_i^{tot}\left(d_i^{tot} - 1\right) - 2A_{ii}^2\right)}$$

where d_i^{tot} depicts the total degree (in-degree + out-degree) of node i. Essentially, in directed networks, this definition reflects the ratio of the number of triangles among a node and its neighbors to the number of all possible triangles that could have been formed (Fagiolo, 2007). The value of c_i ranges from 0 (none of the neighbors are connected to each other) to 1 (all neighbors are mutually connected). The network-wide clustering coefficient (c) is computed by averaging over all local clustering coefficients.

$$c = \frac{1}{n} \sum_i c_i$$

Hubs Versus the Reference Random Attacks

To selectively attack the highly connected hub neurons we started by ranking all neurons according to their total degree (total number of pre- and post-synaptic cells). Then, we performed several attacks at different strengths (the number of removed hubs). In each attack, given required number of cells to attack (s, attack strength), we removed the top degreed cells.

To test the significance of the results observed in hub attacked networks we performed several types of random attacks for comparison. In the first, most naïve random attack, for each hub attack at strength s we performed 10 matching random attacks in which randomly selected s neurons were attacked. In the second, for each hub attack we counted the number of excitatory s_E and inhibitory s_I neurons that were attacked ($s = s_E + s_I$); we then performed 10 matching random attacks in which s_E excitatory neurons and s_I inhibitory neurons were selected randomly. We note that a few hub neurons might also be selected, by chance, in these random selection controls.

Structural Analysis Statistical Tests

To compare the structural disruption of hub attacks to that of random node attacks (**Figure 1**) we compared the structural metric values (mean path length and clustering coefficient) of the strongest attacks. Specifically, we took the ten strongest hub attacks ($n_1 = 10$), and the ten matching random attacks for each strength ($n_2 = 100$). For both metrics (path length or clustering coefficient) a *two-tailed Wilcoxon rank sum test* indicated that the disruption was greater for hub attacks than for matching control ($n_1 = 10$, $n_2 = 100$, $P < 0.001$).

For random edge comparisons (**Supplementary Figure 1**) we took the 100 strongest attacks ($n_2 = 100$) and compared to the 10 closest hub attacks ($n_1 = 10$). In agreement with the previous control, also here, a *two-tailed Wilcoxon rank sum test* indicated that the disruption was greater for hub attacks than for matching control ($n_1 = 10$, $n_2 = 100$, $P < 0.001$), for both metrics.

Dense Model of Neocortical Microcircuit (NMC)

Simulations were performed on a previously published model of the NMC of a two-year-old rat of a neocortical microcircuit. Full details on the constructing of the circuits and its simulation methods were described in Markram et al. (2015). The microcircuit (**Figure 1B**) consisted of 31,346 biophysical Hodgkin-Huxley 3D reconstructed NEURON models with around 7.8 million synaptic connections forming around 36.4 million synapses. Synaptic connectivity between 55 distinct morphological types of neurons (m-types) was predicted algorithmically and constrained by experimental data (Reimann et al., 2015). The densities of ion-channels on morphologically-detailed neuron models were optimized to reproduce the behavior of different electrical neuron types (e-types) and synaptic dynamics recorded *in vitro* (Van Geit et al., 2016). Simulations were run on HPE SGI 8600 supercomputer (BlueBrain 5) using NEURON (Carnevale and Hines, 2006) and CoreNEURON (Kumbhar et al., 2019).

Simulation of Baseline Spontaneous Activity

To account for the missing long-range connections and missing neuromodulators, neurons were depolarized with a noisy somatic current injection of 100% of first spike threshold (Markram et al., 2015, **Figure 15**). In addition, synapses spontaneous release probability was modified by setting the extracellular calcium concentration $[Ca^{2+}]_o$. Two conditions were tested, $[Ca^{2+}]_o$ of 1.25 and 1.4 mM each positioning the circuit in different activity regimes (Markram et al., 2015, **Figure 15**). Synaptic conductances and kinetics are as in Markram et al. (2015). Each attack was simulated twice with different randomization of the noisy step currents and timing of the spontaneous synaptic release, each time for 10 s.

Simulation Oscillatory Thalamocortical Input to the NMC

The oscillatory thalamocortical input to the NMC (**Figure 4**) was generated by following the same principle as in Amsalem et al. (2016) – the spike times of the axons from inhomogeneous Poisson process with time-varying rate as,

$$\lambda(t) = B^*(\sin(t^* f^* 2\pi) + 1)^{1.5} + b$$

where t is time in seconds, f the frequency of the oscillatory input was set to 1 Hz, B 5.83 is a factor, so that the

mean firing rate of the oscillatory part would be equal to 7 Hz, and b is the baseline spontaneous firing rate which was set to 1 Hz. For **Supplementary Figure 1** each simulation was of 10 s, and conducted 5 times with different randomly generated thalamic input.

Burst Detection

We detected bursts by extracting the multivariate SPIKE-synchronization profile (Mulansky and Kreuz, 2016) for each simulation, smoothing the result using a running mean filter of ∼200 ms and then counting the number of events larger than half the maximal synchronization (but at least larger than 0.15).

Force-Directed Graph Layout

Visualization of complex networks in an informative and meaningful way is a challenging task. How to position a large number of nodes, densely interconnected with non-obvious organization, in a two-dimensional layout that can expose inherent symmetries and structures such as hubs and clusters?

To provide a layout in which the distance between nodes (cell types) is more or less proportional to their edge weight (connection probability), we employed a Force-directed graph drawing algorithm. The algorithm is based on a physical model that assigns different forces among the nodes. On one hand, to promote attraction between connected nodes spring-like attractive forces, which depend on the distance and edge weight, are simulated. On the other hand, to avoid overlapping of nodes, repulsive forces (such as Coulomb's law between electrically charged particles) are simulated to separate all pairs of nodes. By iteratively determining all the forces and moving the nodes accordingly, the system gets closer to an equilibrium where all forces add up to zero, and the position of the nodes stays stable.

Here, we used the implementation from D3.js library[1].

Visualization

Figures were created using Matplotlib (Hunter, 2007). For analysis we used Python and Numpy (Harris et al., 2020).

DATA AVAILABILITY STATEMENT

The raw data supporting the conclusions of this article will be made available by the authors, without undue reservation, to any qualified researcher.

[1] https://github.com/d3/d3-force

AUTHOR CONTRIBUTIONS

EG, OA, and IS conceived the study and wrote the manuscript. EG and OA carried out the simulations and the analysis. AS, ML, FS, and HM participated in discussions and helped writing the manuscript. HM and FS developed the *in silico* microcircuit and provided the respective simulation framework and data. All authors contributed to the article and approved the submitted version.

FUNDING

This work was made possible through the Patrick and Lina Drahi Foundation (PLFA), the Blue Brain Project, a research center of the École polytechnique fédérale de Lausanne (EPFL), from the Swiss government's ETH Board of the Swiss Federal Institutes of Technology, the Gatsby Charitable Foundation, and the NIH Grant Agreement U01MH114812.

ACKNOWLEDGMENTS

We thank Noam Kahlon for the helpful discussions related to this project and for conducting the initial hub-attack experiments.

SUPPLEMENTARY MATERIAL

The Supplementary Material for this article can be found online at: https://www.frontiersin.org/articles/10.3389/fncir.2021.718270/full#supplementary-material

Supplementary Figure 1 | Hub attack disruption is stronger than random attacks with matching number of edges. Same as **Figure 1**, only the attack strength (*x*-axis) is measured by the number of removed edges.

Supplementary Figure 2 | Matched *E/I* ratio to hub attack and matched with number of edges **(A–D)** hub attack (black), random attack (orange) and random attack with E/I ratio that is matched to the hub attacks (green) effects on network activity as a function of attack strength. **(A)** Average network firing rate, **(B)** the number of bursts/sec, **(C)** coefficient of variation, and **(D)** global SPIKE-synchronization measure (see section "Materials and Methods" for details about the different attacks and measures). For all measures, hub attack is much more impactful. Panels **(E–H)** same as in **Figure 2**, only the attack strength (*x*-axis) is measured by the number of removed edges.

Supplementary Figure 3 | Effect of hub attacks on the dynamics of the NMC network in the asynchronous regime. **(A)** Raster plot **(top)** and PSTH **(bottom)** of the NMC during spontaneous asynchronous state (see section "Materials and Methods"). **(B,C)** Same as **(A)** after attacking 3,134 and 8,149 hub neurons, respectively. **(D,E)** As in **(B,C)** but for respective random attacks. **(F–G)** Impact of hubs (black) versus random (orange) attacks on network activity as a function of attack strength. **(F)** On the number of bursts/sec, **(G)** on average network firing rate, **(H)** on coefficient of variation, **(I)** on global SPIKE-synchronization measure (see section "Materials and Methods"). For all measures, hub attack is much more impactful.

REFERENCES

Abbott, L. F., Bock, D. D., Callaway, E. M., Denk, W., Dulac, C., Fairhall, A. L., et al. (2020). The mind of a mouse. *Cell* 182, 1372–1376. doi: 10.1016/j.cell.2020.08.010

Adesnik, H., and Scanziani, M. (2010). Lateral competition for cortical space by layer-specific horizontal circuits. *Nature* 464, 1155–1160. doi: 10.1038/nature08935

Amsalem, O., King, J., Reimann, M., Ramaswamy, S., Muller, E., Markram, H., et al. (2020). Dense computer replica of cortical microcircuits unravels

cellular underpinnings of auditory surprise response. *bioRxiv [Preprint]* doi: 10.1101/2020.05.31.126466

Amsalem, O., Van Geit, W., Muller, E., Markram, H., and Segev, I. (2016). From neuron biophysics to orientation selectivity in electrically coupled networks of neocortical L2/3 large basket cells. *Cereb. Cortex* 26, 3655–3668. doi: 10.1093/cercor/bhw166

Avena-Koenigsberger, A., Misic, B., and Sporns, O. (2017). Communication dynamics in complex brain networks. *Nat. Rev. Neurosci.* 19, 17–33. doi: 10.1038/nrn.2017.149

Berg, J., Sorensen, S. A., Ting, J. T., Miller, J. A., Chartrand, T., Buchin, A., et al. (2020). Human cortical expansion involves diversification and specialization of supragranular intratelencephalic-projecting neurons. *bioRxiv [Preprint]* doi: 10.1101/2020.03.31.018820

Bitzenhofer, S. H., Ahlbeck, J., Wolff, A., Wiegert, J. S., Gee, C. E., Oertner, T. G., et al. (2017). Layer-specific optogenetic activation of pyramidal neurons causes beta–gamma entrainment of neonatal networks. *Nat. Commun.* 8:14563. doi: 10.1038/ncomms14563

Boccaletti, S., Latora, V., Moreno, Y., Chavez, M., and Hwang, D. U. (2006). Complex networks: structure and dynamics. *Phys. Rep.* 424, 175–308. doi: 10.1016/j.physrep.2005.10.009

Bullmore, E., and Sporns, O. (2009). Complex brain networks: graph theoretical analysis of structural and functional systems. *Nat. Rev. Neurosci.* 10, 186–198. doi: 10.1038/nrn2575

Cardin, J. A., Carlén, M., Meletis, K., Knoblich, U., Zhang, F., Deisseroth, K., et al. (2009). Driving fast-spiking cells induces gamma rhythm and controls sensory responses. *Nature* 459, 663–667. doi: 10.1038/nature08002

Carnevale, N. T., and Hines, M. L. (2006). *The NEURON Book*. Cambridge: Cambridge University Press, doi: 10.1017/CBO9780511541612

Carrillo-Reid, L., Han, S., Yang, W., Akrouh, A., and Yuste, R. (2019). Controlling visually guided behavior by holographic recalling of cortical ensembles. *Cell* 178, 447–457.e5. doi: 10.1016/j.cell.2019.05.045

de Vries, S. E. J., Lecoq, J. A., Buice, M. A., Groblewski, P. A., Ocker, G. K., Oliver, M., et al. (2020). A large-scale standardized physiological survey reveals functional organization of the mouse visual cortex. *Nat. Neurosci.* 23, 138–151. doi: 10.1038/s41593-019-0550-9

Deisseroth, K. (2015). Optogenetics: 10 years of microbial opsins in neuroscience. *Nat. Neurosci.* 18, 1213–1225. doi: 10.1038/nn.4091

Fagiolo, G. (2007). Clustering in complex directed networks. *Phys. Rev. E - Stat. Nonlinear, Soft Matter Phys.* 76:026107. doi: 10.1103/PhysRevE.76.026107

Fu, H., Hardy, J., and Duff, K. E. (2018). Selective vulnerability in neurodegenerative diseases. *Nat. Neurosci.* 21, 1350–1358. doi: 10.1038/s41593-018-0221-2

Gal, E., London, M., Globerson, A., Ramaswamy, S., Reimann, M. W., Muller, E., et al. (2017). Rich cell-type-specific network topology in neocortical microcircuitry. *Nat. Neurosci.* 20, 1004–1013.

Gal, E., Perin, R., Markram, H., London, M., and Segev, I. (2019). Neuron geometry underlies a universal local architecture in neuronal networks. *bioRxiv [Preprint]* doi: 10.1101/656058

Gouwens, N. W., Sorensen, S. A., Berg, J., Lee, C., Jarsky, T., Ting, J., et al. (2019). Classification of electrophysiological and morphological neuron types in the mouse visual cortex. *Nat. Neurosci.* 22, 1182–1195. doi: 10.1038/s41593-019-0417-0

Guan, J., Lin, Y., Wang, Y., Gao, J., and Ji, G. (2021). An analytical method for the identification of cell type-specific disease gene modules. *J. Transl. Med.* 19:20. doi: 10.1186/s12967-020-02690-5

Guo, J. Z., Graves, A. R., Guo, W. W., Zheng, J., Lee, A., Rodríguez-Gonzá Lez, J., et al. (2015). Cortex commands the performance of skilled movement. *Elife* 4:10774. doi: 10.7554/eLife.10774

Hammond, C., Bergman, H., and Brown, P. (2007). Pathological synchronization in Parkinson's disease: networks, models and treatments. *Trends Neurosci.* 30, 357–364. doi: 10.1016/j.tins.2007.05.004

Harris, C. R., Millman, K. J., van der Walt, S. J., Gommers, R., Virtanen, P., Cournapeau, D., et al. (2020). Array programming with NumPy. *Nature* 585, 357–362. doi: 10.1038/s41586-020-2649-2

Hunter, J. D. (2007). Matplotlib: A 2D graphics environment. *Comput. Sci. Eng.* 9, 90–95. doi: 10.1109/MCSE.2007.55

Kreuz, T., Bozanic, N., and Mulansky, M. (2015). SPIKE-Synchronization: a parameter-free and time-resolved coincidence detector with an intuitive multivariate extension. *BMC Neurosci.* 16:170. doi: 10.1186/1471-2202-16-S1-P170

Kumbhar, P., Hines, M., Fouriaux, J., Ovcharenko, A., King, J., Delalondre, F., et al. (2019). CoreNEURON: An Optimized Compute Engine for the NEURON Simulator. *Front. Neuroinform.* 13:63. doi: 10.3389/fninf.2019.00063

Luccioli, S., Angulo-Garcia, D., Cossart, R., Malvache, A., Módol, L., Sousa, V. H., et al. (2018). Modeling driver cells in developing neuronal networks. *PLoS Comput. Biol.* 14:e1006551. doi: 10.1371/journal.pcbi.1006551

Luo, L., Callaway, E. M., and Svoboda, K. (2018). Genetic dissection of neural circuits: a decade of progress. *Neuron.* 98, 256–281. doi: 10.1016/j.neuron.2018.03.040

Markram, H., Muller, E., Ramaswamy, S., Reimann, M. W., Abdellah, M., Sanchez, C. A., et al. (2015). Reconstruction and simulation of neocortical microcircuitry. *Cell* 163, 456–492. doi: 10.1016/j.cell.2015.09.029

Mulansky, M., and Kreuz, T. (2016). PySpike—A Python library for analyzing spike train synchrony. *SoftwareX* 5, 183–189.

Murray, H. C., Swanson, M. E. V., Dieriks, B. V., Turner, C., Faull, R. L. M., and Curtis, M. A. (2018). Neurochemical characterization of PSA-NCAM+ cells in the human brain and phenotypic quantification in alzheimer's disease entorhinal cortex. *Neuroscience* 372, 289–303. doi: 10.1016/j.neuroscience.2017.12.019

Newman, M. E. J. (2003). The structure and function of complex networks. *SIAM Rev.* 45, 167–256.

Nolte, M., Gal, E., Markram, H., and Reimann, M. W. (2020). Impact of higher order network structure on emergent cortical activity. *Netw. Neurosci.* 4, 292–314. doi: 10.1162/netn_a_00124

Nolte, M., Reimann, M. W., King, J. G., Markram, H., and Muller, E. B. (2019). Cortical reliability amid noise and chaos. *Nat. Commun.* 10:3792. doi: 10.1038/s41467-019-11633-8

Pathak, D., Berthet, A., and Nakamura, K. (2013). Energy failure: does it contribute to neurodegeneration? *Ann. Neurol.* 74:506. doi: 10.1002/ANA.24014

Pouille, F., Marin-Burgin, A., Adesnik, H., Atallah, B. V., and Scanziani, M. (2009). Input normalization by global feedforward inhibition expands cortical dynamic range. *Nat. Neurosci.* 12, 1577–1585. doi: 10.1038/nn.2441

Reimann, M. W., King, J. G., Muller, E. B., Ramaswamy, S., and Markram, H. (2015). An algorithm to predict the connectome of neural microcircuits. *Front. Comput. Neurosci.* 9:120. doi: 10.3389/fncom.2015.00120

Robinson, N. T. M., Descamps, L. A. L., Russell, L. E., Buchholz, M. O., Bicknell, B. A., Antonov, G. K., et al. (2020). Targeted activation of hippocampal place cells drives memory-guided spatial behavior. *Cell* 183, 1586.e–1599.e. doi: 10.1016/j.cell.2020.09.061

Rubinov, M., and Bullmore, E. (2013). Schizophrenia and abnormal brain network hubs. *Dialogues Clin. Neurosci.* 15, 339–349. doi: 10.31887/dcns.2013.15.3/mrubinov

Schirmer, L., Velmeshev, D., Holmqvist, S., Kaufmann, M., Werneburg, S., Jung, D., et al. (2019). Neuronal vulnerability and multilineage diversity in multiple sclerosis. *Nature* 573, 75–82. doi: 10.1038/s41586-019-1404-z

Setareh, H., Deger, M., Petersen, C. C. H., and Gerstner, W. (2017). Cortical Dynamics in Presence of Assemblies of Densely Connected Weight-Hub Neurons. *Front. Comput. Neurosci.* 11:52. doi: 10.3389/fncom.2017.00052

Siegert, S., Cabuy, E., Scherf, B. G., Kohler, H., Panda, S., Le, Y.-Z., et al. (2012). Transcriptional code and disease map for adult retinal cell types. *Nat. Neurosci. 2012* 153, 487–495. doi: 10.1038/nn.3032

Sporns, O. (2013a). Network attributes for segregation and integration in the human brain. *Curr. Opin. Neurobiol.* 23, 162–171. doi: 10.1016/j.conb.2012.11.015

Sporns, O. (2013b). Structure and function of complex brain networks. *Dialogues Clin. Neurosci.* 15, 247–262. doi: 10.1137/S003614450342480

Stam, C. J. (2014). Modern network science of neurological disorders. *Nat. Rev. Neurosci.* 15, 683–695.

Stranahan, A. M., and Mattson, M. P. (2010). Selective vulnerability of neurons in layer II of the entorhinal cortex during aging and Alzheimer's disease. *Neural Plast.* 2010:108190. doi: 10.1155/2010/108190

Syan, S. K., Minuzzi, L., Smith, M., Costescu, D., Allega, O. R., Hall, G. B. C., et al. (2018). Brain structure and function in women with Comorbid bipolar and premenstrual dysphoric disorder. *Front. Psychiatry* 8:301. doi: 10.3389/fpsyt.2017.00301

Turner, N. L., Macrina, T., Alexander Bae, J., Yang, R., Wilson, A. M., Schneider-Mizell, C., et al. (2020). Multiscale and multimodal reconstruction of cortical structure and function. *bioRxiv [Preprint]* doi: 10.1101/2020.10.14.338681

Van Geit, W., Gevaert, M., Chindemi, G., Rössert, C., Courcol, J.-D., Muller, E. B., et al. (2016). BluePyOpt: leveraging open source software and cloud infrastructure to optimise model parameters in neuroscience. *Front. Neuroinform.* 10:17. doi: 10.3389/fninf.2016.00017

Watts, D. J., and Strogatz, S. H. (1998). Collective dynamics of "small-world" networks. *Nature* 393, 440–442. doi: 10.1038/30918

Xue, M., Atallah, B. V., and Scanziani, M. (2014). Equalizing excitation-inhibition ratios across visual cortical neurons. *Nature* 511, 596–600. doi: 10.1038/nature13321

Yuste, R., Hawrylycz, M., Aalling, N., Aguilar-Valles, A., Arendt, D., Arnedillo, R. A., et al. (2020). A community-based transcriptomics classification and nomenclature of neocortical cell types. *Nat. Neurosci.* 23, 1456–1468. doi: 10.1038/s41593-020-0685-8

Conflict of Interest: The authors declare that the research was conducted in the absence of any commercial or financial relationships that could be construed as a potential conflict of interest.

Publisher's Note: All claims expressed in this article are solely those of the authors and do not necessarily represent those of their affiliated organizations, or those of the publisher, the editors and the reviewers. Any product that may be evaluated in this article, or claim that may be made by its manufacturer, is not guaranteed or endorsed by the publisher.

frontiers in Neural Circuits

ORIGINAL RESEARCH
published: 18 February 2022
doi: 10.3389/fncir.2022.843025

Cell-Type Specific Neuromodulation of Excitatory and Inhibitory Neurons *via* Muscarinic Acetylcholine Receptors in Layer 4 of Rat Barrel Cortex

Guanxiao Qi[1]* *and Dirk Feldmeyer*[1,2,3]*

[1] Institute of Neuroscience and Medicine, INM-10, Reseach Centre Jülich, Jülich, Germany, [2] Department of Psychiatry, Psychotherapy and Psychosomatics, RWTH Aachen University, Aachen, Germany, [3] Jülich-Aachen Research Alliance-Brain, Translational Brain Medicine, Aachen, Germany

The neuromodulator acetylcholine (ACh) plays an important role in arousal, attention, vigilance, learning and memory. ACh is released during different behavioural states and affects the brain microcircuit by regulating neuronal and synaptic properties. Here, we investigated how a low concentration of ACh (30 μM) affects the intrinsic properties of electrophysiologically and morphologically identified excitatory and inhibitory neurons in layer 4 (L4) of rat barrel cortex. ACh altered the membrane potential of L4 neurons in a heterogeneous manner. Nearly all L4 regular spiking (RS) excitatory neurons responded to bath-application of ACh with a M4 muscarinic ACh receptor-mediated hyperpolarisation. In contrast, in the majority of L4 fast spiking (FS) and non-fast spiking (nFS) interneurons 30 μM ACh induced a depolarisation while the remainder showed a hyperpolarisation or no response. The ACh-induced depolarisation of L4 FS interneurons was much weaker than that in L4 nFS interneurons. There was no clear difference in the response to ACh for three morphological subtypes of L4 FS interneurons. However, in four morpho-electrophysiological subtypes of L4 nFS interneurons, VIP+-like interneurons showed the strongest ACh-induced depolarisation; occasionally, even action potential firing was elicited. The ACh-induced depolarisation in L4 FS interneurons was exclusively mediated by M1 muscarinic ACh receptors; in L4 nFS interneurons it was mainly mediated by M1 and/or M3/5 muscarinic ACh receptors. In a subset of L4 nFS interneurons, a co-operative activation of muscarinic and nicotinic ACh receptors was also observed. The present study demonstrates that low-concentrations of ACh affect different L4 neuron types in a cell-type specific way. These effects result from a specific expression of different muscarinic and/or nicotinic ACh receptors on the somatodendritic compartments of L4 neurons. This suggests that even at low concentrations ACh may tune the excitability of L4 excitatory and inhibitory neurons and their synaptic microcircuits differentially depending on the behavioural state during which ACh is released.

Keywords: acetylcholine, layer 4, barrel cortex, muscarinic acetylcholine receptor, nicotinic acetylcholine receptor

OPEN ACCESS

Edited by:
Yoshiyuki Kubota,
National Institute for Physiological Sciences (NIPS), Japan

Reviewed by:
Michael M. Kohl,
University of Glasgow, United Kingdom
Rheinallt Parri,
Aston University, United Kingdom

***Correspondence:**
Guanxiao Qi
g.qi@fz-juelich.de
Dirk Feldmeyer
d.feldmeyer@fz-juelich.de

Received: *24 December 2021*
Accepted: *27 January 2022*
Published: *18 February 2022*

Citation:
Qi G and Feldmeyer D (2022) Cell-Type Specific Neuromodulation of Excitatory and Inhibitory Neurons via Muscarinic Acetylcholine Receptors in Layer 4 of Rat Barrel Cortex. Front. Neural Circuits 16:843025. doi: 10.3389/fncir.2022.843025

INTRODUCTION

Normal brain function relies on the participation of diverse neuromodulators such as the acetylcholine (ACh), noradrenaline, dopamine, and serotonin. These neuromodulators are mainly released from different subcortical brain regions during different cognitive and behavioural states and affect neuronal microcircuits differently yet in a collaborative way. ACh plays a critical role in many cognitive functions including arousal, attention, vigilance, learning, and memory (Hasselmo, 2006; Picciotto et al., 2012; Colangelo et al., 2019). While ACh is mainly released from axonal boutons of neurons located in the nucleus basalis of Meynert in the basal forebrain (Mesulam et al., 1983; Zaborszky et al., 2015), it may also be co-released from neocortical choline acetyltransferase (ChAT)-expressing/vasoactive intestinal peptide (VIP)-positive interneurons together with the inhibitory transmitter GABA and/or VIP (Obermayer et al., 2019; Granger et al., 2020). ACh effects are mediated by two different types of receptors, the G-protein-coupled muscarinic ACh receptors (mAChRs) and the ionotropic nicotinic ACh receptors (nAChRs). In the neocortex, both receptor types show layer-specific distributions and effects (Obermayer et al., 2017; Radnikow and Feldmeyer, 2018). In general, ACh increases the excitability of pyramidal cells located in different cortical layers by activating both nAChRs and mAChRs (Gulledge et al., 2007; Zolles et al., 2009; Bailey et al., 2010; Tian et al., 2014; Hay et al., 2016; Yang et al., 2020; Patel et al., 2021). In a minor fraction of deep L2/3 and a subset of L5/6 pyramidal cells, ACh induces an initial small and transient hyperpolarisation followed by a sustained depolarisation mediated by muscarinic M1/3 mAChRs (Gulledge and Stuart, 2005; Gulledge et al., 2007; Eggermann and Feldmeyer, 2009; Patel et al., 2021). In contrast, excitatory neurons located in layer 4 are persistently hyperpolarised by ACh activating M4 mAChRs (Eggermann and Feldmeyer, 2009; Dasgupta et al., 2018). A similar ACh effect was also found in L6A corticocortical neurons (Yang et al., 2020).

Cholinergic effects on GABAergic inhibitory interneurons are heterogenous and dependent on interneuron subtypes (Bacci et al., 2005; Muñoz and Rudy, 2014). Cortical interneurons can be broadly divided into two large groups according to their firing patterns, i.e., fast spiking (FS) and non-FS (nFS) interneurons. ACh induces a depolarisation in the majority of nFS interneurons [e.g., somatostatin-expressing (SST+) adapting firing, VIP+ irregular spiking interneurons] *via* the activation of nAChRs and/or mAChRs but induces a hyperpolarisation in others such as cholecystokinin-expressing (CCK+) regular spiking interneurons (Kawaguchi, 1997; Gulledge et al., 2007). Whether FS interneurons show ACh effects is still a matter of debate (Kawaguchi, 1997; Xiang et al., 1998; Gulledge et al., 2007; Kruglikov and Rudy, 2008; Chen et al., 2015).

The ACh response of a neuron depends on the concentration and the speed and spatial profile of application. In the majority of studies, a high concentration of ACh (∼1 mM) was applied locally through a puff pipette; this approach reveals predominantly the nicotinic ACh response but largely obscures any muscarinic ACh effects. Furthermore, a puff-application mimics (to some extent) phasic ACh release on a short time scale (within a few ms) but does not simulate tonic, non-synaptic ACh release into the extracellular space, the so-called "volume transmission" (Fuxe and Borroto-Escuela, 2016).

In sensory cortices, L4 neurons receive direct thalamocortical input and distribute intracortical excitation and inhibition to other cortical layers. While the neuronal composition and synaptic connectivity of layer 4 have been studied extensively (Feldmeyer et al., 1999; Gibson et al., 1999; Lubke et al., 2000; Beierlein et al., 2003; Xu et al., 2013; Koelbl et al., 2015; Emmenegger et al., 2018; Scala et al., 2019) a comprehensive study on their modulation by ACh or other neuromodulators is still lacking. Here, we investigated how low concentrations of ACh affect the intrinsic properties of different L4 neuron types and subtypes in acute brain slices using patch-clamp recordings and bath-application of cholinergic agonists and antagonists. To reveal the cell-type specific effects of ACh, L4 neurons were classified into three electrophysiological types and ten electro-morphological subtypes as identified previously (Feldmeyer et al., 1999; Staiger et al., 2004; Koelbl et al., 2015; Emmenegger et al., 2018). We found that neuromodulation by mAChRs is a common property of all L4 neurons but is highly cell type-specific. Furthermore, in some L4 nFS interneuron types low concentrations of ACh evoked a strong superthreshold depolarisation mediated by coincident activation of both mAChRs and nAChRs suggesting a cooperative interaction of the two receptor types in cholinergic modulation of neuronal excitability and synaptic transmission.

MATERIALS AND METHODS

All experimental procedures involving animals were performed in accordance with the guidelines of the Federation of European Laboratory Animal Science Association (FELASA), the EU Directive 2010/63/EU, and the German animal welfare law.

Slice Preparation

In this study, Wistar rats (Charles River, either sex) aged 18–33 postnatal days (P18–P33) were maintained on a 12/12-h light/dark cycle with lights on from 7 a.m. to 7 p.m. Rats were anaesthetized with isoflurane at a concentration <0.1% and decapitated between 10:30 a.m. and 11:30 a.m. The brain was quickly removed and placed in an ice-cold modified artificial cerebrospinal fluid (ACSF) containing a high Mg^{2+} and a low Ca^{2+} concentration (4 mM $MgCl_2$ and 1 mM $CaCl_2$), other components are same to that in the perfusion ACSF as described below, to reduce potentially excitotoxic synaptic transmission during slicing. In order to maintain adequate oxygenation and a physiological pH level, the solution was constantly bubbled with carbogen gas (95% O_2 and 5% CO_2). Thalamocortical slices (Feldmeyer et al., 1999; Qi et al., 2017) were cut at 350 μm thickness using a Leica VT1000S vibrating blade microtome and then transferred to an incubation chamber containing preparation solution for a recovery period of at least 30 min at room temperature before being transferred to the recording chamber. After cutting, slices from animals older than P21 were transferred to a holding chamber placed in a water bath at 35°C

for 30 min and then, the water bath was allowed to gradually cool down to the room temperature.

Solution

During recordings, slices were continuously superfused (perfusion speed ∼5 ml/min) with ACSF containing (in mM): 125 NaCl, 2.5 KCl, 1.25 NaH_2PO_4, 1 $MgCl_2$, 2 $CaCl_2$, 25 $NaHCO_3$, 25 D-glucose, 3 mho-inositol, 2 sodium pyruvate, and 0.4 ascorbic acid, bubbled with carbogen gas (95% O_2 and 5% CO_2) and maintained at 30–33°C. Patch pipettes (5–8 MΩ) were pulled from thick-wall borosilicate glass capillaries and filled with an internal solution containing (in mM): 135 K-gluconate, 4 KCl, 10 HEPES, 10 phosphocreatine, 4 Mg-ATP, and 0.3 GTP (pH 7.4 with KOH, 290–300 mOsm). Biocytin at a concentration of 5 mg/ml was added to the internal solution in order to stain patched neurons after recordings.

Electrophysiological Recording and Analysis

Slices and neurons were visualised using an upright microscope equipped with an infrared differential interference contrast (IR-DIC) optics. The barrels can be identified in layer 4 as dark stripes with light "hollows" at low magnification (4× objective) and were visible in 6–8 consecutive slices. Neurons located inside the barrels were randomly selected for recordings. When being visualised at high magnification (40× magnification), putative excitatory neurons have ovoid-shape somata without obvious apical dendrites and putative interneurons have enlarged oval somata. They could also be differentiated by their action potential (AP) firing patterns during recording and by their morphological appearances thereafter. Whole-cell patch clamp recordings were made using an EPC10 amplifier (HEKA, Lambrecht, Germany). Signals were sampled at 10 kHz, filtered at 2.9 kHz using Patchmaster software (HEKA), and later analysed off-line using Igor Pro software (Wavemetrics, United States).

Custom-written macros in Igor Pro 6 (WaveMetrics, Lake Oswego, OR, United States) were used to analyse the recorded electrophysiological signals. Passive and active AP firing properties were assessed by eliciting a series of 1 s current pulses under current clamp configuration. The series resistance and capacitance were carefully adjusted after breaking through the membrane into whole-cell mode and continuously compensated by 80% during recordings. Membrane potentials were not corrected for a junction potential. Neurons with a series resistance exceeding 40 MΩ or with a depolarized resting membrane potential (>-55 mV) after rupturing the cell membrane were excluded from analysis. The resting membrane potential (V_{rest}) was recorded immediately after establishing the whole-cell recording configuration. Other passive membrane properties such as the input resistance R_{in}, membrane time constant τ_m, voltage sag were measured from membrane potential (V_m) traces induced by a series of hyper- and depolarizing subthreshold current pulses. Single AP properties such as the AP threshold, amplitude, half-width, afterhyperpolarisation (AHP) amplitude were measured for the first spike elicited by a rheobase current step. Repetitive firing properties such as the maximum firing frequency, slope of frequency-current curve were measured. The description of most electrophysiological parameters for data analysis has been described previously (Emmenegger et al., 2018).

Drug Application and Analysis

Acetylcholine (30 μM) was applied through the perfusion system. Atropine (ATRO, 200 nM), mecamylamine (MEC, 10 μM), tropicamide (TRO, 1 μM), pirenzepine (PIR, 0.5 μM), dihydro-ß-erythroidine (DHßE, 10 μM), TTX (0.5 μM) and the cocktail of synaptic blockers including CNQX (10 μM), D-AP5 (50 μM), gabazine (10 μM) were all bath-applied; drugs were purchased from Sigma-Aldrich or Tocris. During recordings, a 3 min stable baseline with a V_m fluctuation <1 mV was recorded before applying the drug *via* the perfusion system. The change in V_m was calculated as the difference between the maximum V_m deflection (positive or negative) after drug application and the baseline. To avoid a misclassification of the V_m change because of background V_m fluctuation, we set a threshold of ±0.5 mV so that a V_m change ≤0.5 mV during drug application is considered to be no response.

Immunohistochemical Staining

Slices were fixed after electrophysiological recordings with 4% paraformaldehyde in 100 mM phosphate buffered saline (PBS) for at least 24 h at 4°C. To recover the morphology of biocytin-filled neurons, slices were rinsed several times in 100 mM PBS and then treated with 1% H_2O_2 in PBS for about 20 min in order to reduce any endogenous peroxidase activity. Slices were rinsed repeatedly with PBS and then incubated in 1% avidin-biotinylated horseradish peroxidase (Vector ABC staining kit, Vector Lab. Inc., Burlingame, CA, United States) containing 0.1% Triton X-100 for 1 h at room temperature. The reaction was catalysed using 0.5 mg/ml 3,3-diaminobenzidine (DAB; Sigma-Aldrich, St. Louis, MO, United States) as a chromogen. Slices were then rinsed with 100 mM PBS, followed by slow dehydration with ethanol in increasing concentrations and finally in xylene for 2–4 h. After that, slices were embedded using Eukitt medium (Otto Kindler GmbH, Freiburg, Germany).

Morphological Reconstruction and Analysis

Computer-assisted morphological 3D reconstructions of neurons were made using the NEUROLUCIDA® software (MicroBrightField, Williston, VT, United States) and Olympus BV61 microscopy at 1000× magnification (100× objective, 10× eyepiece). Neurons were selected for reconstruction based on the quality of biocytin labelling when background staining was minimal. The cell body, dendritic and axonal branches were reconstructed manually under constant visual inspection to detect thin and small collaterals. Cytoarchitectonic landmarks such as barrels in the primary somatosensory cortex and layer borders, pial surface and white matter were delineated during reconstructions at a low magnification (4× objective). The position of soma and layers were confirmed by superimposing the DIC images taken during the recording. Tissue shrinkage was

corrected using correction factors of 1.1 in the x–y direction and 2.1 in the z direction (Marx et al., 2012).

Statistical Analysis

For all data, the mean ± s.d. is given. Statistical comparisons among multiple groups were done using a Kruskal–Wallis test followed by a Dunn–Holland–Wolfe non-parametric multiple comparison test. Wilcoxon Mann–Whitney *U* test was performed to assess significant differences between individual groups. To assess the differences between two paired groups under different pharmacological conditions, Wilcoxon signed-rank test was performed. Correlation analysis was performed by calculating Pearson's linear correlation coefficients. Statistical significance was set at $p < 0.05$, n indicates the number of neurons analysed. To prepare box plots for dataset with $n > 10$, the web application PlotsOfData was used[1] (Postma and Goedhart, 2019). In box plots, the interquartile range (IQR) is shown as a box, the range of values that are within 1.5*IQR are shown as whiskers and the median is represented by a horizontal line in the box.

RESULTS

We performed single-cell patch-clamp recordings in combination with biocytin fillings in acute brain slices to characterise the modulatory effect of ACh on the intrinsic properties of L4 neurons in the primary somatosensory (barrel) cortex of rats. In total, we have tested the effects of a low concentration of ACh (30 μM) on 108 L4 excitatory and inhibitory neurons. The ACh responses of L4 neurons was highly diverse depending on their electrophysiological and morphological identities.

Electro-Morphological Classification of Layer 4 Neurons

Based on their electrophysiological characteristics, L4 neurons can be broadly classified as regular spiking (RS) excitatory neurons, FS and nFS inhibitory interneurons (**Figure 1A**). Three L4 neuron types can be easily differentiated by only three electrophysiological parameters, i.e., the maximum firing frequency, AP half-width and the AHP amplitude (**Figures 1B,C**). L4 RS neurons show a regular spiking firing pattern with a prominent spike frequency adaptation during a 1 s depolarising pulse (**Figures 1B,C**). In contrast, L4 FS interneurons show a high-frequency firing pattern without obvious spike frequency adaptation. L4 interneurons of the nFS type show heterogeneous firing patterns including adaptive spiking, irregular spiking, late spiking, etc.

In addition to their electrophysiological diversity, L4 neurons show highly distinct dendritic and in particular axonal morphologies (**Figure 1D**). L4 excitatory neurons fall into two main groups, spiny stellate neurons (SSNs) without an obvious apical dendrite and star pyramidal cells (SPCs) (Feldmeyer et al., 1999; Lubke et al., 2000; but see Staiger et al., 2004). Their axons originate from the soma or the initial part of one basal dendrite and project locally in layer 4 and to supra- and infragranular layers. Dendrites of L4 interneurons are aspiny or sparsely spiny and exhibit small to large multipolar, bipolar, or bitufted orientation patterns. Their axons project either locally in layer 4 and/or to supra- and/or infragranular layers in the vertical direction and/or to neighbouring columns in the horizontal direction. In previous studies, we have classified L4 FS interneurons as small basket cells (sBCs), basket cells (BCs), and translaminar cells (TLCs) (Koelbl et al., 2015) and L4 nFS interneurons as local-projecting (LP; non-Martinotti cell-like), supragranular-projecting (SP; Martinotti cell-like), neurogliaform (NGF), VIP+-like (VIP) and transcolumnar-projecting, interneurons (Emmenegger et al., 2018; **Figure 1D**).

Acetylcholine at Low Concentrations Induces Diverse Changes in the Membrane Potential of Layer 4 Neurons

We bath-applied 30 μM ACh while monitoring changes in the V_m of L4 neurons under current-clamp conditions. Of 44 L4 RS neurons, 42 showed a hyperpolarisation; only two showed no change (**Figures 2A,D**). On average, ACh-induced V_m change in L4 RS neurons was −2.8 ± 1.4 mV (n = 44) (**Figure 3A**). Of 33 L4 FS interneurons, 25 neurons showed a weak but significant depolarisation of the V_m, four a weak hyperpolarisation and another four no change (**Figures 2B,E**). On average, the ACh application resulted in a change in V_m in L4 FS interneurons was 0.9 ± 1.5 mV (n = 33) (**Figure 3A**). Of 31 L4 nFS interneurons, 29 neurons showed a strong depolarisation of the V_m and two a hyperpolarisation (**Figures 2C,F**). For the majority of L4 nFS interneurons (25 out of 31), the ACh-induced depolarisation was subthreshold. In a small fraction of L4 nFS interneurons (4 out of 31), ACh application evoked a suprathreshold depolarisation so that spontaneous AP firing was initiated. On average, the ACh-induced change in V_m in L4 nFS interneurons was 5.2 ± 5.8 mV (n = 31) (**Figure 3A**). Note that the ACh-induced V_m changes were fully reversible by bath application of control ACSF (**Figures 2A–C**). To examine whether these ACh-induced changes in V_m resulted from a direct effect on the neuronal excitability or were caused indirectly by altering the activity of local synaptic microcircuits, a cocktail of synaptic blockers comprising CNQX (10 μM), D-AP5 (50 μM), and gabazine (10 μM) was applied before ACh. There is no difference in the V_m change elicited by ACh in the absence and in the presence of synaptic blockers (**Supplementary Figure 1**). However, a clear decrease in background noise of V_m was observed in the presence of synaptic blockers (**Supplementary Figure 1**). A correlation analysis between the change in V_m and the age of the animal, V_{rest} and R_{in} demonstrated that there is no clear age-dependence of the ACh effect on V_m for any of the three L4 neuron types (**Supplementary Figure 2A**); a significant negative correlation was found between the V_m change and V_{rest} for L4 RS neurons ($r = -0.53$, $p = 1.8 \times 10^{-4}$) and L4 nFS interneurons ($r = -0.48$, $p = 5.9 \times 10^{-3}$) (**Supplementary Figure 2B**). Furthermore, for L4 nFS interneurons, a significant positive correlation was found

[1] https://huygens.science.uva.nl/PlotsOfData/

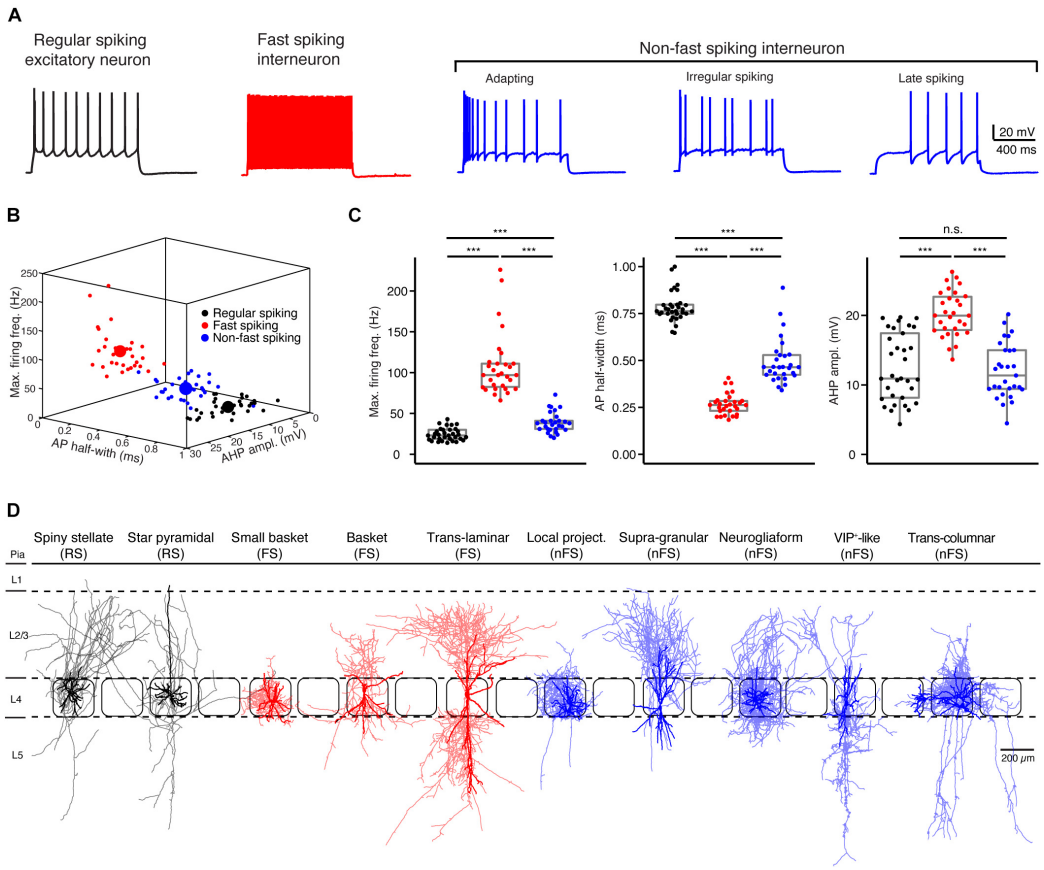

FIGURE 1 | Electro-morphological classification of L4 neurons in the rat barrel cortex. **(A)** Representative firing patterns of L4 regular spiking (RS, black) excitatory neurons, fast spiking (FS, red) and non-fast spiking (nFS, blue) interneurons. **(B)** Electrophysiological differentiation of L4 RS, FS and nFS neurons using the maximal firing frequency, AP half-width and the AHP amplitude. Mean and individual values are shown by large and small dots, respectively. **(C)** Box plots of three electrophysiological parameters for L4 RS, FS and nFS neurons. *P* value was calculated using the non-parametric Wilcoxon–Mann–Whitney two-sample rank test. *** $p < 0.001$, n.s. $p \geq 0.05$. **(D)** Morphological sub-classification of L4 RS, FS and nFS neurons. Somata and dendrites, opaque colour; axons, half-transparent colour.

between the ACh-induced change in V_m and R_{in} ($r = 0.77$, $p = 1.6 \times 10^{-7}$; **Supplementary Figure 2C**), i.e., L4 nFS interneurons with higher R_{in} showed a larger depolarisation.

To evaluate the cell-type specificity of ACh-induced changes in V_m in more detail, we grouped the ACh response with respect to the L4 neuron subtype identified by the electrophysiological and morphological features described above. The two L4 RS excitatory neuron subtypes did not exhibit a significantly different ACh response (SSCs: -2.9 ± 1.4 mV, $n = 25$; SPNs: -2.8 ± 1.6 mV, $n = 19$; $p = 0.85$; **Figure 3B**). Similarly, no significant difference was found in the ACh-induced change in V_m among the three L4 FS interneuron subtypes (sBCs: 0.8 ± 1.0 mV, $n = 17$; BCs: 1.3 ± 2.3 mV, $n = 8$; TLCs: 0.5 ± 1.3 mV, $n = 8$; $p = 0.42$; **Figure 3C**). In contrast, in four subtypes of L4 nFS interneurons the ACh-induced V_m change in VIP interneurons was significantly larger than that in the other three subtypes (LPs: 3.0 ± 2.7 mV, $n = 9$; SPs: 3.8 ± 2.2 mV, $n = 11$; NGFs: 2.8 ± 0.5 mV, $n = 4$; VIPs: 14.3 ± 6.7 mV, $n = 6$; $p = 1.5 \times 10^{-3}$) (**Figure 3D**). We did not record the ACh response of the transcolumnar-projecting L4 nFS interneuron due to their scarcity.

Acetylcholine Differentially Changes the Intrinsic Excitability of Layer 4 Fast Spiking and Non-fast Spiking Interneurons

Acetylcholine not only modulates V_m but also induces changes in other intrinsic properties of L4 neurons. We have previously studied the effects of 100 µM ACh on the intrinsic properties of L4 excitatory neurons (Eggermann and Feldmeyer, 2009) and demonstrated that ACh reduces their excitability through a hyperpolarisation of V_m and a reduction in R_{in}. In this study, we focussed mainly on L4 interneurons. Low concentrations of ACh (30 µM) induced no significant change in the intrinsic properties of L4 FS interneurons except for the V_m (cf. **Figures 2**, **3**). For example, no change was found for the AP half-width (Control: 0.26 ± 0.06 ms, $n = 8$; ACh: 0.26 ± 0.05 ms, $n = 8$; $p = 0.31$) and the AP amplitude (Control: 88.0 ± 12.6 mV, $n = 8$; ACh: 80.0 ± 8.9 mV, $n = 8$; $p = 0.08$) (**Figure 4A** and **Supplementary Table 1**). In contrast, apart from V_m changes (cf. **Figures 2**, **3**) ACh also altered three other intrinsic electrophysiological

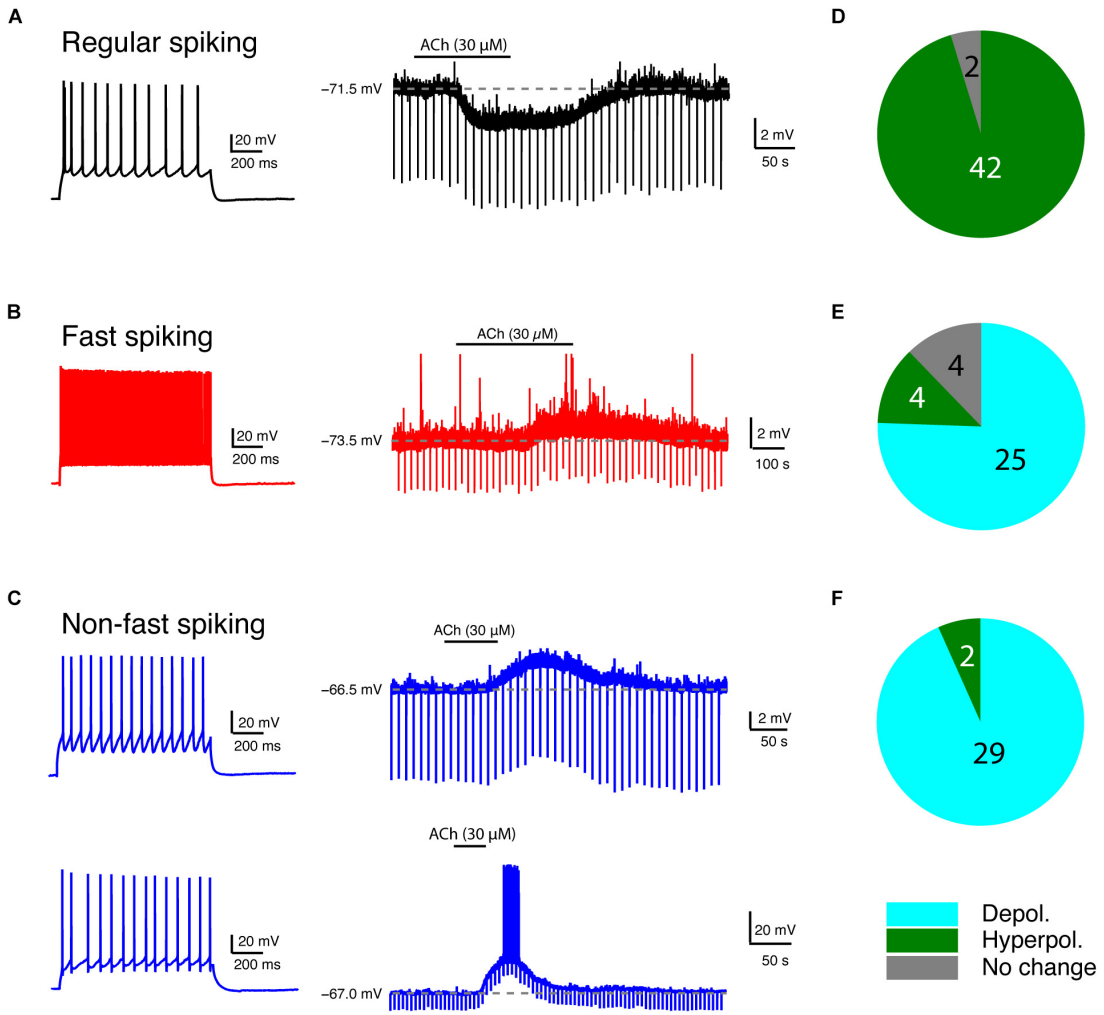

FIGURE 2 | Low concentration of ACh induces diverse V_m changes in L4 RS, FS and nFS neurons. **(A)** An example recording of the time course of ACh-induced Vm change in a L4 RS neuron. **(B)** Same as panel **(A)** but for a L4 FS interneuron. **(C)** Same as panels **(A,B)** but for two different L4 nFS interneurons: top, sub-threshold depolarisation; bottom, supra-threshold depolarisation. **(D–F)** Pie charts summarising the ACh-induced changes in V_m in L4 RS (top), FS (middle), and nFS (bottom) neurons.

properties of L4 nFS interneurons: the AP half-width was increased (Control: 0.44 ± 0.10 ms, n = 10; ACh: 0.48 ± 0.11 ms, n = 10; p = 0.04) and the AP amplitude was decreased (Control: 92.8 ± 10.9 mV, n = 10; ACh: 82.6 ± 11.4 mVs, n = 10; $p = 2.0 \times 10^{-3}$) (**Figure 4B**). Furthermore, the rheobase current was significantly reduced by ACh (Control: 158.08 ± 75.5 pA, n = 10; ACh: 84.0 ± 113.1 pA, n = 10; $p = 5.9 \times 10^{-3}$) (**Supplementary Table 1**). Thus, in contrast to L4 excitatory neurons, ACh enhanced the excitability of all recorded L4 nFS interneuron types.

One particular L4 nFS interneuron (**Figure 4C**) responded to ACh application with a V_m hyperpolarisation, in contrast to most L4 nFS interneurons. Furthermore, ACh changed its repetitive firing property (**Figure 4C**). Under control condition, this neuron showed a regular spiking firing pattern with a small spike-frequency adaptation, which in the presence of 30 µM ACh was transformed to an accelerating firing pattern together with a spike amplitude accommodation. In addition, AP firing persisted even after terminating current injection. Because firing pattern and V_m returned to normal after washout (**Figure 4C**), the marked alteration in the firing pattern cannot be the result of deteriorating recording conditions. Hence, already at low concentrations, ACh can dramatically change the electrophysiological behaviour of a subpopulation of L4 nFS interneurons.

Acetylcholine-Induced Membrane Potential Changes in Layer 4 Neurons Are Mainly Regulated by Muscarinic Receptors

To reveal the molecular mechanism of ACh-induced V_m changes in L4 neurons, slices were superfused with the general mAChR antagonist ATRO (200 nM) before application of

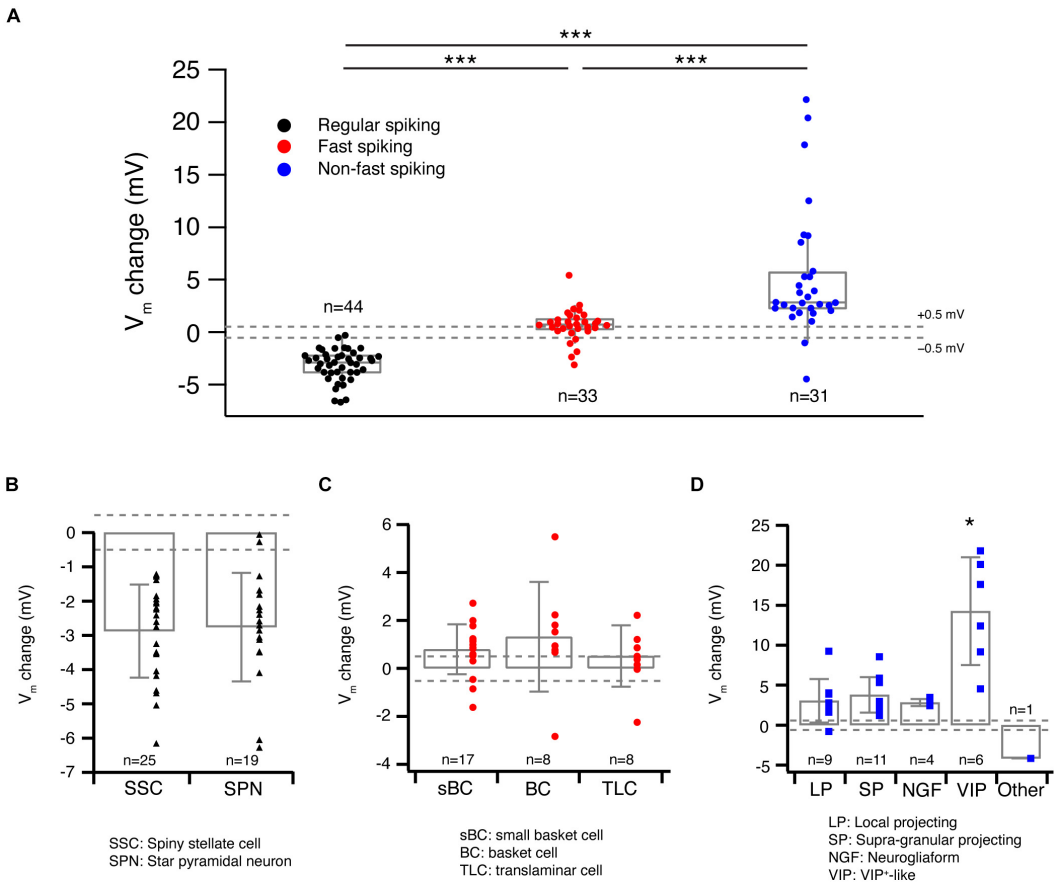

FIGURE 3 | Acetylcholine-induced Vm changes are related to the L4 RS, FS and nFS neuron (sub)types. **(A)** Box plots of ACh-induced Vm changes in L4 RS, FS and nFS neurons. Individual data points are given on the right. *P* value was calculated using the non-parametric Wilcoxon–Mann–Whitney two-sample rank test. *** $p < 0.001$. Dashed lines indicate the Vm change at ±0.5 mV. **(B)** Histograms of ACh-induced V_m changes for two L4 RS neuron subtypes: spiny stellate cells and star pyramidal neurons. No statistically significant difference was found between two subtypes. **(C)** Histograms of ACh-induced V_m changes for three L4 FS neuron subtypes: small basket cells, basket cells, and translaminar cells. No statistically significant difference was found among three subtypes. **(D)** Histograms of ACh-induced V_m changes for five L4 nFS neuron subtypes: local projecting (putative SST+, non-Martinotti cell-like), supragranular projecting (putative SST+, Martinotti cell-like), NGF, VIP+-like and unclassified interneurons. VIP+-like interneurons show the strongest depolarisation of the five subtypes. Statistically significant differences (*) were found between VIP+-like and three other interneuron subtypes (LP, SP, NG).

ACh. A comparison of the ACh-induced change in V_m before and during co-application of ATRO showed that the mAChR antagonist completely blocked the response in all L4 RS excitatory neurons (Control: -3.8 ± 0.9 mV, $n = 9$; ATRO: -0.4 ± 0.5 mV, $n = 9$; $p = 3.9 \times 10^{-3}$) (**Figures 5A,D**) and all L4 FS interneurons (Control: 1.5 ± 0.6 mV, $n = 4$; ATRO: 0.1 ± 0.3 mV, $n = 4$; $p = 0.13$) (**Figures 5B,D**). This suggests that the ACh-induced V_m changes in these L4 neuron types are exclusively mediated by mAChRs. In contrast, in L4 nFS interneurons, ATRO largely (but not completely) blocked the V_m change induced by 30 μM ACh (Control: 9.2 ± 7.2 mV, $n = 11$; ATRO: 3.7 ± 4.5 mV, $n = 11$; $p = 9.8 \times 10^{-4}$) (**Figures 5C,D**). In the majority (8 out of 11) of L4 nFS interneurons, ATRO nearly completely blocked the ACh-induced V_m change while in the remainder (3 out of 11), a residual ACh-induced change in V_m still persisted after the co-application of ATRO. We tested whether this residual depolarisation was mediated by nAChRs (see below). To identify the mAChR type mediating the modulatory effect, TRO (1 μM), a specific M4 mAChR antagonist, and PIR (0.5 μM), a specific M1 mAChR antagonist, were applied before ACh. We found that TRO completely blocked the ACh-induced hyperpolarisation in L4 RS excitatory neurons (**Supplementary Figure 3A**) while PIR completely blocked the ACh-induced depolarisation in L4 FS interneurons (**Supplementary Figure 3B**). However, in L4 nFS interneurons, PIR blocked the ACh-induced depolarisation only partially (**Supplementary Figure 3C**).

Layer 4 VIP+-Like Non-fast Spiking Interneurons Are Strongly Depolarised by Low-Concentration of Acetylcholine *via* Both Muscarinic and Nicotinic Receptors

The fact that a subset of L4 nFS interneurons showed a strong ACh-induced depolarisation (**Figures 2C**, **3A,D**) that was not fully blocked by ATRO (**Figures 5C,D**) indicates that

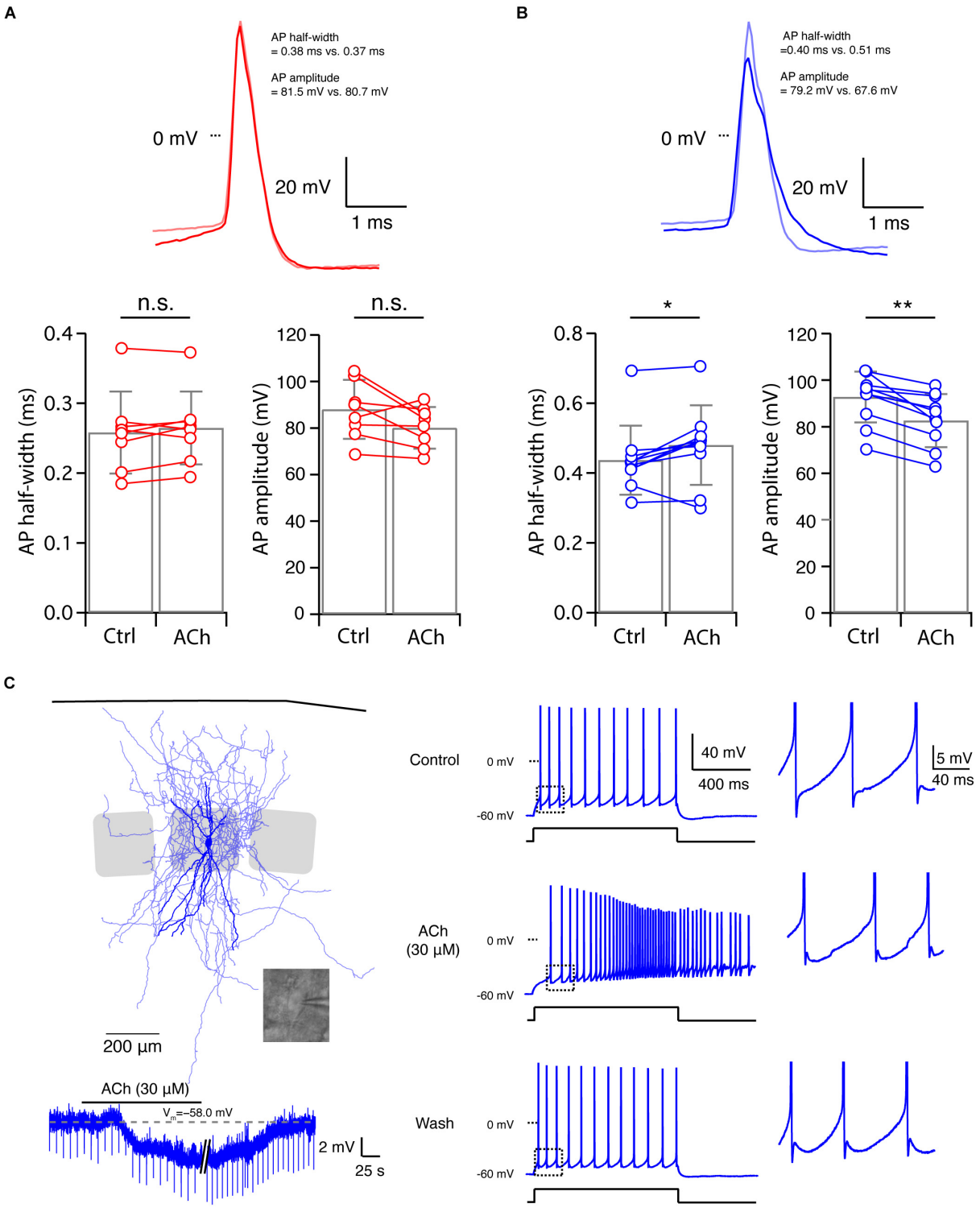

FIGURE 4 | Acetylcholine-induced changes in other intrinsic properties of L4 FS and nFS interneurons. **(A)** Top, overlay of single APs recorded in a L4 FS interneuron before (light red) and after (red) the ACh application. Bottom, comparison histograms for AP half-width and AP amplitude. No statistically significant difference was found. **(B)** Top, overlay of single APs recorded in a L4 nFS interneuron before (light magenta) and after (magenta) ACh application. Bottom, comparison histograms for AP half-width and AP amplitude. A statistically significant increase in AP half-width and a decrease in AP amplitude were found. *P* values were calculated using the non-parametric Wilcoxon signed rank test. * $p < 0.05$, ** $p < 0.01$, n.s. $p \geq 0.05$. **(C)** Example recording from a L4 nFS interneuron; soma and dendrites are in opaque, the axon in half-transparent blue. ACh induced an abnormal V_m in this neuron. Furthermore, a dramatic change in the firing pattern was found during the ACh application.

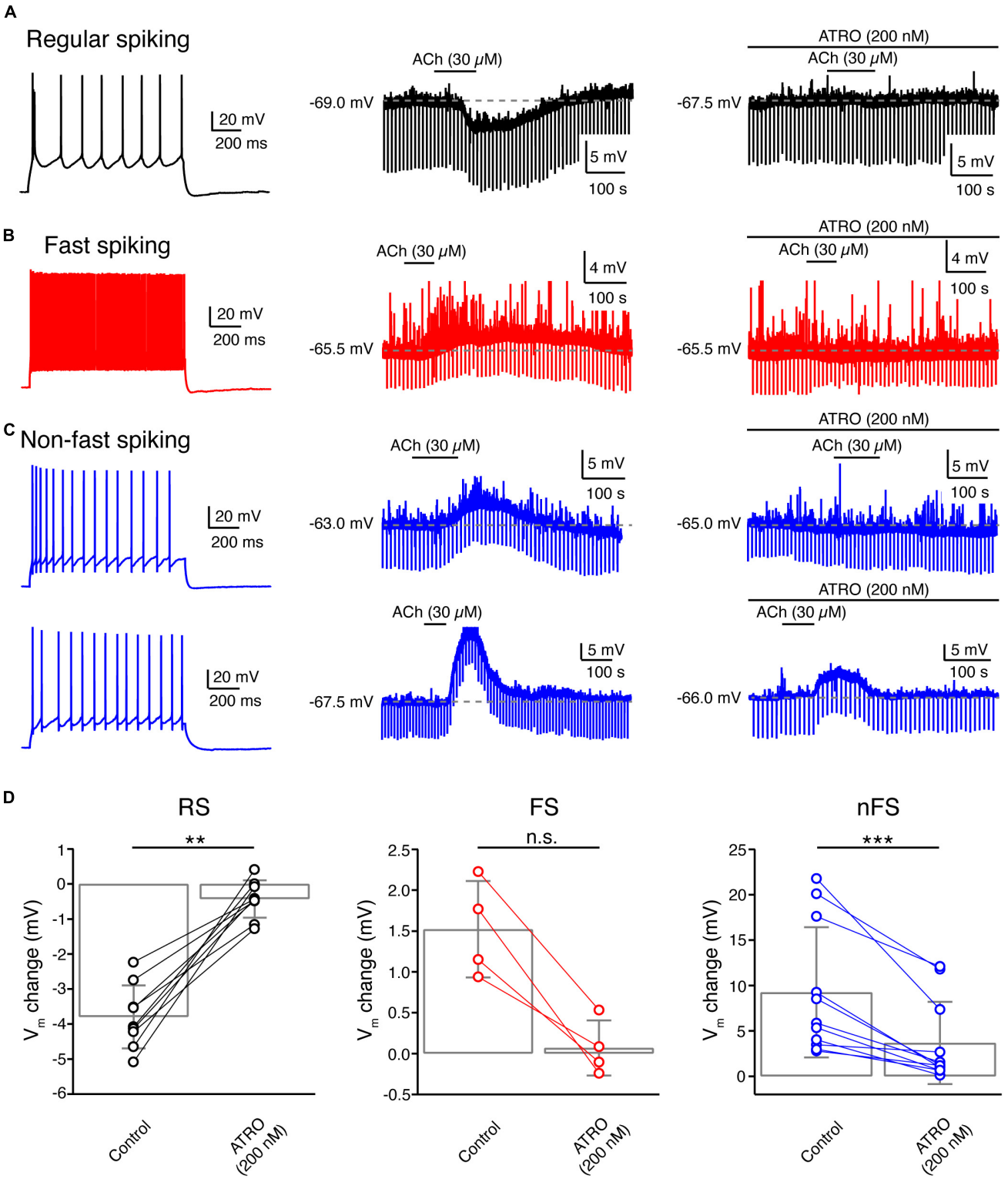

FIGURE 5 | Acetylcholine-induced V_m changes in L4 RS, FS and nFS neurons are mainly mediated by muscarinic ACh receptors. **(A)** An example recording of the time course of ACh-induced Vm change under control condition and in the presence of atropine, a general mAChR antagonist, in a L4 RS neuron. **(B)** Same as panel **(A)** but for a L4 FS interneuron. **(C)** Same as panels **(A,B)** but for two L4 nFS interneurons: upper, sub-threshold depolarisation which could be completely blocked by atropine; lower, supra-threshold depolarisation which could be partly blocked by atropine. **(D)** Comparison histograms for L4 RS (left), FS (middle), and nFS (right) neurons under control conditions and in the presence of atropine. *P* value was calculated using the non-parametric Wilcoxon signed rank test. ** $p < 0.01$, *** $p < 0.001$, n.s. $p \geq 0.05$.

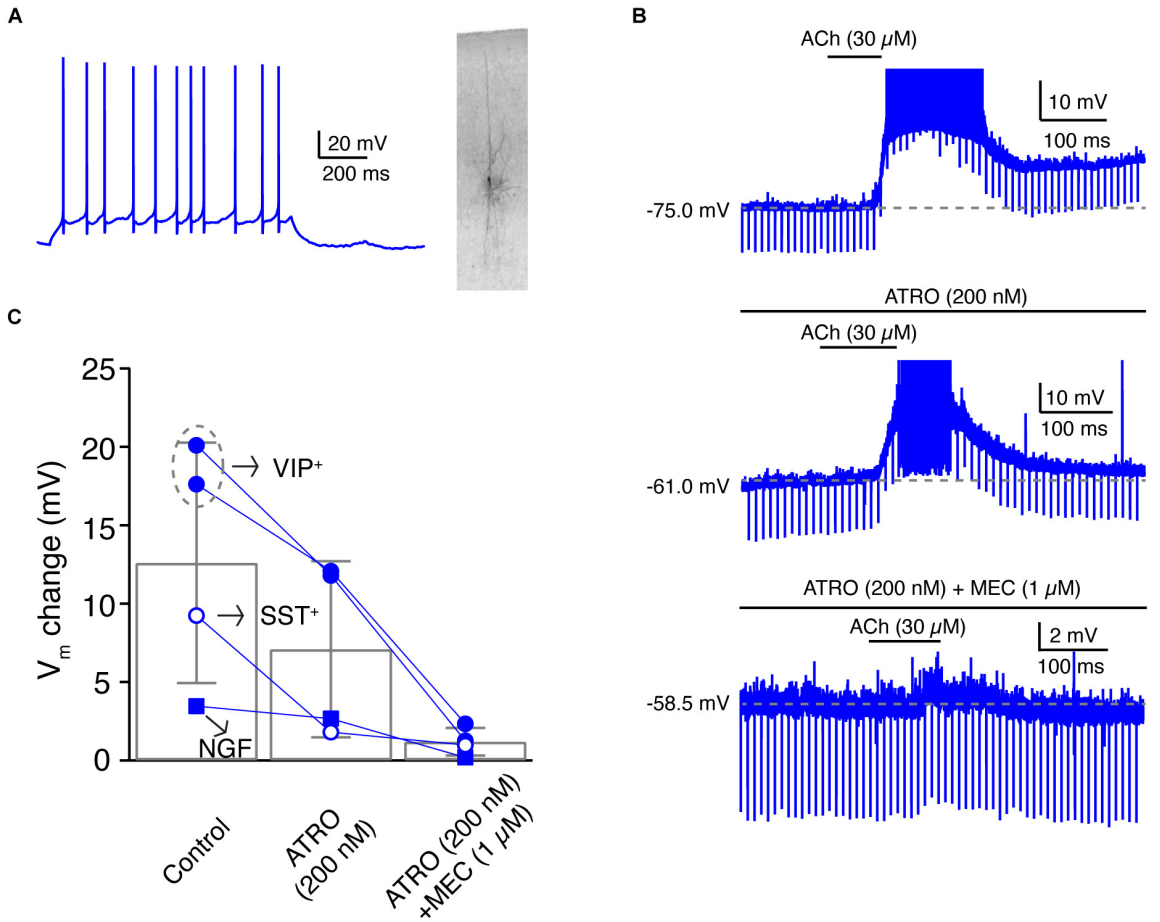

FIGURE 6 | A subpopulation of L4 non-FS interneurons are strongly depolarised by ACh *via* both muscarinic and nicotinic ACh receptors. **(A)** Firing pattern (left) and morphology (right) of an example L4 VIP+-like interneuron. **(B)** Time course of VIP+-like change during ACh application alone (top), during the application of ACh in the presence of atropine (middle), and during the ACh application in the presence of atropine and mecamylamine (bottom). **(C)** Histogram of ACh-induced V_m changes under three conditions. Note that in these four L4 nFS interneurons, two are VIP+-like, one is SST+-like, and one is a NGF cell.

these interneurons may respond to ACh *via* both mAChRs and nAChRs. In those L4 nFS interneurons, in which ATRO blocked the ACh-induced depolarisation only incompletely, MEC (1 μM), a general nAChR antagonist, together with ATRO were applied before ACh. An example recording from a putative L4 VIP+ nFS interneuron (**Figure 6A**) is shown in **Figure 6B**. This neuron exhibits an irregular firing pattern, a bipolar dendritic structure, and a narrow translaminar axonal projection, all of which are characteristics typical of VIP+ interneurons (Porter et al., 1998; Pronneke et al., 2015; Emmenegger et al., 2018). ACh induced a strong depolarisation in this neuron and elicited spontaneous AP firing. Even in the presence of ATRO, the ACh-induced AP firing still exists. Only when ATRO and MEC were applied together, was the ACh-induced change in V_m blocked (**Figure 6B**). A nAChR-mediated depolarisation was observed not only in L4 VIP+ interneurons (n = 2) but also in one putative SST+ interneuron and one NGF cell (**Figure 6C**). However, only VIP+ interneurons showed such a strong nAChR-mediated depolarisation. In one recording from a L4 VIP+ interneuron, we found that the ATRO-resistant depolarisation was completely blocked by DHβE, a specific antagonist for α4β2-subunit containing nAChRs (**Supplementary Figure 3C**).

DISCUSSION

In the present study, we found that all L4 neuron types are persistently modulated by low concentrations of ACh in a cell-type specific way (see **Figure 7**): (1) ACh (30 μM) reduces the intrinsic excitability of L4 RS excitatory neurons by activating the M4 mAChRs presumably located in the soma and/or dendrite, which leads to a hyperpolarisation of V_m and a decreased R_{in}; (2) ACh induces a small but significant depolarisation in L4 FS interneurons by activating M1 mAChRs; (3) ACh elicits a markedly stronger depolarisation in L4 nFS interneurons compared to L4 FS interneurons by activating not only mAChRs (of the M1 and/or M3/5 type) but also nAChRs (presumably of the α4β2* type); (4) In a subset of L4 nFS interneurons, the VIP+-like interneurons, the ACh-induced depolarisation was sufficiently large to induce

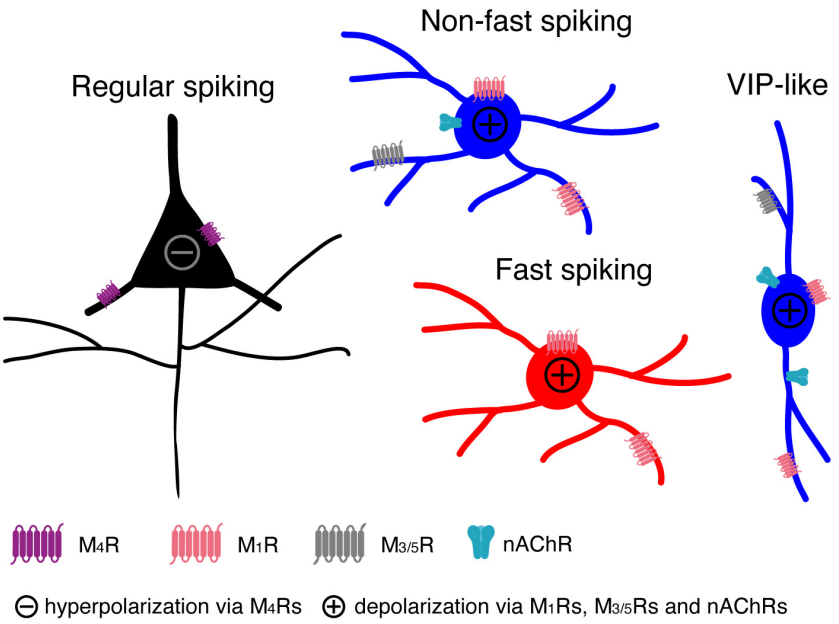

FIGURE 7 | A cartoon summarising the modulatory effects of low concentrations ACh on L4 RS, FS and nFS neurons and their potential molecular mechanisms.

spontaneous AP firing through activation of both mAChRs and nAChRs.

Layer 4 Neuronal Cell-Type Classification

A detailed neuronal cell-type classification is necessary and critical for an in-depth understanding the modulatory effects of ACh. Traditionally, neurons are classified based on their morphological (dendritic and axonal) and electrophysiological (repetitive firing) properties (Petilla Interneuron Nomenclature Group et al., 2008; DeFelipe et al., 2013). With the development and sophistication of single-cell mRNA sequencing techniques, the molecular features of neurons add an additional layer of complexity to neuronal classification (Zeng and Sanes, 2017; Yuste et al., 2020). We have performed a series of studies to dissect the neuronal diversity in layer 4 of rat barrel cortex (Feldmeyer et al., 1999; Lubke et al., 2000; Koelbl et al., 2015; Emmenegger et al., 2018). In general, layer 4 comprises three neuronal cell classes showing distinct repetitive firing properties: regular spiking, fast spiking and non-fast spiking (adapting, irregular, late, etc.). Taking the morphological diversity also into account, L4 RS excitatory neurons have been classified into spiny stellate cells and star pyramidal neurons (Feldmeyer et al., 1999; Lubke et al., 2000) while L4 FS interneurons have been divided into cluster 3 (small basket cells), cluster 2 (basket cells), and translaminar-projecting FS interneurons (Koelbl et al., 2015). Most of these L4 FS interneurons are parvalbumin-positive (PV+) but calbindin-negative. L4 nFS interneurons, on the other hand, have been separated into five morpho-electrophysiological subtypes including transcolumnar-projecting interneurons with an adapting firing pattern, locally projecting with an adapting firing pattern (presumably non-Martinotti cells), supragranular-projecting with an adapting firing pattern with a Martinotti-cell appearance, VIP+ cell-like with an irregular firing pattern (VIP+-like) and neurogliaform cells (Emmenegger et al., 2018). The former three subtypes are somatostatin-positive while the latter two Prox1-positive. Our classification of L4 neurons is in line with several other groups focusing on the barrel cortex or primary visual cortex of rats and mice (Gibson et al., 1999; Porter et al., 2001; Beierlein et al., 2003; Ma et al., 2006; Scala et al., 2019).

The Necessity of Bath-Application of Low-Concentration Acetylcholine to Study the Tonic Neuromodulation Mediated by Muscarinic Receptors

Previously, it has been shown that the ACh concentration in the cerebrospinal fluid is in a low micromolar range, which fluctuates between 1 and 10 μM depending on the brain state (Himmelheber et al., 2000; Mattinson et al., 2011; Teles-Grilo Ruivo et al., 2017). Recently, accumulating evidence indicates that functional synaptic contacts are also established by cholinergic afferents in the neocortex. ACh is released into the synaptic cleft and its concentration can reach a very high concentration (>1 mM) (Turrini et al., 2001; Bennett et al., 2012; Hay et al., 2016; Obermayer et al., 2019). However, the exact extracellular concentration of ACh is still under investigation due to the species differences and difficulties arising from the rapid breakdown by acetylcholinesterase. ACh modulates the intrinsic neuronal properties through both mAChRs and nAChRs. mAChRs are G-protein coupled receptors the activation of which initiates a signalling cascade inside the neuron. In contrast, nAChRs form ligand-gated cation channels (Unwin, 2003; Dani, 2015). These two types of receptors work at

different concentrations of ACh. mAChRs already show a high affinity to ACh at low concentrations (in the range of 1–100 μM) while nAChRs require a high concentration of ACh for maximal activity (in the mM range). Previous studies have used puff-application of 1–10 mM ACh to study the nicotinic effects of ACh on excitatory and inhibitory neurons in several cortical areas (Xiang et al., 1998; Gulledge and Stuart, 2005; Gulledge et al., 2007; Poorthuis et al., 2013a,b). Puff-application of agonists has a high spatiotemporal resolution and is therefore a suitable strategy to simulate phasic ACh release at cholinergic presynaptic terminals; it is also required to minimise the effects of nAChR desensitisation. In addition, at such high concentrations, ACh will not be hydrolysed (and hence inactivated) immediately so that it may persist at low concentrations in the perisynaptic space. Bath application of cholinergic agonists such as ACh and carbachol is a good approach to simulate the latter condition because the agonist concentration will be maintained at a constant level to allow the measurement of neuronal properties at equilibrium. Carbachol shares both the muscarinic and nicotinic actions of ACh but shows a slower binding, dissociation and desensitisation kinetics, in particular at nAChRs. In addition, carbachol is not degraded by acetylcholinesterase. Carbachol is not the natural agonist and the relative affinity of carbachol for mAChRs and nAChRs is likely to be different from that of ACh so that we may observe an activation of nAChRs with low concentrations of carbachol but not with ACh. In order to simulate the *in situ* action of cholinergic agonists, the natural agonist ACh has been used instead of carbachol in this study. It is likely that in the extracellular space, a neurotransmitter/neuromodulator is only present at a μM concentration because of its rapid diffusion from the synaptic release site (Borroto-Escuela et al., 2015). In addition, application of high concentrations of ACh will mask the effects mediated by mAChRs so that the application of low concentrations (∼μM) of ACh is a prerequisite to uncover their functional effects.

Unique Cholinergic Modulation of Layer 4 Excitatory Neurons

We have shown previously that 100 μM ACh persistently hyperpolarises L4 excitatory neurons and reduces their intrinsic excitability (Eggermann and Feldmeyer, 2009), an ACh effect markedly different from that observed in most of pyramidal cells except for L6A corticocortical neurons (Yang et al., 2020). In L2/3, L5 and corticothalamic L6A pyramidal cells, ACh induces a persistent depolarisation and therefore enhances the excitability.

The ACh-induced hyperpolarisation in L4 excitatory neurons is mediated exclusively by M4 mAChRs, a finding that is supported by another study using optogenetic activation of synaptic ACh release (Dasgupta et al., 2018). Here, using a lower concentration of ACh (30 μM), similar results were obtained. Note that, as discussed above, 30 μM is an ACh concentration closer to the physiological range than 100 μM. There was no clear difference between the ACh-induced hyperpolarisation in both L4 RS neuron subtypes suggesting that SSNs and SPCs express the same mAChR subtype at a similar density.

Acetylcholine Persistently Depolarises Layer 4 Fast Spiking Interneurons

The effects of ACh on FS interneurons have been a long-standing matter of debate. Conflicting results have been published by different research groups. Puff-application of 5 mM ACh induced a transient hyperpolarisation that was mediated by mAChRs in rat neocortical L5 FS interneurons (Xiang et al., 1998). Recently, in the mouse visual cortex it has been shown that optogenetically stimulated ACh release led to an indirect inhibition in L2/3 FS interneurons *via* "facilitation" of the cholinergic responses in L2/3 somatostatin-positive interneurons (Chen et al., 2015). On the other hand it has been postulated that ACh does not affect the V_m of FS interneurons. In the rat frontal cortex, bath-application of carbachol (10 μM) had no effect on L2/3 FS interneurons (Kawaguchi, 1997). In a follow-up study the same group used focal application of ACh (100 μM or 5 mM for comparison with the study by Xiang et al., 1998) onto FS interneurons in rat visual and prefrontal cortex; the authors concluded that the focal application itself (i.e., a mechanical artefact but not the transient ACh exposure) caused the hyperpolarising response (Gulledge et al., 2007). Except for Xiang et al. (1998), most investigators have been unable to show a direct effect of ACh on FS interneurons (Muñoz and Rudy, 2014); however, they reported a presynaptic effect of ACh. In contrast to previous studies, we found a persistent ACh-induced V_m depolarisation in L4 FS interneurons, an effect that appeared in all three subtypes of L4 FS interneurons. To the best of our knowledge, this is the first time that a direct depolarising effect of ACh on FS interneurons has been demonstrated conclusively. In addition, we were able to show that this effect is mediated by M1 mAChRs. The ACh-induced depolarisation persisted in the presence of GABA and glutamate receptor antagonists so that indirect effects of ACh can be excluded. We were unable to investigate the effect of ACh on another subtype of FS interneurons, the chandelier or axo-axonic cells, which are very scarce if not absent in cortical layer 4 (Wang et al., 2019).

Acetylcholine Modulates Layer 4 Non-fast Spiking Interneuron Activity in a Subtype-Specific Way

Layer 4 nFS interneurons are a heterogenous population with diverse firing patterns, dendritic/axonal morphologies and molecular expression patterns. To elucidate modulatory effects of ACh on L4 nFS interneurons, a clear separation into identifiable subtypes is required. The local- and supragranular-projecting subtypes of L4 nFS interneurons display an adapting firing pattern similar to that of somatostatin-positive interneurons. Indeed, immunocytochemistry revealed that both subtypes of L4 nFS interneurons are somatostatin-positive (Emmenegger et al., 2018). Here, we found that L4 SST+-like interneurons including both local projecting (non-Martinotti-like) and supragranular projecting (Martinotti-like) cells that responded to ACh with a strong depolarisation that is predominantly mediated by mAChRs. Consistent with our findings, in the mouse barrel cortex it has been shown that L4 SST+ interneurons were depolarised and fired spikes in response to bath-applied

muscarine (3 μM) (Xu et al., 2013). In one L4 SST+-like interneuron, ACh induced a depolarisation mediated by both mAChRs and nAChRs suggesting that even at μM ACh concentrations activation of nAChRs may be also possible. In a previous study, it has been shown that ACh directly excites SST+ neurons *via* both mAChRs and nAChRs in layer 2/3 of mouse visual cortex (Chen et al., 2015). However, a very high concentration of ACh (10 mM) was puff-applied in that study, which is very different from the bath-application of ACh (30 μM) described here.

Excitation of VIP+ interneurons by nAChRs has been observed in several cortical areas of both rat and mouse (Porter et al., 1999; Férézou et al., 2007; Koukouli et al., 2017; Askew et al., 2019; Prönneke et al., 2020). In the rat motor cortex, local pressure application of ACh (100 μM) or the selective nAChR agonist DMPP (100–500 mM) depolarised VIP+ interneurons located in layer 3–5 and induced a discharge of action potentials (Porter et al., 1999). Pharmacological experiments suggested that the ACh effect was mediated by non-α7 nicotinic receptors containing α4β2 and α5 subunits (Koukouli et al., 2017). In another study from the same group, it has been shown that bath-application of nicotine (1 μM) also resulted in a strong depolarisation leading to a sustained action potential discharge in VIP+ interneurons (Férézou et al., 2007). Similarly, bath-application of nicotine (1 μM) in the mouse auditory cortex caused sustained AP discharge in VIP+ interneurons across the layers (Askew et al., 2019). In the mouse barrel cortex, bath-application of ACh (40 μM) efficiently depolarised L2/3 VIP+ interneurons and changed the firing pattern from bursting to tonic spiking in a subpopulation (Prönneke et al., 2020); however, the authors concluded that cholinergic modulation was mediated exclusively by nAChRs. All of the aforementioned studies emphasised the critical role of nAChRs in the cholinergic modulation of VIP+ interneurons but overlooked any direct involvement of mAChRs. However, our recordings from L4 VIP+ interneurons demonstrated that both AChR subtypes participate in the cholinergic modulation in a cooperative way because ATRO partially blocked the depolarisation or shortened the duration of repetitive AP firing induced by ACh; ATRO together with the nAChR antagonist MEC completely blocked the ACh effect. Similarly, in rat frontal cortex, VIP+ cells showed a sustained V_m depolarisation in response to bath-applied muscarine (3 μM) in the presence of TTX (Kawaguchi, 1997) indicating that mAChRs are expressed in these interneurons.

For NGF cells, the focus of attention is mostly cortical layer 1 where NGF cells are abundant (Christophe et al., 2002; Gulledge et al., 2007; Arroyo et al., 2012; Brombas et al., 2014). Puff-application of nicotinic agonists such as ACh, DMPP, choline onto L1 NGF cells or optogenetic stimulation of cholinergic fibres in layer 1 has revealed nicotinic excitation of NGF cells. Similar results have been shown for L2/3 5-HT_{3a}R+ NGF cells of mouse barrel cortex (Lee et al., 2010). Here, we found that in L4 NGF cells of the barrel cortex, low concentrations of ACh led to a mAChR-mediated sustained depolarisation. In one L4 NGF cell, a participation of nAChRs in this depolarisation was also found.

In addition to SST+, VIP+, and NGF cells, layer 4 comprises other nFS subtypes (Tasic et al., 2018). In one L4 nFS interneuron, we were able to show that, in contrast to most other L4 nFS interneurons, ACh application resulted in a hyperpolarisation of this neuron and dramatically changed its repetitive firing pattern during the suprathreshold current injection. The cholinergic response of this neuron together with its firing pattern and morphology, is reminiscent of a subset of CCK+ neurons in L2/3 of rat frontal cortex which exhibited a prominent hyperpolarisation in response to muscarine (3 μM) and had large somata and an extensive axonal arbour (Kawaguchi, 1997). Therefore, the nFS interneuron showing an ACh-induced hyperpolarisation described here could be a L4 CCK+ neuron. Similarly, some hippocampal CA1 CCK+ interneurons showed also an ACh-induced hyperpolarisation mediated by mAChRs (McQuiston and Madison, 1999b; Cea-del Rio et al., 2011). Furthermore, the dramatic change in firing pattern induced by ACh has also been demonstrated in hippocampal CA1 CCK+ interneurons (McQuiston and Madison, 1999a; Lawrence et al., 2006; Cea-del Rio et al., 2010, 2011). In these neurons, through the activation of M1 and M3 mAChRs the AHP was superimposed by an afterdepolarisation which is often sufficiently strong to evoke APs in the absence of further stimulation (McQuiston and Madison, 1999a; Cea-del Rio et al., 2011).

Functional Significance of Cholinergic Neuromodulation for Layer 4 Neuronal Microcircuits

In the neocortex, ACh is continuously released into the extracellular space and its level changes dramatically during the animal's diurnal cycle and different behavioural states (Teles-Grilo Ruivo et al., 2017). Furthermore, there is increasing evidence for changes in ACh receptor expression levels going hand in hand with the diurnal change in ACh drive (Hut and Van der Zee, 2011). Most of the intracortical ACh is not released at synaptic contacts but rather diffusely into the extracellular space through an extrasynaptic volume transmission (Fuxe and Borroto-Escuela, 2016). Under this condition, cholinergic modulation is spatiotemporally slower but broader, thereby tuning neuronal network function. Modulation of neurons and their synaptic interactions through mAChRs may induce neuronal oscillations and therefore change the information processing mode in L4 neuronal microcircuits. Specifically, cholinergic activation of L4 FS, PV+, and nFS, SST+ interneurons by low concentrations of ACh may lead to the generation of persistent activity such as the gamma rhythm, which has been demonstrated to enhance the cortical circuit performance (Bartos et al., 2007; Sohal et al., 2009; Veit et al., 2017). Indeed, it has been demonstrated that bath-application of carbachol (10 μM) to activate mAChRs and kainate (300 nM) to increase the tonic excitatory drive elicited persistent gamma frequency network oscillations in cortical layer 4 of mouse barrel cortex (Buhl et al., 1998). In addition, differential modulation of L4 excitatory and inhibitory neurons, i.e., the persistent hyperpolarisation of L4 excitatory neurons and depolarisation of most L4 inhibitory neurons, will change the excitation-inhibition

balance towards inhibition and reduce the responsiveness of the L4 recurrent excitatory microcircuit. Therefore, our results support the hypothesis that ACh has a filtering action in the major recipient layer of the neocortex (Eggermann and Feldmeyer, 2009). Because neocortical layer 4 is uniquely positioned to gate thalamocortical input to the neocortex, cholinergic modulation of L4 neuronal microcircuits will affect the whole barrel cortex together with the related cortical areas (e.g., M1 and S2) and finally the animal behaviour (Eggermann et al., 2014; Meir et al., 2018). In addition, our finding that mAChRs ubiquitously but differentially modulate the activity of L4 excitatory and inhibitory neurons might open the door to more specific therapeutic strategies to treat cognitive dysfunction or psychiatric disorders linked to degeneration of the cholinergic system in diseases such as Alzheimer's disease and schizophrenia (Marin, 2012; Hampel et al., 2018).

DATA AVAILABILITY STATEMENT

The original contributions presented in the study are included in the article/**Supplementary Material**, further inquiries can be directed to the corresponding authors.

ETHICS STATEMENT

All experimental procedures involving animals were performed in accordance with the guidelines of the Federation of European Laboratory Animal Science Association (FELASA), the EU Directive 2010/63/EU, and the German animal welfare law.

AUTHOR CONTRIBUTIONS

GQ designed research, performed experiments, analysed data, and wrote the draft manuscript. DF supervised the work and wrote the manuscript. Both authors contributed to the article and approved the submitted version.

FUNDING

This work was supported by the Helmholtz Society, the DFG Research Group–BaCoFun (grant no. Fe471/4-2 to DF) and European Union's Horizon 2020 Research Innovation Programme (grant agreement no. 785907; HBP SGA2 to DF).

ACKNOWLEDGMENTS

We are grateful to Danqing Yang for insightful comments and suggestions on the manuscript. We thank Werner Hucko for excellent technical assistance and Karlijn van Aerde for custom-written macros in Igor Pro software. We also thank Vishalini Emmenegger for help with Neurolucida reconstructions.

SUPPLEMENTARY MATERIAL

The Supplementary Material for this article can be found online at: https://www.frontiersin.org/articles/10.3389/fncir.2022.843025/full#supplementary-material

REFERENCES

Arroyo, S., Bennett, C., Aziz, D., Brown, S. P., and Hestrin, S. (2012). Prolonged disynaptic inhibition in the cortex mediated by slow, non-α7 nicotinic excitation of a specific subset of cortical interneurons. *J. Neurosci.* 32, 3859–3864. doi: 10.1523/jneurosci.0115-12.2012

Askew, C. E., Lopez, A. J., Wood, M. A., and Metherate, R. (2019). Nicotine excites VIP interneurons to disinhibit pyramidal neurons in auditory cortex. *Synapse* 73:e22116. doi: 10.1002/syn.22116

Bacci, A., Huguenard, J. R., and Prince, D. A. (2005). Modulation of neocortical interneurons: extrinsic influences and exercises in self-control. *Trends Neurosci.* 28, 602–610. doi: 10.1016/j.tins.2005.08.007

Bailey, C. D., De Biasi, M., Fletcher, P. J., and Lambe, E. K. (2010). The nicotinic acetylcholine receptor alpha5 subunit plays a key role in attention circuitry and accuracy. *J. Neurosci.* 30, 9241–9252. doi: 10.1523/JNEUROSCI.2258-10.2010

Bartos, M., Vida, I., and Jonas, P. (2007). Synaptic mechanisms of synchronized gamma oscillations in inhibitory interneuron networks. *Nat. Rev. Neurosci.* 8, 45–56. doi: 10.1038/nrn2044

Beierlein, M., Gibson, J. R., and Connors, B. W. (2003). Two dynamically distinct inhibitory networks in layer 4 of the neocortex. *J. Neurophysiol.* 90, 2987–3000. doi: 10.1152/jn.00283.2003

Bennett, C., Arroyo, S., Berns, D., and Hestrin, S. (2012). Mechanisms generating dual-component nicotinic EPSCs in cortical interneurons. *J. Neurosci.* 32, 17287–17296. doi: 10.1523/jneurosci.3565-12.2012

Borroto-Escuela, D. O., Agnati, L. F., Bechter, K., Jansson, A., Tarakanov, A. O., and Fuxe, K. (2015). The role of transmitter diffusion and flow versus extracellular vesicles in volume transmission in the brain neural-glial networks. *Philos. Trans. R. Soc. Lond. B Biol. Sci.* 370:0183. doi: 10.1098/rstb.2014.0183

Brombas, A., Fletcher, L. N., and Williams, S. R. (2014). Activity-dependent modulation of layer 1 inhibitory neocortical circuits by acetylcholine. *J. Neurosci.* 34, 1932–1941. doi: 10.1523/jneurosci.4470-13.2014

Buhl, E. H., Tamás, G., and Fisahn, A. (1998). Cholinergic activation and tonic excitation induce persistent gamma oscillations in mouse somatosensory cortex *in vitro*. *J. Physiol.* 513(Pt 1), 117–126. doi: 10.1111/j.1469-7793.1998.117by.x

Cea-del Rio, C. A., Lawrence, J. J., Erdelyi, F., Szabo, G., and McBain, C. J. (2011). Cholinergic modulation amplifies the intrinsic oscillatory properties of CA1 hippocampal cholecystokinin-positive interneurons. *J. Physiol.* 589, 609–627. doi: 10.1113/jphysiol.2010.199422

Cea-del Rio, C. A., Lawrence, J. J., Tricoire, L., Erdelyi, F., Szabo, G., and McBain, C. J. (2010). M3 muscarinic acetylcholine receptor expression confers differential cholinergic modulation to neurochemically distinct hippocampal basket cell subtypes. *J. Neurosci.* 30, 6011–6024. doi: 10.1523/JNEUROSCI.5040-09.2010

Chen, N., Sugihara, H., and Sur, M. (2015). An acetylcholine-activated microcircuit drives temporal dynamics of cortical activity. *Nat. Neurosci.* 18, 892–902. doi: 10.1038/nn.4002

Christophe, E., Roebuck, A., Staiger, J. F., Lavery, D. J., Charpak, S., and Audinat, E. (2002). Two types of nicotinic receptors mediate an excitation of neocortical layer I interneurons. *J. Neurophysiol.* 88, 1318–1327. doi: 10.1152/jn.2002.88.3.1318

Colangelo, C., Shichkova, P., Keller, D., Markram, H., and Ramaswamy, S. (2019). Cellular, Synaptic and Network Effects of Acetylcholine in the Neocortex. *Front. Neural Circuits* 13:24. doi: 10.3389/fncir.2019.00024

Dani, J. A. (2015). Neuronal Nicotinic Acetylcholine Receptor Structure and Function and Response to Nicotine. *Int. Rev. Neurobiol.* 124, 3–19. doi: 10.1016/bs.irn.2015.07.001

Dasgupta, R., Seibt, F., and Beierlein, M. (2018). Synaptic Release of Acetylcholine Rapidly Suppresses Cortical Activity by Recruiting Muscarinic Receptors in Layer 4. *J. Neurosci.* 38, 5338–5350. doi: 10.1523/jneurosci.0566-18.2018

DeFelipe, J., Lopez-Cruz, P. L., Benavides-Piccione, R., Bielza, C., Larranaga, P., Anderson, S., et al. (2013). New insights into the classification and nomenclature of cortical GABAergic interneurons. *Nat. Rev. Neurosci.* 14, 202–216. doi: 10.1038/nrn3444

Eggermann, E., and Feldmeyer, D. (2009). Cholinergic filtering in the recurrent excitatory microcircuit of cortical layer 4. *Proc. Natl. Acad. Sci. U S A.* 106, 11753–11758. doi: 10.1073/pnas.0810062106

Eggermann, E., Kremer, Y., Crochet, S., and Petersen, C. C. H. (2014). Cholinergic signals in mouse barrel cortex during active whisker sensing. *Cell Rep.* 9, 1654–1660. doi: 10.1016/j.celrep.2014.11.005

Emmenegger, V., Qi, G., Wang, H., and Feldmeyer, D. (2018). Morphological and Functional Characterization of Non-fast-Spiking GABAergic Interneurons in Layer 4 Microcircuitry of Rat Barrel Cortex. *Cereb. Cortex* 28, 1439–1457. doi: 10.1093/cercor/bhx352

Feldmeyer, D., Egger, V., Lubke, J., and Sakmann, B. (1999). Reliable synaptic connections between pairs of excitatory layer 4 neurones within a single 'barrel' of developing rat somatosensory cortex. *J. Physiol.* 521(Pt 1), 169–190. doi: 10.1111/j.1469-7793.1999.00169.x

Férézou, I., Hill, E. L., Cauli, B., Gibelin, N., Kaneko, T., Rossier, J., et al. (2007). Extensive overlap of mu-opioid and nicotinic sensitivity in cortical interneurons. *Cereb. Cortex* 17, 1948–1957. doi: 10.1093/cercor/bhl104

Fuxe, K., and Borroto-Escuela, D. O. (2016). Volume transmission and receptor-receptor interactions in heteroreceptor complexes: understanding the role of new concepts for brain communication. *Neural Regen. Res.* 11, 1220–1223. doi: 10.4103/1673-5374.189168

Gibson, J. R., Beierlein, M., and Connors, B. W. (1999). Two networks of electrically coupled inhibitory neurons in neocortex. *Nature* 402, 75–79. doi: 10.1038/47035

Granger, A. J., Wang, W., Robertson, K., El-Rifai, M., Zanello, A. F., Bistrong, K., et al. (2020). Cortical ChAT(+) neurons co-transmit acetylcholine and GABA in a target- and brain-region-specific manner. *Elife* 9:57749. doi: 10.7554/eLife.57749

Gulledge, A. T., and Stuart, G. J. (2005). Cholinergic inhibition of neocortical pyramidal neurons. *J. Neurosci.* 25, 10308–10320. doi: 10.1523/jneurosci.2697-05.2005

Gulledge, A. T., Park, S. B., Kawaguchi, Y., and Stuart, G. J. (2007). Heterogeneity of phasic cholinergic signaling in neocortical neurons. *J. Neurophysiol.* 97, 2215–2229. doi: 10.1152/jn.00493.2006

Hampel, H., Mesulam, M. M., Cuello, A. C., Farlow, M. R., Giacobini, E., Grossberg, G. T., et al. (2018). The cholinergic system in the pathophysiology and treatment of Alzheimer's disease. *Brain* 141, 1917–1933. doi: 10.1093/brain/awy132

Hasselmo, M. E. (2006). The role of acetylcholine in learning and memory. *Curr. Opin. Neurobiol.* 16, 710–715. doi: 10.1016/j.conb.2006.09.002

Hay, Y. A., Lambolez, B., and Tricoire, L. (2016). Nicotinic Transmission onto Layer 6 Cortical Neurons Relies on Synaptic Activation of Non-α7 Receptors. *Cereb. Cortex* 26, 2549–2562. doi: 10.1093/cercor/bhv085

Himmelheber, A. M., Sarter, M., and Bruno, J. P. (2000). Increases in cortical acetylcholine release during sustained attention performance in rats. *Brain Res. Cogn. Brain Res.* 9, 313–325. doi: 10.1016/s0926-6410(00)00012-4

Hut, R. A., and Van der Zee, E. A. (2011). The cholinergic system, circadian rhythmicity, and time memory. *Behav. Brain Res.* 221, 466–480. doi: 10.1016/j.bbr.2010.11.039

Kawaguchi, Y. (1997). Selective cholinergic modulation of cortical GABAergic cell subtypes. *J. Neurophysiol.* 78, 1743–1747. doi: 10.1152/jn.1997.78.3.1743

Koelbl, C., Helmstaedter, M., Lübke, J., and Feldmeyer, D. (2015). A barrel-related interneuron in layer 4 of rat somatosensory cortex with a high intrabarrel connectivity. *Cereb. Cortex* 25, 713–725. doi: 10.1093/cercor/bht263

Koukouli, F., Rooy, M., Tziotis, D., Sailor, K. A., O'Neill, H. C., Levenga, J., et al. (2017). Nicotine reverses hypofrontality in animal models of addiction and schizophrenia. *Nat. Med.* 23, 347–354. doi: 10.1038/nm.4274

Kruglikov, I., and Rudy, B. (2008). Perisomatic GABA release and thalamocortical integration onto neocortical excitatory cells are regulated by neuromodulators. *Neuron* 58, 911–924. doi: 10.1016/j.neuron.2008.04.024

Lawrence, J. J., Statland, J. M., Grinspan, Z. M., and McBain, C. J. (2006). Cell type-specific dependence of muscarinic signalling in mouse hippocampal stratum oriens interneurones. *J. Physiol.* 570, 595–610. doi: 10.1113/jphysiol.2005.100875

Lee, S., Hjerling-Leffler, J., Zagha, E., Fishell, G., and Rudy, B. (2010). The largest group of superficial neocortical GABAergic interneurons expresses ionotropic serotonin receptors. *J. Neurosci.* 30, 16796–16808. doi: 10.1523/jneurosci.1869-10.2010

Lubke, J., Egger, V., Sakmann, B., and Feldmeyer, D. (2000). Columnar organization of dendrites and axons of single and synaptically coupled excitatory spiny neurons in layer 4 of the rat barrel cortex. *J. Neurosci.* 20, 5300–5311. doi: 10.1523/JNEUROSCI.20-14-05300.2000

Ma, Y., Hu, H., Berrebi, A. S., Mathers, P. H., and Agmon, A. (2006). Distinct subtypes of somatostatin-containing neocortical interneurons revealed in transgenic mice. *J. Neurosci.* 26, 5069–5082. doi: 10.1523/JNEUROSCI.0661-06.2006

Marin, O. (2012). Interneuron dysfunction in psychiatric disorders. *Nat. Rev. Neurosci.* 13, 107–120. doi: 10.1038/nrn3155

Marx, M., Gunter, R. H., Hucko, W., Radnikow, G., and Feldmeyer, D. (2012). Improved biocytin labeling and neuronal 3D reconstruction. *Nat. Protoc.* 7, 394–407. doi: 10.1038/nprot.2011.449

Mattinson, C. E., Burmeister, J. J., Quintero, J. E., Pomerleau, F., Huettl, P., and Gerhardt, G. A. (2011). Tonic and phasic release of glutamate and acetylcholine neurotransmission in sub-regions of the rat prefrontal cortex using enzyme-based microelectrode arrays. *J. Neurosci. Methods* 202, 199–208. doi: 10.1016/j.jneumeth.2011.08.020

McQuiston, A. R., and Madison, D. V. (1999a). Muscarinic receptor activity induces an afterdepolarization in a subpopulation of hippocampal CA1 interneurons. *J. Neurosci.* 19, 5703–5710. doi: 10.1523/JNEUROSCI.19-14-05703.1999

McQuiston, A. R., and Madison, D. V. (1999b). Muscarinic receptor activity has multiple effects on the resting membrane potentials of CA1 hippocampal interneurons. *J. Neurosci.* 19, 5693–5702. doi: 10.1523/jneurosci.19-14-05693.1999

Meir, I., Katz, Y., and Lampl, I. (2018). Membrane Potential Correlates of Network Decorrelation and Improved SNR by Cholinergic Activation in the Somatosensory Cortex. *J. Neurosci.* 38, 10692–10708. doi: 10.1523/jneurosci.1159-18.2018

Mesulam, M. M., Mufson, E. J., Levey, A. I., and Wainer, B. H. (1983). Cholinergic innervation of cortex by the basal forebrain: cytochemistry and cortical connections of the septal area, diagonal band nuclei, nucleus basalis (substantia innominata), and hypothalamus in the rhesus monkey. *J. Comp. Neurol.* 214, 170–197. doi: 10.1002/cne.902140206

Muñoz, W., and Rudy, B. (2014). Spatiotemporal specificity in cholinergic control of neocortical function. *Curr. Opin. Neurobiol.* 26, 149–160. doi: 10.1016/j.conb.2014.02.015

Obermayer, J., Luchicchi, A., Heistek, T. S., de Kloet, S. F., Terra, H., Bruinsma, B., et al. (2019). Prefrontal cortical ChAT-VIP interneurons provide local excitation by cholinergic synaptic transmission and control attention. *Nat. Commun.* 10:5280. doi: 10.1038/s41467-019-13244-9

Obermayer, J., Verhoog, M. B., Luchicchi, A., and Mansvelder, H. D. (2017). Cholinergic Modulation of Cortical Microcircuits Is Layer-Specific: Evidence from Rodent, Monkey and Human Brain. *Front. Neural Circuits* 11:100. doi: 10.3389/fncir.2017.00100

Patel, A. V., Codeluppi, S. A., Ervin, K. S. J., St-Denis, M. B., Choleris, E., and Bailey, C. D. C. (2021). Developmental Age and Biological Sex Influence Muscarinic Receptor Function and Neuron Morphology within Layer VI of the Medial Prefrontal Cortex. *Cereb. Cortex* 2021:bhab406. doi: 10.1093/cercor/bhab406

Petilla Interneuron Nomenclature Group, Ascoli, G. A., Alonso-Nanclares, L., Anderson, S. A., Barrionuevo, G., Benavides-Piccione, R., et al. (2008). Petilla terminology: nomenclature of features of GABAergic interneurons of the cerebral cortex. *Nat. Rev. Neurosci.* 9, 557–568. doi: 10.1038/nrn2402

Picciotto, M. R., Higley, M. J., and Mineur, Y. S. (2012). Acetylcholine as a neuromodulator: cholinergic signaling shapes nervous system function and behavior. *Neuron* 76, 116–129. doi: 10.1016/j.neuron.2012.08.036

Poorthuis, R. B., Bloem, B., Verhoog, M. B., and Mansvelder, H. D. (2013a). Layer-specific interference with cholinergic signaling in the prefrontal cortex by smoking concentrations of nicotine. *J. Neurosci.* 33, 4843–4853. doi: 10.1523/jneurosci.5012-12.2013

Poorthuis, R. B., Bloem, B., Schak, B., Wester, J., de Kock, C. P., and Mansvelder, H. D. (2013b). Layer-specific modulation of the prefrontal cortex by nicotinic acetylcholine receptors. *Cereb. Cortex* 23, 148–161. doi: 10.1093/cercor/bhr390

Porter, J. T., Cauli, B., Staiger, J. F., Lambolez, B., Rossier, J., and Audinat, E. (1998). Properties of bipolar VIPergic interneurons and their excitation by pyramidal neurons in the rat neocortex. *Eur. J. Neurosci.* 10, 3617–3628. doi: 10.1046/j.1460-9568.1998.00367.x

Porter, J. T., Cauli, B., Tsuzuki, K., Lambolez, B., Rossier, J., and Audinat, E. (1999). Selective excitation of subtypes of neocortical interneurons by nicotinic receptors. *J. Neurosci.* 19, 5228–5235. doi: 10.1523/jneurosci.19-13-05228.1999

Porter, J. T., Johnson, C. K., and Agmon, A. (2001). Diverse types of interneurons generate thalamus-evoked feedforward inhibition in the mouse barrel cortex. *J. Neurosci.* 21, 2699–2710. doi: 10.1523/JNEUROSCI.21-08-02699.2001

Postma, M., and Goedhart, J. (2019). PlotsOfData—A web app for visualizing data together with their summaries. *PLoS. Biol.* 7:e3000202. doi: 10.1371/journal.pbio.3000202

Pronneke, A., Scheuer, B., Wagener, R. J., Mock, M., Witte, M., and Staiger, J. F. (2015). Characterizing VIP Neurons in the Barrel Cortex of VIPcre/tdTomato Mice Reveals Layer-Specific Differences. *Cereb. Cortex* 25, 4854–4868. doi: 10.1093/cercor/bhv202

Prönneke, A., Witte, M., Möck, M., and Staiger, J. F. (2020). Neuromodulation Leads to a Burst-Tonic Switch in a Subset of VIP Neurons in Mouse Primary Somatosensory (Barrel) Cortex. *Cereb. Cortex* 30, 488–504. doi: 10.1093/cercor/bhz102

Qi, G., van Aerde, K., Abel, T., and Feldmeyer, D. (2017). Adenosine Differentially Modulates Synaptic Transmission of Excitatory and Inhibitory Microcircuits in Layer 4 of Rat Barrel Cortex. *Cereb. Cortex* 27, 4411–4422. doi: 10.1093/cercor/bhw243

Radnikow, G., and Feldmeyer, D. (2018). Layer- and Cell Type-Specific Modulation of Excitatory Neuronal Activity in the Neocortex. *Front. Neuroanat.* 12:1. doi: 10.3389/fnana.2018.00001

Scala, F., Kobak, D., Shan, S., Bernaerts, Y., Laturnus, S., Cadwell, C. R., et al. (2019). Layer 4 of mouse neocortex differs in cell types and circuit organization between sensory areas. *Nat. Commun.* 10:4174. doi: 10.1038/s41467-019-12058-z

Sohal, V. S., Zhang, F., Yizhar, O., and Deisseroth, K. (2009). Parvalbumin neurons and gamma rhythms enhance cortical circuit performance. *Nature* 459, 698–702. doi: 10.1038/nature07991

Staiger, J. F., Flagmeyer, I., Schubert, D., Zilles, K., Kotter, R., and Luhmann, H. J. (2004). Functional diversity of layer IV spiny neurons in rat somatosensory cortex: quantitative morphology of electrophysiologically characterized and biocytin labeled cells. *Cereb. Cortex* 14, 690–701. doi: 10.1093/cercor/bhh029

Tasic, B., Yao, Z., Graybuck, L. T., Smith, K. A., Nguyen, T. N., Bertagnolli, D., et al. (2018). Shared and distinct transcriptomic cell types across neocortical areas. *Nature* 563, 72–78. doi: 10.1038/s41586-018-0654-5

Teles-Grilo Ruivo, L. M., Baker, K. L., Conway, M. W., Kinsley, P. J., Gilmour, G., Phillips, K. G., et al. (2017). Coordinated Acetylcholine Release in Prefrontal Cortex and Hippocampus Is Associated with Arousal and Reward on Distinct Timescales. *Cell Rep.* 18, 905–917. doi: 10.1016/j.celrep.2016.12.085

Tian, M. K., Bailey, C. D., and Lambe, E. K. (2014). Cholinergic excitation in mouse primary vs. associative cortex: region-specific magnitude and receptor balance. *Eur. J. Neurosci.* 40, 2608–2618. doi: 10.1111/ejn.12622

Turrini, P., Casu, M. A., Wong, T. P., De Koninck, Y., Ribeiro-da-Silva, A., and Cuello, A. C. (2001). Cholinergic nerve terminals establish classical synapses in the rat cerebral cortex: synaptic pattern and age-related atrophy. *Neuroscience* 105, 277–285. doi: 10.1016/s0306-4522(01)00172-5

Unwin, N. (2003). Structure and action of the nicotinic acetylcholine receptor explored by electron microscopy. *FEBS Lett.* 555, 91–95. doi: 10.1016/s0014-5793(03)01084-6

Veit, J., Hakim, R., Jadi, M. P., Sejnowski, T. J., and Adesnik, H. (2017). Cortical gamma band synchronization through somatostatin interneurons. *Nat. Neurosci.* 20, 951–959. doi: 10.1038/nn.4562

Wang, X., Tucciarone, J., Jiang, S., Yin, F., Wang, B. S., Wang, D., et al. (2019). Genetic Single Neuron Anatomy Reveals Fine Granularity of Cortical Axo-Axonic Cells. *Cell Rep.* 26, 3145–59e5. doi: 10.1016/j.celrep.2019.02.040

Xiang, Z., Huguenard, J. R., and Prince, D. A. (1998). Cholinergic switching within neocortical inhibitory networks. *Science* 281, 985–988. doi: 10.1126/science.281.5379.985

Xu, H., Jeong, H. Y., Tremblay, R., and Rudy, B. (2013). Neocortical somatostatin-expressing GABAergic interneurons disinhibit the thalamorecipient layer 4. *Neuron* 77, 155–167. doi: 10.1016/j.neuron.2012.11.004

Yang, D., Günter, R., Qi, G., Radnikow, G., and Feldmeyer, D. (2020). Muscarinic and Nicotinic Modulation of Neocortical Layer 6A Synaptic Microcircuits Is Cooperative and Cell-Specific. *Cereb. Cortex* 30, 3528–3542. doi: 10.1093/cercor/bhz324

Yuste, R., Hawrylycz, M., Aalling, N., Aguilar-Valles, A., Arendt, D., Armananzas, R., et al. (2020). A community-based transcriptomics classification and nomenclature of neocortical cell types. *Nat. Neurosci.* 23, 1456–1468. doi: 10.1038/s41593-020-0685-8

Zaborszky, L., Csordas, A., Mosca, K., Kim, J., Gielow, M. R., Vadasz, C., et al. (2015). Neurons in the basal forebrain project to the cortex in a complex topographic organization that reflects corticocortical connectivity patterns: an experimental study based on retrograde tracing and 3D reconstruction. *Cereb. Cortex* 25, 118–137. doi: 10.1093/cercor/bht210

Zeng, H., and Sanes, J. R. (2017). Neuronal cell-type classification: challenges, opportunities and the path forward. *Nat. Rev. Neurosci.* 18, 530–546. doi: 10.1038/nrn.2017.85

Zolles, G., Wagner, E., Lampert, A., and Sutor, B. (2009). Functional expression of nicotinic acetylcholine receptors in rat neocortical layer 5 pyramidal cells. *Cereb. Cortex* 19, 1079–1091. doi: 10.1093/cercor/bhn158

Conflict of Interest: The authors declare that the research was conducted in the absence of any commercial or financial relationships that could be construed as a potential conflict of interest.

Publisher's Note: All claims expressed in this article are solely those of the authors and do not necessarily represent those of their affiliated organizations, or those of the publisher, the editors and the reviewers. Any product that may be evaluated in this article, or claim that may be made by its manufacturer, is not guaranteed or endorsed by the publisher.

frontiers in Neural Circuits

ORIGINAL RESEARCH
published: 28 February 2022
doi: 10.3389/fncir.2022.825735

Response Selectivity of the Lateral Posterior Nucleus Axons Projecting to the Mouse Primary Visual Cortex

Satoru Kondo[1,2]*, *Yuko Kiyohara*[1] *and Kenichi Ohki*[1,2,3]*

[1] *Department of Physiology, School of Medicine, The University of Tokyo, Tokyo, Japan,* [2] *World Premier International Research Center – International Research Center for Neurointelligence (WPI-IRCN), The University of Tokyo Institutes for Advanced Study (UTIAS), Tokyo, Japan,* [3] *Institute for AI and Beyond, The University of Tokyo, Tokyo, Japan*

Neurons in the mouse primary visual cortex (V1) exhibit characteristic response selectivity to visual stimuli, such as orientation, direction and spatial frequency selectivity. Since V1 receives thalamic visual inputs from the lateral geniculate nucleus (LGN) and lateral posterior nucleus (LPN), the response selectivity of the V1 neurons could be influenced mostly by these inputs. However, it remains unclear how these two thalamic inputs contribute to the response selectivity of the V1 neurons. In this study, we examined the orientation, direction and spatial frequency selectivity of the LPN axons projecting to V1 and compared their response selectivity with our previous results of the LGN axons in mice. For this purpose, the genetically encoded calcium indicator, GCaMP6s, was locally expressed in the LPN using the adeno-associated virus (AAV) infection method. Visual stimulations were presented, and axonal imaging was conducted in V1 by two-photon calcium imaging *in vivo*. We found that LPN axons primarily terminate in layers 1 and 5 and, to a lesser extent, in layers 2/3 and 4 of V1, while LGN axons mainly terminate in layer 4 and, to a lesser extent, in layers 1 and 2/3 of V1. LPN axons send highly orientation- and direction-selective inputs to all the examined layers in V1, whereas LGN axons send highly orientation- and direction-selective inputs to layers 1 and 2/3 but low orientation and direction selective inputs to layer 4 in V1. The distribution of preferred orientation and direction was strongly biased toward specific orientations and directions in LPN axons, while weakly biased to cardinal orientations and directions in LGN axons. In spatial frequency tuning, both the LPN and LGN axons send selective inputs to V1. The distribution of preferred spatial frequency was more diverse in the LPN axons than in the LGN axons. In conclusion, LPN inputs to V1 are functionally different from LGN inputs and may have different roles in the orientation, direction and spatial frequency tuning of the V1 neurons.

Keywords: lateral posterior nucleus, lateral geniculate nucleus, primary visual cortex, axons, response selectivity, two-photon calcium imaging, mice

OPEN ACCESS

Edited by:
Yoshiyuki Kubota,
National Institute for Physiological Sciences (NIPS), Japan

Reviewed by:
Miao He,
Fudan University, China
Qi Fang,
University of Southern California, United States

***Correspondence:**
Satoru Kondo
skondo@m.u-tokyo.ac.jp
Kenichi Ohki
kohki@m.u-tokyo.ac.jp

Received: *30 November 2021*
Accepted: *21 January 2022*
Published: *28 February 2022*

Citation:
Kondo S, Kiyohara Y and Ohki K (2022) Response Selectivity of the Lateral Posterior Nucleus Axons Projecting to the Mouse Primary Visual Cortex. Front. Neural Circuits 16:825735. doi: 10.3389/fncir.2022.825735

INTRODUCTION

In mammals, visual information from the retina flows through two major bottom-up pathways and undergoes hierarchical processing (Nassi and Callaway, 2009). One pathway reaches the primary visual cortex (V1) and subsequent higher visual areas (HVAs) via the lateral geniculate nucleus (LGN) of the thalamus. Another pathway reaches the V1 and HVAs in parallel via the lateral

posterior nucleus (LPN) of the thalamus. Both the V1 and HVAs project back to the LPN and form reciprocal circuits with the LPN. The LPN receives strong projections from the superior colliculus (SC) (Gale and Murphy, 2014; Tohmi et al., 2014; Zhou et al., 2017; Bennett et al., 2019), that receives direct retinal input. The V1 sends cortico-collicular feedback projection to the SC and modulate the SC activity (Zhao et al., 2014; Liang et al., 2015), and the SC activity may in turn impact on visual cortical processing via the LPN (Ahmadlou et al., 2018).

LPN is considered the rodent analog of the primate pulvinar (Baldwin et al., 2017; Zhou et al., 2017). LPN/pulvinar receives input from many cortical and subcortical areas, including sensory, motor, association and visuomotor area (Grieve et al., 2000; Wurtz et al., 2011; Gale and Murphy, 2014). LPN/pulvinar combines information from multiple sources and influence the visual processing by linking with the visual, other sensory and the behavioral context (Grieve et al., 2000; Wurtz et al., 2011; Gale and Murphy, 2014; Roth et al., 2016). Previous studies implicated the functional roles of the pulvinar related with higher visual functions in primate, such as attention, saccade movement, and visually guided locomotion (Zhou et al., 2016; Dominguez-Vargas et al., 2017; Soares et al., 2017). In rodent, the LPN transmits motor-related signals to the HVAs and contribute the visual information processing in these cortical area (Tohmi et al., 2014; Beltramo and Scanziani, 2019; Blot et al., 2021), conveys the surround information of the visual field to V1 (Durand et al., 2016; Roth et al., 2016; Fang et al., 2020) and sharpen the orientation selectivity of layer 2/3 neurons in V1 (Fang et al., 2020).

Recent anatomical studies have shown that the LPN is divided into several subregions (Zhou et al., 2017; Bennett et al., 2019) that have specific connections with the cortical and subcortical areas (Tohmi et al., 2014; Bennett et al., 2019). It has been reported that V1 mainly receives projections from the anterior part of the LPN (Bennett et al., 2019), and studies using transsynaptic tracers revealed the bottom-up visual pathway from the SC to V1 through LPN (Fang et al., 2020). In V1, unlike LGN afferents that mainly terminate in layer 4, LPN afferents primarily terminate in layers 1 and 5 (Roth et al., 2016; Zhou et al., 2017). This anatomical segregation of axonal termination in different layers suggests the functional difference between the two thalamic afferents in V1. Among six layers in V1, layer 4 is regarded as the primary input layer of the visual information from the retina (Nassi and Callaway, 2009). On the other hand, layer 1 receives broad range of inputs, such as sensory and higher-order corticocortical, neuromodulatory and thalamic inputs (Mesik et al., 2019). Since the role of cortico-cortical and neuromodulatory inputs to V1 layer 1 has been suggested to be modulatory (Alitto and Dan, 2013; Ibrahim et al., 2016; Leinweber et al., 2017), the role of thalamic inputs to layer 1 may also contribute to the modulation of V1 neuronal activity. However, due to the lack of recordings of the functional properties of the LPN axons distributed in the different V1 layers, the difference in the role of LPN and LGN on the information processing in V1 circuit remains not yet been fully elucidated.

In this study, we performed *in vivo* functional imaging of the LPN axons terminating in various layers in V1 and compared their response selectivity with our previous results on the LGN axons (Kondo and Ohki, 2016). Our studies suggest the differential functional roles of the LPN inputs from LGN inputs on the response selectivity of V1 neurons.

MATERIALS AND METHODS

Animals

C57BL/6 mice (purchased from SLC Hamamatsu, Japan) were used for all experiments. The mice were maintained in an animal facility at the University of Tokyo. The facility housed 2–3 mice per cage in a temperature-controlled animal room with a 12-h/12-h light/dark cycle. All procedures were conducted in accordance with protocols approved by the University of Tokyo Animal Care and Use Committee (approval number: P21-002).

Local Expression of GCaMP6s in the Lateral Posterior Nucleus

The genetically encoded calcium indicator, GCaMP6s, was locally expressed in the LPN using the adeno-associated virus (AAV) infection method. In some experiments, the LGN was infected with green fluorescent protein (GFP)-expressing AAV, and the LPN, with tdTomato-expressing AAV. AAV2/1-CAG-GCaMP6s, GFP, or tdTomato ($\sim 1 \times 10^{13}$ genome copy/ml; purchased from Vector Core, University of Pennsylvania) was used for the desired expression. Mice were anesthetized with isoflurane (5.0% for anesthesia induction and 1.5% for anesthesia maintenance) and fixed on stereotaxic frames. A skin incision was made at the midline, and the periosteum was removed from the skull. For the AAV injection to the LPN and LGN, a small craniotomy was performed just above the dorsal part of the LPN or the LGN using stereotaxic coordinates (LPN: -1.8 mm from the bregma, 2.0 mm lateral from the midline; LGN: -2.3 mm from the bregma, 2.4 mm lateral from the midline). For the AAV injection to the SC, two small craniotomies were performed above the SC using the stereotaxic coordinates (0 mm anterior from the lambda, 1.0 mm lateral from the midline and 0.5 mm anterior from the lambda, 0.5 mm lateral from the midline). A glass pipette filled with AAV vector solution was inserted (2.4 mm depth from the pia for both the LPN and the LGN, 1.0 mm depth from the pia for the SC) and the AAV solution was injected using either pressure (30–50 nL; Nanoject III, Drummond) or iontophoretic methods (3 μA, 7 s-ON and 7 s-OFF, 3 min; Midgard Precision Current Source, Stoelting). The infection area was typically defined as a circular volume with a 400–700 μm diameter from the injection site. The boundaries of the LPN and the LGN were determined according to the mouse brain atlas (Paxinos and Franklin, 2019).

Imaging and Visual Stimulation

For imaging the LPN axons, at 2 weeks after infection, a craniotomy (3 mm in diameter) was performed over V1. Next, the dura mater was removed, and a cranial window was constructed by sealing the area with a cover slip. Two-photon calcium imaging of the axons was performed under anesthesia (0.2% isoflurane with 2.5 mg/kg chlorprothixene). Images were

obtained using a two-photon microscopy system (A1RMP, Nikon) with a 25 × objective lens (CFI Apo LWD 25XW, NA = 1.10, Nikon) at 920 nm wavelength (MaiTai eHP DeepSee, Spectra Physics). The images were obtained in a 2-D plane at 2 Hz. The image size was 512 × 512 pixels (resolution = 0.125 μm/pixel). The average laser power at the sample was modulated between 10 and 40 mW, depending on the imaging depth. To correct the refractive index mismatch in the brain tissue, the axial position of the objective lens was carefully adjusted to obtain the maximum signal intensity. This improved the resolution of axon imaging, especially of those located deep inside the brain. Layers were initially assigned by Nissl staining in the brain section, layer 1: 0–100 μm, layer 2/3: 100–350 μm, layer 4: 350–450 μm, and layer 5: 450–650 μm. Images were then obtained *in vivo* brain at 50–70 μm below the pia for layer 1, at 200–250 μm for layer 2/3, at 350–450 μm for layer 4, and at 450–550 μm for layer 5.

Visual stimulations were presented on a 32-inch LCD display (ME32B, Samsung) using PsychoPy2 (Pierce, 2008). Orientation selectivity was investigated using drifting square-wave gratings moving in 12 directions [each 30° apart, spatial frequency (SPF) = 0.04 cycles per degree (cpd), and temporal frequency = 2 Hz]. These 12 patterns were presented for ∼4 s each (eight frames), with interspersed gray blank (uniform) stimuli of the same duration. The stimuli were repeated 10 times. For SPF preference analysis, drifting sinusoidal-wave gratings moving in eight directions (0.5 s each) were presented for ∼4 s, with interspersed gray blank (uniform) stimuli of the same duration. SPF took one of six different values (0.01, 0.02, 0.04, 0.08, 0.16, and 0.32 cpd) and the temporal frequency was 2 Hz.

Histology

After imaging, each mouse was transcardially perfused with 4% paraformaldehyde, and the brain was removed and submerged in the fixative solution overnight. Thereafter, coronal sections were obtained (thickness of either 50 or 100 μm), which were subsequently examined localization of the infection site in the LPN or LGN and the distribution of LPN or LGN axons in V1. For assigning the V1 layers, the sections were stained using NeuroTrace Red (cat# N-21482, Molecular Probes). All fluorescent photographs were obtained using an epifluorescence microscope (BZX-710, Keyence). The photographs of the retrogradely labeled areas were taken by either the optical sectioning method with structured illumination (BZX-710, Keyence) or confocal microscope (A1R HD25, Nikon).

Data Analysis

All analyses were performed using custom-written programs in MATLAB (Mathworks). Data from the different experimental groups were processed using the same computer code; thus, randomization and blinding were not necessary for data analysis. To obtain an orientation map, calcium signal changes were calculated for all the pixels, and each pixel was colored according to the response to the orientation stimulation [hue: preferred orientation; lightness: response magnitude; and saturation: global orientation selectivity index (gOSI)].

The LPN boutons were automatically detected by a template-matching algorithm using convolution mask images. The centroids of the boutons were determined from a mask image of the boutons. Time courses of fluorescent change were extracted by averaging a circle around the centroid (radius, 0.5 μm).

To estimate the out-of-focus signal around the individual LPN boutons, ring-shaped masks within 10 pixels (1.25 μm) were made from the edge of the boutons, while excluding the pixels at less than 4 pixels (0.5 μm) from the edge of the boutons to reduce the possible overlap with the signal change of the boutons. If a mask overlapped the neighboring boutons/axons or axonal shafts, then the overlapping area was removed from the mask. The out-of-focus signal obtained from these masks was subtracted from the fluorescence signal of the bouton (contamination ratio = 1.0) (Kerlin et al., 2010).

Orientation selectivity was calculated from the corrected time courses. Visually evoked fluorescent changes were calculated as the change in fluorescence normalized to the baseline fluorescence (dF/F). Baseline fluorescence was obtained from the average of the last four frames during the blank periods. The *p*-value for responsiveness was obtained from the analysis of variance across the blank and stimulus periods. The *p*-value for selectivity was obtained from the analysis of variance across the stimulus periods.

The preferred orientation was calculated using vector averaging (Swindale, 1998), defined by the following equations:

$$a = \Sigma R_i \times \cos(2\theta_i),$$

$$b = \Sigma R_i \times \sin(2\theta_i),$$

$$\theta_{pref} = 0.5\arctan(b/a),$$

where R_i is the response to the ith direction θ_i (12 directions; each 30° apart, from 0 to 330°) and θ_{pref} is the preferred orientation.

The gOSI, which is equivalent to 1—circular variance, was calculated using the following formula:

$$gOSI = \mathrm{sqrt}((\Sigma R_i \sin(2\theta_i))\hat{}2 + (\Sigma R_i \cos(2\theta_i))\hat{}2)/\Sigma R_i,$$

where R_i is the response to the ith direction θ_i (Wörgötter and Eysel, 1987).

The OSI was calculated using the following formula:

$$(R_{pref} - R_{ortho})/(R_{pref} + R_{ortho}),$$

where R_{pref} is the response to the preferred orientation and R_{ortho} is the response to the orthogonal orientation to the preferred orientation.

Axonal boutons or neurons were considered responsive when they met the following criteria: *p*-value for responsiveness < 0.001 and maximum response $> 3\%$. Among the responsive boutons or neurons, sharply orientation-selective boutons or neurons were defined when they met the following criteria: *p*-value for selectiveness < 0.001 and gOSI > 0.33.

The preferred direction was calculated using the Gaussian fitting method. A tuning curve was fitted with the sum of two circular Gaussian functions (von Mises distribution), and the peak of the fitting curve was considered as the preferred direction.

The direction selectivity index (DSI) was calculated using the following formula:

$$DSI = (R_{pref} - R_{opp})/(R_{pref} + R_{opp}),$$

where R_{pref} is the response to the preferred direction and R_{opp} is the response in the direction opposite to the preferred direction.

Responsive boutons or neurons were defined using the same criteria as those for the orientation analysis. Among the responsive boutons, sharply direction-selective boutons were defined using the following criteria: p-value for selectiveness < 0.001 and DSI > 0.3.

The responses to the different SPFs were fitted using the difference of the Gaussian (DOG) function (Hawken and Parker, 1987). The preferred SPFs of the boutons were determined from the peak of the DOG fitting curve. The DOG fittings were evaluated using the R-squared values.

The SPF selectivity index was calculated using the following formula:

$$(R_{max} - R_{min})/R_{max},$$

where R_{max} is the maximum response and R_{min} is the minimum response.

Axonal boutons were considered responsive when they met the following criteria: p-value for responsiveness < 0.001 and maximum response $> 3\%$. Among the responsive boutons, the SPF-selective boutons were defined using the following criteria: p-value for selectiveness < 0.001, SPF selectivity index > 0.5, and R-squared value > 0.7. Only the selectively responsive boutons were used for further analysis.

Statistical Analysis

All data are presented as mean ± standard error unless stated otherwise. A two-sided Mann–Whitney U-test or unpaired t-test was used to compare two independent groups. Analysis of variance (ANOVA) or Bonferroni correction was performed when more than two groups were compared. Statistical significance was set at p-value ≤ 0.05 for all the study analyses, except for the definitions of the visually responsive and selective boutons (see "Data Analysis" section). The sample size (n) was defined as the number of mice or images. No statistical analyses were performed to predetermine the sample sizes; the sample size used was similar to that generally employed in the field.

RESULTS

Parallel Projection Pathways From the Thalamus to V1

Of the two vision-related thalamic nuclei—the LGN and the LPN, it has been suggested that only the LGN receives direct input from the retinal ganglion cells that carry visual information (Allen et al., 2016). To identify the anatomical connections between V1 and LGN or LPN, the retrograde tracer, cholera toxin subunit B (CTB), was injected into V1 (**Figure 1A** and **Supplementary Figure 1A**). The CTB injection resulted in retrograde labeling of both the LGN and the anterior part of the LPN neurons, confirming that V1 receives dual inputs from both these thalamic nuclei (**Figure 1B** and **Supplementary Figure 1B**). Retinal visual information is divided into two ascending routes that are formed via the LGN or SC. To examine whether the LPN-V1 pathway is different from the LGN-V1 pathway, but related to the SC, CTB was injected into the anterior part of the LPN (**Figure 1A** and **Supplementary Figure 1A**), the region from where V1 mainly receives inputs (**Figure 1C**; Bennett et al., 2019). The CTB injection led to the retrograde labeling of the superficial layer of the SC (sSC) neurons without labeling the LGN neurons, indicating that the LPN-V1 pathway is different from the LGN-V1 pathway and connected to the SC (**Figure 1C** and **Supplementary Figure 1C**). Furthermore, to examine the projection of the SC neurons to the LPN and LGN, we anterogradely labeled the SC neurons using AAV-tdTomato (**Figure 1D**). We confirmed the projection of the SC neurons to the LPN (**Figure 1D** middle and lower). We observed that the projection from the SC to LPN was denser in the posterior part of LPN (pLPN) (**Figure 1D** lower) than the anterior part of the LPN (aLPN) (**Figure 1D** midle) as described previously (Bennett et al., 2019). Furthermore, we noticed that the shell of the LGN where retinal direction-selective inputs innervate also receives inputs from the SC (**Figure 1D** middle) as reported previously (Bickford et al., 2021). Therefore, the presence of three parallel projection pathways of visual information to V1 were anatomically observed—the LGN (core)-V1 pathway, the SC-LGN (shell)-V1 pathway and the SC-LPN-V1 pathway (**Figure 1A**).

Distinct Laminar Distribution of the Lateral Geniculate Nucleus and Lateral Posterior Nucleus Axons Projecting to V1

To evaluate whether the two parallel pathways are anatomically segregated or mixed in V1, LGN, and LPN neurons were differentially labeled, and the distribution of the projecting axons to V1 was investigated. AAV-GFP and AAV-tdTomato were locally injected into the LGN and LPN, respectively (**Figure 2A**). Local injection of the AAV successfully restricted the expression of GFP and tdTomato in the LGN and LPN, respectively (**Figure 2B**). LGN axons were distributed mainly in the layer 4 and, to a lesser degree, in the layers 1 and 2/3, as previously reported (**Figure 2C**; Kondo and Ohki, 2016). By contrast, LPN axons were mostly distributed in the layers 1 and 5 (**Figure 2C**). In the layer 1, LPN, and LGN axons were mixed, however, the relative density of LPN axons was higher than that of LGN axons (**Figure 2C**). Overall, the parallel LGN and LPN pathways were mostly segregated in the different layers but showed a certain degree of intermingled distribution in V1. With previous work providing evidence that each layer may have a unique functional role in the sensory cortex (Adesnik and Naka, 2018), the results

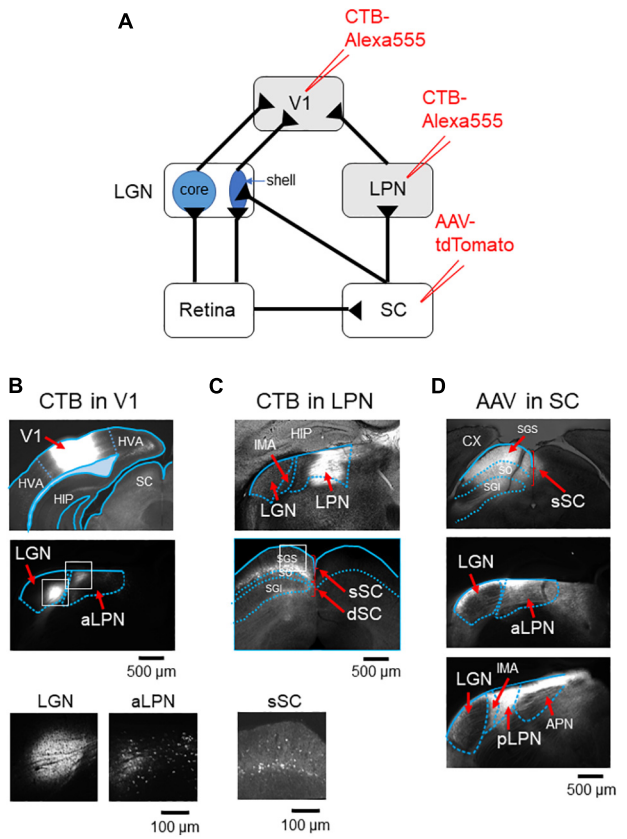

FIGURE 1 | V1 receives inputs from both the LGN and LPN. **(A)** A retrograde labeling by CTB injection into either V1 or LPN. **(B)** CTB was injected into V1 (upper), both the LGN and LPN were retrogradely labeled (middle), and the retrogradely labeled neurons were observed (lower, enlargement of the white rectangles in the middle). **(C)** CTB was injected into the anterior part of the LPN (upper), SC was retrogradely labeled (middle), and the retrogradely labeled neurons were observed (lower, enlargement of the white rectangle in the middle). **(D)** AAV-tdTomato was injected into SC (upper) and both the aLPN (middle) and pLPN (lower) were innervated by SC neurons. Note that the shell of the LGN also received SC inputs (middle). LGN, lateral geniculate nucleus; LPN, lateral posterior nucleus; aLPN, anterior part of LPN; pLPN, posterior part of LPN; CX, cortex; HIP, hippocampus; CTB, cholera toxin subunit B; V1, primary visual cortex; SGS, upper stratum griseum superficial; SO, stratum opticum; SGI, stratum griseum intermedium; sSC, superficial layers of the superior colliculus; dSC, deep layers of the superior colliculus; APN, anterior pretectal nucleus; IMA, intramedullary thalamic area.

of this study suggest that the two inputs may have different functions in visual information processing in V1.

Orientation Selectivity of the Lateral Posterior Nucleus Axons in V1

Previous studies have shown the orientation selectivity of LGN axons distributed in V1 (Kondo and Ohki, 2016; Sun et al., 2016; Zhuang et al., 2021). One study has shown that the projecting axons in the layer 4 have lower orientation selectivity than the projecting axons in the layer 1 (Kondo and Ohki, 2016). However, other studies have reported different results that thalamic axons projecting to both the layers 1 and 4 have high orientation selectivity (Sun et al., 2016; Zhuang et al., 2021). To determine the orientation selectivity of LPN axons projecting to the different layers of V1 and compare their orientation selectivity with that of LGN axons, *in vivo* two-photon calcium imaging of LPN axons was conducted using GCaMP6s. GCaMP6s was locally expressed in the LPN using the AAV method (AAV2/1-CAG-GcaMP6s), and the response to the gratings drifting in 12 different directions was recorded through the cranial imaging window. The fluorescence signal changes in small oval areas, corresponding to the putative axonal boutons, were measured (Glickfeld et al., 2013; Matsui and Ohki, 2013; Kondo and Ohki, 2016). The orientation maps (**Figure 3A** middle) and the distributions of gOSI (**Figure 3A** lower) indicated that the selectivity of the LPN axons projecting to V1 was similar among the different layers (**Figure 3A**, see statistical tests in **Figure 4B**). In contrast, the LGN axons (**Figure 3B** middle and lower) indicated lower orientation selectivity in layer 4 than in layer 1 (**Figure 3B**, see statistical tests in **Figure 4B**), as previously reported (Kondo and Ohki, 2016).

Next, the orientation selectivity was quantified by calculating the gOSI for both the LPN and LGN bouton populations. The proportion of orientation-selective LPN boutons was not significantly different among the different layers (**Figure 4A**). However, the LGN boutons in the layer 4 showed significantly lower orientation selective proportion than the other LGN and LPN boutons (**Figure 4A**). The gOSI of LPN boutons was not significantly different across the different layers (**Figures 4B,C**). However, the gOSI of LGN boutons in the layer 1 showed significantly higher selectivity than in the layer 4 (**Figures 4B,D**). Furthermore, analysis of the distribution of the preferred orientations of the LPN and LGN boutons showed that the LPN boutons had a strongly biased distribution of the preferred orientation in all the layers (**Figure 5A**). The preferred orientations of the LPN boutons showed smaller proportions at 0° (vertical) and 30° than the other orientations. This tendency was similar among LPN boutons recorded from different layers (**Figure 5A**). The preferred orientation of the LGN boutons showed a weak bias toward cardinal orientations (**Figure 5B**), as previously reported (Kondo and Ohki, 2016). Taken together, the results indicate that LPN and LGN axons send differently tuned orientation-selective inputs to V1, even to the overlapping projecting layers.

Direction Selectivity of the Lateral Posterior Nucleus Axons in V1

The proportion of the direction-selective LPN boutons in V1 was similar across the different layers (**Figure 6A**), while the proportion of the direction-selective LGN boutons projecting to the layer 1 was higher than those projecting to the other layers in V1 (**Figure 6A**). LGN boutons in the layer 1 showed the highest direction selective proportion, while LGN boutons in the layer 4 had the lowest direction selective proportion among both LGN and LPN boutons (**Figure 6A**). The DSI of LPN boutons was not significantly different across the different layers (**Figures 6B,C**). However, DSI of LGN boutons in the layer 1 showed significantly higher selectivity than in the layer 4

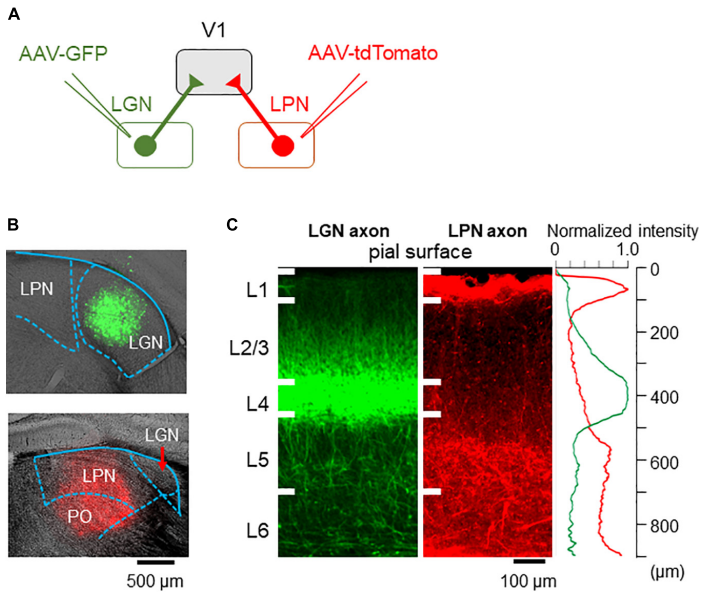

FIGURE 2 | Axonal projections from the LPN and LGN in V1. **(A)** An anterograde labeling of the LGN and LPN axons with different fluorescent proteins. **(B)** A local injection of AAV-GFP in the LGN (upper) and AAV-tdTomato in the LPN (lower). **(C)** The distribution of the LGN (left) and LPN (middle) axons in V1 of the coronal slice. LGN axons project mainly to the layer 4, while LPN axons project mainly to the layer 1 (right). LPN, lateral posterior nucleus; LGN, lateral geniculate nucleus; V1, primary visual cortex; AAV-GFP, adeno-associated virus-green fluorescent protein.

(**Figures 6B,D**). The distribution of the DSI revealed that the boutons in the layer 4 had the lowest mean value, while those in the other layers had similar mean values across both LPN and LGN boutons (**Figures 6B,C**). The preferred directions of the LPN boutons showed strong bias toward specific directions (**Figure 7A**). The preferred directions of the LGN boutons showed a weak bias toward the four cardinal axes (**Figure 7B**). These results suggest that the LPN and LGN axons converging to the same layer carry different direction information.

High Orientation Selectivity of the Mixed Lateral Geniculate Nucleus and Lateral Posterior Nucleus Axons in V1

Because of the difficulty to restrict the expression of GCaMP6s in the small nucleus of LGN, we sometimes encountered the unexpected leakage of GCaMP6s expression in the neighboring LPN (**Figure 8A**). In these cases, we observed that the mixed LGN and LPN axons project to both V1 and HVAs (**Figure 8B**). We analyzed the orientation and direction selectivity of mixed LGN and LPN boutons in V1. The orientation color map of layer 4 indicated that the selectivity of the mixed LGN and LPN boutons was higher (**Figures 8C,D**) than that of LGN boutons in layer 4 (**Figure 3B**; Kondo and Ohki, 2016). The proportion of orientation-selective boutons were statistically higher in the mixed LGN and LPN boutons (**Figure 8E**) than in the LGN boutons in all the layers (**Figure 4A**) (mixed vs. LGN boutons: 58.6 vs. 41.3% in layer 1, $P = 0.017$, unpaired t-test; 49.6 vs. 35.6% in layer 2/3, $P = 0.021$, unpaired t-test; 38.5 vs. 17.8% in layer 4, $P \leq 0.001$, unpaired t-test). These results suggest that high orientation selectivity can be obtained in the mixed LGN and LPN axons projecting to layer 4 of V1 when the expression of GCaMP6s is targeted to LGN but leaked to LPN.

Spatial Frequency Selectivity of the Lateral Posterior Nucleus Axons in V1

The SPF selectivity of the LPN boutons in V1 was examined and compared with that of the LGN boutons (**Figure 9**). SPF selectivity of LPN boutons, including those with low-pass tuning (< 0.01 cpd) and high spatial tuning (> 0.32 cpd), was fitted with a difference of Gaussian (DOG) model and examined the range of preferred SPFs. The proportion of the SPF selective LPN boutons was lower than that of the SPF selective LGN boutons, although the difference was not statistically significant (**Figure 9A**). The mean preferred SPF of the LPN boutons was similar across different layers but significantly higher than that of the LGN boutons (**Figures 9B–D**). The distribution of the preferred SPFs was broader in the LPN boutons than in LGN boutons in all layers (**Figures 9C,D**), indicating that the LPN axons had more diverse SPF selectivity than the LGN axons.

DISCUSSION

In this study, *in vivo* two-photon calcium imaging of LPN axons projecting to V1 was performed to examine their orientation/direction and SPF selectivity, and the findings were compared with the results from our previous study of LGN axons (Kondo and Ohki, 2016). Collectively, the data show that LPN axons project mainly to the layers 1 and 5 and, to a lesser extent, layers 2/3 and 4, while LGN axons project mainly to the layer 4 and, to a lesser extent, layers 1 and 2/3. LPN axons

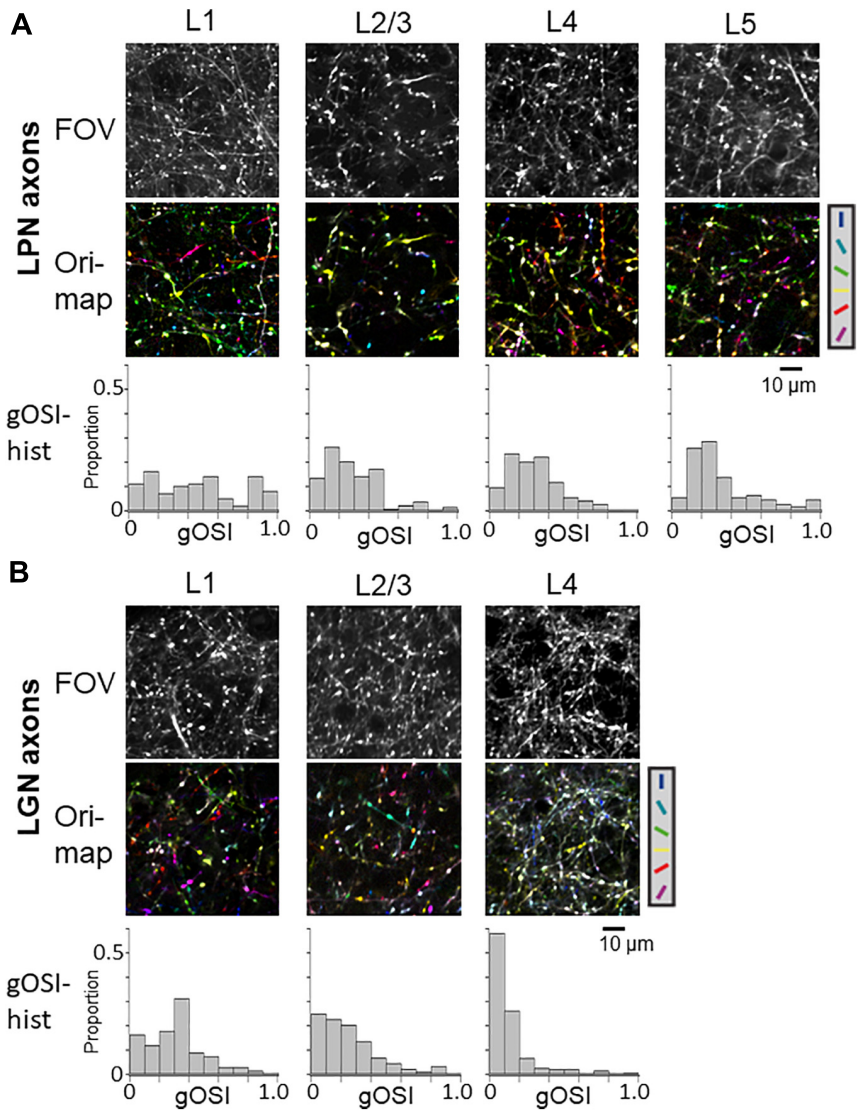

FIGURE 3 | Orientation selectivity of LPN and LGN boutons in V1. **(A)** FOV images (upper), orientation color map (middle) and distribution of gOSI (lower) of the LPN axons in V1. **(B)** FOV images (upper) and orientation color map (middle) and distribution of gOSI (lower) of the LGN axons in V1. Only the LGN axons in the layer 4 indicated low orientation selectivity. LPN, lateral posterior nucleus; LGN, lateral geniculate nucleus; V1, primary visual cortex; FOV, field-of-view. $^{*}P \leq 0.05$, $^{***}P \leq 0.001$ The data of LGN axons are re-use from the previous publication (Kondo and Ohki, 2016).

send orientation- and direction-selective inputs to all the layers, while LGN axons send strong orientation- and direction-selective inputs to the layer 1 and, to a lesser degree, layer 4. Both LPN and LGN axons send SPF-selective inputs to all the layers of V1. However, the SPF selectivity of LPN axons is more diverse than that of LGN axons.

The visual information carried by the LPN neurons has multiple origins. The data from our retrograde labeling study, along with those of other previous study (Bennett et al., 2019), have shown that the LPN receives feedforward inputs from the SC. Furthermore, a transsynaptic retrograde labeling study has shown that the LPN neurons projecting to V1 receive inputs from the SC neurons (Fang et al., 2020). Thus, the LPN activity projecting to V1 could be partly derived from the SC. Many neurons in the superficial layers of the SC (sSC) in mice are tuned for orientation and motion directions (Wang et al., 2010; Gale and Murphy, 2014; Ahmadlou and Heimel, 2015; Feinberg and Meister, 2015; De Franceschi and Solomon, 2018). Therefore, the orientation and direction selectivity of the LPN axons that we observed in this study is potentially derived from the response selectivity of the sSC neurons. Orientation selectivity is heterogeneously distributed in the mouse sSC and is dependent on the retinotopic position (Ahmadlou and Heimel, 2015; Feinberg and Meister, 2015; Kasai and Isa, 2021). Although we did not measure the retinotopic position during the recording, we usually recorded activity of LPN axons at the similar stereotaxic

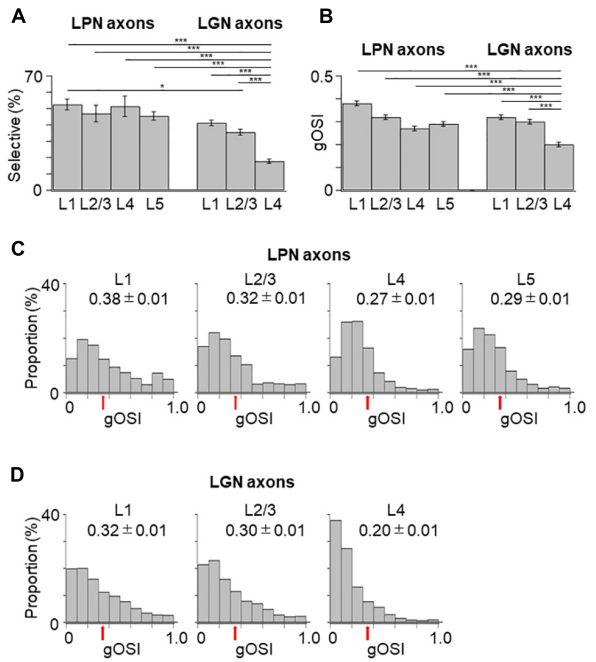

FIGURE 4 | Proportion of orientation-selective axons and distribution of gOSI of LPN and LGN boutons in V1. **(A)** The proportion of orientation-selective LPN and LGN boutons. The proportion of LGN boutons in the layer 4 was significantly different from that of LGN boutons in the remaining layers as well as that of LPN boutons in all the layers ($P \leq 0.001$, Mann–Whitney *U*-test with Bonferroni correction). The proportion of LGN boutons in the layer 2/3 was significantly different from that of LPN boutons in the layer 1 ($p = 0.012$, Mann–Whitney *U*-test with Bonferroni correction) but no significant difference from layers 2/3, 4, and 5 ($p = 1$, Mann–Whitney *U*-test with Bonferroni correction). The proportion of LGN boutons in the layer 1 was not significantly different from that of LPN boutons in all the layers (layer 1, $p = 0.118$; layers 2/3, 4 and 5, $p = 1$, Mann–Whitney *U*-test with Bonferroni correction). **(B)** The mean gOSI of responsive LPN and LGN boutons. gOSI of LGN boutons in the layer 4 was significantly lower than that of LGN boutons in the layers 1, 2/3, LPN axons in the layers 1, 2/3, 4, and 5 ($P \leq 0.001$, Mann–Whitney *U*-test with Bonferroni correction). gOSI of LGN boutons between the layers 1 and 2/3 ($p = 1$, Mann–Whitney *U*-test with Bonferroni correction), and gOSI of LPN boutons among different layers were statistically not different (between the layers 1 and 2/3, $p = 1$; between the layers 1 and 4, $p = 0.105$; between the layers 1 and 5, $p = 0.126$; between the layers 2/3 and 4, $p = 1$; between the layers 2/3 and 5, $p = 0.588$; between the layers 4 and 5, $p = 1$, Mann–Whitney *U*-test with Bonferroni correction). **(C)** The distribution of gOSI of LPN boutons in the layer 1 (left, $n = 562$ boutons from six mice, 11 FOVs), layer 2/3 (second from left, $n = 313$ boutons from six mice, 7 FOVs), layer 4 (second from right, $n = 458$ boutons from five mice, 8 FOVs), and layer 5 (right, $n = 391$ boutons from two mice, 9 FOVs). **(D)** The distribution of gOSI of LGN boutons in the layer 1 (left, $n = 2{,}924$ boutons from 37 mice, 123 FOVs), layer 2/3 (second from left, $n = 2{,}818$ boutons from 36 mice, 97 FOVs), and layer 4 (second from right, $n = 1{,}722$ boutons from 30 mice, 98 FOVs). Arrows **(B,C)** indicate the threshold (gOSI = 0.33) for sharply orientation-selective boutons. gOSI, global orientation-selective index; LPN, lateral posterior nucleus; LGN, lateral geniculate nucleus; V1, primary visual cortex; FOV, field-of-view. $^{*}P \leq 0.05$; $^{***}P \leq 0.001$. The data of LGN axons are re-use from the previous publication (Kondo and Ohki, 2016).

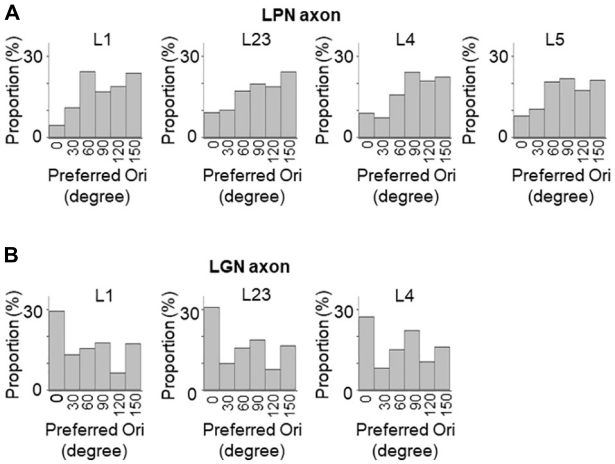

FIGURE 5 | Distribution of preferred orientations of LPN and LGN boutons in V1. The distribution of preferred orientations of LPN boutons **(A)** and LGN boutons **(B)** in each layer of V1. LPN boutons showed skewed bias from horizontal to vertical orientation, whereas LGN boutons showed cardinal bias. LPN, lateral posterior nucleus; LGN, lateral geniculate nucleus; and V1, primary visual cortex. The data of LGN axons are re-use from the previous publication (Kondo and Ohki, 2016).

position in V1. Therefore, biased orientation selectivity observed in this study may reflect the orientation bias of sSC neurons. Given that the sSC receives inputs from the retinal ganglion cells, the characteristic direction selectivity of the LPN neurons can be further traced back to the retinal direction-selective ganglion cells (Shi et al., 2017; Fang et al., 2020).

Another potential origin of the visual information carried by the LPN axons could be V1 or HVA. The LPN has been shown to be reciprocally connected to V1 and HVAs (Bennett et al., 2019; Blot et al., 2021). Thus, LPN activity may also be driven by these feedback visual inputs from the lower and higher visual cortices. Previous studies have shown that lesions or inhibition of the V1 neurons alters neuronal activity in the anterior subregion of the LPN (Bennett et al., 2019), but that it does not largely alter the selectivity of the orientation and direction responses in the sSC neurons (Wang et al., 2010; Ahmadlou and Heimel, 2015). The V1 is connected to the SC unidirectionally and the SC is connected to the LPN unidirectionally as well. Thus, V1-SC-LPN pathway can also be a potential origin of the visual information carried by the LPN axons, but the above results suggest that this pathway may be not so important as reciprocal pathways of the LPN and V1 or LPN and HVAs.

Taken together, the orientation- and direction-selective responses of the LPN axons may originate from either feedforward sSC inputs to the LPN derived from the retinal direction-selective ganglion cells (Shi et al., 2017; Fang et al., 2020) or feedback visual inputs from V1 or the HVAs to the LPN (Zhou et al., 2017; Bennett et al., 2019; Juavinett et al., 2020; Blot et al., 2021). Future studies examining the activity of the LPN axons in V1 under the suppression of the visual cortices or SC will clarify the origin of the visual information carried by the LPN axons in V1.

Our previous study has shown the low orientation selectivity in the LGN axons projecting to the layer 4 of V1 (Kondo and Ohki, 2016), which is different from the results of other

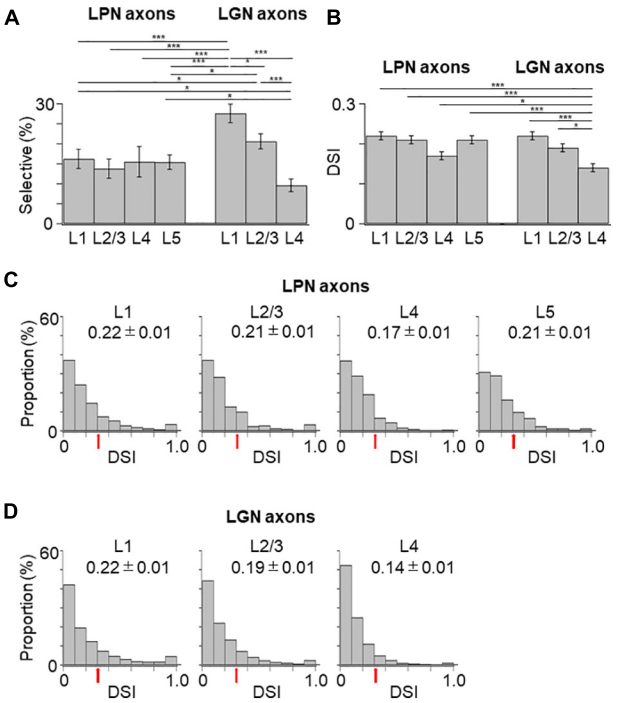

FIGURE 6 | Proportion of direction-selective boutons and distribution of DSI of the LPN and LGN boutons in V1. **(A)** The proportion of direction-selective LPN and LGN boutons. The proportion of the LGN boutons in layer 1 was significantly different from that of the LPN boutons in all the layers ($P \leq 0.001$, Mann–Whitney *U*-test with Bonferroni correction). The proportion of LGN boutons in layer 2/3 was significantly different from that of LPN boutons in layers 2/3 and 5 (layer 2/3, $p = 0.032$; layer 5, $p = 0.045$, Mann–Whitney *U*-test with Bonferroni correction). The proportion of LGN boutons in layer 4 was significantly different from that of LPN boutons in layers 1 and 5 (layer 1, $p = 0.023$; layer 5, $p = 0.031$, Mann–Whitney *U*-test with Bonferroni correction) and LGN boutons in the remaining layers ($p \leq 0.001$, Mann–Whitney *U*-test with Bonferroni correction). **(B)** The mean DSI of responsive LPN and LGN boutons. DSI of LGN boutons in the layer 4 was significantly lower than that of LGN boutons in the layer 1, LPN boutons in the layers 1, 2/3, 5 ($P \leq 0.001$, Mann–Whitney *U*-test with Bonferroni correction) and LGN boutons in the layer 2/3 and LPN boutons in the layer 4 (LGN layer 2/3, $p = 0.015$; LPN layer 4, $p = 0.041$, Mann–Whitney *U*-test with Bonferroni correction). DSI of LGN boutons between the layers 1 and 2/3 ($p = 1$, Mann–Whitney *U*-test with Bonferroni correction) and DSI of LPN boutons among different layers were statistically not different (between layers 1 and 5, $p = 0.882$; other pairs, $p = 1$, Mann–Whitney *U*-test with Bonferroni correction). **(C)** The distribution of DSI of LPN boutons in the layer 1 (left, $n = 187$ boutons from six mice, 11 FOVs), layer 2/3 (second from left, $n = 93$ boutons from six mice, 7 FOVs), layer 4 (second from right, $n = 81$ boutons from five mice, 8 FOVs), and layer 5 (right, $n = 134$ boutons from two mice, 9 FOVs). **(D)** The distribution of DSI of LGN boutons in the layer 1 (left, $n = 1{,}954$ boutons from 37 mice, 123 FOVs), layer 2/3 (middle, $n = 1{,}630$ boutons from 36 mice, 97 FOVs), and layer 4 (right, $n = 931$ boutons from 30 mice, 98 FOVs). Arrows show the threshold (DSI = 0.3) for direction-selective boutons. DSI, direction-selective index; LPN, lateral posterior nucleus; LGN, lateral geniculate nucleus; V1, primary visual cortex; FOV, field-of-view. $^{*}P \leq 0.05$; $^{***}P \leq 0.001$. The data of LGN axons are re-use from the previous publication (Kondo and Ohki, 2016).

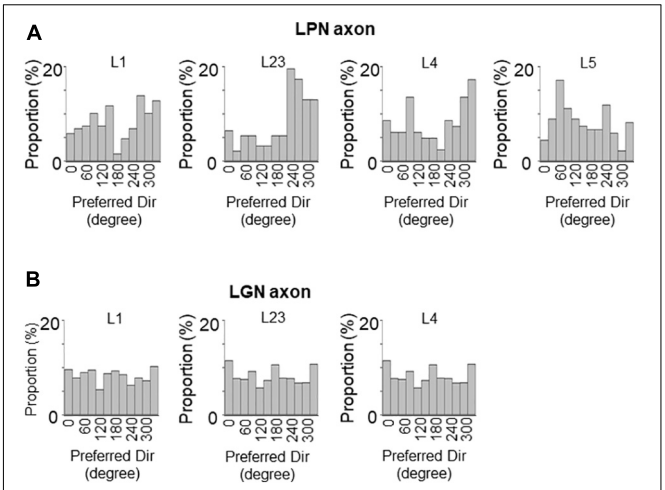

FIGURE 7 | Distribution of preferred directions of LPN and LGN boutons in V1. The distribution of preferred directions of LPN boutons **(A)** and LGN boutons **(B)** in each layer of V1. LPN boutons showed skewed bias from the horizontal to vertical direction, but this bias was less prominent than the orientation bias of LPN boutons. In contrast, LGN boutons showed cardinal bias, which was also less prominent than the orientation bias of LGN boutons. LPN, lateral posterior nucleus; LGN, lateral geniculate nucleus; V1, primary visual cortex. The data of LGN axons are re-use from the previous publication (Kondo and Ohki, 2016).

studies (Sun et al., 2016; Zhuang et al., 2021). The reason for the discrepancy between these studies could be the differences in experimental conditions, particularly, the type of promoter used to express the genetically encoded calcium indicator protein, GCaMP6s. The CAG promoter that we used in our studies (Kondo and Ohki, 2016) is one of ubiquitous promoters and labels a large population of neurons (Jackson et al., 2016). Therefore, our samples may represent a larger population of LGN neurons than other two groups.

Another difference between our study and the two studies is the optics of two-photon microscope. Sun et al. (2016) and Zhuang et al. (2021) used adaptive optics (AO) to improve the distortion of the fluorescence signal due to optical aberrations in the recordings from the deep cortical layers. A previous study showed that the sample-induced aberration during the *in vivo* brain imaging is mostly a spherical aberration (Ji et al., 2012). The spherical aberration can be corrected effectively by adjusting the axial position of the objective lens (Kondo and Ohki, 2016). Since our recordings were done by this method, the effect of sample-aberration was minimized without AO. Indeed, Zhuang et al. (2021) tested this possibility and found that AO improves the signal intensity of visual responses, but does not affect the calculation of the orientation selectivity of axonal boutons in layer 4. In the present study, we found that the LPN axons projecting to the layer 4 of V1 have high orientation selectivity, suggesting that our correction method is enough to see the orientation selectivity, and the low orientation selectivity of the LGN axons projecting to V1 (Kondo and Ohki, 2016) was not due to the sample aberration.

Finally, we observed that LPN axons projecting to the layer 4 of V1 had high orientation selectivity, while LGN axons projecting to the layer 4 of V1 had low orientation selectivity. Because of the difficulty to restrict the expression of GCaMP6s

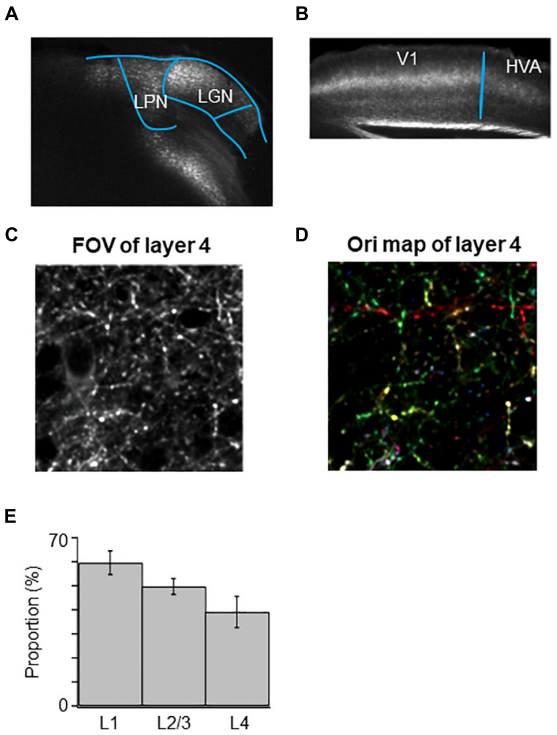

FIGURE 8 | High orientation selectivity of mixed LGN and LPN axons in V1. **(A)** Targeted expression of GCaMP6s to LGN was conducted but expression of GCaMP6s was leaked in LPN. **(B)** Projections of mixed LGN and LPN axons in V1. Projections can be seen not only in the V1 but also in the HVAs. **(C)** A FOV image of the mixed LGN and LPN axons in the layer 4 of V1. **(D)** An orientation color map of the mixed LGN and LPN axons in the layer 4 of V1. Mixed LGN and LPN axons in the layer 4 showed high orientation selectivity. **(E)** The proportion of orientation-selective mixed LGN and LPN boutons in layers 1 (n = 941 boutons from 5 mice, 5 FOVs), 2/3 (n = 1,106 boutons from 5 mice, 5 FOVs) and 4 (n = 1,042 boutons from 5 mice, 5 FOVs). The proportion of orientation-selective mixed LGN and LPN boutons among different layers were statistically not different (between layers 1 and 4, p = 0.258; other pairs, p = 1, Mann–Whitney U-test with Bonferroni correction). LPN, lateral posterior nucleus; LGN, lateral geniculate nucleus; V1, primary visual cortex; FOV, field-of-view.

in the small nucleus of LGN, unexpected leakage of GCaMP6s expression in the neighboring LPN could happen. If it is the case, recordings of the mixed LGN and LPN axons may result in the higher proportion of orientation-selectivity in the layer 4 (**Figure 8**) than the LGN axons.

The orientation-selectivity of LPN axons observed here (mean gOSI = 0.27 ∼ 0.38, gOSI = 0.27 in layer 1) were higher than those of LPN neurons (Durand et al., 2016: mean OSI = 0.22, Fang et al., 2020: mean gOSI = 0.17) but comparable with that of LPN axons in V1 (Roth et al., 2016: mean OSI = 0.38 in layer 1) reported previously (gOSI becomes usually lower than OSI). On the other hand, the DSI was similar between our study and these studies (Our study: mean DSI = 0.17 ∼ 0.22, Durand et al., 2016: mean DSI = 0.34, Roth et al., 2016: mean DSI = 0.27 in layer 1). The location of LPN neurons targeting specific brain regions are localized within the LPN (Bennett et al., 2019, e.g., neurons targeted to V1 and ventral HVA locate mainly in the anterior part of LPN, while neurons targeted to dorsal HVA locate mostly in posterior part of LPN). The stereotaxic coordinates of the recording sites of LPN neurons (Durand et al., 2016, 2.3 mm posterior from Bregma; Fang et al., 2020, 2.2 ∼ 2.3 mm posterior from Bregma) were more posterior than our AAV injected site (our study, 1.8 mm posterior from Bregma). Therefore, the difference in the orientation selectivity between this study and the previous studies may arise from the difference in the population of recorded neurons, where neurons targeting dorsal HVA may be less orientation selective than those targeting V1.

Our recordings of the axonal activities of the LPN and LGN neurons were carried out under the light anesthesia (0.2% isoflurane sedated by chlorprothixene). Since LPN receives inputs from various brain regions such as superior colliculus (SC), higher visual areas, amygdala, and other sensory areas (Zhou et al., 2017; Bennett et al., 2019), these brain regions may affect the response properties of LPN neurons depending on the brain states (Durand et al., 2016, e.g., anesthesia or wakefulness). It is recently reported that the functional organization of orientation-selective SC neurons (Ahmadlou and Heimel, 2015; Feinberg and Meister, 2015; Chen et al., 2021) were dynamically modulated by the brain states (Kasai and Isa, 2021). This state-dependent difference in the orientation-selectivity of SC neurons (Kasai and Isa, 2021) and in neuronal activities of other brain regions (Poulet and Crochet, 2019; Hua et al., 2020) may accordingly affect the orientation-selectivity of LPN neurons.

It is reported that the LPN is reciprocally connected with many cortical areas, such as visual, auditory, and somatosensory cortices (Zhou et al., 2017; Bennett et al., 2019) and possibly integrates multisensory information within the LPN circuit. It has been also suggested that the LPN may function as a hub providing indirect route to transfer sensory information from one cortex to other (Sherman, 2016). Thus, the unique anatomical position of the LPN may have important functional roles for the integration and modulation among the multisensory brain circuits (Chou et al., 2020; Fang et al., 2020). Modulatory function of other higher order thalamus has been also reported in the primary somatosensory cortex, showing that the posterior medial (POm) nucleus of the thalamus enhances the amplitude of whisker deflection (Gharaei et al., 2020).

The orientation- and direction-selective inputs from LPN to different layers in V1 may have different roles in each layer. In layer 4, neurons show sharp orientation selectivity (Niell and Stryker, 2008; Kondo et al., 2016). The orientation selectivity of V1 neurons in layer 4 may be derived from the orientation-non-selective LGN inputs (Hubel and Wiesel, 1962; Lien and Scanziani, 2013) and the orientation-selective LPN inputs may further contribute to the orientation selectivity of V1 neurons in layer 4. The LPN axons send more diverse SPF information than LGN axons to V1. Since the V1 neurons show more diverse SPF selectivity (Niell and Stryker, 2008; Kondo et al., 2016) than LGN axons, diverse SPF selectivity of LPN inputs may contribute to the diverse selectivity of V1 neurons.

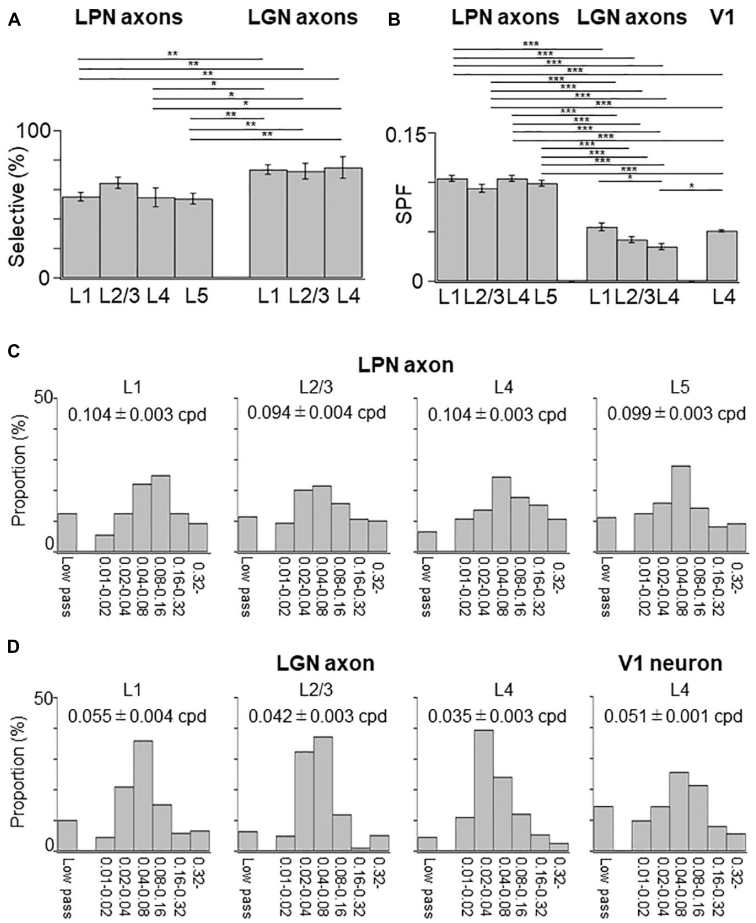

FIGURE 9 | Spatial frequency tuning of LPN and LGN boutons in V1. **(A)** The proportion of SPF-selective LPN and LGN boutons. The proportion of LPN boutons in the layers 1 and 5 was significantly different from that of LGN boutons in all layers ($P \leq 0.01$, Mann–Whitney *U*-test with Bonferroni correction). The proportion of LPN boutons in layer 4 was significantly different from that of LGN boutons in all layers (layer 1, $p = 0.024$; layer 2/3, $p = 0.032$; layer 5, $p = 0.047$, Mann–Whitney *U*-test with Bonferroni correction). **(B)** The mean preferred SPF of responsive LPN and LGN boutons. Mean preferred frequency of LPN boutons of all the layers had significant difference from LGN boutons of all the layers ($P \leq 0.001$, Mann–Whitney *U*-test with Bonferroni correction). Mean preferred frequency among LPN boutons had no significant difference (between layers 1 and 2/3, $p = 0.896$; other pairs, $p = 1$, Mann–Whitney *U*-test with Bonferroni correction). Mean preferred frequency of the layer 4 LGN boutons was significantly different from LGN boutons of layer 1 and V1 neurons in layer 4 (LGN boutons in layer 1, $p = 0.037$; V1 neurons in layer 4, $p = 0.013$, Mann–Whitney *U*-test with Bonferroni correction). **(C)** The distribution of the preferred SPFs of LPN boutons in the layer 1 (left, $n = 893$ boutons from six mice, 13 FOVs), layer 2/3 (second from left, $n = 659$ boutons from six mice, 9 FOVs), layer 4 (second from right, $n = 844$ boutons from five mice, 8 FOVs), and layer 5 (right, $n = 1{,}000$ boutons from three mice, 13 FOVs). **(D)** The distribution of the preferred SPFs of LGN boutons in the layer 1 (left, $n = 3{,}817$ boutons from 20 mice, 42 FOVs), layer 2/3 (second from left, $n = 2{,}669$ boutons from 18 mice, 29 FOVs), and layer 4 (second from right, $n = 5{,}576$ boutons from 20 mice, 55 FOVs), and V1 neurons in the layer 4 (right, $n = 6{,}210$ neurons from 9 mice, 12 volumes). LPN, lateral posterior nucleus; LGN, lateral geniculate nucleus; V1, primary visual cortex; SPF, spatial frequency; FOV, field-of-view; cpd, cycle per degree. $^{*}P \leq 0.05$; $^{**}P \leq 0.01$; $^{***}P \leq 0.001$. The data of LGN axons and V1 neurons are re-use from the previous publication (Kondo and Ohki, 2016).

DATA AVAILABILITY STATEMENT

The data that support the findings of this study and all custom code used in this study are available from the corresponding author upon reasonable request.

ETHICS STATEMENT

The animal study was reviewed and approved by the University of Tokyo Animal Care and Use Committee.

AUTHOR CONTRIBUTIONS

SK and KO designed the research and wrote the manuscript. SK and YK performed the experiments and analyzed the data. All authors contributed to the article and approved the submitted version.

FUNDING

This work was supported by grants from Brain/Minds from AMED (Grant Nos. JP16dm0207034, JP20dm0207048, and

JP21dm0207014 to KO), Institute for AI and Beyond to KO, JSPS KAKENHI (Grant Nos. 25221001, 19H05642, and 20H05917 to KO, 17H03540, 20H03336, and 21H05165 to SK), AMED (Grant No. JP21wm0525013 to SK), and the Mitsubishi Foundation to SK.

ACKNOWLEDGMENTS

We thank all of the members of Ohki Laboratory for support and discussion; A. Hayashi, Y. Kato, M. Taki, T. Inoue, Y. Sono, A. Honda for animal care and genotyping; the Genetically-Encoded Neuronal Indicator and Effector (GENIE) Project for providing GCaMP6s.

SUPPLEMENTARY MATERIAL

The Supplementary Material for this article can be found online at: https://www.frontiersin.org/articles/10.3389/fncir.2022.825735/full#supplementary-material

REFERENCES

Adesnik, H., and Naka, A. (2018). Cracking the Function of Layers in the Sensory Cortex. *Neuron.* 100, 1028–1043. doi: 10.1016/j.neuron.2018.10.032

Ahmadlou, M., and Heimel, J. A. (2015). Preference for concentric orientations in the mouse superior colliculus. *Nat. Commun.* 6:6773. doi: 10.1038/ncomms7773

Ahmadlou, M., Zweifel, L. S., and Heimel, J. A. (2018). Functional modulation of primary visual cortex by the superior colliculus in the mouse. *Nat. Commun.* 9:3895. doi: 10.1038/s41467-018-06389-6

Alitto, H. J., and Dan, Y. (2013). Cell-type-specific modulation of neocortical activity by basal forebrain input. *Front. Syst. Neurosci.* 6:79. doi: 10.3389/fnsys.2012.00079

Allen, A. E., Procyk, C. A., Howarth, M., Walmsley, L., and Brown, T. M. (2016). Visual input to the mouse lateral posterior and posterior thalamic nuclei: photoreceptive origins and retinotopic order. *J. Physiol.* 594, 1911–1929. doi: 10.1113/JP271707

Baldwin, M. K. L., Balaram, P., and Kaas, J. H. (2017). The evolution and functions of nuclei of the visual pulvinar in primates. *J. Comp. Neurol.* 525, 3207–3226. doi: 10.1002/cne.24272

Beltramo, R., and Scanziani, M. (2019). A collicular visual cortex: neocortical space for an ancient midbrain visual structure. *Science* 363, 64–69. doi: 10.1126/science.aau7052

Bennett, C., Gale, S. D., Garrett, M. E., Newton, M. L., Callaway, E. M., Murphy, G. J., et al. (2019). Higher-order thalamic circuits channel parallel streams of visual information in mice. *Neuron* 102, 477–492.e5. doi: 10.1016/j.neuron.2019.02.010

Bickford, M. E., Zhou, N., Krahe, T. E., Govindaiah, G., and Guido, W. (2015). Retinal and tectal "driver-like" inputs converge in the shell of the mouse dorsal lateral geniculate nucleus. *J. Neurosci.* 35, 10523–10534. doi: 10.1523/JNEUROSCI.3375-14.2015

Blot, A., Roth, M. M., Gasler, I., Javadzadeh, M., Imhof, F., and Hofer, S. B. (2021). Visual intracortical and transthalamic pathways carry distinct information to cortical areas. *Neuron* 109, 1996–2008. doi: 10.1016/j.neuron.2021.04.017

Chen, H., Savier, E. L., DePiero, V. J., and Cang, J. (2021). Lack of Evidence for Stereotypical Direction Columns in the Mouse Superior Colliculus. *J. Neurosci.* 41, 461–473. doi: 10.1523/JNEUROSCI.1155-20.2020

Chou, Z., Fang, Q., Yan, L., Zhong, W., Peng, B., Li, H., et al. (2020). Contextual and cross-modality modulation of auditory cortical processing through pulvinar mediated suppression. *Elife* 9:e54157. doi: 10.7554/eLife.54157

De Franceschi, G. D., and Solomon, S. G. (2018). Visual response properties of neurons in the superficial layers of the superior colliculus of awake mouse. *J. Physiol.* 596, 6307–6332. doi: 10.1113/JP276964

Dominguez-Vargas, A. U., Schneider, L., Wilke, M., and Kagan, I. (2017). Electrical microstimulation of the pulvinar biases saccade choices and reaction times in a time-dependent manner. *J. Neurosci.* 37, 2234–2257. doi: 10.1523/JNEUROSCI.1984-16.2016

Durand, S., Iyer, R., Mizuseki, K., de Vries, S., Mihalas, S., and Reid, R. C. (2016). A comparison of visual response properties in the lateral geniculate nucleus and primary visual cortex of awake and anesthetized mice. *J. Neurosci.* 36, 12144–12156. doi: 10.1523/JNEUROSCI.1741-16.2016

Fang, Q., Chou, X. L., Peng, B., Zhong, W., Zhang, L. I., and Tao, H. W. (2020). A differential circuit via retino-colliculo-pulvinar pathway enhances feature selectivity in visual cortex through surround suppression. *Neuron* 105, 355–369.e6. doi: 10.1016/j.neuron.2019.10.027

Feinberg, E. H., and Meister, M. (2015). Orientation columns in the mouse superior colliculus. *Nature* 519, 229–232. doi: 10.1038/nature14103

Gale, S. D., and Murphy, G. J. (2014). Distinct representation and distribution of visual information by specific cell types in mouse superficial superior colliculus. *J. Neurosci.* 34, 13458–13471. doi: 10.1523/JNEUROSCI.2768-14.2014

Gharaei, S., Honnuraiah, S., Arabzadeh, E., and Stuart, G. J. (2020). Superior colliculus modulates cortical coding of somatosensory information. *Nat. Commun.* 11:1693. doi: 10.1038/s41467-020-15443-1

Glickfeld, L. L., Andermann, M. L., Bonin, V., and Reid, R. C. (2013). Cortico-cortical projections in mouse visual cortex are functionally target specific. *Nat. Neurosci.* 16, 219–226. doi: 10.1038/nn.3300

Grieve, K. L., Acuña, C., and Cudeiro, J. (2000). The primate pulvinar nuclei: vision and action. *Trends Neurosci.* 23, 35–39. doi: 10.1016/s0166-2236(99)01482-4

Hawken, M. J., and Parker, A. J. (1987). Spatial properties of neurons in the monkey striate cortex. *Proc. R. Soc. Lond. B Biol. Sci.* 231, 251–288. doi: 10.1098/rspb.1987.0044

Hua, T., Chen, B., Lu, D., Sakurai, K., Zhao, S., Han, B., et al. (2020). General anesthetics activate a potent central pain-suppression circuit in the amygdala. *Nat. Neurosci.* 23, 854–868. doi: 10.1038/s41593-020-0632-8

Hubel, D. H., and Wiesel, T. N. (1962). Receptive fields, binocular interaction and functional architecture in the cat's visual cortex. *J. Physiol.* 160, 106–154. doi: 10.1113/jphysiol.1962.sp006837

Ibrahim, L. A., Mesik, L., Ji, X. X., Fang, Q., Li, H. F., Li, Y. T., et al. (2016). Cross-modality sharpening of visual cortical processing through layer-1-mediated inhibition and disinhibition. *Neuron* 89, 1031–1045. doi: 10.1016/j.neuron.2016.01.027

Ji, N., Sato, T. R., and Betzig, E. (2012). Characterization and adaptive optical correction of aberrations during in vivo imaging in the mouse cortex. *Proc. Natl. Acad. Sci. U. S.A.* 109, 22–27. doi: 10.1073/pnas.1109202108

Jackson, K. L., Dayton, R. D., Deverman, B. E., and Klein, R. L. (2016). Better Targeting, Better Efficiency for Wide-Scale Neuronal Transduction with the Synapsin Promoter and AAV-PHP.B. *Front. Mol. Neurosci.* 9:116. doi: 10.3389/fnmol.2016.00116

Juavinett, A. L., Kim, E. J., Collins, H. C., and Callaway, E. M. (2020). A systematic topographical relationship between mouse lateral posterior thalamic neurons and their visual cortical projection targets. *J. Comp. Neurol.* 528, 95–107. doi: 10.1002/cne.24737

Kasai, M., and Isa, T. (2021). Effects of light isoflurane anesthesia on organization of direction and orientation selectivity in the superficial layer of the mouse superior colliculus. *J. Neurosci.* JN-RM- 1196–1121. doi: 10.1523/JNEUROSCI.1196-21.2021 Epub online ahead of print.

Kerlin, A. M., Andermann, M. L., Berezovskii, V. K., and Reid, R. C. (2010). Broadly tuned response properties of diverse inhibitory neuron subtypes in mouse visual cortex. *Neuron* 67, 858–871. doi: 10.1016/j.neuron.2010.08.002

Kondo, S., and Ohki, K. (2016). Laminar differences in the orientation selectivity of geniculate afferents in mouse primary visual cortex. *Nat. Neurosci.* 19, 316–319. doi: 10.1038/nn.4215

Kondo, S., Yoshida, T., and Ohki, K. (2016). Mixed functional microarchitectures for orientation selectivity in the mouse primary visual cortex. *Nat. Commun.* 7:13210. doi: 10.1038/ncomms13210

Leinweber, M., Ward, D. R., Sobczak, J. M., Attinger, A., and Keller, G. B. (2017). A sensorimotor circuit in mouse cortex for visual flow predictions. *Neuron* 95, 1420–1432. doi: 10.1016/j.neuron.2017.08.036

Liang, F., Xiong, X. R., Zingg, B., Ji, X. Y., Zhang, L. I., and Tao, H. W. (2015). Sensory cortical control of a visually induced arrest behavior via corticotectal projections. *Neuron* 86, 755–767. doi: 10.1016/j.neuron.2015.03.048

Lien, A. D., and Scanziani, M. (2013). Tuned thalamic excitation is amplified by visual cortical circuits. *Nat. Neurosci.* 16, 1315–1323. doi: 10.1038/nn.3488

Matsui, T., and Ohki, K. (2013). Target dependence of orientation and direction selectivity of corticocortical projection neurons in the mouse V1. *Front. Neural Circuits.* 7:143. doi: 10.3389/fncir.2013.00143

Mesik, L., Huang, J. J., Zhang, L. I., and Tao, H. W. (2019). Sensory- and Motor-Related Responses of Layer 1 Neurons in the Mouse Visual Cortex. *J. Neurosci* 39, 10060–10070. doi: 10.1523/JNEUROSCI.1722-19.2019

Nassi, J. J., and Callaway, E. M. (2009). Parallel processing strategies of the primate visual system. *Nat. Rev. Neurosci.* 10, 360–372. doi: 10.1038/nrn2619

Niell, C. M., and Stryker, M. P. (2008). Highly selective receptive fields in mouse visual cortex. *J. Neurosci.* 28, 7520–7536. doi: 10.1523/JNEUROSCI.0623-08.2008

Paxinos, G., and Franklin, K. B. J. (2019). *The Mouse Brain in Stereotaxic Coordinates. 5th Ed.* New York, NY: Elsevier.

Pierce, J. W. (2008). Generating Stimuli for Neuroscience Using PsychoPy. *Front. Neuroinform.* 2:10. doi: 10.3389/neuro.11.010.2008

Poulet, J. F. A., and Crochet, S. (2019). The Cortical States of Wakefulness. *Front. Syst. Neurosci.* 8:64.

Roth, M. M., Dahmen, J. C., Muir, D. R., Imhof, F., Martini, F. J., and Hofer, S. B. (2016). Thalamic nuclei convey diverse contextual information to layer 1 of visual cortex. *Nat. Neurosci.* 19, 299–307. doi: 10.1038/nn.4197

Sherman, S. M. (2016). Thalamus plays a central role in ongoing cortical functioning. *Nat. Neurosci.* 19, 533–541. doi: 10.1038/nn.4269

Shi, X., Barchini, J., Ledesma, H. A., Koren, D., Jin, Y., Liu, X., et al. (2017). Retinal origin of direction selectivity in the superior colliculus. *Nat. Neurosci.* 20, 550–558. doi: 10.1038/nn.4498

Soares, S. C., Maior, R. S., Isbell, L. A., Tomaz, C., and Nishijo, H. (2017). Fast Detector/First Responder: interactions between the Superior Colliculus-Pulvinar Pathway and Stimuli Relevant to Primates. *Front. Neurosci.* 11:67. doi: 10.3389/fnins.2017.00067

Sun, W., Tan, Z., Mensh, B. D., and Ji, N. (2016). Thalamus provides layer 4 of primary visual cortex with orientation- and direction-tuned inputs. *Nat. Neurosci.* 19, 308–315. doi: 10.1038/nn.4196

Swindale, N. V. (1998). Orientation tuning curves: empirical description and estimation of parameters. *Biol. Cybern.* 78, 45–56. doi: 10.1007/s004220050411

Tohmi, M., Meguro, R., Tsukano, H., Hishida, R., and Shibuki, K. (2014). The extrageniculate visual pathway generates distinct response properties in the higher visual areas of mice. *Curr. Biol.* 24, 587–597. doi: 10.1016/j.cub.2014.01.061

Wang, L., Sarnaik, R., Rangarajan, K., Liu, X., and Cang, J. (2010). Visual receptive field properties of neurons in the superficial superior colliculus of the mouse. *J. Neurosci.* 30, 16573–16584. doi: 10.1523/JNEUROSCI.3305-10.2010

Wörgötter, F., and Eysel, U. T. (1987). Quantitative determination of orientational and directional components in the response of visual cortical cells to moving stimuli. *Biol. Cybern.* 57, 349–355. doi: 10.1007/BF00354980

Wurtz, R. H., McAlonan, K., Cavanaugh, J., and Berman, R. A. (2011). Thalamic pathways for active vision. *Trends Cogn. Sci.* 15, 177–184. doi: 10.1016/j.tics.2011.02.004

Zhao, X., Liu, M., and Cang, J. (2014). Visual cortex modulates the magnitude but not the selectivity of looming-evoked responses in the superior colliculus of awake mice. *Neuron* 84, 202–213. doi: 10.1016/j.neuron.2014.08.037

Zhou, H., Schafer, R. J., and Desimone, R. (2016). Pulvinar-Cortex Interactions in Vision and Attention. *Neuron* 89, 209–220. doi: 10.1016/j.neuron.2015.11.034

Zhou, N. A., Maire, P. S., Masterson, S. P., and Bickford, M. E. (2017). The mouse pulvinar nucleus: organization of the tectorecipient zones. *Vis. Neurosci.* 34:E011. doi: 10.1017/S0952523817000050

Zhuang, J., Wang, Y., Ouellette, N. D., Turschak, E. E., Larsen, R. S., Takasaki, K. T., et al. (2021). Laminar distribution and arbor density of two functional classes of thalamic inputs to primary visual cortex. *Cell Rep.* 37:109826. doi: 10.1016/j.celrep.2021.109826

Conflict of Interest: The authors declare that the research was conducted in the absence of any commercial or financial relationships that could be construed as a potential conflict of interest.

Publisher's Note: All claims expressed in this article are solely those of the authors and do not necessarily represent those of their affiliated organizations, or those of the publisher, the editors and the reviewers. Any product that may be evaluated in this article, or claim that may be made by its manufacturer, is not guaranteed or endorsed by the publisher.

frontiers | Frontiers in Neural Circuits

METHODS
published: 12 May 2022
doi: 10.3389/fncir.2022.842748

A Novel Device of Reaching, Grasping, and Retrieving Task for Head-Fixed Mice

Satoshi Manita, Koji Ikezoe and Kazuo Kitamura**

Department of Neurophysiology, University of Yamanashi, Chuo, Japan

Reaching, grasping, and retrieving movements are essential to our daily lives and are common in many mammalian species. To understand the mechanism for controlling this movement at the neural circuit level, it is necessary to observe the activity of individual neurons involved in the movement. For stable electrophysiological or optical recordings of neural activity in a behaving animal, head fixation effectively minimizes motion artifacts. Here, we developed a new device that allows mice to perform reaching, grasping, and retrieving movements during head fixation. In this method, agar cubes were presented as target objects in front of water-restricted mice, and the mice were able to reach, grasp, and retrieve them with their forelimb. The agar cubes were supplied by a custom-made automatic dispenser, which uses a microcontroller to control the two motors to push out the agar cubes. This agar presentation system supplied approximately 20 agar cubes in consecutive trials. We confirmed that each agar cube could be presented to the mouse with an average weight of 55 ± 3 mg and positional accuracy of less than 1 mm. Using this system, we showed that head-fixed mice could perform reaching, grasping, and retrieving tasks after 1 week of training. When the agar cube was placed near the mice, they could grasp it with a high success rate without extensive training. On the other hand, when the agar cube was presented far from the mice, the success rate was initially low and increased with subsequent test sessions. Furthermore, we showed that activity in the primary motor cortex is required for reaching movements in this task. Therefore, our system can be used to study neural circuit mechanisms for the control and learning of reaching, grasping, and retrieving movements under head-fixed conditions.

Keywords: forelimb movements, behavior task, water restriction, agar cube, motor control

OPEN ACCESS

Edited by:
Yoshiyuki Kubota,
National Institute for Physiological Sciences (NIPS), Japan

Reviewed by:
Simon Chen,
University of Ottawa, Canada
Vijay Mohan K. Namboodiri,
University of California, San Francisco, United States

****Correspondence:***
Satoshi Manita
smanita@yamanashi.ac.jp
Kazuo Kitamura
kitamurak@yamanashi.ac.jp

Received: *24 December 2021*
Accepted: *25 April 2022*
Published: *12 May 2022*

Citation:
Manita S, Ikezoe K and Kitamura K (2022) A Novel Device of Reaching, Grasping, and Retrieving Task for Head-Fixed Mice. Front. Neural Circuits 16:842748. doi: 10.3389/fncir.2022.842748

INTRODUCTION

Rodents frequently perform reaching and grasping movements in their daily lives, such as reaching for a seed on the ground, grabbing it, and bringing it to their mouth to eat. Reaching, grasping, and retrieving objects are achieved through a complex neural mechanism. To grasp an object, the neural system (1) must accurately identify the location of the object using visual, auditory, somatosensory, and olfactory information, (2) needs to generate appropriate motor commands based on the location of the object, and (3) needs to accurately move the muscles necessary to grasp that object. Suppose the object's position changes from moment to moment while the forelimb is extended. In that case, the neural system must adjust the trajectory of the forelimb according to a control method that can respond to the changes. Reaching movements and related neural activities have been extensively studied in humans and monkeys (Castiello, 2005; Lemon, 2008;

Alstermark and Isa, 2012; Churchland et al., 2012; Shenoy et al., 2013; Turella and Lingnau, 2014; Thanawalla et al., 2020). Rodents have also been reported to use their forelimbs to reach, grasp, and retrieve objects (Tsai and Maurer, 1930). Since then, many studies on these movements have long been conducted in rodents (Metz and Whishaw, 2000; Whishaw, 2003; Azim et al., 2014; Wang et al., 2017; Yoshida and Isa, 2018; Lemke et al., 2019; Thanawalla et al., 2020; Manns et al., 2021; Nicola et al., 2021).

To investigate how single neuronal activities are involved in reaching, grasping, and retrieving movements, it is necessary to measure or control their activities during these behaviors. For these purposes, it is useful to utilize a wide variety of transgenic mice expressing calcium sensors or light-activated proteins. Several studies using these transgenic mice have shown correlations and causal relationships between various neural activities and behaviors under head-fixed conditions (Helmchen et al., 2018; Svoboda and Li, 2018). Since head fixation can restrict the behavior of mice compared to freely moving conditions, it is relatively easy to observe the movement of mouse limbs and whiskers and present sensory stimuli. Recently, with head fixation in mice, several studies have shown neuronal activity during reaching, grasping, and retrieving movements (Guo et al., 2015, 2021; Galinanes et al., 2018; Levy et al., 2020; Sauerbrei et al., 2020). In these studies, the mouse was head-fixed and performed a task in which they had to reach, grab, and retrieve a target such as a food pellet or water droplets. This manuscript presents a new method for investigating the reaching, grasping, and retrieving behavior of head-fixed mice. In this method, a single agar cube is automatically supplied in front of a mouse with a restricted water supply, allowing the mouse to reach, grasp, and retrieve it as a target with its forelimb. This system can be used to study the mechanisms of neural circuits for motor control and motor learning under head-fixed conditions.

MATERIALS AND EQUIPMENT

Animals and Surgery

The experiments and procedures were approved by the Animal Experiment Committee of University of Yamanashi. Male and female C57BL/6J mice (>6 weeks old) were purchased from Japan SLC (Hamamatsu, Japan). Female VGAT-ChR2 mice [B6.Cg-Tg(Slc32a1-COP4*H134R/EYFP)8Gfng/J, strain #:014548, The Jackson Laboratory, Bar Harbor, ME, United States] were used for optogenetics experiments. They were kept on a reversed 12-h/12-h light-dark cycle and allowed to eat food freely, and all behavioral experiments were performed in the dark phase. To immobilize the head of a mouse during behavior, we implanted an aluminum head plate [40 mm × 25 mm (the mediolateral: ML and the anteroposterior: AL axis), 1.5 mm thick, with a 15 mm × 10 mm (ML and AL axis) hole in the center or 40 mm × 20 mm, 1.5 mm thick, with a hole of 10 mm diameter in the center] to the head of the mouse. The mouse was anesthetized by inhalation of isoflurane (1.5–3%, 0.2–0.3 L/min), and the body temperature was maintained using a heater. For the surgery we used an artificial cerebrospinal fluid (ACSF) containing: 150 mM NaCl, 2.5 mM KCl, 10 mM HEPES, 2 mM $CaCl_2$, and 1 mM $MgCl_2$ (pH = 7.4 adjusted with NaOH). Eye ointment (0.3% ofloxacin, TOA Pharmaceuticals, Toyama, Japan) was applied to the eyes of the mice during surgery. The hair on the scalp was removed with a hair removal cream, and a surface anesthetic (Xylocaine Jelly 2%, Aspen Japan, Tokyo, Japan) was applied, and the skull was exposed by incision. The head plate was fixed to the skull with dental cement (Super-bond, SUN Medical, Moriyama, Japan) such that the plate did not cover the eyes of the mice. The exposed skull was covered with dental cement to attach the head plate to the skull and keep the bone from becoming infected with bacteria.

Behavior System

We developed a new behavioral experimental system where head-fixed mice could grasp an agar cube using their forelimb (**Figure 1**). An agar dispenser for making agar cubes consists of an agar mold, two plungers, and a control unit.

Agar Mold

The procedure of making an agar cube is as follows: to prepare a 3% agar solution, agar powder (010-15815, FUJIFILM Wako Pure Chemical Corporation, Osaka, Japan) was mixed with deionized water, heated in a microwave oven, and stirred to dissolve. A custom-made mold (outer size (W × H × D): 12 cm × 2.4 cm × 1.2 cm) consists of two acrylic plates. One acrylic plate has a thin channel (4 mm × 4 mm width and depth), and the other covers the channel. These acrylic plates are joined by screws before pouring the agar solution. The prepared agar solution was poured into the mold and hardened at room temperature (**Figure 1C**).

Plungers

The hardened agar was extruded from the agar mold using two orthogonal plungers (push 1 and push 2) to form a cube. The movements of the push 1 and push 2 plungers were controlled by independent self-made linear actuators (**Figures 1A–F**). The push 1 actuator consists of a stepper motor (SM-42BYG011, Mercury Motor, Shenzhen, China), a linear guide, and a ball screw (**Figures 1B,D**). To determine the start and end positions of the push 1 plunger, a slot-type photomicrosensor (EE-SX671A, OMRON, Kyoto, Japan) was placed at each location (**Figure 1D**). The push 2 actuator consists of a servo motor (DS3218, DSSERVO, Dongguan, China), a linear guide, and a slider-crank (**Figures 1E,F**).

Control Unit

A microcontroller (Arduino Uno Rev3, Arduino, Somerville, MA, United States) and a motor drive shield (L293D Motor Drive Shield for Arduino, SainSmart, Las Vegas, NV, United States) attached to the Arduino were used to control the movements of the two motors used in the push 1/2 actuators (**Figure 1A**). For the movement of the push 1 plunger per trial, the stepper motor rotated 270°, corresponding to a 3.75 mm horizontal displacement calculated by the operating angle per step of the stepping motor: 1.8° (0.025 mm) and travel per rotation of the ball screw: 5 mm. For the movement of the push 2 plunger per trial, the servo motor rotated from 31° to 90°, corresponding to a

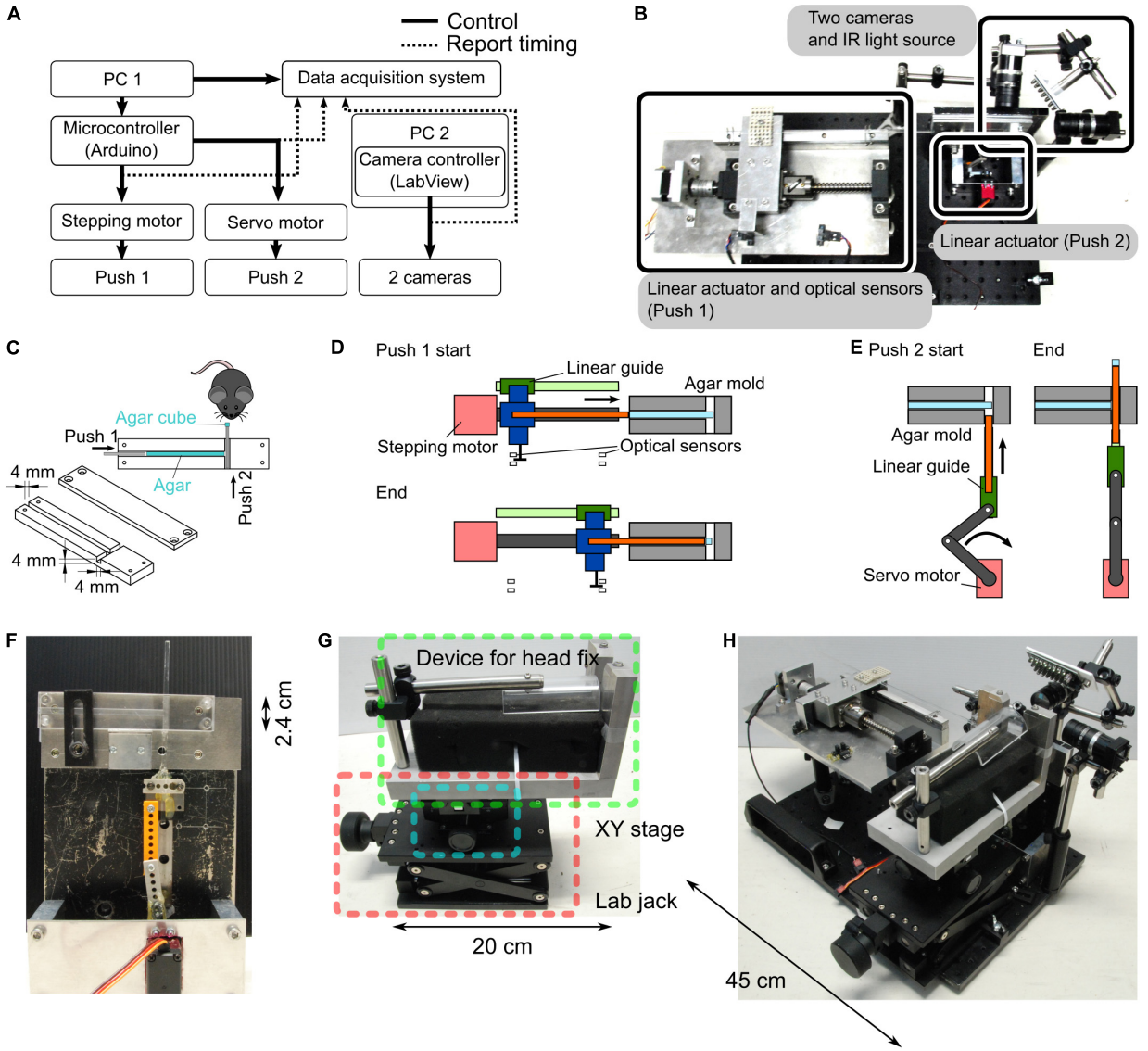

FIGURE 1 | Agar dispenser. **(A)** Configuration of the agar dispenser system. A microcontroller connected to the PC1 regulates the stepping and servo motors, forming two linear actuators. The orthogonal linear actuators push agar in the agar mold twice (Push 1 and 2), which creates an agar cube. We used another PC (PC2) to observe and record mouse behavior with two cameras. Push timings and camera triggers are stored on the PC1 by a data acquisition board. **(B)** Photograph showing the top view of the behavior task system. **(C)** Schematic of the agar mold. Successive pushes by orthogonal plungers (Push 1 → Push 2) create and present the agar cube in front of a mouse. **(D)** A schematic diagram of the molds before and after extrusion of all the agars is shown. Approximately 20 agar cubes are produced from the start to the end of this process. The position of optical sensors determined the start and end positions of the agar extrusion. The main parts are indicated by the following colors; stepping motor: red, linear guide: green, ball screw: dark gray, push 1 plunger: orange, and connecter between linear guide, ball screw, and push 1 plunger: blue. **(E)** Schematic of the push 2. For each agar cube (one trial), the agar extruded by push 1 plunger converted into a cube by push 2. The main parts are color-coded as follows; stepping motor: red, linkage: dark gray, linear guide: green, and push 2 plunger: orange. **(F)** Photograph of a side view of the agar mold and the push 2 mechanism. **(G)** Apparatus for fixing the head of mice. A manual XY stage (blue square) and a laboratory jack (red square) were placed at the bottom of the device that fixes the mouse head (green square) so that the position of the mouse can be adjusted. **(H)** Photograph of the whole system (the agar dispenser system with the head fix apparatus).

vertical displacement of 5 mm in 360 ms. The timing of the push 1 and push 2 movements was determined by the experimenter's keyboard input using a PC connected to the Arduino.

The state parameters of the task, such as the trial number, session start signal, request for trial start trigger, and message to inform the session end, were reported by the PC. Reaching, grasping, and retrieving movements of the mouse were recorded at a 100 Hz frame rate with an infrared LED illumination (an array of 940 nm LED × 56) using two USB3 cameras (BU031, Toshiba TELI, Tokyo, Japan) controlled by custom software written in LabVIEW (National Instruments, Austin, TX, United States).

Water Restriction

To motivate the mice to grab the agar cubes, we limit the water supply in the following manner. Before starting water restriction, mice were allowed to rest for a week to recover from the surgery to install the head plate (**Figure 2A**). During rest, the mice were allowed to drink water freely. We removed the water bottle from the cage during the water restriction period, and mice were given 1–2 g of 3% agar cubes instead of water in their home cages, regardless of the consumption of agar cubes during the behavioral sessions. When mice did not train for multiple days, they were given water from a water bottle, and the water supply was restricted the day before training. If mice weighed less than 80% of their weight before starting water restriction, the amount of agar was increased to 3 g per day. If the mice showed signs of dehydration or pain [e.g., ruffled fur or abnormal gait (Guo et al., 2014)], training was stopped, and the water bottle was fed into the home cage until they recovered.

Habituation and Training Periods

As a preparatory period for behavioral tests, 2–4 days of habituation period were provided to acclimate the mice to the apparatus, followed by 2–5 days of training (**Figure 2A**). During the habituation period, the experimenter supplied approximately 1 mL of water from a plastic disposable pipette to the mouse under head-fixed conditions in the apparatus for 15–30 min. Some mice drank water from day one, while others needed several days to start drinking. For this reason, the habituation period varied from mouse to mouse and ranged from 2 to 4 days. During the training period, 10–20 agar cubes were administered to the mice simultaneously (**Figure 2B**). The agar cubes were placed by the experimenter at a distance that was easy for the mice to grasp. Some mice did not reach out and grab and eat the many agars placed in front of mice at the start of training. Even when the mice did not eat the agars, the agar cubes were kept supplied for 1 min, and this was repeated for several days. Then, when mice were able to grab the agar cubes with their forelimbs and eat them (**Figure 2B**) and gained at least 0.5 g of body weight after 1 day of training, they were moved from the training phase to the test phase. For these reasons, the training period varied from 2 to 5 days, depending on the mouse.

Reaching, Grasping, and Retrieving Test

After the training period, the reaching, grasping, and retrieving (RGR) test was performed. Agar cubes were placed in front of the mice using the agar dispenser during the test period. One trial was defined as the time when the mouse either acquired or dropped one agar cube, and all trials per day were defined as one session. The position of the mouse and the agar cube was such that the agar cube was directly under the mouse's jaw, and the agar cube was placed about 2–3 mm to the right of the mouse's midline so that it could be grasped by the mouse's right hand. The following steps were performed so that the position of the mouse in relation to the agar dispenser was the same each time. On the first day, we imaged the position of the mouse relative to the agar cube, which was provided by the agar dispenser under head-fixed conditions. We adjusted the position of the mouse in the following sessions based on the position of the eyes and nose in this image. A manual XY linear stage and a laboratory jack built into the head-fixation device were used to adjust the position (**Figure 1G**). When the agar mold ran out of agar, we replaced it with another mold filled with agar. The mice were kept under head fixation during the exchange of the mold. When the dissolved agar was poured into the mold, some spaces were occasionally created where agar did not exist, presumably due to the contamination with air bubbles. The agar cube could not be supplied to the mouse from this agar-free space. In this case, the trial was considered a catch trial. The trial was excluded from the analysis when an agar cube was small, or two cubes came out simultaneously. The number of trials in each session was to be 40 or 100. If the mouse did not reach for the agar for 1 min, the trial was considered a time-out trial. Two consecutive time-out trials resulted in the termination of the session for that day. If the mouse did not take the agar cube, the experimenter manually removed the agar cube. We conducted at least 13 trials per session during the test period (67.4 ± 32.0 trials/session, 13–103 trials, $n = 13$ mice, 103 sessions). Test sessions were performed under a constant blue light illumination in a light shield box [inner size (W × H × D): 100 cm × 110 cm × 75 cm] unless otherwise stated.

Agar Cube Measurements

To examine the reproducibility of the agar cubes, we measured the weight, position, and size of the agar cubes produced by the agar dispenser. The operating conditions of the linear actuators for extruding the agar cube were fixed (the stepper motor rotation: 270° per trial, the servo motor angles: 31° and 90° for rest and active states, respectively). The weight of each agar cube was measured individually with an electronic balance. Two cameras captured the front and side images of the agar cubes, from which the area and location of the centroid of the agar cube were measured (**Figures 3B–D**). At the coordinates in the camera's field of view, the centroid of 99 agar cubes was measured, and the average coordinates were calculated. The difference between the coordinates of each cube and the average was measured.

Optogenetic Suppression of the Primary Motor Cortex

To suppress the primary motor cortex (M1) activity, we used mice expressing ChR2 in all GABAergic neurons (VGAT-ChR2 mice) and wild-type mice as control. After completing the training period, the skulls of these mice were thinned with a dental drill. Prior to the light illumination experiment, mineral oil was applied to increase the transparency of the skull. Blue light (470 ± 24 nm) from a fiber-coupled LED photostimulator (Spectra X, Lumencor, Beaverton, OR, United States) was illuminated to the forelimb area of the M1 (0.5 mm anterior and 1.5 mm lateral from the bregma) through the skull. The diameter of the optical fiber core was 1 mm, and the light intensity was 61 mW at the fiber end. The light was delivered as a 40 Hz square wave with a 50% duty cycle for 10 s. The stimulus onset was synchronized with the movement onset of the push 2, which

presents the agar cube in front of the mouse. Light illumination trials were randomly chosen with a probability of 20%.

Analysis

The behavior of the mice was manually analyzed by watching the video recorded by the cameras. The results of the trial were classified as success (success score: 1), type 1 failure (grasped the agar but could not put it into the mouth, success score: 0.5), or type 2 failure (unable to grasp the agar, success score: 0), and the mean scores were calculated for each session (**Figures 4**, **5**). To evaluate the time course of success scores during each session, the sequence of success scores was three-point moving averaged which was used as the data for the third window point (**Figure 4C**). The success score of each session was the mean score of all trials (**Figures 4E**, **5C,E**). To examine whether successful grasping is increased by repetition of sessions, we calculated a parameter called the grab ratio, the number of successful grabs (success and type 1 failure trials) divided by the total number of reach (success, type 1 failure, and type 2 failure trials) in each session. In the optogenetics experiment, we counted the number of trials in which mice extended their forelimb toward the agar cube for 10 s after the agar was presented. Data analysis, statistical testing, and graph creation were performed using custom analysis programs written in Python 3 (SciPy library for statistical testing). All error bars indicate the standard error.

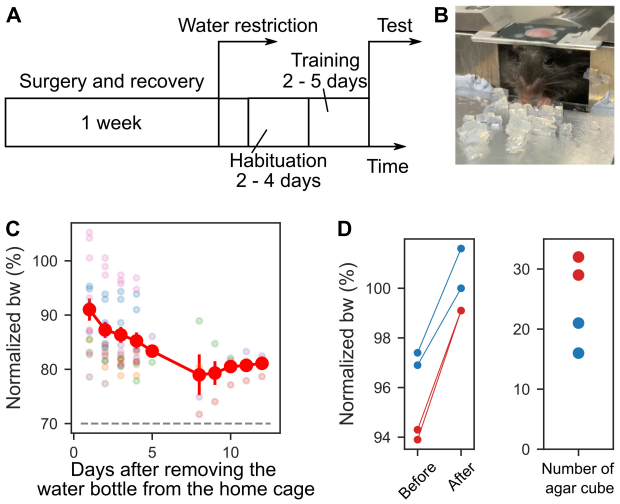

FIGURE 2 | Time course of experiment and body weights. **(A)** Time course of the experiment. One week after the recovery period from the surgery, water restriction was started. Before the test session, habituation and training periods were scheduled. **(B)** Photograph of a mouse during the training. **(C)** Mice body weights (bw) during habituation, training, and test sessions. The body weights were normalized to that on the day water restriction was started. The dashed gray line indicates 70%. Each color represents a different mouse (n = 7). **(D)** Left, the normalized weights of four sessions from two mice before they ate the agar cubes and after they could no longer eat them. Right, the number of agar cubes eaten by the mice.

RESULTS

Reproducible Agar Cube Production and Presentation

We examined the precision of the reproducibility of the agar cubes produced by the device. The average weight of the agar cube was 0.055 ± 0.003 g (mean ± standard deviation, range: 0.045–0.060 g, n = 95 cubes, four agar molds, **Figure 3A**). The standard deviations of the centroid of the agar cube were 0.36 and 0.088 mm (Y and Z axes) for camera 1, and 0.11 and 0.083 mm (X and Z axes) for camera 2, respectively (n = 99 cubes, five agar molds, **Figure 3C**). The areas of the agar cubes were 16 ± 0.8 mm^2 for camera 1, and 11 ± 0.54 mm^2 for camera 2, respectively (**Figure 3D**). These data showed that the size of agar cubes created by the dispenser was very similar, and each agar cube could be presented with an accuracy of less than 1 mm.

The Mice Performed the Task Under the Water Restriction

For mice to perform the task, drinking water was restricted, and 3% agar cubes were given as a reward (body weights normalized to those before water restriction: 84.85 ± 5.88%, **Figure 2C**). After eating the agar cubes in the training or test sessions, the weights of those mice were measured. Even in mice whose body weight was 90% of that before water restriction, the weight gain exceeded 1 g (9 sessions, 2 mice). These results indicate that the mice performed the task with mild water restriction (less than 20% body weight loss) during training and testing periods. We next examined the number of agar cubes that mice could eat. Mice that weighed more than 90% of their pre-restriction weight were given agar cubes until they did not eat anymore. The weight of the mice before and after eating and the number of agar cubes they ate were measured. We found that the mice stopped eating once they reached approximately their pre-restriction weight (2 mice, **Figure 2D**). This amount corresponded to an average of 24.5 agar cubes (range: 16–32 cubes, n = 4 sessions, 2 mice, **Figure 2D**).

The Mice Performed the Reaching, Grasping, and Retrieving Task With a High Success Rate in the Post-training Test

During the training period, the mice were given several agar cubes simultaneously and grabbed them (**Figure 2B**). Even if the mouse could not grab an agar cube once, it was allowed to grab it again as long as the agar cube was within its reach. After 2–5 days of this training, test sessions were conducted. In the test session, the dispenser automatically presented the agar cube, and the mouse was required to grab it and bring it to its mouth. Once the mouse dropped the agar cube, it was unable to grab the same agar cube again. We then examined whether mice performed the task better with the subsequent test session. Unexpectedly, mice performed this task with a high success score even in the early test sessions (success score in session 1: 0.81 ± 0.048, four mice, **Figure 4E**). Success scores did not change with the number of sessions (one-way ANOVA, F = 1.94, p = 0.09, **Figure 4E**) but tended to decrease and then increase again as the number of sessions increased. We also examined whether behavioral

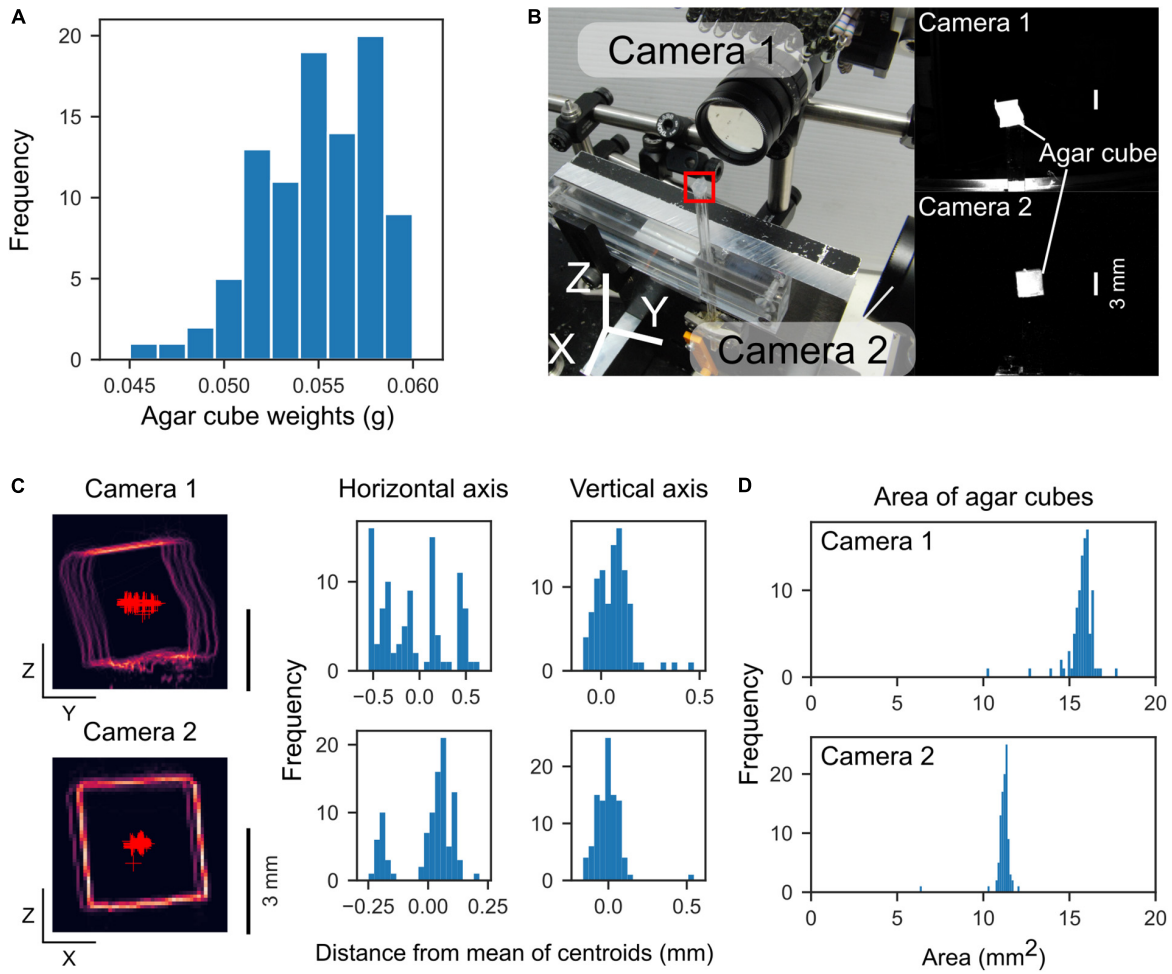

FIGURE 3 | Weight and location of the extruded agar cubes. **(A)** Histogram of agar cube weights (mean: 0.055 g, n = 95 cubes, 4 sets). **(B)** Left, Photograph of the measurement configuration. Two orthogonally positioned cameras capture front and side images of the agar cube. The red square indicates the location of an agar cube. Right, Agar cube images by the cameras. **(C)** Left, Outlines of agar cubes captured by the two cameras. The outlines of 99 agar cubes were overlaid. Red "plus" markers indicate centroids of the agar cubes. Right, Histograms of the distance from the mean of centroids along with horizontal and vertical axes. **(D)** Histograms of the area of the agar cubes captured by each camera.

performance increased within a single session. However, success scores did not change as the number of trials within a session was increased (one-way ANOVA, F = 0.30, p = 1.00, n = 36 trials in four mice, **Figure 4D**). These data indicate that trained mice can perform tasks with high performance even when a single agar cube is presented automatically.

We sought to determine why the success rate was very high from the beginning of the testing session and found that the mouse jaw was very close to the agar cube (0 mm away, **Figures 4A**, **5A**). Therefore, we placed the agar cube at a more distant location (1.3 mm away) to make it more difficult for the mice to grasp the agar. As shown in **Figures 5B,C**, the success scores in the early sessions were low and gradually increased over four sessions by repeated practice ($p < 0.001$, 1–8 sessions: 0.081 ± 0.015, n = 24 sessions, three mice, 9–16 sessions: 0.21 ± 0.028, n = 24 sessions, three mice, one-way ANOVA, **Figure 5C**). Moreover, we examined whether placing the ager cube farther away would increase the difficulty of this task. We found that success scores decreased when the agar cube was placed at 4.2 mm compared to those at 1.3 mm ($p < 0.001$, 1.3 mm: 0.38 ± 0.06, n = 6 sessions, two mice, 4.2 mm: 0.14 ± 0.04, n = 9 sessions, two mice, one-way ANOVA, **Figures 5D,E** and **Supplementary Movies 1**, **2**). These results indicate that we can change the difficulty of this task by changing the distance between the mice and the agar cubes.

We next examined whether the task could also be used for evaluating the learning of grasping. Mice might not need to learn to grasp the agar cube because the agar cube is softer and presumably easier to grab than the food pellet used in the classical methods. We tested whether agar cube grasping improves with repeated practice by measuring the ratio of successful grasping trials in each session. We found that the grab ratio increased with the number of sessions ($p < 0.001$, one-way ANOVA, 1–8 sessions: 0.10 ± 0.02, n = 24 sessions, 9–16 sessions: 0.25 ± 0.03,

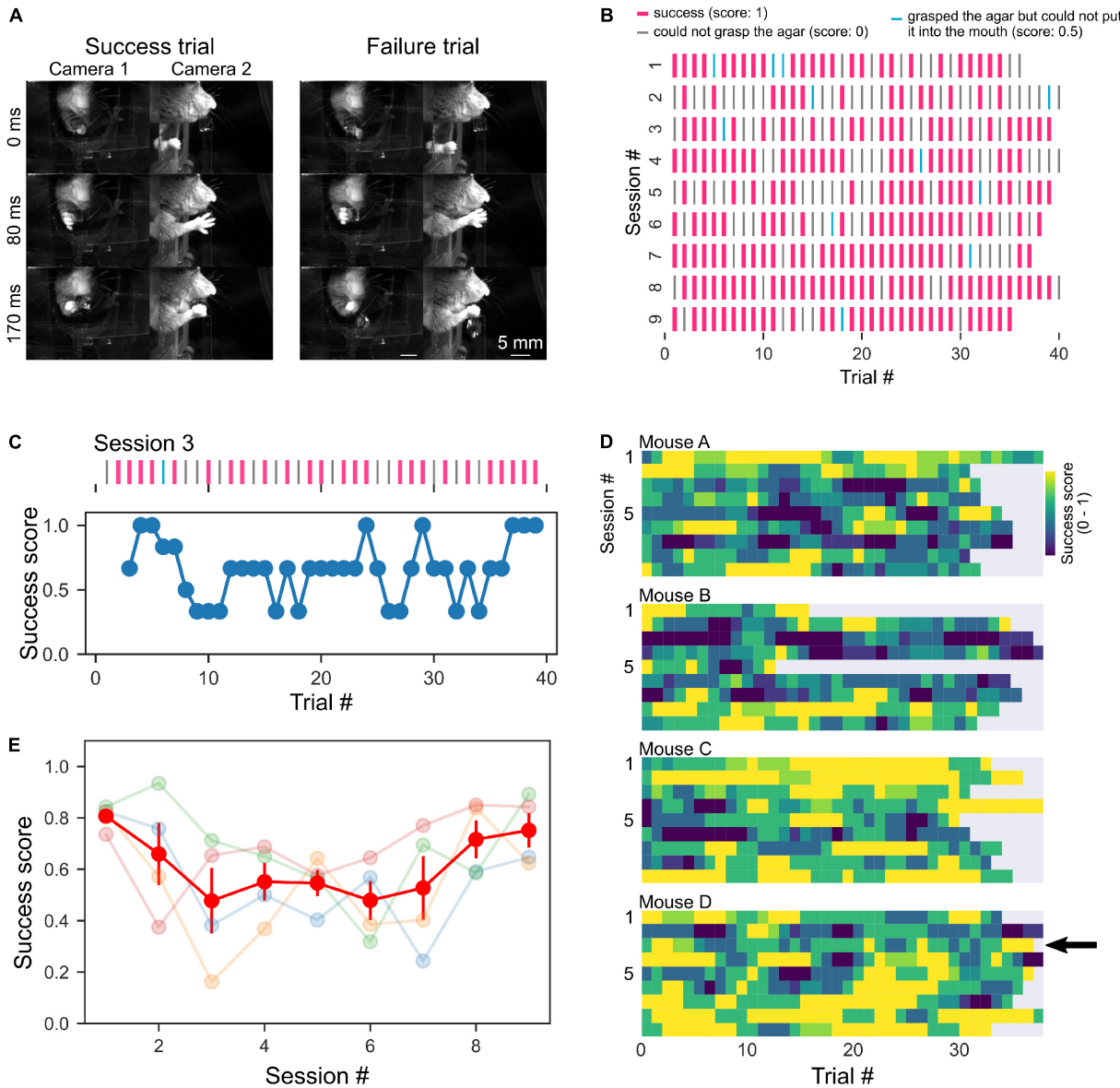

FIGURE 4 | High behavioral performance with short training. **(A)** Sequential photographs of RGR behavior by head-fixed mouse. Examples of success and failure (could not grasp the agar, "type 2 failure", score: 0) trials of the same mouse are shown. The timestamp represents the time from the beginning of the right forelimb movement of the mouse. **(B)** A representative raster plots of the success and failure trials of a mouse. Pink lines indicate successful trials. Cyan lines indicate trials where the mouse grabbed the cube but dropped it before putting it in its mouth (type 1 failure). Gray lines indicate failure trials where the mouse dropped the cube before grabbing it (type 2 failure). **(C)** A representative example of moving average from raster plot in a session [session 3 shown in panel **(B)**]. **(D)** Color plots of success scores in individual mice. The arrow indicates data in panel **(C)**. **(E)** Mean success scores were plotted across sessions. The light color plots show data from individual mice, and the red plot indicates the average.

n = 24 sessions, three mice, **Supplementary Figure**), suggesting that motor skill learning is necessary for grasping the agar cube.

The Reaching Is Dependent on M1 Activity

To examine whether this task depends on M1 activity, we used transgenic mice expressing ChR2 in GABAergic neurons (VGAT-ChR2 mice). Reaching was suppressed during photostimulation of M1 on the contralateral (left) side of VGAT-ChR2 mice (p < 0.001, Chi-square test, with photostim.: 55/80 trials, without photostim.: 9/391 trials, two mice, **Figure 5F**, left and **Supplementary Movie 3**). In 37 of the 55 suppressed trials, the forelimb was extended after photostimulation (**Supplementary Movie 1**). This result is consistent with the results of a previous manuscript (Guo et al., 2015) and is presumably due to rebound activity that activates the motor engram of the trained behavior. On the other hand, reaching movements were not suppressed by photostimulation to the ipsilateral (right side)

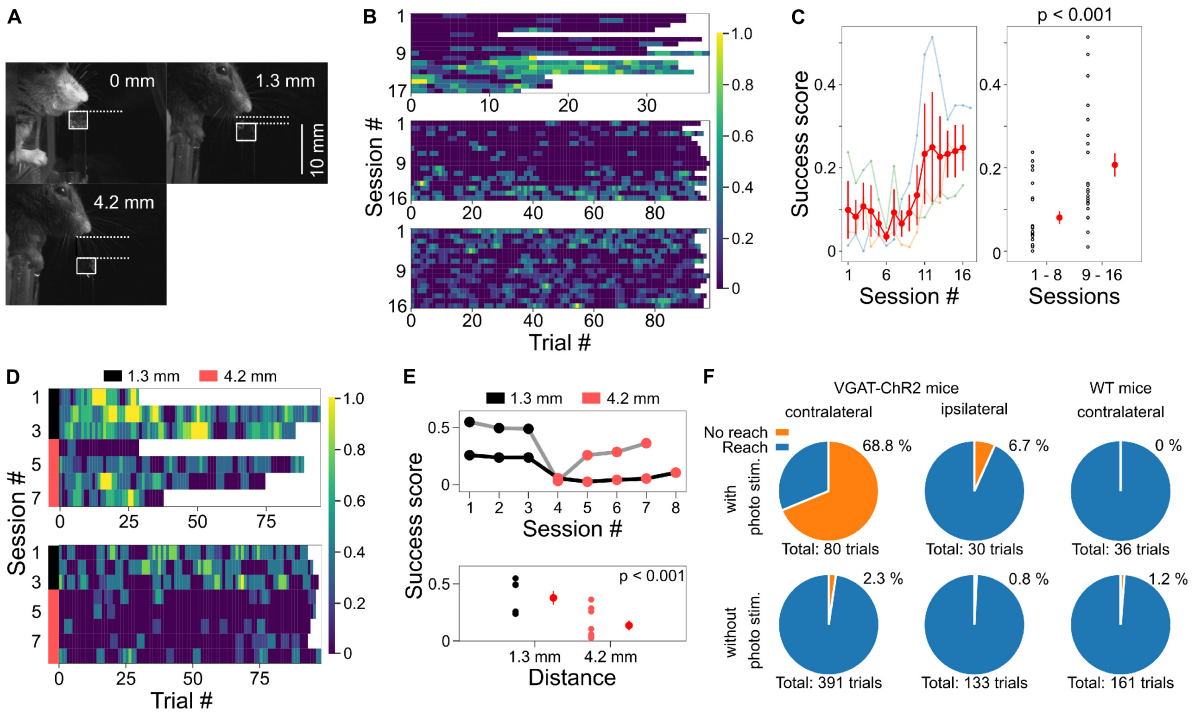

FIGURE 5 | Placing the agar cubes farther away made the task more difficult. **(A)** Examples of different agar cube positions are shown. In each image, the distance from the jaw of the mouse to the agar top is shown. White squares indicate the position of the agar. **(B)** Example of changes in success scores in three mice during test sessions when the agar cube was presented at 1.3 mm from the jaw. **(C)** Left, the relationship between session number and success scores from three mice shown in panel **(B)**. Data plotted in light color represent data from individual mice. Red plots and error bars represent mean and standard error, respectively. Right, Success scores in the second half of the session increased compared to the first half ($p < 0.001$, one-way ANOVA). **(D)** Success scores are shown in color plots when the distance from the mouse jaw to the ager was changed from 1.3 to 4.2 mm. Data obtained from two mice are shown. The black and pink bar lines indicate sessions in which the agars were located at 1.3 and 4.2 mm, respectively. **(E)** Top, from the data in panel **(D)**, the relationship between session number and mean success score are shown. Gray and black lines indicate data from two different mice. Bottom, success scores decreased when the agar cube was placed at 4.2 mm compared to the condition with the agar cube placed at 1.3 mm ($p < 0.001$, one-way ANOVA). **(F)** The reaching movements depend on M1 activity. Left, reaching was suppressed by the photostimulation to M1 on the left (contralateral) side of VGAT-ChR2 mice; with photostim.: 55/80 trials (68.8%), without photostim.: 9/391 trials (2.3%), 2 mice, $p < 0.001$, Chi-square test. Middle, reaching was not suppressed by the photostimulation of M1 on the right (ipsilateral) side; with photostim.: 2/30 trials (6.7%), without photostim.: 1/133 trials (0.8%). Right, reaching was not suppressed by the photostimulation of M1 on the left (contralateral) side of wild-type mice; with photostim.: 0/36 trials (0%), without photostim.: 2/161 trials (1.2%).

M1 of the same mice (with photostim.: 2/30 trials, without photostim.: 1/133 trials) or the contralateral M1 of wild-type mice (with photostim.: 0/36 trials, without photostim.: 2/161 trials, **Figure 5F**, middle and right). These results suggest that the reaching movements and the performance of this task are dependent on the M1 activity.

DISCUSSION

In this study, we developed a reaching, grasping, and retrieving task device for mice. This device can automatically present agar cubes in front of a head-fixed mouse. This task can be performed in mice with mild water restrictions. Mice could reach, grasp and retrieve the agar cube presented in front at a high success rate without extensive training. The success rate depended on the distance between the mouse and the agar cube. However, with repeated test sessions, the mouse gradually grasped the agar cubes even from a large distance.

Differences From Previous Methods

Our method allowed mice to perform the task with only drinking water restriction. RGR tasks for rodents generally use food pellets as rewards (Azim et al., 2014; Guo et al., 2015, 2021; Levy et al., 2020; Sauerbrei et al., 2020). To obtain food pellets as rewards during the task, mice must be restricted in their diet, which is a huge burden on rodent health (Heiderstadt et al., 2000; Toth and Gardiner, 2000; Tucci et al., 2006). On the other hand, the agar cube was given as a reward for this behavioral task. Therefore, mice only had restrictions on drinking water, which is less burdensome (Schwarz et al., 2010; Guo et al., 2014; Galinanes et al., 2018), and are more motivated to perform a task for reward (Goltstein et al., 2018). Recently, it has been shown that mice can perform RGR tasks by restricting drinking water (Galinanes et al., 2018). Consistently, we also found that mice can be sufficiently motivated to perform the task by mild restriction of water supply, that is, 1–2 g of agar per day in addition to the agar cubes ingested during the task (~1 g), instead of total water deprivation. Indeed, mice performed up to ~100 trials/session

without substantial weight loss (∼85% of body weight before training). The number of trials per session showed variability in three out of nine mice tested (**Figure 4D** Mouse B, **Figure 5B** top, **Figure 5D** upper). On the contrary, the number of trials was stable in the other six mice. Therefore, variation in the number of trials is different from mouse to mouse. The reason for this variability is still unclear, and it should be investigated in future studies.

It was reported that using the acetic acid solution as drinking water can maintain mice's motivation to perform the task while minimizing the burden on their health (Urai et al., 2021). Drinking acetic acid as water control would also be effective in our behavioral task. Furthermore, our method has an additional advantage over the water droplet reaching task (Galinanes et al., 2018). It can evaluate grasping function using solid agar cubes instead of liquid water droplets.

The difficulty of the task can be easily changed using this method. This was achieved by changing the position of the agar cube, which was done by simply changing the displacement of the push 2 plunger (**Figure 5A**), and thus it can be changed during a session. Therefore, it is possible to investigate more complex functions such as error-based adaptation. Under difficult conditions (4.2 mm ager cube distance), success scores increased slightly as the number of sessions increased (**Figure 5E**). This result implies that mice adapted to the new location for grasping the agar cubes. Furthermore, our system also allows changing the size of the agar. We expect that this will also change the difficulty of the task.

M1 Contributes to the Reaching Movements

When M1 in the left hemisphere of VGAT-ChR2 mice was suppressed by photostimulation, reaching movement in the right forelimb was inhibited (**Figure 5F** and **Supplementary Movie 3**). This is because GABAergic neurons activated by photostimulation suppressed the surrounding excitatory neurons in M1, and their activity was required to initiate the reaching movements (Zhao et al., 2011). M1 was stimulated for 10 s immediately before the agar cube was presented in front of the mouse. Inhibiting M1 during reaching or grasping may stop the movement (Guo et al., 2015). Changing the intensity and timing of photostimulation to M1 makes it possible to test how the M1 activity affects the different phases of forelimb movements. In addition to M1, behavioral bias similar to that observed in lick movements (Li et al., 2016; Svoboda and Li, 2018) may also be found in forelimb reaching movements by briefly suppressing the premotor cortex before the onset of movement. Different timing or location of photostimulation can provide clues to the neural basis of the complex movement.

What Can We Do With This Device?

The movements of the mouse are filmed by multiple high-speed (100 Hz) cameras. The markerless pose estimation algorithms such as DeepLabCut (Mathis et al., 2018) allow us to estimate how the mice use their forelimb and fingers to reach and grasp the agar cube and how they change during the learning of the task. Since these movements can be performed under head fixation, simultaneous recording and manipulation of neural activity using a combination of calcium imaging, electrophysiological recordings, and optogenetic perturbation becomes possible. Furthermore, since head fixation suppresses brain vibration, it is effective for measurements that require spatial resolution at the sub-cellular level, such as dendrite and spine imaging (Schwarz et al., 2010; Guo et al., 2014; Burgess et al., 2017; Bjerre and Palmer, 2020; Wagner et al., 2020). These future experiments allow us to unveil the correlation and causal relationship between brain activity and motor parameters or motor learning and to understand the neural circuit mechanisms of these movements.

DATA AVAILABILITY STATEMENT

The raw data supporting the conclusions of this article will be made available by the authors, without undue reservation.

ETHICS STATEMENT

The animal study was reviewed and approved by the Animal Experiment Committee of University of Yamanashi.

AUTHOR CONTRIBUTIONS

SM designed and performed the experiments, analyzed the data, and wrote the manuscript. KI designed the experiments and wrote the manuscript. KK designed the project and wrote the manuscript. All authors contributed to the article and approved the submitted version.

FUNDING

This work was partly supported by Grants-in-Aid for Scientific Research (19K06883 and 21H05621 to SM, 17H06313 to KK) from the Japan Society for the Promotion of Science (JSPS), Grant-in-Aid for Brain Mapping by Integrated Neurotechnologies for Disease Studies (Brain/MINDS) (JP19dm0207079h0002 to SM, JP19dm0207080 to KK), Narishige Neuroscience Research Foundation (to SM), Grant for Young Researcher from Yamanashi Prefecture (to SM), and Takeda Science Foundation (to SM).

ACKNOWLEDGMENTS

We thank the Center for Creative Technology, University of Yamanashi for making the agar mold and the mouse head fixation device and N. Yaguchi and K. Okazaki for animal care and technical assistance, and the members of the Kitamura lab for helpful discussions.

SUPPLEMENTARY MATERIAL

The Supplementary Material for this article can be found online at: https://www.frontiersin.org/articles/10.3389/fncir.2022.842748/full#supplementary-material

The four files are figure, and video recordings of the mouse's behavior in success (movie_1.mp4), failure (movie_2.mp4) trials, and M1 inhibition with the optogenetic method (movie_3.mp4), respectively.

The following materials created in this study will be deposited and shared in a public repository GitHub (https://github.com/Satoshi-Manita/RGR_test).

- Design files for linear actuators, agar mold, head-fixing apparatus, and head plate.
- Codes for Arduino and LabVIEW files for camera and data acquisition.

REFERENCES

Alstermark, B., and Isa, T. (2012). Circuits for skilled reaching and grasping. *Annu. Rev. Neurosci.* 35, 559–578. doi: 10.1146/annurev-neuro-062111-150527

Azim, E., Jiang, J., Alstermark, B., and Jessell, T. M. (2014). Skilled reaching relies on a V2a propriospinal internal copy circuit. *Nature* 508, 357–363. doi: 10.1038/nature13021

Bjerre, A. S., and Palmer, L. M. (2020). Probing cortical activity during head-fixed behavior. *Front. Mol. Neurosci.* 13:30. doi: 10.3389/fnmol.2020.00030

Burgess, C. P., Lak, A., Steinmetz, N. A., Zatka-Haas, P., Bai Reddy, C., Jacobs, E. A. K., et al. (2017). High-yield methods for accurate two-alternative visual psychophysics in head-fixed mice. *Cell Rep.* 20, 2513–2524. doi: 10.1016/j.celrep.2017.08.047

Castiello, U. (2005). The neuroscience of grasping. *Nat. Rev. Neurosci.* 6, 726–736. doi: 10.1038/nrn1744

Churchland, M. M., Cunningham, J. P., Kaufman, M. T., Foster, J. D., Nuyujukian, P., Ryu, S. I., et al. (2012). Neural population dynamics during reaching. *Nature* 487, 51–56. doi: 10.1038/nature11129

Galinanes, G. L., Bonardi, C., and Huber, D. (2018). Directional reaching for water as a cortex-dependent behavioral framework for mice. *Cell Rep.* 22, 2767–2783. doi: 10.1016/j.celrep.2018.02.042

Goltstein, P. M., Reinert, S., Glas, A., Bonhoeffer, T., and Hubener, M. (2018). Food and water restriction lead to differential learning behaviors in a head-fixed two-choice visual discrimination task for mice. *PLoS One* 13:e0204066. doi: 10.1371/journal.pone.0204066

Guo, J. Z., Graves, A. R., Guo, W. W., Zheng, J., Lee, A., Rodriguez-Gonzalez, J., et al. (2015). Cortex commands the performance of skilled movement. *eLife* 4:e10774. doi: 10.7554/eLife.10774

Guo, J. Z., Sauerbrei, B. A., Cohen, J. D., Mischiati, M., Graves, A. R., Pisanello, F., et al. (2021). Disrupting cortico-cerebellar communication impairs dexterity. *eLife* 10:e065906. doi: 10.7554/eLife.65906

Guo, Z. V., Hires, S. A., Li, N., O'Connor, D. H., Komiyama, T., Ophir, E., et al. (2014). Procedures for behavioral experiments in head-fixed mice. *PLoS One* 9:e88678. doi: 10.1371/journal.pone.0088678

Heiderstadt, K. M., McLaughlin, R. M., Wright, D. C., Walker, S. E., and Gomez-Sanchez, C. E. (2000). The effect of chronic food and water restriction on open-field behaviour and serum corticosterone levels in rats. *Lab. Anim.* 34, 20–28. doi: 10.1258/002367700780578028

Helmchen, F., Gilad, A., and Chen, J. L. (2018). Neocortical dynamics during whisker-based sensory discrimination in head-restrained mice. *Neuroscience* 368, 57–69. doi: 10.1016/j.neuroscience.2017.09.003

Lemke, S. M., Ramanathan, D. S., Guo, L., Won, S. J., and Ganguly, K. (2019). Emergent modular neural control drives coordinated motor actions. *Nat. Neurosci.* 22, 1122–1131. doi: 10.1038/s41593-019-0407-2

Lemon, R. N. (2008). Descending pathways in motor control. *Annu. Rev. Neurosci.* 31, 195–218. doi: 10.1146/annurev.neuro.31.060407.125547

Levy, S., Lavzin, M., Benisty, H., Ghanayim, A., Dubin, U., Achvat, S., et al. (2020). Cell-type-specific outcome representation in the primary motor cortex. *Neuron* 107, 954.e9–971.e9. doi: 10.1016/j.neuron.2020.06.006

Li, N., Daie, K., Svoboda, K., and Druckmann, S. (2016). Robust neuronal dynamics in premotor cortex during motor planning. *Nature* 532, 459–464. doi: 10.1038/nature17643

Manns, M., Basbasse, Y. E., Freund, N., and Ocklenburg, S. (2021). Paw preferences in mice and rats: meta-analysis. *Neurosci. Biobehav. Rev.* 127, 593–606. doi: 10.1016/j.neubiorev.2021.05.011

Mathis, A., Mamidanna, P., Cury, K. M., Abe, T., Murthy, V. N., Mathis, M. W., et al. (2018). DeepLabCut: markerless pose estimation of user-defined body parts with deep learning. *Nat. Neurosci.* 21, 1281–1289. doi: 10.1038/s41593-018-0209-y

Metz, G. A., and Whishaw, I. Q. (2000). Skilled reaching an action pattern: stability in rat (Rattus norvegicus) grasping movements as a function of changing food pellet size. *Behav. Brain Res.* 116, 111–122. doi: 10.1016/s0166-4328(00)00245-x

Nicola, F. D. C., Hua, I., and Levine, A. J. (2021). Intersectional genetic tools to study skilled reaching in mice. *Exp. Neurol.* 347:113879. doi: 10.1016/j.expneurol.2021.113879

Sauerbrei, B. A., Guo, J. Z., Cohen, J. D., Mischiati, M., Guo, W., Kabra, M., et al. (2020). Cortical pattern generation during dexterous movement is input-driven. *Nature* 577, 386–391. doi: 10.1038/s41586-019-1869-9

Schwarz, C., Hentschke, H., Butovas, S., Haiss, F., Stuttgen, M. C., Gerdjikov, T. V., et al. (2010). The head-fixed behaving rat–procedures and pitfalls. *Somatosens. Mot. Res.* 27, 131–148. doi: 10.3109/08990220.2010.513111

Shenoy, K. V., Sahani, M., and Churchland, M. M. (2013). Cortical control of arm movements: a dynamical systems perspective. *Annu. Rev. Neurosci.* 36, 337–359. doi: 10.1146/annurev-neuro-062111-150509

Svoboda, K., and Li, N. (2018). Neural mechanisms of movement planning: motor cortex and beyond. *Curr. Opin. Neurobiol.* 49, 33–41. doi: 10.1016/j.conb.2017.10.023

Thanawalla, A. R., Chen, A. I., and Azim, E. (2020). The cerebellar nuclei and dexterous limb movements. *Neuroscience* 450, 168–183. doi: 10.1016/j.neuroscience.2020.06.046

Toth, L. A., and Gardiner, T. W. (2000). Food and water restriction protocols: physiological and behavioral considerations. *Contemp. Top. Lab. Anim. Sci.* 39, 9–17.

Tsai, L. S., and Maurer, S. (1930). "Right-handedness" in white rats. *Science* 72, 436–438. doi: 10.1126/science.72.1869.436

Tucci, V., Hardy, A., and Nolan, P. M. (2006). A comparison of physiological and behavioural parameters in C57BL/6J mice undergoing food or water restriction regimes. *Behav. Brain Res.* 173, 22–29. doi: 10.1016/j.bbr.2006.05.031

Turella, L., and Lingnau, A. (2014). Neural correlates of grasping. *Front. Hum. Neurosci.* 8:686. doi: 10.3389/fnhum.2014.00686

Urai, A. E., Aguillon-Rodriguez, V., Laranjeira, I. C., Cazettes, F., International Brain, L., Mainen, Z. F., et al. (2021). Citric acid water as an alternative to water restriction for high-yield mouse behavior. *eNeuro* 8:ENEURO.0230-20.2020. doi: 10.1523/ENEURO.0230-20.2020

Wagner, M. J., Savall, J., Kim, T. H., Schnitzer, M. J., and Luo, L. (2020). Skilled reaching tasks for head-fixed mice using a robotic manipulandum. *Nat. Protoc.* 15, 1237–1254. doi: 10.1038/s41596-019-0286-8

Wang, X., Liu, Y., Li, X., Zhang, Z., Yang, H., Zhang, Y., et al. (2017). Deconstruction of corticospinal circuits for goal-directed motor skills. *Cell* 171, 440.e14–455.e14. doi: 10.1016/j.cell.2017.08.014

Whishaw, I. Q. (2003). Did a change in sensory control of skilled movements stimulate the evolution of the primate frontal cortex? *Behav. Brain Res.* 146, 31–41. doi: 10.1016/j.bbr.2003.09.027

Yoshida, Y., and Isa, T. (2018). Neural and genetic basis of dexterous hand movements. *Curr. Opin. Neurobiol.* 52, 25–32. doi: 10.1016/j.conb.2018.04.005

Zhao, S., Ting, J. T., Atallah, H. E., Qiu, L., Tan, J., Gloss, B., et al. (2011). Cell type-specific channelrhodopsin-2 transgenic mice for optogenetic dissection of neural circuitry function. *Nat. Methods* 8, 745–752. doi: 10.1038/nmeth.1668

Conflict of Interest: The authors declare that the research was conducted in the absence of any commercial or financial relationships that could be construed as a potential conflict of interest.

Publisher's Note: All claims expressed in this article are solely those of the authors and do not necessarily represent those of their affiliated organizations, or those of the publisher, the editors and the reviewers. Any product that may be evaluated in this article, or claim that may be made by its manufacturer, is not guaranteed or endorsed by the publisher.

frontiers | Frontiers in Neural Circuits

ORIGINAL RESEARCH
published: 22 July 2022
doi: 10.3389/fncir.2022.933201

Anatomical and Functional Connectivity at the Dendrodendritic Reciprocal Mitral Cell–Granule Cell Synapse: Impact on Recurrent and Lateral Inhibition

*S. Sara Aghvami[1], Yoshiyuki Kubota[2] and Veronica Egger[3]**

[1] School of Cognitive Sciences, Institute for Research in Fundamental Sciences (IPM), Tehran, Iran, [2] Division of Cerebral Circuitry, National Institute for Physiological Sciences (NIPS), Okazaki, Japan, [3] Neurophysiology, Institute of Zoology, Regensburg University, Regensburg, Germany

In the vertebrate olfactory bulb, reciprocal dendrodendritic interactions between its principal neurons, the mitral and tufted cells, and inhibitory interneurons in the external plexiform layer mediate both recurrent and lateral inhibition, with the most numerous of these interneurons being granule cells. Here, we used recently established anatomical parameters and functional data on unitary synaptic transmission to simulate the strength of recurrent inhibition of mitral cells specifically from the reciprocal spines of rat olfactory bulb granule cells in a quantitative manner. Our functional data allowed us to derive a unitary synaptic conductance on the order of 0.2 nS. The simulations predicted that somatic voltage deflections by even proximal individual granule cell inputs are below the detection threshold and that attenuation with distance is roughly linear, with a passive length constant of 650 μm. However, since recurrent inhibition in the wake of a mitral cell action potential will originate from hundreds of reciprocal spines, the summated recurrent IPSP will be much larger, even though there will be substantial mutual shunting across the many inputs. Next, we updated and refined a preexisting model of connectivity within the entire rat olfactory bulb, first between pairs of mitral and granule cells, to estimate the likelihood and impact of recurrent inhibition depending on the distance between cells. Moreover, to characterize the substrate of lateral inhibition, we estimated the connectivity *via* granule cells between any two mitral cells or all the mitral cells that belong to a functional glomerular ensemble (i.e., which receive their input from the same glomerulus), again as a function of the distance between mitral cells and/or entire glomerular mitral cell ensembles. Our results predict the extent of the three regimes of anatomical connectivity between glomerular ensembles: high connectivity within a glomerular ensemble and across the first four rings of adjacent glomeruli, substantial connectivity to up to eleven glomeruli away, and negligible connectivity

OPEN ACCESS

Edited by:
Gordon M. Shepherd, Yale University, United States

Reviewed by:
Charles A. Greer, Yale University, United States
Shawn D. Burton, Lehigh University, United States

***Correspondence:**
Veronica Egger
Veronica.Egger@ur.de

Received: *30 April 2022*
Accepted: *27 May 2022*
Published: *22 July 2022*

Citation:
Aghvami SS, Kubota Y and Egger V (2022) Anatomical and Functional Connectivity at the Dendrodendritic Reciprocal Mitral Cell–Granule Cell Synapse: Impact on Recurrent and Lateral Inhibition. Front. Neural Circuits 16:933201. doi: 10.3389/fncir.2022.933201

beyond. Finally, in a first attempt to estimate the functional strength of granule-cell mediated lateral inhibition, we combined this anatomical estimate with our above simulation results on attenuation with distance, resulting in slightly narrowed regimes of a functional impact compared to the anatomical connectivity.

Keywords: olfactory bulb, recurrent inhibition, lateral inhibition, network model, mitral cell, granule cell, reciprocal synapse, glomerular column

INTRODUCTION

The massive presence of inhibitory interneurons at the early processing level is a hallmark of olfactory systems (Shepherd and Greer, 2004). Inhibitory synaptic circuits are thus likely to constitute the core of the central processing unit in early olfactory coding. Since most olfactory receptors detect structural features of odor molecules rather than entire odorants, olfactory coding is synthetic and combinatorial. At the input level of the rodent olfactory bulb, each activated receptor type in turn usually targets two glomeruli and thereby activates their associated sets of principal neurons and interneurons downstream that we will denote as glomerular columns hereafter (**Figure 1A**). Another specific feature of bulbar circuitry is the large lateral dendritic field span of its principal neurons of up to 2 mm, allowing them to interact with several hundred glomerular columns across the bulb. These long-range dendrodendritic interactions are enabled by quasi-axonal action potential (AP) propagation along the lateral dendrites from which excitation is passed on to inhibitory interneurons, which in turn contact the principal neurons both within and across columns. By now, several subtypes of anaxonic inhibitory interneurons are known to form dendrodendritic reciprocal synapses with the smooth lateral dendrites of the principal mitral cells (MC) and tufted cells (TC): (1) granule cells (GC), with their somata in the GC layer and their apical dendrite extending into the external plexiform layer (EPL) and bearing the reciprocal synapses within large, electrically isolated spines (Price and Powell, 1970b; Woolf et al., 1991; Bywalez et al., 2015) and (2) other types of neurons whose somata are located in the EPL and who feature smooth dendrites. These EPL interneurons consist of various, partially overlapping subpopulations such as parvalbumin neurons, corticotropin-releasing hormone neurons, and somatostatin neurons (e.g., Toida et al., 1994; Hamilton et al., 2005; Kosaka and Kosaka, 2008; Lepousez et al., 2010; Huang et al., 2013); the parvalbumin subtype is by now known to exert substantial inhibition of MCs (Kato et al., 2013; Miyamichi et al., 2013; Liu et al., 2019).

Here, we focused on the role of GCs (1) because GCs are the most abundant neuronal type of the olfactory bulb (in rat $> 2{\cdot}10^6$, Richard et al., 2010, versus EPL interneurons $<1{\cdot}10^5$, e.g., Parrish-Aungst et al., 2007, in mouse) and also provide the majority of inhibitory inputs onto MCs and TCs compared to parvalbumin interneurons (approximately 90%, Matsuno et al., 2017), (2) because their contribution to inhibition is not well understood (e.g., Fukunaga et al., 2014; Burton, 2017), and (3) because of our long-standing interest in the function of the reciprocal GC spine that has by now allowed us to characterize the operation of the spine microcircuit with regard to its output to MCs. For example, recurrent inhibition by GCs can already be exerted at the single-spine level, since a local glutamatergic MC input can activate the reciprocal microcircuit (Lage-Rupprecht et al., 2020), whereas it is as of yet unknown whether EPL interneuron dendrites can release GABA in response to a single MC AP without further excitation from other inputs.

For similar reasons, we restricted our study to MCs, excluding TC types. There is increasing evidence for a substantial degree of functional and molecular diversity across TCs (e.g., Imamura et al., 2020; Zeppilli et al., 2021); at this point, these subtypes are less well characterized than MCs, especially with regard to their synaptic interactions with GCs (but see Section "Discussion"). Conversely, MC lateral dendrites have been studied both experimentally and in simulations (e.g., Lowe, 2002; Xiong and Chen, 2002; Debarbieux et al., 2003; McTavish et al., 2012; Li and Cleland, 2013; McIntyre and Cleland, 2016). Here, we supplemented these studies with functional data on unitary GC input to MC lateral dendrites (from Lage-Rupprecht et al., 2020) and anatomical data on synaptic density (see Section "Anatomical Basis of Mitral Cell–Granule Cell Dendrodendritic Connectivity") in order to estimate GC-mediated recurrent inhibition.

A key question in olfactory processing is whether the concept of lateral inhibition as we know it from visual processing can be generalized to the olfactory system. While earlier experimental and modeling results have argued in favor of isotropic contrast enhancement as performed by retinal circuits (e.g., Yokoi et al., 1995; Davison et al., 2003), the discontinuous nature of the olfactory representation itself, where chemotopy may exist only in a limited way (e.g., Soucy et al., 2009), along with observations of sparse and patchy lateral inhibition (e.g., Fantana et al., 2008; Kim et al., 2012; Economo et al., 2016; Lehmann et al., 2016; Shmuel et al., 2019), is sounding a note of caution. However, the used methods are quite diverse in their approaches and both glomerular layer and EPL circuits may well contribute to both isotropic (i.e., radially symmetric) and anisotropic (i.e., patchy) lateral inhibition across glomerular columns. Based on others' and own functional observations (Arevian et al., 2008; Fukunaga et al., 2014; Bywalez et al., 2015; Burton, 2017; Lage-Rupprecht et al., 2020; Mueller and Egger, 2020), we devised a hypothesis on the role of GCs in olfactory processing, which states that GCs serve to provide lateral inhibition exclusively between coactivated glomerular columns *via* an activity-dependent mechanism located within the reciprocal spines (Lage-Rupprecht et al., 2020; Egger and Kuner, 2021). This hypothesis could reconcile the abovementioned divergent findings on the spatial structure of

lateral inhibition. It predicts that the anatomical connectivity between MCs and GCs across glomerular columns should be isotropic in order to allow for maximal flexibility with regard to the functional interaction between coactivated glomerular columns, whereas functional lateral connectivity *via* GCs will be patchy. The prediction of isotropic anatomical connectivity is also one of our key assumptions here. Thus, after first investigating recurrent inhibition, we asked what amount of lateral inhibition could be exerted between any two MCs or the MC ensembles associated with glomerular columns *via* far-reaching dendrodendritic interactions with GCs, based on the anatomical connectivity.

This part of the study builds on an earlier, less elaborate model of anatomical connectivity (Egger and Urban, 2006). Although back then most of the relevant parameters could already be gathered from existing anatomical studies, there were also several less well-defined essential parameters (see below). These gaps have been mostly closed, and thus an update appears timely. Moreover, in the present study, we refined the earlier model by accounting for MC branching and by also covering glomerular columnar ensembles of MCs rather than only single MCs. In addition, as mentioned above, we have now obtained detailed physiological data on synaptic transmission at the reciprocal synapse from GCs to MCs, allowing us to go one step further to estimate the functional impact of both GC-mediated recurrent and lateral inhibition, which so far has been studied in computational network models based on more generic assumptions about synaptic properties (e.g., Davison et al., 2003; Migliore and Shepherd, 2008; McIntyre and Cleland, 2016; Kersen et al., 2022; see Section "Discussion").

Most important with regard to the level of precision and detail in the description of the anatomical network that governs both recurrent and lateral inhibition are the following recent results:

(1) A crucial anatomical parameter, the linear density of reciprocal synapses along MC lateral dendrites n_LD_{MC}, was established only recently in a quantitative manner in various studies in mice (Bartel et al., 2015; Sailor et al., 2016; Matsuno et al., 2017), beyond an early seminal study that focused mostly on the ultrastructure and the arrangement of GC spines (Woolf et al., 1991). Because of the importance of this parameter, we also experimentally verified its order of magnitude for juvenile rats (see Section "Anatomical Basis of Mitral Cell–Granule Cell Dendrodendritic Connectivity"), since our functional data were mostly obtained in juvenile rats.

(2) Measurements of the number of MCs per glomerulus N_{MC_GL} were significantly improved; recent studies were based on electroporation of single glomeruli in mice converge on $N_{MC\_GL} \approx 10$ (Sosulski et al., 2011; Ke et al., 2013; Liu et al., 2016; Schwarz et al., 2018), while earlier studies estimated larger numbers based on large-scale cell counting (e.g., Allison, 1953; Meisami and Safari, 1981; but see Royet et al., 1989). This parameter is of particular importance for estimating the connectivity between glomerular ensembles of MCs.

MATERIALS AND METHODS

Compilation of Anatomical Parameters

All anatomical parameters in **Table 1** are based on the available literature and own data. Whenever possible, data from rat olfactory bulbs were used.

Comments on Some Parameters

(1, 2) The average number N_LD_{MC} and the total length of MC lateral dendrites L_LD_{MC} were obtained by averaging the data of Orona et al. (1984) on dendritic lengths for type I and type II individual MCs. Since the relative fractions of MC type I and II cells are not known, we used the arithmetic mean. The delineation between type II MCs and deep or internal TCs seems not entirely clear at this point.

(3) The total effective length of MC dendrites L_LD_{MC}eff here refers to the projection of MC dendrites into the plane of the EPL; MC dendrites (but not those of TCs) also extend into the vertical direction such that their length extends the horizontal field span of 850 μm by 300 μm (Mori et al., 1983; see Assumption 3 for more details).

(5, 6) The average positions of MC lateral dendrite branch points $b_{1,2,3}$ were estimated based on the large data set by Mori et al. (1983; **Figure 4**) from rabbits and chosen such that L_LD_{MC}eff is met for a total number of 5 lateral dendrites and 15 branch points (Orona et al., 1984); there is no similarly detailed study of rat MC branching patterns yet.

(7) Following an early EM study that reconstructed short segments of MC dendrites and the associated GC spines (Woolf et al., 1991), several recent studies analyzed the linear density of inhibitory synapses onto MC lateral dendrites in mice in a quantitative manner (Bartel et al., 2015; Sailor et al., 2016; Matsuno et al., 2017). From the large data set in Sailor et al. (2016), one can gather an inhibitory synapse density of $0.64 \pm 0.37\ \mu m^{-1}$ ($n = 56$ segments with mean length 78 ± 20 μm, average number of puncta per segment 50 ± 29). Bartel et al. (2015) found a mean linear density of $1.1\ \mu m^{-1}$. Similar values can be derived from Matsuno et al. (2017) for proximal segments (their Figure 9, 0.2 contacts/dendrite area corresponds to roughly $1.2\ \mu m^{-1}$ for a proximal radius of 1 μm). Interestingly, these authors costained for parvalbumin and found that the total fraction of parvalbumin+ puncta was below 10%. Similarly, Bartel et al. (2015) argued that, because of the large population of GCs compared to other neuron types, most detected contacts are likely to be formed by GCs. Our own measurements in rat MCs complement these data (see Sections "Measurement of Inhibitory Synapse Density on Rat Mitral Cell Lateral Dendrites n_LD_{MC}" and "Anatomical Basis of Mitral Cell–Granule Cell Dendrodendritic Connectivity"). It is under debate whether inhibitory contacts are clustered or rather homogenously distributed; in any case, sections devoid of any GC synapses are probably shorter than 10 μm (Bartel et al., 2015, their Figure 5). Lacking more precise data, we decided to assume a uniform

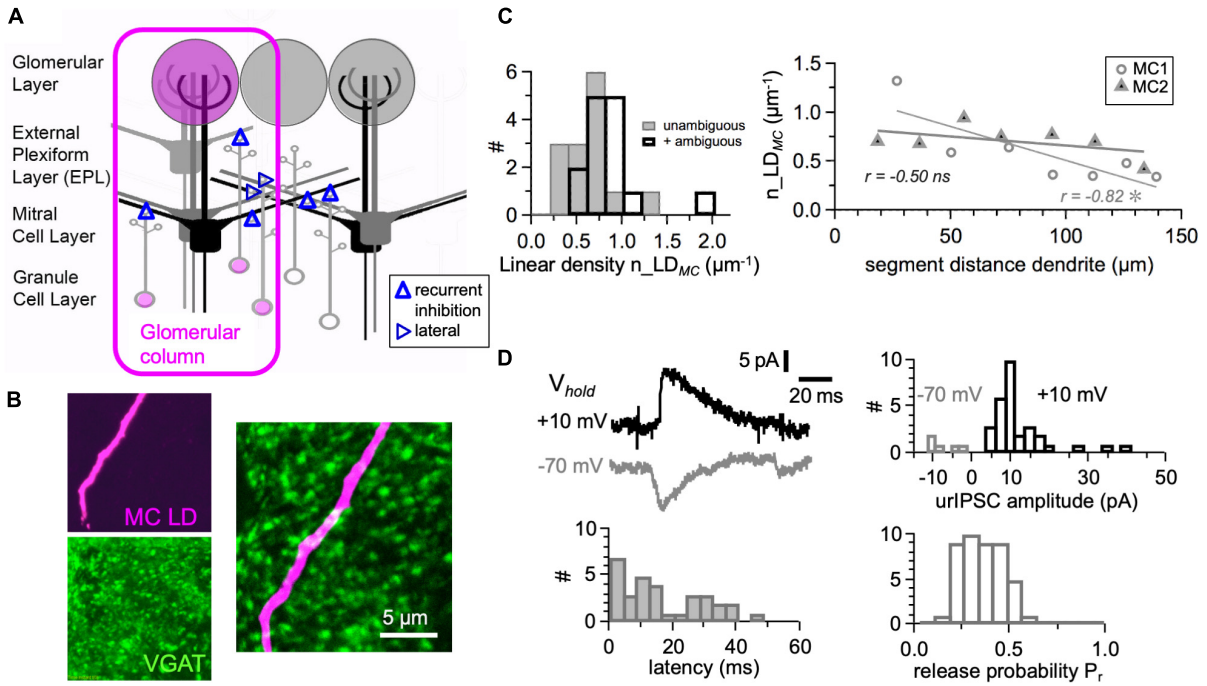

FIGURE 1 | Dendrodendritic interactions between mitral cells and granule cells. **(A)** Scheme of mitral cell–granule cell network. Glomerular column: Ensemble of mitral cells and granule cells that can be excited from a glomerulus. Recurrent inhibition will occur widely, lateral inhibition can happen only *via* the granule cells that are sufficiently excited within the columnar ensemble to generate a global or local spike (if at all, see Section "Discussion"). **(B)** Example double stain of juvenile rat mitral cell lateral dendrite segment and GABAergic presynapses (see Section "Materials and Methods"). Top left: Biocytin label. Bottom left: VGAT-stain. Both z-projections of 5 µm-deep image stack (sectioning at 0.2 µm). Right: Overlay of z-projections within a 1 µm selection of the stack. **(C)** Cumulative histochemical data: Left: Synaptic input density distribution for certain synapses and upper limit ($n = 14$ segments). Right: Density versus distance on the segment. Linear fit (significance of correlation 1-tailed for MC1 $P = 0.012$, MC2 $P = 0.127$, $n = 7$ data points each). **(D)** Unitary-like mitral cell IPSCs are evoked by uncaging of glutamate onto granule cell spines (data from Lage-Rupprecht et al., 2020). Top left: Averaged example traces from two mitral cells at two different holding potentials (−70 mV, +10 mV) and equilibrium potentials E_{Cl} (+16 mV, −130 mV). Top right, bottom: Distribution of amplitudes, response latencies, and release probabilities (modified from Figure 1 in Lage-Rupprecht et al., 2020).

density along the dendrites as the first approximation (see Assumption 2).

(8) We accounted for the reduced effective length of MC dendrites [see comment on (3) above and Assumption 3] by increasing our result for the density n_LD_{MC} to an effective density $n\_LD_{MC}eff = 1\ \mu m^{-1}$.

(9) Because of the restriction of our approach to the GC-MC subnetwork, we reduced the literature value for the total number of GCs by the number of cells that might be part of TC subnetworks (see Assumption 1 for more details).

(10) While the number of reciprocal spines per GC N_{recGC} is not relevant for our connectivity estimate (see below, Eq. 6), it is useful to validate the above parameter choices (see Assumption 1).

(11) The lateral extent of the GC dendritic field was measured from the reconstructed GCs shown in Orona et al. (1983) ($n = 40$ cells) and from a set of GCs filled with a fluorescent dye and imaged with two-photon microscopy (Egger et al., 2003, 2005; $n = 29$ cells). The two groups had a virtually identical mean horizontal dendritic field radius of $R_{GC} = 50 \pm 40\ \mu m$ (S.D.).

Measurement of Inhibitory Synapse Density on Rat Mitral Cell Lateral Dendrites n_LD_{MC}

Inhibitory synapse density on rat MC lateral dendrites was measured based on colocalization of a cytoplasmic dendritic stain and VGAT-puncta (Panzanelli et al., 2007) in a set of $n = 14$ dendritic segments from 2 MC proximal lateral dendrites. MCs from acute brain slices (300 µm thickness) of juvenile rats (P14; see Chatterjee et al., 2016 for ethics statement and brain slice preparation, since the slices used here were prepared for that study) were filled with Biocytin (0.5 mg/500 µl internal solution) for 10 min *via* the recording pipette during whole-cell recordings (pipette resistance < 5 MΩ). Slices were fixed (4% paraformaldehyde, 0.2% picric acid, and 0.1% glutaraldehyde in 0.1 M PB) and kept at least overnight. Slices were embedded in agar and resectioned (50 µm thickness). After washing, slices were incubated in 1% sodium borohydrate in PBS for 30 min, washed, and then incubated in primary antiserum overnight (anti-VGAT, developed in rabbit, dilution 1:5000, # A-2052, SIGMA, Taufkirchen, Germany). After washing, slices were incubated in secondary antiserum

TABLE 1 | Anatomical parameters (see Section "Compilation of Anatomical Parameters" for further explanation).

#	Parameter	Symbol	Values used in the model	Comments	Source (Species)	Robustness to ±10% change
(1)	Number of MC lateral dendrites	N_LD_{MC}	5	Average of type I and II MC	Orona et al., 1984 (rat)	
(2)	Total Length of MC lat. dend. per MC	L_LD_{MC}	12500 μm	Average of type I and II MC	Orona et al., 1984 (rat)	
(3)	Effective total Length of MC lat. dendrites	L_LD_{MC}eff	10000 μm	Required for model	Mori et al., 1983 (rabbit)	High (±20%) affects only scaling
(4)	Radius of MC dendritic field	R_{MC}	850 μm	500–1300 μm	Orona et al., 1984 (rat), Mori et al., 1983 (rabbit)	High (∼ ±20%), affects mainly scaling
(5)	Number of branchpoints	N_{BP}	15	Type I MC	Orona et al., 1984 (rat)	
(6)	Position of branchpoints on MC dendrite (relative to field)	b_1, b_2, b_3	150 μm, 550 μm, 750 μm	see **Figure 2A**	Mori et al., 1983 (rabbit); with N_LD_{MC} and N_{BP} matched to obtain L_LD_{MC}eff	Low (0/-3%; 1/-4%, 2/-5%)
(7)	Average density of synapses on MC lateral dendrite	n_LD_{MC}	Not used, instead 8	0.64–1.1 μm^{-1}	Woolf et al., 1991 (mouse, age 5 weeks), Bartel et al., 2015 (mouse, 2 weeks, 10 weeks), Matsuno et al., 2017 (mouse, 8–10 weeks), Sailor et al., 2016 (mouse, several weeks), own data (rat 2 weeks, see Section "Results")	High (±20%) affects only scaling
(8)	Effective density on MC lateral dendrite	n_LD_{MC}eff	1 μm^{-1}		Based on ratio dendritic length/field radius (Orona et al., 1984, rat)	
(9)	Total number of GCs that interact with MCs	N_{GC}	$1.5{\cdot}10^6$	$2.2{\cdot}10^6$ at 2 weeks, $5{\cdot}10^6$ in adults	Richard et al., 2010 (rat)	Medium (−11%, +8%) affects only scaling
(10)	Number of reciprocal spines per GC	N_{recGC}	200		Price and Powell, 1970b (rat), Shepherd and Greer, 2004 (rat), Geramita et al., 2016 (mouse)	Does not enter estimate, is used for cross-validation of n_LD_{MC}eff
(11)	Radius of GC dendritic field	R_{GC}	50 μm		Orona et al., 1983 (rat), own data	Low (±2%)
(12)	Size of 2D sheet (mid-EPL xy-area)	A_{EPL}	$20{\cdot}10^6$ μm^2	$15–25{\cdot}10^6$ μm^2	Royet et al., 1989 (rat), Struble et al., 2001 (rat)	Medium (±10%) affects only scaling
(13)	Number of MCs per glomerulus	N_{MC_GL}	10	Type I and II MC	Liu et al., 2016: M72 mouse: 10 MCs 7 TCs; Royet et al., 1989 (rat): 13 MCs; Schwarz et al., 2018: mouse M174-9 only 6 MC, 6 d/mTC, 19 sTCs	High (+21/-19%) affects only scaling

*Robustness of connectivity estimate (**Figure 5C** top): change of parameter value to 110% or 90% of setting.*

overnight (Alexa 488-anti rabbit IgG, dilution 1:200, #A-11008, Invitrogen, Waltham, MA, United States) and finally incubated with Alexa 594-streptavidin (1:2000, Invitrogen) for 90 min. Dual-channel Z-stacks (sectioning 0.2 μm) were taken on a confocal microscope (Olympus Fluoview 300, Hamburg, Germany) and analyzed manually by Fluoview software within the first top 5 μm of the slices. Contacts were counted as unambiguous if there was a clear overlap between puncta and dendrite in at least two of the three projection planes (xy, xz, and yz) and as ambiguous if there was an overlap only within one of the three projections. In an earlier study from our laboratory, contacts established by light microscopical techniques were verified by subsequent electron microscopy, yielding a correct hit rate of approximately 80% (Karube et al., 2004).

Simulations

We used a compartmental cable model of an MC to simulate the inhibitory synaptic inputs onto it. The morphology of the dendritic tree was adopted from Orona et al. (1984); one primary dendrite and five similar lateral dendrites tapered non-linearly from 4 to 0.5 μm along the trunks and branches, based on the study of Mori et al. (1983). **Figure 2A** shows the lateral dendrite geometry (see also **Table 1**). The total extent of the dendrite matches the radius of the MC dendritic field $R_{MC} = 850$ μm within the xy-plane.

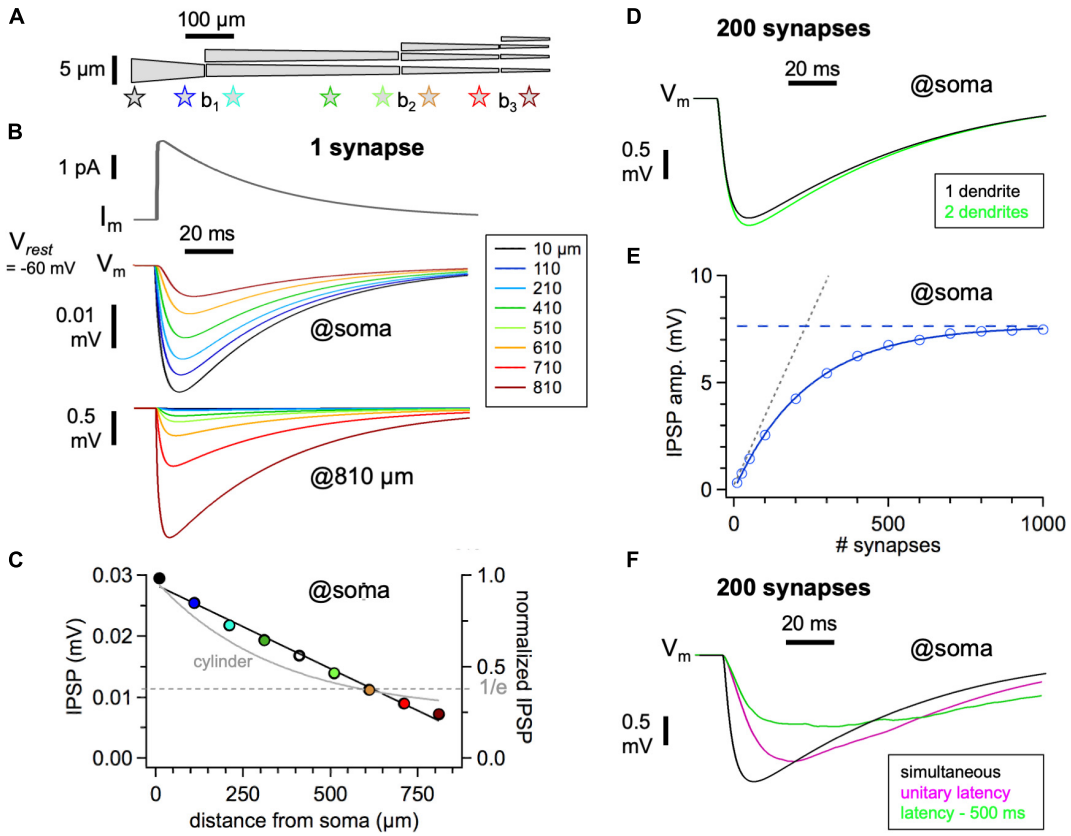

FIGURE 2 | Simulation of granule cell-mediated recurrent inhibition. **(A)** Model anatomy of one mitral cell lateral dendrite. Branchpoints at $b_1 = 150$ µm, $b_2 = 550$ µm, $b_3 = 750$ µm. Total length 850 µm, the total number of branchpoints 3. Tapering: first segment 4–2.5 µm, second segment 2.5–2 µm, third segment 2–1 µm, fourth segment 1–0.5 µm. **(B)** Top: Simulation of IPSC recorded at the soma under physiological conditions (10 µm from soma, $g_{syn} = 200$ pS, $V_m = -60$ mV, $E_{Cl} = -80$ mV). Middle: Simulation of IPSP generated at the same location and at various distances, as recorded at the soma. Bottom: IPSP at the same locations as in panel **C** but recorded at the distal site (810 µm). **(C)** Cumulative somatopetal attenuation along the dendrite, absolute (left axis) and normalized to the extrapolated amplitude at 0 µm (normalized IPSP, right axis). Gray line: Simulation in a cylindrical neurite without tapering. **(D)** Somatic recurrent inhibition exerted by 200 synapses distributed equally across 1 lateral dendrite of the mitral cell model (black trace) and with the proximal 80% of synapses shifted to another lateral dendrite (green trace). The difference between the traces indicates the reduced shunting of the distal 20% of synapses in the second case. **(E)** Recurrent summated IPSP amplitude at the soma versus a number of (equidistant) synapses on one dendrite. Dotted line: linear summation of unitary IPSP. Dashed line: saturation due to shunting and reduction in driving force. **(F)** Black trace: same simulation as in panel **(D)**. Magenta trace: same, but with onset latencies distributed according to **Figure 1D**. Green trace: the temporal extent of latency values further expanded, to 500 ms.

The model was implemented in NEURON 7.4 along with Python (Hines et al., 2009) for both a passive and an active dendritic tree. In both cases, the axial resistance is set to be 100 Ωcm and the membrane conductance is $2e^{-4}$ S/cm^2. These passive parameters were adjusted to match the measured unitary IPSCs proximal to the soma (Lage-Rupprecht et al., 2020), considering both the amplitude and time course of the IPSC (**Figure 2B**). The unitary synaptic inhibition is obtained by mimicking a single square pulse of 1 mM GABA release for 3 ms (as in our previous simulations of glutamate release, e.g., Bywalez et al., 2015) and by implementing GABA receptor kinetics according to Destexhe (1998), with a maximum conductance of 200 pS (based on our functional data, see Section "Results") and a reversal potential $E_{Cl} = -80$ mV (or $E_{Cl} = -70$ mV in a subset of simulations). We did not implement a gradient in synaptic conductance along the lateral dendrite, since the available experimental evidence is ambiguous (Lowe, 2002). The random onset latency of the inhibitory synapses used in **Figure 2F** was generated from a Gamma distribution function fitted to the experimental data presented in **Figure 1D**.

Implementation of the Anatomical Connectivity Model

All routines were implemented in IGOR (Wavemetrics, OR, United States). Integrations were performed numerically. We evaluated the robustness of the connectivity function (Eq. 9) to parameter variations of ±10%. The rightmost column of **Table 1** shows the resulting sensitivities in terms of the average percentage change in the connectivity. Connectivity model assumptions aside from the parameter choices in **Table 1** are described in the Section "Model for Recurrent Mitral Cell–Granule Cell Connectivity and Lateral Mitral Cell–Granule Cell–Mitral Cell Connectivity."

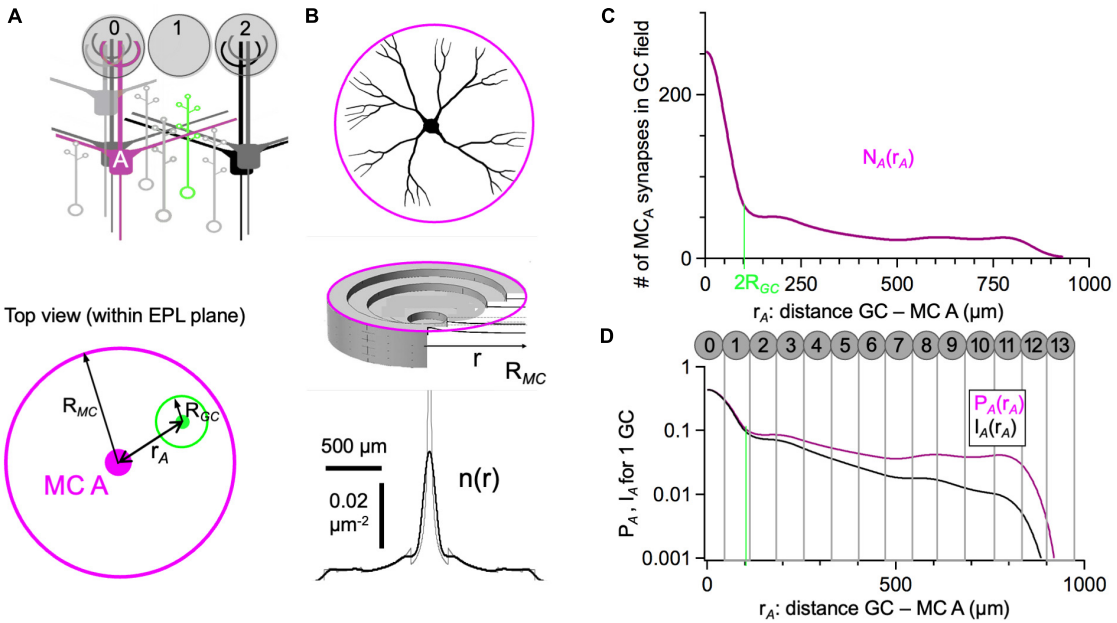

FIGURE 3 | Anatomical connectivity between individual mitral cells and granule cells. **(A)** Scheme of the MC-GC network, below the top view of the dendritic fields of MC A (magenta, field radius R_{MC}) and a GC (green, field radius R_{GC}). r_A: distance MC-GC. **(B)** Synaptic density for single mitral cell with branching secondary dendrites as described in Eq. 1. The top graph shows a schematic view of a branching neuron, and the middle graph illustrates how the synaptic density was calculated with the position of the steps corresponding to the average branchpoint position. The bottom graph shows the average radial synaptic density n(r) for a branching cell including smoothing of the branchpoint positions. The gray line corresponds to the unsmoothed density as given in Eq. 1. **(C)** Number of synapses of MC A that a given GC at position r_A can access (Eq. 3). $2R_{GC}$ indicates the distance at which there is no more overlap with the GC dendritic field with the peak of n(r). **(D)** Probability P_A that a GC at position r_A will indeed connect to MC A (Eq. 6) and effective inhibitory impact I_A (Eq. 7, from **Figure 2C**). The spacing of glomeruli is indicated (diameter of glomeruli scaled to fit all 4,000 glomeruli into A_{EPL}, see Section "Results").

RESULTS

Anatomical Basis of Mitral Cell–Granule Cell Dendrodendritic Connectivity

Apart from a seminal early EM study that was restricted to shorter segments of MC lateral dendrites (total summed length 63 µm, Woolf et al., 1991), the density of inhibitory contacts along lateral MC dendrites n_LD_{MC} was established only recently (see Section "Introduction"). Since this synapse density is a crucial parameter for the efficiency of both recurrent and lateral inhibition and all the published studies were done in mice, we performed a qualitative test in juvenile rats (inhibitory synapses labeled with Anti-VGAT and lateral dendrite with Biocytin, see Section "Materials and Methods"; **Figures 1B,C**) and obtained a lower limit of $0.65 \pm 0.26\ \mu m^{-1}$ ($n = 14$ lateral dendrite segments from $n = 2$ MCs, counting only unambiguous puncta; upper limit including ambiguous puncta: $0.83 \pm 0.33\ \mu m^{-1}$; mean segment length 19.2 ± 4.7 µm, total analyzed length 269 µm). This result is in rather a close accordance with the mouse immunohistochemistry data, especially with the study of Sailor et al. (2016). Across segments, linear density was fairly homogenous with the exception of the first segment in MC 1 (**Figure 1C**).

For the two-dimensional connectivity model described further below, we used an increased effective synaptic density $n\_LD_{MC}eff = 1\ \mu m^{-1}$ that accounts for the fact that MC dendrites are not running in a planar fashion (Mori et al., 1983; Orona et al., 1984; see also **Table 1**).

Functional Inhibitory Impact of Individual Granule Cell Spine Inputs

Our previous study of single GC spine output triggered by local two-photon uncaging of glutamate yielded a set of IPSCs from proximal inhibitory inputs (<50 µm from the soma, Lage-Rupprecht et al., 2020). Since these IPSCs are caused by the vesicular release of GABA upon local excitation of the reciprocal spine, we considered them to reflect true unitary inputs. At a holding potential $V_{hold} = +10$ mV and a chloride Nernst potential $E_{Cl} = -130$ mV, these inputs had an average amplitude of 12 ± 8 pA ($n = 32$, mean $\pm$ *SD*, example in **Figure 1D**). This amplitude was increased by a factor of two because of antagonistic interactions of the uncaging compound DNI-Glu with GABAergic currents (block of spontaneous IPSC amplitudes by 50%, Lage-Rupprecht et al., 2020), resulting in a synaptic conductance $g_{syn} = I_{syn}/(V_{hold} - E_{Cl}) = 170 \pm 120$ pS. Using this conductance to predict the IPSC amplitude under different conditions ($E_{Cl} = +16$ mV, $V_{hold} = -70$ mV, used in another subset of experiments) yields −15 pA, or −7.5 pA in DNI. This value is very close to the measured mean value of -8 ± 4 pA in these experiments (in DNI, $n = 5$, **Figure 1D**), further validating g_{syn}.

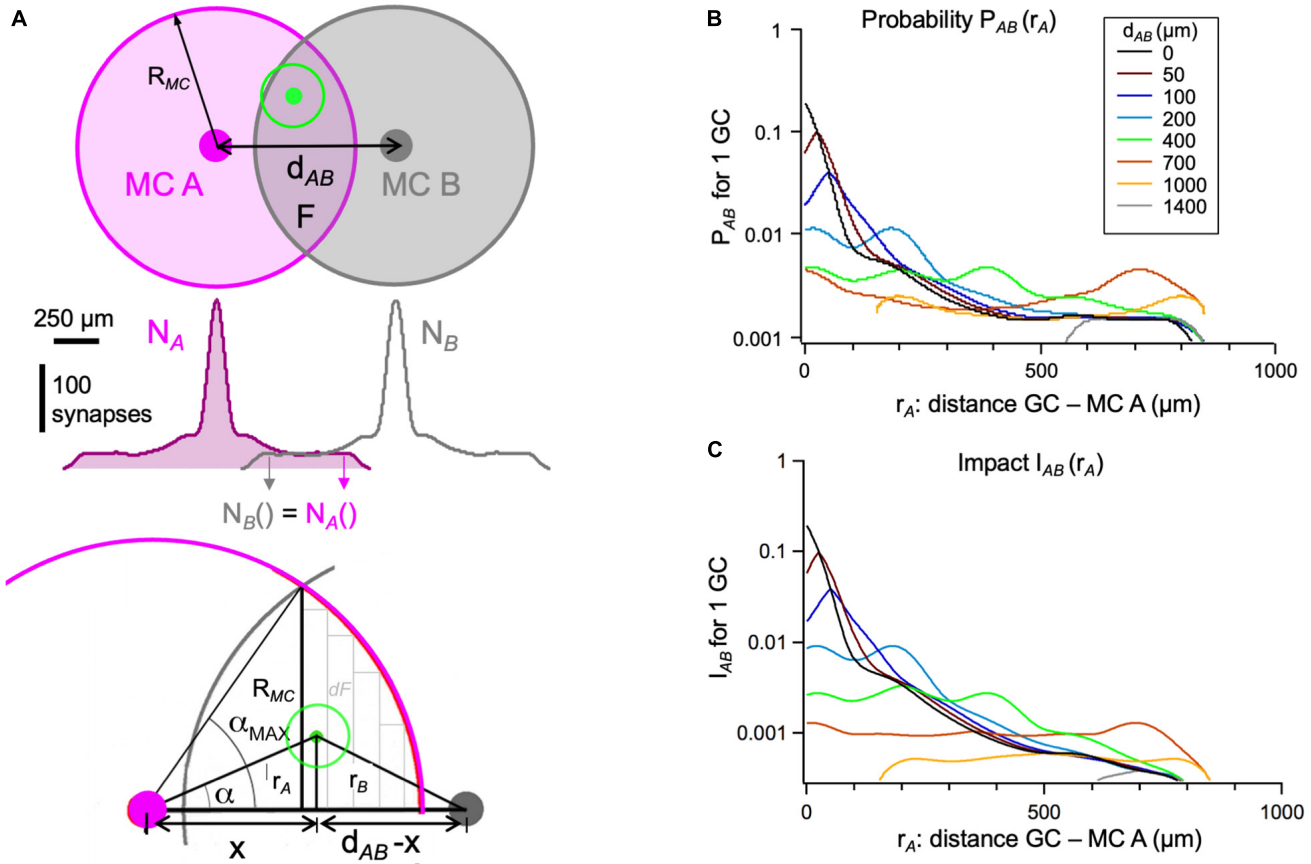

FIGURE 4 | Anatomical connectivity between pairs of mitral cells *via* one granule cell. **(A)** Top: Top view of the dendritic fields of MC A (magenta), a second MC B (gray) at distance d_{AB}, and a GC (green) within the overlap area F of the MCs' dendritic fields. Middle: Illustration of symmetry in $N_A(r)$ and $N_B(r)$. Bottom: Geometrical parameters relevant for the calculus in Eqs 9, 10 (see also **Table 2**). r_A, r_B: distance of GC from MC A resp. B. α: angle between the position of GC soma r_A and d_{AB}. α_{MAX}: maximally possible α for the respective d_{AB}. x: distance of projection of GC position onto d_{AB} from MC A; relevant for integration. The gray rectangles represent the integration increments *dF*. **(B)** Probability P_{AB} of a GC at position r_A to connect to both A and B (Eq. 6), plotted for a set of distances d_{AB} between mitral cells A and B (0–1400 µm). The righthand peak in the curves for 200–700 µm is due to the increased synaptic density around the soma of MC B. Parameters as given in **Table 1**. **(C)** I_{AB}: correction of P_{AB} for a distance-dependent reduction in IPSP impact because of attenuation (**Figure 2C**, Eq. 7).

Thus, under more physiological conditions ($V_m = -60$ mV, $E_{Cl} = -80$ mV), we obtained $I_{syn} = 3.4 \pm 2.4$ pA. For lack of more precise data, we assumed that the conductance does not depend on its distance to the soma (Lowe, 2002). We also used a less hyperpolarized $E_{Cl} = -70$ mV in a second set of simulations, following the argument by McIntyre and Cleland (2016) that this choice better reflects the physiological situation in adult animals *in vivo*, where then $I_{syn} = 1.7$ pA.

Simulation of Recurrent Inhibition

For the simulation of recurrent inhibition, we used a compartmental model (see Section "Materials and Methods"), with the dendritic morphology of an MC lateral dendrite as shown in **Figure 2A**. **Figure 2B** shows a single IPSC originating from a synapse at a distance of 10 µm from the soma, based on the unitary conductance established above. Passive parameters and kinetics of GABA release were adjusted to match our recorded IPSC kinetics and also previously established kinetics in the current clamp condition (based on spontaneous IPSPs recorded in MCs at −60 mV, rise time 12 ± 7 ms, half duration 40 ± 15 ms, $n = 27$ IPSPs in 9 MCs, data set from Egger et al. (2005); these IPSPs might originate from different sources than GCs but the passive parameters should be similar, see Section "Discussion"). Unitary IPSPs were simulated originating from synapses at the indicated distances from the soma. Our simulations (**Figure 2B**) thus predict a unitary IPSP amplitude on the order of 0.03 mV for proximal input and below 0.01 mV for inputs beyond 700 µm from the soma. Such small amplitudes are below the detection limit in conventional, non-averaged whole-cell current-clamp recordings (see Section "Discussion").

Figure 2C shows that the attenuation with distance is almost linear, a result of the implemented dendrite tapering (not of branching, not shown). The somatopetal space constant is on the order of 650 µm, close to the space constant used in a detailed earlier simulation of inhibition in MC lateral dendrites (McIntyre and Cleland, 2016, their

TABLE 2 | Additional important variables and their symbols.

Variable	Symbol
Number of reciprocal synapses per MC	N_{synMC}
Density of granule cells on EPL sheet	n_{GC}
Synaptic density of single MC (radial coordinates)	n(r)
Synaptic density of glomerular MC ensemble (radial coordinates)	n_{GL}(r)
Distance of GC from MC A, B, respectively	r_A, r_B
Distance between MCs A, B	d_{AB}
Coordinate of projection of r_A onto d_{AB}	x
Number of synapses of MC A and B within the dendritic field of GC	N_A, N_B
Probability of connection between a GC and MC A or B	P_A, P_B
Inhibitory impact of GC on MC A	I_A
Probability of connection between MC A and B *via* GC	P_{AB}
Number of interconnecting GCs between MC A/glomerulus Y and MC B/glomerulus Z	N_{AB}, N_{AZ}, N_{YZ}
Angle between the position of GC soma relative of MC A and shortest distance d_{AB} between MC somata	α
Area of overlap between dendritic fields of MC A and B	F
Inhibitory impact of MC A/glomerulus Y on MC B/glomerulus Z	I_{AB}, I_{AZ}, I_{YZ}

lambda 850 μm in a dendrite with a diameter of 2 μm). Note that our MC anatomy is scaled down by a factor of 0.75 to account for the projection into the EPL/xy-plane (see Section "Compilation of Anatomical Parameters"); thus, in a real geometry, attenuation of distal inputs will be accordingly stronger because of the longer extent of the dendrite. Importantly, the result on attenuation is used further below to estimate the recurrent and lateral inhibitory impact of GCs based on our anatomical connectivity models, including a robustness test for modified degrees of attenuation (**Figures 3D**, **4C**, **5C**). Finally, synapses situated on the distal dendrite cause a much larger simulated local voltage deflection due to the higher input resistance (**Figure 2B** bottom).

Next, we investigated the summation of multiple simultaneous IPSPs at the soma, with active synapses distributed with equal spacing along the dendrite. **Figure 2D** shows the result for 200 co-active synapses, and **Figure 2E** the amplitude of inhibition versus the number of coactive synapses, indicating a saturation at ∼1000 coactive synapses that lies at −67.5 mV, well below the maximally possible IPSP amplitude of 20 mV (at $E_{Cl} = -80$ mV). This limitation is due both to a decrease in the driving force, characteristic of purely passive dendritic integration (e.g., Tran-Van-Minh et al., 2015), and to increased shunting of distal inputs by proximal inputs, as can be illustrated by simulations with different numbers and distributions of synapses (Vida et al., 2006; David et al., 2008; **Figures 2D,E**).

In order to approximate the strength of GC-mediated inhibition to be expected in the wake of an MC AP that propagates into the lateral dendrites, we chose the fraction of activated synapses in accordance with our finding for the probability of unitary reciprocal GABA release, which factors in the probability of release of glutamate from the MC dendrite ($P_r = 0.5$, Egger et al., 2005) yielding $P_{rec} = 0.15$ (Lage-Rupprecht et al., 2020; **Figure 1D**), and distributed the onset of release according to the measured latency distribution (also **Figure 1D**), which was smoothed before random assignment of values to individual synapses. The resulting recurrent IPSP was accordingly reduced in amplitude and broadened (**Figure 2F**). Asynchronicity of GABA release is likely to be yet more expanded, since our experiments did not account for potentially delayed release from MCs, and time constants on the order of 500 ms were obtained in classical dendrodendritic inhibition experiments. Further broadening will ensue, as shown also in **Figure 2F**.

Model for Recurrent Mitral Cell–Granule Cell Connectivity and Lateral Mitral Cell–Granule Cell–Mitral Cell Connectivity

As first described in Egger and Urban (2006), we reduced the connectivity problem within the external plexiform layer (EPL) to the connectivity on a two-dimensional sheet, projecting all reciprocal synapses onto this area, i.e., the mean surface area of the EPL. The first task was to determine the recurrent connectivity between a given MC-GC pair. Next, the estimate of lateral connectivity corresponded to the number of GCs within the overlap area of the dendritic fields of two MCs A and B that are connected to both. The connectivities between two glomerular ensembles, i.e., between all the MCs that are part of a glomerular columnar ensemble or between a single MC and its own or another glomerular ensemble, can be calculated *via* the same approach. Aside from the parameter settings listed in **Table 1**, the connectivity model is based on the following five assumptions:

Assumption 1: The Density of Mitral Cell and Granule Cell Synapses Is Homogenous in the External Plexiform Layer

The density of granule cells n_{GC} can be estimated by projecting the total number of GCs onto the mean surface area of the external plexiform layer (EPL).

$$n_{GC} \approx N_{GC}/A_{EPL} \quad (1)$$

The size of this sheet is roughly given by the EPL volume (6.6 mm^3, e.g., Royet et al., 1989; Struble et al., 2001) divided by the EPL depth (300–400 μm, e.g., Orona et al., 1984): $A_{EPL} \approx 20\ mm^2$ (extent in mid-EPL).

However, not all bulbar GCs are available for MC connectivity. While there might be GCs that connect to both MCs and TCs (Arnson and Strowbridge, 2017, identity of interneuron subtype unclear), there is also the notion of anatomically segregated subnetworks (Mori et al., 1983; Orona et al., 1983), which has been reinforced by functional data indicating different connectivities and roles of TCs versus MCs in odor processing (e.g., Ezeh et al., 1993; Nagayama et al., 2004; Fukunaga et al., 2012; Geramita and Urban, 2017). Based on the total dendritic lengths (12000 μm MCs versus 5000 μm TCs, Orona et al., 1984), the rather similar linear synapse

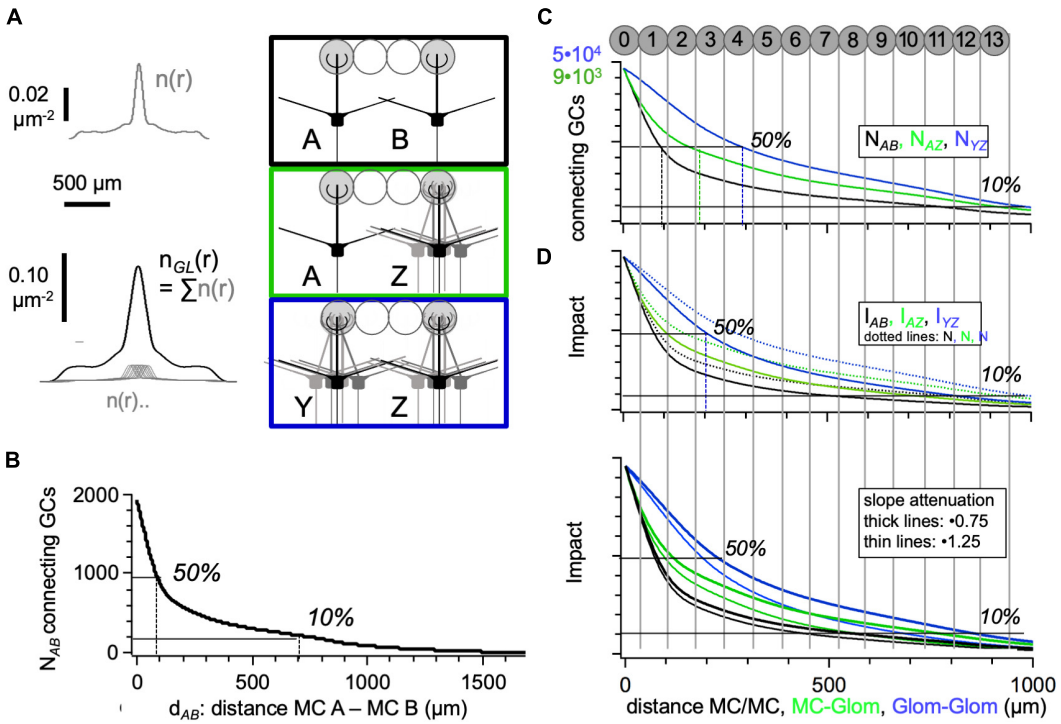

FIGURE 5 | Number of granule cells providing connectivity between two mitral cells or glomerular mitral cell ensemble. **(A)** Synaptic density distribution for single MC n(r) as in **Figure 3B** and for a glomerular ensemble of mitral cells $n_{GL}(r)$ (see Section "Materials and Methods"). **(B)** Number of GCs N_{AB} that interconnects a pair of MCs versus their distance d_{AB} (Eq. 9). The gray bars illustrate the average dimensions of glomeruli within the network ($2 \cdot r_{GL} = 120$ µm). **(C)** Number of GCs that interconnect a pair of glomerular MC ensembles (blue line) or a single MC and an ensemble (green line), compared to the MC-MC case (black line). For better comparison, all three connectivity functions are scaled to the same size at $d_{AB} = 0$, with the respective maximal numbers indicated in the respective color. **(D)** Top: Number of GCs as above but corrected for their functional impact. Dotted lines: Functions from above for comparison. Arbitrary units on the y-scale. Bottom: Impact with varying degrees of attenuation. The slope of the linear attenuation (fit in **Figure 2C**) is increased or decreased by 25%. The spacing of glomeruli is indicated (diameter of glomeruli scaled to fit all 4000 glomeruli into A_{EPL}, see Section "Results").

densities on both MCs and TCs (Sailor et al., 2016), and the somewhat lower numbers of TCs versus MCs per glomerulus (e.g., Liu et al., 2016; this is the least well-defined number), the number of synapses provided by MCs alone is roughly 70% of the total number of MC and TC synapses, and therefore the number of possibly connecting GCs is reduced from the total number N_{GC} by the same fraction to $1.5 \cdot 10^6$ GCs. Thus, for the MC-GC network modeled here, we used $n_{GC} \approx 1.5 \cdot 10^6 / 20\ mm^2 = 0.075\ \mu m^{-2}$.

The validity of these settings can be checked by comparing the total number of synapses in the projected EPL area from the GC and the MC points of view:

Granule Cell View

$N_{GC} \cdot N_{recGC} = 1.5 \cdot 10^6$ GCs·200 spines per GC yields a total number of GC spine output synapses of $300 \cdot 10^6$.

Mitral Cell View

Synapses on lateral dendrites per glomerular ensemble: $N_{MC\_GL} \cdot L\_LD_{MC}eff \cdot n\_LD_{MC}eff = 10 \cdot 10^4 \cdot 1 = 10^5$, then, the total number of MC synapses (4000 glomeruli in rat, Royet et al., 1989) is $400 \cdot 10^6$. This synapse number also contains synapses with other interneurons, the fraction of which is estimated to be at least ∼10% (Matsuno et al., 2017).

Hence, the total GC and MC synapse numbers are roughly consistent, also validating our setting of $n\_LD_{MC}eff = 1\ \mu m^{-1}$.

Assumption 2: Synapses Are Evenly Distributed Along the Lateral Dendrites of Mitral Cells

While anatomical and functional data indicate both short-range and long-range inhomogeneities in synaptic distribution (Price and Powell, 1970a; Mori, 1987; Woolf et al., 1991; Lowe, 2002; Bartel et al., 2015), these data do not allow for a more precise description: other recent measurements did not find any systematic variation (Sailor et al., 2016; see also Section "Materials and Methods") and our own qualitative data in rat did also not show high fluctuations across the analyzed segments (**Figure 1D**). A decrease in linear density n_LD_{MC} with distance from the soma might be expected because of the tapering of lateral dendrites, but according to Bartel et al. (2015), this effect is not very strong, because the surface density of contacts is actually increasing with smaller dendritic diameters (see e.g., their **Figure 5F**). Future evidence for systematic changes in linear density with distance could easily be incorporated into the density function (Eq. 2 below).

Assumption 3: The Synaptic Density Profile of Mitral Cells and of Glomerular Ensembles of Mitral Cells Is Radially Symmetric

This approach represents the average MC synaptic distribution, neglecting the position of individual lateral dendrites (see also Davison et al., 2003). The average MC dendritic fields are radially symmetric (Price and Powell, 1970a; Mori et al., 1983; Orona et al., 1984). More importantly, labeling of glomerular MC ensembles *via* electroporation has confirmed that a glomerular ensemble's lateral dendrite distribution is by and large symmetric (Sosulski et al., 2011; Ke et al., 2013; Liu et al., 2016; Schwarz et al., 2018).

Since MC lateral dendrites are not running straight in parallel with the EPL orientation (in contrast to TC lateral dendrites, Mori et al., 1983; Orona et al., 1984) but instead wiggle in the vertical dimension such that the total length of a dendrite (without branches) surpasses its actual field span of 850 by 300 μm or ∼35%, we accounted for this property by decreasing the effective lengths of lateral dendrites (with regard to the projection into the EPL plane) and at the same time increasing the synaptic density on the lateral dendrite n_LD_{MC} accordingly, such that the effective density $n\_LD_{MC}eff$ is 1 μm^{-1} instead of 0.65 μm^{-1} (see also Section "Materials and Methods," **Table 1**). We distributed the total number of synapses per MC $N_{synMC} = L\_LD_{MC} \cdot n\_LD_{MC} = L\_LD_{MC}eff \cdot n\_LD_{MC}eff = 10000$ dropping off with 1/r on a disk with radius R_{MC}. The branching of the lateral dendrites was taken into account by adding three rings of synaptic densities that also dropped off with 1/r, with an inner radius at the average position of branch points b_1, b_2, b_3, and with outer radius R_{MC} (**Figures 3A,B**; Eq. 1). In our model, there was just one additional branchpoint per lateral dendrite for every further ring (**Figure 2A**), yielding a total number of 15 branchpoints (in line with type I MCs in Orona et al., 1984).

$$
\begin{aligned}
n(r) &= \textstyle\sum_{i=0} n_i(r) \\
n_i(r) &= 0 \quad \text{for} \quad r < b_i \\
n_i(r) &= n_0(r) \quad \text{for } b_i < r < R_{MC} \\
\text{with} \qquad n_0(r) &= \frac{N_o}{R_{MC}} \cdot \frac{1}{2\pi r} \\
\text{and} \quad N_o \text{ such that } &\textstyle\int_0^{R_{MC}} n(r) \cdot 2\pi r \, dr \\
&= N_{synMC}
\end{aligned}
\tag{2}
$$

The synaptic density needs to satisfy the condition that its integral is equal to the total number of dendrodendritic synapses per MC; the factor N_0 must be chosen accordingly. The soma and apical dendrite also bear reciprocal synapses with GCs, albeit possibly at a reduced density in comparison to the lateral dendrites (Price and Powell, 1970a; see also Benson et al., 1984; Naritsuka et al., 2009). To account for these synapses and to avoid singularities, we used a constant density value around the MC soma that corresponds to the synaptic density n(r) at 10 μm. Finally, n(r) was smoothed with a Gaussian function with width $\sigma = 40$ μm (**Figure 3B**).

To assemble an ensemble of MC lateral dendrites belonging to the same glomerular column $n_{GL}(r)$, we distributed the $N_{MC\_GL} = 10$ MCs per glomerulus according to the distribution of "sister mitral cells" (Buonviso et al., 1991), with a mean average distance of ∼50 μm and a total radius of 200 μm (9 cells placed at distances ±10, ±30, ±50, −70, +90, −110 μm from a first central cell, **Figure 5A**). Similar distributions have also been observed in more recent research (Kikuta et al., 2013; Schwarz et al., 2018).

Assumption 4: The Granule Cells-Mediated Anatomical Connectivity Between Individual Glomerular Ensembles Is Spatially Isotropic

While detailed anatomical data on this issue are not available as of yet (since their quantification would require large-scale electron microscopy and reconstruction), currently available evidence indicates that dedicated dendrodendritic connections between certain glomeruli seem unlikely to play a major role in MC-GC connectivity: MCs and yet more so glomerular MC ensembles have radially symmetric dendritic fields as described above, probably to maximize the spatial range of the glomerular input/output. Using a multi-electrode stimulation device, we also consistently observed that a given GC can be excited (and even fired) from several adjacent glomeruli both in rats and mice (Stroh et al., 2012; Chatterjee et al., 2016; Lukas et al., 2018), in line with results based on optogenetic activation (Burton and Urban, 2015). Thus, a given GC is likely to belong to more than one glomerular column, again arguing against specific connectivities.

Yet, this assumption may be a major simplification; for example, structural and synaptic plasticity (Chatterjee et al., 2016; Huang et al., 2016; Sailor et al., 2016) may result in specifically enhanced connectivity between glomerular ensembles belonging to relevant odor representations (e.g., behaviorally relevant odors that were chosen for a discrimination task or odors of a newly discovered type of food source in the wild). In any case, as outlined in the introduction, isotropic anatomical connectivity would allow for maximal flexibility with regard to the binding of co-active columns.

Assumption 5: There Is Just One Reciprocal Synaptic Contact per Coupled Granule Cell–Mitral Cell Pair

This assumption relies both on the previous assumption (no preferred targets) and morphological evidence: Since a given GC dendritic branch was so far not found to contact the same MC branch two times (Woolf et al., 1991; see also Pressler and Strowbridge, 2017) and because of the geometric arrangement of cells, with GC dendrites oriented perpendicularly to the MC dendrites, it appears unlikely that a given GC will contact the same MC more than one time, except for GCs very close to the MC soma. This assumption is further supported by our estimate (**Figure 3D**): the probability for one contact P_1 between any GC-MC pair that is within reach of each other is fairly low (on the order of <0.1 for GCs whose dendritic fields do not overlap with the MC soma where the density of MC synapses is highest). The probability for two contacts between the same MC-GC pair, P_2, is then in first approximation equal to $(P_1)^2$, i.e., on the order of $<10^{-2}$.

However, if we applied this stochastic view to the contacts between a GC and a glomerular ensemble of MCs, the probability

that a proximal GC will contact the ensemble more than one time would be rather high and would need to be corrected for if the number of connected GCs is of interest. In particular, if a GC was situated right below the glomerulus, P_{1_10} was close to 1; thus, in this case, the chance for multiple contacts was also very high. We accounted for the possibility of multiple contacts between a GC and a glomerular ensemble of MCs by a binomial correction [subtracting the probabilities for double and triple contacts from the probability for at least one contact by the same cell, which is $1-(1-P_1)^{10}$, with the probability for no contact at all being $(1-P_1)^{10}$].

Connectivity Between a Mitral Cell and a Granule Cell Depending on Their Distance

To estimate the connectivity between two mitral cells A and B, we first calculated the number of synapses of MC A that a GC at a certain position r_A within the dendritic field of cell A can "see" in its own dendritic field D, N_A. This function can be approximated rather well by integrating the density of mitral cell synapses $n_A(r)$ over the radius of a GC's dendritic arbor, at the known distance between the GC and the mitral cell A, r_A, which itself is in the first approximation

$$N_A(r_A) = \int n_A(r)\ dD \approx n_A(r_A) \cdot \pi \cdot R_{GC}^2 \tag{3}$$

We did this for all possible GC positions, which yielded the function $N_A(r_A)$ as shown in **Figure 3D**. Now $N_B(r)$ can be calculated from $N_A(r)$ using the geometric relationship between r_A and r_B shown in **Figure 4A**, which depends on the distance between A and B, d_{AB}, and the angle α of the GC position relative to d_{AB}.

$$N_B(r_A) = N_A(r_B) \tag{4}$$

$$r_B = \sqrt{d_{AB}^2 - 2d_{AB}x + x^2 \cdot \left(1+\tan^2\alpha\right)} \tag{5}$$

The probability that the GC at position r_A is connected to MC A, $P_A(r_A)$, is the number of available MC synapses N_A times the number of the GC's spines (i.e., the chances for the GC to make a contact) divided by the number of all the GC spines of all GCs within the dendritic field D (i.e., the partner synapses of all GCs available for A). Equation 6 is a first approximation that relies on our Assumption 5, i.e. that there is just one reciprocal synaptic contact per coupled GC-MC pair. Note that the number of reciprocal spines per GC N_{recGC} was canceled.

$$\begin{aligned} P_A &= \frac{N_A \cdot N_{recGC}}{N_{recGC} \cdot n_{GC} \cdot \pi \cdot r_{GC}^2} \Rightarrow \\ P_A(r_A) &= \frac{N_A(r_A)}{n_{GC} \cdot \pi \cdot r_{GC}^2} \end{aligned} \tag{6}$$

P_A is shown in **Figure 3D**, along with the functional inhibitory impact I_A (Williams and Stuart, 2003) of the GC at position r_A on the somatic voltage of MC A. Because of the attenuation of the IPSP with distance, factored in as the normalized IPSP nIPSP(r) (**Figure 2C**), inhibition originating from more distal GCs is reduced accordingly:

$$I_A(r_A) = P_A(r_A) \cdot \mathrm{nIPSP}(r_A) \tag{7}$$

P_A and I_A can be related to the arrangement of glomeruli above, showing that there is high connectivity/impact within the first to the second surrounding ring of glomeruli and a rather constant connectivity and decaying impact further out. The glomeruli were scaled in order to fit onto $A_{EPL} \approx 20\ \mathrm{mm}^2$ (4000 glomeruli in rat ⇒ area per glomerulus ≈ 5000 $\mu\mathrm{m}^2$, resulting in an effective glomerular diameter of ≈ 70 μm).

Connectivity Between Two Mitral Cells and/or Glomerular Ensembles of Mitral Cells *via* Granule Cells Depending on Their Distance

The probability that a certain GC at position r_A in the overlap area F will be connected to both A and B is the product of the individual probabilities for connections to A and B (**Figure 4B**):

$$P_{AB}(r_A) = P_A(r_A) \cdot P_B(r_A) \overset{\text{Eq. 4}}{=} P_A(r_A) \cdot P_A(r_B) \tag{8}$$

The inhibitory impact I_{AB} of such an MC-GC-MC connection can be estimated by replacing either P_A or P_B with its impact (Eq. 7), since the spreading IPSP within the lateral dendrite of the receiving MC is attenuated, whereas the conduction of the action potential along the lateral dendrite of the excited MC is not much affected by attenuation (e.g., Lowe, 2002; Xiong and Chen, 2002; Djurisic et al., 2004; **Figure 4C**).

Finally, to obtain the number of all GCs in F that will be connected to both A and B, we integrated the product of P_{AB} and the density of GCs within the overlap area F.

$$\begin{aligned} N_{AB}(d_{AB}) &= \int n_{GC} \cdot P_{AB}(r,\alpha)\, dF \\ &= 2 \cdot n_{GC} \int_{d_{AB}/2}^{R_{MC}} \overline{P_{AB}(r)} \frac{dF}{dr} dr \\ F(r) &= r_{MC}^2 \arccos\left(\frac{r}{R_{MC}}\right) - r\sqrt{R_{MC}^2 - r^2} \Rightarrow dF \\ &= -2\sqrt{r_{MC}^2 - r^2}\, dr \end{aligned} \tag{9}$$

Since $P_{AB}(r)$ was not fixed within an increment of the integration dF (see **Figure 4A**) but depended on the angle α, its mean value within dF should to be calculated beforehand:

$$\begin{aligned} \overline{P_{AB}(r)} &= \frac{\int_0^{\alpha\_\max} P_{AB}(r,\alpha)\, d\alpha}{\alpha\_\max} \\ P_{AB}(r,\alpha) &= \frac{N_A(r_A) \cdot N_A(r_B)}{n_{GC}^2 \cdot \pi^2 \cdot R_{GC}^4} \\ &\text{with } r_A = \frac{r}{\cos\alpha},\ r_B \text{ from Eq. 4} \\ \alpha\_\max &= \arccos\left(\frac{r}{R_{MC}}\right) \end{aligned} \tag{10}$$

The result for the set of parameters in **Table 1** is shown in **Figures 5B,C**. The relation to the glomerular map

above is indicated by vertical lines, with glomeruli sized as in **Figure 3D**. There are three regimes: Connectivity is the highest for connections between MCs within the same home glomerulus 0 and/or the first ring of adjacent glomeruli and then drops off rather quickly, with another decline at the border of the regime where the MC somata are farther apart than the effective dendritic field span, $d_{AB} > R_{MC} = 850\ \mu m$. This second drop is explained by the lost overlap between the proximal somatic regions with their high synaptic density and the lateral dendrites of the other MC, respectively.

Next, we calculated the connectivities for either single MCs and a glomerular MC ensemble or between two entire glomerular ensembles. Glomerular MC ensembles are better captured by our mean-field approach than individual MCs since the synaptic density of a glomerular ensemble of MC lateral dendrites would be smoother and better resemble the assumed isotropic density n(r) (Assumption 3). However, a correction for multiple contacts between a given GC and the MC ensemble should be introduced (Assumption 5). To calculate the number of GCs that connect 2 glomerular ensembles Y and Z within the MC-GC network, we assembled the synaptic density of a glomerular ensemble from a set of $N_{MC\_GL} = 10$ MCs based on the reported distributions of sister MCs, which were substantially broader than a glomerular diameter, on the order of 200 μm (Buonviso et al., 1991; Ke et al., 2013; Kikuta et al., 2013; Schwarz et al., 2018; Assumption 3). Therefore, the synaptic density distribution $n_{GL}(r)$ was considerably broadened in comparison to the density n(r) of a single MC (**Figure 5A**).

While the resulting numbers of connecting GCs (**Figure 5C** top left) may appear high at first glance, they are not implausible. If, for example, we looked at the maximal number of GCs that could provide intraglomerular inhibition across the MCs within a glomerular ensemble (≈50.000 GCs), these would constitute roughly 25% of the entire set of GCs within the dendritic field of the glomerulus' MCs ($n_{GC} \cdot \pi \cdot (R_{MC} + 100\ \mu m)^2 \approx 210.000$ GCs). **Figure 5C** also shows the connectivity between a single MC and an MC glomerular ensemble.

We found that, for glomerular MC ensembles instead of single MCs, the observed connectivity regimes were substantially broadened. Now the steep initial drop to 50% was extending well into the fourth ring of glomeruli. The switch to the intermediate regime was far less pronounced than for the single MC case. This intermediate region ranged from the fourth ring to at least the eleventh, where connectivity might still be sufficient to excite GCs *via* all the MCs that belong to MC A's glomerular ensemble and thus could potentially mediate lateral inhibition (but see Section "Discussion").

However, this broadening is reduced if we took into account the reduced inhibitory impact of more distant GCs due to the attenuation of IPSPs, as shown in **Figure 5D**. As stated above, the attenuation was accounted for by multiplying P_{AB}, i.e., the integrand in Eq. 10, with the normalized distance-dependence of the IPSP, nIPSP(r) (from **Figure 2D**). Now the regime of high impact between two MC ensembles was narrowed to three rings of glomeruli and the impact beyond these three rings was also substantially reduced in comparison to the purely anatomical model.

Robustness of Results

Our anatomical estimate is fairly robust with respect to parameter variations (**Table 1**). Only changes in parameters that determine the areas of integration (R_{MC}, R_{GC}) also change the shape of the connectivity function. All other parameter changes solely affect its scaling.

As to the combination of the anatomical connectivity estimate with our results from compartmental modeling, we also tested for variations in the degree of attenuation/effective space constant, since this parameter is not well established experimentally (see Section "Discussion") and influences the inhibitory impact by more distal synapses. **Figure 5D** (bottom) shows the result of modifying the linear slope of the normalized attenuation from **Figure 2D** by a factor of 0.75 (shallower) and 1.25 (steeper). The second modification can be interpreted to account for the reduced dendritic length in our model since a synapse that is located at 800 μm in the model is located at 1100 μm in the real morphology. These modifications affected the inhibitory impact across interconnected glomeruli more substantially than the impact between single MCs, but overall, their effect was rather weak.

DISCUSSION

Ever since the 1980s, detailed quantitative anatomical studies of the vertebrate olfactory system have contributed to our knowledge of the underpinnings of neural networks in the olfactory bulb, and by now, many parameters that contribute to GC-MC connectivity are well characterized. Yet, while our general approach is based on substantial experimental evidence, both anatomical and functional, there are still many assumptions on insufficiently well-known parameters, so our results are to be interpreted with a grain of salt and should certainly not be taken as precise predictions.

Functional Implications for Inhibition Originating From Granule Cell Reciprocal Spines

One lesser-known property is electrotonic conduction within MC lateral dendrites. So far, investigations of passive spread have been mostly restricted to the MC apical dendrite. Lowe (2002) characterized lateral dendritic inhibitory inputs using flash photolysis of GABA with high spatial resolution at distances up to 150 μm and obtained somewhat ambiguous results. Investigation of more distal inputs, direct dendritic recordings, or voltage-sensitive dye imaging of passive conduction in lateral dendrites has not been performed yet. While it is by now safe to assume that active conduction in lateral dendrites works almost as well as in the apical dendrite, the passive properties, in particular the passive space constant, remain poorly characterized. Still, in line with earlier studies (McIntyre and Cleland, 2016), our simulations predict a substantial attenuation of distal IPSPs.

Our simulations based on experimental data show that even for proximal inputs the size of a unitary IPSP originating from a GC spine is <0.05 mV, i.e., below the noise threshold at the MC soma (e.g., noise $\sigma = 0.11$ mV at $V_{rest} = -60$ mV, Diba et al., 2004), and thus is unlikely to exert any influence on MC spiking at all. However, in the case of recurrent inhibition, it has to be considered that there will be the release of GABA from ∼ 200 GC spine inputs per lateral dendrite: there are up to 10,000 reciprocal spines per MC of which up to 15% will release GABA, according to the experimentally established reciprocal release probability P_r (**Figure 1D**). This population response will summate (**Figure 2**) and thereby can substantially hyperpolarize the MC soma. Still, this GC-mediated hyperpolarization is unlikely to prevent MC spiking (e.g., Fukunaga et al., 2014) because it cannot prevent the glomerular MC spike (Chen et al., 2002) from depolarizing the MC soma beyond the threshold of voltage-gated sodium channels. Nevertheless, the summated IPSP can delay spiking and thus possibly infer synchronization of MCs, as also pointed out earlier (e.g., Schoppa, 2006; McTavish et al., 2012; McIntyre and Cleland, 2016). Such synchronization in the gamma-beta range in turn is likely to promote the binding of odor representations across the olfactory bulb and/or to enable transmission of stimulus features other than identity to the piriform cortex (e.g., Kashiwadani et al., 1999; Doucette et al., 2011; Dalal and Haddad, 2022).

GCs are known to also establish dendrosomatic contacts with MCs (Price and Powell, 1970a; Benson et al., 1984; Naritsuka et al., 2009; Pressler and Strowbridge, 2017). For type S GCs, it has been observed that these contacts are housed in spines much larger than the usual gemmule (Naritsuka et al., 2009), thus the functional impact of these synapses might also be more substantial than what we predicted here. Thus, the detectable spontaneous IPSPs recorded from MCs elsewhere and also by us (e.g., Desmaisons et al., 1999; Egger et al., 2005) might originate either from EPL interneurons, dendrosomatic (GC) inputs and/or synchronous release of GABA from several GCs.

Summation/integration of inhibitory inputs has received little attention so far but should follow similar rules as the passive integration of excitatory inputs. We predict substantial shunting effects to occur during recurrent inhibition, resulting in a saturation of the amplitude with an increasing number of activated synapses that happens well below the limitation by the decreasing driving force and thus is related to shunting. The effect of shunting on MC AP timing and its ensuing ability to mediate synchronization of MCs has been explored in a previous simulation (David et al., 2008).

Anatomical Connectivity

Our connectivity model is based on a statistical mean-field approach that projects all synaptic contacts into two dimensions and provides an analytical solution for averaged morphologies (Egger and Urban, 2006). While this approach might overly simplify interactions between individual MCs, it is likely to cover interactions between and within glomerular ensembles of MCs fairly well. Other recent studies used three-dimensional approaches (Migliore et al., 2014; Kersen et al., 2022) with realistic MC morphologies, also restricted to the MC-GC subnetwork, to generate reduced OB network models. Because of the reduced numbers of cells and different connectivity rules, their network connectivity measures are difficult to compare with our results, which are based on the inclusion of the entire MC-GC OB network. The Kersen et al. (2022) model found that, for a pair of MCs, the number of shared GCs and lateral inhibition (in terms of a reduction of MC firing rate) dropped off less rapidly with distance, reaching 50% at 200–300 μm distance (rather than at 100 μm), but then there was no intermediate regime of connectivity/impact. As to experimentally established connectivities, pairwise MC-GC connections have been notoriously difficult to investigate, even though the detection of MTC inputs activated by glomerular stimulation is unproblematic (e.g., Schoppa and Westbrook, 1999; Egger et al., 2005, etc.). In a heroic slice study, MC-GC connectivity of GCs positioned vertically below MCs was found to be well below the values predicted by our model (Pressler and Strowbridge, 2017, 3–5% compared to our >10%; 4% in Kato et al., 2013). Several factors might contribute here: MCs are mostly contacted by deep GCs which are more likely to be damaged during slicing, as well as part of the lateral dendrites of any MC. Moreover, our mean-field approach might systematically overestimate connectivity, at least between single cells.

Anatomical Versus Functional Lateral Connectivity

Specific GC-mediated lateral connectivity (rather than isotropic) might exist and be subject to learning (e.g., Fantana et al., 2008; Huang et al., 2016); in any case, the isotropic substrate used here as a first approximation serves to facilitate such experience-dependent changes, which may affect not so much the anatomical network but the functional lateral connectivity emerging from it, which underlies several additional influences. First, electrotonic attenuation within the lateral MC dendrites will strongly reduce inputs from the more distal parts of the lateral dendrite, even though the space constant of these dendrites is rather large. We included this attenuation in our estimate of inhibitory impact. Second, the propagation of APs in MC lateral dendrites is very likely dynamically regulated: later APs in a burst might propagate not as far into the lateral dendrite as early APs because of recurrent inhibition (Egger and Urban, 2006). Third, asynchronous unitary release from GCs will broaden the response (Chen et al., 2000; Lage-Rupprecht et al., 2020; Ona Jodar et al., 2020). Lastly, activation of GCs beyond their threshold for lateral signaling requires more than one input to the GC, depends on the activity of both interconnected MCs, and might also occur in a delayed manner (Arevian et al., 2008; Giridhar and Urban, 2012; Burton and Urban, 2015; Lage-Rupprecht et al., 2020; Mueller and Egger, 2020). Thus, the functional or effective connectivity will vary dynamically.

The small size of unitary inputs and their substantial attenuation along the lateral dendrite make it unlikely that distal

GC spine inputs activated *via* lateral excitation from other MCs will exert a substantial influence on somatic spike timing (see also McIntyre and Cleland, 2016), since these lateral inputs are unlikely to occur in similarly high numbers and temporal coincidence compared to recurrent inhibition. However, they can be expected to involve coordinated inhibitory inputs from GC glomerular ensembles associated with coactive columns (Egger and Kuner, 2021) and might shape recurrent output from the involved sets of GCs in a manner that indeed allows influencing MC temporal coding (McTavish et al., 2012).

Apparently, the overall structure of our connectivity estimate is reproduced fairly well by a reported measurement of lateral inhibition by Christie et al. (2001, their Figure 4). These data were obtained by recording IPSCs at MC and TC somata in acute brain slices in response to a glomerular stimulation electrode that was gradually stepped away from the glomerular region above the recorded cell. IPSC amplitude data were normalized to the IPSC amplitude in response to stimulation of the cell's "home glomerulus." This setting corresponds to the connectivity between a single MC and a glomerular ensemble (green lines in **Figures 5C,D**), even though a substantial amount of connections is removed within brain slices. *In vivo*, Peace et al. (BioRxiv 2017) used optogenetic glomerular activation, observing substantial lateral excitation of GCs even at 500 μm away and also far-ranging lateral inhibition of MCs. In other *in vivo* data sets, lateral inhibition was reported as strongest rather close to the home glomerulus and as occurring in a non-isotropic manner (Ezeh et al., 1993; Luo and Katz, 2001; Lehmann et al., 2016). In all such studies, however, the aforementioned EPL interneurons together with glomerular layer circuits are likely to dominate the recorded lateral MC inhibition because of the activity-dependence of GC-mediated lateral inhibition.

Outlook

Previous findings indicate the existence of rather isolated functional glomerular column-like ensembles of GCs (Kauer and Cinelli, 1993; Willhite et al., 2006), which might form in an activity-dependent manner based on an isotropic substrate (Kim et al., 2011). Such ensembles may provide specific connectivity between populations of related MCs and TCs in different glomeruli. In our view, specific functional connectivity between coactive glomerular columns could emerge based on a coincidence detection mechanism that involves presynaptic NMDA receptors within the GC spine's presynaptic active zone (Lage-Rupprecht et al., 2020); such connectivity might indeed be enhanced by learning, reconciling the existing divergent notions on patchy versus continuous olfactory mapping.

Since lateral inhibition is activity-dependent and thus unlikely to happen without recurrent inhibition, the main effect of lateral inhibition will be to amplify recurrent inhibition from the sets of GC spines belonging to mother GCs that are part of coactive glomerular columns. Therefore, these GCs fire global or dendritic spikes that also invade the spines (Egger and Kuner, 2021). How exactly this amplification is enacted will be the subject of future computational and experimental investigations. Certainly, it will increase the probability for GABA release, but by how much and during which time window after an MC AP? There are already experimental hints on the short-term plasticity of MC inputs to GCs (Dietz and Murthy, 2005; Chatterjee et al., 2016; Pressler and Strowbridge, 2017) and on the summation of Ca^{2+} entry into GC spines upon coincident local and global activation (Aghvami et al., 2019; Mueller and Egger, 2020). This question is also highly important in the context of repetitive MC firing during a theta-gamma burst – how are recurrent and possibly lateral release probability modified over time within a succession of MC spikes? Finally, how are the massive excitatory centrifugal cortical inputs onto GCs (e.g., Matsutani, 2010; Markopoulos et al., 2012) integrated with recurrent and lateral inhibition?

Extensions of our approach could be used to model TC subnetworks (Mori et al., 1983; Orona et al., 1983). In addition, the input from axon collaterals from MCs and various TC subtypes that are known to also terminate on GCs could also be accounted for. These types of inputs are highly likely to provide strong excitation and thus contribute to the formation of columnar GC ensembles (Pressler and Strowbridge, 2020); more detailed knowledge of these connections is required to estimate the number of GCs belonging to a glomerular ensemble (**Figure 1A**) that can be excited from a glomerulus beyond the (local) spiking threshold. Here, it would also be advisable to explore the effect of such inputs within the respective subnetworks of MCs and TCs, since their axonal collaterals within the bulb have different projection patterns (e.g., Kishi et al., 1984; Lodovichi et al., 2003; Hirata et al., 2019; Lukas et al., 2019; Sun et al., 2020).

Another interesting option might be to explore the impact of adult neurogenesis (Altman, 1969, recent review Tufo et al., 2022) on the bulbar network, depending on the percentage of exchanged GCs. Late newborn GCs are preferentially deep GCs (Lemasson et al., 2005) and may thus preferentially synapse onto MCs rather than TCs (Mori et al., 1983; Orona et al., 1983), influencing the MC subnetwork. We presume that the value of the synapse density on lateral dendrites n_LD_{MC} for juvenile rats observed here might increase later because of the overall doubling of GC numbers in rats in the course of development (Richard et al., 2010). Conversely, such an increase in contacts might be balanced by a reduction in release probability and other plastic adaptations.

DATA AVAILABILITY STATEMENT

The original contributions presented in this study are included in the article/supplementary material, further inquiries can be directed to the corresponding author.

ETHICS STATEMENT

According to German animal ethics legislature, experiments in acute brain slices do not require approval by an ethics committee.

Other rules apply (e.g., proof of qualification of the involved researchers for brain slice preparations has to be provided to the institutional veterinarians). For this study, brain slices were taken from ongoing experiments for Chatterjee et al. (2016).

AUTHOR CONTRIBUTIONS

VE conceived the study, constructed the anatomical network model, and wrote the manuscript. SA performed the functional simulations. YK contributed to the histochemical part of the study. All authors contributed to manuscript revision and read and approved the submitted version.

FUNDING

This work was supported by DFG (SFB 870, SPP 1392, and SPP2205) and BMBF/FKZ GQ 01GQ1502 to VE.

ACKNOWLEDGMENTS

We wish to thank N. Urban and S. Chandra and the reviewers of earlier manuscripts for comments and valuable suggestions, H. Ellrich for anatomical analysis, and M. Hines and J. Ashcroft for ongoing advice with regard to simulations.

REFERENCES

Aghvami, S. S., Muller, M., Araabi, B. N., and Egger, V. (2019). Coincidence detection within the excitable rat olfactory bulb granule cell spines. *J. Neurosci.* 39, 584–595. doi: 10.1523/JNEUROSCI.1798-18.2018

Allison, A. C. (1953). The morphology of the olfactory system in the vertebrates. *Biol. Rev. Camb. Philos. Soc.* 28, 195–244.

Altman, J. (1969). Autoradiographic and histological studies of postnatal neurogenesis. IV. Cell proliferation and migration in the anterior forebrain, with special reference to persisting neurogenesis in the olfactory bulb. *J. Comp. Neurol.* 137, 433–457. doi: 10.1002/cne.901370404

Arevian, A. C., Kapoor, V., and Urban, N. N. (2008). Activity-dependent gating of lateral inhibition in the mouse olfactory bulb. *Nat. Neurosci.* 11, 80–87. doi: 10.1038/nn2030

Arnson, H. A., and Strowbridge, B. W. (2017). Spatial structure of synchronized inhibition in the olfactory bulb. *J. Neurosci.* 37, 10468–10480. doi: 10.1523/JNEUROSCI.1004-17.2017

Bartel, D. L., Rela, L., Hsieh, L., and Greer, C. A. (2015). Dendrodendritic synapses in the mouse olfactory bulb external plexiform layer. *J. Comp. Neurol.* 523, 1145–1161. doi: 10.1002/cne.23714

Benson, T. E., Ryugo, D. K., and Hinds, J. W. (1984). Effects of sensory deprivation on the developing mouse olfactory system: a light and electron microscopic, morphometric analysis. *J. Neurosci.* 4, 638–653. doi: 10.1523/JNEUROSCI.04-03-00638.1984

Buonviso, N., Chaput, M. A., and Scott, J. W. (1991). Mitral cell-to-glomerulus connectivity: an HRP study of the orientation of mitral cell apical dendrites. *J. Comp. Neurol.* 307, 57–64. doi: 10.1002/cne.903070106

Burton, S. D. (2017). Inhibitory circuits of the mammalian main olfactory bulb. *J. Neurophysiol.* 118, 2034–2051. doi: 10.1152/jn.00109.2017

Burton, S. D., and Urban, N. N. (2015). Rapid feedforward inhibition and asynchronous excitation regulate granule cell activity in the mammalian main olfactory bulb. *J. Neurosci.* 35, 14103–14122. doi: 10.1523/jneurosci.0746-15.2015

Bywalez, W. G., Patirniche, D., Rupprecht, V., Stemmler, M., Herz, Andreas, V. M., et al. (2015). Local postsynaptic voltage-gated sodium channel activation in dendritic spines of olfactory bulb granule cells. *Neuron* 85, 590–601.

Chatterjee, M., Perez de los Cobos Pallares, F., Loebel, A., Lukas, M., and Egger, V. (2016). Sniff-like patterned input results in long-term plasticity at the rat olfactory bulb mitral and tufted cell to granule cell synapse. *Neural Plast.* 2016:9124986. doi: 10.1155/2016/9124986

Chen, W. R., Shen, G. Y., Shepherd, G. M., Hines, M. L., and Midtgaard, J. (2002). Multiple modes of action potential initiation and propagation in mitral cell primary dendrite. *J. Neurophysiol.* 88, 2755–2764.

Chen, W. R., Xiong, W., and Shepherd, G. M. (2000). Analysis of relations between NMDA receptors and GABA release at olfactory bulb reciprocal synapses. *Neuron* 25, 625–633. doi: 10.1016/s0896-6273(00)81065-x

Christie, J. M., Schoppa, N. E., and Westbrook, G. L. (2001). Tufted cell dendrodendritic inhibition in the olfactory bulb is dependent on NMDA receptor activity. *J. Neurophysiol.* 85, 169–173. doi: 10.1152/jn.2001.85.1.169

Dalal, T., and Haddad, R. (2022). Upstream gamma-synchronization enhances odor processing in downstream neurons. *Cell Rep.* 39:110693. doi: 10.1016/j.celrep.2022.110693

David, F., Linster, C., and Cleland, T. A. (2008). Lateral dendritic shunt inhibition can regularize mitral cell spike patterning. *J. Comput. Neurosci.* 25, 25–38. doi: 10.1007/s10827-007-0063-5

Davison, A. P., Feng, J., and Brown, D. (2003). Dendrodendritic inhibition and simulated odor responses in a detailed olfactory bulb network model. *J. Neurophysiol.* 90, 1921–1935. doi: 10.1152/jn.00623.2002

Debarbieux, F., Audinat, E., and Charpak, S. (2003). Action potential propagation in dendrites of rat mitral cells in vivo. *J. Neurosci.* 23, 5553–5560. doi: 10.1523/JNEUROSCI.23-13-05553.2003

Desmaisons, D., Vincent, J. D., and Lledo, P. M. (1999). Control of action potential timing by intrinsic subthreshold oscillations in olfactory bulb output neurons. *J. Neurosci.* 19, 10727–10737. doi: 10.1523/JNEUROSCI.19-24-10727.1999

Destexhe, A. (1998). Spike-and-wave oscillations based on the properties of GABAB receptors. *J. Neurosci.* 18, 9099–9111. doi: 10.1523/JNEUROSCI.18-21-09099.1998

Diba, K., Lester, H. A., and Koch, C. (2004). Intrinsic noise in cultured hippocampal neurons: experiment and modeling. *J. Neurosci.* 24, 9723–9733. doi: 10.1523/JNEUROSCI.1721-04.2004

Dietz, S. B., and Murthy, V. N. (2005). Contrasting short-term plasticity at two sides of the mitral-granule reciprocal synapse in the mammalian olfactory bulb. *J. Physiol.* 569, 475–488. doi: 10.1113/jphysiol.2005.095844

Djurisic, M., Antic, S., Chen, W. R., and Zecevic, D. (2004). Voltage imaging from dendrites of mitral cells: EPSP attenuation and spike trigger zones. *J. Neurosci.* 24, 6703–6714. doi: 10.1523/JNEUROSCI.0307-04.2004

Doucette, W., Gire, D. H., Whitesell, J., Carmean, V., Lucero, M. T., and Restrepo, D. (2011). Associative cortex features in the first olfactory brain relay station. *Neuron* 69, 1176–1187. doi: 10.1016/j.neuron.2011.02.024

Economo, M. N., Hansen, K. R., and Wachowiak, M. (2016). Control of mitral/tufted cell output by selective inhibition among olfactory bulb glomeruli. *Neuron* 91, 397–411. doi: 10.1016/j.neuron.2016.06.001

Egger, V., and Kuner, T. (2021). Olfactory bulb granule cells: specialized to link coactive glomerular columns for percept generation and discrimination of odors. *Cell Tissue Res.* 383, 495–506. doi: 10.1007/s00441-020-03402-7

Egger, V., and Urban, N. N. (2006). Dynamic connectivity in the mitral cell-granule cell microcircuit. *Semin. Cell Dev. Biol.* 17, 424–432. doi: 10.1016/j.semcdb.2006.04.006

Egger, V., Svoboda, K., and Mainen, Z. F. (2003). Mechanisms of lateral inhibition in the olfactory bulb: Efficiency and modulation of spike-evoked calcium influx into granule cells. *J. Neurosci.* 23, 7551–7558. doi: 10.1523/JNEUROSCI.23-20-07551.2003

Egger, V., Svoboda, K., and Mainen, Z. F. (2005). Dendrodendritic synaptic signals in olfactory bulb granule cells: local spine boost and global low-threshold spike. *J. Neurosci.* 25, 3521–3530. doi: 10.1523/JNEUROSCI.4746-04.2005

Ezeh, P. I., Wellis, D. P., and Scott, J. W. (1993). Organization of inhibition in the rat olfactory bulb external plexiform layer. *J. Neurophysiol.* 70, 263–274. doi: 10.1152/jn.1993.70.1.263

Fantana, A. L., Soucy, E. R., and Meister, M. (2008). Rat olfactory bulb mitral cells receive sparse glomerular inputs. *Neuron* 59, 802–814. doi: 10.1016/j.neuron.2008.07.039

Fukunaga, I., Berning, M., Kollo, M., Schmaltz, A., and Schaefer, A. T. (2012). Two distinct channels of olfactory bulb output. *Neuron* 75, 320–329. doi: 10.1016/j.neuron.2012.05.017

Fukunaga, I., Herb, J. T., Kollo, M., Boyden, E. S., and Schaefer, A. T. (2014). Independent control of gamma and theta activity by distinct interneuron networks in the olfactory bulb. *Nat. Neurosci.* 17, 1208–1216. doi: 10.1038/nn.3760

Geramita, M. A., Burton, S. D., and Urban, N. N. (2016). Distinct lateral inhibitory circuits drive parallel processing of sensory information in the mammalian olfactory bulb. *eLife* 5:e16039. doi: 10.7554/eLife.16039

Geramita, M., and Urban, N. N. (2017). Differences in glomerular-layer-mediated feedforward inhibition onto mitral and tufted cells lead to distinct modes of intensity coding. *J. Neurosci.* 37, 1428–1438. doi: 10.1523/JNEUROSCI.2245-16.2016

Giridhar, S., and Urban, N. N. (2012). Mechanisms and benefits of granule cell latency coding in the mouse olfactory bulb. *Front. Neural Circuits* 6:40. doi: 10.3389/fncir.2012.00040

Hamilton, K. A., Heinbockel, T., Ennis, M., Szabo, G., Erdelyi, F., and Hayar, A. (2005). Properties of external plexiform layer interneurons in mouse olfactory bulb slices. *Neuroscience* 133, 819–829. doi: 10.1016/j.neuroscience.2005.03.008

Hines, M. L., Davison, A. P., and Muller, E. (2009). NEURON and python. *Front. Neuroinform* 3:1. doi: 10.3389/neuro.11.001.2009

Hirata, T., Shioi, G., Abe, T., Kiyonari, H., Kato, S., Kobayashi, K., et al. (2019). A novel birthdate-labeling method reveals segregated parallel projections of mitral and external tufted cells in the main olfactory system. *eNeuro* 6, doi: 10.1523/ENEURO.0234-19.2019

Huang, L., Garcia, I., Jen, H.-I., and Arenkiel, B. R. (2013). Reciprocal connectivity between mitral cells and external plexiform layer interneurons in the mouse olfactory bulb. *Front. Neural Circuits* 7:32. doi: 10.3389/fncir.2013.00032

Huang, L., Ung, K., Garcia, I., Quast, K. B., Cordiner, K., Saggau, P., et al. (2016). Task learning promotes plasticity of interneuron connectivity maps in the olfactory bulb. *J. Neurosci.* 36, 8856–8871. doi: 10.1523/JNEUROSCI.0794-16.2016

Imamura, F., Ito, A., and LaFever, B. J. (2020). Subpopulations of projection neurons in the olfactory bulb. *Front. Neural Circuits* 14:561822. doi: 10.3389/fncir.2020.561822

Karube, F., Kubota, Y., and Kawaguchi, Y. (2004). Axon branching and synaptic bouton phenotypes in GABAergic nonpyramidal cell subtypes. *J. Neurosci.* 24, 2853–2865. doi: 10.1523/JNEUROSCI.4814-03.2004

Kashiwadani, H., Sasaki, Y. F., Uchida, N., and Mori, K. (1999). Synchronized oscillatory discharges of mitral/tufted cells with different molecular receptive ranges in the rabbit olfactory bulb. *J. Neurophysiol.* 82, 1786–1792. doi: 10.1152/jn.1999.82.4.1786

Kato, H. K., Gillet, S. N., Peters, A. J., Isaacson, J. S., and Komiyama, T. (2013). Parvalbumin-expressing interneurons linearly control olfactory bulb output. *Neuron* 80, 1218–1231. doi: 10.1016/j.neuron.2013.08.036

Kauer, J. S., and Cinelli, A. R. (1993). Are there structural and functional modules in the vertebrate olfactory bulb? *Microsc. Res. Tech.* 24, 157–167. doi: 10.1002/jemt.1070240207

Ke, M.-T., Fujimoto, S., and Imai, T. (2013). SeeDB: a simple and morphology-preserving optical clearing agent for neuronal circuit reconstruction. *Nat. Neurosci.* 16, 1154–1161. doi: 10.1038/nn.3447

Kersen, D. E. C., Tavoni, G., and Balasubramanian, V. (2022). Connectivity and dynamics in the olfactory bulb. *PLoS Comput. Biol.* 18:e1009856. doi: 10.1371/journal.pcbi.1009856

Kikuta, S., Fletcher, M. L., Homma, R., Yamasoba, T., and Nagayama, S. (2013). Odorant response properties of individual neurons in an olfactory glomerular module. *Neuron* 77, 1122–1135. doi: 10.1016/j.neuron.2013.01.022

Kim, D. H., Chang, A. Y., McTavish, T. S., Patel, H. K., and Willhite, D. C. (2012). Center-surround vs. distance-independent lateral connectivity in the olfactory bulb. *Front. Neural Circuits* 6:34. doi: 10.3389/fncir.2012.00034

Kim, D. H., Phillips, M. E., Chang, A. Y., Patel, H. K., Nguyen, K. T., and Willhite, D. C. (2011). Lateral connectivity in the olfactory bulb is sparse and segregated. *Front. Neural Circuits* 5:5. doi: 10.3389/fncir.2011.00005

Kishi, K., Mori, K., and Ojima, H. (1984). Distribution of local axon collaterals of mitral, displaced mitral, and tufted cells in the rabbit olfactory bulb. *J. Comp. Neurol.* 225, 511–526. doi: 10.1002/cne.902250404

Kosaka, T., and Kosaka, K. (2008). Heterogeneity of parvalbumin-containing neurons in the mouse main olfactory bulb, with special reference to short-axon cells and beta IV-spectrin positive dendritic segments. *Neurosci. Res.* 60, 56–72. doi: 10.1016/j.neures.2007.09.008

Lage-Rupprecht, V., Zhou, L., Bianchini, G., Aghvami, S. S., Mueller, M., Rozsa, B., et al. (2020). Presynaptic NMDARs cooperate with local spikes toward GABA release from the reciprocal olfactory bulb granule cell spine. *Elife* 9:e63737. doi: 10.7554/eLife.63737

Lehmann, A., D'Errico, A., Vogel, M., and Spors, H. (2016). Spatio-temporal characteristics of inhibition mapped by optical stimulation in mouse olfactory bulb. *Front. Neural Circuits* 10:15. doi: 10.3389/fncir.2016.00015

Lemasson, M., Saghatelyan, A., Olivo-Marin, J. C., and Lledo, P. M. (2005). Neonatal and adult neurogenesis provide two distinct populations of newborn neurons to the mouse olfactory bulb. *J. Neurosci.* 25, 6816–6825. doi: 10.1523/JNEUROSCI.1114-05.2005

Lepousez, G., Csaba, Z., Bernard, V., Loudes, C., Videau, C., Lacombe, J., et al. (2010). Somatostatin interneurons delineate the inner part of the external plexiform layer in the mouse main olfactory bulb. *J. Comp. Neurol.* 518, 1976–1994. doi: 10.1002/cne.22317

Li, G., and Cleland, T. A. (2013). A two-layer biophysical model of cholinergic neuromodulation in olfactory bulb. *J. Neurosci.* 33, 3037–3058. doi: 10.1523/JNEUROSCI.2831-12.2013

Liu, A., Savya, S., and Urban, N. N. (2016). Early odorant exposure increases the number of mitral and tufted cells associated with a single glomerulus. *J. Neurosci.* 36:11646. doi: 10.1523/JNEUROSCI.0654-16.2016

Liu, G., Froudarakis, E., Patel, J. M., Kochukov, M. Y., Pekarek, B., Hunt, P. J., et al. (2019). Target specific functions of EPL interneurons in olfactory circuits. *Nat. Commun.* 10:3369. doi: 10.1038/s41467-019-11354-y

Lodovichi, C., Belluscio, L., and Katz, L. C. (2003). Functional topography of connections linking mirror-symmetric maps in the mouse olfactory bulb. *Neuron* 38, 265–276. doi: 10.1016/s0896-6273(03)00194-6

Lowe, G. (2002). Inhibition of backpropagating action potentials in mitral cell secondary dendrites. *J. Neurophysiol.* 88, 64–85. doi: 10.1152/jn.2002.88.1.64

Lukas, M., Holthoff, K., and Egger, V. (2018). Long-term plasticity at the mitral and tufted cell to granule cell synapse of the olfactory bulb investigated with a custom multielectrode in acute brain slice preparations. *Methods Mol. Biol.* 1820, 157–167. doi: 10.1007/978-1-4939-8609-5_13

Lukas, M., Suyama, H., and Egger, V. (2019). Vasopressin cells in the rodent olfactory bulb resemble non-bursting superficial tufted cells and are primarily inhibited upon olfactory nerve stimulation. *eNeuro* 6, doi: 10.1523/ENEURO.0431-18.2019

Luo, M., and Katz, L. C. (2001). Response correlation maps of neurons in the mammalian olfactory bulb. *Neuron* 32, 1165–1179. doi: 10.1016/s0896-6273(01)00537-2

Markopoulos, F., Rokni, D., Gire, D. H., and Murthy, V. N. (2012). Functional properties of cortical feedback projections to the olfactory bulb. *Neuron* 76, 1175–1188. doi: 10.1016/j.neuron.2012.10.028

Matsuno, T., Kiyokage, E., and Toida, K. (2017). Synaptic distribution of individually labeled mitral cells in the external plexiform layer of the mouse olfactory bulb. *J. Comp. Neurol.* 525, 1633–1648. doi: 10.1002/cne.24148

Matsutani, S. (2010). Trajectory and terminal distribution of single centrifugal axons from olfactory cortical areas in the rat olfactory bulb. *Neuroscience* 169, 436–448. doi: 10.1016/j.neuroscience.2010.05.001

McIntyre, A. B., and Cleland, T. A. (2016). Biophysical constraints on lateral inhibition in the olfactory bulb. *J. Neurophysiol.* 115, 2937–2949. doi: 10.1152/jn.00671.2015

McTavish, T. S., Migliore, M., Shepherd, G. M., and Hines, M. L. (2012). Mitral cell spike synchrony modulated by dendrodendritic synapse location. *Front. Comput. Neurosci.* 6:3. doi: 10.3389/fncom.2012.00003

Meisami, E., and Safari, L. (1981). A quantitative study of the effects of early unilateral olfactory deprivation on the number and distribution of mitral and tufted cells and of glomeruli in the rat olfactory bulb. *Brain Res.* 221, 81–107. doi: 10.1016/0006-8993(81)91065-9

Migliore, M., and Shepherd, G. M. (2008). Dendritic action potentials connect distributed dendrodendritic microcircuits. *J. Comput. Neurosci.* 24, 207–221. doi: 10.1007/s10827-007-0051-9

Migliore, M., Cavarretta, F., Hines, M. L., and Shepherd, G. M. (2014). Distributed organization of a brain microcircuit analyzed by three-dimensional modeling: the olfactory bulb. *Front. Comput. Neurosci.* 8:50. doi: 10.3389/fncom.2014.00050

Miyamichi, K., Shlomai-Fuchs, Y., Shu, M., Weissbourd, B. C., Luo, L., and Mizrahi, A. (2013). Dissecting local circuits: parvalbumin interneurons underlie broad feedback control of olfactory bulb output. *Neuron* 80, 1232–1245. doi: 10.1016/j.neuron.2013.08.027

Mori, K. (1987). Membrane and synaptic properties of identified neurons in the olfactory bulb. *Prog. Neurobiol.* 29, 275–320. doi: 10.1016/0301-0082(87)90024-4

Mori, K., Kishi, K., and Ojima, H. (1983). Distribution of dendrites of mitral, displaced mitral, tufted, and granule cells in the rabbit olfactory bulb. *J. Comp. Neurol.* 219, 339–355. doi: 10.1002/cne.902190308

Mueller, M., and Egger, V. (2020). Dendritic integration in olfactory bulb granule cells upon simultaneous multispine activation: low thresholds for nonlocal spiking activity. *PLoS Biol.* 18:e3000873. doi: 10.1371/journal.pbio.3000873

Nagayama, S., Takahashi, Y. K., Yoshihara, Y., and Mori, K. (2004). Mitral and tufted cells differ in the decoding manner of odor maps in the rat olfactory bulb. *J. Neurophysiol.* 91, 2532–2540. doi: 10.1152/jn.01266.2003

Naritsuka, H., Sakai, K., Hashikawa, T., Mori, K., and Yamaguchi, M. (2009). Perisomatic-targeting granule cells in the mouse olfactory bulb. *J. Comp. Neurol.* 515, 409–426. doi: 10.1002/cne.22063

Ona Jodar, T., Lage-Rupprecht, V., Abraham, N. M., Rose, C. R., and Egger, V. (2020). Local postsynaptic signaling on slow time scales in reciprocal olfactory bulb granule cell spines matches asynchronous release. *Front. Synaptic Neurosci.* 12:551691. doi: 10.3389/fnsyn.2020.551691

Orona, E., Rainer, E. C., and Scott, J. W. (1984). Dendritic and axonal organization of mitral and tufted cells in the rat olfactory bulb. *J. Comp. Neurol.* 226, 346–356. doi: 10.1002/cne.902260305

Orona, E., Scott, J. W., and Rainer, E. C. (1983). Different granule cell populations innervate superficial and deep regions of the external plexiform layer in rat olfactory bulb. *J. Comp. Neurol.* 217, 227–237. doi: 10.1002/cne.902170209

Panzanelli, P., Fritschy, J. M., Yanagawa, Y., Obata, K., and Sassoe-Pognetto, M. (2007). GABAergic phenotype of periglomerular cells in the rodent olfactory bulb. *J. Comp. Neurol.* 502, 990–1002. doi: 10.1002/cne.21356

Parrish-Aungst, S., Shipley, M. T., Erdelyi, F., Szabo, G., and Puche, A. C. (2007). Quantitative analysis of neuronal diversity in the mouse olfactory bulb. *J. Comp. Neurol.* 501, 825–836. doi: 10.1002/cne.21205

Peace, S. T., Johnson, B. C., Li, G., Kaiser, M. E., Fukunaga, I., Schaefer, A. T., et al. (2017). Coherent olfactory bulb gamma oscillations arise from coupling independent columnar oscillators *bioRxiv* 213827. doi: 10.1101/213827

Pressler, R. T., and Strowbridge, B. W. (2017). Direct recording of dendrodendritic excitation in the olfactory bulb: divergent properties of local and external glutamatergic inputs govern synaptic integration in granule cells. *J. Neurosci.* 37, 11774–11788. doi: 10.1523/JNEUROSCI.2033-17.2017

Pressler, R. T., and Strowbridge, B. W. (2020). Activation of granule cell interneurons by two divergent local circuit pathways in the rat olfactory bulb. *J. Neurosci.* 40, 9710–9714. doi: 10.1523/JNEUROSCI.0989-20.2020

Price, J. L., and Powell, T. P. (1970a). The mitral and short axon cells of the olfactory bulb. *J. Cell Sci.* 7, 631–651. doi: 10.1242/jcs.7.3.631

Price, J. L., and Powell, T. P. (1970b). The morphology of the granule cells of the olfactory bulb. *J. Cell Sci.* 7, 91–123.

Richard, M. B., Taylor, S. R., and Greer, C. A. (2010). Age-induced disruption of selective olfactory bulb synaptic circuits. *Proc. Natl. Acad. Sci. U.S.A.* 107, 15613–15618. doi: 10.1073/pnas.1007931107

Royet, J. P., Jourdan, F., Ploye, H., and Souchier, C. (1989). Morphometric modifications associated with early sensory experience in the rat olfactory bulb: II. Stereological study of the population of olfactory glomeruli. *J. Comp. Neurol.* 289, 594–609. doi: 10.1002/cne.902890406

Sailor, K. A., Valley, M. T., Wiechert, M. T., Riecke, H., Sun, G. J., Adams, W., et al. (2016). Persistent structural plasticity optimizes sensory information processing in the olfactory bulb. *Neuron* 91, 384–396. doi: 10.1016/j.neuron.2016.06.004

Schoppa, N. E. (2006). Synchronization of olfactory bulb mitral cells by precisely timed inhibitory inputs. *Neuron* 49, 271–283. doi: 10.1016/j.neuron.2005.11.038

Schoppa, N. E., and Westbrook, G. L. (1999). Regulation of synaptic timing in the olfactory bulb by an A-type potassium current. *Nat. Neurosci.* 2, 1106–1113. doi: 10.1038/16033

Schwarz, D., Kollo, M., Bosch, C., Feinauer, C., Whiteley, I., Margrie, T. W., et al. (2018). Architecture of a mammalian glomerular domain revealed by novel volume electroporation using nanoengineered microelectrodes. *Nat. Commun.* 9:183. doi: 10.1038/s41467-017-02560-7

Shepherd, G. M., and Greer, C. A. (2004). "Olfactory bulb," in *The Synaptic Organization of the Brain*, 3rd Edn, ed. G. M. Shepherd (New York, NY: Oxford University Press), 133–169.

Shmuel, R., Secundo, L., and Haddad, R. (2019). Strong, weak and neuron type dependent lateral inhibition in the olfactory bulb. *Sci. Rep.* 9, 1602–1602. doi: 10.1038/s41598-018-38151-9

Sosulski, D. L., Bloom, M. L., Cutforth, T., Axel, R., and Datta, S. R. (2011). Distinct representations of olfactory information in different cortical centres. *Nature* 472, 213–216. doi: 10.1038/nature09868

Soucy, E. R., Albeanu, D. F., Fantana, A. L., Murthy, V. N., and Meister, M. (2009). Precision and diversity in an odor map on the olfactory bulb. *Nat. Neurosci.* 12, 210–220. doi: 10.1038/nn.2262

Stroh, O., Freichel, M., Kretz, O., Birnbaumer, L., Hartmann, J., and Egger, V. (2012). NMDA-receptor dependent synaptic activation of TRPC channels in olfactory bulb granule cells. *J. Neurosci.* 32, 5737–5746. doi: 10.1523/JNEUROSCI.3753-11.2012

Struble, R. G., Beckman, S. L., Fesser, E., and Nathan, B. P. (2001). Volumetric and horseradish peroxidase tracing analysis of rat olfactory bulb following reversible olfactory nerve lesions. *Chem. Senses* 26, 971–981. doi: 10.1093/chemse/26.8.971

Sun, X., Liu, X., Starr, E. R., and Liu, S. (2020). CCKergic tufted cells differentially drive two anatomically segregated inhibitory circuits in the mouse olfactory bulb. *J. Neurosci.* 40, 6189–6206. doi: 10.1523/JNEUROSCI.0769-20.2020

Toida, K., Kosaka, K., Heizmann, C. W., and Kosaka, T. (1994). Synaptic contacts between mitral/tufted cells and GABAergic neurons containing calcium-binding protein parvalbumin in the rat olfactory bulb, with special reference to reciprocal synapses between them. *Brain Res.* 650, 347–352. doi: 10.1016/0006-8993(94)91804-x

Tran-Van-Minh, A., Cazé, R. D., Abrahamsson, T., Cathala, L., Gutkin, B. S., and DiGregorio, D. A. (2015). Contribution of sublinear and supralinear dendritic integration to neuronal computations. *Front. Cell. Neurosci.* 9:67. doi: 10.3389/fncel.2015.00067

Tufo, C., Poopalasundaram, S., Dorrego-Rivas, A., Ford, M. C., Graham, A., and Grubb, M. S. (2022). Development of the mammalian main olfactory bulb. *Development* 149:dev200210. doi: 10.1242/dev.200210

Vida, I., Bartos, M., and Jonas, P. (2006). Shunting inhibition improves robustness of gamma oscillations in hippocampal interneuron networks by homogenizing firing rates. *Neuron* 49, 107–117. doi: 10.1016/j.neuron.2005.11.036

Willhite, D. C., Nguyen, K. T., Masurkar, A. V., Greer, C. A., Shepherd, G. M., and Chen, W. R. (2006). Viral tracing identifies distributed columnar organization in the olfactory bulb. *Proc. Natl. Acad. Sci. U.S.A.* 103, 12592–12597. doi: 10.1073/pnas.0602032103

Williams, S. R., and Stuart, G. J. (2003). Voltage- and site-dependent control of the somatic impact of dendritic IPSPs. *J. Neurosci.* 23, 7358–7367. doi: 10.1523/JNEUROSCI.23-19-07358.2003

Woolf, T. B., Shepherd, G. M., and Greer, C. A. (1991). Serial reconstructions of granule cell spines in the mammalian olfactory bulb. *Synapse* 7, 181–192. doi: 10.1002/syn.890070303

Xiong, W., and Chen, W. R. (2002). Dynamic gating of spike propagation in the mitral cell lateral dendrites. *Neuron* 34, 115–126. doi: 10.1016/s0896-6273(02)00628-1

Yokoi, M., Mori, K., and Nakanishi, S. (1995). Refinement of odor molecule tuning by dendrodendritic synaptic inhibition in the olfactory bulb. *Proc. Natl. Acad. Sci. U.S.A.* 92, 3371–3375. doi: 10.1073/pnas.92.8.3371

Zeppilli, S., Ackels, T., Attey, R., Klimpert, N., Ritola, K. D., Boeing, S., et al. (2021). Molecular characterization of projection neuron subtypes in the mouse olfactory bulb. *Elife* 10:e65445. doi: 10.7554/eLife.65445

Conflict of Interest: The authors declare that the research was conducted in the absence of any commercial or financial relationships that could be construed as a potential conflict of interest.

Advantages of publishing in Frontiers

OPEN ACCESS
Articles are free to read for greatest visibility and readership

FAST PUBLICATION
Around 90 days from submission to decision

HIGH QUALITY PEER-REVIEW
Rigorous, collaborative, and constructive peer-review

TRANSPARENT PEER-REVIEW
Editors and reviewers acknowledged by name on published articles

Frontiers
Avenue du Tribunal-Fédéral 34
1005 Lausanne | Switzerland

Visit us: www.frontiersin.org
Contact us: frontiersin.org/about/contact

REPRODUCIBILITY OF RESEARCH
Support open data and methods to enhance research reproducibility

DIGITAL PUBLISHING
Articles designed for optimal readership across devices

FOLLOW US
@frontiersin

IMPACT METRICS
Advanced article metrics track visibility across digital media

EXTENSIVE PROMOTION
Marketing and promotion of impactful research

LOOP RESEARCH NETWORK
Our network increases your article's readership